

DISSERTATION

Employing Symmetry in Dynamics and Motion Control of Robotic Mechanisms

Ausgeführt zum Zwecke der Erlangung des akademischen Grades eines Doktors der technischen Wissenschaften (Dr. techn.)

unter der Leitung von

Univ.Prof. Dr.-Ing. Dipl.-Ing. Christian Ott (Betreuung)
Univ.-Prof. Dipl.-Ing. Dr. techn. Andreas Kugi (Zweitbetreuung)
E376

Institut für Automatisierungs- und Regelungstechnik

eingereicht an der Technischen Universität Wien Fakultät für Elektrotechnik und Informationstechnik

von

Hrishik Mishra Matrikelnummer: 12046005

Wien, May 14, 2025

Studiendekan: Univ.Prof. Dr.sc. Silvan Schmid

Betreuer: Univ.Prof. Dr.-Ing. Dipl.-Ing. Christian Ott

Zweitbetreuer: Univ.-Prof. Dipl.-Ing. Dr. techn. Andreas Kugi

Tag des Rigorosums: 26.06.2025

Prüfungsvorsitzender:

Erster Gutachter: Prof. Dr. Kristin Y. Pettersen

Zweiter Gutachter: Univ.Prof. Dr.-Ing. Wolfgang Kemmetmüller

DEDICATION

 $To\ my\ siblings\ who\ taught\ without\ speaking...$



Preface

This thesis is based on my research activity within the horizontal of *space robotics* and the vertical of *motion control of floating-base robots* in the Institute of Robotics and Mechatronics at the German Aerospace Center (DLR). The institute has innovated a myriad of advanced robotic systems and tools for control prototyping, and serves as a crucible for several state-of-the-art robotics projects within European Union (EU), especially Germany.

I am grateful to my mentor Prof. Christian Ott for providing his guidance and supervision. During this research, he provided well-educated inputs to the many theoretical problems I was faced with. Although the inputs were not always an immediate solution, they illuminated the path that eventually led me to it. For this education, I am deeply thankful to him. I am also grateful to Prof. Andreas Kugi, who appreciated my interest in the geometry of motion, and accepted my doctoral candidacy under his supervision at TU Wien. In the same vein, I am also thankful to the Prof. Alin Albu-Schäfer who is one of the greatest scientific minds in present day robotics. His novel ideas on topology and geometric mechanics have inspired my efforts in determining the flavour of this thesis.

I am thankful to the DLR On-Orbit Servicing Simulator (OOS-SIM) team: Dr. Roberto Lampariello, Dr. Marco De Stefano, Dr. Ribin Balachandran, Bernhard Brunner, Martin Stelzer, who have contributed towards developing the state-of-the-art robotic facility, not only in terms of scientific methods, but also the software framework behind it. I am indebted to the intellectual discussions with Fabian Beck, whose deep understanding of the geometry of motion invigourated new ideas. I am thankful to the other team members of Newton: Jongseok Lee, Dr. Ribin Balachandran, Dr. Konstantin Kondak, Dr. Marco De Stefano, who inspired pertinent action to bring deep-tech robotics for space to the domain of industrial maintenance. I thank the upper management involved in space robotics at the institute, who have actively promoted my research in the proposals and results of several international projects.

Science without engineering is philosophy, and through the research activity in this thesis, I was able to witness both work in harmony towards the common goal of bringing out novelty and creativity in robotics. I was fortunate for being a part of an endeavour that encouraged equal focus on theory and practice.

I express my gratitude towards my parents: Mr. Manoranjan Mishra and Mrs. Manjushree Mishra, who have always inspired me to pursue my goals despite the challenges they might have faced due to them. I thank my grandfather, Mr. Netrananda Mishra, who not only set the example of reading books to learn, but he also taught me to set boundaries on knowledge to gain wisdom. I am indebted to my close friends, who have acted as my family, advisers and critics to teach me the philosophy of the hammer.

Munich, Germany, May 14, 2025

Place, Date

Hrishik Mishra

Full Name

Kurzzusammenfassung

Land, Meer, Luft und Raum – In all diesen Bereichen sind robotische Mechanismen im Dienst des menschlichen Strebens. Darunter haben frei schwebende Roboter, wie z.B. Orbitalroboter oder Humanoiden, in letzter Zeit an Bedeutung gewonnen, aufgrund ihrer Mobilität. Diese mobilen Mechanismen sind einzigartig durch den Erhalt des Momentes, wenn die Schwerkraftwirkung entfernt wird. Diese Eigenschaft folgt aus der Einhaltung der kinetischen Energie des Mechanismus unabhängig von seinem räumlichen Standort, wie von Noethers Theorem dargestellt wird. Ein solches System ist ein Euler-Lagrange-System mit Symmetrie (Invarianz), auch gennant ein Lagrange-Poincaré-System. Bei solchen mobilen Mechanismen sind die frei schwebende Basis und der Gelenkmechanismus mit Sensoren und Aktoren ausgestattet, die auf unterschiedlichen Grundprinzipien beruhen. Dies beeinträchtigt die Steuerungsleistung, falls traditionelle Methoden angewendet werden, die Symmetrie ignorieren. Dasselbe gilt für die Simulation ihrer Dynamik ohne Berücksichtigung der Symmetrie, was bei kritischen Anwendungen, wie etwa der Bodensimulation von Orbitalrobotermissionen zur Validierung vor dem Start, nachteilig sein kann. Doch selbst bei Robotermechanismen ohne inhärente Symmetrie erscheint diese notwendig, wenn eine hierarchische Aufgabenausführung für Ganzkörperbewegungen erforderlich ist. Dies bedeutet, dass die Bewegung zur Erfüllung der sekundären Aufgabe eine Symmetrie der primären Aufgabe sein sollte. Trotz der Vielfalt ihrer Erscheinungsformen fehlt eine gemeinsame, auf Symmetrie basierende Theorie, die Dynamik und Steuerungssynthese für diese Klasse von Problemen in der Robotik vereinheitlicht.

Um dies zu erreichen, leistet diese Dissertation, wie der Titel andeutet, Beiträge zur Nutzung der Lagrangian-Symmetrie für die Dynamik und Bewegungskontrolle von robotischen Mechanismen. Für einen freischwebender-Roboter wird eine neue Berechnung seiner Lagrange-Poincaré-Dynamik bereitgestellt, die vorteilhafte Eigenschaften für die Bewegungs-kontrolle aufdeckt. Unter Verwendung

dieser Berechnung werden neue geometrische Aspekte seiner Bewegung offenbart. Die Struktur der vorgeschlagenen Dynamik wird ausgenutzt, um ein Hardware-inthe-Loop-Simulationsrahmen für Orbitalroboter zu entwickeln. Der vorgeschlagene Rahmen erfordert weniger Sensoren als der Stand der Technik und skaliert gemäß den Entwicklungsphasen der Mission. Letzteres ist auf die implizite Substrukturierung der Lagrange-Poincaré-Dynamik zurückzuführen. Die Symmetrie in der Lagrange-Poincaré-Dynamik wird ausgenutzt, um ein Steuerungsrahmen zu entwickeln, der die oben genannten Probleme, die aus der hybriden Sensorik und Aktuation eines freischweibende-Roboters entstehen, adressiert. Dieser Steuerungsrahmen nutzt das innere Modell der Dynamik und minimalistische Sensorik, um eine vollständige Bewegungsstabilisierung zu erreichen, während er in unsicheren Umgebungen kontaktbewusst ist. Um eine hierarchische Bewegungssteuerung in robotischen Mechanismen ohne inhärente Symmetrie zu erreichen, werden zwei Steuerungsansätze vorgeschlagen zur Synthese von künstlicher Symmetrie. Dies ermöglicht die Nutzung der Steuerungssynthese für Lagrange-Poincaré-Systeme, wie bei den freischweibende-Robotermechanismen. Daher bietet diese Dissertation eine vereinte Theorie basierend auf der Symmetrie für die oben genannten Klassen von Problemen in Bezug auf Dynamik und Bewegungssteuerung in der Robotik. Die Methoden werden an den Stand der Technik-Robotersystemen validiert und in mehreren Fachzeitschriften und Konferenzen veröffentlicht. Die Anwendbarkeit der Arbeit aus dieser Dissertation wird durch ihren Nutzen in mehreren Projekten belegt, die von KUKA AG, EU, ESA und NASA gefördert wurden, und ist ebenfalls berichtet.

Wenn man die Gleichheit zweier Zahlen a und b beweist, indem man zuerst zeigt, dass a ≤ b und dann, dass a ≥ b, ist das unfair: Man sollte stattdessen zeigen, dass sie wirklich gleich sind, indem man den inneren Grund für ihre Gleichheit aufdeckt. [1, pp. 64].))

Emmy Noether, Weyl's Levels of infinity, 1935

Abstract

Land, sea, air and space - Across all the media, robotic mechanisms are in service of human endeavour. Among them, floating-base robotic mechanisms, e.g., orbital robots, humanoids etc., have recently gained prominence due to their mobility. These mobile mechanisms are uniquely characterized by conservation of momentum if the effect of gravity is removed. This property follows from the invariance of the mechanism's kinetic energy w.r.t. its spatial location, as stated by Noether's theorem. Such a system is an Euler-Lagrange system with symmetry (invariance), or a Lagrange-Poincaré system. For such mobile mechanisms, the floating-base and the articulated mechanism are equipped with sensors and actuators that differ in their underlying principles. This negatively affects control performance while employing traditional methods which disregard its symmetry. Likewise, simulation of its dynamics without considering symmetry can be detrimental in critical applications, e.g., on-ground simulation of orbital robotic missions for validation before launch. Even in robotic mechanisms that do not possess an inherent symmetry, it still appears as a requirement if hierarchical execution of tasks is required for whole-body motion. This means that the motion towards fulfilment of the secondary task should be a symmetry of the primary task. Thus, despite raising its head in many guises, a common theory based on symmetry that unifies the dynamics and control synthesis for this class of problems in robotics is missing.

To this end, as the title suggests, this thesis makes its contributions towards employing Lagrangian symmetry for dynamics and motion control of robotic mechanisms. For a floating-base robotic mechanism, a novel computation of its Lagrange-Poincaré dynamics is provided, which reveals advantageous properties for motion control. Using this computation, new geometric aspects of its motion are revealed. The structure of the proposed dynamics is exploited to design a hardware-in-the-loop simulation framework for orbital robots. The proposed framework has lower sensory requirements than the state-of-the-art and also

scales according to mission development phases due to the implicit substructuring of the Lagrange-Poincaré dynamics. The symmetry in Lagrange-Poincaré dynamics is exploited to design a control framework that addresses the aforementioned problems arising from the hybrid sensing and actuation of a floating-base robot. This control framework exploits the internal model of the dynamics and uses minimal sensing to achieve full motion stabilization, while being contact-aware in uncertain environments. To achieve hierarchical motion control in robotic mechanisms without any inherent symmetry, two control approaches are proposed to synthesize artificial symmetry. This enables exploiting the control synthesis for Lagrange-Poincaré systems, as for the floating-base robotic mechanisms. Thus, this thesis provides a unified theory based on symmetry for the aforementioned class of problems related to dynamics and motion control in robotics. The methods are validated on state-of-the-art robotic systems and are published in several peer-reviewed conferences and journals. The applicability of the work from this thesis is evidenced by its utility in several projects funded by KUKA AG, EU, ESA and NASA, which are also reported.

If one proves the equality of two numbers a and b by showing first that $a \leq b$ and then that $a \geq b$, it is unfair; one should instead show that they are really equal by disclosing the inner ground for their equality. [1, pp. 64].

Emmy Noether, Weyl's Levels of infinity, 1935

99

Contents

A	crony	yms		$\mathbf{X}\mathbf{V}$
Li	st of	Figur	es x	xii
Li	st of	Table	s xx	xiii
1	Intr	oduct	ion	1
	1.1	Relate	ed Work	3
	1.2	Contr	ibution Overview	7
2	Me	chanic	s of Mechanisms	17
	2.1	Config	guration of Mechanisms	18
	2.2	Lagra	ngian Mechanics	19
	2.3	Symm	netry in \mathcal{EL} Systems	22
		2.3.1	The Metric and its Killing vectors	24
	2.4	Const	rained Motion of Mechanisms	26
		2.4.1	Modeling Constraints	26
		2.4.2	Integral flows of Vertical Subspace	28
		2.4.3	Local Integrability of the Vertical Subspace	29
		2.4.4	Structure Group-(oid) of Vertical Subspace	30
		2.4.5	Constrained \mathcal{EL} Systems: Vertical Subspace	34
		2.4.6	The Horizontal Subspace	36
		2.4.7	Topology of Fiber Bundle and \mathcal{EL} equations	37
		2.4.8	Nonholonomic nature of Constraints	41
	2.5	Mecha	anical Attributes for Motion Control	43
		2.5.1	Impedance/Compliance Control	43
		2.5.2	Passivity in Euler-Lagrange (\mathcal{EL}) systems	44
		2.5.3	Variable Inertia in \mathcal{EL} systems	45

x Contents

	2.6	Computations for Multibody mechanisms		. 4	5
		2.6.1 Rigid-Body Motion		. 40	6
		2.6.2 Recursive Lagrangian Mechanics		. 48	8
		2.6.3 Constraints and Transformations		. 50	0
	2.7	Conclusion		. 52	2
3	Mo	tion of Floating-base Robotic Mechanism (FRM)		53	3
	3.1	Introduction		. 53	3
	3.2	Related Work		. 54	4
	3.3	Key Contributions		. 5	5
	3.4	Dynamics of the Floating-base Robotic Mechanism (FRM)		. 50	6
		3.4.1 Floating-base Dynamics or Hamel's Equations		. 5'	7
		3.4.2 Lagrange-Poincaré (\mathcal{LP}) Equations: The Motivation		. 58	8
		3.4.3 A Geometric View of FRM Motion			1
	3.5	Main Contribution		. 60	6
		3.5.1 Choice of Iterative Computation		. 60	6
		3.5.2 Fundamental Matrices of Locked Inertia		. 60	6
		3.5.3 Proposed form of the Lagrange-Poincaré (\mathcal{LP}) equation	ions	. 68	8
	3.6	Properties of the \mathcal{LP} Equations			2
		3.6.1 Commutativity			2
		3.6.2 Skew-symmetry/Passivity		. 75	2
		3.6.3 SE(3) Transformation of Momentum Dynamics			3
		3.6.4 SE(3) Invariance of Shape Dynamics			4
		3.6.5 Analytical Computation of Curvature		. 74	4
		3.6.6 Nonholonomic locomotion of FRM		. 7	5
		3.6.7 Passive Interconnection of Momentum & Shape			9
	3.7	Generalization of the FRM		. 80	0
		3.7.1 Symmetry-breaking Potential Fields			0
		3.7.2 Potential Fluid Flow		. 83	3
	3.8	Conclusion		. 8	5
4	Mo	tion Substructuring for Validation & Verification (V&	zV)	8'	7
	4.1	Introduction		. 8'	7
		4.1.1 Related Work			7
		4.1.2 Key Contributions		. 88	8
	4.2	V&V-Problem for an Orbital Mechanism			0
		4.2.1 Orbital Mechanism		. 90	0
		4.2.2 Problem Statement			1
	4.3	On-ground Robotic facilities (OGRF)			2
		4.3.1 Fixed-base Manipulator			2
		4.3.2 Vehicle with Simulated Manipulator			3
		4.3.3 Vehicle-Manipulator			4
		4.3.4 Gravity-compensated OGRF			

Contents

	4.4		n Substructuring Approach
		4.4.1	Method of Controlled Lagrangians
	, -	4.4.2	\mathcal{LP} Equations of an Orbital Mechanism
	4.5	_	sed method and Modalities
		4.5.1	Dynamics equivalence
		$\frac{4.5.2}{-}$	Generating Motion for V&V
	4.6	-	imental Validation
		4.6.1	M1-A on KUKA Light Weight Robot 4+ (LWR4+) 107
		4.6.2	M3-B on OOS-SIM
		4.6.3	
	4.7	Concl	usion
5			sed Motion Control of \mathcal{LP} Systems 113
	5.1		luction
		5.1.1	State-of-the-art: Full-state feedback
		5.1.2	State-of-the-art: Output feedback
		5.1.3	Problem Statement: \mathcal{LP} Systems
		5.1.4	Summary of Contributions
	5.2		ling Motion for Control
	5.3	Passiv	rity-Based Control (PBC) Framework
		5.3.1	Potential Shaping
		5.3.2	Structure-Preserving Damping Injection
		5.3.3	Passivity-Based Control (PBC) Design: \mathcal{LP} Systems 124
	5.4	Propo	sed Method: Internal Model-PBC (IM-PBC) 127
		5.4.1	Differential-Geometric Perspective
		5.4.2	Direct Internal Model-PBC (IM-PBC)
		5.4.3	Stability/Passivity Analysis of Direct IM-PBC 132
		5.4.4	Subsystem IM-PBC
		5.4.5	Stability/Passivity Analysis of Subsystem IM-PBC 138
	5.5	Sensor	ry/Model Extension of IM-PBC
			Velocity: Sensing and Models
		5.5.2	Force: Sensing, Models and Estimation
		5.5.3	Integral Action for $Ver(\mathcal{LP})$ in Direct IM-PBC 144
	5.6		ation of the Proposed Methods
		5.6.1	Simulation Results: Subsystem IM-PBC
		5.6.2	Experimental Results: Direct IM-PBC
	5.7		usion
c			
6	6.1		ced Variational Symmetry in Motion Control 159 luction
		6.1.1	Related Work
		6.1.2	Motivating Case
			Key Contributions

xii Contents

	6.2	Preliminaries	162
		6.2.1 Symmetry Generation: Concept	163
	6.3	Task-induced Fiber Bundle	
	6.4	The Horizontal subspace	
		6.4.1 Restriction of the Secondary Task	170
	6.5	\mathcal{EL} equations of Motion on the Fiber Bundle	171
	6.6	Symmetry Generating Controller Design	172
		6.6.1 Shaping the Inertia Metric Tensor	172
		6.6.2 Passive Interconnection of Subsystems	176
		6.6.3 Stabilizing the Shape Space	178
		6.6.4 Stabilizing the Momentum	179
		6.6.5 Symmetry-breaking Potential: I	179
		6.6.6 Symmetry-breaking Potential: II	181
		6.6.7 Relation to Floating-base Mechanics	
	6.7	Validation	
		6.7.1 Symmetry Generation and Shape Regulation	
		6.7.2 Motion Control with Symmetry-breaking Potential	184
	6.8	Conclusion	
7	Тос	sk-induced Algebraic Symmetry in Motion Control	189
1	7.1	Introduction	
	1.1	7.1.1 Related Work	190
		7.1.2 Key Contributions	190
	7.2	Preliminaries	191
	1.2	7.2.1 The considered \mathcal{EL} system	192
		7.2.2 Proportional Action	192
	7.3	\mathcal{EL} Mechanics on Fibered Manifolds	196
	1.5	7.3.1 Task-induced Fiber Bundle	190
		7.3.2 Restriction of the Secondary Task	
		7.3.3 \mathcal{EL} equations of Motion on the Fiber Bundle	
	7.4	Conserved Hamiltonian and Motion Control	
	1.1	7.4.1 Comparison of Force Fields	
		7.4.2 Wandering Equilibrium in the Fiber	
		7.4.3 The Conserved Hamiltonian	
	7.5	Conclusion	
	1.0	Conclusion	210
8		plications	219
	8.1	NASA/DLR/MIT ROAM/Tumbledock: ISS Experiments	
	8.2	V&V Strategy for Orbital Robotics	
		8.2.1 Co-simulation: MIL/SIL/PIL	
		8.2.2 Hardware-in-the-loop (HIL) on OOS-SIM	
	8.3	EU EROSS+: On-orbit Servicing	
		8.3.1 Co-simulation: Initial Analysis	224

xiii

		8.3.2 HIL: Control Prototyping	26
	8.4	V 1 G	$\frac{20}{27}$
	0.4		27 27
			$\frac{21}{30}$
	8.5	9	31
	8.6		33
	8.7	· · · · · · · · · · · · · · · · · · ·	36
	0.1		36
		· / -	40
	8.8	. , ,	42
9	Con	aclusion 24	45
\mathbf{A}	App	pendix 24	49
	A.1	SE(3) Group and Properties	49
			49
		A.1.2 Matrix Representation	50
		A.1.3 Proof in Property 2.3	50
	A.2	Multibody Dynamics	51
			51
		A.2.2 Proof of Lemma 2.14	51
		A.2.3 Proof of Lemma 3.2	52
	A.3	Stokes' Theorem for the FRM	52
		A.3.1 Stokes' Theorem	52
		±	53
	A.4	Derivations in Lemma 3.3	54
			54
			54
	A.5	Computation of LID Matrix: Lemma 3.7 2	55
	A.6	v i	56
		-	56
		i	56
			56
		v	57
		1	57
		A.6.6 Proofs used in Theorem 3.2	57
Bi	bliog	graphy 20	61

Acronyms

- $\mathcal{EL} \ \ \text{Euler-Lagrange. vii, ix, xii, xix, 1, 2, 3, 4, 6, 8, 9, 10, 12, 17, 19, 20, 22, 23, 24, 25, 31, 34, 35, 36, 37, 38, 39, 44, 45, 53, 54, 79, 89, 93, 94, 96, 97, 113, 115, 127, 157, 159, 160, 161, 162, 163, 165, 166, 170, 171, 173, 174, 187, 189, 190, 191, 192, 194, 195, 196, 197, 199, 200, 201, 202, 203, 206, 207, 208, 211, 212, 213, 214, 215, 216, 245, 246, 247$
- \mathcal{EP} Euler-Poincaré. 20, 53, 54, 57, 58, 89, 229, 230
- Lagrange-Poincaré. vii, viii, x, xi, xx, 1, 3, 4, 7, 8, 9, 10, 11, 12, 42, 44, 52, 54, 55, 56, 58, 59, 60, 61, 66, 68, 71, 72, 73, 75, 77, 79, 81, 82, 84, 85, 86, 87, 89, 90, 91, 95, 98, 99, 100, 103, 104, 113, 114, 115, 116, 117, 118, 119, 120, 121, 122, 124, 125, 126, 127, 128, 130, 132, 134, 135, 136, 138, 140, 142, 143, 144, 145, 146, 148, 150, 152, 153, 154, 156, 157, 161, 162, 165, 175, 182, 183, 187, 188, 189, 221, 223, 224, 234, 238, 245, 246, 247
- **BLF** Body-level factorization. 131
- BTC Bilateral Teleoperation Controller. 237, 238, 239
- cBVI corrected Body Velocity Integral. 77, 253
- CC Coriolis/Centrifugal. 6, 7, 11, 22, 54, 55, 56, 58, 59, 60, 61, 66, 68, 69, 70, 71, 72, 73, 74, 79, 84, 85, 90, 92, 94, 95, 96, 97, 101, 102, 120, 121, 131, 154, 160, 161, 164, 171, 181, 187, 190, 194, 200, 202, 208, 209, 230, 247
- CCF Constraint Curvature Function. xxii, 75, 78, 253, 254
- CL Controlled Lagrangian. 2, 4, 99, 159, 160
- **CoM** Center-of-Mass. 61, 62, 63, 82, 83, 231

CPT Continuous Point Transformation. 22, 23, 24, 29, 168, 174

DCV Direction Cosine Vector. 241

DLR German Aerospace Center. iii, 12, 106, 116, 119, 148, 149, 154, 219, 222, 223, 224, 225, 226, 235, 237, 240

DoF Degrees-of-Freedom. 159, 163, 189, 232, 239, 240

EKF Extended Kalman Filter. xiii, 221, 227, 229

EROSS+ European Robotic Orbital Support Services. xii, 224, 225, 227

ESA European Space Agency. viii, 11, 111, 219, 242, 247

EU European Union. iii, viii, xii, 11, 111, 119, 219, 224, 225, 233, 243, 247

FRM Floating-base Robotic Mechanism. x, xiii, xix, xx, xxiii, 2, 3, 4, 5, 6, 7, 8, 10, 11, 17, 19, 24, 26, 30, 38, 40, 41, 42, 52, 53, 54, 55, 56, 57, 58, 59, 60, 61, 62, 63, 64, 65, 66, 67, 68, 69, 70, 72, 73, 74, 75, 76, 77, 78, 79, 80, 81, 82, 83, 84, 85, 86, 88, 89, 90, 94, 95, 98, 100, 113, 114, 115, 116, 117, 118, 119, 120, 121, 122, 123, 124, 125, 127, 128, 132, 134, 135, 136, 138, 139, 140, 141, 142, 143, 144, 145, 146, 148, 149, 150, 151, 152, 153, 154, 155, 156, 157, 160, 161, 176, 182, 187, 223, 224, 226, 227, 228, 230, 231, 236, 237, 238, 239, 243, 245, 246, 247, 252, 253, 254

FTS Force-Torque Sensor. 88, 89, 103, 106, 143, 144, 235, 238

GNC Guidance, Navigation & Control. 149, 222, 223, 229

HIL Hardware-in-the-loop. xii, xiii, xx, xxi, xxiii, 6, 86, 87, 88, 89, 90, 91, 92, 93, 94, 99, 101, 102, 103, 104, 105, 106, 107, 108, 109, 110, 111, 223, 226, 227, 230, 233, 234, 235, 236, 239, 246, 247

ID Inertia Derivative. 45, 163, 164, 183

IM-PBC Internal Model-PBC. xi, xx, 116, 117, 118, 119, 126, 127, 128, 129, 131, 132, 133, 135, 136, 137, 138, 139, 140, 141, 142, 143, 144, 145, 146, 147, 148, 149, 151, 152, 153, 154, 156, 157, 225, 226

IMU Inertial Measurement Unit. 117, 127, 142, 220

ISS International Space Station. xii, 11, 219, 220, 221, 227

IV Inertia Velocity. 45, 163, 164

Acronyms xvii

- LID Locked Inertia Derivative. xiii, 255
- LWR4+ Light Weight Robot 4+. xi, 90, 105, 106, 107, 146, 148, 227, 235
- **MAR** Multi-Arm Robot. xxi, 232, 233, 234
- MPC Minimum Perturbation Coordinate. 77
- **NE** Newton-Euler. 113
- NPS Noether Point Symmetry. 24, 160, 175
- **OBSW** On-board Software. 6, 88, 90, 91, 98, 99, 101, 102, 103, 104, 105, 106, 107, 108, 109, 230, 232
- **OFC** Output Feedback Control. 10, 115, 117, 118, 119, 126, 127, 246
- **OGRF** On-ground Robotic facilities. x, xx, 6, 88, 89, 90, 91, 92, 93, 95, 97, 98, 99, 100, 101, 102, 103, 104, 105, 106, 107, 108, 109, 110, 247
- OOS-SIM On-Orbit Servicing Simulator. iii, xi, xii, xxi, xxii, 106, 107, 116, 117, 118, 119, 148, 149, 154, 223, 225, 226, 227, 230, 231, 235
- **OSP** Output Strict Passivity. 44, 80, 117, 119, 124, 125, 126, 132, 134, 135, 138, 140, 142, 143, 144, 145, 154, 181
- **PBC** Passivity-Based Control. xi, xvi, xx, 2, 4, 7, 9, 10, 52, 114, 117, 118, 119, 121, 123, 124, 125, 127, 128, 136, 149, 159, 188, 190, 191, 195, 207, 209, 217, 232, 233, 245, 246, 247
- **PFB** Principal Fiber Bundle. 17, 21, 38, 39, 40, 59, 160, 161, 174, 176, 179, 182, 184, 187, 246
- **PoE** Product of Exponentials. 29, 31, 32
- **PSC** Partitioned Shared Controller. 237, 238, 239
- SAM Suspended Aerial Manipulator. 237, 239
- **SGC** Symmetry Generating Controller. xii, xx, xxi, 8, 9, 12, 161, 162, 172, 173, 175, 177, 179, 181, 183, 184
- SI Standard Interface. 232, 233, 234, 235
- SVD Singular Value Decomposition. 29, 30, 62, 242
- UAGAS Uniform Almost Global Asymptotic Stability. 119

xviii Acronyms

ZSD Zero-State Detectable. 44

ZSO Zero-State Observable. 44, 136, 178

List of Figures

1.1	Non-Euclidean topology in robotics	4
1.2	Orbital robotics and its V&V	5
1.3	Subject intersection in this thesis	8
1.4	Chapter-wise outline of the thesis	10
2.1	Symmetry: Concept for \mathcal{EL} systems	23
2.2	Killing vectors on a Sphere $Q = \mathbb{S}^2$	25
2.3	Commonly encountered constrained mechanisms	26
2.4	Constrained mechanism as a surjective submersion	27
2.5	Integrability of the vertical subspace (nullspace)	30
2.6	Motion along the nullspace	32
2.7	A fibered bundle in which the fiber is not a homogeneous space	34
2.8	Non-integrability of the horizontal subspace	37
2.9	Step-wise classification of fiber bundles in increasing sophistication.	38
2.10	Floating-base Robotic Mechanism (FRM) with group symmetry	40
2.11	Net displacement of the FRM-base due to a gait	42
2.12	Passive interconnection of subsystems	45
2.13	Articulated robotic mechanisms	46
3.1	Floating-base Robotic Mechanism (FRM) in robotics	54
3.2	Differential-geometric illustration of the FRM configuration space.	60
3.3	Generalized Poinsot's construction for the FRM	65
3.4	A sketch of proof for Theorem 3.2	69
3.5	Nonholonomic locomotion in FRM	76
3.6	Stokes' theorem applied to FRM locomotion	78
3.7	Passive interconnection block diagrams	80
3.8	Generalization of the FRM	83

XX LIST OF FIGURES

4.1	HIL of orbital robotic mission using fixed-base flight prototype	91
4.2	On-ground Robotic facilities (OGRF)	92
4.3	CAESAR manipulator in operation with carrier mechanism	96
4.4	Concept of converse Lagrangian matching	99
4.5	HIL: Orbital mechanism using a fixed-base flight prototype	103
4.6	HIL: Vehicle with impedance causality and simulated manipulator.	104
4.7	HIL: Vehicle-manipulator with impedance causality in vehicle	105
4.8	HIL: Vehicle-manipulator with admittance causality in vehicle	105
4.9	Mission orbital robot and its V&V facility	106
	Comparison between P1 and M1-A HIL methods	108
4.11	HIL using M3-B setup	109
5.1	\mathcal{LP} systems: Mechanisms with group symmetry	114
5.2	Conventional approach vs Anticipatory robotic control paradigm.	116
5.3	Localizer outliers during the ROAM-2 ISS flight experiment	117
5.4	Orbital FRM: Divergence of the localizer in close proximity	117
5.5	Limit cycle due to heterogeneous actuation in FRM	118
5.6	Estimation in \mathcal{LP} system: Differential-geometric illustration	128
5.7	Direct IM-PBC as passive interconnection	132
5.8	Subsystem IM-PBC as passive interconnection	138
5.9	Convergence evidence of Subsystem IM-PBC	147
5.10	Velocity convergence in Subsystem IM-PBC	148
5.11	Experimental setup for validation of direct PBC	149
5.12	FRM-base configuration: measurement vs observer	150
	FRM locked velocity: measurement vs observer	150
5.14	Total actuation for the direct IM-PBC	151
5.15	Disturbance wrench estimation	151
5.16	FRM-base control with integral action	152
5.17	FRM locked velocity control with integral action	152
5.18	Regulation of symmetry-breaking tasks: Positions	153
5.19	Regulation of symmetry-breaking tasks: Orientations	153
5.20	Total actuation for the direct IM-PBC: Integral action	154
5.21	Estimated disturbance wrench: Integral action	154
5.22	FRM-base configuration during interactions	155
5.23	FRM locked velocity during interactions	155
5.24	Total actuation for the direct IM-PBC during interactions	156
5.25	Estimated disturbance wrench during interactions	156
6.1	Symmetry results in reduction of dynamics into shape and group.	161
6.2	Geodesics on \mathbb{S}^2 sphere	173
6.3	Symmetry Generating Controller (SGC): Motion control concept.	176
6.4	Passive interconnection of $Hor(\mathcal{LP})$ and $Ver(\mathcal{LP})$ subsystems	178
6.5	Passive interconnection: primary task, nullspace, secondary task	180
	· · · · · · · · · · · · · · · · · · ·	

LIST OF FIGURES xxi

(6.6	Passive interconnection: primary/secondary/nullspace momenta	182
(5.7	Computation for SGC using robotic libraries	183
6	6.8	Simulation using the ESA MIRROR robot	185
(5.9	Motion characteristics on the total space	185
(5.10	Joint-space SGC: Conserved quantities	186
(5.11	Cartesian space SGC: Conserved quantities	186
(5.12	SGC: Energy function based on Casimir invariant	187
(5.13	Motion characteristics on the fiber space (nullspace)	187
,	7 1	Matter and all and the table and the	190
	7.1	Motion control scenario with desirable symmetry	
	7.2	Motion control scenario for a particle in affine space	193
	7.4	Secondary potential restricted to nullspace of primary	201
	7.5	Force fields: Superposition vs nullspace-projected control	204
	7.6	Time-evolution of the fiber equilibrium	207
	7.7	Time-evolution of the fiber origin and equilibrium.	207
	7.8	Motion Characteristics with the proposed control action	211
	7.9	Time evolution of fiber origin and equilibrium	212
		2D particle orbit: undamped and damped	213
		Fully damped control motion characteristics	214
		Motion with damping in either primary or secondary subspaces	215
		Fiber origin and equilibrium: Damping in primary or secondary.	215
-	(.14	2D particle orbit: Damping in primary or secondary	216
8	3.1	Validation of the Observer: NASA Ames/ISS	220
	3.2	Astrobee controller block diagram.	221
	3.3	ISS experiment results: Astrobee state estimation	222
	3.4	ISS experiment results: Disturbance wrench estimation	222
	3.5	Co-simulation environment for control prototyping	224
	3.6	Momentum conservation on OOS-SIM during capture	225
	3.7	Incremental V&V strategy using co-simulation	226
	3.8	EROSS+: Co-simulation environment for control prototyping	
	3.9	EROSS+ results from Co-simulation environment	227
8	3.10	ESA COMRADE: Motion control using robotic navigation filter	228
		ESA COMRADE: Estimation results for camera and LiDAR	229
8	3.12	ESA COMRADE scenario of robotic capture of ENVISAT	231
		Controller position errors on HIL for ESA COMRADE	231
		ESA MIRROR: Robot morphologies for on-orbit assembly	233
		2-arms Multi-Arm Robot (MAR)-morphology: Walking	233
		2-arms MAR-morphology: Control errors	234
		ORU-BOAS Scenario: Two satellite docking using SIROM	234
		Wrenches during docking.	235
		Reaction wheel motion using centralized free-flying controller	
		Control errors in centralized free-flying controller	

xxii LIST OF FIGURES

8.21	KUKA Innovation Award 2023 scenario: Shared control	237
8.22	Shared control: Experimental validation on OOS-SIM	238
8.23	Control sequence in the shared control experiment	239
8.24	Control errors in configuration	239
8.25	Transparency of proposed shared control approach	240
8.26	Cartesian control of robotic arm with pointing requirement	241
8.27	Controller performance for KUKA Innovation Award 2024	243
9.1	Contributions of the thesis	246
A 1	Constraint Curvature Function surface plots: Stokes' theorem	254

List of Tables

1.1	First author contributions	14
1.2	Patents filed	14
1.3	Collaborative contributions	15
3.1	Comparison of FRM dynamics formulations	85
4.1	Classification of HIL facilities for orbital FRM \ldots	89
8 1	Available Measurements on Orbital Robot	228

CHAPTER 1

Introduction

99

(6 Inertia tells Space how to curve, and curved Space tells Inertia how to move [2].

John A. Wheeler, A Journey into Gravity and Spacetime, 1990

We are the universe trying to understand itself. The question of how it evolves in time and space is answered by our comprehension of the geometry of motion. We have stood on the shoulders of giants like J. Kepler, I. Newton, L. Euler, J.L. Lagrange, W. Hamilton, G. Riemann, S. Lie, F. Klein, E. Cartan, E. Noether, A. Einstein, C. Ehresmann et al. to answer the very fundamental principles of motion. Variational principles naturally arose in the minds of physicists and scientists to explain motion phenomena using a single dynamical quantity called the Lagrangian. Using this, the application of Hamilton's principle leads us to the Euler-Lagrange equations that determine how the state evolves while conserving energy. Noether's theorem and her concept of invariance (symmetry) was instrumental in propelling the modern understanding of mechanics. The concept was elegant and simple: the absence of a position variable in the Lagrangian results in a special structure of the Euler-Lagrange equations that exhibit a conservation law. In this case, the variable is said to be a "symmetry of the Lagrangian", and the resulting Euler-Lagrange systems with symmetry are called Lagrange-Poincaré systems. The higher dimensional motion is quantified by the variations of a lower dimensional shape in the level-sets of conserved momenta. Today, we can unambiguously state that energy conservation is a symmetry in time and momentum conservation is a symmetry in space. In the context of this thesis,

1 Introduction

symmetry refers to the invariance of the Lagrangian of a system w.r.t. motion along certain directions in its configuration space.

In the present day, a large class of contemporary engineering systems, e.g., mechanical systems, are modeled as Euler-Lagrange systems, which are based on variational principles emerging from the definition of energy functions [3]. Our understanding of motion phenomena and its stability has shaped the development of motion control approaches for Euler-Lagrange systems. The ability to steer (control) the state of an Euler-Lagrange system from point A to point B is still considered the first principle of motion control. The works of A. Lyapunov, J.P. LaSalle, N. N. Krasovskii, V. M. Matrosov et al. have cumulatively provided a foundation to ascertain stability of Euler-Lagrange systems using energy, or energy-like functions without analysing the Euler-Lagrange equations directly. Thus, the variational modeling method is one of the most powerful techniques of dynamics because it abstracts the sophisticated Euler-Lagrange system into a single energy function, which aids analysis of stability, dissipative behaviour and interconnection of Euler-Lagrange systems through energy exchange. The generality of this approach is evidenced by its widespread application for electrical, mechanical, eletro-mechanical and robotic systems. In fact, in the robotics domain, where interactions with the environment are a requirement and not a disturbance to be rejected, energetic behavioural control serves as a framework to balance safety, stability and performance.

Humanity's fascination with robotic mechanisms dates back to characters from ancient Greece like Talos: the bronze machine who guarded Crete, and the Indian subcontinent like Bhuta Vahana Yanta: autonomous motion machines that guarded the relics of King Asoka. While the fascination continues to this day through science fiction, robotic mechanisms have emerged as a practical reality to address conveniences and contingencies of human endeavour. For instance, robotic mechanisms have emerged as sophisticated tools to deal with the space debris problem, infrastructure maintenance, large-scale manufacturing etc. The curiosity of the past is the reality of today, and our understanding of motion phenomena and its control enables us to realize a desired behaviour from these mechanisms. In particular, robotic mechanisms are treated as constrained Euler-Lagrange systems and motion control boils down to stabilizing its energetic behaviour in fulfilment of a task. The key idea is to synthesize a desired variational principle by virtue of control actions, e.g., Passivity-Based Control and Controlled Lagrangian, so that the robot moves from point A to point B while minimizing an energy functional.

However, all robotic mechanisms are not created equal. A typical robot mounted to the machine floor in a factory, i.e., fixed-base robotic manipulator, has no discernible symmetry of its Lagrangian (momentum conservation). It possesses homogeneous proprioceptive sensing (e.g., encoders) for motion control. On the other hand, a Floating-base Robotic Mechanism is an articulated mechanism mounted on a movable platform. In contrast to a fixed-base robot, a free

1.1 Related Work

Floating-base Robotic Mechanism exhibits a natural symmetry of its Lagrangian w.r.t. position and orientation of its platform. Thus, it is a Lagrange-Poincaré system and the symmetry implies conservation of its total momentum. Even the nature of sensing and actuation for the platform and the articulated mechanism differ in their underlying physical principles. In particular, while the articulated structure uses proprioceptive sensing like the fixed-base robot, the platform configuration is determined using exteroceptive sensing (e.g., image processing), which is slow-sampled. This negatively affects control performance while employing traditional methods (as in fixed-base robots) which disregard its symmetry. Thus, formulating the motion control in terms of energy functions that employ the underlying symmetry is not only structure-preserving, but also enables exploiting the structure for model-based design. The latter is key to addressing the heterogeneity in sensors and actuators. Before a robotic mechanism is deployed in a remote environment, like a planetary orbit where its momentum is conserved (symmetry), its motion control is required to be validated on-ground (no symmetry) using hardware simulation methods. Simulation of its dynamics without considering symmetry is detrimental to maintaining momentum consistency. Thus, recreating faithfully the symmetry behaviour is of practical relevance, since it directly affects key mission control parameters, e.g., fuel usage. At the same time, even the fixed-base robot is often required to perform a primary task along a task surface while optimizing its configuration as a secondary task without affecting the primary. This means that the motion towards the secondary task should be a symmetry (by requirement) of the primary. Thus, despite being a topic of practical relevance, a common theory based on symmetry that unifies the dynamics and control synthesis for this class of problems in robotics was missing. This is the primary contribution of this thesis.

1.1 Related Work

Motion control in robotics has emerged as a key applied field of geometric mechanics. Naturally, advanced concepts from mechanics drive novel developments in robotics. In robotics, we often deal with constrained mechanisms (through joints) which feature a non-Euclidean geometry of the configuration space. Thus, a robotic mechanism is viewed as a particle in a higher-dimensional curved space, and this makes it a direct descendant of the same mechanics that govern the theory of general relativity, see Fig. 1.1. This link has been explored over the years through textbooks, some of which have focused on theoretical robotics [4–6], while others have been closer to applied robotics [7, 8].

This has led to practical manifestation of theoretical concepts like topology, energetic behaviour and holonomy. Today, there is a rich heritage of Lie group (e.g., SE(3)) theory for motion control [9, 10] and observer design [11, 12], which are encountered frequently in robotics. The energy-based stabilization of Euler-

4 1 Introduction

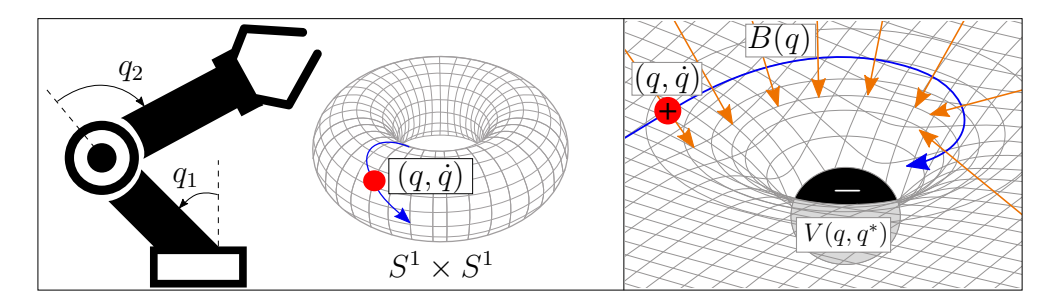


Figure 1.1: Left: A 2-joint robot has a 2-Torus configuration space. Right: Motion (blue) of a particle in an electromagnetic field (scalar potential: V, vector potential: B) in a non-Euclidean space.

Lagrange systems is one of the most powerful techniques, and has been addressed through Passivity-Based Control [3] and Controlled Lagrangian [13] approaches. The motion characteristics of systems with symmetry and constraints are well understood [14], [15], [16]. Through these works, we know that a variational symmetry of any Euler-Lagrange system splits the dynamics into momentum dynamics (which is conserved) and shape variations, which is known as the Lagrange-Poincaré system. In such systems, periodic motions in shape can induce a net displacement in an external (group) configuration variable. This is how astronauts reorient themselves in space and a falling cat lands on its feet. This displacement is achieved by moving the limbs in a periodic fashion to displace the overall body orientation. The displacement is actually the consequence of Stokes' theorem, and is the cornerstone of locomotion of robotic systems [17, 18]. For practical implementation, numerical computations of this displacement and the optimal frame in which the Stokes's law is useful have been proposed [19–21]. In the subcategory of robot dynamics, the equations of motion for serial kinematic chain robotic mechanisms are computed using efficient iterative Newton-Euler algorithms in real-time implementation [22, 23]. The link between the Lagrangian formulation from geometric mechanics and the robotics-based Newton-Euler formulation has been established thoroughly [24]. This lets us write Newton's second law for the robot as a constrained Euler-Lagrange system in a coordinate-invariant manner.

Among such systems, Floating-base Robotic Mechanism is an articulated robotic mechanism mounted on a movable platform, and is ubiquitous in several domains [25–27], as shown in Fig. 3.1. The commonly-known equations of motion for the Floating-base Robotic Mechanism are the inertia-coupled dynamics of its configuration (base and shape) velocities. These dynamics are efficiently computed by considering the Floating-base Robotic Mechanism as a kinematic chain using the standard iterative algorithms [22, 26, 28], [23, §9.4]. However, it is also well known that the Floating-base Robotic Mechanism exhibits the property of conservation of linear and angular momentum [29, 30]. This is simply a

1.1 Related Work 5

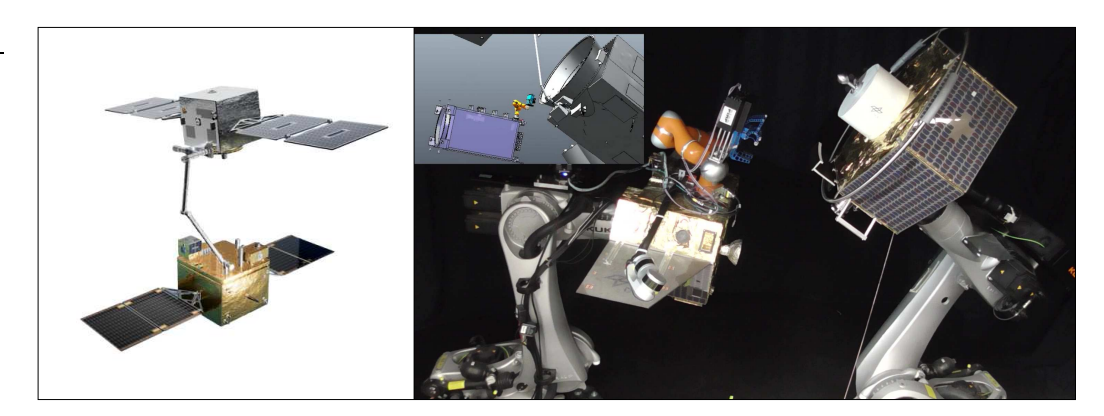


Figure 1.2: Left: Orbital Floating-base Robotic Mechanism in the EROSS IOD scenario [41]. Right: ESA COMRADE [42] mission scenario inset, and Validation & Verification facility in the main picture.

consequence of the symmetry of the Lagrangian w.r.t. the configuration of the base. The Floating-base Robotic Mechanism is further distinguished by its motion characteristics in that a closed path in its shape space (joints) might cause a net displacement of the base, just like a falling cat [31]. The natural habitat of a Floating-base Robotic Mechanism is in a planetary orbit, in the absence of symmetry-breaking potentials, like gravity, although the concept of modeling also applies to other domains, e.g., humanoids [22, 25].

For the Floating-base Robotic Mechanism in its natural habitat, i.e., orbital robotics, see Fig. 1.2, a wide variety of motion control approaches have been adopted [27, 32–36]. From an actuation perspective, control approaches are classified as free-floating if only shape actuation is used, while free-flying exploits the full actuation capability [37, 38]. Free-floating approaches are practically advantageous because they are fuel-efficient and the Validation & Verification complexity in a mission preparation is reduced. The latter results from the reduction in interfaces between spacecraft and robotic subsystems which enables mission validation in a geographically distributed manner. However, the freefloating approach is prone to position drifts due to inadvertent interactions with the environment during operation and second-order external forces (e.g., gravity gradient). Free-flying approaches can stabilize the motion during interactions, but suffer from hybrid actuation problems because the base is actuated using actuators like thrusters, which are commonly discrete by design. In [27], the discrete thrust problem was addressed using an explicit passivity-preserving control approach while posing regulation tasks on the end-effector and the base. In [37], the approach of splitting the dynamics into momentum and shape was exploited. The key approach was that the momentum subsystem was driven to convergence, and in this set the required task was achieved. This concept of shape-momentum decomposition is also popular in motion control of humanoid robots [39, 40].

In recent years, orbital mechanisms have emerged as a key mission element in

6 1 Introduction

on-orbit servicing [43–45], active debris removal [46], on-orbit assembly [47] and sample acquisition from remote sites on a comet/asteroid [48]. The controller software for the whole bespoke orbital mechanism is executed on subsystem-specific On-board Software computers. In order to achieve the necessary technology readiness levels, the Validation & Verification of the On-board Software algorithms are carried out using Hardware-in-the-loop simulation using On-ground Robotic facilities due to their inherent integration of available hardware and software models [46–50], see Fig. 1.2. Hence, to meaningfully interface the On-board Software with a Hardware-in-the-loop facility, it is imperative to generate motion in a physically consistent way. This means that the conservation of momentum corresponding to the symmetry of the Floating-base Robotic Mechanism should be preserved during Validation & Verification testing.

Descending towards terrestrial robotics, where fixed-base kinematic chain robotic mechanisms are frequently used to perform automation tasks, it is noted that there is no discernible symmetry. Indeed, these systems naturally do not feature momentum conservation. Yet, a form of symmetry is often required in task execution. For instance, it might be required to perform a primary task, e.g., polishing a task surface, with the highest priority, while a secondary task, e.g., keeping the elbow pointed upward, might be required to achieve an optimal configuration. However, this should be executed in a way that the motion due to the secondary task does not affect the primary task potential, i.e., it is a symmetry of the primary task. The seminal work on this topic was proposed in [51, 52]. In these works, the Euler-Lagrange dynamics was written alternatively using the primary task velocity and a non-integrable nullspace velocity. Motion stabilization was achieved by cancelling the off-diagonal Coriolis/Centrifugal terms. However, the approach relied on semi-definite functions for proof of stability because the method failed to specify a metric tensor behaviour for the hierarchical motion control task. Thus, the underlying principle behind hierarchy in motion and the associated symmetry is still unknown in literature. Even with the recent advent of methods which aim to learn Lyapunov functions for multi-task execution, the key challenge is in specifying the metric tensor [53].

From a bird's eye view, it is evident that although the dynamics and control of both Floating-base Robotic Mechanism and the hierarchical motion of terrestrial robots look like different problem statements and have been treated independently in literature, they are connected through the common concept of symmetry. However, the unifying theory of dynamics and the associated control synthesis is missing in robotics. For hierarchical control, it is still not known if a single energy-like function can be employed to ascertain stability, and if not, why. Similarly, while the parlance between Lagrangian and robotics computation of dynamics are well-understood for fixed-base robots, the Floating-base Robotic Mechanism has not enjoyed this juxtaposition. This is because the Lagrangian formalism for generalized coordinates is commonly known, but the Floating-base Robotic Mechanism has a Lie group as a configuration variable, and thus, the

commonly-known Hamilton's principle ends up with parametrized coordinates (e.g., using Euler angles). To obtain singularity-free dynamics, it is viewed as a kinematic chain mechanism and the dynamics are written using standard iterative algorithms. But this conceals the special structure of the Lagrange-Poincaré equations resulting from the symmetry. Thus, the momentum conservation property has to be explicitly invoked in literature, and the nonholonomic behaviour due to the symmetry is hidden in the iterative computations, and has appeared disconnected from it. Even when it comes to the motion control of the Floatingbase Robotic Mechanism, the underlying shape-momentum interconnection has not been revealed before. Consequently, motion control has not benefited from the added structure of the Lagrange-Poincaré equations due to symmetry. Furthermore, it is often assumed that the sensing and actuation of the shape and the group of Lagrange-Poincaré systems is homogeneous. However, the group variable is commonly measured using exteroceptive sensing in Lagrange-Poincaré systems, which are slow-sampled. The motion control approaches above have ignored this unique feature of majority of the Lagrange-Poincaré-type robotic systems. This negatively affects controller performance, as I show later, and hence, diminishes their applicability. Similarly, for the case of Validation & Verification testing, the preservation of the momentum conservation property has also not been exploited in the state-of-the-art simulation facilities. This results in low fidelity of the Validation & Verification method while increasing sensory overheads. Thus, it is of both practical and theoretical significance to bring forward the concept of symmetry in dynamics and motion control of robotic mechanisms.

1.2 Contribution Overview

The overarching theme of this thesis is to employ the advantages of symmetry in dynamics description and motion control of robotic systems. At the very core, the thesis prescribes the way to employ symmetry, when available, and if absent, it shows the way to generate a symmetry through control action so that the proposed theory can be applied. In spirit, this thesis could be considered as an extension of the work in [3] to Lagrange-Poincaré systems as it focuses on Passivity-Based Control of Lagrange-Poincaré systems. It addresses problems of practical relevance by bringing together the germane topics from the disciplines of geometric mechanics, motion control and robotics, as shown in Fig. 1.3. The thesis balances the theoretical contribution with empirical validation through simulations and experiments in the field. The contribution begins by considering a quintessential Lagrange-Poincaré system that has symmetry: a Floating-base Robotic Mechanism (FRM). Its equations of motion are derived as an efficient recursive computation that reveals the special structure of its Coriolis/Centrifugal matrix due to the underlying symmetry. These Lagrange-Poincaré equations also feature a block-diagonalized inertia, and this is exploited to reconstruct the be8 1 Introduction

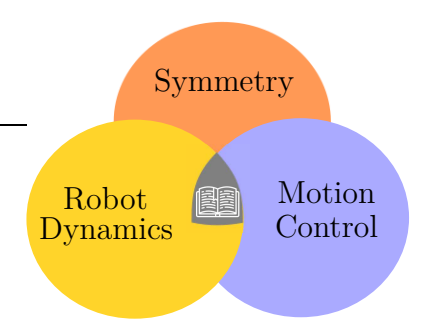


Figure 1.3: Subject intersection in this thesis.

haviour of a Floating-base Robotic Mechanism in a validation facility with high fidelity while avoiding sensory overheads. For general Lagrange-Poincaré systems, a motion control framework is developed that employs an internal model of the symmetry variable dynamics to combine slow-sampled exteroceptive and fast-sampled proprioceptive sensing for high performance. For the Floating-base Robotic Mechanism, the special structure of the Lagrange-Poincaré equations revealed earlier proves to be crucial in this model-based approach. For general Euler-Lagrange systems that do not possess a desirable symmetry, a Symmetry Generating Controller is developed that, firstly, transforms the Euler-Lagrange system into an Lagrange-Poincaré system, and, secondly, exploits this symmetry for hierarchical motion control. Finally, for this case of hierarchy, the taskinduced symmetry is imposed such that motion stability can be ascertained using a single energy function, which was never done earlier. A chapter-wise outline of the thesis is shown in Fig. 1.4, which highlights the contents of the chapter and also the flow of ideas between the chapters. The main idea of a Chapter is written in dark grey with key points highlighted in light grey. The outline will be explained next.

Chapter 2 provides the formal concepts that are required in the remainder of the thesis. This includes Lie group theory, fiber bundle theory, constrained mechanics and multibody computations that are used in robotics. In particular, the Hamilton's principle for deriving the equations of motion for Euler-Lagrange systems having a Lie group as a configuration variable, e.g., Floating-base Robotic Mechanism, is shown. A theoretical framework for constrained mechanics is provided using tools from geometric mechanics which unifies systems with symmetry, operational space control and systems with physical constraints. To the best of my knowledge, such a framework is not available in robotics literature. These concepts are used in the later chapters to develop the main contributions. Herein, the Lagrangian formalism and robotics notation are correlated.

Chapter 3 focuses on the dynamics of the Floating-base Robotic Mechanism. A novel geometrical construction is derived for visualizing its nonholonomic motion. The Lagrange-Poincaré equations of such a mechanism are derived with

a novel recursive formulation that match the analogous equations from geometric mechanics. In particular, the dynamics are split into shape and momentum variations, and the structure reveals additional properties due to the underlying symmetry. The shape and momentum subsystems are proved to be in a passive interconnection, which forms the basis of motion control. The Lagrange-Poincaré equations are extended for the presence of symmetry-breaking potential fields like gravity and buoyancy, while being surrounded by a potential fluid flow for applications in different domains, e.g., underwater robotics.

Chapter 4 deals with the subject of dynamic substructuring in Validation & Verification, which is required for testing algorithms on a facility before deploying a robot in a remote environment. Specifically, the structure of the Lagrange-Poincaré equations for the shape and momentum dynamics is exploited to reduce sensory overhead in the Validation & Verification facility. This also enables realizing the motion with high fidelity such that the symmetry (momentum) is preserved. The Lagrange-Poincaré dynamics derived in Chapter 3 are implemented on Validation & Verification robotic systems to emphasize the benefits of the proposed approach through several experiments.

Chapter 5 provides a novel Passivity-Based Control framework with an internal model for motion stabilization of general Lagrange-Poincaré systems. In particular, two methods are proposed, which differ in the energy functions used for stabilization. In the first method, the whole system is abstracted as a single energy function, while in the latter, the shape subsystem is prioritized over the momentum subsystem, and the corresponding energy functions are used hierarchically to ascertain stability. Since in Lagrange-Poincaré systems, the group variable is measured using exteroceptive sensing, which are slow-sampled, the proposed approach has a built-in model observer for high performance. The additional states of the observer error dynamics elegantly behave as a part of the shape subsystem of the Lagrange-Poincaré system. This preserves the passive interconnection between momentum and shape subsystems from Chapter 3.

Chapter 6 deals with motion control with a task-induced hierarchy of general Euler-Lagrange systems, which lack variational symmetry in desirable directions. A novel Symmetry Generating Controller is proposed to, first, generate a symmetry along the primary task to transform the Euler-Lagrange system into an Lagrange-Poincaré system. This enables the application of the passive interconnection of the shape (primary task) and momentum (nullspace) subsystems from Chapter 3. Consequently, this approach of motion stabilization assumes the form of the second method in Chapter 5, i.e., the shape subsystem is prioritized over the momentum subsystem, and the corresponding energy functions are used hierarchically to ascertain stability. In particular, for the momentum subsystem, two scalar functions are used: the natural energy and the squared-momentum, both of which are conserved quantities for Lagrange-Poincaré systems.

Chapter 7 deals with general Euler-Lagrange systems which lack any discernible symmetry and answers positively the fundamental question, if it is pos-

1 Introduction

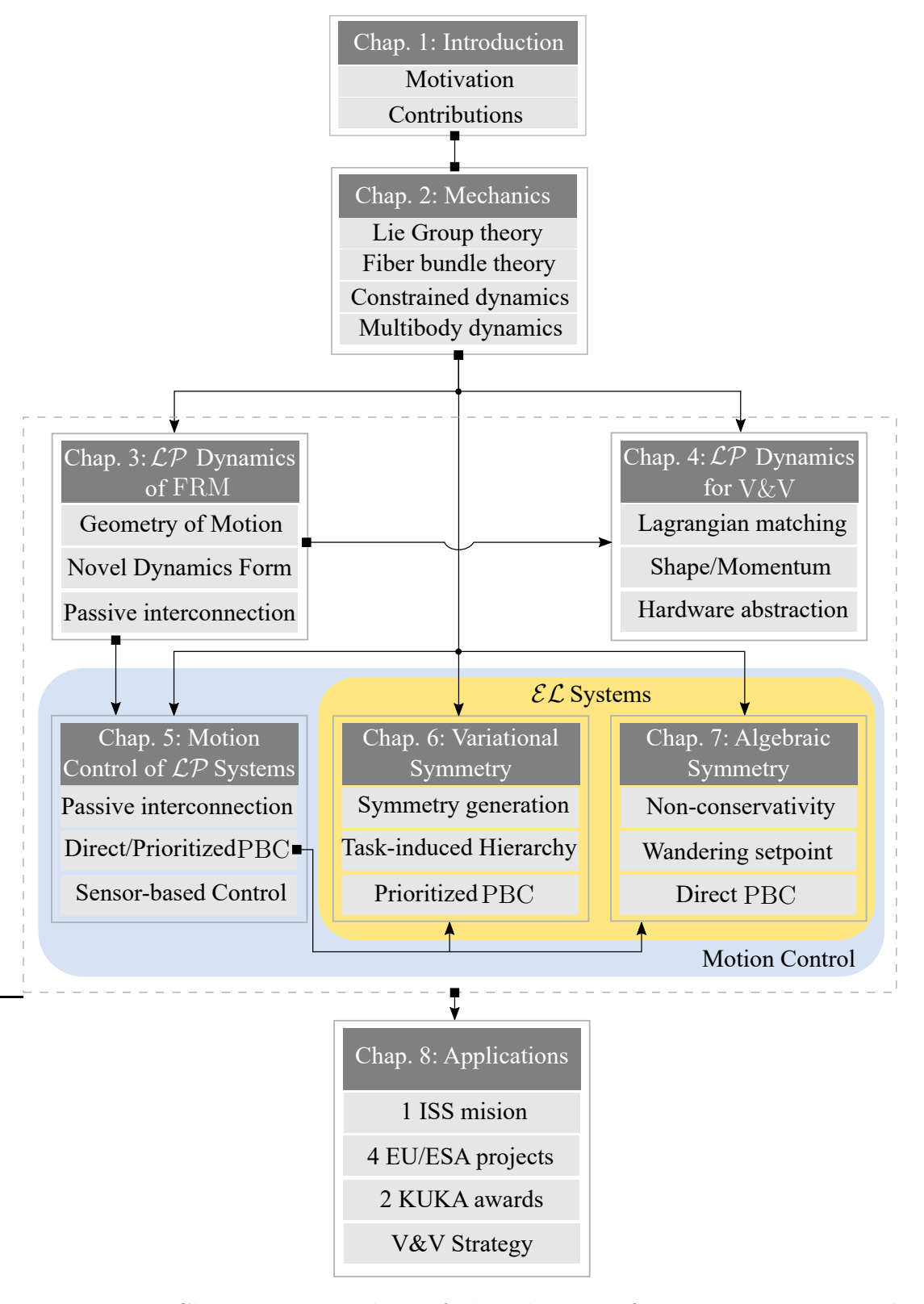


Figure 1.4: Chapter-wise outline of the thesis. \mathcal{LP} : Lagrange-Poincaré, FRM: Floating-base Robotic Mechanism, V&V: Validation & Verification, PBC: Passivity-Based Control, \mathcal{EL} : Euler-Lagrange.

sible to achieve a task-induced hierarchy using a single energy-like function. It is proved that task-induced hierarchy is actually a non-conservative problem because the projection of a potential generates an equilibrium that varies with the primary task motion. By tracking this wandering setpoint, a novel method that operates similarly to the first method in Chapter 5 is provided.

Chapter 8 contains a list of practical applications resulting from this thesis's research work. As is evident from above, the contributions are towards: dynamics and Validation & Verification methods, sensor-based control, motion control and also its extension to shared control (with teleoperation). The contributions include work on: an intravehicular ISS mission, four projects (2 EU and 2 ESA) on servicing and assembly in space robotics, a Validation & Verification strategy for orbital robotics that space agencies and companies are increasingly adopting for early-phase mission analysis, and two industry engagements through KUKA-sponsored innovation awards.

In the thesis, smaller concepts are structured as Lemmas, while major contributions are written as Theorems. The specific contributions (one or more Theorems) of this thesis are listed below in the ascending order of chapters:

- i) In Theorem 3.1, a novel geometric visualization of the unforced motion of the Floating-base Robotic Mechanism is derived, which serves as the multibody extension of the Poinsot construction (1834) for rigid body motion.
- ii) Theorem 3.2 provides a novel factorization of the Coriolis/Centrifugal matrix of the Lagrange-Poincaré equations for the Floating-base Robotic Mechanism. This reveals a special structure of these equations derived from geometric mechanics and exhibits the symmetry. This formulation and its properties enable model-based control, e.g., observer design, which was not possible while using prior iterative algorithms in robotics.
- iii) In Theorem 3.3, a novel closed-form computation of the curvature that quantifies the nonholonomic behaviour of the Floating-base Robotic Mechanism is derived. This is used to compute the displacement of the base per periodic motion in shape, and is required for nonholonomic motion planning without explicitly integrating the equations of motion.
- iv) Theorem 3.4 proves that the shape and momentum subsystems in systems with symmetry (Lagrange-Poincaré systems) e.g. Floating-base Robotic Mechanism, are in a passive feedback interconnection. This provides an elegant structure for motion control design using subsystems, and is the foundation for hierarchical motion control.
- v) Theorem 3.5 generalizes the Lagrange-Poincaré equations for the Floating-base Robotic Mechanism to consider the presence of a symmetry-breaking potential field and a potential fluid flow surrounding the Floating-base Robotic Mechanism, and is useful for underwater and aerial robotics.

1 Introduction

vi) Through Theorems 4.1 and 4.2, two control laws are derived based on Lagrangian matching that map the shape and momentum dynamics of the Lagrange-Poincaré equation of an orbital robot to on-ground robotic facilities. These theorems serve to create a Validation & Verification framework that replicate the motion of a specimen orbital robot on ground. The proposed theorems do not require acceleration measurements and ensure momentum consistency, unlike prior methods.

- vii) Theorem 5.1 proposes a novel control law with with an internal model observer to achieve motion control of Lagrange-Poincaré systems without a group velocity measurement, while stabilizing a single energy-like function. This provides robustness against slow-sampled exteroceptive measurement of the group variable. This is further extended in Theorem 5.3 to include the group velocity measurement, however, provides an additional estimation of forces affecting the momentum subsystem.
- viii) Theorem 5.2 proposes an observer-based control law, as in Theorem 5.1, but achieves hierarchical motion control of Lagrange-Poincaré systems while stabilizing the shape and momentum subsystem energies sequentially. By prioritizing the shape convergence, Theorem 5.2 posits the geometric framework for hierarchical motion control of general \mathcal{EL} systems.
- ix) For Euler-Lagrange systems that lack symmetry in desirable directions, e.g., in hierarchical motion control, Theorems 6.1 and 6.2 employ a Symmetry Generating Controller to generate a partial symmetry, and provide a control law to stabilize the geodesic motion in the primary operational space. While the former stabilizes the secondary task using the natural energy of the momentum subsystem, the latter achieves this using the squared momentum in the Lyapunov function. In contrast to prior works, the metric behaviour of hierarchical motion control is explicitly prescribed.
- x) For a task-induced hierarchy, which is proved to be a non-conservative problem in this thesis, Theorem 7.1 provides a novel control action that generates a new conserved Hamiltonian for the Euler-Lagrange system. Using this new Hamiltonian, asymptotic stabilization is achieved through damping injection while preserving the natural metric tensor.

The research findings reported in this thesis have found applications that have been published in **five journal** and **six conferences** publications, and **two patents** (four more submitted). The main publications which are based on the work in this thesis are listed in Table 1.1. Furthermore, the contents of **Chapter 6** and **Chapter 7** of this thesis are currently being prepared for two journal submissions. The patents filed during the research period together with German Aerospace Center are listed in Table 1.2 and are highlighted with

the percentage of my contribution. Finally, one book chapter, seven journals and seven conference proceedings have been published collaboratively with other research activities, which are related to the topic, but not directly integrated in this thesis. These are summarized in Table 1.3.

	Journals					
[54]	M. De Stefano, H. Mishra ¹ , A. M. Giordano, R. Lampariello, C. Ott					
	A relative dynamics formulation for hardware-in-the-loop					
	simulation of on-orbit robotic missions.					
	IEEE Robotics and Automation Letters, 2021					
[55]	H. Mishra, R. Balachandran, M. De Stefano and C. Ott,					
	A Compliant Partitioned Shared Control Strategy for					
	an Orbital Robot, IEEE Robotics and Automation Letters, 2021					
[56]	H. Mishra, G. Garofalo, A. M. Giordano, M. De Stefano, C. Ott,					
	A. Kugi, Reduced Euler-Lagrange equations of floating-base robots:					
	Computation, properties, & applications,					
	IEEE Transactions on Robotics (T-RO), 2022					
[57]	H. Mishra ¹ , T. Vicariotto and M. De Stefano,					
	Dynamics, Simulation & Control of Orbital Modules					
	for On-Orbit Assembly, IEEE Robotics and Automation Letters, 2025					
[58]	H. Mishra, M. De Stefano, C. Ott					
	Is there a Closed-loop Lagrangian for Hierarchical Motion Control?					
	IEEE Control Systems Letters (first review), 2025					
	Conferences					
[61]	H. Mishra, M. De Stefano, A. M. Giordano, C. Ott,					
	Tracking Control with Robotic Systems for a Moving Target:					
	A Vector Lyapunov Function Approach, IFAC-PapersOnLine, 2018					
[62]	H. Mishra, M. De Stefano, A. M. Giordano, C. Ott,					
	A Nonlinear Observer for Free-Floating Target Motion using					
	only Pose Measurements, American Control Conference (ACC), 2019					
[63]	H. Mishra, M. De Stefano, A. M. Giordano and C. Ott,					
	Output Feedback Stabilization of an Orbital Robot,					
[0.4]	IEEE Conference on Decision and Control (CDC), 2020					
[64]	H. Mishra, M. De Stefano, A. M. Giordano, R. Lampariello, C. Ott,					
	A Geometric Controller for Fully-Actuated Robotic Capture					
[0]	of a Tumbling Target, American Control Conference (ACC), 2020					
[65]	H. Mishra, A. M. Giordano, M. De Stefano, R. Lampariello, C. Ott,					
	Inertia-Decoupled Equations for Hardware-in-the-Loop Simulation					
	of an Orbital Robot with External Forces,					
	IEEE/RSJ International Conference on Intelligent Robots					
	and Systems, 2020					

 $^{^{1}\}mathrm{The}$ first two authors contributed equally to the paper.

1 Introduction

[66] H. Mishra, M. De Stefano, C. Ott, Dynamics and Control of a Reconfigurable Multi-Arm Robot for In-Orbit Assembly, IFAC-PapersOnLine, 2022

Table 1.1: First author contributions

[67]	M. De Stefano, C. Ott, R. Vijayan, H. Mishra (5%), F. Elhardt,
	Method for controlling a robot device,
	accepted (US20240391102), US, 2024

[68] R. Balachandran, **H. Mishra** (50%)

Verfahren zum kooperativen Kontrollieren eines autonomen Systems durch einen menschlichen Operator und/oder ein automatisches Kontrollsystem und Computerprogrammprodukt pending (DE102020114574.8A), DE, 2020

Table 1.2: Patents filed

[73]	R. Lampariello, H. Mishra , N. Oumer, P. Schmidt,					
	M. De Stefano, A. Albu-Schäffer, Tracking Control for the Grasping of					
	a Tumbling Satellite With a Free-Floating Robot,					
	IEEE Robotics and Automation Letters, 2018					

- [74] M. De Stefano, H. Mishra, R. Balachandran, R. Lampariello,
 C. Ott, C. Secchi, Multi-Rate Tracking Control for a Space Robot on a Controlled Satellite: A Passivity-Based Strategy,
 in IEEE Robotics and Automation Letters, 2019
- [75] A. Poó Gallardo, H. Mishra, A. Massimo Giordano, R. Lampariello, Robust Estimation of Motion States for Free-Floating Tumbling Target Capture, *IEEE Aerospace Conference*, 2019
- [76] R. Balachandran, H. Mishra, M. Cappelli, B. Weber, C. Secchi, C. Ott, Adaptive Authority Allocation in Shared Control of Robots Using Bayesian Filters, IEEE International Conference on Robotics and Automation, 2020
- [77] A. Coelho, Y. Sarkisov, X. Wu, **H. Mishra**, H. Singh, A. Dietrich, A. Franchi, K. Kondak, C. Ott, Whole-body teleoperation and shared control of redundant robots with applications to aerial manipulation. *Journal of Intelligent & Robotic Systems*, 2021
- [78] R. Balachandran, H. Mishra, M. Panzirsch and C. Ott, A Finite-Gain Stable Multi-Agent Robot Control Framework

п	
	with Adaptive Authority Allocation,
	IEEE International Conference on Robotics and Automation, 2021
[79]	A. M. Giordano, D. Calzolari, M. De Stefano, H. Mishra ,
	C. Ott, A. Albu-Schäffer, Compliant Floating-Base Control of
	Space Robots, IEEE Robotics and Automation Letters, 2021
[80]	R. Lampariello, H. Mishra , N. W. Oumer, J. Peters, Robust Motion
	Prediction of a Free-Tumbling Satellite with On-Ground Experimental
	Validation, Journal of Guidance, Control, and Dynamics, 2021
[81]	I. Rodríguez, JP. Lutze, H. Mishra , P. Lehner and M. A. Roa,
	Hybrid Planning to Minimize Platform Disturbances during
	In-orbit Assembly Tasks, IEEE Aerospace Conference, 2022
[82]	J. Jeong, H. Mishra, C. Ott and M. J. Kim,
	A Memory-based SO(3) Parameterization: Theory and Application to
	6D Impedance Control with Radially Unbounded Potential Function,
	International Conference on Robotics and Automation (ICRA), 2022
[83]	M. Rothammer, A. Coelho, H. Mishra , C. Ott, A. Franchi,
	A. Albu-Schaeffer, A Rigid Body Observer (BObs) Considering
	Pfaffian Constraints With a Pose Regulation Framework,
	IEEE Control Systems Letters, 2023
[84]	A. Coelho, A. Albu-Schaeffer, A. Sachtler, H. Mishra, D. Bicego,
	C. Ott, A. Franchi, EigenMPC: An Eigenmanifold-Inspired
	Model-Predictive Control Framework for Exciting Efficient Oscillations
	in Mechanical Systems,
	IEEE Conference on Decision and Control, 2022
[85]	JP. Lutze, R. Schuller, H. Mishra , I. Rodríguez and M. A. Roa,
	Optimization of multi-arm robot locomotion to reduce satellite
	disturbances during in-orbit assembly,
	IEEE Aerospace Conference, 2023
[86]	R. Balachandran, M. De Stefano, H. Mishra, C. Ott,
	A. Albu-Schaeffer, Passive arbitration in adaptive shared control
	of robots with variable force and stiffness scaling, <i>Mechatronics</i> , 2023
[87]	M. De Stefano, M. A. Roa, R. Balachandran, A. M. Giordano,
	H. Mishra, N. Oumer,,
	Design and Validation of Orbital Robotic Missions,
	In Space Robotics: The State of the Art and Future Trends,
	Cham: Springer Nature Switzerland, 2024

Table 1.3: Collaborative contributions

CHAPTER 2

99

Mechanics of Mechanisms

(6) In the absence of a constraint or the propulsive energy of an action, motion is by virtue of inertia towards a state of equilibrium or a new constraint [88, pp. 198].

Kanad, Vaisesika Sutra, 6th century BC

This chapter summarizes the preliminary concepts from geometric mechanics and robotics that are relevant to the contributions of this thesis. In particular, relevant ideas of Lagrangian mechanics, Noether's symmetry, nonholonomic constrained mechanics, impedance control and multibody dynamics are introduced and expanded. Despite this chapter being preliminary in nature, there are minor contributions within it, and they are explicitly pointed out. In particular, a detailed treatise on the mechanics of constrained mechanisms is given, which is the main contribution of this chapter.

The organization of this chapter is as follows. The notations that aid in the construction of the theory are provided in Sec. 2.1. Importantly, I revisit the Hamilton's principle for \mathcal{EL} systems on Lie groups and trivial *Principal Fiber Bundles* (PFBs) in Sec. 2.2 which is relevant for deriving the equations of motion of a Floating-base Robotic Mechanism within the Lagrangian formalism. The concepts of symmetry and its relevance to motion control are outlined mathematically in Sec. 2.3. Based on this, a comprehensive theory of constrained mechanisms is developed in Sec. 2.4, which is the main contribution of this chapter. The concepts of impedance control, passivity and multibody dynamics are introduced through Sections 2.5-2.6 to aid the reader in navigating the contents of this thesis.

2.1 Configuration of Mechanisms

The configuration of a mechanism is usually denoted by a non-Euclidean variable $x \in Q \subset \mathbb{R}^d$, where d is the dimension of the configuration manifold Q. An element X of the tangent space at x is denoted as $X \in T_xQ \subset \mathbb{R}^d$, and $Y \in T_x^\top Q \subset R^d$ for an element on the cotangent space. The tangent and cotangent spaces at a point x are isomorphic to vector (velocities) and covector (forces) spaces, respectively. Given two vectors $X, Y \in T_xQ$ and a symmetric weighing matrix $A \in \mathbb{R}^{n \times n}$, $\langle X, Y \rangle_A$ denotes an inner-product of the tangent space. The natural inner product of the tangent space results when A is the metric tensor. In case A is the identity matrix, it is not explicitly written. For a covector, $Z \in T_x^\top Q$, a pairing product can be naturally defined as $\langle X, Z \rangle$ using the identity weight. Given a metric tensor A on any configuration space Q, $(\bullet)^{\sharp}: T_x^\top Q \to T_x Q$ and $(\bullet)^{\flat}: T_xQ \to T_x^\top Q$ are inverse musical isomorphisms that use the metric tensor to transform the argument quantity from cotangent space to tangent space, and vice versa [89, pp. 341]. In this thesis, the configuration space on which the isomorphisms are applied are implicitly clear.

Property 2.1. [89, ch. 12] Consider two manifolds X and Y. Let there be a surjective map, $\pi: X \to Y$. This map provides a tangent space pushforward $d\pi: T_x X \to T_y Y$ and a cotangent space pullback $T_y^\top Y \to T_x^\top X$ in the reverse direction. The pullback property applies to all k-forms, i.e., any k-form, e.g., a scalar potential, or a covector force, can be pulled back from Y to the corresponding exact quantity on X.

Note that Prop. 2.1 enables canonical pullbacks only from Y to X. For the reverse direction, a connection choice must be made, and will be made clear later. Mechanisms can also possess a non-commutative configuration variable, e.g. attitude (orientation) of a satellite. In this case, the variable belongs to a non-Abelian Lie group, $g \in G$, e.g. SO(3), SE(2), SE(3) etc, which has a matrix representation. Given a vector in the tangent space at $g, X \in T_gG$, its left invariant (right invariant) form is written as $x_l = g^{-1}X$ ($x_r = Xg^{-1}$, respectively)¹. Both these forms belong to the Lie algebra, $x_l, x_r \in \mathfrak{g}$, which is also a matrix representation of vectors on the tangent space at the group identity. It is useful to write vector fields on Lie groups as invariant forms because \mathfrak{q} is isomorphic to \mathbb{R}^d , where d is the dimension of the configuration variable, e.g. d = 3, 3, 6 for SO(3), SE(2), SE(3), respectively. This isomorphism is denoted as $(\bullet)^{\vee}: \mathfrak{g} \mapsto \mathbb{R}^d$ and its inverse is $(\bullet)^{\wedge}: \mathbb{R}^d \mapsto \mathfrak{g}$. The left and right invariant forms of a vector are related as, $x_r = gx_lg^{-1}$, which is written using the Adjoint representation of the group as $x_r^{\vee} = \operatorname{Ad}_q x_l^{\vee}, \operatorname{Ad} : \mathfrak{g} \mapsto \mathfrak{g}.$ Given two vectors $X, Y \in T_q G$, the non-commutativity in configuration due to displacements along X, Y is captured by the Lie bracket,

¹The left (right) invariant form is known as a body (spatial, respectively) velocity of the group [90, ch. 2].

i.e., $[X,Y] = [x_r,y_r] = \operatorname{ad}_{x_r^{\vee}} y_r^{\vee}$, where $\operatorname{ad}: \mathfrak{g} \to \mathfrak{g}$ is the adjoint map of \mathfrak{g} onto itself, and it is the differential of the Ad map. Likewise, for elements on the cotangent space, the duals $\operatorname{Ad}^{\top}: \mathfrak{g}^{\top} \mapsto \mathfrak{g}^{\top}$ and $\operatorname{ad}^{\top}: \mathfrak{g}^{\top} \to \mathfrak{g}^{\top}$, serve the same purpose. The group and its algebra are endowed with a local diffeomorphism map, $\exp: \mathfrak{g} \to G$ and its inverse map, $\log: G \to \mathfrak{g}$. In general, the configuration of a sophisticated mechanism can occur in a form $(x,g) \in G \times Q$, which comprises of commutative and non-commutative bases, e.g. a FRM. While $G \times Q$ denotes a left group action, the same mechanism can be written alternatively as a right group action, $Q \times G$, and this is only a matter of notation.

2.2 Lagrangian Mechanics

In this subsection, the uncommon topics related to Lagrangian mechanics are revisited to highlight the difference between the variational principles of mechanisms with commutative and non-commutative basis, e.g., Lie group. This section ends with the Hamel's equations, which is used to model the motion of a FRM. This will serve as a starting point for the contribution in Chapter 3.

Lemma 2.1. Hamilton's principle [91, §2.1]: Given a mechanical system with the Lagrangian $L(x, \dot{x}) = T(x, \dot{x}) - V(x)$, where T and V are the kinetic and potential energies, respectively, its motion from time t_1 to time t_2 is such that the line integral (called the action integral), $I = \int_{t_1}^{t_2} L(x, \dot{x}) dt$, has a stationary value for the actual path of the motion, i.e., $\delta I = \int_{t_1}^{t_2} \delta L(x, \dot{x}) dt = 0$.

Lemma 2.2. Derivation of \mathcal{EL} equations [91, §2.3]: Expanding the result of Lemma 2.1,

$$\int_{t_1}^{t_2} \delta L(x, \dot{x}) dt = \int_{t_1}^{t_2} \frac{\delta L}{\delta x} \delta x dt + \int_{t_1}^{t_2} \frac{\delta L}{\delta \dot{x}} \delta \dot{x} dt = 0$$
 (2.1)

For simplification of (2.1), a crucial step is the application of integration by parts to the second term as,

$$\int_{t_1}^{t_2} \frac{\delta L}{\delta \dot{x}} \delta \dot{x} dt = \int_{t_1}^{t_2} \frac{\delta L}{\delta \dot{x}} \delta x dt - \int_{t_1}^{t_2} \frac{d}{dt} \frac{\delta L}{\delta \dot{x}} dt$$
 (2.2)

where $\int_{t_1}^{t_2} \frac{\delta L}{\delta \dot{x}} \delta x dt = 0$ because $\delta x(t_i) = 0$, and applying (2.2) in (2.1), leads to,

$$\int_{t_1}^{t_2} \left(\frac{\delta L}{\delta x} - \frac{d}{dt} \frac{\delta L}{\delta \dot{x}} \right) \delta x dt = \int_{t_1}^{t_2} \mathcal{E} \mathcal{L}(x, \dot{x}, \ddot{x}) \delta x dt = 0$$
 (2.3)

Finally, applying the fundamental lemma of calculus of variations, i.e., if the integral in (2.3) is 0 for arbitrary δx , then $\mathcal{EL} = 0$ is the \mathcal{EL} equation.

Lemma 2.3. Given a generalized force f, which produces a virtual displacement δx , the forced \mathcal{EL} equation are given by a direct application of the D'Alembert's principle [91, §1.4] as,

$$\langle \mathcal{EL}(x, \dot{x}, \ddot{x}), \delta x \rangle = \langle f, \delta x \rangle \Rightarrow \mathcal{EL}(x, \dot{x}, \ddot{x}) = f$$
 (2.4)

The lemmas above apply to mechanisms with commutative configuration spaces, e.g. fixed-base robotic manipulator. However, in mechanisms with a non-commutative configuration variable, e.g. attitude (orientation) of a satellite, the variable is a matrix representation of a non-Abelian Lie group, which prevents straightforward application of the Lemmas above. To this end, an alternative form of Hamilton's principle for Lie groups is required, and is recalled below.

Lemma 2.4. Hamilton's principle on Lie groups [92, §9.1]: Given a configuration $g \in G$ which evolves as $\dot{g} = gV^{\wedge}$, where $V^{\wedge} \in \mathfrak{g}$ is the left-invariant velocity, the Hamilton's principle is independent of g and reduces to the Lie algebra \mathfrak{g} , i.e.,

$$\delta \int_{t_1}^{t_2} L_0(g, \dot{g}) dt = \delta \int_{t_1}^{t_2} l_0(V) dt = \int_{t_1}^{t_2} \langle \frac{\delta l_0}{\delta V}, \delta V \rangle dt = 0$$
 (2.5)

Given a differential displacement, $\delta g \in T_gG$, like δx in Lemma 2.2, the reduced left-invariant form is $\beta = g^{-1}\delta g \in \mathfrak{se}(3)$. Using this, the non-commutative variational principle is written as $\delta V = \operatorname{ad}_V \beta + \dot{\beta}$, and applied to (2.5), i.e.,

$$\int_{t_1}^{t_2} \langle \frac{\delta l_0}{\delta V}, \delta V \rangle dt = \int_{t_1}^{t_2} \langle \frac{\delta l_0}{\delta V}, \operatorname{ad}_V \beta^{\vee} \rangle dt + \int_{t_1}^{t_2} \langle \frac{\delta l_0}{\delta V}, \dot{\beta} \rangle dt$$
 (2.6)

As in (2.2) of Lemma 2.2, integration by parts is applied to the second term in (2.6) with $\beta(t_i) = 0$, followed by applying the fundamental lemma of calculus, finally resulting in the unforced Euler-Poincaré (\mathcal{EP}) equation as,

$$\frac{d}{dt}\frac{\delta l_0}{\delta V} - \operatorname{ad}_V^{\top} \frac{\delta l_0}{\delta V} = \mathcal{E}\mathcal{P}(V, \dot{V}) = 0$$
(2.7)

Given a generalized force, $F \in \mathfrak{g}^{\top}$, which produces a virtual left-invariant displacement β , the forced \mathcal{EP} equation is obtained by applying D'Alembert principle as in Lemma 2.3 as,

$$\langle \mathcal{EP}(V, \dot{V}), \beta \rangle = \langle F, \beta \rangle \Rightarrow \mathcal{EP}(V, \dot{V}) = F$$
 (2.8)

In many cases, as is also encountered in this work later, the Lagrangian is explicitly a function of a Lie group variable. In this case, \mathcal{EP} reduction as in Lemma 2.4 is not feasible. To this end, the following is useful.

Lemma 2.5. [93, eq. 1.1] Consider a mechanism with a configuration variable $g \in G$, which varies as $\dot{g} = gV^{\wedge}$. Given a left-invariant Lagrangian $\check{l}(g, V)$, which explicitly depends on the pose g, its motion is described by the unforced Left-invariant \mathcal{EL} equation for the Lie group as follows,

$$\frac{d}{dt}\frac{\delta \ddot{l}}{\delta V} - \left(g^{-1}\frac{\delta \ddot{l}}{\delta g}\right)^{\vee} - \operatorname{ad}_{V}^{\top}\frac{\delta \ddot{l}}{\delta V} = \mathcal{E}\mathcal{L}_{G}(g, V, \dot{V}) = 0$$
(2.9)

As in Lemma 2.4, for a generalized force F, the forced \mathcal{EL}_G equation is obtained by applying D'Alembert's principle as,

$$\mathcal{EL}_G(g, V, \dot{V}) = F \tag{2.10}$$

Proof. Computing the first variation of the action integral, i.e., $\delta \int_{t_1}^{t_2} \check{l} dt$, using the left-invariant form of the variation $\beta = g^{-1}\delta g$ (as in Lemma 2.4), we obtain,

$$\int_{t_1}^{t_2} \delta \breve{l}(g, V) dt = \int_{t_1}^{t_2} \left(\langle \frac{\delta l}{\delta V}, \delta V \rangle + \langle \frac{\delta l}{\delta g}, \delta g \rangle \right) dt
= \int_{t_1}^{t_2} \left(\langle \frac{\delta l}{\delta V}, \delta V \rangle + \langle \left(g^{-1} \frac{\delta l}{\delta g} \right)^{\vee}, \beta^{\vee} \rangle \right) dt$$
(2.11)

where the final step is converted to a left-invariant inner product. Applying Lemma 2.4, the result follows.

Remark 1. Note that the result of Lemma 2.5 structurally encapsulates the results of Lemma 2.2 and 2.4, i.e., the L.H.S. consists of the derivative of the Lagrangian relative to the configuration and the non-commutative ad-term.

Correspondingly, the right invariant form using the spatial velocity is written using a negative sign for the ad-term as,

$$\frac{d}{dt}\frac{\delta \tilde{l}}{\delta \tilde{V}} - \left(\frac{\delta \tilde{l}}{\delta g}g^{-1}\right)^{\vee} + \operatorname{ad}_{\tilde{V}}^{\top}\frac{\delta \tilde{l}}{\delta \tilde{V}} = \tilde{F}$$
(2.12)

where $\tilde{V}^{\wedge} \in \mathfrak{g}$ and $\tilde{F} \in \mathfrak{g}^{\top}$ are the right invariant forms of velocity and force.

Lemma 2.6. Hamel's equations Consider a mechanism with a configuration consisting of non-commutative and commutative bases, $(g, x) \in G \times Q$, i.e., a trivial PFB [14]. If the Lagrangian, $L(g, \dot{g}, x, \dot{x})$, can be written in a left-invariant form, $l(V, x, \dot{x})$, i.e., independent of the group variable g, then its motion is described by the Hamel's equations [94, §. 6], [31, eq. 4, 5], written as follows,

$$\frac{d}{dt}\frac{\delta l}{\delta V} - \operatorname{ad}_{V}^{\top}\frac{\delta l}{\delta V} = F, \quad \frac{d}{dt}\frac{\delta l}{\delta \dot{x}} - \frac{\delta l}{\delta q} = f$$
 (2.13)

where $(F, f) \in \mathfrak{g} \times T_x^{\top}Q$ are the generalized forces.

Proof. The proof exploits the Hamilton's principle from Lemmas 2.2 and 2.4. Computing the first variation of the action integral, i.e., $\delta \int_{t_1}^{t_2} l dt$, we obtain,

$$\int_{t_1}^{t_2} \delta l(V, x, \dot{x}) dt = \int_{t_1}^{t_2} \left(\langle \frac{\delta l}{\delta V}, \delta V \rangle + \langle \frac{\delta l}{\delta x}, \delta x \rangle + \langle \frac{\delta l}{\delta \dot{x}}, \delta \dot{x} \rangle \right) dt \tag{2.14}$$

in which directly applying the commutative variational principle from Lemma 2.1 for the variations δx , and the non-commutative variational principle from Lemma 2.4 for the variations δg leads to the unforced equations. Finally, applying D'Alembert's principle for generalized forces $(F, f) \in \mathfrak{g} \times T_x^{\top} Q$, which correspond to the arbitrary displacements $(\beta, \delta x)$, the result follows.

Remark 2. In the special case of Lemma 2.6 with G as an Abelian group (commutative basis), e.g. robotic manipulator mounted on a linear guide, the non-commutative term, i.e., $\operatorname{ad}_{V}^{\top} \frac{\delta l}{\delta V} = 0$.

In \mathcal{EL} systems, we are often interested in symmetry along certain directions. For example, consider a fixed-base robot with configuration $q \in Q$. It is required to control its motion on an operational space of a dimension lower than Q. Then, the motion along the nullspace basis to the primary task vector field acts as its symmetry, and is relevant in analysis. Since the contributions of this thesis are based around such a symmetry, it is formally introduced next.

2.3 Symmetry in \mathcal{EL} Systems

While \mathcal{EL} equations describe the general motion, they do not reveal information about its symmetry, i.e., invariance to transformations. For the following analytical treatment, let the configuration manifold of an \mathcal{EL} system be $Q \subset \mathbb{R}^n$ with its configuration as $q \in Q$. It is endowed with an inertia tensor, M(q), which yields the kinetic energy metric $K = \frac{1}{2} \langle \dot{q}, \dot{q} \rangle_{M(q)}$. Given a scalar potential, $V(q): Q \to \mathbb{R}$, its Lagrangian is $L = K(q, \dot{q}) - V(q)$. Using the Hamilton's principle and D'Alembert's principle (Lemmas 2.1 and 2.3 from Chapter 2), the \mathcal{EL} equations are written as follows with their corresponding subject on the R.H.S.,

$$\frac{d}{dt}\frac{\delta L}{\delta \dot{q}} - \frac{\delta L}{\delta q} = \tilde{\tau}, \text{ Lagrangian}$$
 (2.15a)

$$\nabla_{\dot{q}}\dot{q} = (\tilde{\tau} - \frac{\partial V}{\partial q})^{\sharp}, \text{ Riemannian}$$
 (2.15b)

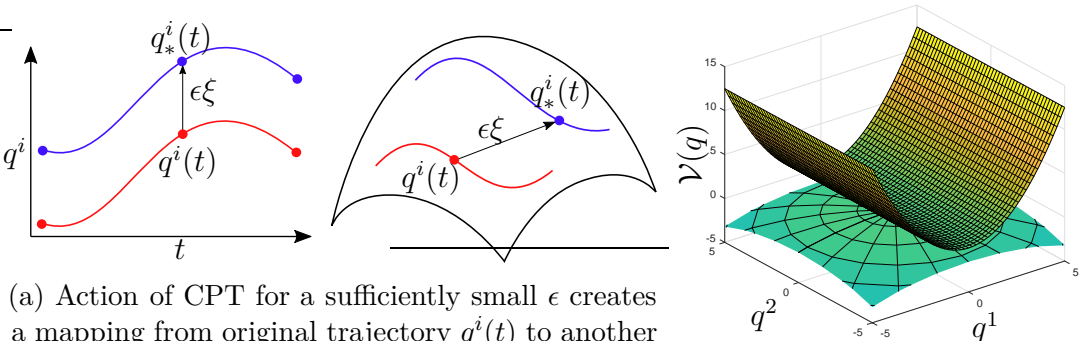
$$M(q)\ddot{q} + C(q,\dot{q})\dot{q} = \tilde{\tau} - \frac{\partial V}{\partial q}$$
, Robotics (2.15c)

where ∇ is the covariant derivative on Q, $\tilde{\tau} \in T_q^{\top}Q$ is the total force (including the control action), and C is the matrix of the Coriolis/Centrifugal (CC) forces containing the Christoffel symbols corresponding to M [8, ch. 4].

Def. 2.1. [95, §II.A] Let ξ be a smooth vector field, e.g., nullspace basis of a primary task in operational space control [51]. The flow of ξ gives a transformation Φ on Q called Continuous Point Transformation (CPT), i.e., a displacement of the point q along ξ , such that $\Phi(q,0) = q$, see Fig. 2.1a. In coordinates,

$$\Phi(q,\epsilon): q \mapsto q_* = q + \epsilon \xi(q) + \mathcal{O}(\epsilon) \tag{2.16}$$

where the parameter ϵ takes a value around 0, indicating the infinitesimal nature of the transformation.



(a) Action of CPT for a sufficiently small ϵ creates a mapping from original trajectory $q^i(t)$ to another $q_*^i(t)$ along the vector field ξ . In this work, we do not consider time-like transformations.

(b) A scalar potential, $V = \frac{1}{2}||q^1||^2$, with a symmetry along q_2 -axis.

Figure 2.1: Symmetry: Concept for \mathcal{EL} systems.

Def. 2.1 is a critical concept in analysing infinitesimal symmetries, i.e., symmetries along a vector field rather than a trivial symmetry along a coordinate variable. Given a scalar quantity $\mathcal{V}(q)$, its variation along the flow of ξ is determined by the Lie derivative,

$$\mathcal{L}_{\xi}\mathcal{V}(q) = \mathcal{V}(\Phi(q, \epsilon)) - \mathcal{V}(q) = \epsilon \langle \xi, \frac{\partial \mathcal{V}}{\partial q}(q) \rangle$$
 (2.17)

The function $\mathcal{V}(q)$ is considered to be ξ -invariant, or ξ is a symmetry of \mathcal{V} , if $\mathcal{L}_{\xi}\mathcal{V}(q) = 0$, i.e., the function remains invariant along the flow of ξ .

Example 1. In Fig. 2.1b, a scalar potential $V(q) = \frac{1}{2}||q^1||^2$ is shown on $q(q^i) \in Q$. Considering the vector,

$$\xi = \xi^{1}(q) \frac{\partial}{\partial q^{1}} + \xi^{2}(q) \frac{\partial}{\partial q^{2}} = \begin{bmatrix} \xi^{1}(q) & \xi^{2}(q) \end{bmatrix} \begin{bmatrix} \frac{\partial}{\partial q^{1}} \\ \frac{\partial}{\partial q^{2}} \end{bmatrix}, \tag{2.18}$$

for $\xi^1 = 0$ and $\xi^2 = 1$, ξ is a symmetry of \mathcal{V} by inspection. In (2.18), $\xi \in \mathbb{R}^{1 \times n}$ is the matrix form of the symmetry basis (nullspace), and may depend on q in a general case.

To use this notion for a velocity-dependent scalar quantity on Q, $\mathcal{K}(q,\dot{q})$, the first prolongation of the infinitesimal generator is defined as [95, §II.C],

$$\hat{\xi} = \xi \frac{\partial}{\partial q} + \dot{\xi} \frac{\partial}{\partial \dot{q}} \tag{2.19}$$

Thus, the variation along the flow of $\hat{\xi}$ is determined as,

$$\mathcal{L}_{\hat{\xi}}\mathcal{K}(q,\dot{q}) = \epsilon \left(\langle \xi, \frac{\partial \mathcal{K}}{\partial q}(q,\dot{q}) \rangle + \langle \dot{\xi}, \frac{\partial \mathcal{K}}{\partial \dot{q}}(q,\dot{q}) \rangle \right)$$
(2.20)

As before, \mathcal{K} is ξ -invariant, or ξ is a symmetry of \mathcal{K} , if $\mathcal{L}_{\hat{\xi}}\mathcal{K} = 0$.

Example 2. In Example 1, consider a kinetic energy $\mathcal{K} = \frac{1}{2} \langle \dot{q}, \dot{q} \rangle_{M(q^1)}$, in which $M(q^1)$ is the inertia tensor with only q^1 dependency. The first prolongation can be written as,

$$\hat{\xi} = \xi(q) \begin{bmatrix} \frac{\partial}{\partial q^1} \\ \frac{\partial}{\partial q^2} \end{bmatrix} + \dot{\xi}(q, \dot{q}) \begin{bmatrix} \frac{\partial}{\partial \dot{q}^1} \\ \frac{\partial}{\partial \dot{q}^2} \end{bmatrix}$$
(2.21)

Since, $\xi^1 = 0$ and $\xi^2 = 1$, are constants, we get $\mathcal{L}_{\hat{\xi}} \mathcal{K} = 0$, implying that the kinetic energy is ξ -invariant, with symmetry along q^2 axis. This type of symmetry is observed in FRM, in which the kinetic energy is independent of the floating platform's configuration [56].

Def. 2.2. Noether Point Symmetry (NPS): A CPT which is a symmetry of the Lagrangian of the \mathcal{EL} system in (2.15), i.e.,

$$\mathcal{L}_{\hat{\xi}} \int L dt = \int \left(L(q_*, \dot{q}_*) - L(q, \dot{q}) \right) dt = \epsilon \mathbb{F}(q)$$
 (2.22)

where \mathbb{F} is the Bessel-Hagen term, and it can only be the total derivative² of a scalar field, i.e., $\mathbb{F} = \int \frac{d\alpha(q)}{dt} dt$ [95, §III]. In this case, Φ with generator ξ is simply a Lie symmetry of the \mathcal{EL} equations, whereas, in the particular case that $\mathbb{F} = 0$, the symmetry is strict. The term $\hat{\xi}(L) = \dot{\alpha}$ is called the Rund-Trautman identity, and the Rund-Trautman expression for the \mathcal{EL} equations gives a momentum-related term as,

$$\langle \hat{\xi}, \mathcal{EL}(L) \rangle = \frac{d}{dt} (\alpha(q) - p_i \xi^i), \ p = \frac{\partial L}{\partial \dot{q}}$$
 (2.23)

A key point is that for Φ to be a Noether Point Symmetry (NPS), $I = \alpha - p_i \xi^i$ is a momentum-related conserved quantity during motion dictated by the \mathcal{EL} equations. In this subsection, the concept of symmetry in a \mathcal{EL} system was provided.

2.3.1 The Metric and its Killing vectors

A deeper understanding of the infinitesimal symmetry of the kinetic energy is gained from the inertia metric tensor next. The following theory will be exploited in Chapter 6 to achieve hierarchical motion control by synthesizing an artificial symmetry of the metric tensor. Consider the \mathcal{EL} system in (2.15) with the kinetic energy $\mathcal{K}(q,\dot{q}) = \frac{1}{2}\langle \dot{q},\dot{q}\rangle_{M(q)}$. In this case, (2.20) is rewritten to get the NPS as,

$$\mathcal{L}_{\xi} \mathcal{K}_{ij}(q) = \xi(\mathcal{K}_{ij}(q)) + \mathcal{K}_{ij}(q) \frac{\partial \xi^{j}}{\partial q_{i}} + \mathcal{K}_{ij}(q) \frac{\partial \xi^{k}}{\partial q_{j}} = 0$$
 (2.24)

which is the Killing equation [97]. The key concept behind (2.24) is that it shows that \mathcal{K} does not vary as one translates along the vector field ξ . The metric

²Note that this is because the addition of a total time derivative of a scalar field to the Lagrangian leaves the \mathcal{EL} equations invariant [96].

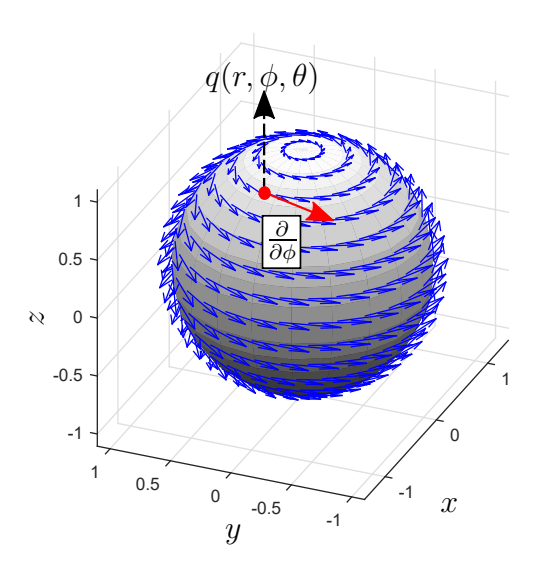


Figure 2.2: Killing vectors along $\frac{\partial}{\partial \phi}$ on a Sphere $Q = \mathbb{S}^2$ in a surrounding Euclidean space (\mathbb{R}^3) , which create rotations around z-axis.

of the \mathcal{EL} system can maximally have upto n(n+1)/2 Killing vectors, where $n = \dim(Q)$ [98], e.g. Euclidean space. Of these, n killing vectors are translation symmetries ∂_q , and the remaining $\frac{n(n-1)}{2}$ indicate the O(n) rotational symmetries. A manifold possessing maximal killing vectors is a constant curvature manifold. Thus, in an n-dimensional Riemannian space, there can be maximally $\frac{n(n+1)}{2}$ conserved momenta.

Lemma 2.7. Consider a Riemannian manifold (Q, M(q)) having k < n Killing vectors, ξ^i . A coordinate system exists such that the metric is independent of k coordinates corresponding to the Killing vector flows. The converse is also true.

Proof. See [98, Prop. 2.2]. \Box

Example 3. Considering a sphere, $Q = \mathbb{S}^2$, a configuration point is denoted as $q \equiv q(r, \phi, \theta)$, see Fig. 2.2. The Riemannian metric on \mathbb{S}^2 is written in matrix form as $\operatorname{blkdiag}(\mathbb{I}, r^2 \sin^2 \theta, r^2)$.

The vector, $\xi = \begin{bmatrix} \xi^1(q) & \xi^2(q) & \xi^3(q) \end{bmatrix}$ with $\xi^1 = \xi^3 = 0$ and $\xi^2 = 1$, is a killing vector of the metric tensor because it does not depend upon ϕ explicitly. The killing vectors (blue arrows) have been shown in Fig. 2.2 for the the particular case of ξ , which cause rotations about the z-axis.

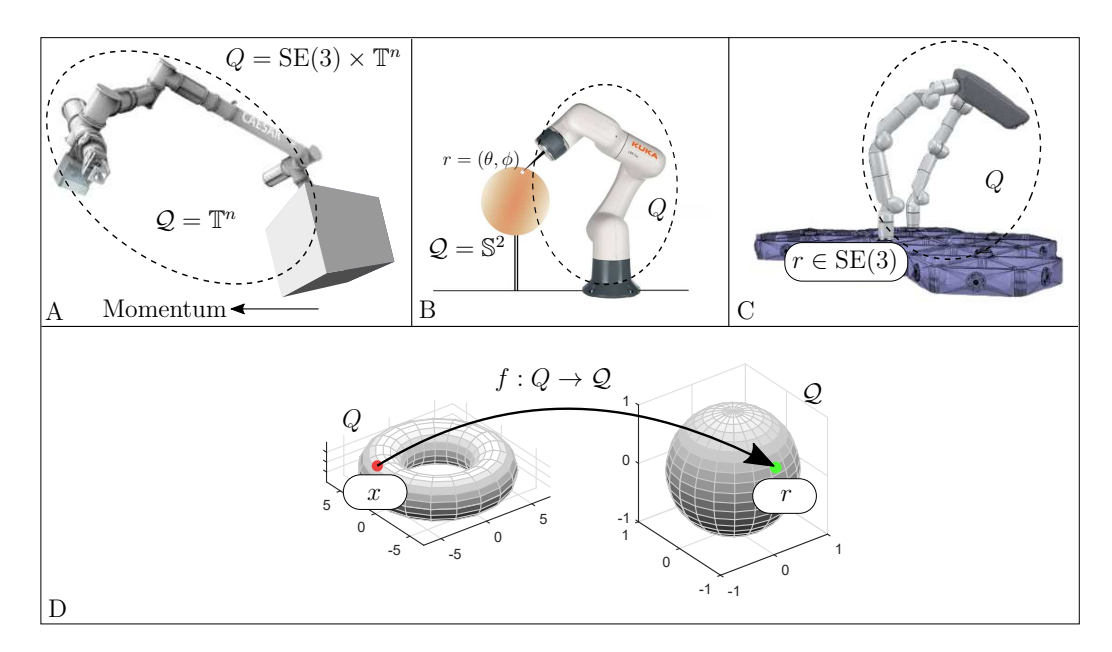


Figure 2.3: Constrained mechanisms. A: System with symmetry, FRM which features momentum conservation. B: Operational space control, the end-effector tip of the fixed-base robot is controlled on a sphere. C: A serial kinematic chain robot kinematically constrained at both end-effectors for torso operation. D: Constraint modeled as a submersion.

2.4 Constrained Motion of Mechanisms

Constraints in mechanisms, see Fig. 2.3, are encountered in two ways: Physical constraints, which are satisfied by the equations of motion of the system; and virtual constraints, e.g. operational space motion, Fig. 2.3-B, which are required to be satisfied by the closed-loop dynamics through motion control. The former type can further be classified into two. While presence of a physical (kinematic) constraint, Fig. 2.3-C, is an obvious one, the dynamic constraint that are a mathematical consequence of symmetry, Fig. 2.3-A, are unintuitive because they are not physically present but still satisfied by the dynamics [14]. The contributions of this thesis encompass physical and virtual constraints. Therefore, in the following, a comprehensive theory of constrained mechanisms is developed to highlight the aspects of modeling, integrability of subspaces and the group structure induced by the constraint. To the best of my knowledge, such a theory is not available in robotics literature and this is the main contribution of this chapter.

2.4.1 Modeling Constraints

Consider a mechanism with a configuration manifold Q. In geometric mechanics, a constrained mechanism appears in an abstract form as shown in Fig. 2.4.

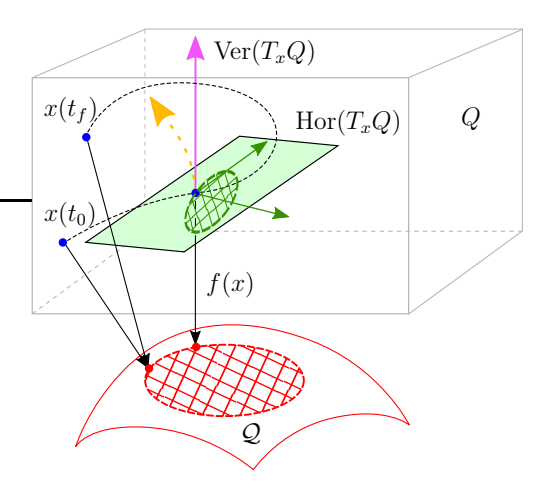


Figure 2.4: An illustration of a constrained mechanism with a configuration space Q as a fiber bundle with map f, which maps points in Q to base space Q. At a point x, the Ehresmann connection decomposes the tangent space into $\text{Hor}(T_xQ)$ (green plane) and $\text{Ver}(T_xQ)$ (magenta line) directions. $\text{Ver}(T_xQ)$ is tangent to all points (arrowed orange line) which map to the same point in Q. A periodic motion in $\text{Hor}(T_xQ)$ projected to Q results in net displacement in Q, i.e., $x(t_0) \neq x(t_f)$.

The presence of a constraint implies a bundle structure, i.e., there exists a map $f: Q \to \mathcal{Q}$, where \mathcal{Q} is known as the base space and Q assumes the role of a total space [99, Ch. 3], see Fig. 2.3-D. The following assumption is required for theoretical development.

Assumption 2.1. Given the \mathcal{EL} system, the bundle map f corresponding to the constraint is not singular, i.e., $\operatorname{rank}(df(x)) = m$.

Def. 2.3. For a \mathcal{EL} system, let Q (dim(Q) = n) be the configuration space and Q (dim(Q) = m) be the operational space such that both are differentiable manifolds with k = n - m > 0. Then, the differentiable map $f: Q \mapsto Q$ is a surjective submersion at $x \in Q$ if its differential, $df: T_xQ \mapsto T_{f(x)}Q$ is a surjective map.

The map, f, from Def. 2.3 is a surjective submersion if it satisfies Assumption 2.1, i.e., J = df is such that $\operatorname{rank}(J) = m$. Generally, f is a surjective submersion, i.e., non-invertible map, as r = f(x), where $x \in Q$. This results in a fibered manifold, denoted as a triplet (Q, f, Q). Each fiber $f^{-1}(r)$ for $r \in Q$ is an embedded submanifold of Q with dimension k [100], commonly known as a the manifold of self-motions [101]. Formally, this is a fiber space³, $\{f^{-1}(r) : r \in Q\}$. The fiber bundle can be denoted by the short exact sequence as,

$$f^{-1}(r) \xrightarrow{\Psi} Q \xrightarrow{f} Q$$
 (2.25)

³Alternatively, Q appears as a disjoint and connected set of self-motion submanifolds [89, Ch. 19], parametrized by any r. The partition of Q into the disjoint nullspaces parametrized by r is a foliation [102].

where $\Psi: f^{-1}(r) \to Q$ is the inclusion map of the embedded submanifold at each r. The inclusion map has the form $\Psi(r, s^*) = x^*$, which for a given fiber coordinate s^* gives a configuration in $x^* \in Q$ [103, §1]. The map Ψ determines a section in Q for a given r, and allows determining fiber coordinate. In particular, it satisfies $\pi \circ \Psi = \operatorname{Id}_{\mathcal{Q}}$ and $\Psi(f(q)) = x$, which determines the origin in the fiber. Note that, Ψ is determined such that s^* is an origin of the fiber at r. To understand the topology of the fiber, it is prudent to identify its tangent space.

For every $x \in Q$, the primary submersion f canonically⁴ describes a vertical subspace, \mathbb{V} , on the tangent bundle TQ, as, $\mathbb{V}_x = \operatorname{Kern}(J(q))$, where \mathbb{V}_x is a k-dimensional vector space. The vertical component of T_xQ at a point x of the bundle is denoted by $\operatorname{Ver}(T_xQ) = \operatorname{Kern}(df(x))$, which we denote as a matrix basis $Z \in \mathbb{R}^{n \times k}$. The fibered manifold provides canonical exact sequences for the tangent and the cotangent spaces as follows [104, eq. 1.4.3],

$$\mathbb{V}_x \xrightarrow{Z} T_x Q \xrightarrow{J} T_r \mathcal{Q} \tag{2.26}$$

$$T_r^{\top} \mathcal{Q} \xrightarrow{J^{\top}} T_x^{\top} Q \xrightarrow{Z^{\top}} \mathbb{V}_x^{\top}$$
 (2.27)

Assumption 2.2. For any $r \in Q$, rank $(\text{Ver}(T_rQ)) = \text{rank}(\text{Kern}(J)) = k$, where $\text{Kern}(\bullet)$ is the kernel, or the nullspace, of the argument.

In general, the set of points in which Assumption 2.2 is fulfilled is dense in Q, and it specifies that the mechanism is free of algorithmic singularities [105, 106]. The assumption merely states that the vertical subspace \mathbb{V}_x is full rank. In this work, the motion of the \mathcal{EL} system is considered in the local region which satisfies Assumptions 2.1 and 2.2.

Let a vertical velocity be $(x, \tilde{\mu}) \in \mathbb{V}_x$, where $\tilde{\mu} \in \mathbb{R}^k$. The velocity $\tilde{\mu}$ is canonically projected to a vertical component $\dot{x}_v \in \operatorname{Ver}(T_qQ)$ on the tangent space, as $\dot{x}_v = Z(x)\tilde{\mu}$, where $Z \in \mathbb{R}^{n \times k}$ denotes the set of vertical (nullspace) basis. Motion along Z ensures the invariance of f(q) = r. Since \mathbb{V}_x is tangent to the fiber $f^{-1}(r)$, $Z = d\Psi$ is the Jacobian (differential) w.r.t. s of the inclusion map Ψ in (2.25), as we shall prove next.

2.4.2 Integral flows of Vertical Subspace

In the following, the objective is to uncover the structure group that acts on the fiber (nullspace). Consider a fixed point in operational space $r \in \mathcal{Q}$ defining a distribution \mathcal{D} , allowing motions only along the fiber, i.e., $\dot{x} \in \mathcal{D}$.

The *integral curve* of the i^{th} vertical vector $Z^i \in \mathbb{V}_x$ on Q is a smooth curve $x(t) = \gamma(\epsilon_i)$, parametrized with $\gamma(\epsilon_i) : I \subset \mathbb{R} \mapsto Q$, whose tangent vector coincides with Z^i at that point, i.e., $\frac{d}{dt}\gamma(\epsilon) = Z^i(\gamma(\epsilon_i))$. A unique parametrization of

⁴The vertical subspace is canonical, whereas its orthogonal complement is chosen using a connection [14], as shall be described later.

 γ might not be found, however, there is a maximal integral curve defined on the largest possible domain interval, denoted as $\Psi^{i}(x_0, \epsilon_i)$, which is written as,

$$\Psi^{i}(x_0, \epsilon_i) = x_0 + Z^{i}(x_0)\epsilon_i + \mathcal{O}(\epsilon_i^2)$$
(2.28)

Note that (2.28) has the structure of a CPT from Def. 2.1, and we get,

$$Z^{i}(q) = \frac{d}{d\epsilon_{i}} \Big|_{\epsilon_{i}=0} \Psi^{i}(x, \epsilon_{i}), \ \Psi^{i}(x, s_{i}) = x_{0}$$
 (2.29)

whose integral solution is a left action⁵ of the flow, $\Psi^{i}(q, \epsilon_{i}) = \exp(Z^{i}(x_{0})\epsilon_{i}) \cdot x_{0}$. For all the fiber (nullspace) basis, the CPT is written using the Product of Exponentials (PoE) as, $\Psi(x, \epsilon) = \prod_{i=1}^{k} \exp(Z^{i}(x_{0})\epsilon_{i})x_{0}$ [107, Th. 1.51].

Assumption 2.3. Let $Q_{\delta} \subset Q$ and $Q_{\delta} \subset Q$ exist such that the fiber bundle arising from the constraint (Q, f, Q) is locally a Cartesian product $Q \cong Q \times f^{-1}(r)$ $\forall r \in Q_{\delta}$.

From a topological perspective, (Q, f, Q) can be non-trivial, i.e., it does not admit a global product space trivialization, e.g., Möbious strip. The local triviality condition in Assumption 2.3 is necessary to limit the scope to continuous motions along a chosen trivialization of the fiber, i.e. the nullspace.

2.4.3 Local Integrability of the Vertical Subspace

The vertical velocity $\tilde{\mu} \in \mathbb{V}_x$ can be written using its tangent space component at a fixed $r \in \mathcal{Q}$ as $\dot{x}_v \in \text{Ver}(T_q Q)$ as,

$$Z(x)\tilde{\mu} = \dot{x}_v = \dot{x} \Rightarrow Z^{\top}Z\tilde{\mu} = Z^{\top}\dot{x} \Rightarrow \tilde{\mu} = Z^{\top}\dot{x}$$
 (2.30)

which means $\dot{x}_v = \mathcal{Z}\dot{x}$, where $\mathcal{Z} = ZZ^{\top} \in \mathbb{R}^{n \times n}$ is a tangent space (endomorphism) projector, i.e., $\mathcal{Z}: TQ \mapsto TQ$. I point out that Z is a Stiefel manifold, giving a set of orthonormal k-frames on Q, and consequently, \mathcal{Z} is the corresponding Grasmannian projector [108], if Z is composed of orthonormal basis, e.g., computed using Singular Value Decomposition (SVD).

Lemma 2.8. Given Assumption 2.3, the vertical subspace, \mathbb{V} , of TQ, is integrable [89, Ch. 13], and $\operatorname{Ver}(T_xQ)$ forms a closed subalgebra of T_qQ .

Proof. To prove this, Frobenius theorem is invoked to show that, given $X, Y \in \mathbb{V}$, the commutator, $[X, Y] \in \mathbb{V}$. Using f as the surjective submersion,

$$df([X,Y]) = [df(X), df(Y)] = 0$$
 (2.31)

which proves that $[X, Y] \in \text{Kern}(df) = \mathbb{V}$, and is a closed subalgebra.

 $^{^5{}m The}$ solution is also equivalently given by a right action.

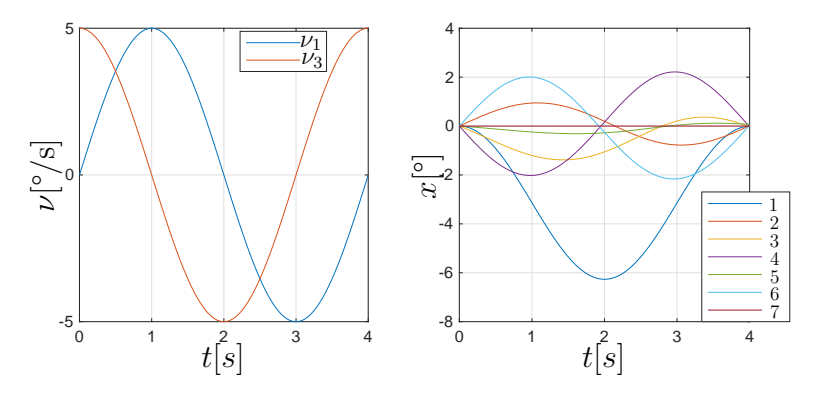


Figure 2.5: Integrability of the vertical subspace (\mathbb{V}) of the forward kinematics as a surjective submersion, $f: \mathbb{T}^7 \to \mathbb{R}^3$.

Example 4. An articulated system with n=7 revolute joints, $Q=\mathbb{T}^7$, is considered with the task space as the inertial position of the end-effector tip in the reachable subspace, i.e., $Q \subset \mathbb{R}^3$. Thus the kinematics map, $f: \mathbb{T}^7 \mapsto \mathbb{R}^3$ defines a vertical subspace, whose basis is determined by a matrix $Z \in \mathbb{R}^{7\times 4}$ obtained using SVD from spectral geometry. A trajectory along Z^1, Z^3 is chosen to create a periodic circular motion of diameter $10[\degree]$, see Fig. 2.5, as follows,

$$q(t) = \int_0^4 (Z^1 \nu_1 + Z^3 \nu_3) dt \tag{2.32}$$

where $(\nu_1, \nu_2) = 5(\sin \frac{\pi}{2}t, \cos \frac{\pi}{2}t)[°/s]$. In the right of Fig. 2.5, it is seen that all joints during the trajectory are displaced from their initial condition and return to it at the end, t = 4, demonstrating integrability of \mathbb{V} . This is a special case because the Lie Algebra of \mathbb{T}^7 is Abelian, and hence solvable, i.e., given $X, Y \in T_x \mathbb{T}^7$, [X,Y] = 0, see [89, Ex. 8.40c]. Consequently, the Lie subalgebra \mathbb{V} is also solvable by Lie's theorem, see [109, §3]. Hence, the vertical vector fields commute and the mechanism returns to the initial configuration after a loop.

Remark 3. Note that, in general, the Lie Algebra of T_xQ is not Abelian, e.g., FRM. In this case, the Lie subalgebra spanned by the vertical subspace \mathbb{V} of the submersion might not commute. This occurs when one of the configuration coordinates is non-Abelian. Hence, the joint positions, as on the right of Fig. 2.5, might not return to their initial condition. This, however, is the property of non-commutative Lie Algebra, but the vertical subspace is integrable.

2.4.4 Structure Group-(oid) of Vertical Subspace

In the following, the objective is to uncover the structure group that acts on the fiber (nullspace). From Lemma 2.8, at a given r, \mathbb{V} is a closed Lie subalgebra of T_xQ satisfying the submersion f(x) = r. In (2.29), Z^i is the *infinitesimal*

generator of the integral curve on Q, and Ψ denotes the left flow action, because it acts from the R.H.S. Corresponding to this flow action is a local Lie group, G, parameterized by ϵ_i as follows.

Lemma 2.9. Consider the \mathcal{EL} system satisfying Def. 2.3 as a constraint f(q) = r, which restricts its velocities to the distribution $\dot{x} \in \mathcal{D}$. The vertical subspace (nullspace) $\mathbb{V} = \text{Kern}(df)$ of the submersion is the allowable motion, and the fiber velocity is obtained using (2.30). In this case,

1. $\forall Z, \exists (x, \tilde{\mu}) \in \mathbb{V}_x$, and the following isomorphism holds:

$$\tilde{\mu} \in \mathbb{V}_x \cong \mathfrak{g}, \ Z(x)\tilde{\mu} \in \mathfrak{g}^Q \cong \operatorname{Ver}(T_x Q)$$
 (2.33)

- 2. The Lie algebra \mathfrak{g} generates a k-dimensional Lie group, G, which results in an analogous left group action on Q as $\Psi(x,\epsilon) = g(\epsilon) \cdot x$, where $g \in G_0$, see Fig. 2.6.
- 3. At a fixed r, $x(0) \equiv (r, z)$, where $z \in f^{-1}(r)$ is the fiber element at r. Thus, a group element $g \in G_0$ acts only on the second argument as $x(t) \equiv (r, g \cdot z)$, and (r, g) parametrizes the motions on Q w.r.t. x(0).
- 4. The group element is written as the PoE,

$$g = \prod_{i=1}^{k} \exp(Z^{i}(q)\epsilon_{i}), \ g \in G_{0}.$$
 (2.34)

5. The Lie group reconstruction is determined by a right-invariant vector field $\dot{g} = \tilde{\mu}^{\wedge} \cdot g$, where $\tilde{\mu}$ denotes the spatial velocity in the basis of $e(r_0)$, see Fig. 2.6.

where (ϵ_i) parameterize the Lie group G_0 , and \mathfrak{g} denotes the Lie algebra basis corresponding to the vertical velocity, $\tilde{\mu}$, and \mathfrak{g}^Q denotes the vector field corresponding \mathfrak{g} , which in turn corresponds to \dot{x}_v .

Proof. Recall from Lemma 2.8 that $\operatorname{Ver}(T_xQ)$ is a closed subalgebra of T_xQ . In item 1, for all the vector fields Z^i , i=1..k in Q ((2.29)), there exists a fiber velocity, which forms a Lie algebra $\tilde{\mu} \in \mathfrak{g} \cong \mathbb{V}$, see [110, Def. 557]. For item 2, by the Fundamental Theorem on Lie Algebra Actions [89, Lemma 20.16], there is a k-parameter local Lie group G with the corresponding left group action $\Psi(q, \epsilon)$, which is the same result obtained in Sec. 2.4.2. Item 3 results by fixing the chart at x(t=0). Note that the action of G_0 depends upon the choice of variables [111, §1.9]. For example, a group element $g \in \operatorname{SO}(2)$ parametrized with an angle, $\delta\theta$, acts on $x=(x_1,x_2)\in\mathbb{R}^2$ in Euclidean coordinates as $\hat{x}=g(\delta\theta)x$. However, in polar coordinates, g acts as $\hat{x}_\theta=(R,\theta+\delta\theta)$. The submersion, f, creates a polar decomposition as $x\equiv(r,z)$, and g acts on z by left translation. For item 4, each velocity Z^i generates a flow given by a one-parameter subgroup, as shown

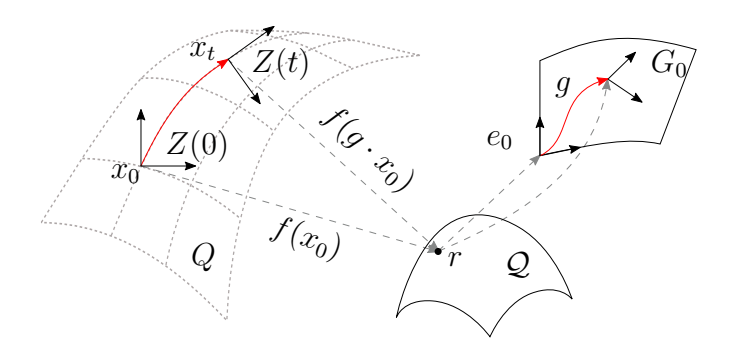


Figure 2.6: Motion along the nullspace of a distribution \mathcal{D} , which arises from a constraint on the forward kinematics submersion, f(x) = r.

in Sec. 2.4.2. The flow is given by the exponential map [107, Th. 1.51] and [112, Th 5.3]. The overall group displacement is simply the PoE. For item 5, note that the infinitesimal generator of the flow due to a left group action is produced by right-invariant Lie algebra, see [4, Prop. 9.3.7], i.e., which denotes a spatial velocity [5, Def. 2.8.13] in the basis of e_0 , see Fig. 2.6.

Remark 4. The reader might be aware of the concept of PoE from its application in robotics to determine forward kinematics of open-chain multibody systems, see $[8, \S2.2]$ [113, Th. 3.1], for a point in operational space, $u \in S$ as,

$$u(x) = PoE(x)u(0), PoE(x) = \prod_{i=1}^{n} \exp(\hat{\zeta}_i(x)\vartheta_i)$$
 (2.35)

where $\hat{\zeta}_i$ and ϑ_i define the Lie algebra basis (twist) and the displacement of the i^{th} -joint, respectively. Note the similarity in (2.34) of Lemma 2.9 and (2.35).

Remark 5. Note that the vertical vectors corresponding to the basis, Z^i , are a vector representation (\mathbb{R}^n), and are the infinitesimal generator of the group action. The vectors can be converted to a matrix algebra by Ado's theorem, see [89, Th. 8.49]. This step is required for the $\exp(\bullet)$ functions in Lemma 2.9.

Hence, using Lemma 2.9, let G_0 be the local k-dimensional Lie group [107, Def. 1.20] with a matrix representation in GL(n). Given $g \in G_0$, a new configuration along the nullspace at r is obtained as $x^* = g \cdot x$, where \cdot represents the matrix multiplication. Let the corresponding Lie algebra be $\mathfrak{g} \cong \mathbb{V}_x$, where $\mathfrak{g} \subset \mathfrak{gl}(n)$ is also a matrix representation of \mathbb{V}_x , as discussed in Remark 5. A vector $\tilde{\mu} \in \mathfrak{g}$ is tangent to the curve produced by the exponential map, $\tilde{\mu} = \frac{d}{dt}(\exp(t\tilde{\mu}))$.

Thus, the submersion f creates a vertical space \mathbb{V} as a closed Lie subalgebra, \mathfrak{g} , which is an infinitesimal generator for the group displacement, g, in the nullspace given by Lemma 2.9. This group displacement, like in (2.35), is determined using PoE, such that Z^i determines the Lie algebra basis, and ϵ is the group parameter change. At this point, it is worth noting that given the Lie algebra basis for \mathfrak{g} ,

the group element's parameters $(\epsilon_i(t) \text{ in } (2.34))$ can be obtained using the Wei-Norman formula to form the group element g [114, 115]. The problem here is that the Lie Group G_0 is not equipped with a defined identity, e. It is convenient to choose the configuration at t = 0, i.e., x(0), to define e.

Lemma 2.10. Let the bundle map of a constrained \mathcal{EL} system be denoted as $f: Q \mapsto Q$, and be a surjective submersion. Let $\mathbb{V} = \mathrm{Kern}(df)$ be its vertical subspace that defines an action of a k-parameter group G_0 on Q at a fixed $r \in Q$. Then, G_0 is local symmetry group of the algebraic system of f, i.e., there exist k G_0 -invariant functions that define a submanifold of Q, and the group orbit induced by Z^i is denoted as $Q/G_0 \cong Q$.

Proof. Firstly, note that if the forward kinematics, f, satisfies f(x) = r, it also satisfies $f(g \cdot x) = r$. Here, G_0 determines the *symmetry group of the algebraic system* given by the submersion [107]. This invariance is written in terms of the Lie algebra as,

$$\mathcal{L}_{Z^{i}} f = Z^{i} (df) = Z^{i} (q)^{\top} J(q)^{\top} = 0$$
(2.36)

where $J(q) \in \mathbb{R}^{m \times n}$ is the Jacobian matrix corresponding to the submersion f. From [107, Def. 2.3], the result follows.

Property 2.2. For the fiber bundle (Q, f, Q), the action of $g \in G_0$ corresponding to the basis Z leaves the distribution \mathcal{D} invariant, i.e.,

$$\langle df(g \cdot x), \dot{x} \rangle = \langle df(x), \dot{x} \rangle.$$

Furthermore, once the group G_0 is fixed at x(0), \dot{x}_v is translated using the Adjoint group action as $(\mathrm{Ad}_g \tilde{\mu})_Q = \Psi(g^{-1})\dot{x}_v$, see [5, pp 233]. Consequently, it follows that, $Z_1\tilde{\mu} = (\mathrm{Ad}_g^{-1}\tilde{\mu})_Q$, implying that $Z \cong \mathrm{Ad}_{g^{-1}}$ is the adjoint action of G_0 .

In motion control of \mathcal{EL} systems, a virtual constraint on the primary operational space is desired, see Fig. 2.3-B. However, it is required to regulate a part of the motion as if it is described on \mathcal{Q} . This means that $r \equiv r(t)$ is not stationary. Note that Lemma 2.10 indicates only a point-dependent (local) symmetry. This is because the group identity e(r(t)) is not defined along the trajectory r(t). This is a topological obstruction to finding coordinates for the fiber, while motion occurs in the base space, \mathcal{Q} . However, the fiber is point-wise, for each $r \in \mathcal{Q}$ integrable.

This kind of point-wise symmetry is Cartan geometry, as opposed to Klein geometry, in which the fiber is homogeneous [116]. For the fiber bundle, (Q, f, Q), G_t is a Lie groupoid, which is the many-object generalization of a Lie group with a point-dependent identity map [117, 118]. A treatment of the groupoid formalism is beyond the scope of this work. However, the key conclusion here is that the foliation of Q arising from submersion, f, viewed as a Lie algebroid is integrable [118]. Thus, its vertical subspace integrates to a Lie Groupoid [119]. A topological

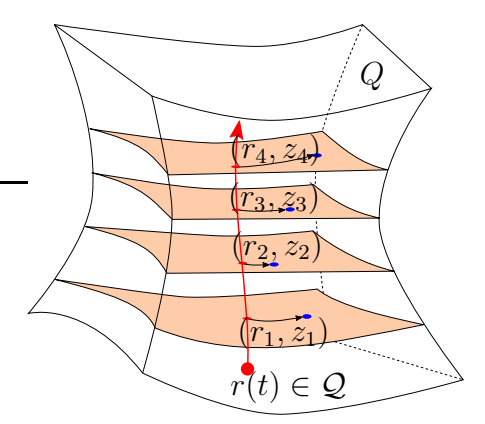


Figure 2.7: A fibered bundle (Q, f, Q, G_t) in which the fiber is not a homogeneous space resulting in non-continuous group action, i.e., $\forall r(t)$, (r_{i+1}, z_{i+1}) cannot be obtained through group action, $g.(r_i, z_i)$ for $g \in G_t$. This is because the group identity e(r(t)) varies along the trajectory r(t).

abstraction is shown in Fig. 2.7, in which the fiber space (orange leaves) do not make up a homogeneous space, and cause an obstruction to determining distances in the fiber. Although direct motion control on the Groupoid coordinates is not treated here, its Jacobian map, Z is useful.

Remark 6. In [102], it was concluded that the nullspace (vertical) subspace is non-integrable because given a closed loop in operational space $r(t) \in \mathcal{Q}$ such that $r(t_0) = r(t_f)$, $x(t_0) \neq x(t_f)$. This is, however, the non-integrability (geometric phase like a falling cat [94]) of the horizontal subspace - the orthogonal complement of the vertical subspace \mathbb{V} , which we shall explain next, but \mathbb{V} is integrable.

With the above analysis, a point $r \in \mathcal{Q}$ was fixed to uncover the structure Lie group acting on the fibers. At t = 0, the identity (0-element) of the group is fixed as $g(r) = e_0$, and thus, the fiber $f^{-1}(r)$, i.e., the nullspace, is isomorphic to the group G_0 . In the following, the condition f(x) = r is used to describe the motion of a constrained \mathcal{EL} system.

2.4.5 Constrained \mathcal{EL} Systems: Vertical Subspace

Commonly, constrained mechanics is handled using well-known mathematical tools like Lagrange multipliers [8, §6.1] and Lagrangian reduction [5]. In the former, the dynamics of $\dot{x} \in T_xQ$ are written in a constraint-consistent form, whereas, in the latter, the constraint is treated as a vertical subspace and the dynamics are written in new invariant coordinates, $w \in f^{-1}(r)$, see [5] and [8, §4.6]. In the latter case, $f^{-1}(r)$ denotes the manifold of allowable motions and its parametrization is assumed to be known.

In the following, the allowable motion is described perversely along the vertical subspace, while assuming a constraint on the submersion f. To achieve this, the fiber bundle structure (Q, f, Q, G_0) from the previous section is employed. This approach is uncommon but falls under the subject of Lagrangian mechanics on fibered manifolds [119]. This aids modeling the motion violating the submersion constraint as its horizontal subspace, which helps model the base space, Q, in terms of a quotient description, Q/G_0 . Another consequence of the sequences in (2.26) and (2.27) is the canonically defined metric on the submanifold $f^{-1}(r)$.

Def. 2.4. Induced metric on the submanifold [89, pp. 333]: Given the Riemannian manifold (Q, M) characterizing the \mathcal{EL} system, the submanifold $f^{-1}(r)$ induced by the submersion automatically inherits a pullback metric using the Jacobian, Z, of the inclusion map, Ψ , as $\Lambda(x) = Z^{\top}MZ$.

To that end, using (2.30), the canonical vertical metric is defined using the infinitesimal generator, $\mathcal{K}_v = \frac{1}{2} \langle \tilde{\mu}, \tilde{\mu} \rangle_{\Lambda}$, and Λ , is the locked inertia [14, Def. 5.2] of the system. From Lemma 4, $\tilde{\mu}$ is a spatial velocity, and hence, Λ is resolved in the spatial frame of the group motion, i.e., at e_0 .

Lemma 2.11. Consider a \mathcal{EL} system with its configuration $x \in Q$ such that $\dim(Q) = n$. Let the \mathcal{EL} system be holonomically constrained, such that the constraint is defined on another manifold Q with $\dim(Q) = m$. Correspondingly, there is a submersion $f: Q \mapsto Q$, which is a surjective submersion, i.e., k = n - m > 0. The constraint is written as, f(q) = r, where $\frac{d}{dt}r = 0$. The subspace of the tangent space TQ with allowable motion is the vertical subspace, $\mathbb{V} = \mathrm{Kern}(df)$, which is a closed Lie subalgebra isomorphic to \mathfrak{g} . Thus, the constrained \mathcal{EL} system's configuration is $g \in G_0$, where G_0 is the Lie group corresponding to \mathfrak{g} obtained through PoE. Then, the equations of motion on the k = n - m submanifold, $f^{-1}(r)$ are written by the right-trivialized Euler-Lagrange equations for the Lie group,

$$\frac{d}{dt}\frac{\delta l}{\delta \tilde{\mu}} - \left(\frac{\delta l}{\delta g}g^{-1}\right)^{\vee} = -\operatorname{ad}_{\tilde{\mu}}^{\top}\frac{\delta l}{\delta \tilde{\mu}} + F, \ \dot{g} = \tilde{\mu}^{\wedge} \cdot g$$
(2.37)

where $F \in \mathfrak{g}^{\top} \cong \mathbb{V}_{x}^{\top}$ is the right-invariant (spatial) force restricted to the submanifold $f^{-1}(r)$.

Proof. The Lagrangian for the constrained \mathcal{EL} system is $l = \mathcal{K}_v(g, \tilde{\mu}) - \mathcal{V}(g)$, where $\mathcal{V}: G \mapsto \mathbb{R}$ is the scalar potential on the Lie group G_0 . For such a system, the dynamics are given by the forced right-trivialized Euler-Lagrange equations for the Lie group G_0 , as we recall from the corollary in (2.12) of Lemma 2.5. The forcing is simply obtained using D'Alembert's work principle.

Let $\tau \in T_x^{\top}Q$, then it can be mapped to F as,

$$\langle \tau, \dot{x} \rangle = \langle F, \tilde{\mu} \rangle = \langle F, Z^{\top} \dot{x} \rangle \Rightarrow \tau = Z(x)F$$
 (2.38)

Remark 7. It is worth pointing out that $\tilde{\mu}$ is a velocity expressed relative to a configuration-dependent frame of the \mathcal{EL} system. In that sense, it is a quasivelocity, and the dynamics in Lemma 2.11 are also given by the Hamel's equations, as shown in [120, eq. 2.5].

Lemma 2.12. Consider the constrained \mathcal{EL} system described in Lemma 2.11. For the unforced case, i.e., $F = -\left(\frac{\delta \mathcal{V}}{\delta g}g^{-1}\right)^{\vee}$, the constrained Hamiltonian for the nullspace (vertical) motion is

$$\tilde{\mathcal{H}} = \mathcal{K}_v(g, \tilde{\mu}) + \mathcal{V}(g) = \langle \frac{\delta l}{\delta \tilde{\mu}}, \xi \rangle - l(q, \xi)$$
 (2.39)

and satisfies energy conservation, $\dot{\tilde{\mathcal{H}}} = 0$.

Proof. Taking the time-derivative of (2.39),

$$\dot{\tilde{\mathcal{H}}} = \frac{d}{dt} \langle \frac{\delta l}{\delta \tilde{\mu}}, \tilde{\mu} \rangle - \dot{l} \tag{2.40}$$

Computing the time-derivative of the constrained Lagrangian l,

$$\dot{l} = \langle \left(\frac{\delta l}{\delta g}g^{-1}\right)^{\vee}, \tilde{\mu} \rangle + \langle \frac{\delta l}{\delta \tilde{\mu}}, \dot{\tilde{\mu}} \rangle = \langle \left(\frac{\delta l}{\delta g}g^{-1}\right)^{\vee}, \tilde{\mu} \rangle + \frac{d}{dt} \langle \frac{\delta l}{\delta \tilde{\mu}}, \tilde{\mu} \rangle - \langle \frac{d}{dt} \frac{\delta l}{\delta \tilde{\mu}}, \tilde{\mu} \rangle \quad (2.41)$$

Using (2.41) in (2.40),

$$\dot{\tilde{\mathcal{H}}} = \langle \operatorname{ad}_{\tilde{\mu}}^{\top} \frac{\delta l}{\delta \tilde{\mu}}, \tilde{\mu} \rangle = 0 \Rightarrow \tilde{\mathcal{H}} = \text{const.}$$
 (2.42)

because of the skew-symmetry of the Lie bracket in ad-operator [10]. \Box

Lemma 2.12 is further proof of the integrability of the vertical space V.

2.4.6 The Horizontal Subspace

So far, the canonical structure available for the constraint has been discussed. To write the equations of motion using fiber bundle velocities, a geometric concept called the *connection* is required. A connection fundamentally provides a mechanism to compute a vertical velocity, $\tilde{\mu}$ using the velocity \dot{x} of the \mathcal{EL} system.

Def. 2.5. An Ehresmann connection \mathcal{A} is a vertical valued quantity on Q defined as, $\mathcal{A}_x : T_x Q \mapsto \mathbb{V}_x$ and $\mathcal{A}(\operatorname{Ver}(\tilde{\mu})) = \tilde{\mu}$, where $\tilde{\mu} \in \mathbb{V}$ [14].

Using the Ehresmann connection in Def. 2.5, the tangent space decomposes as $T_xQ = \text{Ver}(T_xQ) \oplus \text{Hor}(T_xQ)$, where $\text{Hor}(T_xQ)$ is the horizontal subspace and is orthogonal to the canonical vertical subspace. This formulation is applicable for *both*, motion analysis of constrained mechanisms and also the operational

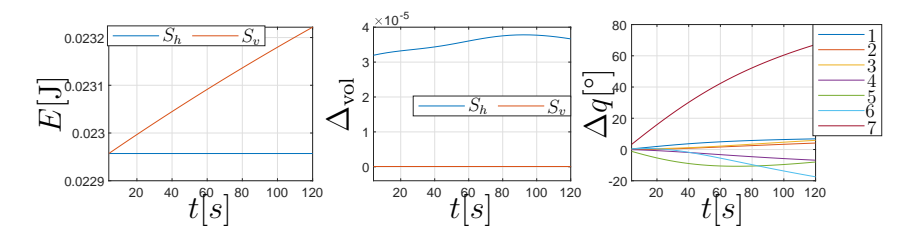


Figure 2.8: Non-integrability of the horizontal subspace (Hor (T_xQ)) of the surjective submersion, $\mathbb{T}^7 \to \mathbb{R}^3$.

space motion control of mechanisms. In particular, the connection defines the endomorphism map, $T_xQ \to T_xQ$, through the projector matrix $\mathcal{Z} = Z\mathcal{A}$, which splits any tangent velocity vector $\dot{x}^* \in T_xQ$ as,

$$\dot{x}^* = \dot{x}_v^* + \dot{x}_h^* = (\mathcal{Z})\dot{x}^* + \text{Kern}(\mathcal{Z})\dot{x}^* \tag{2.43}$$

Note that in (2.30), a subconscious choice was made as $\mathcal{A} = Z^{\top}$, while considering a fixed \dot{r} . However, the connection is a choice, and can be chosen in a way that aids or simplifies analysis. The horizontal subspace is generally the non-integrable distribution, and corresponds to the velocity \dot{r} for the submersion f. Example 4 is used to illustrate this in Fig. 2.8. In particular, the \mathcal{EL} system was initialized to run two different simulations, with $\dot{x}(0) = \dot{x}_v(0)$, say S_v , and $\dot{x}(0) = \dot{x}_h(0)$, S_h . On the left, it can be seen that the energy corresponding to S_v is conserved, as proved in Lemma 2.12. In contrast, there is no such conservation property in S_h , indicating a non-integrable behaviour. In the center, a volumetric quantity is computed as $\Delta_{\text{vol}} = \langle \Delta p, \Delta q \rangle$ for the \mathcal{EL} system, where Δp denotes change in momentum and Δq denotes the change in configuration w.r.t. the same quantities at t = 0. The latter quantity is plotted on the right. From these plots, we can empirically verify the integrability of the vertical subspace and the non-integrability of the horizontal subspace.

2.4.7 Topology of Fiber Bundle and \mathcal{EL} equations

Using the aforementioned machinery, the motion of the \mathcal{EL} system can be described using the fiber bundle velocity $(\dot{r}, \tilde{\mu})$ instead of using (2.15). The variational problem for describing the motion on the fiber bundle is not trivial. A bottom-up classification of sophistication in fiber bundles in provided in Fig. 2.9 to show how topology affects the \mathcal{EL} mechanics. Consider a fixed $r \in \mathcal{Q}$. In this case, as shown in Lemma 2.11, the Lagrangian on the fiber can be written as,

$$l(g, \tilde{\mu}) = \frac{1}{2} \langle \tilde{\mu}, \tilde{\mu} \rangle_{\Lambda(g)} - \mathcal{V}(g)$$
 (2.44)

where the \mathcal{EL} dynamics describe the variation of the structure group of the fiber $f^{-1}(r)$. For the case in which r(t) varies, a family of such Lagrangians is obtained

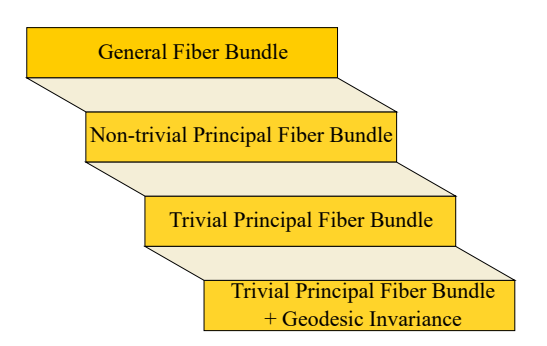


Figure 2.9: Step-wise classification of fiber bundles in increasing sophistication.

[119]. This situation has been encountered previously in the field of \mathcal{EL} systems with symmetry [5], in which $f: Q \to \mathcal{Q}$ is the submersion such that $\mathcal{Q} \cong Q/G$ is a quotient space of the Lie group G. In these special cases, the fiber space is itself the Lie group resulting in a PFB. Consequently, the velocity $(\dot{r}, \tilde{\mu})$ and its dynamics correspond to the shape velocity and the group velocity (could be non-Abelian), respectively, and their dynamics e.g., FRM [56]. Importantly, at each r, the same group G determines the fiber. In case of a trivial fiber bundle, i.e., $Q = G \times Q$, the identity of G can be globally trivialized. In a simpler topology, the metric in the fiber, Λ , is constant $\forall x$. This in turn leads to geodesic invariance, i.e., for every geodesic in $Q, x : [a, b] \to Q$, if $\dot{x} \in \mathcal{D}(x(a))$, then $\dot{x} \in \mathcal{D}(x(t))$ [121, §3]. However, in case of non-trivial fiber bundles, i.e., $Q \neq G \times Q$ is not globally a Cartesian product, the identity of G is only locally defined at each r. So, for motion control, there is an obstruction to measuring distances in the fiber while considering motion in Q. Already, for this case, the Lagrangian formalism is not readily available. Indeed, the only work I could find on this topic is [121], for which a published version was not available. This does not affect our subsequent work, as we are able to derive the dynamics using robotics tools. But this emphasizes exotic topologies that are encountered in robotics and are extremely rare in geometric mechanics. In the non-trivial case, $\Lambda \equiv \Lambda(x)$, whereas in the trivial case, $\Lambda \equiv \Lambda(r)$. In case of general fiber bundles, however, as is the case in this chapter, the structure group of the fiber is not globally the same $\forall r \in \mathcal{Q}$, and is actually a Groupoid structure, which is a relatively new topic.

In the general case considered here, the quotient map $f: Q \to Q/G_t$ holds locally for each r(t), where G_t is the Lie group locally defined at r. From a global perspective, this defines a Lie groupoid, i.e., a set of Groups [119]. Recall that this was also our conclusion from Sec. 2.4.4. In this case, the tangent space that is isomorphic to the groupoid yields a Lie algebroid. Hence, the dynamics of $(\dot{r}, \tilde{\mu})$ correspond to the dynamics of the shape velocity and the Lie algebroid of G_t . This implies that, $\forall r \in \mathcal{Q}$, the \mathcal{EL} dynamics of l gives the dynamics of the structure group G_t at r.

2.4.7.1 Operational Space as a Constraint

In operational space motion control, as in Fig. 2.3-B, the \mathcal{EL} system is not controlled directly on its configuration space Q. Instead, it is controlled on an alternative operational space given by the submersion f, e.g., on a sphere, i.e., $Q = \mathbb{S}^2$. In this case, the total motion of the mechanism decomposes into motions along operational space and internal motions [122]. In other words, the tangent space decomposes as $T_xQ = \text{Hor}(T_xQ) + \text{Ver}(T_xQ)$, where $\text{Hor}(T_xQ)$, for instance corresponds to motion on Cartesian space, Q = SE(3), that is required to be constrained, while $\text{Ver}(T_xQ)$ denotes the space of null-space motions. It is worth pointing out that, generally, such a formulation does not result in a trivial fiber bundle, i.e., $Q \neq G \times Q$. In fact, the \mathcal{EL} system need not have any symmetry of the Lagrangian along the fibers, therefore, resulting in a general fiber bundle with a Groupoid toplogy in the nullspace (fiber).

2.4.7.2 Symmetry as a Constraint

In the case of mechanisms with continuous symmetry, i.e., the Lagrangian is invariant to some configuration variables, the corresponding conjugate momenta is conserved by the equations of motion. This is a simple restatement of Noether's theorem [14, §4.1]. Let the configuration be written as $x = (q, q) \in Q$, as in Lemma 2.6, where $Q = G \times Q$ assumes a PFB topology. Let the group reconstruction formula be $\dot{q} = qV^{\wedge}$, where $V^{\wedge} \in \mathfrak{g}$ is the left-invariant group velocity written using the Lie algebra. Thus, the submersion in Def. 2.3 is trivially written as, $f: G \times \mathcal{Q} \to \mathcal{Q}$, which projects to the second argument, and its differential is $df = J = [0_{m,k} \ \mathbb{I}_{m,m}]$. Due to the presence of a global Lie group, the leftinvariant Lagrangian can be explicitly written as $l = \frac{1}{2} \langle \zeta, \zeta \rangle_{M(q)} - \mathcal{V}(q)$, where $\zeta = \begin{bmatrix} V^{\top} & \dot{q}^{\top} \end{bmatrix}$, M is the left-invariant inertia metric tensor of the whole mechanism and $\mathcal{V}:\mathcal{Q}\to\mathbb{R}$ is the symmetry-preserving potential, respectively. Generally, the inertia assumes a form, $M(q) = \begin{bmatrix} M_1(q) & M_{1q}(q) \\ M_{1q}(q)^\top & M_q(q) \end{bmatrix}$, where M_1 is the body locked-inertia, M_{1q} is the inertia coupling and M_q is the inertia metric tensor on \mathcal{Q} when V=0. Note that M_1 is the left-trivialized form of Λ in Def. 2.4, and will be shown below. This description generalizes a wide class of systems, e.g. see Fig. 5.3a, manipulator-equipped spacecraft, spacecraft with rotors (Astrobee), etc. Note that l is clearly independent of g. The conjugate momentum map is defined below.

Def. 2.6. The momentum map [5, §3.7] is a mapping, $\mathcal{J}: TQ \to \mathfrak{g}^{\top}$, which is defined as $\mathcal{J} = \langle Z, \frac{\delta l}{\delta \zeta} \rangle$, and physically represents the total right-invariant momentum of the mechanism.

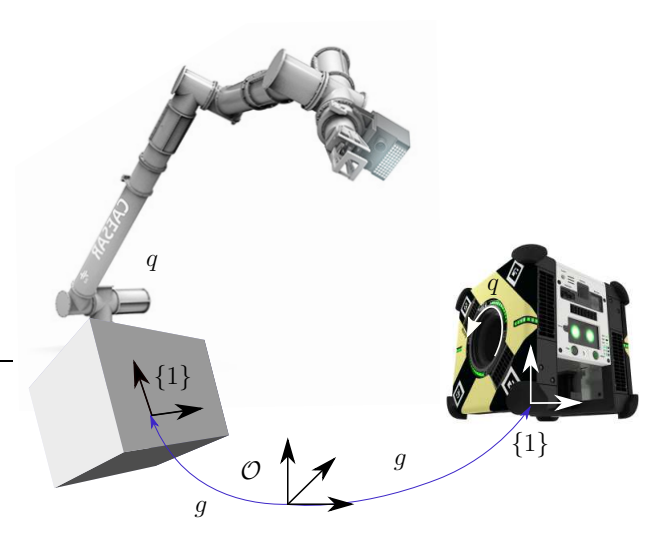


Figure 2.10: FRM with group symmetry. On left, a manipulator-equipped space-craft. On right, the Astrobee free-flyer with internal rotors.

Using Def. 2.6 and Def. 2.4, for the PFB topology, \mathcal{J} [31, App.] and Λ are

$$\mathcal{J} = \begin{bmatrix} \operatorname{Ad}_g^{-\top} & 0 \end{bmatrix} M(q) \zeta, \ \Lambda = \begin{bmatrix} \operatorname{Ad}_g^{-\top} & 0 \end{bmatrix} M(q) \begin{bmatrix} \operatorname{Ad}_g^{-1} \\ 0 \end{bmatrix}$$
 (2.45)

because $Z^{\top} = \begin{bmatrix} \operatorname{Ad}_g^{\top} & 0 \end{bmatrix}$ contains the group Adjoint action as shown in Property 2.2. In such mechanisms, the conservation principle itself imposes a mathematical constraint, which is modeled using a special type of Ehresmann connection. The conservation of \mathcal{J} is written as a constraint on the tangent-space using a geometric quantity called the *mechanical connection* [17, §3.2], defined below.

Def. 2.7. Mechanical connection: A map, $\mathcal{A}: TQ \to \mathfrak{se}(3)$, which quantifies the right-invariant velocity corresponding to \mathcal{J} , and is written as $\tilde{\mu} = \mathcal{A}\zeta = \Lambda^{-1}\mathcal{J}$. Using the momentum map in Def. 2.6,

$$\tilde{\mu} = \Lambda^{-1} \mathcal{J} = \Lambda^{-1} Z^{\top} \frac{\delta l}{\delta \zeta} = \Lambda^{-1} Z^{\top} M(q) \zeta = \underbrace{\operatorname{Ad}_{g} \left[\mathbb{I}_{6,6} \quad \mathcal{A}_{l}(q) \right]}_{\mathcal{A}} \begin{bmatrix} V \\ \dot{q} \end{bmatrix}$$
(2.46)

where $A_l = M_1^{-1} M_{1q}$ is alternatively called the local mechanical connection, and Λ is the right-invariant locked inertia [14, eq. 5.3.1] defined in Def. 2.4.

Just like the Ehresmann connection, in Def. 2.7, \mathcal{A} is the connection for the bundle map $G \times \mathcal{Q} \to \mathcal{Q}$ [123, §2]. In fact, the mechanical connection is the Ehresmann connection on the PFB, which arises due to the symmetry action of a Lie group.

Lemma 2.13. Given Def. 2.7, the tangent space decomposes as

$$\mathfrak{g} \times T_a \mathcal{Q} = \operatorname{Hor}(\mathfrak{g} \times T_a \mathcal{Q}) + \operatorname{Ver}(\mathfrak{g} \times T_a \mathcal{Q}),$$
 (2.47)

where $\mathcal{A} = 0$ defines $\operatorname{Hor}(\mathfrak{g} \times T_q \mathcal{Q})$ and the latter is the orthogonal complement. Consequently, the horizontal velocity is $\zeta_h = (-\mathcal{A}_l \dot{q}, \dot{q})$ and the vertical velocity is $\zeta_v = \zeta - \zeta_h = (V_1 + \mathcal{A}_l \dot{q}, 0) = (\mu, 0)$, respectively, which are identified using the shape and left-invariant (body) locked velocities, i.e., \dot{q} and μ , respectively.

In FRM, $\operatorname{Hor}(T_xQ)$ refers to the reduced joint-space, while $\operatorname{Ver}(T_xQ)$ denotes the space of the momentum variation. A key difference between the two types of constraints discussed in subsections 2.4.7.1 and 2.4.7.2 is the following. While in operational space motion control, $\operatorname{Hor}(T_xQ)$ denotes the space of motions parallel to the constraint, i.e., deformation along the constraint, it refers to the space of internal motions perpendicular to the momentum constraint for a FRM.

2.4.8 Nonholonomic nature of Constraints

In general, constraints are nonholonomic in nature, i.e, the constraint map of the Ehresmann connection is not preserved over a closed path in $\operatorname{Hor}(T_xQ)$, i.e., gait, see Fig. 2.4. In fact, this is observed through a net displacement in the mechanism's configuration, i.e., $x(t_0) \neq x(t_f)$. For example, in robotics, it is well known that gaits in end-effector operational space, i.e., $\operatorname{Hor}(T_xQ)$, result in a net displacement in the mechanism's natural configuration in Q [105]. Likewise, for FRM, a gait in the shape-space (internal motions) results in a net-displacement of the inertial configuration, the falling-cat phenomenon [94]. The amount of non-preservation of the constraint is quantified by its curvature, which, in simpler commutative spaces, is the exterior derivative of the constraint map. In case of non-commutative spaces, the curvature is given by the covariant exterior derivative, which also accounts for the change due to non-commutativity [19]. Informally speaking, the curvature or the exterior derivative gives the differential change in the constraint per infinitesimal area displacement due to the gait in the base space Q (chequered red in Fig. 2.4).

2.4.8.1 Curvature of Floating-base Robotic Mechanism (FRM)

A unique characteristic of the FRM is that \mathcal{A} is not preserved over a closed path in shape space, i.e., gait. In fact, this is observed through a net displacement of the FRM-base pose g due to the gait, as shown in Fig. 2.11. This is the falling-cat phenomenon [94]. Due to its g-dependency, \mathcal{A} in (3.6) is not preserved over a gait, and the amount of non-preservation is quantified by its curvature. Based on the g-dependency, just as \mathcal{A} is defined locally by \mathcal{A}_l , the curvature of \mathcal{A} is defined by the local curvature of \mathcal{A}_l [14, Def. 3.5], denoted as $D\mathcal{A}_l$, where D is the exterior covariant derivative operator, see [20, §B.6]. The local curvature, DA_l , is significant because it appears explicitly in the \mathcal{LP} equations, as I shall see later, and is also employed for locomotion analysis in geometric mechanics [20, 124, 125], as described below.

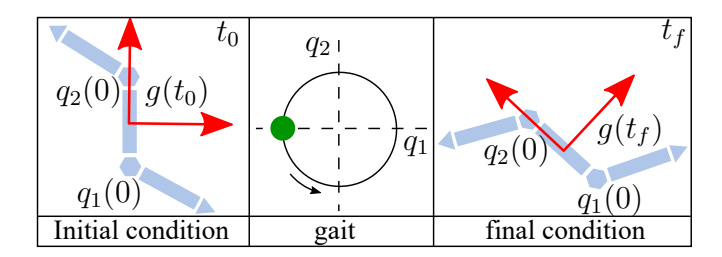


Figure 2.11: Net displacement of the FRM-base, $\delta g = g(t_0)^{-1}g(t_f)$, due to a gait. Left: FRM initial (t_0) configuration; Center: gait with starting point (green) and direction (arrow); Right: FRM final (t_f) configuration.

In particular, DA_l is exploited to estimate the net displacement of the FRM-base over a gait, i.e., $\delta g = g(t_0)^{-1}g(t_f)$ in Fig. 2.11. Common approaches presuppose that the time-integral in $\dot{g} = gV^{\wedge}$, for $\tilde{\mu} = 0_6$, is converted into an area integral by invoking Stokes' theorem, see Appendix A.3.1. In short, given an infinitesimal path displacement in shape space, $dq \in \mathbb{R}^n$, $(-A_l dq)^{\wedge}$ in $\dot{g} = gV^{\wedge}$ defines a $\mathfrak{se}(3)$ infinitesimal displacement of the FRM-base. Similarly, for an infinitesimal area displacement over a gait in shape space $dA \in \mathbb{R}^n \times \mathbb{R}^n$, $(-DA_l dA)^{\wedge}$ also quantifies a net displacement. Note that the area dA requires two base vectors to be uniquely determined.

Def. 2.8. The local curvature is $(DA_l)(q, x)y = (dA_l)(q, x)y - \operatorname{ad}_{A_lx}A_ly$, where $x, y \in \mathbb{R}^n$ are the two vectors in shape space that uniquely define the basis for an oriented differential area in the shape. The term $dA_l(x)y$ is the exterior derivative operator and measures the intrinsic change in A_l across the shape space; and $\operatorname{ad}_{A_lx}A_ly$ is the Lie bracket, which measures the extrinsic change in A_l , as the allowable velocity space rotates with the FRM-base body frame due to the non-abelian property of SE(3) [20].

Since SE(3) is non-abelian, an exact solution for δg in Fig. 2.11 is not feasible for the FRM. However, an approximate $\delta \hat{g}$ over a gait area \mathcal{U} is estimated as [20],

$$\zeta = \log(\delta \hat{g}) = -\int \int_{\mathcal{U}} D\mathcal{A}_l dA \approx \log(\delta g),$$
 (2.48)

using visual tools to compute the area integral in (2.48), see Appendix A.3.2. The approximation errors in (2.48) are mitigated by computing the area integral therein in the minimum perturbation coordinate frame, which minimizes non-commutativity, instead of the group frame of the floating platform in the FRM, see [19, 20]. In [125], an alternative approximation of the integral of $\dot{g} = gV^{\wedge}$ was used. In such locomotion approaches, DA_l is essential, and is traditionally computed using symbolic or numeric methods.

2.5 Mechanical Attributes for Motion Control

In the following, the mechanical attributes that are relevant for characterization of motion control of mechanisms in this thesis are defined.

2.5.1 Impedance/Compliance Control

Consider a mechanism with $x, \hat{x} \in Q$ as the current and the setpoint equilibrium configurations, respectively. The relative motion between the two configurations is quantified by $\dot{\tilde{x}} = x - T(x, \hat{x})\dot{\tilde{x}}$, where $T: T_{\hat{x}}Q \to T_xQ$ is the linear map to transform a vector from one tangent space to another.

Def. 2.9. Mechanical Impedance: It is a tuple (M, γ, ψ) , where $M: T_xQ \to T_x^\top Q$ is the inertia metric tensor, $\gamma: Q \to T_x^\top Q$ is the differential of a scalar potential, i.e., $\gamma = -d_x \mathcal{V}_x(x,\hat{x})$, and $\psi: T_xQ \to T_x^\top Q$ is the differential of a Rayleigh dissipation potential, i.e., $\psi = -d_x \mathcal{V}_x(\dot{x},\dot{x})$, which characterizes the equations of motion about an equilibrium point $(\hat{x},\dot{\hat{x}}) \in T_{\hat{x}}Q$. By characterizes, I mean that the equation of motion is,

$$M(x)\nabla_{\dot{x}}\dot{\tilde{x}} + \gamma(x,\hat{x}) + \psi(x,\hat{x},\dot{\hat{x}}) = F_d$$
(2.49)

where ∇ is the Levi-Civita connection of the Riemannian metric on Q [10], and $F_d \in T_x^\top Q$ is the input force.

In Def. 2.9, (2.49) is simply the Newton's law on non-Euclidean spaces. The map γ is commonly called the stiffness force, while ψ is the damping force. Together, (γ, ψ) constitute the commonly-known Proportional-Derivative (PD) control action. In the following two definitions, damping is inherently assumed in the motion control system.

Def. 2.10. Impedance Control: Given a displacement $(\delta x, \delta \dot{x})$ from the equilibrium $(\hat{x}, \dot{\hat{x}}) \in T_{\hat{x}}Q$, it is the motion control to ensure that closed-loop equations of motion are characterized by a configurable impedance $(\hat{M}, \hat{\gamma}, \hat{\psi})$. A subset of impedance control is stiffness control, which characterizes $(\hat{\gamma}, \hat{\psi})$ for the closed-loop motion with the natural inertia M. In essence, impedance control configures the tuple of scalars $(\hat{T}, \hat{V}_x, \hat{V}_{\hat{x}})$, which are the configurable kinetic energy metric, scalar potential and the Rayleigh dissipation potential, respectively.

In many mechanisms, the motion control system is indirectly commanded as a $(\delta x, \delta \dot{x})$ displacement relative to $(x, \dot{x}) \in T_x Q$. In this case, the inverse tuple, $(\hat{M}^{-1}, \hat{\gamma}^{-1}, \hat{\psi}^{-1})$ is configured, which is commonly called *admittance control*. If $(\hat{\gamma}^{-1}, \hat{\psi}^{-1})$ are instead specified, it is *compliance control*.

2.5.2 Passivity in \mathcal{EL} systems

In the following, key concepts about L_2 -stability, asymptotic stability and feedback interconnection of systems are introduced. These concepts will be employed in Chapter 5 for motion control analysis. For further details on passivity and Lyapunov stability, the reader is referred to [3, Def. A.8] and [126], respectively.

Def. 2.11. Given, the state of a \mathcal{EL} system, $x \in X \subset \mathbb{R}^a$, with input $u \in U \subset \mathbb{R}^b$ and output $y \in Y \subset \mathbb{R}^c$, the dynamical system

$$\Sigma : \dot{x} = h(x, u), \ y = k(x, u)$$
 (2.50)

is said to be passive if there exists a continuously differentiable function $V \geq 0$ (storage function), such that $\dot{V} \leq y^{\top}u$. Moreover, it satisfies Output Strict Passivity (OSP) if $\dot{V} \leq -\delta ||y||^2 + y^{\top}u$, $\delta > 0$. If (2.50) satisfies stability of the origin, i.e., $h(0,0) = 0_a$, $k(0,0) = 0_c$, and is also OSP, then it is finite-gain L_2 -stable and its L_2 -gain $\leq \frac{1}{\delta}$ [126], which implies bounded input bounded output for the map $u \mapsto y$. The notion of asymptotic stability using passivity is introduced below.

In Def. 2.11, OSP is a formal way of explaining terminal velocity, i.e., a system experiencing an input u like gravity will reach a finite terminal velocity, y, as $t \to \infty$. This is a powerful concept to prove robustness against disturbances, e.g., interactions of a robot with its environment.

Def. 2.12. Zero-state observability and detectability [3, Def. A.8] An \mathcal{EL} system of the form $\dot{x} = h(x)$, $x \in \mathbb{R}^n$ is Zero-State Observable (ZSO) from the output y = k(x), if for all initial conditions $x(0) \in \mathbb{R}^n$, we have $(y(t) \equiv 0 \Rightarrow x(t) = 0)$. It is Zero-State Detectable (ZSD) if the output satisfies $y(t) \equiv 0 \Rightarrow \lim_{t \to \infty} x(t) = 0$.

Def. 2.13. [3, Prop. A.9]Suppose the system Σ is OSP with positive semidefinite storage function H > 0.

- 1. If Σ is ZSO, then H(x) > 0, $\forall x \neq 0$.
- 2. If H(x) > 0, $\forall x \neq 0$, H(0) = 0 and Σ is ZSD, then x is a locally asymptotically stable equilibrium of (2.50)

In this thesis, feedback interconnection of subsystems will be encountered in the context of systems with symmetry (\mathcal{LP} systems), and the following concept is introduced as a starting point for the analysis.

Def. 2.14. Invariance of Passivity [3, Prop. A.6] Consider the input-output system in a feedback interconnection as depicted in Fig. 2.12 with state $x = (x_1, x_2)$, output $y = (y_1, y_2)$ and input $u = (u_1, u_2)$. If Σ_1 and Σ_2 are both passive then, $\Sigma: u \mapsto y$ is also passive. If furthermore they are OSP then $\Sigma: u \mapsto y$ is also OSP.

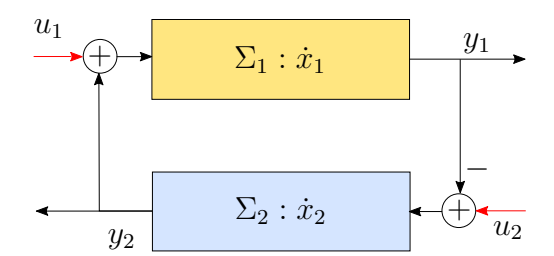


Figure 2.12: Passive interconnection of subsystems.

2.5.3 Variable Inertia in \mathcal{EL} systems

In this thesis, I consider general \mathcal{EL} systems with configuration-dependent inertia, e.g., a robotic manipulator. For such systems, the following fundamental matrices [127] provide two key variations of inertia, and are employed in Chapters 3 and 6. Consider the \mathcal{EL} system in Lemma 2.2 with inertia tensor M(x).

Def. 2.15. Given velocities $y, z \in T_xQ$, the partial derivative of the scalar product $\langle y, z \rangle_{M(x)}$ relative to the configuration (x) is written using the Inertia Derivative (ID) matrix [127, Def. 1], $M_d(x,y)^{\top}$, as $\frac{\partial \langle y, z \rangle_M}{\partial x} = M_d(x,y)^{\top}z$. In (2.3), the ID matrix is required to define the partial derivative of the kinetic energy relative to the configuration as $\frac{\partial \langle \dot{x}, \dot{x} \rangle_M}{\partial x} = M_d(q, \dot{x})^{\top}\dot{x}$.

Def. 2.16. The Inertia Velocity (IV) matrix [127, Def. 2] is a symmetric matrix, $M_v(x,y)$, given any velocity, $y \in T_xQ$, which is interpreted as $M_v(\dot{x}) = \frac{dM}{dt}$ when $y = \dot{q}$, and appears in (2.3).

2.6 Computations for Multibody mechanisms

The development of computationally efficient multibody algorithms in the robot dynamics community [23, 128, 129] has been pivotal not only in control of robotic mechanisms, but has also pervaded to other branches of mechanics, like molecular dynamics [130]. While direct symbolic computation is the closest in structure to the purely Lagrangian formulation, it is computationally inefficient [131]. Thus, the fast iterative/recursive algorithms have been favoured for real-time control purposes. In such approaches, each link is treated as a constrained rigid body [23]. Its configuration lies on a non-Abelian Lie group, and the kinematic constraint defines the joint type, e.g. revolute, prismatic. The group depends on the nature of spatial complexity, e.g. SE(3) (SE(2)) for spatial (planar, respectively) cases. Its kinematic quantities (position, velocity and acceleration) and dynamic quantities (forces) are computed using the same quantities of the previous link and its own joint quantities in an iterative loop. Applying D'Alembert's principle using the external forces yields the forced equation of motion. These algorithms are classified as Newton-Euler [128] or Lagrangian [129, 132], and are equally

competitive [133]. The topics outlined in this section provide the preliminary material for the computations derived in Chapter 3.

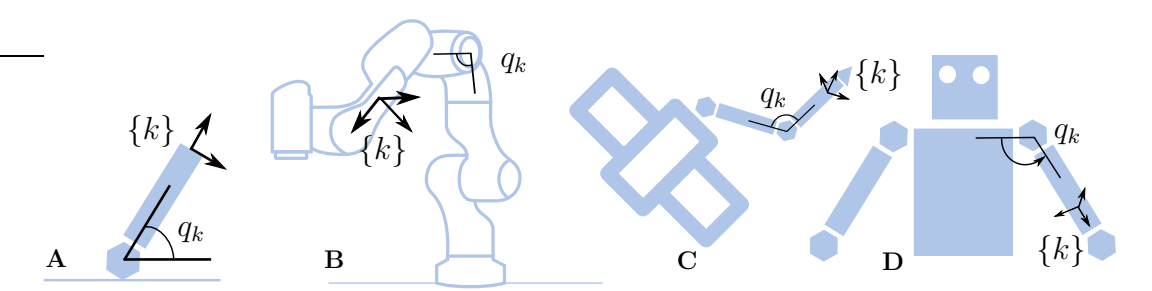


Figure 2.13: Articulated robotic mechanisms. **A**: An inverted pendulum, **B**: a fixed-base manipulator, **C**: a manipulator-equipped spacecraft and **D**: a humanoid torso with manipulators, in which $\{k\}$ is the k^{th} -link frame and q_k is the position of the k^{th} joint.

2.6.1 Rigid-Body Motion

To this end, the constrained motion of a rigid body is revisited. The k^{th} link in Fig. 2.13 is modeled as a rigid-body with pose $g_k \in SE(3)$. Its time variation is given by the reconstruction formula,

Kinematics
$$\{\dot{g}_k = g_k V_k^{\wedge}, g_k \equiv g_k(R_k, p_k),$$
 (2.51)

where $V_k^{\wedge} \in \mathfrak{se}(3)$ is its left-invariant body velocity. Its left-invariant Lagrangian is $l_k = \frac{1}{2} \langle V_k, V_k \rangle_{M_k}$, where $M_k \in \mathbb{R}^{6 \times 6}$ is the rigid-body inertia tensor (see Appendix A.1.2). The link motion is governed by the forced *Euler-Poincaré* equation, as in (2.8), which is written as,

Dynamics
$$\left\{ \mathcal{EP}(V_k, \dot{V}_k) = M_k \dot{V}_k + (-\operatorname{ad}_{V_k}^{\top} M_k) V_k = F_k \right\},$$
 (2.52)

where $F_k \in \mathbb{R}^6 \cong \mathfrak{se}(3)^{\top}$ is the left-invariant body wrench arising due to the joint constraint, joint actuation, etc. In (2.52), $\operatorname{ad}_{V_k}^{\top} M_k$ encapsulates the SE(3) structural coefficients, see (A.1) in Appendix A.1.2,.

2.6.1.1 Body-level factorization

In Lyapunov-based stability analysis for motion control of mechanisms, the passivity or the skew-symmetry of the matrix of Coriolis/centrifugal (CC) terms is required [10, 62, 134]. While the former is the energy conservation property of the unforced dynamics, the latter is a stronger property required in tracking control and observer design, as explained in Appendix A.2.1. The CC matrix of a multibody mechanism is obtained using (2.52) for each link. Thus, the CC matrix

in (2.52), which is known as the *body-level factorization* has ramifications on the properties of multibody dynamics equations, as shall be demonstrated later.

Abstracting the group notation, the dynamics in (2.52) is written purely in vector notation as,

$$M_k \dot{V}_k + \mathcal{C}(V_k) V_k = F_k \tag{2.53}$$

where $C(V_k) \in \mathbb{R}^{6\times 6}$ is the body-level factorization [135] of the Coriolis/Centrifugal (CC) terms. A key property is that while $C(V_k)V_k$ is unique, $C(V_k)$ is non-unique. In the following, I state the commonly used choices below.

1. Natural \mathcal{EP} factorization: $\mathcal{C}(V_k) = \operatorname{ad}_{V_k}^{\top} M_k$. It satisfies passivity, i.e.,

$$V_k^{\top} \operatorname{ad}_{V_k}^{\top} M_k V_k = (\operatorname{ad}_{V_k} V_k)^{\top} M_k V_k = 0$$
 (2.54)

However, it does not satisfy skew-symmetry. Additionally, due to the non-abelian property of SE(3), the bivariate map $(\operatorname{ad}_v^\top M_k)w$ is not commutative, i.e., $(\operatorname{ad}_v^\top M_k)w \neq (\operatorname{ad}_w^\top M_k)v$, given $v, w \in \mathbb{R}^6$.

2. Augmented \mathcal{EP} factorization: Using the property $\mathrm{ad}_x x = 0$, the natural \mathcal{EP} factorization was augmented in [22] with an extra term as follows,

$$C(V_k) = \left(\operatorname{ad}_{V_k}^{\top} M_k - M_k \operatorname{ad}_{V_k}\right)$$
 (2.55)

which satisfies $C(V_k)V_K = \operatorname{ad}_{V_k}^{\top} M_k V_K$ and skew-symmetry by construction.

3. Bilinear \mathcal{EP} factorization: For common Lie groups in robotics, e.g. SE(3), SO(3), SE(2) etc., the natural \mathcal{EP} factorization in the \mathcal{EP} equation of Lemma 2.4 leads to a bilinear map, i.e., $\operatorname{ad}^{\top}: (\mathfrak{g}, \mathfrak{g}^{\top}) \to \mathfrak{g}^{\top}$. Due to the bilinearity, an alternative bilinear map exists, $\operatorname{ad}_{(\bullet)}^{\sim}: (\mathfrak{g}^{\top}, \mathfrak{g}) \to \mathfrak{g}^{\top}$, such that, given $v \in \mathbb{R}^d \cong \mathfrak{g}$, $(\operatorname{ad}_v^{\top}) \frac{\delta l_0}{\delta V} = \operatorname{ad}_{\frac{\delta l_0}{\delta V}}^{\sim}v$. For the k^{th} -link on SE(3),

$$(\operatorname{ad}_{v}^{\top})\frac{\delta l_{k}}{\delta V_{k}} = \operatorname{ad}_{\frac{\delta l_{k}}{\delta V_{k}}}^{\sim} v = \operatorname{ad}_{M_{k}V_{k}}^{\sim} v.$$
(2.56)

Although I proposed this factorization in the context of observer design in [62], see (A.2) in Appendix A.1.2, I attribute the contribution to the earlier works [30], [26] and [28] in the context of multibody mechanisms.

Property 2.3. The dynamics in (2.52) written alternatively using the property in (2.56) satisfies skew-symmetry, i.e., $x^{\top} \left(\frac{d}{dt} M_k - 2(-\operatorname{ad}_{M_k V_k}^{\sim}) \right) x = 0$ for $x \in \mathbb{R}^6$. A corollary is that this property is invariant to a time-varying change of basis.

Proof. See Lemma A.1.3 in Appendix A.1.2.

Therefore, using the skew-symmetric operator, $\operatorname{ad}_{(\bullet)}^{\sim}$, (2.56) enables the exchange of velocity arguments with the $\operatorname{ad}_{(\bullet)}^{\top}$ operator to compute the equivalent CC wrench. Using (2.56), $\mathcal{C}(V_k) = \operatorname{ad}_{M_k V_K}^{\sim}$.

4. The Riemannian connection [10, eq. 8], [6]: For a Lie group, G, the Riemannian connection is written as,

$$\nabla_v w = \frac{1}{2} \mathrm{ad}_v w - \frac{1}{2} \mathbb{M}^{-1} \left(\mathrm{ad}_v^{\top} \mathbb{M} w + \mathrm{ad}_w^{\top} \mathbb{M} v \right)$$
 (2.57)

where $\mathbb{M}: \mathfrak{g} \to \mathfrak{g}^{\top}$ is the left-invariant metric on G. In (2.57), $\nabla_v w$ denotes the left-invariant covariant derivative of the vector field w along the vector field v, which is computed using the Levi-Civita (torsion-free) connection ∇ on G. Using ∇ for the rigid body, G = SE(3),

$$C(v)w = M_k \nabla_v w = \frac{1}{2} M_k \operatorname{ad}_v w - \frac{1}{2} \left(\operatorname{ad}_v^\top M_k w + \operatorname{ad}_v^\top M_k w \right)$$
$$= \frac{1}{2} \left(M_k \operatorname{ad}_v - \left(\operatorname{ad}_v^\top M_k + \operatorname{ad}_{M_k v}^\sim \right) \right) w$$
(2.58)

where in the last equality the bilinear \mathcal{EP} factorization is used. By inspection, one can verify that this choice of $\mathcal{C}(V_k)$ satisfies skew-symmetry. This factorization was used in [136], and shown in [135] to be Christoffel-consistent. The main reason for this is that (2.57) results directly from the torsion-free connection property, see [6], which is used in differential geometry to compute the Christoffel symbols. A geometric picture of this choice was missing, which I have provided here.

2.6.2 Recursive Lagrangian Mechanics

Let the configuration of the mechanisms in Fig. 2.13 be $r \in Q \subset \mathbb{R}^n$, where Q is the configuration manifold. Note that Q might contain basis which is commutative (**A** and **B**), non-commutative (e.g. SO(3) for a rigid-body satellite) or both (**C** and **D**). Thus, the configuration velocity is written as $\zeta \in T_r Q \subset \mathbb{R}^n$. In the case that Q contains purely commutative basis, $\zeta = \dot{r}$, while in case that Q contains a Lie group as a configuration variable, ζ might contain trivialized velocity (left or right) of the Lie group, see Sec. 2.1. The pose of the k^{th} -link is obtained as a map $g_k = f_k(r)$, where $f_k : Q \to \text{SE}(3)$ is the forward kinematics map. The link velocity is obtained using the pushforward, i.e., the differential of the map along system velocity as $df_k(\dot{r}) = J_k(r)\zeta = V_k$, where $J_k = g_k^{-1}\frac{\delta g_k}{\delta r}$ such that $J_k : T_r Q \to \mathbb{R}^6 \cong \mathfrak{se}(3)$ is the left-invariant (body) Jacobian of the forward kinematics map [90]. The joint torques/forces are obtained using the pullback, i.e., $df^{\top}(F_k) = J_k(r)^{\top} F_k = F_k$, where $F_k \in T_r^{\top} Q$ denote the torques/forces on the mechanism due to the wrenches acting on the k^{th} -link.

Assumption 2.4. The mechanisms considered in Fig. 2.13 are characterized by a simple Lagrangian, i.e., $L = \mathcal{T} - \mathcal{V}$, where $\mathcal{T} = \frac{1}{2} \langle \zeta, \zeta \rangle_{M(r)}$ is the kinetic energy metric based on the inertia tensor M(r) and $\mathcal{V}(r) : Q \to \mathbb{R}$ is the potential energy.

Let us first consider that Q constitutes a commutative basis. In this case, the motion is governed by the \mathcal{EL} equation from Lemma 2.2. Under Assumption 2.4, the forced \mathcal{EL} equation from Lemma 2.3 is written in vector notation as,

$$\mathcal{EL}(r,\dot{r},\ddot{r}) = M(r)\ddot{r} + C(r,\dot{r})\dot{r} = F + \nabla_r V \tag{2.59}$$

where $M, C \in \mathbb{R}^{n \times n}$ are the matrices of inertia and CC terms, respectively, and $\tau \in T_r^\top Q \subset \mathbb{R}^n$ contains the generalized torques/forces acting on the mechanism. By inspection, it can be seen that, $\frac{dM(r)}{dt}\dot{r} - \frac{1}{2}\frac{\delta}{\delta r}\langle \dot{r}, \dot{r}\rangle_M = C(r, \dot{r})\dot{r}$.

Secondly, consider that $Q = \mathrm{SE}(3) \times \tilde{Q}$, i.e., Q is a direct product of the non-commutative $\mathrm{SE}(3)$ group and commutative topology \tilde{Q} , e.g. \mathbf{C} and \mathbf{D} . Let the configuration of the mechanism be denoted as $r = (g_1, q)$. Considering symmetry-breaking potential forces (e.g. gravity) as external, the presence of the group coordinate g_1 yields a reduced Lagrangian with inertia, $M \in \mathbb{R}^{(6+n)\times(6+n)}$, as $l(q,\zeta) = \mathcal{T} - \mathcal{V}$, where $\mathcal{T} = \frac{1}{2}\langle \zeta, \zeta \rangle_M$, $\zeta = \begin{bmatrix} V_1^\top & \dot{q}^\top \end{bmatrix}^\top$ is the configuration velocity, $\zeta^{\wedge} = g_1^{-1}\dot{g}_1 \in \mathfrak{se}(3)$ for the pose. The motion resulting from $l(q,\zeta)$ are governed by the Hamel's equations (Lemma 2.6). In robot dynamics, the floating-base formulation [22, 23, 26] for the Hamel's equations are written as,

$$\underbrace{\begin{bmatrix} M_b(q) & M_{bq}(q) \\ M_{bq}(q)^\top & M_q(q) \end{bmatrix}}_{M(q)} \begin{bmatrix} \dot{V}_1 \\ \ddot{q} \end{bmatrix} + C(q, \zeta) \begin{bmatrix} V_1 \\ \dot{q} \end{bmatrix} = \underbrace{\begin{bmatrix} \mathcal{F}_1 \\ \tau \end{bmatrix}}_{F} + \nabla_q \mathcal{V}, \tag{2.60}$$

where M_b, M_{bq}, M_q are the locked, coupling and manipulator inertias, respectively, $C \in \mathbb{R}^{(6+n)\times(6+n)}$ is the CC matrix, and $\mathcal{F}_1 \in \mathbb{R}^6 \cong \mathfrak{se}(3)^{\top}$ and $\tau \in \mathbb{R}^n$ are the forces acting on the base and joints, respectively.

Remark 8. Abstracting the commutative/non-commutative basis, both (2.59) and (2.60) can be written compactly as,

$$M(r)\dot{\zeta} + C(r,\zeta)\zeta = F + \nabla_r \mathcal{V}$$
 (2.61)

A notable advantage of modeling each link as a rigid-body in Sec. 2.6.1 is the efficient multibody computation using the recursive Newton-Euler algorithm [28, 137]. The recursive form yields an iterative computation of the dynamic matrices M, C in the equations of motion in (2.61) [22, 26, 28], which are outlined below.

Lemma 2.14. The matrices M, C in the motion equation in (2.61), are computed, e.g. see [28, eq. 18], using the body-level factorization, C, as follows,

$$M = \sum_{k} J_{k}^{\top} M_{k} J_{k}, \quad C = \sum_{k} J_{k}^{\top} (\mathcal{C}(V_{k}) J_{k} + M_{k} \dot{J}_{k}). \tag{2.62}$$

where J_k is the link Jacobian relative to the base frame.

Proof. The velocity of the k^{th} link is $V_k = J_k(r)\zeta$ and its time-derivative is written as $\dot{V}_k = J_k(r)\dot{\zeta} + \dot{J}_k(\zeta)\zeta$. Substituting this in (2.53) for all links, pre-multiplying J_k^{\top} on both sides and considering that the constraint reaction wrenches disappear after projection results in (2.61) with M, C as in (3.2). Note that an iterative loop is required in Lemma 2.14, and J_k and \dot{J}_k are obtained beforehand in this loop through a recursive computation, as shown in [22, §VI].

Lemma 2.14 is directly applicable to serial kinematic mechanisms. For general tree mechanisms, an outward summation for each branch of the tree is required in (3.2).

Property 2.4. Given the equation of motion in (2.61), and the computation of Lemma 2.14 using any body-level factorization in (2.53), the dynamic matrices M, C satisfy the passivity property $\zeta^{\top}(\frac{dM}{dt}(\zeta) - 2C(\zeta))\zeta = 0$ [28]. However, only the augmented \mathcal{EP} , bilinear \mathcal{EP} and the Riemannian connection factorizations satisfy the skew-symmetric property, i.e., $w^{\top}(\frac{dM}{dt}(\zeta) - 2C(\zeta))w = 0$ for an arbitrary $w \in \mathbb{R}^n$ [135]. Among these factorizations, the latter provides a Christoffel-consistent factorization, i.e., preserves the structural coefficients of Q.

Remark 9. Contrasting (2.61) with \mathcal{EL} and Hamel's equations from Lemmas 2.1 and 2.6, it is clear that the ease of computation in Lemma 2.14 comes at the cost of abstracting the structure of the Lagrangian equations. In particular, C has no discernible structure, and does not provide much insight for model-based control design. This has been well-known in robotics [131].

2.6.3 Constraints and Transformations

Lemma 2.14 provides an efficient computation of (2.61), which is the dynamics of the mechanism's natural configuration residing on Q. In such mechanisms, it is common to encounter constraints which arise from a kinematic coupling or conservation of momenta due to symmetry. As I revealed in Sec. 2.4, these constraints decompose the tangent space T_rQ along horizontal (perpendicular to the constraint) and vertical (parallel to the constraint) directions. It is convenient for motion analysis to rewrite (reduce) the equations of motion. In the following, Lemma 2.14 is exploited to obtain the variation of the vertical and horizontal velocities as an alternative dynamics description of the mechanism. This alternative emphasizes the symmetry explicitly, and will be employed in Chapter 3.

2.6.3.1 Newtonian Transformation

Consider the mechanism in (2.61), for which the equation of motion on the natural configuration manifold Q is known. An arbitrary velocity ξ can be defined simply by using a linear map, $\xi = L(r)\zeta$, such that ξ generalizes a velocity (or quasi-velocity) in operational space, horizontal and (or) vertical tangent space due to

constraints or symmetry. In robotics, L can be the push-forward Jacobian map of forward kinematics of the mechanism, i.e., $L(r) = \frac{\delta f}{\delta r}$, or appear from the Pfaffian form of a constraint (symmetry), which is non-integrable, i.e., $dL(r)\xi \neq 0$. In this case, the motion equations in (2.61) are written using the new velocities ξ . I call this a Newtonian transformation because although (2.61) is derived from a scalar Lagrangian through variational principles, the same cannot be concluded for the transformed equations of motion.

Assumption 2.5. The linear map L satisfies $\operatorname{rank}(L) = \dim(Q)$ (full-rank) and is invertible, at least, in a local neighbourhood of a configuration $r_0 \in Q$.

Lemma 2.15. Given the mechanism in (2.61), with a non-integrable linear map $\xi = L(r)\zeta$ satisfying Assumption 2.5, the dynamics of ξ are written as,

$$\Lambda(r)\dot{\xi} + \Gamma(r,\zeta)\xi = \mathcal{F} + L^{-\top}\nabla_r \mathcal{V}$$
(2.63)

which is obtained in two of the following ways.

- 1. ζ -Iteration+ ξ -Transformation: Applying Lemma 2.14, $\forall k, \ \dot{V}_k = J_k \dot{\zeta} + \dot{J}_k \zeta$ is substituted in (2.52), and pre-multiplied with J_k^{\top} on both sides, resulting in the dynamics of the configuration velocity, ζ . Following this, $\dot{\xi} = L^{-1}\dot{\zeta} + \dot{L}^{-1}\zeta$ is substituted in $\dot{\zeta}$ from the previous result. This results in $\Lambda(r) = L^{-\top}ML^{-1}$ and $\Gamma(r,\zeta) = L^{-\top}(M\dot{L}^{-1} + CL^{-1})$ and $\mathcal{F} = L^{-\top}F$.
- 2. Direct ξ -Iteration: Secondly, I propose an alternative way of using direct iteration to compute the dynamics of ξ . In particular, $\forall k$, V_k is rewritten as a map of the new velocity, ξ , as

$$V_k = J_k \zeta = J_k L^{-1} \xi \Rightarrow \dot{V}_k = J_k L^{-1} \dot{\xi} + \frac{d}{dt} (J_k L^{-1}) \xi$$
 (2.64)

Substituting R.H.S in (2.52), and pre-multiplying $(J_k L^{-1})^{-\top}$ yields the result in a link-wise iterative fashion. This method was published in [56].

Both approaches in Lemma 2.15 yield the same motion equations, and hence, the same inertia and CC matrix (see [135, Rem. 6]). However, as will be seen later, in some cases, J_kL^{-1} can be partitioned further, which enables the factorization of the CC matrix with more structure. Although a computational comparison merits its own scope, I provide a preliminary idea below. The computation of Γ in Lemma 2.15-1 requires one pass of n iterations (link-wise), and an additional numerical transformation. Lemma 2.15-2, however, requires 2 passes with n iterations in each pass. One pass is nominally given by the computation of L, J_k and J_k , followed by another pass to obtain (3.4).

Property 2.5. For mechanisms, the equations of motion obtained using a Newtonian transformation preserves passivity or energy conservation property, i.e.,

$$x^{\top} \left(\frac{d}{dt}\Lambda(r) - 2\Gamma(r,\zeta)\right) x = 0, \ x = \zeta$$
 (2.65)

If the body-level factorization of Γ is chosen to be skew-symmetric, then the above property holds for arbitrary x. Additionally, if the Riemmanian connection factorization is used as the body-level factorization, then the transformed CC matrix Γ is Christoffel-consistent [135].

2.7 Conclusion

This chapter introduced the preliminary material that is relevant for the exposition of concepts in this thesis. In particular, the concept of symmetry in the context of Lagrangian mechanics was formally introduced. A detailed theory on constrained motion of mechanisms was provided. This is a unified framework to generalize the dynamics and motion control problem of FRM and hierarchical control. Such a theory has not been reported earlier, and this was the key contribution of this chapter. The concepts of impedance control and passivity were introduced to familiarize the reader with the preliminaries of PBC. A short treatment of multibody dynamics was provided as a preliminary to derive the \mathcal{LP} dynamics of the FRM in the next chapter.

Motion of Floating-base Robotic Mechanism (FRM)

(6 The falling-cat (FRM) can right itself using the concept of inducing a change in the state of a system by exploiting the underlying geometry of the system itself, which connects it to quantum physics, optics, and Foucault's pendulum mechanics [138].

G. J. Gbur, Falling Felines and Fundamental Physics, 2019

3.1 Introduction

A FRM is an articulated robotic mechanism mounted on a movable platform, and is ubiquitous in several domains [25–27], as shown in Fig. 3.1. The commonly-known equations of motion for the FRM are the inertia-coupled dynamics of its configuration (FRM-base and shape) velocities. These dynamics are efficiently computed by considering the FRM as a kinematic chain using the standard iterative algorithm in Lemma 2.14. These equations also exhibit the skew-symmetry (or passivity) property, which is useful for stability analyses in motion control [27]. From the Lagrangian perspective in geometric mechanics (Lemma 2.6), the dynamics above are seen as a set of an \mathcal{EP} equation and an \mathcal{EL} equation, which correspond to the motion of the FRM-base and the shape (joints), respectively. This set is called a system of Hamel's equations [31, 94]. Among kinematic chain systems, the FRM is unique in its well-known property of momentum conservation, i.e., it is an \mathcal{EL} system with inherent symmetry. This property is modeled as a Pfaffian-like velocity constraint using the mechanical connection, as I outlined

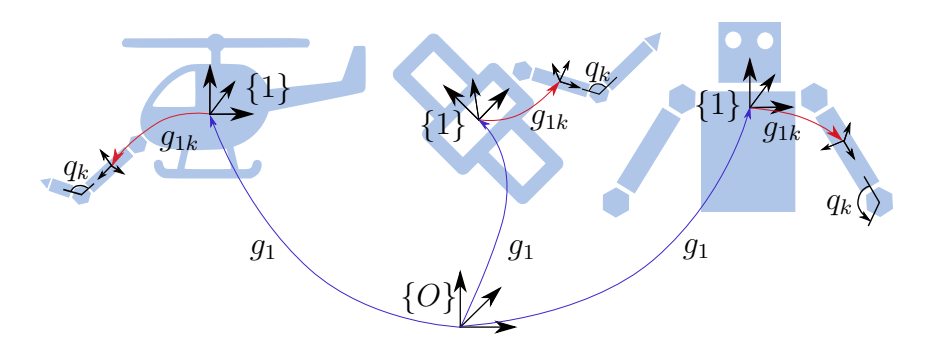


Figure 3.1: Floating-base Robotic Mechanism (FRM) with configuration (g_1, q) , where $g_1 \in SE(3)$ is the pose of the FRM-base frame, $\{1\}$, relative to the inertial frame $\{O\}$, and $q \in \mathbb{R}^n$ are the *n*-joint positions.

in Sec. 2.4.7.2. The FRM is further distinguished by its distinct non-flatness (curvature) of this connection [31], i.e., the constraint is not preserved over a closed path (gait) in shape space. In other words, a gait might cause a net displacement of the FRM-base, recall Sec. 2.4.8.1.

3.2 Related Work

Noether's invariance arising from Lie group action was first observed for rotational dynamics of a rigid body, and the Poinsot construction provided a geometric visualization of this symmetry [139]. While the FRM is also a system with symmetry, an analogue of Poinsot construction for multibody systems is missing in literature. For the dynamics of this class of mechanical systems, the \mathcal{LP} equations, were proposed in the early nineties [14, §5.3][94, pp. 141]. In particular, the \mathcal{LP} equations consist of momentum and shape variations as an \mathcal{EP} equation and an \mathcal{EL} equation with curvature-related gyroscopic forces, respectively. The structure of the \mathcal{LP} equations provide a useful insight into the FRM dynamics through a block-diagonal inertia, the separation of velocity dependencies in the CC terms and the apparentness of the curvature form. A first step in this direction by the robot dynamics community was a matrix transformation of the Hamel's equations [25], which revealed the useful block-diagonal inertia property.

However, a direct link between kinematic chain iterative dynamics and \mathcal{LP} equations has not been established before. A negative consequence was that only the block-diagonal structure of inertia was exploited, as in [25, 140], whereas the structural properties of the CC matrix were not examined. In fact, the use of matrix transformations resulted in a placeholder CC matrix, which concealed its precise structure. This resulted in a CC matrix, which (a) had an apparent coupling between the shape dynamics and the group variable, (b) lacked a commutative property (like fixed-base robots, see [141]), and (c) did not reveal the FRM curvature. I point out that the curvature computation in FRM locomotion

analyses [19, 20, 124, 142] is traditionally performed using numeric or symbolic methods, and an analytical computation method is missing. In fact, locomotion approaches in geometric mechanics approximate this displacement per gait using area integrals of the curvature [19, 20, 124, 125, 143].

The CC matrix of multibody systems is required in applications that include, but are not limited to, motion tracking [134], velocity observers [141] and contact detection [144]. The skew-symmetry of an iteratively computed CC matrix [22] was extended in [135] with Christoffel-symbol consistency. In [127], the CC matrix was structured as the sum of inertia variations relative to time and shape, defined as fundamental matrices. However, prior CC matrix factorizations were limited to configuration velocity dynamics, and the added structure due to velocity constraints, as in the FRM¹, remains unexamined.

3.3 Key Contributions

To this end, the contributions of this chapter are the following.

- 1. In Theorem 3.1, I provide a novel Poinsot's construction to provide a geometrical method for visualizing the nonholonomic unforced motion of the FRM. This is the multibody equivalent of the original Poinsot construction (1834) for rigid body motion, and is a direct contribution towards understanding the geometry of motion for FRMs.
- 2. In Theorem 3.2, I propose a novel CC matrix for the \mathcal{LP} equations of a FRM as a sum of two matrices, in which the partitions of each are computed using an iterative expression with a specific velocity dependency. In particular, the first CC matrix depends on the shape velocity, while the second depends on the locked velocity (momentum). I prove that the former CC matrix of block-diagonal terms satisfies the skew-symmetry (passivity) property, while the latter is itself skew-symmetric. This structure is a result of the inherent symmetry of the FRM, and was not revealed in prior works.
- 3. The proposed CC matrix structure is used to reveal the following properties. By extending the notion of fundamental matrices [127] for fixed-base robots to the FRM, I identify the parts of the CC matrix with commutativity. This enables the reordering of velocity arguments in the CC forces for simplification, e.g. in velocity observers, which was previously limited to fixed-base robots [141]. I prove that the shape dynamics is invariant to a transformation of the momentum dynamics, e.g. to a centroidal frame [25].
- 4. In Theorem 3.4, it is proved that in the FRM the momentum and the shape subsystems are in a passive feedback interconnection with each other. This

¹In the FRM, the velocity constraint is not externally imposed, but is a mathematical consequence of the symmetry (conservation law) in the motion equations.

is a property of immense utility in motion control, that is unique to the FRM due to its inherent symmetry in the \mathcal{LP} dynamics.

- 5. From the proposed CC matrix, in Theorem 3.3, I derive the curvature as an analytic matrix-based expression. This is useful for computing the FRM-base displacement per gait in the shape space.
- 6. Finally, in Theorem 3.5, I generalize the motion of the FRM in the presence of symmetry-breaking potential fields like gravity and buoyancy, while being surrounded by a potential fluid flow. In contrast to prior works, this work extends the momentum-shape formulation of FRM-dynamics to also include fluid effects. This formulation is useful for aerial and underwater robotics applications.

The work proposed here exhaustively focuses on the derivation of the dynamics, notably, as an iterative formulation, and its properties, which can appeal to a broad robotics audience. To achieve that, I establish an interdisciplinary link between the forms of \mathcal{LP} equations from *both* communities, robot dynamics and geometric mechanics.

The chapter is organized as follows. In Sec. 3.4, the \mathcal{LP} equations of motion for the FRM from both, robot dynamics and geometric mechanics, are reviewed. I also propose the Poinsot construction to provide a geometric visualization of the FRM's motion. The main result, i.e., the CC matrix factorization, is stated and derived in Sec. 3.5. In Sec. 3.6, the novel properties of the CC matrix are proved and the closed form expression of curvature is derived. It is proved that the momentum and the shape subsystems of the FRM are in a passive feedback interconnection. In Sec. 3.7, the \mathcal{LP} dynamics of a free FRM is generalized in the presence of a symmetry-breaking potential and the surrounding potential fluid flow. The chapter concludes with remarks in Sec. 3.8. A sectioned Appendix is given to aid the analysis.

3.4 Dynamics of the FRM

In this section, due to the interdisciplinary nature of this chapter, the relevant details of FRM dynamics descriptions from *both* communities, robot dynamics [23, 25] and geometric mechanics [14, 16, 94] are examined. The presentation is structured in order to facilitate a link between the two dynamic descriptions. For the sake of clarity, I consider the FRM as a single kinematic chain, which is formalized as follows.

Def. 3.1. A FRM is a multibody system of n+1 rigid links (see Fig. 3.1), which comprises of a movable platform and an articulated mechanism with n holonomic joints. Its configuration space is $Q \equiv SE(3) \times \mathbb{R}^n$ with coordinates

 $r = (g_1, q) \in \mathcal{Q}$, where $g_1 \equiv (R_1, p_1) \in SE(3)$ is the pose of the FRM-base and $q \in \mathbb{R}^n$ is the shape (joint positions) of the mechanism.

For general kinematic tree structures, the following computations will have an outer summation, as in [23]. In the text, the shape (q) and velocity dependencies of the dynamic quantities are provided in declaration and omitted later for brevity. For details specific to SE(3) notation and properties, the reader is referred to Appendix A.

3.4.1 Floating-base Dynamics or Hamel's Equations

Considering potential forces (e.g. gravity) as external, the Lagrangian of the FRM is independent of the g_1 [14, §5] with inertia, $M(q) \in \mathbb{R}^{(6+n)\times(6+n)}$, as $l(q,V) = \frac{1}{2}\langle V,V\rangle_M$, where $V = \begin{bmatrix} V_1^\top & \dot{q}^\top \end{bmatrix}^\top$ is the FRM configuration velocity, and $V_1^\wedge = g_1^{-1}\dot{g}_1 \in \mathfrak{se}(3)$ for the FRM-base pose. The equations of motion that result from l(q,V) are given by the Hamel's equations (see Lemma 2.6). It is the Lagrangian equivalent of the floating-base formulation in (2.60) [22, 23, 26] from robot dynamics, and written as,

$$\underbrace{\begin{bmatrix} M_b(q) & M_{bq}(q) \\ M_{bq}(q)^{\top} & M_q(q) \end{bmatrix}}_{M(q)} \begin{bmatrix} \dot{V}_1 \\ \ddot{q} \end{bmatrix} + C(q, V) \begin{bmatrix} V_1 \\ \dot{q} \end{bmatrix} = \underbrace{\begin{bmatrix} \mathcal{F}_1 \\ \tau \end{bmatrix}}_{F}, \tag{3.1}$$

where M_b, M_{bq}, M_q are the locked, coupling and manipulator inertias, respectively, $C \in \mathbb{R}^{(6+n)\times(6+n)}$ is the CC matrix, and $\mathcal{F}_1 \in \mathbb{R}^6 \cong \mathfrak{se}(3)^{\top}$ and $\tau \in \mathbb{R}^n$ are the forces acting on the FRM-base and joints, respectively.

A notable advantage of (3.1) is its efficient computation using the recursive Newton-Euler algorithm [28, 137]. For the contribution of this chapter, Lemma 2.14 is used for the iterative computation of M, C as follows.

Lemma 3.1. The matrices M, C in the motion equation, (3.1), are computed using the natural \mathcal{EP} body-level factorization as,

$$M = \sum_{k} T_{k}^{\top} M_{k} T_{k}, C = \sum_{k} T_{k}^{\top} (-\operatorname{ad}_{V_{k}}^{\top} M_{k} T_{k} + M_{k} \dot{T}_{k}).$$
 (3.2)

where $T_k = \begin{bmatrix} Ad_{1k}^{-1}(q) & J_k(q) \end{bmatrix}$, and J_k is the link Jacobian relative to the FRM-base.

The partitioning in T_k is used to add detail to the dynamic matrices, e.g.

$$M = \begin{bmatrix} M_b & M_{bq} \\ M_{bq}^{\top} & M_q \end{bmatrix}, \ M_b = \sum_k \operatorname{Ad}_{1k}^{-\top} M_k \operatorname{Ad}_{1k}^{-1},$$

$$M_{bq} = \sum_k \operatorname{Ad}_{1k}^{-\top} M_k J_k, \ M_q = \sum_k J_k^{\top} M_k J_k.$$
(3.3)

Note that the natural \mathcal{EP} factorization in Lemma 3.1 does not satisfy skew-symmetry, i.e., $x^{\top}(\dot{M}-2C)x=0, \ x\in\mathbb{R}^{6+n}$. This is commonly achieved using alternative factorizations, see 2.6.1.1. In this paper, Lemma 3.1 serves as a starting point to ease into the derivation of the main result, which satisfies skew-symmetry.

3.4.2 Lagrange-Poincaré (\mathcal{LP}) Equations: The Motivation

The dynamics in Sec. 3.4.1 only describe the FRM as a kinematic chain. However, the FRM is also uniquely characterized by a conservation property on its momentum map, i.e., $\mathcal{J} = \operatorname{Ad}_{1}^{-\top} (M_{b}V_{1} + M_{bq}\dot{q})$, using Def. 2.6.

The alternative dynamics description, which explicitly shows this property, is the set of Lagrange-Poincaré (\mathcal{LP}) equations [14, §5.3]. In this chapter, I develop a body formulation of the \mathcal{LP} equations, i.e., using body velocity quantities. To this end, I define the locked velocity for the FRM as follows.

Def. 3.2. Locked velocity is the velocity of the instantaneous equivalent rigid FRM (locked shape), and is written as $\mu = V_1 + \mathcal{A}_l(q)\dot{q}$, where $\mathcal{A}_l = M_b^{-1}M_{bq}$ is the dynamic-coupling factor in robot dynamics. It is the body velocity corresponding to the momentum map, i.e., $\mu = M_b^{-1} \mathrm{Ad}_1^{\top} \mathcal{J}$.

3.4.2.1 \mathcal{LP} Equations in Robot Dynamics

In the robot dynamics community, a matrix-based form of the \mathcal{LP} equations is obtained by applying the Newtonian transformation (of type 1) from subsection 2.6.3.1 to (3.1), and is summarized in the Lemma below.

Lemma 3.2. Considering $\xi = \begin{bmatrix} \mu^{\top} & \dot{q}^{\top} \end{bmatrix}^{\top}$ as the new mechanism velocity, which is related to the configuration velocity, V, through a transformation as $V = L(q)\xi$, $L = \begin{bmatrix} \mathbb{I}_{6,6} & -\mathcal{A}_l \\ 0_{n,6} & \mathbb{I}_{n,n} \end{bmatrix}$, the dynamics of the FRM are alternatively given as,

$$\underbrace{\begin{bmatrix} M_b(q) & 0_{6,n} \\ 0_{n,6} & \Lambda_q(q) \end{bmatrix}}_{\Lambda(q) = L^\top ML} \dot{\xi} + \underbrace{\begin{bmatrix} \Gamma_b(q,V) & \Gamma_{bq}(q,V) \\ \Gamma_{qb}(q,V) & \Gamma_q(q,V) \end{bmatrix}}_{\Gamma(q,V) = L^\top (M\dot{L} + CL)} \xi = \underbrace{\begin{bmatrix} \mathcal{F}_1 \\ (\tau - \mathcal{A}_l^\top \mathcal{F}_1) \end{bmatrix}}_{\mathcal{F}}, \quad (3.4)$$

where Λ , Γ are the transformed matrices of inertia and CC terms, and \mathcal{F} denotes the transformed covector of forces acting on the FRM.

Accordingly, the FRM-base pose, g_1 , is reconstructed alternatively as,

$$\dot{g}_1 = g_1 \Big(\mu - \mathcal{A}_l(q) \dot{q} \Big)^{\wedge}, \quad : \quad V_1 = \begin{bmatrix} \mathbb{I}_{6,6} & -\mathcal{A}_l \end{bmatrix} \xi \tag{3.5}$$

Remark 10. In [25, eq. 15], the approach in Lemma 3.2 was used to obtain the dynamics of (\mathcal{J}, \dot{q}) instead of ξ . Due to the g_1 -dependency of \mathcal{J} in Def. 2.6, however, the shape dynamics had an apparent g_1 -dependency [16, eq. 8], which is not physical. Although the shape dynamics in Lemma 3.2 (bottom row) does not have a g_1 -dependency, its invariance to frame transformations as a property is unproved, but often assumed.

Remark 11. In (3.4), Γ is a placeholder CC matrix, and does not provide a special structure like the block-diagonal inertia, Λ . In particular, there is no clear separation of velocity dependencies, i.e., μ, \dot{q} , in the partitions of Γ . This limits specific applications, e.g. model-based control [63], and dynamics linearization, like $\frac{\partial(\Gamma V)}{\partial \mu}$, $\frac{\partial(\Gamma V)}{\partial \dot{q}}$, which require the partitioned CC terms, preferably with closed form computation.

It is worth appreciating that the analytic form of the \mathcal{LP} equations was revealed by the geometric mechanics community [14, 16, 94]. In this structure, notable aspects of the CC terms are velocity dependency separation and the apparentness of the curvature term. Therefore, I will subsequently review the concepts from geometric mechanics that lead to the analytic form of the \mathcal{LP} equations. Juxtaposing it with robot dynamics in (3.4) will pave the way for the main result.

3.4.2.2 \mathcal{LP} Equations in Geometric Mechanics

Using Def. 2.7, the conservation of \mathcal{J} is written as a Pfaffian-like velocity constraint using the mechanical connection, as follows

$$(\mathrm{Ad}_{1}^{-\top} M_{b} \mathrm{Ad}_{1}^{-1})^{-1} \mathcal{J} = \underbrace{\mathrm{Ad}_{1} \left[\mathbb{I}_{6,6} \quad \mathcal{A}_{l}(q) \right] \begin{bmatrix} V_{1} \\ \dot{q} \end{bmatrix}}_{\mathcal{A}(q,V)}, \tag{3.6}$$

and \mathcal{A}_l is alternatively called the local mechanical connection. Note that \mathcal{A} is simply the right-invariant (spatial) velocity corresponding to the momentum, \mathcal{J} . Applying Lemma 2.13, $\mathcal{A} = 0_6$ defines horizontal and vertical subspaces with velocities $V_h = (-\mathcal{A}_l \dot{q}, \dot{q})$ and $V_v = V - V_h = (V_1 + \mathcal{A}_l \dot{q}, 0_n)$, respectively, which are minimally written using the shape and locked velocities, i.e., \dot{q} and μ , respectively. Using these minimal velocity forms in the orthogonal subspaces, Lemma 2.13 provides a geometric interpretation of $V = L\xi = V_v + V_h$ in Lemma 3.2.

The FRM configuration space, SE3 × \mathbb{R}^n , shown as grey box in Fig. 3.2, has a PFB structure [14, §3.2]. This means that its motion r(t) (blue dot trajectory) in SE(3) × \mathbb{R}^n is composed of SE(3) as the fiber (black dashed lines) and \mathbb{R}^n as the shape-space, see red bordered manifold and reduced-space trajectory, q(t). Projecting (black arrows) V_h into \mathbb{R}^n , i.e. shape-space, yields the reduced dynamics. Secondly, the vertical part V_v (blue arrow), is identified with the locked velocity.

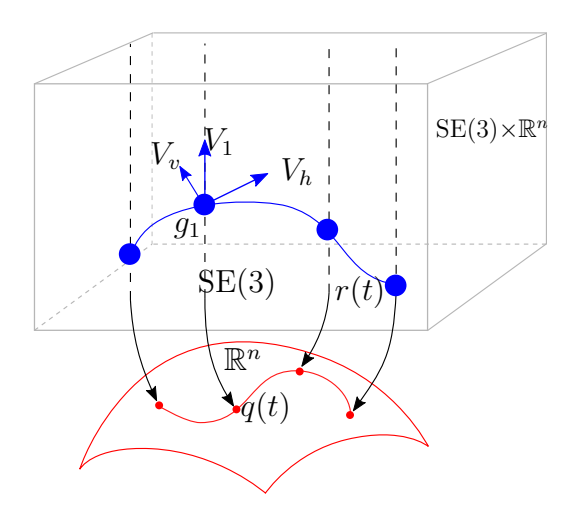


Figure 3.2: A differential-geometric illustration of the FRM configuration space.

 $\text{hor}_r, \text{ver}_r, V_b$ have been marked as blue arrows in Fig. 3.2. The \mathcal{LP} equations (shown next) are a direct consequence of this orthogonal split.

I recall from subsection 2.4.8.1 that a FRM has a non-null curvature, which is employed for locomotion analysis in geometric mechanics. A supplementary goal in this chapter is to derive an analytical computation of DA_l using iterative robot dynamics. To facilitate a comparison with the robot dynamics notation in (3.4), the unforced \mathcal{LP} equations are stated below in matrix-vector notation.

Lemma 3.3. For the unforced FRM, the horizontal and vertical velocity decomposition of the velocity due to the mechanical connection results in the Lagrangian, $\hat{l}(q,\xi) = \frac{1}{2} \langle \dot{q}, \dot{q} \rangle_{\Lambda_q} + \frac{1}{2} \langle \mu, \mu \rangle_{M_b}$. Using \hat{l} , the dynamics is given by the \mathcal{LP} equations, which in matrix-based notation [16], [145] read as,

$$M_b \dot{\mu} + \frac{dM_b}{dt} \mu = \operatorname{ad}_{\mu}^{\top} M_b \mu - \operatorname{ad}_{\mathcal{A}_l \dot{q}}^{\top} M_b \mu, \tag{3.7}$$

$$\Lambda_{q}\ddot{q} + \frac{d\Lambda_{q}}{dt}\dot{q} - \frac{\partial}{2\partial q}\langle\dot{q},\dot{q}\rangle_{\Lambda_{q}} = \tilde{N}(q,\mu,\dot{q})$$

$$= -\left((D\mathcal{A}_{l})(\dot{q})\right)^{\top}M_{b}\mu + \frac{\partial\langle\mu,\mu\rangle_{M_{b}}}{2\partial q} - \mathcal{A}_{l}^{\top}\mathrm{ad}_{\mu}^{\top}M_{b}\mu.$$
(3.8)

In Lemma 3.3, the *unforced* case of the full FRM dynamics is interpreted as the momentum dynamics in body basis, (3.7), which defines the level-set on which the shape dynamics, (3.8), evolve. Lemma 3.3 further highlights the following aspects of the CC terms. Firstly, there is not only an elegant separation of the CC couplings in terms of velocity dependencies, i.e., (\dot{q}, \dot{q}) on L.H.S and $(\dot{q}, \mu), (\mu, \mu)$ on R.H.S, but they also have physical interpretations. Secondly, note that the curvature appears explicitly in (3.8). This structure is in contrast to (3.4), see Remark 11. However, (3.7) and (3.8) do not satisfy the skew-symmetric property, which is desirable, see Appendix A.2.1.

Hence, the main idea in this chapter is to modify the iterative computations from the previous works in robot dynamics [22, 25] to directly obtain the forced dynamics in (3.4), and separate the CC couplings as in geometric mechanics (Lemma 3.3). Instead of the original form of the \mathcal{LP} equations, I derive a reformulation, which provides a skew-symmetric property. Before proceeding towards this, however, I first present a geometric visualization of the motion of the FRM, which gives the reader an intuition about the locked velocity μ .

3.4.3 A Geometric View of FRM Motion

In this subsection, the unforced motion of the FRM is considered in (3.7)-(3.8). Firstly, I recall that using (3.6),

$$\mathcal{A} = \mathrm{Ad}_1 M_b^{-1} \mathrm{Ad}_1^{\mathsf{T}} \mathcal{J} = \mathrm{Ad}_1 \mu \tag{3.9}$$

The geometric interpretation is split into subsections (3.4.3.1) and (3.4.3.2), corresponding to the linear and angular parts, respectively. In (3.4.3.2), I propose a new *generalized Poinsot's construction* to provide a geometric interpretation of the angular part of μ .

3.4.3.1 Center-of-Mass (CoM) velocity

Def. 3.3. For the FRM in Def. 3.1, in which the k^{th} -link pose relative to an inertial frame $\{O\}$ is $g_k \equiv (R_k, p_k)$, the CoM is,

$$p = \frac{\sum_{k=1}^{n} (m_k p_k)}{\sum_{k=1}^{n} m_k} = \frac{\sum_{k=1}^{n} (m_k p_k)}{m} \Rightarrow \dot{p} = \frac{\sum_{k=1}^{n} (m_k \dot{p}_k)}{m} = \frac{\sum_{k=1}^{n} (m_k R_k v_k)}{m} \quad (3.10)$$

where m is the total mass of the FRM, and v_k is the body trivialized translational velocity of the k^{th} link.

Def. 3.4. For the FRM defined in Def. 3.1, the virtual chassis frame of a FRM is an instantaneous locked body frame, $\{C\}$, located at the CoM, and is oriented along the instantaneous principal axes of the FRM's locked inertia [146]. The pose of $\{C\}$ relative to $\{O\}$ is denoted as $g_c \equiv (R_c, p) \in SE(3)$.

Lemma 3.4. For the FRM defined in Def. 3.1, for which the locked inertia trivialized at $\{1\}$ is M_b , the instantaneous locked principal axes inertia about the frame $\{C\}$ (Def. 3.4) is completely diagonalized as

$$M_c = \begin{bmatrix} I_c & 0 \\ 0 & m \cdot \mathbb{I}_{3,3} \end{bmatrix}, \ I_c = \text{diag}([I_x(q) \ I_y(q) \ I_z(q)])$$
(3.11)

where I_c is the locked moment of inertia about $\{C\}$.

Proof. Firstly, trivializing M_b at the intermediate frame $\{C'\}$, which is located on the CoM, $g_{c'} \equiv (\mathbb{I}_{3,3}, p)$, removes the product of inertia terms, i.e., linear and angular parts are decoupled as blkdiag $(m \cdot \mathbb{I}_{3,3}, I'_c)$ [25]. Secondly, Sylvester's law of inertia is invoked which states that for a positive definite $I_{c'}$, $I_c = R_{c'c}I_{c'}R_{c'c}^T$, where $I_c = \sum_{k=1}^n R_{ck}I_kR_{ck}^T$ is the completely diagonalized and $R_{c'c}$ is the orientation of the principal axes relative to $\{C'\}$. This result is obtained using a right-handed SVD, which leads to the result.

The total body momentum resolved in the virtual chassis frame, $\{C\}$, is $\bar{\Pi} = \sum_{k=1}^{n} \operatorname{Ad}_{ck}^{-\top} M_k V_k$, and expanding,

$$\bar{\Pi} = \sum_{k=1}^{n} \begin{bmatrix} p_{ck} \times R_{ck} m_k v_k + R_{ck} I_k \omega_k \\ R_{ck} m_k v_k \end{bmatrix}$$
(3.12)

Let $\bar{\mu}$ be the locked velocity trivialized at $\{C\}$. Trivializing \mathcal{A} and \mathcal{J} at $\{C\}$, $\mathcal{A} = \operatorname{Ad}_c \bar{\mu}$ and $\mathcal{J} = \operatorname{Ad}_c^{-\top} \bar{\Pi}$. Using (3.9),

$$\bar{\mu} = \sum_{k=1}^{n} \left(A d_{ck}^{-\top} M_k^{-1} A d_{ck}^{-1} \right) \bar{\Pi} = M_c^{-1} \bar{\Pi}$$
(3.13)

Using (3.12) in (3.13),

$$\bar{\mu} = \begin{bmatrix} I_c^{-1} & 0 \\ 0 & \frac{1}{m} \end{bmatrix} \sum_{k=1}^n \begin{bmatrix} p_{ck} \times R_{ck} m_k v_k + R_{ck} I_k \omega_k \\ R_{ck} m_k v_k \end{bmatrix}$$
(3.14)

Multiplying the terms in (3.14) and applying Def. 3.3 to simplify the linear part,

$$\bar{\mu} = \begin{bmatrix} I_c^{-1} h_\omega \\ R_c^T \dot{p} \end{bmatrix} = \mathrm{Ad}_{1c}^{-1} \mu \tag{3.15}$$

where $h_{\omega} = \sum_{k=1}^{n} p_{ck \times} R_{ck} m_k v_k + R_{ck} I_k \omega_k$. Thus, the linear part of $\bar{\mu}$ is simply the CoM velocity of the FRM and thus, we conclude the following.

Remark 12. For the FRM defined in Def. 3.1, the linear part of the velocity (bottom 3 components) of both the mechanical connection \mathcal{A} and the locked velocity μ is simply CoM velocity trivialized at $\{1\}$.

3.4.3.2 Generalized Poinsot's Construction

In this section, the *Poinsot's construction* [147] for rigid body is generalized to a multibody FRM. To that end, I first recall the Poinsot's theorem for rigid bodies.

Def. 3.5. Classical Poinsot's theorem [147, pp. 493] for rigid body: The moment of inertia ellipsoid in space rolls without slipping on the invariable plane.

For the generalization to a FRM, the following Lemma is required.

Lemma 3.5. For the FRM defined in Def. 3.1, the total kinetic energy is

$$\mathcal{K} = \underbrace{\frac{1}{2}m\dot{p}^Tp}_{\mathcal{K}_{\mu_v}} + \underbrace{\frac{1}{2}\bar{\mu}_{\omega}^TI_c(q)\bar{\mu}_{\omega}}_{\mathcal{K}_{\mu_{\omega}}} + \underbrace{\frac{1}{2}\dot{q}^T\Lambda_q\dot{q}}_{\mathcal{K}_{\dot{q}}}$$
(3.16)

and the exchange of energy between $\mathcal{K}_{\dot{q}}$ and $\mathcal{K}_{\mu_{\omega}}$ takes place due to variations in shape-space. Furthermore,

$$\bar{\Pi} = \begin{bmatrix} \bar{\Pi}_{\omega} \\ \bar{\Pi}_{v} \end{bmatrix} = M_{c}\overline{\mu} = \begin{bmatrix} I_{c}\bar{\mu}_{\omega} \\ m\bar{\mu}_{v} \end{bmatrix}$$
 (3.17)

Proof. Using $\bar{\mu}$ from (3.15) instead of μ , the kinetic energy is,

$$\mathcal{K} = \frac{1}{2} \left(\bar{\mu}^T M_c \bar{\mu} + \dot{q}^T \Lambda_q(q) \dot{q} \right) \tag{3.18}$$

Using (3.15) on (3.18), and noting that M_c is diagonalized according to Lemma 3.4 and $\bar{\mu}_{\omega} = R_{bc}^T \mu_{\omega}$ from (3.15), the result follows. Furthermore, \mathcal{K}_{μ_v} is independent of q and $\mathcal{K}_{\dot{q}}$ is independent of p and hence there is no energy exchange between \mathcal{K}_{μ_v} and $\mathcal{K}_{\dot{q}}$. Finally, using the diagonal structure of M_c from Lemma 3.4, the final part of the proof follows.

Next, I provide a generalization of Poinsot's theorem to the FRM, which reveals the geometry of its motion.

Theorem 3.1. Generalized Poinsot's theorem: For the FRM defined in Def. 3.1, the locked moment of inertia ellipsoid in space rolls without slipping on a momentum plane, which translates to accommodate the ellipsoid's shape deformation.

Proof. I begin the proof using a local trivialization of μ about the instantaneous locked frame, $\{C\}$, which is defined in Lemma 3.4, and state the following. Using Lemma 3.5, the total kinetic energy, $\mathcal{K} = \mathcal{K}_{\mu_v} + \mathcal{K}_{\mu_\omega} + \mathcal{K}_{\dot{q}} = \mathcal{K}_0$, $\mathcal{K}_0 \geq 0$. In the following, like Poinsot, I consider $\mathcal{K}_{\mu_v} = c_v$, $c_v \geq 0$ and $\dot{\mathcal{K}}_{\mu_v} = 0$. This implies that the inertial CoM velocity is invariant and this follows from unforced motion of FRM. With no loss of generality, I restrict to the level set of the total kinetic energy given by,

$$\tilde{\mathcal{K}} = \{ \mathcal{K}_{\mu_{\omega}} + \mathcal{K}_{\dot{q}} | \mathcal{K}_{\mu_{v}} = c_{v} \} = \tilde{\mathcal{K}}_{0}, \ \tilde{\mathcal{K}}_{0} \ge 0$$
(3.19)

Furthermore,

$$\tilde{\mathcal{K}}_{0} = \mathcal{K}_{\mu_{\omega}} + \mathcal{K}_{\dot{q}} \Rightarrow \mathcal{K}_{\mu_{\omega}} = \tilde{\mathcal{K}}_{0} - \mathcal{K}_{\dot{q}} \Rightarrow \sum_{k=x,y,z} \bar{\mu}_{\omega_{k}}^{2} I_{k} = 2(\tilde{\mathcal{K}}_{0} - \mathcal{K}_{\dot{q}})$$

$$\Rightarrow \sum_{k=x,y,z} \left(\frac{I_{k}}{2(\tilde{\mathcal{K}}_{0} - \mathcal{K}_{\dot{q}})} \right) \bar{\mu}_{\omega_{k}}^{2} = 1 \Rightarrow \rho^{T} I_{c} \rho = 1 = F(\rho), \text{ (see [91, pp. 201])}$$
(3.20)

where $\rho = \frac{1}{\sqrt{2(\mathcal{K}_0 - \mathcal{K}_{\dot{q}})}} \bar{\mu}_{\omega}$ is a normalized vector pointing along locked angular velocity in the instantaneous $\{C\}$ frame. The final result of (3.20), is the *ellipsoid* of inertia in body [147] in the body ρ -space in the locked system.

In (3.20), let $\sigma = I_c \rho = \frac{1}{\sqrt{2K_{\mu\omega}}} \bar{\Pi}_{\omega}$. Using equivalence of inner products, see Lemma A.1 in Appendix, (3.20) is, thus, written as $\langle \rho, \sigma \rangle = 1 = \langle \rho', \sigma' \rangle$. Using this, the corresponding *ellipsoid of inertia in space* is simply, $F'(\rho') = \rho'^T R_c I_c R_c^T \rho' = 1$, where F' is defined in (x, y, z) of an inertial ρ' -space. For the FRM, this Locked Inertia Ellipsoid has been shown in Fig. 3.3a.

Remark 13. The locked inertia ellipsoid, $F(\rho)$ which is defined in the instantaneous frame $\{C\}$ (see Lemma 3.4), in contrast to the rigid body formulation (see [147, pp. 492]), is not fixed in its principal semi-axes. For the FRM, which is a multibody, these semi-axes are given from (3.20) as $(\frac{1}{\sqrt{I_x(q)}}, \frac{1}{\sqrt{I_y(q)}}, \frac{1}{\sqrt{I_z(q)}})$ and vary as q changes. This fact is clearly visible in Fig. 3.3b, where the inertia ellipsoid has been shown for $t = \{0, 45, 57\}[s]$ during the FRM's unforced motion.

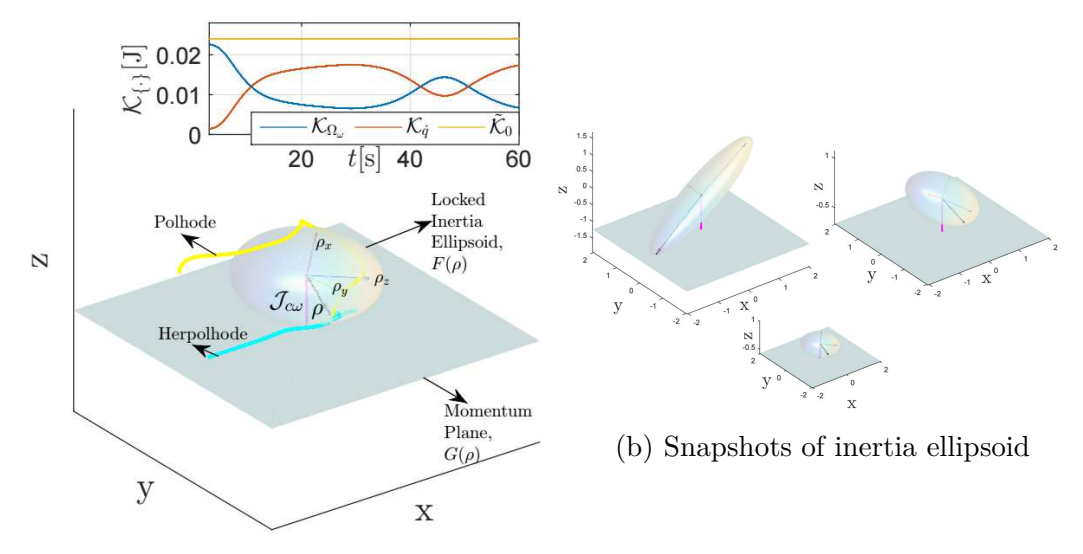
Furthermore, taking the gradient of F' at ρ' (point at which ρ meets the ellipsoid), $\nabla_{\rho'}F'(\rho')=2\sigma'=2\frac{1}{\sqrt{2\mathcal{K}_{\mu\omega}}}R_cI_c\bar{\mu}_\omega=\sqrt{\frac{2}{\mathcal{K}_{\mu\omega}}}\mathcal{J}_\omega$, where \mathcal{J}_ω is the angular momentum map and is conserved in inertial space. Thus, \mathcal{J}_ω is normal to a plane in the inertial ρ' -space and is written as $G(\rho)=\sqrt{\frac{2}{\mathcal{K}_{\mu\omega}}}J_\omega^T\rho'=\sqrt{\frac{2}{\mathcal{K}_{\mu\omega}}}\bar{\Pi}_\omega^T\rho=1$.

Remark 14. The momentum plane, $G(\rho)$, as mentioned above, is expressed in either body (ρ) or inertial (ρ') basis. However, it is clearly seen through (3.20) that these bases are not invariant and change in scale as $\mathcal{K}_{\dot{q}}$ changes. This is in contrast to the rigid body, where the invariance of kinetic energy results in fixed bases. Hence, in the case of the FRM, the momentum plane, $G(\rho)$ translates in a direction parallel to \mathcal{J}_{ω} as the basis of ρ scale up and down.

The endpoint of the vector ρ is thus the point of contact of the inertia ellipsoid $F(\rho)$ and the momentum plane $G(\rho)$, and therefore, the inertia ellipsoid rolls on this plane without slipping.

In other words, as the shape of the inertia ellipsoid changes, the momentum plane translates correspondingly in a way that ensures that the ellipsoid rolls without slipping.

Remark 15. Using the plane equation $G(\rho)$, the normal distance of the ellipsoid from the momentum plane is given as, $d = \left| \sqrt{\frac{2}{\mathcal{K}_{\mu\omega}}} \bar{\Pi}_{\omega}^T \rho \right|$. In case of a rigid body, the conservation of both kinetic energy and angular momentum ensures that $\dot{d} = 0$. Since the semi-axes of the inertia ellipsoid for the FRM change with change in shape-space q, it is natural that d is not fixed. This can be seen through its dependence on the ρ which varies with $\mathcal{K}_{\dot{q}}$.



(a) Generalized Poinsot's construction

Figure 3.3: (a): Generalized Poinsot's construction (isometric view) for the FRM showing the Locked Inertia Ellipsoid, $F(\rho)$, that rolls on the Momentum Plane, $G(\rho)$. G is parameterized by its normal, the generalized angular momentum \mathcal{J}_{ω} (magenta), which is constant in inertial space. The normalized locked angular velocity, ρ , (black) is shown in the locked local basis, $\{\rho_x, \rho_y, \rho_z\}$ (RGB), and touches both F and G. The trajectories on the ellipsoid (Polhode, yellow) and the plane (Herpolhode, cyan) are only instantaneous since the basis, $\{x, y, z\}$, depend on $\mathcal{K}_{\dot{q}}$. The total energy $\tilde{\mathcal{K}}_0$ (top) remains constant while $\mathcal{K}_{\mu_{\omega}}$ and $\mathcal{K}_{\dot{q}}$ exchange energy. (b): Isometric views of Locked Inertia Ellipsoid, $F(\rho)$ rolling on the Momentum Plane $G(\rho)$ at t = 0[s] (left), t = 45[s] (right) and t = 57[s] (bottom) for a torque-free FRM motion. $F(\rho)$ varies as shape changes, and $G(\rho)$ translates accordingly. The angular momentum map \mathcal{J}_{ω} remains invariant.

Remark 16. In case of rigid body motion, the trajectories of ρ on the inertia ellipsoid and the momentum plane are called the Polhode and Herpolhode respectively. For the FRM, these trajectories exist but can only be considered in an instantaneous sense. In Fig. 3.3a, it can be seen that because the parameters of the ellipsoid and the plane change (see remarks 13 and 14), the Polhode and the Herpolhode exist only at the point of contact.

Hence, in this subsection, the locked velocity of the FRM trivialized about the virtual chassis frame was used to provide a geometric interpretation. Clearly, μ and \mathcal{A} are simply the same (see (3.9) and (3.15)) but trivialized in $\{B\}$ and $\{I\}$, respectively. This contribution of the chapter is towards mechanics of the FRM, which has not been reported earlier in literature. In particular, the generalized Poinsot construction was possible due to the use of the virtual chassis frame from robotics and the classical Poinsot construction from geometric mechanics.

3.5 Main Contribution

In this section, the proposed form of the \mathcal{LP} equations and its properties are derived. To ease the subsequent derivation, firstly, a direct computation is chosen to obtain (3.4) and avoid the transformation in Lemma 3.2. Secondly, the variations of the locked inertia are expressed as fundamental matrices so that they can be used in the resulting CC matrix factorization.

3.5.1 Choice of Iterative Computation

From subsection 2.6.3.1, I recall that both iterative computations for Newtonian transformations can be used to obtain the dynamics of ξ . Both approaches yield the same motion equations, and hence, the same inertia and CC matrix (see [135, Rem. 6]). However, Lemma 2.15-1 provides a numerical computation of the CC matrix in a way that its structure is concealed due to \dot{L} , which might be difficult to obtain in closed form. This computation was used for the FRM ($\hat{\nu} = \xi$) by [25], see Lemma 3.2. In contrast, Lemma 2.15-2 directly provides a closed form computation of the CC matrix.

Remark 17. In this chapter, Lemma 2.15-2 is exploited as the first step in the derivation of the main result for the FRM ($\hat{\nu} = \xi$). To this end, the decomposition of V into velocities in the vertical and horizontal subspaces from Lemma 2.13 is exploited to redefine the link velocity, V_k , from Lemma 2.14 as, $V_k = T_k(V_v + V_h)$, which is written as,

$$V_k = \tilde{T}_k(q)\xi, \ \tilde{T}_k(q) = \begin{bmatrix} Ad_{1k}^{-1}(q) & \tilde{J}_k(q) \end{bmatrix},$$
 (3.21)

where $\tilde{J}_k = J_k - Ad_{1k}^{-1} \mathcal{A}_l$ is the generalized Jacobian [25] for the k^{th} link.

3.5.2 Fundamental Matrices of Locked Inertia

For fixed-base robots, the CC matrix was shown as the sum of variations of the inertia matrix relative to time and shape in Def. 2.15 and Def. 2.16, also see [127]. These two variations were expressed as fundamental matrices (operators) that described the CC terms in the Euler-Lagrange equations. For the FRM case, I extend the notion of the fundamental matrices to describe the CC terms that arise from the variations of the locked inertia, M_b , in the \mathcal{LP} equations of the FRM, i.e., (3.7)-(3.8). To this end, I define three operators in the respective Lemmas below.

Lemma 3.6. Locked Inertia Velocity (LIV) matrix: It is a symmetric matrix, P(q, x), given an arbitrary shape velocity, $x \in \mathbb{R}^n$, which gives $P(\dot{q}) = \frac{dM_b}{dt}$ when $x = \dot{q}$, and appears in (3.7). It is computed as,

$$P(\dot{q}) = -\sum_{k} Ad_{1k}^{-\top} \left(ad_{J_{k}\dot{q}}^{\top} M_{k} + M_{k} ad_{J_{k}\dot{q}} \right) Ad_{1k}^{-1}.$$
 (3.22)

Proof. Computing $\frac{d}{dt}M_b(q)$ using M_b in (3.3) and the time-derivative of the Ad operator (see Prop. A.2, Appendix A.1), the expression of the LIV matrix, $P(q, \dot{q})$, is obtained as (3.22).

Lemma 3.7. Locked Inertia Derivative (LID) matrix: Given arbitrary velocities $x, y \in \mathbb{R}^6 \cong \mathfrak{se}(3)$, the partial derivative of the scalar product $\langle x, y \rangle_{M_b}$ relative to shape (q) is written in matrix notation using the LID matrix, $S(q, x)^{\top}$, as $\frac{\partial \langle x, y \rangle_{M_b}}{\partial q} = S(q, x)^{\top}y$. In (3.8), the LID matrix serves to define the partial derivative of the locked kinetic energy relative to shape as $\frac{\partial \langle \mu, \mu \rangle_{M_b}}{\partial q} = S(q, \mu)^{\top}\mu$, where,

$$S(\mu)^{\top} = \sum_{k} J_{k}^{\top} \left(\operatorname{ad}_{Ad_{1k}^{-1}\mu}^{\top} M_{k} + \operatorname{ad}_{M_{k}Ad_{1k}^{-1}\mu}^{\sim} \right) Ad_{1k}^{-1}.$$
 (3.23)

Proof. Given arbitrary x, y, the closed form computation of $S(q, x)^{\top}y$ is derived in Lemma A.4 of the Appendix A.5. The expression in (3.23) follows as a corollary of Lemma A.4 for the specific case of the locked velocity, i.e. $x = y = \mu$.

In the SE(3) group, the time-derivative of a covector in the body frame has an ad^T-term (apparent wrench) to account for changing body basis and encapsulates the SE(3) structural coefficients, as shown in Prop. A.3 of Appendix A.1. For the FRM, the body frame is the moving FRM-base frame, $\{1\}$, which has a body velocity V_1 that depends on the shape velocity due to the mechanical connection, i.e., $V_1 = \mu - \mathcal{A}_l \dot{q}$. Hence, there is an additional term that accounts for the changing body basis in SE(3) due to the local mechanical connection through $\mathcal{A}_l \dot{q}$. This is captured by the matrix below.

Lemma 3.8. Given an arbitrary locked velocity $x \in \mathbb{R}^6 \cong \mathfrak{se}(3)$, and shape velocity $y \in \mathbb{R}^n$, such that $x = V_1 + \mathcal{A}_l y$, the apparent forces due to the change in the SE(3) body basis resulting from the mechanical connection is $\operatorname{ad}_{M_b x}^{\sim} \mathcal{A}_l y$, where $\operatorname{ad}_{M_b x}^{\sim} \mathcal{A}_l$ is the Interaction Matrix (IM) which encapsulates the product of the structure coefficients of the local mechanical connection, \mathcal{A}_l , and the SE(3) group.

Proof. The time-derivative of the locked momentum $z = M_b x$, is obtained using Prop. A.3 of Appendix A.1.2 as,

$$\frac{dz}{dt} = \mathring{z} - \operatorname{ad}_{V_1}^{\top} M_b x = \mathring{z} - \operatorname{ad}_x^{\top} M_b x + \operatorname{ad}_{\mathcal{A}_{l}y}^{\top} M_b x, \tag{3.24}$$

where \mathring{z} is the componentwise time-derivative (see [23, §2.10]). Note that (3.24) already reveals the R.H.S of (3.7) for $x = \mu, y = \dot{q}$. In particular, the last R.H.S term in (3.24) yields the apparent forces due to the change in the SE(3) body basis resulting from the mechanical connection. Applying the property (2.56) to it as $(\operatorname{ad}_{\mathcal{A}_{l}y}^{\top}M_{b})x = (\operatorname{ad}_{M_{b}x}^{\sim}\mathcal{A}_{l})y$ in the spirit of the arguments of Sec. 2.6.1 results in the IM.

The \mathcal{LP} equations are presented next with the proposed CC matrix factorization as the main contribution of this paper.

3.5.3 Proposed form of the \mathcal{LP} equations

Theorem 3.2. Let us consider the Floating-base Robotic System in Def. 3.1, given the Pfaffian-like constraint (mechanical connection) arising from the SE(3) symmetry in Lemma 2.13. Its motion is governed by the \mathcal{LP} equations. This system of equations is proposed with the following factorization of the matrix of CC terms, and is written as:

$$\underbrace{\begin{bmatrix} M_{b}(q) & 0_{6,n} \\ 0_{n,6} & \Lambda_{q}(q) \end{bmatrix}}_{\Lambda(q)} \begin{bmatrix} \dot{\mu} \\ \ddot{q} \end{bmatrix} + \underbrace{\begin{bmatrix} \frac{1}{2}P(\dot{q}) & 0_{6,n} \\ 0_{n,6} & \tilde{\Gamma}'_{q}(\dot{q}) \end{bmatrix}}_{\mathcal{D}_{\dot{q}}(q,\dot{q})} \underbrace{\begin{bmatrix} \mu \\ \dot{q} \end{bmatrix}}_{\xi} \\
= \underbrace{\begin{bmatrix} \operatorname{ad}_{M_{b}\mu}^{\sim} & -\frac{1}{2}S(\mu) - \operatorname{ad}_{M_{b}\mu}^{\sim} \mathcal{A}_{l} \\ \frac{1}{2}S(\mu)^{\top} - \mathcal{A}_{l}^{\top} \operatorname{ad}_{M_{b}\mu}^{\sim} & -\tilde{\mathcal{B}}(q,\mu) \end{bmatrix}}_{\mathcal{D}_{\mu}(q,\mu)} \begin{bmatrix} \mu \\ \dot{q} \end{bmatrix} + \underbrace{\begin{bmatrix} \mathcal{F}_{1} \\ \tau - \mathcal{A}_{l}^{\top} \mathcal{F}_{1} \end{bmatrix}}_{\mathcal{F}}.$$
(3.25)

In (5.3), Λ is the block-diagonal inertia tensor, which is composed of the locked inertia, M_b , and the reduced shape inertia, Λ_q . The two proposed CC matrices are $\mathcal{D}_{\dot{q}}$ and \mathcal{D}_{μ} , which have velocity dependencies of \dot{q} and μ , respectively. These CC matrices contain the fundamental matrices defined in Lemmas 3.6-3.8. Additionally, $\tilde{\mathcal{B}}$ is related to the curvature of the local mechanical connection, and $\tilde{\Gamma}'$ is the reduced shape CC matrix that results in the (\dot{q}, \dot{q}) -coupling in the shape dynamics. The external forces acting on the FRM are concatenated in \mathcal{F} , and include the actuation and the potential (gravity) forces. In particular, given the initial conditions (t=0) for (q, \dot{q}, g_1, μ) , (5.3) is solved by computing the matrices as,

$$\bullet \Lambda_q(q) = \sum_k J_k^{\top} M_k J_k - \mathcal{A}_l^{\top} M_b \mathcal{A}_l$$
 (3.26a)

$$\bullet P(\dot{q}) = -\sum_{k} \operatorname{Ad}_{1k}^{-\top} \left(\operatorname{ad}_{J_{k}\dot{q}}^{\top} M_{k} + M_{k} \operatorname{ad}_{J_{k}\dot{q}} \right) \operatorname{Ad}_{1k}^{-1}$$
(3.26b)

•
$$S(\mu)^{\top} = \sum_{k} J_k^{\top} \left(\operatorname{ad}_{Ad_{1k}^{-1}\mu}^{\top} M_k + \operatorname{ad}_{M_k Ad_{1k}^{-1}\mu}^{\sim} \right) A d_{1k}^{-1}$$
 (3.26c)

$$\bullet \ \tilde{\Gamma}'_{q}(\dot{q}) = \sum_{k} \tilde{J}_{k}^{\top} (-\operatorname{ad}_{M_{k}\tilde{J}_{k}\dot{q}}^{\sim} \tilde{J}_{k} + M_{k} \, \dot{\tilde{J}}_{k})$$
(3.26d)

$$\bullet \tilde{\mathcal{B}}(\mu) = -\mathcal{A}_l^{\top} \operatorname{ad}_{M_b \mu}^{\sim} \mathcal{A}_l + S(\mu)^T \mathcal{A}_l - \mathcal{A}_l^{\top} S(\mu) - \sum_k (J_k^{\top} M_k \nabla_{(\operatorname{Ad}_{1k}^{-1} \mu)} J_k)$$
(3.26e)

where, $\tilde{J}_k = J_k - Ad_{1k}^{-1} \mathcal{A}_l$ for the k^{th} link, and given a velocity $X \in \mathbb{R}^6 \cong \mathfrak{se}(3)$,

$$\nabla_X = M_k^{-1} (\text{ad}_X^{\top} M_k + \text{ad}_{M_k X}^{\sim} - M_k \text{ad}_X).$$
 (3.27)

Proof. A sketch of proof for Theorem 3.2 is shown in Fig. 3.4 as incremental steps that are followed here. In the following steps, the identities (A.10a)-(A.10e) from Lemma A.2 related to \tilde{J}_k , which are listed in Appendix A.2, will be referred.

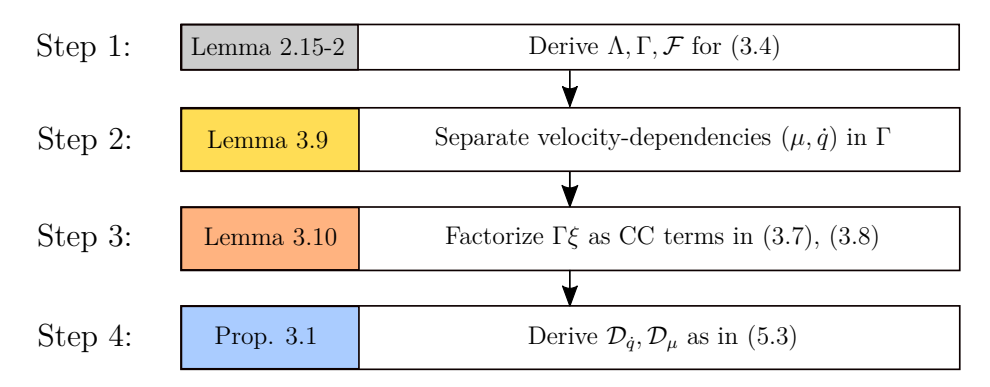


Figure 3.4: A sketch of proof for Theorem 3.2.

Step 1

As stated in Remark 17, Lemma 2.15-2 is invoked with link velocity $V_k = T_k \xi$ to compute (3.4). This leads to three inferences, the first two of which corroborate the earlier results from Lemma 3.2, and are stated here for completeness. Firstly, the inertia matrix is obtained as, $\Lambda(q) = \sum_k \tilde{T}_k^{\top} M_k \tilde{T}_k$. Using (A.10a), Λ is obtained in the exact block-diagonal form of (3.4). Secondly, $\mathcal{F} = \sum_k \tilde{T}_k^{\top} F_k$ reduces to the same form as (3.4) after considering that the constraint forces in the articulated mechanism of the FRM vanish after projection.

Thirdly, the CC matrix is obtained as,

$$\Gamma(q, V_k) = \tilde{T}^{\top} \left(-\operatorname{ad}_{V_k}^{\top} M_k \tilde{T} + M_k \dot{\tilde{T}} \right). \tag{3.28}$$

By analysing further the closed form computation of Γ , the structure in $\mathcal{D}_{\dot{q}}$, \mathcal{D}_{μ} in (5.3) is revealed, and this is the main contribution of this paper.

Step 2

To this end, I separate the FRM velocity dependencies, i.e., μ and \dot{q} , in Γ . The computations are summarized in the following Lemma.

Lemma 3.9. The CC matrix, Γ , in (3.28) is obtained through the computation

of its block partitions, $\Gamma_b, \Gamma_{bq}, \Gamma_{qb}, \Gamma_q$, as functions of μ and \dot{q} , as follows:

$$\Gamma_b = -\operatorname{ad}_{\mu}^{\mathsf{T}} M_b + \operatorname{ad}_{\mathcal{A}_t \dot{q}}^{\mathsf{T}} M_b + P(\dot{q})$$
(3.29)

$$\Gamma_{bq} = 0_{6,n} \tag{3.30}$$

$$\Gamma_{qb} = \mathcal{A}_l^{\mathsf{T}} \operatorname{ad}_{\mu}^{\mathsf{T}} M_b - \underbrace{\sum_k J_k^{\mathsf{T}} \operatorname{ad}_{Ad_{1k}^{-1}\mu}^{\mathsf{T}} M_k A d_{1k}^{-1}}_{\tilde{S}(q,\mu)^{\mathsf{T}}}$$

$$-\underbrace{\sum_{k} \left(\tilde{J}_{k}^{\top} \operatorname{ad}_{\tilde{J}_{k}\dot{q}}^{\top} M_{k} + \tilde{J}_{k}^{\top} M_{k} \, ad_{J_{k}\dot{q}} \right) Ad_{1k}^{-1}}_{B_{1}(q,\dot{q})}$$
(3.31)

$$\Gamma_q = -\underbrace{\sum_{k} \tilde{J}_k^{\top} \operatorname{ad}_{Ad_{1k}^{-1}\mu}^{\top} M_k \tilde{J}_k}_{B_2(q,\mu)} + \underbrace{\sum_{k} \tilde{J}_k^{\top} \left(-\operatorname{ad}_{\tilde{J}_k \dot{q}}^{\top} M_k \tilde{J}_k + M_k \dot{\tilde{J}}_k\right)}_{\Gamma_q'(q,\dot{q})}.$$
(3.32)

Proof. See Appendix A.6.6.1.

We note here that $\Gamma \neq \mathcal{D}_{\dot{q}} + \mathcal{D}_{\mu}$.

Remark 18. The last term in (3.29) is the LIV matrix in Lemma 3.6. Additionally, applying Γ_b , Γ_{bq} in (3.29) to the top row of (3.4) results in the momentum equation of (3.7).

This concludes the simplification obtained through separation of dependencies in the iterative formulation. On the R.H.S of (5.3), I see that the \mathcal{D}_{μ} matrix only has μ -dependency whereas Γ_{qb} in Γ from (3.31) has \dot{q} -dependency too. Also, note that in (3.32), $\dot{\Lambda}_q \neq \Gamma_q' + \Gamma_q'^{\top}$, which implies that the standard reduced shape space skew-symmetric property [25] for the FRM is not satisfied.

Step 3

For this, the following factorization is used to obtain the CC terms in (3.8) from the result in Lemma 3.9.

Lemma 3.10. Given the iterative computation of Γ in Lemma 3.9, the computed CC forces acting on the FRM, i.e., $\Gamma(q,\xi)\xi$ give the closed form computation of the CC forces in (3.7) and (3.8) with velocity dependencies of μ, \dot{q} .

Proof. Given Γ_{qb} and Γ_q in Lemma 3.9, the CC torques of the shape dynamics (bottom row) in (3.4) are computed as,

$$\Gamma_{qb}\mu + \Gamma_q \dot{q} = -\frac{1}{2} S(\mu)^\top \mu + \mathcal{A}_l^\top \operatorname{ad}_{\mathcal{A}_l \dot{q}}^\top M_b \mu + \tilde{\mathcal{B}}(q, \mu) \dot{q} + \tilde{\Gamma}_a'(\dot{q}) \dot{q},$$
(3.33)

where all the CC matrices on R.H.S are the same as in Theorem 3.2. The proof of (3.33) is given in Appendix A.6.6.2.

71

Remark 19. With the above observations, note that (3.33) provides the velocity dependency separation which matches the shape dynamics in (3.8). Also, in the shape dynamics $\tilde{\Gamma}'_q(\dot{q})\dot{q} = \left(\frac{d\Lambda_q(\dot{q})}{dt}\dot{q} - \frac{\partial \langle \dot{q},\dot{q}\rangle_{\Lambda_q}}{2\partial q}\right)$.

Using the Remarks 18 and 19, I conclude that the above simplifications of the iteratively computed $\Gamma(q,\xi)\xi$ results in the CC terms of (3.7) and (3.8).

However, these equations do not jointly satisfy skew-symmetry, which is often required, as noted in Appendix A.2.1.

Step 4

Hence, I observe the following commutative property which leads to the main result in (5.3).

Property 3.1. Given locked velocities, $x, y \in \mathbb{R}^6$, and shape velocity, $z \in \mathbb{R}^n$, the following commutativity properties for the fundamental matrices from Lemmas 3.6 and 3.7 hold.

$$S(q, x)^{\mathsf{T}} y = S(q, y)^{\mathsf{T}} x, \ P(q, z) y = S(q, y) z.$$
 (3.34)

Proof. For the first, S^{\top} from (3.23) of Lemma 3.7 is used with (2.56). For the second, (2.56) and $ad_x y = -ad_y x$ are used.

The Prop. 3.1 leads to the following corollary, which is used to obtain the result in Theorem 3.2.

Corollary 1. Given locked velocity $\mu \in \mathbb{R}^6 \cong \mathfrak{se}(3)^*$ and shape velocity $\dot{q} \in \mathbb{R}^n$, $P(\dot{q})\mu = \frac{1}{2}P(\dot{q})\mu + \frac{1}{2}S(\mu)\dot{q}$.

Using Corollary 1 on Γ_b in Lemma 3.9, followed by using (2.56) for both ad^{\top} terms, I obtain the first row in (5.3). Using the same property for the $\mathcal{A}_l^{\top} \operatorname{ad}_{\mu}^{\top} M_b \mu$ term in (3.33) provides the second row in (5.3). Rearranging as (\dot{q}, \dot{q}) on L.H.S and all $(\dot{q}, \mu), (\mu, \mu)$ on R.H.S, I obtain the proposed $\mathcal{D}_{\dot{q}}, \mathcal{D}_{\mu}$ matrices in (5.3). \square

With Theorem 3.2, the CC matrix for the \mathcal{LP} equations was obtained as a sum of two novel CC matrices, namely $\mathcal{D}_{\dot{q}}$ and \mathcal{D}_{μ} . Notably, their block partitions have an explicit velocity dependency on \dot{q} and μ , respectively. In contrast, the Γ matrix in (3.4) and the result in [25, eq. 18] have functional dependencies on V for all the block partitions instead of the velocity of the inertia-decoupling transformation, i.e., ξ . By defining the IM matrix as in Lemma 3.8, the same operator is used in the momentum dynamics (top) and the shape dynamics (bottom, with a transpose) of (5.3), in contrast to the last R.H.S term in both, (3.7) and (3.8). The structure of $\mathcal{D}_{\dot{q}}$ and \mathcal{D}_{μ} reveals key properties, which are provided next.

3.6 Properties of the \mathcal{LP} Equations

In this section, the properties of the \mathcal{LP} equations of the FRM that are useful in motion control design, e.g., observers, tracking control etc. are outlined. The properties outlined below have not been revealed in literature and are a key contribution of this chapter. With each property, a corresponding application area is also given.

3.6.1 Commutativity

For fixed-base robots, I recall that the commutativity property of the CC matrix is well known [127, 141]. This property, however, does not hold for a rigid-body due to the non-abelian nature of SE(3), as discussed in Sec. 2.6.1. Consequently, for the FRM, the complete CC matrix in (3.4) does not exhibit this property.

The separation of velocity dependencies in the CC terms of (5.3) enabled the isolation of the LIV matrix, P, and the LID matrix, S, for which I proved commutativity in Prop. 3.1. In the context of FRM dynamics, such a property has not been reported before and is neither apparent in (3.4) nor the pair (3.7)-(3.8). Two uses of this property are demonstrated below.

Given two velocities, $x, y \in \mathbb{R}^6$, the dynamics of the error z = x - y is encountered in the stability analysis of tracking [10] and observer design [62, 141] problems. The following corollary of Prop. 3.1 is useful to eliminate y in such cases.

$$S(x)^{\mathsf{T}}x - S(y)^{\mathsf{T}}y = (2S(x)^{\mathsf{T}} - S(z)^{\mathsf{T}})z.$$
 (3.35)

Prop. 3.1 is also useful for linearization, e.g. in Kalman filtering, as is demonstrated next. Given the velocity state ξ , linearisation of the function $w = S(\mu)\dot{q}$, which appears in the top row of (5.3), about $\hat{\xi} = \begin{bmatrix} \hat{\mu}^{\top} & \hat{q}^{\top} \end{bmatrix}$, gives,

$$\frac{\partial w}{\partial \xi}\Big|_{\xi=\hat{\xi}} = \begin{bmatrix} \frac{\partial w}{\partial \mu}\Big|_{\mu=\hat{\mu}} & \frac{\partial w}{\partial \dot{q}}\Big|_{\dot{q}=\hat{q}} \end{bmatrix} = \begin{bmatrix} P(\hat{q}) & S(\hat{\mu}) \end{bmatrix}$$
(3.36)

after applying the second of Prop. 3.1.

3.6.2 Skew-symmetry/Passivity

This property is pivotal to motion control analysis, and is stated next.

Property 3.2. Given $x \in \mathbb{R}^6$, $y \in \mathbb{R}^n$, and $z = \begin{bmatrix} x^\top & y^\top \end{bmatrix}^\top$, the skew-symmetric property, $z^\top (\dot{\Lambda} - 2\Gamma)z = 0$, can be viewed in (5.3), as satisfying the following,

$$x^{\mathsf{T}} \left(\frac{dM_b}{dt} - P(\dot{q})\right) x = 0, \ y^{\mathsf{T}} \left(\frac{d\Lambda_q}{dt} - 2\tilde{\Gamma}_q'\right) y = 0,$$

$$x^{\mathsf{T}} \operatorname{ad}_{M_b \mu}^{\sim} x = 0, \ y^{\mathsf{T}} \tilde{\mathcal{B}}(q, \mu) y = 0, \ z^{\mathsf{T}} \mathcal{D}_{\mu} z = 0.$$

$$(3.37)$$

73

The CC matrix, $\mathcal{D}_{\dot{q}}$, which depends on \dot{q} , satisfies the skew-symmetry property (top row in (3.37)), while the CC matrix, \mathcal{D}_{μ} , which depends on μ , is skew-symmetric (bottom row in (3.37)).

Proof. See Appendix A.6.1. \Box

Prop. 3.2 is crucial for Lyapunov-based stability analysis in specific problems like motion tracking [134] and observer design [62], as explained in Appendix A.2.1.

3.6.3 SE(3) Transformation of Momentum Dynamics

Considering an arbitrary frame as $\{C\}$, its pose $g_c(t) \in SE(3)$, which may be time-varying, is a right SE(3) translation of g_1 , i.e., $g_c = g_1g_{1c}(t)$, where $\dot{g}_{1c} = g_{1c}V_{1c}^{\wedge}$, and $V_{1c}^{\wedge} \in \mathfrak{se}(3)$. Correspondingly, this change of basis of μ to $\{C\}$ is an Adjoint transformation of g_{1c} , i.e., $\mu_c = \mathrm{Ad}_{1c}^{-1}\mu$. For this case, the following is useful.

Property 3.3. The momentum dynamics in top row of (5.3) transform to any frame $\{C\}$ with a pose $g_c(t) \in SE(3)$ through a right SE(3) translation as,

$$\bar{M}_{b}(q)\dot{\mu}_{c} + \bar{P}(q,\dot{q},g_{1c})\mu_{c} = \operatorname{ad}_{\bar{M}_{b}(q)\mu_{c}}^{\sim}\mu_{c}
- \left(\frac{1}{2}\bar{S}(q,\operatorname{Ad}_{1c}\mu_{c}) + \operatorname{ad}_{\bar{M}_{b}(q)\mu_{c}}^{\sim}\bar{\mathcal{A}}_{l}(q,g_{1c})\right)\dot{q} + \bar{\mathcal{F}}_{b},$$
(3.38)

where the dynamic transformations are:

 $\bullet \, \bar{M}_b = \operatorname{Ad}_{1c}^{\top} M_b \operatorname{Ad}_{1c} \qquad \bullet \, \bar{\mathcal{A}}_l = \operatorname{Ad}_{1c}^{-1} \mathcal{A}_l$ $\bullet \, \operatorname{ad}_{\bar{M}_b \mu_c}^{\sim} = \operatorname{Ad}_{1c}^{\top} \operatorname{ad}_{M_b \mu}^{\sim} \operatorname{Ad}_{1c} \qquad \bullet \, \bar{\mathcal{F}}_1 = \operatorname{Ad}_{1c}^{\top} \mathcal{F}_1$ $\bullet \, \bar{S} = \operatorname{Ad}_{1c}^{\top} S(\operatorname{Ad}_{1c} \mu_c) \qquad \bullet \, \operatorname{ad}_{\bar{M}_b \mu_c}^{\sim} \bar{\mathcal{A}}_l = \operatorname{Ad}_{1c}^{\top} \operatorname{ad}_{M_b \mu}^{\sim} \mathcal{A}_l$ $\bullet \, \bar{P} = \operatorname{Ad}_{1c}^{\top} \frac{P}{2} \operatorname{Ad}_{1c} + \bar{M}_b \operatorname{ad}_{V_{1c}}$

and all the L.H.S terms above have an implicit g_{1c} -dependency.

Proof. Multiplying Ad_{1c}^{\top} to the first row in (5.3), and rewriting $\mu = \mathrm{Ad}_{1c}\mu_c$, (3.38) follows.

Prop. 3.3 is useful for FRM applications that require the momentum dynamics (top row, (5.3)) in a more suitable frame, e.g. centroidal frame in humanoids [25], for control design and motion planning purposes.

3.6.4 SE(3) Invariance of Shape Dynamics

Two key observations are made here as a corollary.

Property 3.4. The shape dynamics (bottom row, (5.3)) is invariant to the right SE(3) translation in Prop. 3.3, i.e., invariant to the transformation of the momentum dynamics like (3.38). Additionally, the system skew-symmetric Prop. 3.2 is preserved.

Proof. We note that the transformations in Prop. 3.3 with $\mu = \mathrm{Ad}_{1c}\mu_c$ satisfy,

$$\bar{\mathcal{A}}_l^{\top} \bar{M}_b \bar{\mathcal{A}}_l = \mathcal{A}_l^{\top} M_b \mathcal{A}_l, \ \bar{\mathcal{A}}_l^{\top} \bar{\mathcal{F}}_1 = \mathcal{A}_l^{\top} \mathcal{F}_1, \tag{3.39}$$

$$\bar{S}(\mu_c)^{\top} \mu_c = S(\operatorname{Ad}_{1c}\mu_c)^{\top} \operatorname{Ad}_{1c}\mu_c = S(\mu)^{\top} \mu,
\bar{\mathcal{A}}_l^{\top} \operatorname{ad}_{\bar{M}_b\mu_c}^{\sim} \mu_c = \mathcal{A}_l^{\top} \operatorname{ad}_{M_b\mu}^{\sim} \mu, \quad \tilde{\mathcal{B}}(\operatorname{Ad}_{1c}\mu_c) = \tilde{\mathcal{B}}(\mu).$$
(3.40)

These properties are used for the proof in Appendix A.6.2.

Note that although the first in Prop. 3.4 appears obvious, prior works [25] have not revealed this invariance, as discussed in Remark 10. The aforementioned proof is a direct consequence of the proposed factorization of $\mathcal{D}_{\dot{q}}$, \mathcal{D}_{μ} in (5.3).

Using Properties 3.3 and 3.4, (5.3) is rewritten with a transformation of the proposed CC matrices as,

$$\bar{\mathcal{D}}_{\dot{q}} = \begin{bmatrix} \bar{P}(\dot{q}) & 0_{6,n} \\ 0_{n,6} & \tilde{\Gamma}'_{q}(\dot{q}) \end{bmatrix},
\bar{\mathcal{D}}_{\mu} = \begin{bmatrix} \operatorname{ad}_{\bar{M}_{b}\mu_{c}}^{\sim} & -\frac{\bar{S}(\mu_{c})}{2} - \operatorname{ad}_{\bar{M}_{b}\mu_{c}}^{\sim} \bar{\mathcal{A}}_{l} \\ \frac{\bar{S}(\mu_{c})^{\top}}{2} - \bar{\mathcal{A}}_{l}^{\top} \operatorname{ad}_{\bar{M}_{b}\mu_{c}}^{\sim} & \tilde{\mathcal{B}}(\operatorname{Ad}_{1c}\mu_{c}) \end{bmatrix}.$$
(3.41)

Applications that require the momentum in another frame (as in Prop. 3.3) exploit shape (joints) for control [25]. The invariance in Prop. 3.4 obviates the measurement of g_1 for local joint control, as I shall also demonstrate later.

3.6.5 Analytical Computation of Curvature

Deriving an analytical iterative computation of the local curvature for the FRM was a supplementary goal of the factorization in Theorem 3.2. Although symbolic forms of the FRM curvature have been proposed in geometric mechanics [142] for up to 3-shape variable systems, the iterative forms typically used in robot dynamics² have not been derived before. To this end, I report the following.

Theorem 3.3. Given the FRM in Def. 3.1, its curvature quantifies the non-holonomy (see Def. 2.8), $(DA_l)(x)y = ((dA_l)(x) - ad_{A_lx}A_l)y$, in iterative form is written using the CC matrix structure in Theorem 3.2 as,

$$(D\mathcal{A}_l)(q,x)y = -M_b(q)^{-1}\mathcal{B}^{\top}(q,x)y, \ x,y \in \mathbb{R}^n,$$
 (3.42)

²Note that the curvature does not appear explicitly in the CC matrix (Γ) of (3.4).

where,

$$\mathcal{B}(q,x) = \sum_{k} \left(J_k^{\top} (M_k \nabla_{J_k x} + 2M_k \operatorname{ad}_{J_k x}) A d_{1k}^{-1} \right)$$

$$- S(\mathcal{A}_l x)^T + \mathcal{A}_l^{\top} P(x) + \mathcal{A}_l^{\top} \operatorname{ad}_{A_l x}^{\top} M_b.$$
(3.43)

Proof. See Appendix A.6.3.

Corollary 2. In (3.42), if x = y, $DA_l = 0_6$.

Proof. See Appendix A.6.4. \Box

Property 3.5. (Contravariance of curvature, [14, Def. 3.5]): Given $g_c \in SE(3)$ such that $g_c = g_1g_{1c}$, the body curvature, DA_l , transforms contravariantly to the new basis of g_c as $DA_l^c = Ad_{1c}^{-1}DA_l$.

Proof. See Appendix A.6.5. \square

The Prop. 3.5 is essential to transform Theorem 3.3 from the FRM-base frame, {1}, to a minimum perturbation coordinate frame (see [20, 142]), in which the approximation of Stokes's theorem on SE(3), (2.48), is optimal. Theorem 3.3 enables curvature computation for more than 2-shape variables, which will be demonstrated in the next section, and is useful for locomotion analysis, i.e., gait planning and initialization [19].

3.6.6 Nonholonomic locomotion of FRM

I recall from Sec. 2.4.8.1, see Fig. 2.11, that locomotion methods address the synthesis of a gait i.e., closed path in shape space, and its optimization to induce a desired displacement (in FRM-base) [19, 20, 124, 143]. Therein, the inverse problem is commonly posed as: Given a gait, $q(t) \in \mathbb{R}^n$, can the net FRM-base displacement, δg_1 , be estimated without explicitly integrating (5.4). To answer this, I refer to the well-known result from geometric mechanics [19, 20, 124] for $\mu = 0$, which, firstly, converts the integral of (5.4) into an area integral of curvature, as shown in Appendix A.3.1. As a second step, a visual representation of the curvature, Constraint Curvature Function (CCF), is used to compute the resulting area integral, summarized in Appendix A.3.2. This integral is an approximation of the FRM-base displacement per gait.

For optimal gait planning, the CCF, firstly, aids in gait synthesis, i.e., identify regions in shape space that induce negative, positive or zero displacement, for initialization and heuristics, see [143, §5]. Secondly, given a gait parameter, e.g. its perimeter, the CCF is used to solve an optimality criteria, e.g. maximize displacement and minimize perimeter [143, §6]. Recently, in [142], the idea was extended for n > 2 shape variables. While the aforementioned works compute the CCF map using symbolic or numeric methods for planar systems, in the following

treatment, I demonstrate the application of the analytical form in Theorem 3.3 for a spatial FRM with $n \ge 2$, and use the CCF to answer the question posed above.

3.6.6.1 Motivating Scenario

To this end, let us consider the FRM in Def. 3.1, in which m joints (shape variables) such that $2 \le m \le n$ execute a gait. This gait is considered on a static embedded two-dimensional hyper-plane, H(q)=0, which has local coordinates $r=\begin{bmatrix} r_1 & r_2 \end{bmatrix}^{\top}$ about the origin $q_c=\nabla H(q)$. Thus, there exists a unique map between the gait-space and the shape space, ψ , as,

$$q = \psi(q_c, r) \Rightarrow \dot{q} = \Psi(q_c, r)\dot{r},$$
 (3.44)

where $\Psi = \frac{\partial \psi}{\partial r} \in \mathbb{R}^{n \times 2}$ is the gait Jacobian with n-m zero-rows. The concept is illustrated in Fig. 3.5, in which a circular gait (on a hyperplane) in an anti-clockwise sense is executed using m=3 shape variables, denoted as (q_1,q_2,q_3) . This scenario was considered in [148, § V.B], however, for a planar FRM with symbolically computed CCF. This motivating scenario is a typical application, in which Theorem 3.3 serves to generate the CCF surface map point-wise analytically.

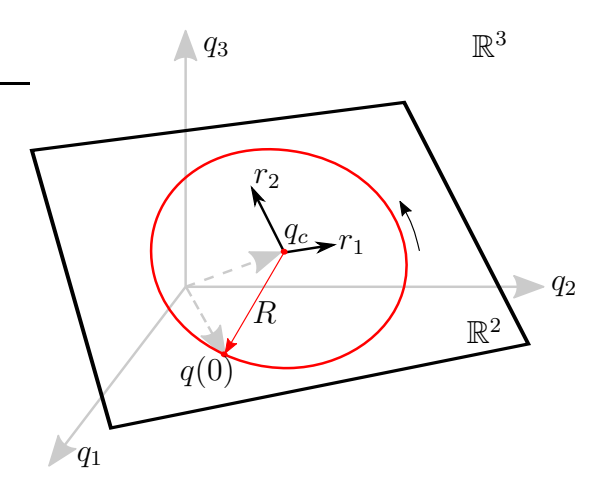


Figure 3.5: A 2-Degree-of-Freedom gait-space (hyperplane) with variables (r_1, r_2) and its origin at q_c in a surrounding 3-D shape space with variables (q_1, q_2, q_3) , which execute an anti-clockwise gait starting at q(0).

To this end, the Algorithm 1 is the novel contribution here.

Given a gait with initial condition, q(0), the following steps from [19, 20] yield an approximate FRM-base displacement.

1. Using the output of Algorithm 1, the CCF surface map is plotted over the gait-space, ϑ_r , and the CCF volume under the gait, r(t), is computed to

Algorithm 1 Generate CCF Surface Map

Input:

 Ψ , ψ , $g_1(0)$, q_c

Minimum Perturbation Coordinate (MPC) frame [19, 20], $\{C\}$, with pose $g_c \in SE(3)$

Output: CCF

- 1: Assign basis: $e_1 = \Psi(1), e_2 \in \Psi(2) \in \mathbb{R}^n$, where $\Psi(i)$ is its i^{th} column
- 2: Compute relative pose: $g_{1c} = g_1(0)^{-1}g_c$
- 3: Create discretized domain (grid) of gait-space, $\vartheta_r \subset \mathbb{R}^2$ such that $r(t) \in \vartheta_r$
- 4: for each $r \in \vartheta_r$ do
- 5: Compute the configuration point in shape space: $q = \psi(q_c, r) \in \theta_q \subset \mathbb{R}^m$
- 6: Compute curvature using (3.42) from Theorem 3.3 in the FRM-base frame, $\{1\}: D\mathcal{A}_l(q, e_1)e_2$
- 7: Transform curvature to the MPC frame, $\{C\}$ using Prop. 3.5: $D\mathcal{A}_l^c = \operatorname{Ad}_{1c}^{-1} D\mathcal{A}_l$
- 8: CCF(index of r) $\leftarrow DA_l^c$
- 9: end for
- 10: Save CCF to file.

obtain the corrected Body Velocity Integral (cBVI) (see Appendix A.3.2) component-wise, i.e., ζ_i in (2.48).

- 2. The net displacement in $\{C\}$, i.e., $g_c(t_0)^{-1}g_c(t_f)$ is approximated as $\exp(\zeta)$ using (2.48).
- 3. Since $g_{1c}(t_0) = g_{1c}(t_f)$ over a gait, the net displacement of the FRM-base is approximated as $\delta \hat{g}_1 = \exp(\mathrm{Ad}_{1c}\zeta) \approx \delta g_1$.

3.6.6.2 Example

For the FRM, I considered the LWR-4+ robot with n=7 joints, dynamic and kinematic parameters of which were reported in [27]. The FRM-base was modeled with a mass, $m_b = 3.5 [\text{kg}]$ and principal inertia, $I_b \equiv (0.12, 0.14, 0.12) [\text{kg.m}^2]$. As an example, a circular gait, as in Fig. 3.5, was considered with $q_c = q(0) = 0_7$, the gait-shape map and the gait Jacobian as $\psi = \Psi = \begin{bmatrix} 0 & 1/\sqrt{2} & 1/\sqrt{2} & 0 & 0_3 \\ 0 & 0 & 0 & 1 & 0_3 \end{bmatrix}^{\top}$, such that the joints numbered 2,3,4, m=3 are used. The circular gait was $\dot{r} = \frac{\pi}{2} [\sin(\pi t) & \cos(\pi t)]^{\top}$. As in [21], the virtual chassis frame, i.e., a coordinate system located at the CoM of the FRM and oriented along its instantaneous principal axes, was chosen as the MPC frame $\{C\}$. In this frame, the locked inertia is diagonalized. Due to this choice, the translation components k=4,5,6 can be ignored since the CoM of the FRM is invariant to shape motion, i.e., the curvature components are zero. This was also verified in the computed \mathcal{DA}_c^c . The

Algorithm 1 from Sec. 3.6.6.1 was executed with a discrete grid size of 30×30 for ϑ_r to obtain the CCF surface data. The specific CCF surfaces are shown in Fig. 3.6 with the gait overlaid in blue. By visual inspection, it can be seen that the encased volumes in k=1,2 bases are small and the maximal displacement is expected along the negative k=3 basis (enlarged). Indeed, upon integrating (5.4) with $\mu=0_6$ and $g_1(0)=\mathbb{I}_{4,4}$, the final FRM-base orientation after the gait was found to be (-0.4228,0.1682,-13.73)[°] in XYZ sense. By using the approximation in Sec. 3.6.6.1, it was found to be (-0.9623,0.9873,-13.25)[°]. The error metric of the pose estimate was $||\log(\delta g_1^{-1}\delta \hat{g}_1)||=0.017$ with an orientation error of 1.0450[°], which is comparable to the mean error, 3.7242[°], reported in [19]. From the similarity in the approximation error, we conclude the suitability of Theorem 3.3 for generating the CCF surface map using Algorithm 1 towards usage in the gait planning [19, 124, 143]. I note that the approximation method itself is not in the scope of this paper, and is used from these works here as a use-case.

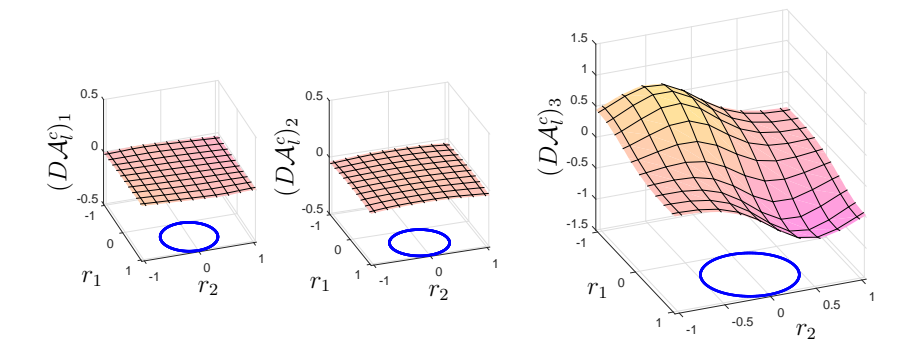


Figure 3.6: CCF surface plots for the rotational bases k = 1, 2, 3 of the virtual chassis frame, $\{C\}$, for a 2-DoF gait (blue) using 3-shape variables.

The key point here is that the analytical method in Theorem 3.3 yields the exact curvature value at a given shape (q) in step 6 of Algorithm 1 to generate the CCF map. In contrast, numerical methods perform a numerical differentiation of \mathcal{A}_l at q to obtain $D\mathcal{A}_l$, which introduces approximation errors. The advantage of the recursive computation in Theorem 3.3 over symbolic methods [148] is the ease of adding/removing joints seamlessly to the locomotion analysis using the same FRM model. For example, in Sec. 3.6.6.2, if the same analysis was required for joints (1,2,3,4), instead of the joints (2,3,4), the symbolic computation would require a modification of the FRM model accordingly. In contrast, Theorem 3.3 always uses the same FRM model, and thus, offers scalability to arbitrary FRM kinematic structures, which are not restricted to be planar, i.e., $g_1 \in SE(3)$. Moreover, the proposed computation provides a valid alternative to numerical and symbolic methods.

3.6.7 Passive Interconnection of Momentum & Shape

In \mathcal{EL} systems, the block-diagonal structure of the inertia tensor implies a decomposition of the Lagrangian into two subsystems, which further implies a passive interconnection of both subsystems, [3, §2.4]. In the following, I extend the result in [3, Prop. 2.10] to the case of \mathcal{LP} systems, i.e., systems with symmetry like the FRM, which also possess a block-diagonal inertia tensor, but have a non-commutative configuration variable (SE(3)).

Theorem 3.4. Consider the \mathcal{LP} system, whose motion is given by Theorem 3.2. Its Lagrangian can be decomposed as,

$$\hat{l}(q,\xi) = \underbrace{\frac{1}{2} \langle \mu, \mu \rangle_{M_b(q)}}_{\hat{l}_{\mu}} + \underbrace{\frac{1}{2} \langle \dot{q}, \dot{q} \rangle_{\Lambda_q(q)} - \mathcal{V}(q)}_{\hat{l}_{\dot{q}}}$$
(3.45)

where $\mathcal{V}: \mathbb{R}^n \to \mathbb{R}$ is a scalar potential field on the shape. The dynamics in (5.3) is represented as the negative feedback interconnection of two passive subsystems (as shown in Fig. 3.7a)

$$\Sigma_1 : (\tau - \mathcal{A}_l^{\top} \mathcal{F}_1) + \frac{D\hat{l}_{\mu}}{Dq} \mapsto \dot{q}, \quad \Sigma_2 : \begin{bmatrix} \mathcal{F}_1 \\ -\dot{q} \end{bmatrix} \mapsto \begin{bmatrix} \mu \\ \frac{D\hat{l}_{\mu}}{Dq} \end{bmatrix}$$
 (3.46)

with the subsystem Hamiltonians, $\mathcal{H}_{\mu} \equiv \hat{l}_{\mu}$ and $\mathcal{H}_{\dot{q}} = \langle \frac{\delta \hat{l}_{\dot{q}}}{\delta \dot{q}}, \dot{q} \rangle - \hat{l}_{\dot{q}}$ as storage functions, where $\frac{D \hat{l}_{\mu}}{D q}$ is the covariant derivative of the locked kinetic energy relative to the shape (q), see [149, §4.2], and serves as the subsystem coupling signal.

Proof. Under the presence of \mathcal{V} , the R.H.S. of the shape dynamics for forcing is $\tau - \mathcal{A}_l^{\mathsf{T}} F_1 - \frac{\partial \mathcal{V}}{\partial q}$. In the shape dynamics (bottom row of (5.3)), the CC terms with (μ, μ) coupling are actually the covariant derivative of the locked kinetic energy, \hat{l}_{μ} , relative to the shape, see [149, §4.2], i.e.,

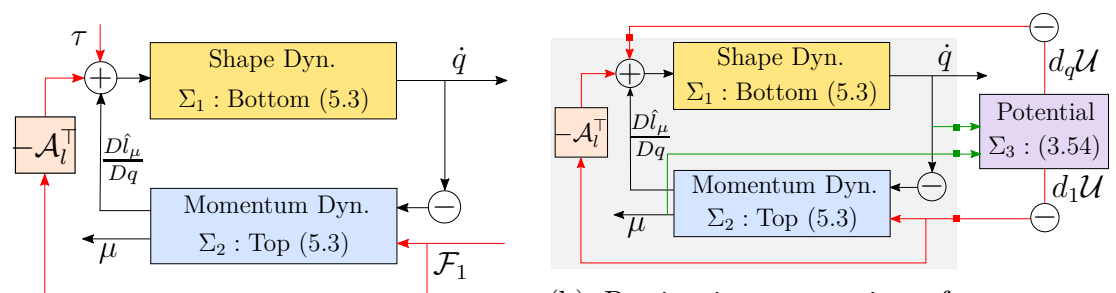
$$\frac{D\hat{l}_{\mu}}{Dq} = \frac{\delta\hat{l}_{\mu}}{\delta q} - \mathcal{A}_{l}^{\top} \operatorname{ad}_{\mu}^{\top} \frac{\delta\hat{l}_{\mu}}{\delta \mu}$$
(3.47)

Thus, taking the time-derivative of $\mathcal{H}_{\dot{q}}$ for Σ_1 ,

$$\mathcal{H}_{\dot{q}} = \langle (\tau - \mathcal{A}_{l}^{\top} \mathcal{F}_{1}) + \frac{D\hat{l}_{\mu}}{Dq}, \dot{q} \rangle$$
 (3.48)

by using the skew-symmetry of $\tilde{\mathcal{B}}$ and $\tilde{\Gamma}'$ in Prop. 3.2. Likewise, computing the time-derivative of \mathcal{H}_{μ} for Σ_2 , and using passivity in Prop. 3.2,

$$\dot{\mathcal{H}}_{\mu} = \langle \mathcal{F}_{1}, \mu \rangle - \langle \mu, \left(\frac{1}{2}S(\mu) + \operatorname{ad}_{M_{b}\mu}^{\sim} \mu \mathcal{A}_{l}\right) \dot{q} \rangle
= \langle \mathcal{F}_{1}, \mu \rangle + \langle -\dot{q}, \left(\frac{1}{2}S(\mu)^{\top} - \mathcal{A}_{l}^{\top} \operatorname{ad}_{\mu}^{\top} M_{b}\right) \mu \rangle = \langle \mathcal{F}_{1}, \mu \rangle + \langle -\dot{q}, \frac{D\hat{l}_{\mu}}{Dq} \rangle$$
(3.49)



- (a) Passive interconnection of momentum and shape subsystems.
- (b) Passive interconnection of momentum and shape subsystems with a symmetrybreaking potential.

Figure 3.7: Passive interconnection block diagrams.

It is worth highlighting the significance of Theorem 3.4 in the context of motion control. Prior works from pedal robotics [25, 150–152] and orbital robotics [34, 36] have exploited momentum-based motion control methods. In these works, the momentum subsystem motion is analysed as a linear system (not energy-based), while passivity analysis is applied only for the whole system (not subsystem). The main reason that prevents subsystem motion analysis is the interconnection term $\frac{D\hat{l}_{\mu}}{Dq}$. Theorem 3.4 concludes that the momentum and shape subsystems are in a passive negative feedback interconnection, and hence ensuring OSP of each subsystem is enough to ensure OSP of the whole system. Note also that this passive interconnection is a direct result of Noether's symmetry in the FRM dynamics, and would not result from the general inertia-decoupled form in Lemma 3.2.

3.7 Generalization of the FRM

In Sec. 3.5, I considered the FRM with a Lagrangian, \hat{l} , that was independent of the group variable g_1 . In this section, I generalize the following case: The motion of the FRM in Def. 3.1 is governed by a symmetry-breaking potential field in the presence of a surrounding potential fluid flow, see Fig. 3.8.

3.7.1 Symmetry-breaking Potential Fields

A symmetry-breaking potential field, $\mathcal{U}(g_1,q): \mathrm{SE}(3) \times \mathbb{R}^n \to \mathbb{R}$, is a scalar potential, which breaks the Lagrangian symmetry of the FRM, i.e., $\hat{l} = \hat{l}_{\mu} + \hat{l}_{\dot{q}} - \mathcal{U}(g_1,q)$ depends explicitly on the FRM-base pose g_1 . Common examples of such potential fields are gravity and buoyancy. Considering the *unforced*³ FRM under such

³The following analysis is performed for the unforced case for ease of illustration, but obviously the extension of the passive interconnection also holds in the forced case with the forces acting as additional inputs as in Theorem 3.4.

a symmetry-breaking potential field, the \mathcal{LP} equations are written by applying the same transformation as for the forces in the proof of Theorem 3.2, but with a negative sign, as,

$$\mathcal{LP}^*(q, \dot{\mu}, \ddot{q}) = - \begin{bmatrix} d_1 \mathcal{U}(g_1, q) \\ d_q \mathcal{U}(g_1, q) - \mathcal{A}_l^{\top} d_1 \mathcal{U}(g_1, q) \end{bmatrix}$$
(3.50)

where d_1 and d_q are the differentials of the argument relative to the coordinates g_1 and q, respectively. In the following, the SE(3)-dependency of the differentials on the SE(3) group will be denoted by the subfixes, as in (3.50). Despite symmetry-breaking, I extend the result of Theorem 3.4 below.

Corollary 3. Consider the \mathcal{LP} system, whose motion is given by Theorem 3.2 with forces purely arising from a symmetry-breaking potential, $\mathcal{U}(g_1, q)$. Its Lagrangian in (3.45) is,

$$\hat{l}(q,\xi) = \hat{l}_{\mu}(q,\mu) + \hat{l}_{\dot{q}}(q,\dot{q}) - \mathcal{U}(g_1,q)$$
(3.51)

The passive feedback interconnection of the momentum and shape subsystems in Theorem 3.4 is in a negative feedback interconnection with the dynamics of \mathcal{U} , which are together represented as three passive subsystems (as shown in Fig. 3.7b)

$$\Sigma_1 : - \left(d_q \mathcal{U} - \mathcal{A}_l^{\top} d_1 \mathcal{U} \right) + \frac{D\hat{l}_{\mu}}{Dq} \mapsto \dot{q}, \quad \Sigma_2 : \begin{bmatrix} -d_1 \mathcal{U} \\ -\dot{q} \end{bmatrix} \mapsto \begin{bmatrix} \mu \\ \frac{D\hat{l}_{\mu}}{Dq} \end{bmatrix}$$
(3.52)

$$\Sigma_3 : \begin{bmatrix} \mu \\ \dot{q} \end{bmatrix} \mapsto \begin{bmatrix} d_1 \mathcal{U} \\ d_q \mathcal{U} - \mathcal{A}_l^\top d_1 \mathcal{U} \end{bmatrix}$$
 (3.53)

with the subsystem Hamiltonians \mathcal{H}_{μ} , $\mathcal{H}_{\dot{q}}$ and the potential \mathcal{U} as the storage functions

Proof. For Σ_3 , the dynamics of \mathcal{U} is given by,

$$\frac{d}{dt}\mathcal{U} = \langle d_1 \mathcal{U}, V_1 \rangle + \langle d_q \mathcal{U}, \dot{q} \rangle = \langle d_1 \mathcal{U}, \mu \rangle + \langle d_q \mathcal{U} - \mathcal{A}_l^\top d_1 \mathcal{U}, \dot{q} \rangle$$
 (3.54)

The unforced variant of \mathcal{LP} equations in (3.50) is,

$$\mathcal{LP}^*(q, \dot{\mu}, \ddot{q}) = -\begin{bmatrix} d_1 \mathcal{U}(g_1, q) \\ d_q \mathcal{U}(g_1, q) - \mathcal{A}_l^{\top} d_1 \mathcal{U}(g_1, q) \end{bmatrix}$$
(3.55)

Computing the time-derivatives of $\mathcal{H}_{\dot{q}}$ and \mathcal{H}_{μ} for Σ_1 and Σ_2 , as in Theorem 3.4,

$$\dot{\mathcal{H}}_{\dot{q}} = -\langle -(d_q \mathcal{U} - \mathcal{A}_l^{\top} d_1 \mathcal{U}), \dot{q} \rangle - \langle \frac{D\hat{l}_{\mu}}{Dq}, \dot{q} \rangle, \dot{\mathcal{H}}_{\mu} = -\langle d_1 \mathcal{U}, \mu \rangle + \langle \dot{q}, \frac{D\hat{l}_{\mu}}{Dq} \rangle$$
(3.56)

Remark 20. Resolving the top row of Theorem 3.2 in the CoM frame of the FRM provides the CoM translational dynamics $(\dot{\mu}_v)$, which is the only part affected by the gravity potential forces, see [25]. However, this simplification only works for the gravity potential. For a general symmetry-breaking potential, e.g. buoyancy, there might be yet another frame of relevance. Thus, I have provided a general expression in (3.50), which includes the result in [25].

Consider the FRM in Fig. 3.8 with a body frame positioned at the CoM, $\{CM\}$, but oriented along $\{1\}$. The gravity potential is

$$\mathcal{U}_q = m\gamma h = m\gamma \langle E_3, p_c \rangle = m\gamma \langle E_3, p_1 + R_1 p_{1c}(q) \rangle \tag{3.57}$$

where $\gamma = 9.81 [\text{m/s}^2]$ is the gravity constant, $E_3 = (0, 0, 1)$ is the vertical direction of $\{O\}$, and $p_{1c} \in \mathbb{R}^3$ is the position of CoM ($\{CM\}$) relative to $\{1\}$. Considering $\mathcal{U}_g \equiv \mathcal{U}_g(g_c)$,

$$d_{cm}\mathcal{U}_g(g_{cm}) = \left(g_{cm}^{-1} \frac{\delta \mathcal{U}_g}{\delta g_{cm}}\right)^{\vee} = f_g = (\hat{\gamma}, 0)$$
(3.58)

where $\hat{\gamma} = R_1^{\top} E_3 m \gamma$ is the left trivialized gravity force at $\{CM\}$. Similarly,

$$d_q \mathcal{U}_g(g_1, q) = \frac{\delta U_g}{\delta q} = \langle \frac{\delta g_c}{\delta q}, \frac{\delta U_g}{\delta g_c} \rangle = J_{1c}^{\top} d_{cm} U_g$$
 (3.59)

where $J_{1c} \in \mathbb{R}^{6 \times n}$ is the Jacobian (push-forward) of $g_{1cm} \equiv g_{1cm}(q)$ as a forward kinematics map. For any arbitrary body frame $\{1\}$, considering $\mathcal{U}_g \equiv \mathcal{U}_g(g_1, q)$,

$$d_1 \mathcal{U}_g(g_1, q) = \left(g_1^{-1} \frac{\delta \mathcal{U}_g}{\delta g_1}\right)^{\vee} = \left(\hat{\gamma}, (p_{1cm})_{\times} \hat{\gamma}\right) = \operatorname{Ad}_{1cm}^{-\top} f_g = \operatorname{Ad}_{1cm}^{-\top} d_{cm} \mathcal{U}_g \qquad (3.60)$$

Thus, the total gravity contribution in \mathcal{LP}^* in (3.50) is compactly written as,

$$\left(\operatorname{Ad}_{1cm}^{-\top} d_{cm} \mathcal{U}_g, (J_{1cm} - \operatorname{Ad}_{1cm}^{-\top} \mathcal{A}_l)^{\top} d_{cm} U_g\right) = \left(\operatorname{Ad}_{1cm}^{-\top} d_{cm} \mathcal{U}_g, \tilde{J}_{1cm}^{\top} d_{cm} U_g\right)$$
(3.61)

where \tilde{J}_{1cm} is the corresponding generalized Jacobian. In the same way, consider the body frame positioned at the buoyancy center, $\{CB\}$, but oriented along $\{1\}$. Let the buoyancy potential be written as $\mathcal{U}_b(g_{cb}) \equiv \mathcal{U}_b(g_1, q)$. Following the same steps as above, the buoyancy contribution appears in the form of (3.61) as

$$\left(\operatorname{Ad}_{1cb}^{-\top} d_{cb} \mathcal{U}_b, (J_{1cb} - \operatorname{Ad}_{1cb}^{-\top} \mathcal{A}_l)^{\top} d_{cb} U_b\right) = \left(\operatorname{Ad}_{1cb}^{-\top} d_{cb} \mathcal{U}_b, \tilde{J}_{1cb}^{\top} d_{cb} U_b\right)$$
(3.62)

where the subfixes $_{cm}$ have been replaced with analogous $_{cb}$ terms.

Thus, using the above machinery, symmetry-breaking potential fields (gravity and buoyancy) can be considered for the FRM as an \mathcal{LP} system. This is relevant for applications in aerial and underwater robotics, especially keeping the passive feedback interconnection in perspective for motion control.

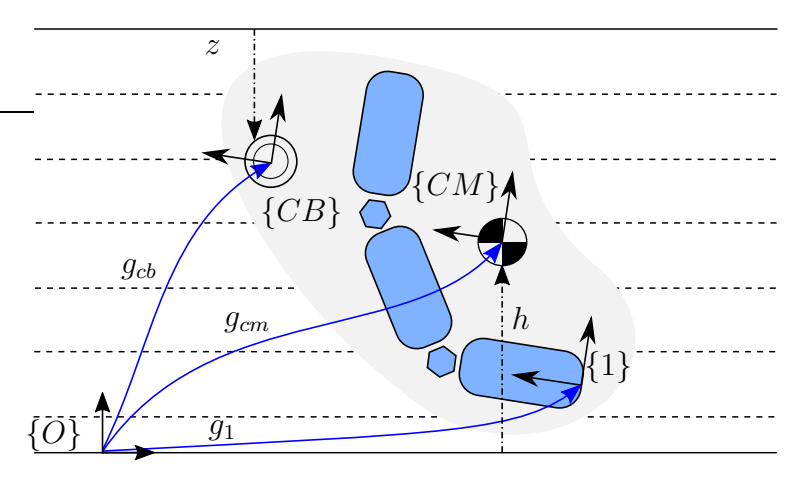


Figure 3.8: Floating-base Robotic Mechanism (FRM) in presence of symmetry-breaking potentials in the form of gravity at CoM $\{CM\}$ and buoyancy at $\{CB\}$, while being submerged in a potential fluid flow. Motion of FRM results in motion of liquid envelope (grey), and vice versa.

3.7.2 Potential Fluid Flow

For the second generalization, the FRM is considered submerged in a fluid, e.g. in underwater robotics, microrobotics. Three key simplifications are exploited for analysis of this case. Firstly, the fluid flow is considered to be a potential flow, i.e., motion is considered in absence of a vortex-shedding mechanism [153]. This framework is sufficient to describe the motion of the FRM due to transfer of momentum between itself and the surrounding fluid. Secondly, the fluid is considered incompressible [154], which makes the FRM-fluid system independent (symmetric) of fluid variables, and the dynamics of (g_1, q) is sufficient to completely describe the motion of the FRM. Thirdly, in the absence of the symmetry-breaking potentials, the total Lagrangian of the FRM-fluid system is independent of g_1 , i.e.,

$$\hat{l} = \frac{1}{2} \langle \mu, \mu \rangle_{M_b} + \frac{1}{2} \langle \dot{q}, \dot{q} \rangle_{\Lambda_q} + \mathcal{K}_f(q, \dot{q}, \mu)$$
(3.63)

where \mathcal{K}_f is the kinetic energy of the fluid. Together with the potential flow consideration, (3.63) is written as, $\hat{l} = \frac{1}{2} \langle \mu, \mu \rangle_{\hat{M}_b} + \frac{1}{2} \langle \dot{q}, \dot{q} \rangle_{\hat{\Lambda}_q}$, where \hat{M}_b and $\hat{\Lambda}_q$ are the new inertia tensors with added inertia effects due to the surrounding fluid [153–156]. Consequently, the local mechanical connection, $\hat{\mathcal{A}}_l = \hat{M}_b^{-1} \hat{M}_{bq}$, where \hat{M}_{bq} is the coupling inertia with added inertia. Note that for these inertia tensor transformations, each link inertia $\hat{M}_k = M_k + \sum \bar{M}_{kj}$, where \bar{M}_{kj} is the inertia added to the k^{th} -link due to the surrounding fluid and the j^{th} -link due to hydrodynamic coupling, see [153, §7.2].

Thus, considering the link-wise inertia mappings, the result of Theorem 3.2 holds, as all the matrices in (3.26) are computable using \hat{M}_k . In this case, μ is the

locked velocity of the FRM-fluid system, and the top row of (5.3) encapsulates its total momentum dynamics. Using this, the following generalization of \mathcal{LP} dynamics of the FRM is stated.

Theorem 3.5. Consider the Floating-base Robotic System in Fig. 3.8 in the presence of an effective symmetry-breaking potential $\mathcal{U}(g_1,q)$, e.g. gravity, buoyancy, spatial spring etc., and surrounded by a potential fluid flow with kinetic energy \mathcal{K}_f . The Lagrangian of the FRM-fluid system is of the form,

$$\hat{l} = \frac{1}{2} \langle \mu, \mu \rangle_{M_b} + \frac{1}{2} \langle \dot{q}, \dot{q} \rangle_{\Lambda_q} + \mathcal{K}_f(q, \dot{q}, \mu) - \mathcal{U}(g_1, q)$$
(3.64)

and its motion is governed by a variation of the \mathcal{LP} equations. This system of equations is written using the factorization of the matrix of CC terms, as in Theorem 3.2, and is written as:

$$\underbrace{\begin{bmatrix} \hat{M}_{b}(q) & 0_{6,n} \\ 0_{n,6} & \hat{\Lambda}_{q}(q) \end{bmatrix}}_{\hat{\Lambda}(q)} \begin{bmatrix} \dot{\mu} \\ \ddot{q} \end{bmatrix} + \underbrace{\begin{bmatrix} \frac{1}{2}\hat{P}(\dot{q}) & 0_{6,n} \\ 0_{n,6} & \hat{\Gamma}'_{q}(\dot{q}) \end{bmatrix}}_{\hat{\mathcal{D}}_{\dot{q}}(q,\dot{q})} \underbrace{\begin{bmatrix} \mu \\ \dot{q} \end{bmatrix}}_{\dot{\xi}}$$

$$= \underbrace{\begin{bmatrix} \operatorname{ad}_{\hat{M}_{b}\mu}^{\sim} & -\frac{1}{2}\hat{S}(\mu) - \operatorname{ad}_{\hat{M}_{b}\mu}^{\sim} \hat{\mathcal{A}}_{l} \\ \frac{1}{2}\hat{S}(\mu)^{\top} - \hat{\mathcal{A}}_{l}^{\top} \operatorname{ad}_{\hat{M}_{b}\mu}^{\sim} & -\hat{\mathcal{B}}(q,\mu) \end{bmatrix}}_{\hat{\mathcal{D}}_{\mu}(q,\mu)} \begin{bmatrix} \mu \\ \dot{q} \end{bmatrix} \qquad (3.65)$$

$$+ \begin{bmatrix} \mathcal{F}_{1} \\ \tau - \mathcal{A}_{l}^{\top} \mathcal{F}_{1} \end{bmatrix} + \begin{bmatrix} d_{1}\mathcal{U} \\ d_{q}\mathcal{U} - d_{1}\mathcal{U} \end{bmatrix}$$

where the $\hat{\bullet}$ matrices are computed using \hat{M}_k for the link inertia.

Theorem 3.5 is a generalized form of the \mathcal{LP} dynamics of the FRM under the action of symmetry-breaking potential fields and in the presence of a surrounding potential flow. In this way, this form is applicable to orbital, aerial and underwater robotics. The key advantages of Theorems 3.2-3.5 over the prior results from robot dynamics (Lemma 3.2) and geometric mechanics (Lemma 3.3) are summarized in Table 3.1 through a comparison. From Theorem 3.2, the closed form expressions of $\mathcal{D}_{\dot{q}}$, \mathcal{D}_{μ} enable the linearization of the CC terms, e.g. $\frac{\partial \mathcal{D}_{\alpha}\xi}{\partial \dot{q}}$, $\frac{\partial \mathcal{D}_{\mu}\xi}{\partial \mu}$ using existing methods, as in [22], which is not possible in Lemmas 3.2 and 3.3. Although a computational comparison merits its own scope, I provide a preliminary idea below. The computation of Γ in Lemma 3.2 required one pass of n iterations (link-wise), and an additional numerical transformation. The computation of $\mathcal{D}_{\dot{q}}$, \mathcal{D}_{μ} in Theorem 3.2 requires 2 passes with n iterations in each pass. One pass is nominally given by the expressions in (3.26), which in turn require \mathcal{A}_l that is computed in a preceding pass. For the extension in Theorem 3.5 to consider surrounding fluid, an additional pass of n+1 iterations is

required to compute \hat{M}_k with added inertia effects for each link to account for the hydrodynamic coupling between the links. While the simplification of the gravity force was given before in robot dynamics [25], I provide a general framework for symmetry-breaking potential fields to account for other effects like buoyancy and parasitic stiffness acting on the FRM-base.

Property	Rob. Dyn. (Lem. 3.2)	Geom. Mech. (Lem. 3.3)	•
Commut. (Prop. 3.1)	*	×	√
Skew-sym. (Prop. 3.2)	✓	*	✓
SE(3) Transf. (Prop. 3.3)	✓	✓	✓
Invariance (Prop. 3.4)	*	*	✓
Curvature (Th. 3.3)	*	✓	✓
CC Linearization	*	*	✓
Computation	Iterative	Symbolic	Iterative
Complexity	n+Transform.	_	2n
Symmetry-breaking	✓	✓	✓
Potential Generalization			
Extension with	*	✓	✓
Fluid Flow (Th. 3.5)			

Table 3.1: Comparison of FRM dynamics formulations

3.8 Conclusion

In this paper, I proposed a novel factorization of the Coriolis/Centrifugal (CC) matrix for the inertia-decoupled equations of a Floating-base Robotic Mechanism (FRM). The factorization was a consequence of simplifying the CC matrix computation from robot dynamics and deriving the Lagrange-Poincaré (\mathcal{LP}) equations from geometric mechanics. The proposed CC matrix is separated into two parts based on velocity dependency. The first part, which depends only on the shape velocity, was proved to satisfy the skew-symmetry (passivity) property. The second part, which depends only on the locked velocity, was proved to be skew-symmetric. I also derived novel commutative properties between two fundamental matrices that feature in the proposed CC matrices. I proved that the shape dynamics are invariant to the transformation of momentum dynamics. From a geometric perspective, I derived the generalized Poinsot's construction to visualize the motion of the FRM. Using the proposed CC matrix factorization, I derived the iterative expression to compute the curvature form of the FRM. I also used the proposed

curvature computation to estimate the FRM-base displacement due to a planar gait, while considering more than two shape variables. Using the proposed form of the \mathcal{LP} dynamics, the passive feedback interconnection between the momentum and shape subsystems was revealed. Furthermore, the proposed form was extended to include symmetry-breaking potentials (e.g., gravity) and the presence of a surrounding potential fluid flow. In this way, the contributions of this chapter are applicable in multiple robotics domains. The publication resulting from the contributions of this chapter is:

1. H. Mishra, G. Garofalo, A. M. Giordano, M. De Stefano, C. Ott, and A. Kugi, "Reduced Euler-Lagrange equations of floating-base robots: Computation, properties, and applications", *IEEE Transactions on Robotics*, pp. 1–19, 2022

In the following two chapters, the proposed form of the \mathcal{LP} dynamics will be exploited to simulate momentum-consistent dynamics for HIL simulation and for designing observer-based motion control for the FRM.

Motion Substructuring for V&V

Oriven by the principle of being (on-orbit), the vehicular mechanism (on-ground) appears in its specific role by association with the principle of becoming (Lagrangian matching) [157, pp. 35].

Ishvarakrishna, Samkhya-karika, 4th century AD

4.1 Introduction

Dynamic substructuring is an engineering approach to model the dynamical behaviour of a multi-system mechanism by decomposing it into meaningful domain-specific subsystems [158]. A key advantage of substructuring is that it enables the interfacing of model-based and real subsystems in a HIL simulation. In large-scale orbital projects for on-orbit servicing/assembly, HIL serves as a key element for V&V of control, estimation and planning algorithms of orbital mechanisms [46]. In this chapter, the main contribution is a HIL framework for V&V of orbital motion control algorithms from the phases of control prototyping to flight-ready prototype tests. To achieve this, the inertia-decoupled \mathcal{LP} dynamics from the previous chapter will be exploited for substructuring.

4.1.1 Related Work

Orbital mechanisms, e.g. a manipulator-equipped spacecraft, have emerged as a key mission element in on-orbit servicing [43–45], active debris removal [46], on-

orbit assembly [47] and sample acquisition from remote sites on a comet/asteroid [48]. The controller software for the whole bespoke orbital mechanism, which includes navigation, control law, planner etc. [73], is executed on subsystem-specific On-board Software (OBSW) computers. For the V&V of the OBSW algorithms, which is required to achieve the necessary technology readiness levels [159, 160], HIL simulation using On-ground Robotic facilities (OGRF) have increasingly gained eminence [46–50] due to their inherent integration of available hardware and software models. Hence, to meaningfully interface the OBSW with a HIL facility, it is imperative to generate motion in a physically consistent way.

A classification of the reported HIL facilities is provided in Table. 4.1 and is summarized below. In [161, 162], HIL for an underactuated and unforced orbital FRM was proposed by exploiting its momentum map conservation and combining a numerical simulation of spacecraft states with a fixed-base OGRF. In an alternative strategy in [162], the orbital FRM was mounted on a vehicle (another manipulator), which effected the spacecraft motion. In [49, 163], the end-effector poses of fixed-base reference robot and OGRF were modeled with a kinematic constraint and drift-compensation schemes were proposed. The vehicle emulation system II [164] used Force-Torque Sensor (FTS) measurements instead of model-based dynamics to command the spacecraft motion, which results from interaction between the orbital manipulator and its spacecraft. A fixed-base HIL approach was used in [165] to simulate a dual-arm orbital FRM for contact scenarios. A common attribute of HIL in [161, 165] was the use of a fixed-base OGRF and a vehicle with the satellite-prototype to simulate the relative motion between the test satellite and the orbital FRM. In [73, §3], a predefined momentum and kinematic model of a grasped satellite were added to the reduced orbital FRM dynamics computation to simulate interaction dynamics. Alternatively, in [50, 166], inertia-coupled Hamel's equations [31] were integrated using FTS measurements to compute the dynamics of the orbital FRM's spacecraft. In [166], joint positions were commanded to a fixed-base OGRF in admittance causality and the spacecraft motion was numerically simulated. Contrastingly, in [50], the orbital manipulator was considered as an impedance on a vehicle, which effected spacecraft motion in admittance causality. To summarize, in the aforementioned works, for the free-floating case, reduced dynamics on momentum map level-set were exploited while, the Hamel's equations were used for the case with external forces. Note that only the former method preserves implicitly the symmetry, i.e. momentum is conserved.

4.1.2 Key Contributions

In this chapter, the *emphasized* items from Table 4.1 are considered. I use a model-based dynamic interaction between orbital manipulator and spacecraft because the interaction forces depend directly on the HIL state-space, i.e. actual motion in OGRF. Like [162], I also analyse *both* fixed-base and vehicle-driven OGRF, but,

4.1 Introduction 89

Attribute	Classification		
Dynamic interaction	Model-based, FTS sensor		
between manipulator			
and spacecraft			
• Spacecraft	Fixed-base (software),		
$\operatorname{simulation}$	$Vehicle ext{-}driven$		
• Vehicle causality	$Impedance,\ Admittance$		
• Commanded motion	Absolute, Relative		

Table 4.1: Classification of HIL facilities for orbital FRM

for the vehicle, both causalities, admittance and impedance, are considered. By describing absolute dynamics, I ensure that the OGRF experiences the correctly computed Coriolis/Centrifugal (CC) forces during HIL validation. An orbital manipulator in impedance causality is considered due to its suitability for contact-oriented tasks [43–45]. To this end, the main result of this chapter is obtained by proving equivalence between the Controlled Lagrangians (CL) corresponding to the OGRF and the orbital robot. However, instead of the Hamel's equations or the reduced dynamics, I exploit the inertia-decoupled structure of the \mathcal{LP} [167, eq. 2.9] equations to fully describe the orbital robot dynamics and, therefore, include spacecraft-actuation and external forces.

The contributions of this chapter are the following.

- 1. In Theorem 4.1, a converse Lagrangian matching method is proposed that shapes the behaviour of the \mathcal{EL} equations of an OGRF to replicate the \mathcal{EL} equations of the shape (joints) of the orbital FRM. This enables control prototyping using the OGRF, while considering the mission orbital FRM.
- 2. In Theorem 4.2, a converse Lagrangian matching method is proposed that shapes the behaviour of the \mathcal{EL} equations of an OGRF to replicate the \mathcal{EP} equations of the spacecraft (base) of the orbital FRM. To simulate spacecraft motion, the block-diagonal inertia of \mathcal{LP} equations from Chapter 3 are exploited. This obviates the need for joint acceleration/torque measurements, which can be noisy and bias-prone. In fact, to simulate interactions between manipulator and spacecraft even in presence of external forces, I show that tangent space variables and a FTS of the HIL are sufficient.
- 3. The physical (momentum) consistency in previous free-floating HIL is extended to the case of a forced orbital robot by using \mathcal{LP} equations to completely describe its fully-actuated dynamics.
- 4. Finally, I demonstrate the effectiveness of the proposed methods through comparative experiments on two OGRF platforms, a fixed-base KUKA

LWR4+ and the OOS-SIM [50]. In particular, for the latter case, I also provide experimental results for the HIL of a fully-actuated orbital robot while considering environment interactions.

The layout of the chapter is as follows. The problem statement of HIL for the orbital robot is described in Sec. 4.2. In Sec. 4.3, the motion of the OGRF in a typical HIL facility are modeled. In Sec. 4.4, the main idea is proposed using the method of Controlled Lagrangians (CL), and \mathcal{LP} equations are introduced. In Sec. 4.5, I propose two converse theorems for dynamics equivalence and three modalities for simulating spacecraft motion in HIL. In Sec. 5.6.2, I provide experimental results, followed by concluding remarks in Sec. 4.7.

4.2 V&V-Problem for an Orbital Mechanism

Orbital FRMs are a key technology for on-orbit servicing/assembly operations [41, 168] and active debris removal [169]. In projects related to early-phase mission analysis and flight-prototype validation, HIL testing is a necessary requirement to increase the technology readiness level. Therefore, it is important to replicate the motion of the mission orbital FRM on the OGRF faithfully to maximize the scope of V&V. To that end, let us first formalize it.

4.2.1 Orbital Mechanism

Def. 4.1. An orbital mechanism, e.g. a manipulator-equipped spacecraft, is a FRM of n+1 rigid links, which are connected with n holonomic-joints. The simplified configuration space of the orbital robot, as seen in Fig. 4.1 (blue box), is $\hat{Q} \cong SE(3) \times \mathbb{R}^n$ with coordinates $z = (g_b, q) \in \hat{Q}$.

Using Def. 4.1, the orbital mechanism's total velocity is $\zeta = (V_b, \dot{q})$, where $\dot{g}_b = g_b V_b^{\wedge}$, $V_b^{\wedge} \in \mathfrak{se}(3)$ refers to the spacecraft velocity. Considering the fully-coupled inertia tensor, $\hat{M}(q) \in \mathbb{R}^{(6+n)\times(6+n)}$, its reduced Lagrangian takes the form $\hat{l}(q,\zeta) = \frac{1}{2}\zeta^{\top}\hat{M}(q)\zeta$. The Hamel's equations describe its dynamics as,

$$\underbrace{\begin{bmatrix} \hat{M}_b & \hat{M}_{bq} \\ \hat{M}_{bq}^{\top} & \hat{M}_q \end{bmatrix}}_{\hat{M}} \dot{\zeta} + \hat{C}(q, \zeta) \zeta = \begin{bmatrix} \hat{\mathcal{F}}_b \\ \hat{\tau} \end{bmatrix} + \begin{bmatrix} \hat{J}_b(q)^{\top} \\ \hat{J}(q)^{\top} \end{bmatrix} \mathcal{F}_e, \tag{4.1}$$

where \hat{M} and \hat{C} are the matrices of inertia and CC terms, respectively, $(\hat{F}_b, \hat{\tau})$ are the actuator forces commanded from OBSW, and $\mathcal{F}_e \in \mathbb{R}^6 \cong \mathfrak{se}(3)^{\top}$ is the external interaction wrench at a material point $\{\mathcal{E}\}$ on the mechanism's structure. Given the pose $g_e = \hat{f}(q)$, where $f: \hat{Q} \to \text{SE}(3)$ is the forward kinematics map of $\{\mathcal{E}\}$, and $\hat{J}_b \in \mathbb{R}^{6 \times 6}$ and $\hat{J} \in \mathbb{R}^{6 \times n}$ are the Jacobians for base and articulated mechanism displacements, respectively.

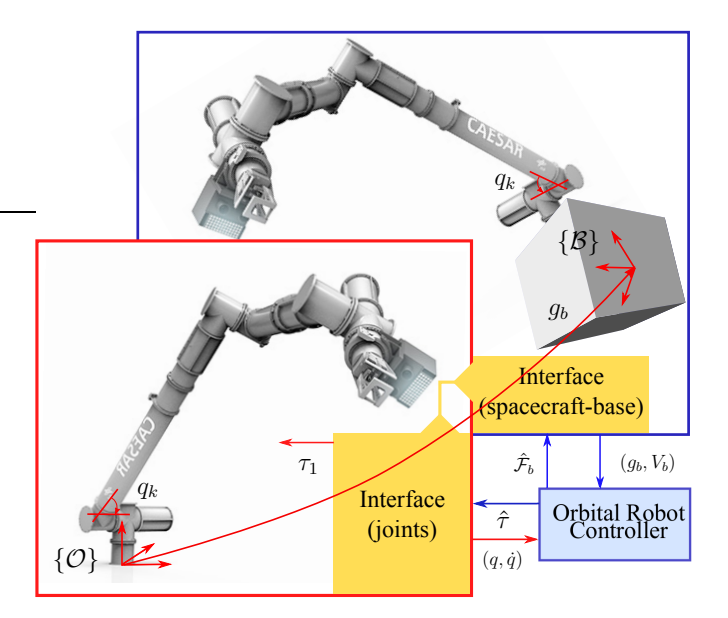


Figure 4.1: Diagram of an orbital robot (CAESAR [170], blue) on right. The forced dynamics of this system can be simulated on a fixed-base CAESAR manipulator (red) for HLS validation.

4.2.2 Problem Statement

Orbital mechanisms can have a articulated structures with length of 2-4[m] [43, 170] depending on mission requirements. Firstly, the HIL V&V of these unwieldy-sized mechanisms poses additional complexities [46] to simulate the base motion, which can be avoided using a fixed-base setup. This is illustrated in Fig. 4.1, where an OBSW is interfaced with the fixed-base CAESAR arm [170] (red box). Secondly, for HIL validation of sensor-based navigation, physical floating-base dynamics is also necessary. In this case, a scaled-down model might be used while simulating floating-base dynamics. Therefore, in both cases outlined above, a common interface (Fig. 4.1, yellow) between an OBSW and OGRF is required, which maps the OBSW commands, $(\hat{\mathcal{F}}_b, \hat{\tau})$, to that of OGRF, such that the latter's state-space trajectories are identical to that of the orbital mechanism.

Past HIL methods have relied on Hamel's equations for simulating the forced dynamics of the orbital robot. On one hand, this requires \ddot{q} or τ measurements for reconstructing spacecraft motion (first row in (4.1)), which is a sensory overhead for the HIL. On the other hand, the Hamel's equations lack the momentum consistency of free-floating dynamics. Note that free-floating dynamics are physically consistent due to the momentum map level-set constraint but are restricted to an unforced case. Therefore, alternatively, I use the \mathcal{LP} description of the orbital mechanism, to ensure consistency.

4.3 On-ground Robotic facilities (OGRF)

During the course of a large-scale project, e.g. an orbital mission, the required technology-readiness level [159, 160] dictates the complexity of the HIL OGRF that is used for V&V. In the following, the OGRF that are commonly available for prototyping and V&V of the motion system on an orbital mechanism are classified, see Fig. 4.2. In the following treatment, the HIL-specific quantities are denoted by their corresponding subfix.

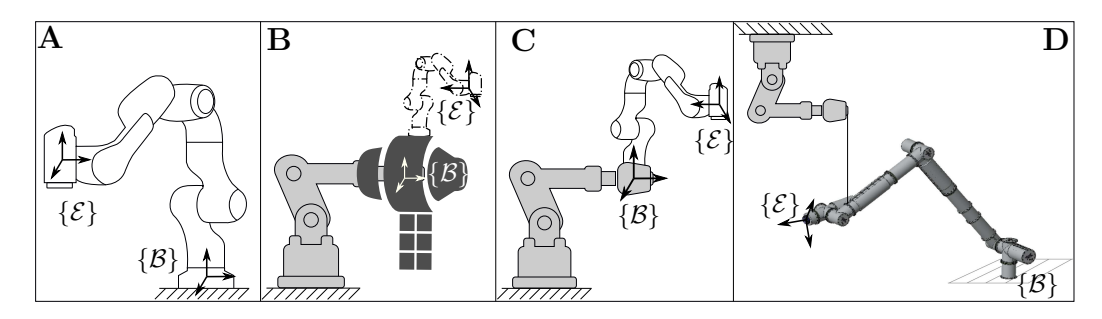


Figure 4.2: On-ground Robotic facilities (OGRF). A: Fixed-base manipulator, B: Flight-ready prototype of vehicle with simulated manipulator, C: Vehicle-manipulator with mechanical mounting on another manipulator end-effector, $\{\mathcal{B}\}$, D: Gravity-compensated OGRF for flight-ready prototype of manipulator.

4.3.1 Fixed-base Manipulator

A fixed-base manipulator is often a starting point to initiate prototyping [48]. It is formalized below.

Def. 4.2. A fixed-base manipulator is a multibody with n holonomic-joints, see left of Fig. 4.2-**A**. Its configuration is denoted with coordinates, $q_1 \in Q_1$, corresponding to the joint positions and Q_1 is a Riemannian manifold with manipulator inertia, $\Lambda_1(q_1) \in \mathbb{R}^{n \times n}$, as its metric tensor.

The Lagrangian for this manipulator is $L_1 = \frac{1}{2} \langle \dot{q}_1, \dot{q}_1 \rangle_{\Lambda_1} - U_1(q_1)$, where $U_1(q_1)$ is the gravity potential. The dynamics are written using the Euler-Lagrange operator, $\mathcal{EL}(L_1)$ [167, eq. 2.3] as,

$$\mathcal{EL}(L_1) = \Lambda_1(q_1)\ddot{q}_1 + \Gamma_1(q_1, \dot{q}_1)\dot{q}_1 = \tau_1 + \tau_{1d} + J_1(q)^{\top} \mathcal{F}_e$$
 (4.2)

where $C_1 \in \mathbb{R}^{n \times n}$ is the matrix of joint-space CC terms, and $\tau_1, \tau_{1d} \in \mathbb{R}^n$ are actuation and other lumped torques (including gravity potential torques, i.e. $\frac{\partial U_1(q_1)}{\partial q_1}$), respectively. $J_1(q_1) \in \mathbb{R}^{6 \times n}$ and $\mathcal{F}_e \in \mathbb{R}^6 \cong \mathfrak{se}(3)^*$ are the manipulator Jacobian and wrench at end-effector, respectively.

93

Remark 21. The fixed-base OGFM in Def. 4.2 is capable of executing only the motion of an orbital robot's manipulator. So, the spacecraft pose, g_b , is entirely reconstructed in software using the simulated actuation $\bar{\mathcal{F}}_b$, and I denote this HIL configuration space as $Q = SE(3) \times \mathbb{R}^n$.

4.3.2 Vehicle with Simulated Manipulator

For a mission, the spacecraft platform and the manipulator subsystems are developed by different stakeholders. In this case, the former might already have a HIL OGRF for the spacecraft [171, 172], see Fig. 4.2-B.

Def. 4.3. A mechanism (e.g. a manipulator) which models the platform's motion, e.g. spacecraft, with configuration $g_2 \in SE(3)$, i.e., the inertial pose of $\{\mathcal{B}\}$.

4.3.2.1 Lagrangian Modeling and Computation

Let the vehicle system in Def. 4.3 be a mechanism with configuration $q_2 \in Q_2$, which has a Lagrangian $\frac{1}{2}\langle \dot{q}_2, \dot{q}_2 \rangle_{M_2(q_2)} - U_2(q_2)$. Its motion is described by the \mathcal{EL} equations as,

$$\mathcal{EL} = M_2(q_2)\ddot{q}_2 + C_2(q_2, q_2)\dot{q}_2 = \tau_2 + \tau_{2d} \tag{4.3}$$

where $M_2, C_2, \tau_2, \tau_{2d}$ follow the same definitions as in subsection 4.3.1.

Assumption 4.1. The vehicle mechanism is a non-redundant robotic manipulator, dim $Q_2 = \dim (SE(3))$.

The pose of $\{\mathcal{B}\}$, $g_2 = f_2(q_2)$, where $f_2 : Q_2 \to SE(3)$ is the forward kinematics map of the vehicle mechanism. The push-forward differential map is $df_2(\dot{q}_2) = T_2(q_2)\dot{q}_2$. Using Assumption 4.1, f_2^{-1} and T_2^{-1} exist locally by the inverse function theorem. In the neighbourhood of q_2 , the Lagrangian is rewritten as, $L_2 = \frac{1}{2} \langle V_2, V_2 \rangle_{M(g_2)} + U(g_2)$, where $V_2 = (g_2^{-1}\dot{g}_2)^{\vee}$. Note that L_2 is not independent of g_2 , and hence, the dynamics is given by the left-invariant Euler-Lagrange equation on SE(3), see Lemma 2.5, and written as,

$$\mathcal{EL}_{SE(3)}(L_2) = \mathcal{M}_2(g_2)\dot{V}_2 + \Gamma_2(g_2, V_2)V_2 = \mathcal{F}_2 + \mathcal{F}_{2d}$$
(4.4)

where the transformed quantities for the analytical result in Lemma 2.5 are computed using the Newtonian transformation in Lemma 2.15-1. In particular,

$$\mathcal{M}_{2} = T_{2}^{-\top} M_{2} T_{2}^{-1}$$

$$\Gamma_{2} V_{2} = \dot{M}_{2} V_{2} - \left(g_{2}^{-1} \frac{\delta l}{\delta g_{2}}\right)^{\vee} - \operatorname{ad}_{V_{2}}^{\top} \Lambda V_{2} = \dot{M}_{2} V_{2} - J_{2}^{-\top} \frac{\delta L}{\delta q} - \operatorname{ad}_{V_{2}}^{\top} \Lambda V_{2}$$

$$= T_{2}^{-\top} (M_{2} \dot{T}_{2}^{-1} + C_{2} T_{2}^{-1}) V_{2}$$

$$\mathcal{F}_{2} = T_{2}^{-\top} \tau_{2}, \ \mathcal{F}_{2d} = T_{2}^{-\top} \tau_{2d}$$

$$(4.5)$$

For the complete motion simulation of an orbital mechanism, the coupling with a simulated manipulator is required.

4.3.3 Vehicle-Manipulator

Def. 4.4. A vehicle-manipulator [26] (Fig. 4.2-C) is a multibody system consisting of a fixed-base manipulator of n holonomic-joints mounted on a vehicle at a frame $\{\mathcal{B}\}$. The configuration of the manipulator and vehicle are denoted with coordinates, q_3 , and $g_3 \in SE(3)$ (see App.), respectively.

4.3.3.1 Lagrangian Modeling and Computation

For model-based HIL, the vehicle-manipulator is modeled as a fully-coupled system on the simplified configuration space, $Q_3 \cong SE(3) \times \mathbb{R}^n$. Its Lagrangian is $L_3(q_3, g_3, V_3) = \frac{1}{2} \langle \zeta_3, \zeta_3 \rangle_{\mathbb{M}_3}$, with inertia tensor, $\mathbb{M}_3(q_3, g_3) \in \mathbb{R}^{(6+n) \times (6+n)}$, mechanism velocity $\zeta_3 = \begin{bmatrix} V_3^\top & \dot{q}_3^\top \end{bmatrix}^\top$, $V_3^{\wedge} \in \mathfrak{se}(3)$ (see App.) is the body velocity for the vehicle pose, g_3 , and $\dot{g}_3 = g_3 V_3^{\wedge}$. As was in subsection 4.3.2, L_3 is not independent of g_3 , and hence a straightforward Hamel's equation form is not possible. Instead, the dynamics are given by the $\mathcal{EL}_{SE(3)}$ equation for the motion of $\{\mathcal{B}\}$, and the \mathcal{EL} equations for the joints.

Specifically, using L_3 , the dynamics are obtained using recursive computations, and are written in vector algebra notation as,

$$\mathbb{M}_3(g_3, q_3) \begin{bmatrix} \dot{V}_3 \\ \ddot{q}_3 \end{bmatrix} + \mathbb{C}_3(g_3, \zeta_3) \begin{bmatrix} V_3 \\ \dot{q}_3 \end{bmatrix} = \begin{bmatrix} \mathcal{F}_3 + \mathcal{F}_{3d} \\ \tau_3 + \tau_{3d} \end{bmatrix} + \begin{bmatrix} T_3(q_3)^\top \\ J_3(q_3)^\top \end{bmatrix} \mathcal{F}_e$$
(4.6)

where, \mathcal{F}_3 , $\mathcal{F}_{3d} \in \mathbb{R}^6 \cong \mathfrak{se}(3)^*$ are the actuation and lumped wrenches (including gravity wrench), of the vehicle, respectively. And, τ_3 , $\tau_{3d} \in \mathbb{R}^n$ are the actuation and lumped torques (including gravity torques) of the manipulator, respectively. Also, $\mathbb{C}_3 \in \mathbb{R}^{(6+n)\times(6+n)}$ is the non-unique CC matrix and $\mathbb{M}_3 = \begin{bmatrix} \mathcal{M}_3 & M_{3q} \\ M^\top & M_2 \end{bmatrix}$ is

Also, $\mathbb{C}_3 \in \mathbb{R}^{(6+n)\times(6+n)}$ is the non-unique CC matrix and $\mathbb{M}_3 = \begin{bmatrix} \mathcal{M}_3 & M_{3q} \\ M_{3q}^\top & M_3 \end{bmatrix}$ is the coupled inertia¹. $J_3 \in \mathbb{R}^{6\times n}$, $T_3 \in \mathbb{R}^{6\times 6}$ are the end-effector Jacobians for the manipulator and vehicle, respectively, and $\mathcal{F}_e \in \mathbb{R}^6 \cong \mathfrak{se}(3)^*$ is end-effector wrench.

4.3.3.2 Momentum Constraint

If the vehicle in the vehicle-manipulator is left unactuated, a trajectory of the manipulator causes a vehicle displacement due to momentum exchange². In particular, the momentum quantity is $\mathcal{J}_3 = \operatorname{Ad}_{q_b}^{\top}(\mathcal{M}_3V_3 + M_{3q}\dot{q}_3)$. Using \mathcal{J}_3 , the

 $^{{}^{1}\}mathcal{M}_{3}, M_{3q}, M_{3}$ are the locked, coupling and manipulator inertias, respectively [50].

²Note that M_3 does not have a symmetry in g_3 like the orbital FRM, and hence, the momentum is not conserved, but momentum exchange occurs.

95

mechanical connection (see Def. 2.7) is, $A_3(g_3, q_3, \zeta_3) = \operatorname{Ad}_3\left[\mathbb{I}_{6,6} \quad \mathcal{A}_3(g_3, q_3)\right] \begin{bmatrix} V_3 \\ \dot{q}_3 \end{bmatrix}$,

where $\mathcal{A}_3 = \mathcal{M}_3^{-1} M_{3q}$ is the local form of the connection. Note that the vehicle-manipulator contrasts with the FRM in Chapter 3, in which the Lagrangian and the mechanical connection were independent of the SE(3) pose. Although there is no such symmetry for the vehicle-manipulator, the same framework is exploited to rewrite the dynamics in (4.6) in a Ver – Hor form with block-diagonal inertia. To this end, as in Chapter 3, A_3 is parameterized by a locked velocity, μ_3 .

Next, I follow the steps to rewrite the dynamics of the vehicle-manipulator. The vehicle-manipulator velocity is $\xi_3 = (\mu_3, \dot{q}_3)$, which is obtained using the linear transformation $\mathcal{T}_3(g_3, q_3) = \begin{bmatrix} \mathbb{I} & \mathcal{A}_3 \\ 0 & \mathbb{I} \end{bmatrix}$, as $\xi_3 = \begin{bmatrix} \mu_3^\top & \dot{q}_3^\top \end{bmatrix}^\top = \mathcal{T}_3(q)\zeta_3$. Applying the Newtonian transformation in Lemma 2.15-1 on (4.6),

$$\hat{\mathbb{M}}_3(g_3, q_3) \begin{bmatrix} \dot{\mu}_3 \\ \ddot{q}_3 \end{bmatrix} + \hat{\mathbb{C}}_3(g_3, q_3, \zeta_3) \begin{bmatrix} \mu_3 \\ \dot{q}_3 \end{bmatrix} = \begin{bmatrix} \bar{\mathcal{F}}_3 + T_3^{\top} \mathcal{F}_e \\ \tau_3 - \mathcal{A}_3^{\top} \bar{\mathcal{F}}_3 + \tilde{J}_3^{\top} \mathcal{F}_e \end{bmatrix}$$
(4.7)

where $\bar{\mathcal{F}}_3 = \mathcal{F}_3 + \mathcal{F}_{3d}$, $\tilde{J}_3 = J_3 - \operatorname{Ad}_{g_{be}}^{-1} \mathcal{A}_3$ is the generalized Jacobian, and $\hat{\mathbb{M}}_3$ and $\hat{\mathbb{C}}_3$ are the transformed inertia and CC matrix, obtained as,

$$\hat{\mathbb{M}}_{3} = \text{blkdiag}(\mathcal{M}_{3}, \Lambda_{3}(q_{3})) = \mathcal{T}_{3}^{-\top} \mathbb{M}_{3} \mathcal{T}_{3}^{-1}$$

$$\hat{\mathbb{C}}_{3} = \begin{bmatrix} \Gamma_{3}(\zeta_{3}) & \Gamma_{3q}(\zeta_{3}) \\ -\Gamma_{3q}(\zeta_{3})^{\top} & \bar{\Gamma}_{3}(\zeta_{3}) \end{bmatrix} = \mathcal{T}_{3}^{-\top} (\mathbb{M}_{3} \dot{T}_{3}^{-1} + \mathbb{C}_{3} \mathcal{T}_{3}^{-1})$$
(4.8)

In particular, the momentum equation is the top row of (4.7) as,

$$\operatorname{Ver}(\mathcal{LP})(l_3) = \mathcal{M}_3 \dot{\mu}_3 + \begin{bmatrix} \Gamma_3(\zeta_3) & \Gamma_{3q}(\zeta_3) \end{bmatrix} \zeta_3 = \bar{\mathcal{F}}_3 + T_3^{\top} \mathcal{F}_e$$
 (4.9)

and the shape-space dynamics is the bottom row,

$$\operatorname{Hor}(\mathcal{LP})(l_3) = \Lambda_3 \ddot{q}_3 + \begin{bmatrix} -\Gamma_{3q}(\zeta_3)^\top & \bar{\Gamma}_3(\zeta_3) \end{bmatrix} + \mathcal{A}_3^\top \bar{\mathcal{F}}_3 = \tau_3 + \tau_{3d} + \tilde{J}_3^\top \mathcal{F}_e \quad (4.10)$$

By following the above procedure, the two pairs, (4.17), (4.18) and (4.9), (4.10) have decoupled inertias. This removes acceleration dependencies between the two equations in each pair, and this addresses the problem described in Sec. 4.2.2.

4.3.4 Gravity-compensated OGRF

Typically, a flight-ready orbital manipulator (e.g. CAESAR [170]) might not have enough torque capability to support its own gravity during on-ground V&V. It is common to use passive (fixed mass) [47] or active gravity-compensation schemes. The latter approach exploits a *carrier*, which is another serial-chain or parallel mechanism to generate gravity-support torques [173]. The analysis shown in the following is related to the patent [67] in Table 1.2.

Def. 4.5. A gravity-compensated manipulator, see Fig. 4.2-**D**, is a fixed-base manipulator, which is constrained to a carrier mechanism to compensate for its own gravity [173]. Its configuration is $x_4 = (q_4, \theta_4) \in Q_4 \equiv \hat{Q}_4 \times \tilde{Q}_4$, where $q_4 \in \hat{Q}_4$ and $\theta_4 \in \tilde{Q}_4$ are the position variables of the fixed-base manipulator and the carrier, respectively.

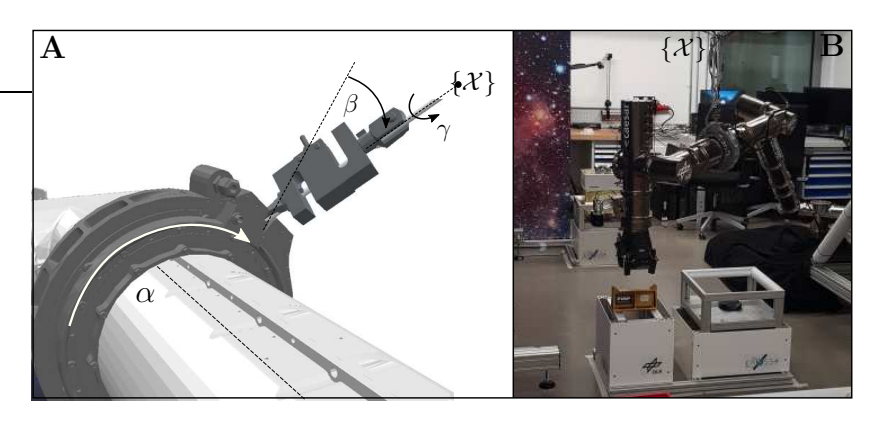


Figure 4.3: A: Unconstrained SO(3)-motion of attachment, $\{\mathcal{X}\}$, between CAE-SAR and carrier, B: CAESAR manipulator in operation with carrier mechanism.

4.3.4.1 Lagrangian Modeling and Computation

The carrier and the flight-prototype manipulator are multibody mechanisms with commutative configuration spaces. Let the corresponding unconstrained Lagrangians be $\tilde{L}_4 = \frac{1}{2} \langle \dot{\theta}_4, \dot{\theta}_4 \rangle_{H_4} - \tilde{U}_4(\theta_4)$, and $\hat{L}_4 = \frac{1}{2} \langle \dot{q}_4, \dot{q}_4 \rangle_{M_4} + \hat{U}_4(q_4)$, where M_4, H_4 are the inertia tensors and \tilde{U}_4, \hat{U}_4 are the scalar potentials, e.g. gravity. The motion is given by their corresponding \mathcal{EL} equations as follows,

$$\mathcal{E}\mathcal{L}(\tilde{L}_4) = H_4(\theta_4)\ddot{\theta}_4 + N_4(\theta_4, \dot{\theta}_4)\dot{\theta}_4 = t_4 + t_{4d}$$

$$\mathcal{E}\mathcal{L}(\hat{L}_4) = M_4(q_4)\ddot{q}_4 + C_4(q_4, \dot{q}_4)\dot{q}_4 = \tau_4 + \tau_{4d} + J_4(q_4)^{\top}\mathcal{F}_e$$
(4.11)

where C_4 , N_4 are the CC matrices, τ_4 , t_4 are the actuator torques, τ_{4d} , t_{4d} contain the lumped torques, like gravity, i.e., $\frac{\partial \tilde{U}_4}{\partial \theta_4}$ and $\frac{\partial \hat{U}_4}{\partial q_4}$, respectively. For V&V, the external interaction wrench, \mathcal{F}_e is of interest for the manipulator, at a point, e.g. end-effector, given by its forward kinematics map $g_4: \hat{Q}_4 \to \mathrm{SE}(3)$. The wrench is pulled back using using the map Jacobian as $J_4^{\top} \mathcal{F}_e$.

The constraint between the manipulator and the carrier, see Figs. 4.2-**D** and 4.3, is realized at a material 3*D*-point $\{\mathcal{X}\}$. Let $f_4: \hat{Q} \to G$ and $h_4: \tilde{Q} \to G$ denote the forward kinematics maps for the manipulator and carrier of $\{\mathcal{X}\}$, respectively. Note that G is a subgroup of SE(3), e.g. SO(3), \mathbb{R}^3 , or SE(3) itself [174], which generalizes a family of holonomic motion constraints in 3*D*-space.

Assumption 4.2. The carrier mechanism is non-redundant, i.e., h_4^{-1} exists locally by the inverse function theorem.

97

Note that using the theory on constrained mechanics in Chapter 2, the constraint between the vehicle and the CAESAR manipulator is written as a map, $\pi: Q_4 \to G$, see Def. 2.3. Given the subgroup positions of the carrier and manipulator as, $\tilde{g}_4, \hat{g}_4 \in G$, respectively, the relative position gives the holonomic constraint as,

$$g_x = \pi(x_4) = \hat{g}_4^{-1} \tilde{g}_4 = \text{const.} \Rightarrow W_4 - \text{Ad}_{g_x}^{-1} V_4 = \underbrace{\left[\tilde{T}_4 - \text{Ad}_{g_x}^{-1} \hat{T}_4\right]}_{I} \begin{bmatrix} \dot{\theta}_4 \\ \dot{q}_4 \end{bmatrix} = 0$$
 (4.12)

where $W_4 = (\tilde{g}_4^{-1}\dot{\tilde{g}}_4)^{\vee}$ and $V_4 = (\hat{g}_4^{-1}\dot{\hat{g}}_4)^{\vee}$ are the body velocities of the carrier and manipulator at $\{\mathcal{X}\}$, respectively.

In the particular case of CAESAR in Fig. 4.3, note that the motion in SO(3) at $\{\mathcal{X}\}$ is unconstrained by virtue of rotational motions in α, β, γ , where α, β are the rotational joints from an attached sleeve mechanism, and γ is the assumed rotational degree of freedom about the cable length axis. Hence, the constraint is purely translational, i.e., $g_x \in \mathbb{R}^3$.

Using Assumption 4.2, \tilde{T}_4 is invertible and $\theta_4 = h_4^{-1} f_4(q_4)$. Using this invertible transformation, (4.12) is written in the form $\mu_4 = A(\theta_4, q_4) \left[\dot{\theta}_4^\top \quad \dot{q}_4^\top \right]^\top$, where $A = \left[\mathbb{I} \quad \tilde{T}_4^{-1} \mathrm{Ad}_{g_x}^{-1} \hat{T}_4 \right]$ is the Ehresmann connection in Def. 2.5. Due to the kinematic constraint, however, the vertical velocity $\mu_4 = 0$. Thus, the constrained Lagrangian of Fig. 4.2-**D** is written as $L_4 = \frac{1}{2} \langle \dot{q}_4, \dot{q}_4 \rangle_{\Lambda_4} - U_4(q_4)$, while considering $\mu_4 = 0$, where Λ_4 is the constrained inertia, and $U_4(q_4) = \tilde{U}_4(h_4^{-1} f_4(q_4)) + \hat{U}_4(q_4)$ such that $dU_4 = d\hat{U}_4 + A^\top d\tilde{U}_4$, see [14, §2.1]. The constrained dynamics are obtained by simply taking the $\mathrm{Hor}(\mathcal{EL})$ part of the motion. To enable computation, note that $\left[\mu_4^\top \quad \dot{q}_4^\top \right]^\top = T_4 \left[\dot{\theta}_4^\top \quad \dot{q}_4^\top \right]^\top$, where $T_4 = \begin{bmatrix} \mathbb{I} & A \\ 0 & \mathbb{I} \end{bmatrix}$ is the invertible tangent space map. Using the Newtonian transformation in Lemma 2.15-1 on (4.11), the dynamics are written using $\mu_4 = 0$ as,

$$\operatorname{Hor}(\mathcal{EL})(L_4) = \Lambda_4(x_4)\ddot{q}_4 + \Gamma_4(x_4, \dot{q}_4) = \tau_4 - A^{\top}(t_4 + t_{4d}) + \tau_{4d} + J_4(q_4)^{\top}\mathcal{F}_e \quad (4.13)$$

where Γ_4 is the the matrix of CC terms, and computed as,

$$\Lambda_{4} = M_{4} - A^{T} H_{4} A
\Gamma_{4} \dot{q}_{4} = \dot{\Lambda}_{4} - \frac{\delta L_{4}}{\delta q_{4}} + A^{T} \frac{\delta L_{4}}{\delta \theta_{4}} + \left((dA)(\dot{x}_{1}) \right)^{T} \frac{\delta L_{4}}{\delta \mu}, [14, \text{ eq. } 2.1.6]
= \text{Hor} \left(T_{4}^{-T} (\text{blkdiag}(H_{4}, M_{4}) \dot{T}_{4}^{-1} + \text{blkdiag}(N_{4}, C_{4}) T_{4}^{-1}) \right) \begin{bmatrix} 0 \\ \dot{q}_{4} \end{bmatrix}$$
(4.14)

where $\operatorname{Hor}(\bullet)$ above considers the CC terms of only the $\operatorname{Hor}(\mathcal{EL})$ (bottom row) dynamics.

4.3.4.2 Energetic behaviour of Gravity-Compensation

In (4.13), let the actuation be decomposed as $\tau_4 = \tau_{4c} + \tau_{4g}$, where τ_{4c} and τ_{4g} are the torques for motion control from OBSW (mission element) and gravity-compensation (on-ground element), respectively. The motion control task is identified using a scalar potential $\Phi_4(q_4): \hat{Q} \to \mathbb{R}_+$.

Lemma 4.1. Given the gravity-compensated OGRF in Fig. 4.2-**D**, if the motion control torque τ_4 satisfies a passivity property with the motion control task, i.e., $\tau_{4c} + d\Phi_4 \mapsto \dot{q}_4$, $\tau_{4g} - A^{\top}(t_4 + t_{4d}) + \tau_{4d} = \Delta_g = 0$, and $\mathcal{F}_e = 0$, then the complete manipulator-carrier mechanism is Lyapunov stable, i.e., the OGRF states (x_4, \dot{x}_4) are bounded. In case $\mathcal{F}_e, \Delta_g \neq 0$, the OGRF is passive with the passivity-map $(J_4^{\top} \mathcal{F}_e + \Delta_g) \mapsto \dot{q}_4$.

Proof. Consider the function $\mathcal{H}_4 = \frac{1}{2} \langle \dot{q}_4, \dot{q}_4 \rangle_{\Lambda_4} + \tilde{U}_4(\theta_4) + \hat{U}_4(q_4) + \Phi_4(q_4)$, where $\Phi_4 : \hat{Q} \to \mathbb{R}_+$ is a potential for the motion control task. Taking its time-derivative using (4.13) with $\mathcal{F}_e = 0$,

$$\dot{\mathcal{H}}_4 = \dot{q}_4^{\top} \left(\tau_4 - A^{\top} (t_4 + t_{4d}) + \tau_{4d} \right) = \dot{q}_4^{\top} (\tau_{4c} + d\Phi_4) \le 0 \tag{4.15}$$

where the passivity property, $\dot{q}_4^{\top}(\dot{\Lambda}_4 - 2\Gamma_4)\dot{q}_4 = 0$, for the constrained OGRF is applied, and (4.15) implies Lyapunov stability. For the latter part, considering $\mathcal{F}_e, \Delta_g \neq 0$, and computing time-derivative of \mathcal{H}_4 ,

$$\dot{\mathcal{H}}_4 \le (J_4^{\top} \mathcal{F}_e + \Delta_g)^{\top} \dot{q}_4 \Rightarrow \mathcal{H}_4(t) - \mathcal{H}_4(0) \le \int_0^t (J_4^{\top} \mathcal{F}_e + \Delta_g)^{\top} \dot{q}_4 dt \tag{4.16}$$

Lemma 4.1 is important because it provides a stability guarantee for the V&V of a gravity-compensated OGRF. It also gives the condition for the OBSW to ensure stability during the V&V testing phase.

Remark 22. The solution of $\tau_{4g} + A^{\top}(t_4 + t_{4d}) + \tau_{4d} = \Delta_g = 0$ might be an underdetermined problem if the manipulator has more degrees-of-freedom than the carrier mechanism. In this case, an optimization problem is formulated with $\Delta_g = 0$ as a constraint function, as shown by [173]. This method was solved as an optimality constraint problem in the patent [67], which resulted from the work during this thesis.

4.4 Motion Substructuring Approach

In the following, the key idea of using the Controlled Lagrangian method [167, 175] towards substructuring the orbital FRM in terms of shape and momentum variations of its \mathcal{LP} dynamics is described.

4.4.1 Method of Controlled Lagrangians

In this chapter, I use the method of Controlled Lagrangian (CL). Its basic idea is as follows: Given the problem to asymptotically stabilize an equilibrium of a mechanical system, I find a control law such that the closed-loop dynamics emerge from a chosen Lagrangian. The method of CL leads to an actuation mapping, which is the key concept used in this chapter. For control synthesis details, I refer the reader to [175, §2.2.1].

Firstly, I specify that in contrast to control synthesis, it has to be *proved* that the CLs for the HIL OGRF and the orbital robot are equivalent for the chosen actuation mapping. This is exactly analogous to stating the converse theorem for CL-equivalence [167, Prop. 2.4]. The time-evolution of the orbital mechanism state in the mission scenario for a given actuation is different to that of the OGRF. This is because the configuration spaces are different (see Fig.8.14), i.e. $\hat{Q} \neq Q_i$, because the inertia tensors, which depend on kinematic/dynamic parameters, are different. An OBSW designed for (4.1) can be meaningfully interfaced with OGRF, if and only if, the time-trajectories of z (red dot) in OGRF (dashed blue) and orbital robot (dashed pink) are identical. This is achieved by creating a configuration-dependent mapping between the actuation in cotangent spaces of \hat{Q} (pink) and Q_i (blue), and is the main contribution of this chapter.

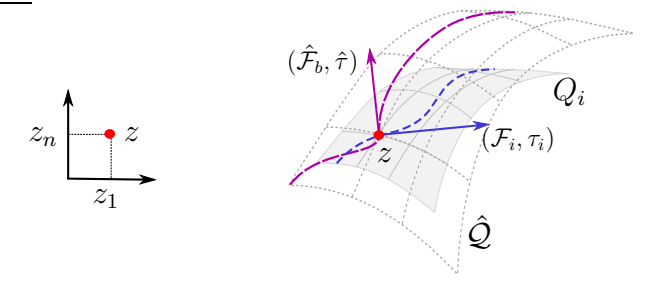


Figure 4.4: At any given time, the configuration (red dot) of the mechanical systems in \hat{Q} (dotted) and Q_i (grey) have the same local coordinates z and identical time-trajectories. To achieve this, a mapping between (\mathcal{F}_i, τ_i) (blue) and $(\hat{\mathcal{F}}_b, \hat{\tau})$ (pink) has to be enforced.

Although this idea can also be applied to the Hamel's equations, (4.6) and (4.1), the coupled inertia leads to the problem described in Sec. 4.2.2. So, alternatively, I use \mathcal{LP} equations, which reveal a block-diagonal inertia.

4.4.2 \mathcal{LP} Equations of an Orbital Mechanism

In this section, the \mathcal{LP} equations from Theorem 3.2 are used for substructuring the motion of the orbital robot. These equations reveal a block-diagonalized inertia, and hence can be written as a pair of $Ver(\mathcal{LP})$ and $Hor(\mathcal{LP})$ equations, which correspond to locked and shape dynamics, respectively. The \mathcal{LP} equations

describe the dynamics using a new system velocity $\hat{\xi} = \begin{bmatrix} \hat{\mu}^{\top} & \dot{q}^{\top} \end{bmatrix}^{\top} \in \mathbb{R}^{6+n}$ with locked velocity, $\hat{\mu}$, which is obtained as $\hat{\mu} = V_b + \hat{\mathcal{A}}_l(q)\dot{q}$, where $\hat{\mathcal{A}}_l = \hat{M}_b^{-1}\hat{M}_{bq}$ is the local mechanical connection. The locked velocity, $\hat{\mu}$, has a physical interpretation of being the velocity of the instantaneous equivalent rigid body system by locking the joints of the orbital robot.

A key consequence of defining the new system velocity, $\hat{\xi}$, is a block-diagonal inertia, which leads to a decoupled reduced Lagrangian, $\hat{l}(q,\xi)$. The dynamics resulting from \hat{l} are the \mathcal{LP} equations, which is computed using Theorem 3.2, and decomposes the motion of the orbital mechanism into momentum and shape substructures. The top row of \mathcal{LP} equations in (5.3) gives,

$$\operatorname{Ver}(\mathcal{LP})(l) = \hat{M}_b \dot{\hat{\mu}} + P(q, \dot{q})\hat{\mu} - \operatorname{ad}_{\hat{M}, \hat{\mu}}^{\sim}(\hat{\mu} - \hat{\mathcal{A}}_l \dot{q}) = \hat{\mathcal{F}}_b + \hat{J}_b^{\top} \mathcal{F}_e$$
(4.17)

after applying Property 3.1. Note that $\text{Ver}(\mathcal{LP})(l)$ is related to the locked kinetic energy, $l = \frac{1}{2} \langle \hat{\mu}, \hat{\mu} \rangle_{\hat{M}_b}$. Also, the second row in (5.3) is compactly written as,

$$\operatorname{Hor}(\mathcal{LP})(l) = \hat{\Lambda}_{q}\ddot{q} + \Gamma_{q}(\dot{q})\dot{q} - \Gamma_{\mu}(\mu)\hat{\xi} = \hat{\tau} - \hat{\mathcal{A}}_{l}^{T}\hat{\mathcal{F}}_{b} + \hat{J}^{\top}\mathcal{F}_{e},$$

$$\Gamma_{\mu}(\mu) = \left[\left(\frac{1}{2}S(\hat{\mu})^{\top} - \mathcal{A}_{l}^{\top}\operatorname{ad}_{M_{b}\hat{\mu}}^{\sim} \right) - \tilde{\mathcal{B}}(\hat{\mu}) \right]$$
(4.18)

where $\text{Hor}(\mathcal{LP})(l)$ corresponds to the shape kinetic energy, $\frac{1}{2}\dot{q}^{\top}\hat{\Lambda}_q(q)\dot{q}$. The base (spacecraft) pose g_b is reconstructed as,

$$\dot{g}_b = g_b V_b^{\wedge} = g_b \left(\hat{\mu} - \hat{\mathcal{A}}_l(q) \dot{q} \right)^{\wedge} \tag{4.19}$$

4.5 Proposed method and Modalities

This section describes the main contribution of this chapter. In particular, two theorems are presented that shape the behaviour of the dynamics of an OGRF to replicate the motion of the shape (joints) and momentum of the orbital FRM. Furthermore, these theorems are applied to common OGRF, as shown in Fig. 4.2, to derive platform-specific control laws.

4.5.1 Dynamics equivalence

The main objective of this section is to establish conditions of equivalence between dynamics of an orbital robot and OGRF. To this end, I first state the following.

Assumption 4.3. For the on-ground V&V of control, planning and estimation algorithms of the orbital mechanism in Sec. 4.2 using the OGRF in Sec. 4.3, the initial state-space, $(q(0), \dot{q}(0), g_b(0), \mu(0))$, are identical.

The following two theorems result in the actuation maps that are required for dynamics equivalence.

Theorem 4.1. (Converse matching for \mathcal{EL} equations): Given shape (joints) dynamics of an orbital mechanism in (4.18), which is required to be produced on a fixed-base OGRF (i = 1) in (4.2), vehicle-manipulator OGRF (i = 3) in (4.10) and a gravity-compensated OGRF (i = 4) in (4.13), respectively, they produce the same equations of motion, i.e. ($q(t), \dot{q}(t)$), if and only if, Ass. 4.3 holds and,

• There is a map between the control torques $\hat{\tau} \mapsto \tau_i$, as,

$$\tau_{i} = \mathcal{E}\mathcal{L}(L_{i}, X) - \partial_{\dot{q}\dot{q}}(L_{i})\hat{\Lambda}_{q}^{-1}\mathcal{E}\mathcal{L}(L, \xi) + \partial_{\dot{q}\dot{q}}(L_{i})\hat{\Lambda}_{q}^{-1}(\hat{\tau} - \hat{\mathcal{A}}_{l}(q)^{\top}\hat{\mathcal{F}}_{b}) + (\partial_{\dot{q}\dot{q}}(L_{i})\hat{\Lambda}_{q}^{-1}\hat{J}^{\top} - J_{i}^{\top})\mathcal{F}_{e} - \tau_{id}$$

$$(4.20)$$

where $\partial_{\dot{q}\dot{q}}(L_i) = \frac{\partial^2 L_i}{\partial \dot{q}^2}$, i = 1, 2 corresponding to (4.2) and (4.10), respectively. For fixed-base manipulator and gravity-compensated OGRF, $i = 1, 3, X = \dot{q}$, and for vehicle-manipulator, $i = 2, X = \xi_3$.

Proof. Like [175, Prop. 2.1.5], I denote the resulting accelerations in CLs, L_i and L, as \ddot{q}_i , \ddot{q} corresponding to actuation torques τ_i , $\hat{\tau}$, respectively. Taking the inertia-scaled difference in these accelerations,

$$\hat{\Lambda}_{q}(\ddot{\hat{q}} - \ddot{q}_{i}) = -\mathcal{E}\mathcal{L}(L, \xi) + \hat{\tau} - \hat{\mathcal{A}}_{l}^{\mathsf{T}}\hat{\mathcal{F}}_{b} + \hat{J}_{g}^{\mathsf{T}}\mathcal{F}_{e} - \hat{\Lambda}_{q}\partial_{\dot{q}\dot{q}}(L_{i})^{-1} \Big(-\mathcal{E}\mathcal{L}(L_{i}, X) + \tau_{i} + \tau_{id} + J_{i}^{\mathsf{T}}\mathcal{F}_{e} \Big)$$

$$(4.21)$$

Substituting τ_i as (4.20) in (4.21), $\hat{\Lambda}_q(q)(\ddot{q} - \ddot{q}_i) = 0$. In addition to this equality, if and only if, Ass. 4.3 holds true, trajectories for $(q(t), \dot{q}(t))$ are identical, thereby proving equivalence of L_i , L.

To illustrate the result, for example, applying Theorem 4.1 on a fixed-base OGRF (i = 1) in (4.2),

$$\tau_{1} = \underbrace{C_{1}(\dot{q})\dot{q} - M_{1}\hat{\Lambda}_{q}^{-1}\Gamma_{q}(\dot{q})\dot{q}}_{1} + \underbrace{M_{1}\hat{\Lambda}_{q}^{-1}\Gamma_{\mu}(\hat{\mu})\hat{\xi}}_{2} + M_{1}\hat{\Lambda}_{q}^{-1}\left(\underbrace{\hat{\tau} - \hat{\mathcal{A}}_{l}^{\top}\hat{\mathcal{F}}_{b}}_{3}\right) + \underbrace{\left(M_{1}\hat{\Lambda}_{q}^{-1}\hat{J}^{\top} - J_{i}^{\top}\right)\mathcal{F}_{e}}_{4} - \underbrace{\tau_{1d}}_{5} \tag{4.22}$$

where the numbered items are described as follows,

- 1. Joint-space CC terms using actual HIL joint measurements
- 2. CC terms arising from non-zero simulated momentum
- 3. Actuation commands from OBSW
- 4. Mapping of interaction wrenches measured on HIL facility

5. Feedforward gravity-compensation and disturbance models, e.g. friction

This means that Theorem 4.1 enforces an interface between the OBSW and the OGRF such that the joint-space trajectories of *both* robots in Fig. 4.1 are identical. Theorem 4.1 also guarantees that the state-feedback (q, \dot{q}) (red arrow) to the OBSW is consistent with expected orbital robot dynamics.

Theorem 4.2. (Converse matching for \mathcal{EP} equations): Given locked dynamics of an orbital robot in (4.17), which is required to be produced on a vehicle with a simulated manipulator (i = 2) in (4.4) and a vehicle-manipulator (i = 3) in (4.9), respectively, they produce the same equations of motion, i.e. $(g_b(t), \mu(t))$, if and only if, Ass. 4.3 holds and,

• There is a map between the control torques $\hat{\mathcal{F}}_b \mapsto \mathcal{F}_i$ as,

$$\mathcal{F}_{i} = -\mathcal{F}_{id} + \mathcal{E}\mathcal{P}(l_{2}, \xi) - \mathcal{M}_{i}\hat{M}_{b}^{-1}\mathcal{E}\mathcal{P}(l, \xi) + \mathcal{M}_{i}\hat{M}_{b}^{-1}\hat{\mathcal{F}}_{b} + (\mathcal{M}_{i}\hat{M}_{b}^{-1}\hat{J}_{b}^{\top} - T_{i}^{\top})\mathcal{F}_{e}$$

$$(4.23)$$

Proof. Taking the inertia-scaled difference in resulting locked accelerations,

$$\hat{M}_b(\hat{\mu} - \dot{\mu}_i) = \operatorname{ad}_{\hat{M}_b\hat{\mu}}^{\sim}(\hat{\mu} - \hat{\mathcal{A}}_l\dot{q}) - P(\dot{q})\hat{\mu} + \hat{\mathcal{F}}_b + \hat{J}_b^{\top}\mathcal{F}_e
- \hat{M}_b\mathcal{M}_i^{-1} \left(\Gamma_i(q_i, Y)Y + \mathcal{F}_i + T_i^{\top}\mathcal{F}_e\right)$$
(4.24)

If \mathcal{F}_i is chosen as,

$$\mathcal{F}_{i} = \underbrace{\mathcal{M}_{i} \hat{M}_{b}^{-1} \left(\operatorname{ad}_{\hat{M}_{b} \hat{\mu}}^{\sim} (\hat{\mu} - \hat{\mathcal{A}}_{l} \dot{q}) - P(\dot{q}) \hat{\mu} \right) - \Gamma_{i}(Y) Y}_{1} + \underbrace{\mathcal{M}_{i} \hat{M}_{b}^{-1} \hat{\mathcal{F}}_{b}}_{2} + \underbrace{\left(\mathcal{M}_{i} \hat{M}_{b}^{-1} \hat{J}_{b}^{\top} - T_{i}^{\top} \right) \mathcal{F}_{e}}_{3} - \underbrace{\mathcal{F}_{id}}_{4}}$$

and substituted in (4.24), $\hat{M}_b(q)(\dot{\hat{\mu}} - \dot{\mu}_i) = 0$. In addition to this equality, if and only if, Ass. 4.3 holds true, $(g_b(t), \mu(t))$ is identical for the orbital mechanism and OGRF, and the result of the theorem is obtained by taking $\mu_i(t) = \hat{\mu}(t)$. The numbered items in (4.2) are described as follows,

- 1. CC terms arising for the momentum dynamics
- 2. Mapping of Actuation commands from OBSW
- 3. Mapping of interaction wrenches measured on HIL facility
- 4. Feedforward gravity-compensation for vehicle

I note that one would obtain the same equations as (4.20) and (4.23) if the problem was formulated as an impedance control/matching task in locked and shape spaces [176, eq. 15].

4.5.2 Generating Motion for V&V

In this section, I outline three modalities of HIL and provide block diagrams for clarity on complete implementation using Theorems 4.1 and 4.2.

4.5.2.1 Fixed-base OGRF, M1-A

In this mode, the floating-base (e.g. spacecraft) motion is simulated in software by integrating the equations of motion, while the hardware component of the HIL contains the articulated mechanism, its joint sensors and a FTS at the point of interaction. For the former, instead of using (4.1), I propose integrating $\text{Ver}(\mathcal{LP})$ equation from (4.17), i.e. $\mathcal{F}_1 = \hat{\mathcal{F}}_b$ in Fig. 8.14, and (5.4) to close the HIL loop as shown in Fig. 4.5.

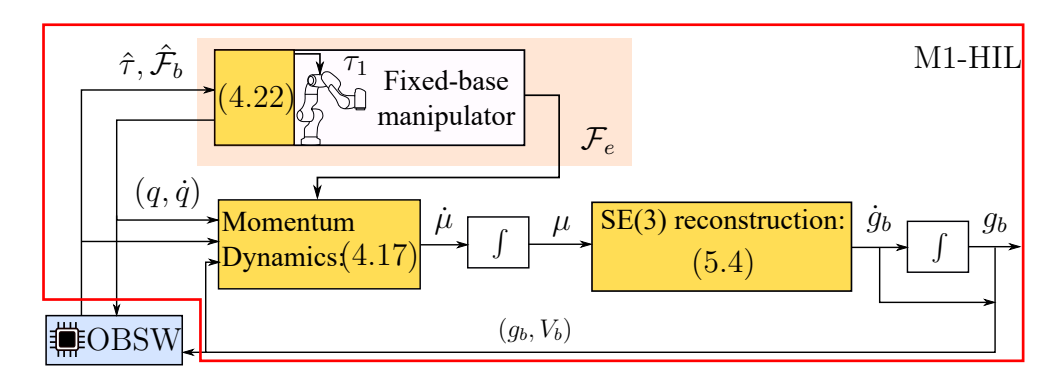


Figure 4.5: A HIL for an orbital mechanism using a fixed-base OGRF.

4.5.2.2 Gravity-compensated OGRF, M1-B

As in the previous case, the floating-base (e.g. spacecraft) motion is simulated in software, while the hardware component of the HIL contains the articulated mechanism, its joint sensors, the gravity-compensation system, and a FTS at the point of interaction. For the floating-base simulation, $Ver(\mathcal{LP})$ equation from (4.17) is integrated, i.e. $\mathcal{F}_1 = \hat{\mathcal{F}}_b$ in Fig. 8.14, and (5.4) to close the HIL loop as shown in Fig. 4.5.

4.5.2.3 Impedance Vehicle-Simulated Manipulator, M2-A

In this mode, the joints motion of the articulated mechanism is simulated in software by integrating the equations of motion, while the hardware component of the HIL contains the vehicle that simulates the floating-base and its sensing. In impedance causality, the vehicle in Def. 4.2 has a torque-interface to effect base motion. Following the principle in M1-A, I propose integrating $\text{Hor}(\mathcal{LP})$ equation from (4.18), i.e. $\tau_2 = \hat{\tau}$, to close the loop as shown in Fig. 4.6.

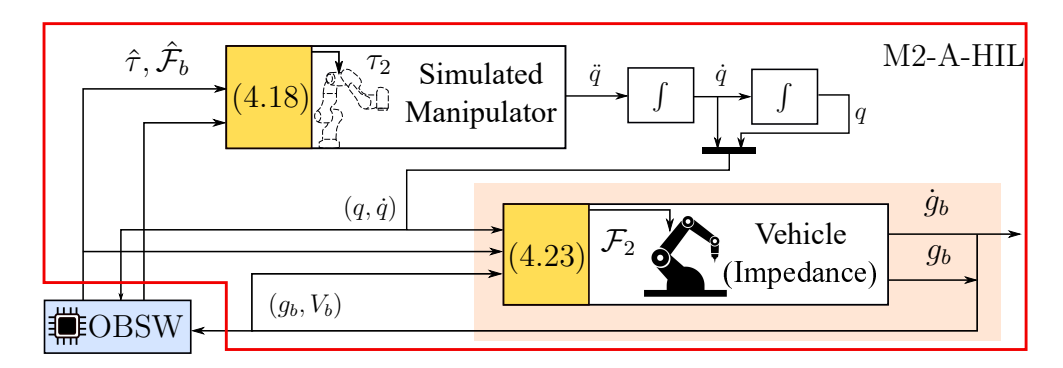


Figure 4.6: A HIL for an orbital mechanism using a vehicle with impedance causality and a simulated manipulator.

4.5.2.4 Admittance Vehicle-Simulated Manipulator, M2-B

This modality is the same as the previous, except that the vehicle in Def. 4.2 has a position-interface for motion control to effect base motion. The desired locked inertia for the admittance controller can be straightforwardly chosen as, $\hat{M}_b = M_2$. This simplifies the map in (4.23) of Theorem 4.2 as,

$$\mathcal{F}_2 = -\mathcal{F}_{2d} + \mathcal{E}\mathcal{L}(l_2, \xi) - \mathcal{E}\mathcal{L}(l, \xi) + \hat{\mathcal{F}}_b$$
(4.25)

which is substituted in (4.9). Satisfying Theorems 4.1 and 4.2 ensures that the OGRF motion dynamics match (4.17) and (4.18), which implies $V_b = \hat{\mu} - \hat{\mathcal{A}}_l \dot{q}$. Hence, the admittance controller commands, $(g_b(t), V_b(t))$, are obtained by integrating $\text{Ver}(\mathcal{LP})$ equation in (4.9) and the SE(3) reconstruction in (5.4).

4.5.2.5 Vehicle-Manipulator Impedance mode, M3-A

In impedance causality, the vehicle in Def. 4.2 has a torque-interface to effect spacecraft motion. This might be a use-case for simulating dynamics of a small-sized arm on a small satellite [177], in which the vehicle is a KUKA LWR-4, for instance. In this case, Theorem 4.2 is invoked to enforce a mapping, namely (4.23), between actuation torques $\hat{\mathcal{F}}_b$, \mathcal{F}_3 . The complete strategy has been shown in Fig. 4.7.

4.5.2.6 Vehicle-Manipulator Admittance mode, M3-B

In admittance causality, the vehicle, e.g. an industrial robot, is used in position-control mode to simulate the spacecraft motion [50]. The desired locked inertia for the admittance controller can be straightforwardly chosen as, $\hat{M}_b = \bar{M}_b$. This simplifies the map in (4.23) of Theorem 4.2 as,

$$\mathcal{F}_3 = -\mathcal{F}_{3d} + \mathcal{E}\mathcal{L}(l_2, \xi) - \mathcal{E}\mathcal{L}(l, \xi) + \hat{\mathcal{F}}_b + (\hat{J}_b^{\top} - T_3^{\top})\mathcal{F}_e$$
(4.26)

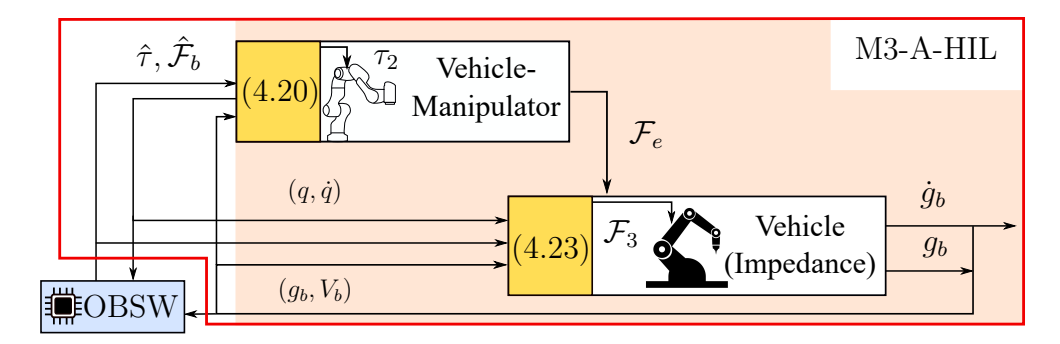


Figure 4.7: A HIL for an orbital mechanism using a vehicle-manipulator with impedance causality in vehicle.

which is substituted in (4.9). Satisfying Theorems 4.1 and 4.2 ensures that the OGRF motion dynamics match (4.17) and (4.18), which implies $V_b = \mu - \hat{\mathcal{A}}_l \dot{q}$. Hence, the admittance controller commands, $(g_b(t), V_b(t))$, are obtained by integrating (4.9) and (5.4). This strategy has been shown in Fig. 4.8.

Note that the proposed methods account for different manipulator models in the OGRF and the orbital robot. A consequence of Theorems 4.1 and 4.2 is the stability M1 and M2, given that OBSW stabilizes (4.1). For M3, the closed-loop stability is a function of the vehicle's admittance dynamics.

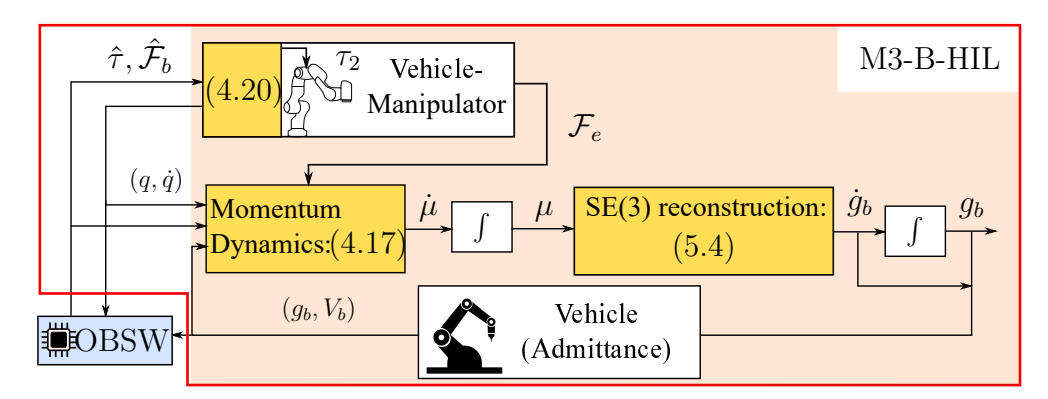
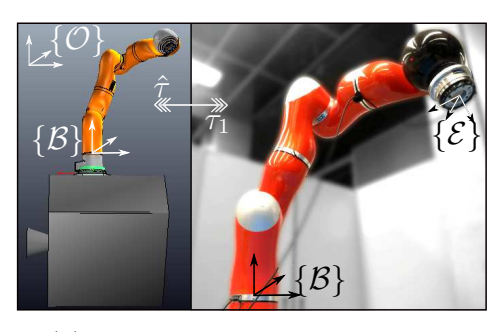


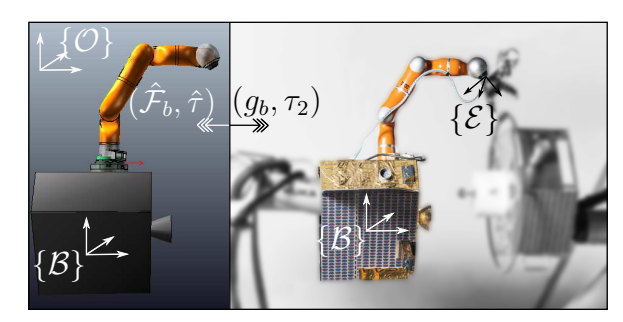
Figure 4.8: A HIL setup for an orbital robot using a vehicle-manipulator with admittance causality in vehicle.

4.6 Experimental Validation

In this section, the experimental results are summarized. From a practical perspective, vehicle in impedance causality (M3-A) has low disturbance-rejection against errors, e.g. gravity-compensation, through (4.23), which might affect the HIL accuracy. Therefore, results for M1-A and M3-B methods are shown, see Fig. 4.9. In both approaches, a KUKA LWR4+ was used as the manipulator for

both, the reference orbital robot and the OGRF. The mass and inertia parameters of LWR4+ are the same as reported in [27, Table 1]. In the following, $(\tilde{\bullet})$ refers to a measured quantity. I denote the twist velocity basis of the frame $\{\mathcal{B}\}$ as e_i , i=1..6 where i=1,2,3 and i=4,5,6 denote the instantaneous translation and rotational basis, respectively.





(a) M1-A with KUKA LWR4+.

(b) M3-B on DLR OOS-SIM.

Figure 4.9: In both figures, orbital robot on left and OGRF on right, with $\{\mathcal{B}\}$ as the common frame on spacecraft. The simulation and hardware elements have identical initial conditions.

Scenario 1. A joint trajectory between two configurations was commanded while considering initial momentum $\mathcal{J}(0) = 0_6$. The OBSW was a free-floating controller, i.e. unactuated spacecraft. Therefore, the actuation, $(0_6, \hat{\tau})$, which was generated by the OBSW, was used in (4.20) to obtain τ_i commands for the two LWR4+ OGRF. During the maneuver, contacts were made at the end-effector, $\{\mathcal{E}\}$, and the resulting wrench, \mathcal{F}_e , was measured using a FTS sensor.

For this scenario, the HIL spacecraft dynamics was computed using the following three methods.

- 1. P0: Using the dynamics in (4.1), \dot{V} was integrated with state, $(g_b, V_b, \tilde{q}, \dot{\tilde{q}})$, and actuation, $\begin{bmatrix} 0_6^\top & \hat{\tau}^\top \end{bmatrix}^\top$, to obtain the spacecraft state, (g_b, V_b) .
- 2. P1: Using only the first row of (4.1), \dot{V}_b was integrated using the same actuation as P0. However, this requires \ddot{q} measurements, which was obtained by numerical differentiation of \dot{q} and a first order low-pass filter with cut-off frequency of 10[Hz].
- 3. M1-A: The proposed method was used with identical state and actuation as that of P0.

The P0 method has a dependency on $\hat{\tau}$, which results in a drift in \dot{V}_b due to the compensation of residual torques, e.g. gravity-compensation errors. Indeed, it was observed that even in static condition, the OBSW applied control action

in the order of 0.1[N.m], which caused a non-physical motion in the spacecraft. Although an ad-hoc deadzone was implemented, the configuration-dependence of these torques made it ineffective. Hence, results for P1 and M1-A were compared since they are independent of $\hat{\tau}$.

4.6.1 M1-A on KUKA LWR4+

M1-A was validated using Scenario 1 on the setup in Fig. 4.9a, in which the reference orbital robot (Fig. 4.9a, left) and the fixed-base OGRF (Fig. 4.9a, right) are shown. A joint-space PD-controller [29] was implemented as the OBSW. The mass of the spacecraft was 105[Kg] and principal inertias were (47.5, 34.9, 46.2)[Kg.m²].

In Fig. 4.10a, the comparison between results from P1 (left) and M1-A (right) for the Scenario 1 are presented. In the first row, the measured momentum map $\tilde{\mathcal{J}}$ has been presented for both approaches in basis e_2, e_3, e_4 , since the contacts affected $\tilde{\mathcal{J}}$ in these directions by the highest magnitude. During t = [0, 13][s] (before first contact), it can be clearly seen that the initial condition, $\mathcal{J}(0)$, holds during manipulator motion for M1-A (right), whereas in P1 (left), this condition is violated, which makes the HIL non-physical during manipulator motion. The measured contact forces referenced at $\{\mathcal{B}\}$, $J_b^{\top}\mathcal{F}_e$, are presented in the second row, where J_b is the spacecraft Jacobian of end-effector. Despite the applied forces being of a similar magnitude, the change in $\tilde{\mathcal{J}}(t)$ is characterized by spikes in P1 (left), whereas M1-A provides consistent increments. In Fig. 4.10b, the resulting free-floating spacecraft velocity V_b during t = [0, 9][s] is shown for P1 (dashed) and M1-A (solid) for e_i , i = 1..6 (colored). Due to the non-physical momentum behavior, it can be seen that P1 results in an underestimated velocity, especially in e_4, e_5 .

4.6.2 M3-B on OOS-SIM

The OOS-SIM [50] is a HIL facility (Fig. 4.9b, right), which uses an industrial robot in admittance causality to simulate dynamics for the orbital robot's spacecraft. The simulated spacecraft mass was 600[Kg] and principal inertias were $(500, 600, 500)[\text{Kg.m}^2]$. First, I note that since orbital robot and OGRF are identical, (4.26) simplifies further to $\bar{\mathcal{F}}_b = -\bar{\mathcal{F}}_{bd} + \hat{\mathcal{F}}_b$ for the admittance controller. Secondly, (4.20) simplifies to $\tau_2 = -\tau_{2d} + \hat{\tau}$. Thus, the HIL simplifies to feed-through of the OBSW commands with additional gravity-compensation. For the validation procedure, \tilde{V}_b was obtained by numerically differentiating the industrial robot's forward kinematics \tilde{g}_b and using a first-order low-pass filter with 10[Hz] cut-off frequency.

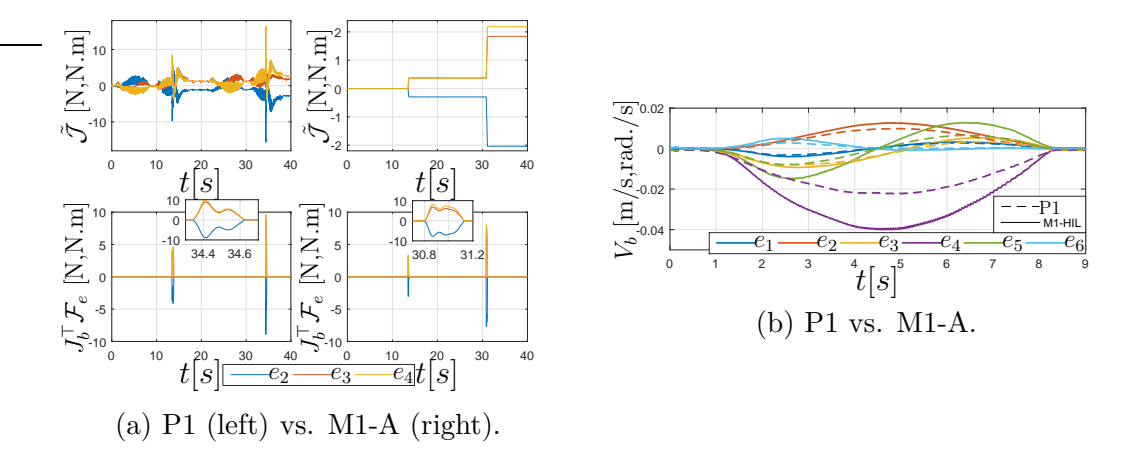


Figure 4.10: (a): Comparison between P1 (left) and M1-A (right) during OGRF motion and contacts. Top row: Momentum, Bottom row: Contact forces. Difference in contact events is due to manually induced contacts. (b): Comparison of $V_b(t)$ (colored) during a trajectory between P1 (dashed) and M1-A (solid).

4.6.2.1 M3-B: Momentum Consistency

A free-floating Cartesian PD-controller [29] was used in Scenario 1 to approach the stationary satellite structure on the right of Fig. 4.9b till contact was made. The comparative results from P1 and M3-B are presented in Fig. 4.11a. In first row, \mathcal{J} is plotted for e_1, e_3, e_5 , since the contact affected its magnitude more significantly in these basis. Note that, the second order response at $t \geq 0[s]$ in both approaches is due to the admittance controller's transient response. However, during t = [0, 10] (plot insets), it can be seen that $\tilde{\mathcal{J}} \to 0_6$ for M3-B, whereas, this condition is violated for P1. This corroborates the same observation made in Sec. 4.6.1. I also note that, in experiments for both, M3-B and P1, the controller parameters, trajectory and initial conditions were kept identical. However, I observe in second row that the contact duration is longer for P1. This might be explained as follows. In P1, g_b is integrated from an erroneous V_b , which was observed clearly in Fig. 4.10 of Sec. 4.6.1. This is due to a non-physical momentum, which is also seen in left of Fig. 4.11a. As a result of the ensuing non-physical behavior, the generalized Jacobian for $\mathcal{J}=0_6$, that is used in OBSW is not in agreement with HIL, resulting in modified Cartesian forces and hence a different contact behavior. In fact, a direct result of this was that the orbital robot gained twice as much more momentum in t > 11[s] for P1 than M3-B.

4.6.2.2 M3-B for a V&V Scenario

In this scenario, the conditions of Scenario 1 were the same, however, with space-craft actuation ($\hat{\mathcal{F}}_b \neq 0_6$). The goal of this validation was to emphasize that the

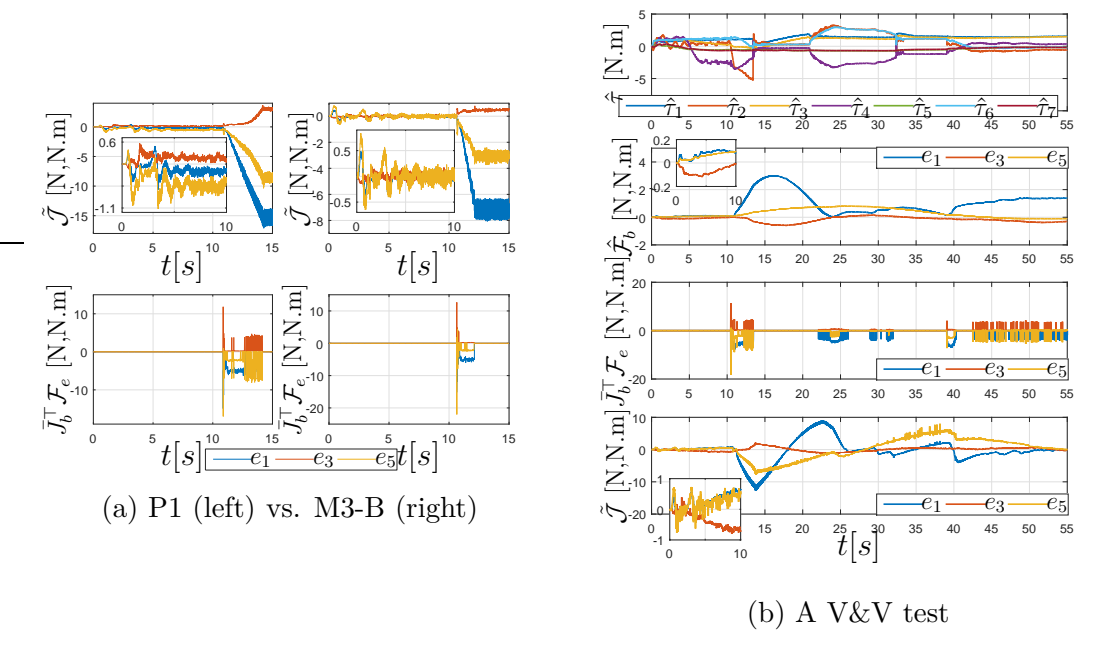


Figure 4.11: (a): Comparison between P1 (left) and M3-B (right) during OGRF motion and contacts. Top row: Momentum map, Bottom row: Contact forces. (b): Experimental result for M3-B HIL of a fully-actuated orbital robot with multiple contacts. OBSW actuation in top two rows, contact forces in third row and momentum map in bottom row.

proposed method is applicable to a fully-actuated orbital robot while interacting with a passive environment. A fully-actuated orbital robot controller [27] was used to regulate poses of end-effector, $\{\mathcal{E}\}$, and spacecraft, $\{\mathcal{B}\}$. The desired end-effector pose was chosen to induce a contact at $\{\mathcal{E}\}$ with the client structure on right of Fig.4.9b. The results have been presented in Fig. 4.11b.

In the first row, the OBSW joint-actuation $\hat{\tau}$ has been plotted. The quantities $\hat{\mathcal{F}}_b$, $J_b^{\top} \mathcal{F}_e$ and $\tilde{\mathcal{J}}$ have been plotted for e_1, e_3, e_5 bases, since the contacts affected their magnitude more significantly in these basis. Note that, as soon as the manipulator moves at $t \geq 0[\mathbf{s}]$, $\mathcal{F}_b \neq 0_6$ (plot inset). This causes a consequent change in $\tilde{\mathcal{J}}$ (plot inset). The first contact occurs at $t = 10.5[\mathbf{s}]$, which drastically changes $\tilde{\mathcal{J}}$. However, control action $\hat{\mathcal{F}}_b$ also increases to compensate for resulting pose errors. And finally, through consequent contacts (third row) in $t > 40[\mathbf{s}]$, the controller is able to stabilize motion $(\tilde{\mathcal{J}} \to 0_6, t > 50[\mathbf{s}])$ by achieving force balance between $\hat{\mathcal{F}}_b$ and $J_b^{\top} \mathcal{F}_e$. This is achieved through the manipulator torques $\hat{\tau}$, which act between $\{\mathcal{E}\}$ and $\{\mathcal{B}\}$.

4.6.3 Discussion

In sections 4.6.1-4.6.2, I observed that the combined effect of noisy \tilde{q} and filter dynamics in P1 negatively affects a HIL by injecting non-physical momentum during manipulator motion. This diminishes the physical consistency of HIL validation. For instance, on-ground estimation of spacecraft fuel-consumption to perform tasks, e.g. spacecraft pose regulation, is affected by erroneous V_b and alteration of contact dynamics in P1. In contrast, the proposed M1-A and M3-B methods simulate an orbital robot without requiring \tilde{q} . In fact, this imparts a physically correct behaviour to the HIL without precluding external forces in dynamics. Thus, the problem statement in Sec. 4.2.2 has been duly addressed using the proposed methods and which were also experimentally validated. A key observation from Sec. 4.6.2 is that force feedback of \mathcal{F}_e is not required to simulate interactions if the manipulators for the orbital robot and the OGRF are identical.

I remark that the proposed methods enable HIL of a fully-actuated orbital robot with contacts. However, model-based discontinuous thruster actuation requires high bandwidth in the vehicle-manipulator OGRF. In practice, time delays in the force loop and admittance characteristics might negatively affect HIL fidelity. This may limit stability during contacts, and addressing this issue with the proposed methods defines our future scope of work.

4.7 Conclusion

In this chapter, a Hardware-in-the-loop framework was proposed to simulate a fully-actuated orbital robot in the presence of external forces. To this end, two converse theorems of Controlled Lagrangian equivalence were proved and applied to the Lagrange-Poincaré equations of an orbital robot. By exploiting the block-diagonal inertia of these equations, the need of joint acceleration/torque measurements for simulating spacecraft motion was avoided. The main benefit of the proposed approaches was physical (momentum) consistency, which was validated through experiments on two facilities, a fixed-base KUKA LWR-4 and OOS-SIM. Furthermore, the specific case of a fully-actuated orbital robot with multiple contacts was experimentally validated using the proposed method to prove its effectiveness. The publications resulting from the contributions of this chapter are:

- 1. H. Mishra, A. M. Giordano, M. De Stefano, R. Lampariello, and C. Ott, "Inertia-decoupled equations for hardware-in-the-loop simulation of an orbital robot with external forces", in 2020 IEEE/RSJ International Conference on Intelligent Robots and Systems (IROS), 2020, pp. 1879–1886
- 2. M. De Stefano, H. **Mishra**, A. M. Giordano, R. Lampariello, and C. Ott, "A relative dynamics formulation for hardware- in-the-loop simulation of

4.7 Conclusion 111

on-orbit robotic missions", *IEEE Robotics and Automation Letters*, vol. 6, no. 2, pp. 3569–3576, 2021

3. H. **Mishra**, T. Vicariotto, and M. De Stefano, "Dynamics, simulation & control of orbital modules for on-orbit assembly", *IEEE Robotics and Automation Letters*, vol. 10, no. 1, pp. 200–207, 2025

The HIL framework proposed here was exploited in several projects funded by the EU and European Space Agency (ESA). The results are detailed later in Chapter 8.

Sensor-based Motion Control of \mathcal{LP} Systems

(6 A goal-oriented motion is meaningful if it is driven by the right cognition, which, in turn, is incrementally achieved through sense-perception of things present, estimation of things present as well as not, and comparison with the previously known. [178, pp. 15].

Gautama, Nyaya Sutra, 2nd-century AD

5.1 Introduction

Rapid developments in robotics research have rendered mechanisms kinetic in their environment, rather than being affixed spatially, see Fig. 5.1. In such mechanisms, apart from the internal shape, the spatial position is an additional variable (usually a group, e.g. SE(3), SO(3)) for motion control. The group position is often a symmetry variable, i.e., the Lagrangian does not depend on it. Lagrangian symmetry implies a conservation or a continuity equation for momentum by Noether's theorem [14, §4.1]. These mechanisms are a particular form of \mathcal{EL} systems, called \mathcal{LP} systems [149]. In Chapter 3, I derived the \mathcal{LP} dynamics using efficient Newton-Euler (NE)-like iterative computations for FRM. The FRM has emerged as a key element for complex tasks, e.g. on-orbit servicing [179, 180], aerial [181, 182] and underwater manipulation [155, 183]. Meaningful motion control in such a task requires effective feedback of the mechanism states and a coordinated actuation of the whole FRM. However, the heterogeneous sensing and actuation between the group and shape subsystems make motion control

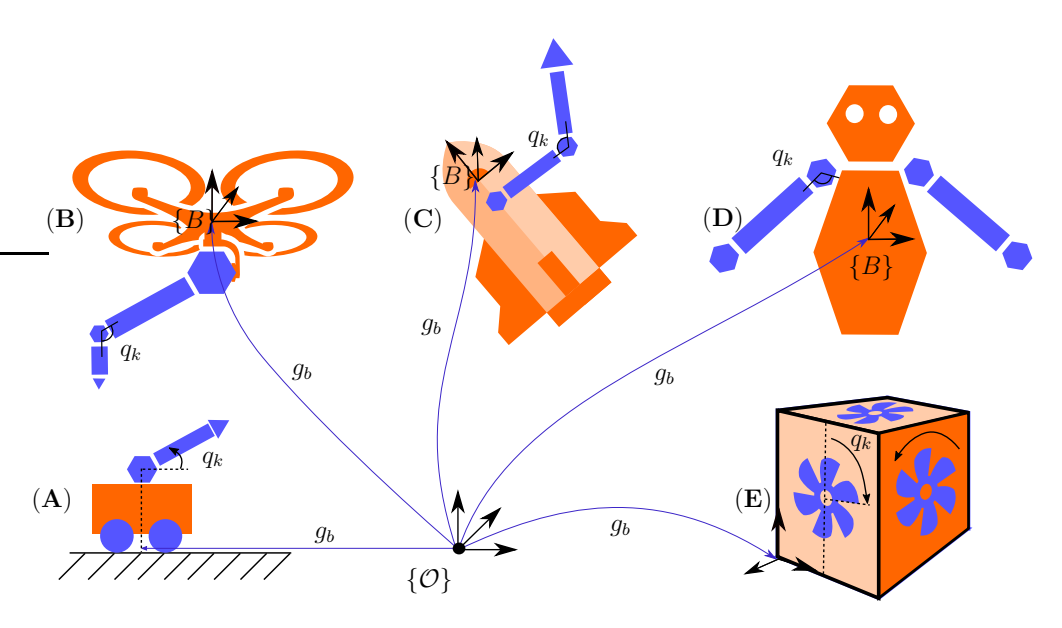


Figure 5.1: \mathcal{LP} systems: Mechanisms with group symmetry (g_b) . (A): Cart-Pendulum toy, (B): Aerial manipulator, (C), Orbital manipulator, (D): Humanoid, (E): Satellite with rotors.

non-trivial, which is the main topic of this chapter. Although the analytical treatment is posed for the FRM, it applies to any \mathcal{LP} system without loss of generality.

5.1.1 State-of-the-art: Full-state feedback

The first approach to motion control for a FRM, or any \mathcal{LP} system, is stabilization of its relative equilibria (or the shape), i.e., joints on a momentum level-set. This approach exploits only the internal actuation, e.g. joints, reaction wheels etc., and is commonly known as free-floating motion control [73, 140, 184]. With this approach, the reachable workspace of the FRM is restricted by the momentum level-set assumption. Furthermore, while the motion control is passive relative to disturbances in its internal motion, an external disturbance (impact) can cause an irreversible drift in operational space variables. Both these demerits are mitigated by exploiting the fully-actuated capability (momentum transfer actuators, e.g. thrusters) of the FRM, termed as free-flying motion control, [27, 34, 35, 134]. This approach, is further classified as hierarchical [34, 35] and direct PBC [27, 134]. In the former approach, the symmetry (momentum) property of the FRM is exploited by prioritizing the momentum-related task as primary, and the operational space task as secondary. The latter approach exploits the passivity of the FRM-dynamics for motion control with equal priority tasks. In all the aforestated approaches so far, full-state feedback is often assumed, and the controller development is made in a manner that the FRM's sensing and actuation

5.1 Introduction 115

is equivalent for its shape and external motions.

5.1.2 State-of-the-art: Output feedback

In contrast to full-state feedback, Output Feedback Control (OFC) specifically considers available sensing. In this approach, the overall controller is a dynamic feedback system, wherein the unmeasured states are estimated to realize the motion control law. OFC approaches exploiting velocity observers of mechanical systems have a rich history in robotics [185–187] and motion control [62, 141, 188]. Kalman filter designs, which are purely based on kinematics equations, have used *both* proprioceptive and exteroceptive measurements for the estimation of the FRM-base states [185–187]. In the absence of velocity sensors, the dynamics model of the mechanism is exploited [62, 141, 188]. Despite the vast literature, the OFC approach often gets misinterpreted within the research community.

Remark 23. While a perception system provides an estimate of a physical quantity only using sensory data, an OFC exploits the applied control effort and available sensing in a feedback loop to stabilize motion. The observer in the latter is similar to a perception system only in error injection, i.e., correction of the estimated quantity using sensory feedback. However, the stability analyses of OFC is usually non-trivial due to the lack of a separation principle, i.e. the error dynamics of the observer and the control law are mutually dependent. Therefore, the observer design fits a particular choice of a control law [141, 188]. It might also be worth noting that an OFC approach is associated with a convergence guarantee, and is starkly different from a controller that tracks a model-free interpolation.

The properties of the mechanism's dynamics are crucial in observer design. In particular, the analysis in [141] relied upon the commutative and the skew-symmetric properties of the Coriolis/Centrifugal (CC) matrix for a fixed-base robot. In [189], the controller was dynamically extended to possess a \mathcal{EL} structure with damping using the estimated velocity, whereas the motion control of the \mathcal{EL} plant was achieved purely through an interconnection potential. In [188, 190], intrinsic observers that conform to the Riemannian manifold structure of the mechanism's configuration space were designed. The authors proved that the observer convergence for a general mechanism was local due to the manifold curvature forces, which are quadratic in velocities.

5.1.3 Problem Statement: \mathcal{LP} Systems

Full-state feedback of the \mathcal{LP} system's (FRM) internal shape is often available through proprioceptive sensing, e.g. joint encoders, and hence using a dirty derivative or a first order observer [3] is sufficient for shape velocity feedback. However, its external motion (momentum) and the group variable are not directly measured. Exteroceptive sensing, e.g. camera and its image processing, are used

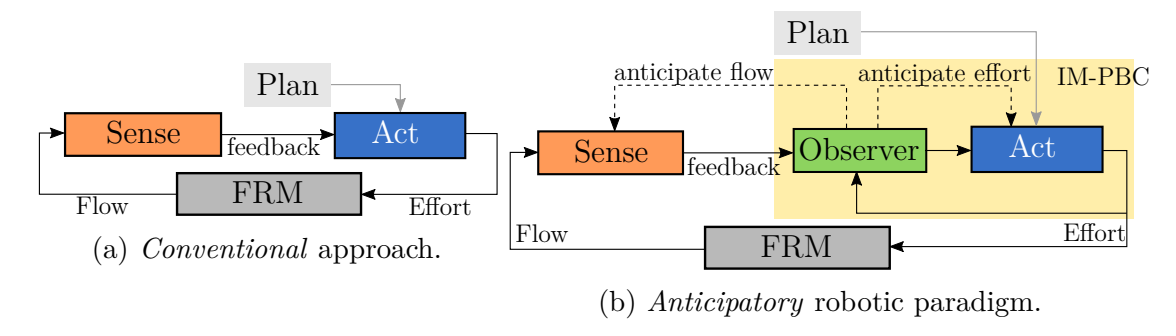
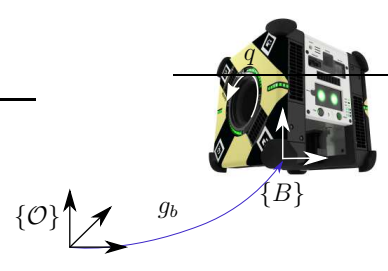


Figure 5.2: Conventional approach vs Anticipatory robotic control paradigm.

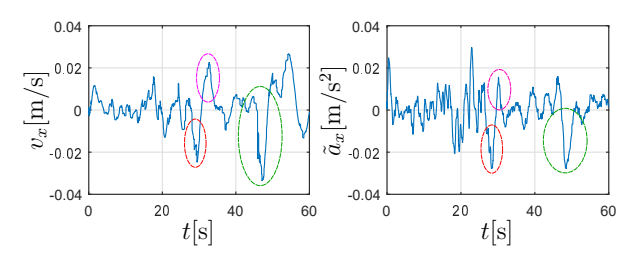
to locate the FRM in its environment. The circuitry on such sensors is limited in its sampling time. Additionally, the sensor pipeline introduces a transport delay due to processing and data transmission. Hence, the closed-loop motion control is affected not only by low feedback rate, but also by transport delay [191]. Furthermore, a pure exteroceptive approach does not provide velocity feedback of the floating-base, and a numerical differentiation of a slow-sampled, noisy and latency-affected signal is ineffective for feedback control. To mitigate this, the exteroceptive signal is combined with high-rate proprioceptive measurements, e.g. IMU, in a sophisticated sensor-fusion algorithm (commonly known as 'perception system' or 'localizer' or 'navigation filter'). Although this approach is effective in some 'slow' applications, abrupt changes in visible feature count result in outliers and non-physical discontinuities in the feedback signal [192, 193].

In the conventional approach, the feedback results from a direct interconnection of the perception system (orange) and a control law (blue), see Fig. 5.2a. However, the outliers in feedback (due to occlusions, feature count losses etc.) of the external motion of the FRM results in high-frequency effort commands to the actuator. Furthermore, high-frequency effort leads to abrupt flow (momentum) changes, which adversely affects the perception system, e.g. due to large pixel velocities. Consequently, the feedback nature of Fig. 5.2a restricts the motion control stability [192, 194]. These observations highlight a key issue. There is a coupling between sensor-actuator system of the FRM's external motion, through the effort-flow variables [195]. An example is shown in Fig. 5.3 from the ROAM-2 ISS flight experiment of the Astrobee robot. On the right, the outliers in estimated linear velocity and acceleration bias from the localizer are shown. A similar problem had been observed in my earlier work [73] at the DLR-OOS-SIM, as shown in Fig. 5.4, in which the quaternion estimate jumps in close range due to feature count reduction. At the same time, the heterogeneous actuation for the shape and the FRM-base also affects the motion control negatively, as is shown in Fig. 5.5. In particular, the static friction in the shape coupled with the slow actuation dynamics of the FRM-base create a limit cycle. Thus, to achieve meaningful motion stabilization of the FRM, a sophisticated

5.1 Introduction 117



(a) The Astrobee free-flyer FRM with internal rotors.



(b) Localizer outliers (ovals) during motion: velocity, v_x , and Inertial Measurement Unit (IMU)-accelerometer bias, \tilde{a}_x , in x-direction.

Figure 5.3: Localizer outliers during the ROAM-2 ISS flight experiment.

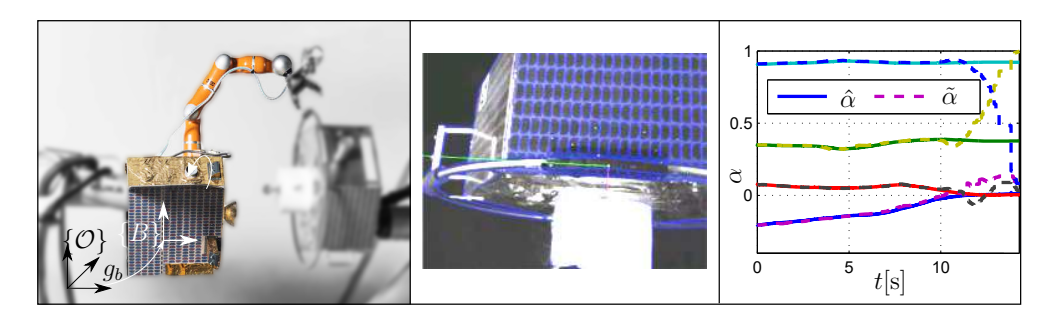


Figure 5.4: Left: The orbital FRM at OOS-SIM; Center: Camera-view with image-processing overlay; Right: Divergence of the localizer quaternion $\tilde{\alpha}$ relative to ground truth $\hat{\alpha}$ in close proximity.

approach is required.

5.1.4 Summary of Contributions

To this end, this chapter provides a motion control framework for \mathcal{LP} systems, especially the FRM, to deal with sensing and actuator heterogeneity of the shape and momentum subsystems. The contributions of this chapter are listed below.

1. A motion control framework consisting of two full-state feedback PBC-design approaches: Direct IM-PBC and Subsystem IM-PBC, is proposed through Lemmas 5.1 and 5.2, respectively. In Direct PBC, the passivity of the whole \mathcal{LP} -dynamics is exploited in control design, whereas in Subsystem PBC, the shape subsystem stabilization is given precedence. The key significance of the two approaches is the assertion of OSP of the interconnected system of momentum and shape, without requiring OSP for both subsystems, as is commonly known from literature, see [189, Appendix A.3]. The proposed approaches hold for any \mathcal{LP} system, i.e., mechanism with block-diagonalized inertia, as is the case for the FRM. This acts as a starting point for the OFC problem.

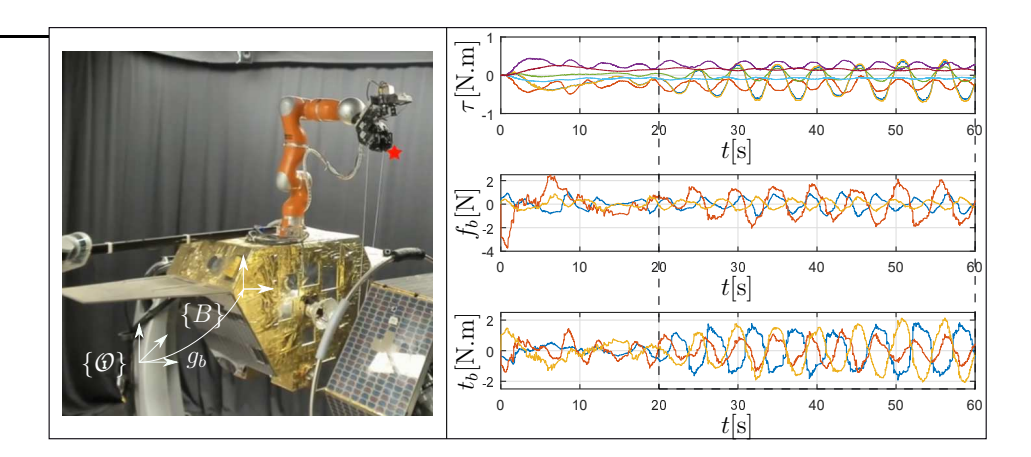


Figure 5.5: Left: Coordinated control of the orbital FRM at OOS-SIM; Right: Limit cycle (t > 20[s]) of a FRM between heterogeneous actuation of articulated mechanism (top, τ) and FRM-base (wrench, (f_b, t_b)) arising from static friction in the shape (joints) and the slow (50[Hz]) actuation of the FRM-base.

- 2. To address the OFC problem, two novel IM-PBC approaches are proposed by extending the Direct PBC and Subsystem PBC modalities. The IM-PBC methods exploit an observer based on the internal model of the Ver(\mathcal{LP}) dynamics to achieve full motion stabilization, while considering symmetry-breaking potentials, e.g. gravity, buoyancy and global control tasks (endeffector pose). In particular, the IM-PBC methods consist of the observer system for the momentum and the group variable in feedback with the motion control law. The methods are novel in that, they use a minimal set of measurements in form of the shape's state-space and the exteroceptive group variable (FRM-base pose) of the FRM. Hence, inertial sensors (velocity measurements) of the group-momentum variables are not strictly required, as in [185–187]. To the best of the authors' knowledge, such a method has not been reported for FRM. By exploiting the block-diagonal inertia in the \mathcal{LP} equations, the need for shape acceleration measurements is avoided in motion control.
- 3. The two IM-PBC methods are dynamic extensions of the full-state feedback direct and subsystem PBC approaches in item 1. In particular, Lemmas 5.1 and 5.2 are extended with the observer through Theorems 5.1 and 5.2, respectively. Importantly, in the momentum and shape interconnection (Fig. 3.7a of Chap. 3), the observer states elegantly extend the shape subsystem. In contrast to the dynamic extension in [189], the estimated quantity is directly used in the control law. In this way, the IM-PBC methods intuitively extend the corresponding approaches in item 1, and it also reveals gain criteria for convergence.

- 4. Both methods are proved to be OSP to external disturbances, which are suitable for contact-oriented tasks. Furthermore, the free-space motion is Uniform Almost Global Asymptotic Stability (UAGAS) [188], which is in contrast to [188, 190]. To achieve this, I reveal a skew-symmetric form of the curvature-related forces specific to \mathcal{LP} systems.
- 5. Furthermore, the proposed methods are extended to include additional sensory and model information to improve performance. The proposed IM-PBC extension with velocity sensing is able to perform contact-detection, shown in Theorem 5.3, and provide an integral action (Lemma 5.9) to deal with the heterogeneity in actuation of the FRM. The Subsystem IM-PBC is validated through simulations to highlight key aspects of convergence, and the Direct IM-PBC is validated experimentally on the DLR-OOS-SIM within the context of the EU EROSS+ mission project.

The chapter is organized as follows. In Sec. 5.2, the dynamics descriptions of the FRM are revisited. In Sec. 5.3, the PBC approach for \mathcal{LP} systems is introduced consisting of potential shaping and damping injection. Therein, two full-state feedback PBC approaches, namely direct PBC and subsystem PBC are introduced. While the former exploits the passivity of \mathcal{LP} dynamics with symmetry-breaking potentials, the latter prioritizes the shape subsystem for convergence. In Sec. 5.4, the aforementioned PBC approaches are extended for the OFC problem, denoted as the IM-PBC framework. Within this framework, direct IM-PBC and subsystem IM-PBC are proposed. Herein, the observer and control feedback laws are provided. The presentation of each method is followed by a stability/passivity analysis. In Sec. 5.5, the sensory and model extensions for the proposed IM-PBC are provided, which can be exploited for performance improvement. Within this extension, the proposed framework is shown to exploit contact detection and integral actions. In Sec. 5.6, the validation summary of the IM-PBC is provided, with relevant plots that highlight convergence and performance characteristics. Finally, concluding remarks, accompanying publications and future work are summarized in Sec. 5.7.

5.2 Modeling Motion for Control

A FRM is a system consisting of a floating-base and n joints/links, see Def. 3.1. In this chapter, its configuration is denoted as $r = (g_b, q) \in SE(3) \times \mathbb{R}^n$, where g_b, q are the inertial pose of the floating-base and articulated mechanism's joint positions, respectively. For generality, I consider the FRM as a multibody in the presence of symmetry-breaking potential field(s), e.g. gravity and/or buoyancy, and surrounded by a potential fluid flow, as in Sec. 3.7 of Chap. 3. To this end, the motion of purely rigid FRM is introduced first, followed by the result from Theorem 3.5 of Chap. 3. To ease the notation, the q-dependency of the dynamic

matrices is clarified in declaration but is omitted thereafter. The dynamics of an FRM are introduced next.

5.2.0.1 Hamel's equations

Denoting the total velocity as $V = (V_b, \dot{q})$, the dynamics of a FRM are commonly described using the Hamel's equations (see Lemma 2.6), which is written in robotics as,

$$\begin{bmatrix} \Lambda_b(q) & M_{bq}(q) \\ M_{bq}(q)^{\top} & M_q(q) \end{bmatrix} \begin{bmatrix} \dot{V}_b \\ \ddot{q} \end{bmatrix} + C(q, V) \begin{bmatrix} V_b \\ \dot{q} \end{bmatrix} = \begin{bmatrix} \mathcal{F}_b \\ \tau \end{bmatrix} + \begin{bmatrix} F_d \\ \tau_d \end{bmatrix}$$
 (5.1)

where, Λ_b , M_{bq} , M_q are the locked, coupling and manipulator inertias, respectively, C is the CC matrix, τ , $\tau_d \in \mathbb{R}^n$ are the actuation and disturbance torques, respectively, and \mathcal{F}_b , $F_d \in \mathbb{R}^6 \cong \mathfrak{se}(3)^*$ are the actuation wrenches, respectively.

The demerit of the inertia coupling in (5.1) is that \ddot{q} measurements are required to solve the spacecraft dynamics, i.e. \dot{V}_b . This is a sensory overhead for the observer design. Additionally, the CC-coupling terms in (5.1) render the observer's stability analysis non-trivial.

5.2.0.2 Lagrange-Poincaré (\mathcal{LP}) equations

Contrary to Hamel's equations, that use (q, V) to describe the dynamics of an FRM, the \mathcal{LP} equations use (q, ξ) , where $\xi = (\mu, \dot{q}) \in \mathbb{R}^{6+n}$ is a new system velocity with locked velocity, μ (see Def. 3.2). Using the transformation $T(q) = \begin{bmatrix} \mathbb{I}_{6,6} & \mathcal{A}_l \\ 0_{n,6} & \mathbb{I}_{n,n} \end{bmatrix}$, such that $\xi = TV$, \mathcal{LP} equations can be obtained using the Newtonian Transformation in Lemma 2.15-1, as,

$$\Lambda(q)\dot{\xi} + \Gamma(q, V)\xi = \begin{bmatrix} \mathcal{F}_b + F_d \\ \tau + \tau_d - \mathcal{A}_l^{\top}(\mathcal{F}_b + F_d) \end{bmatrix}$$
 (5.2)

A key consequence of the transformation leading to (5.2) is that Λ is block-diagonal [25]. This avoids the need for \ddot{q} measurements to solve for $\dot{\mu}$ in (5.2). However, note that Γ is a place-holder CC matrix, which lacks specific structure and has velocity dependencies of V instead of ξ . This prevents using its Lagrangian structure in model-based design. Furthermore, it does not generalize symmetry-breaking potentials like buoyancy and the effects of surrounding fluid.

In Chap. 3, I revealed the \mathcal{LP} equations with a special structure of the CC matrix with properties that will prove to be useful here. Furthermore, by exploiting Theorem 3.5, I generalize the proposed method for FRM in symmetry-breaking potential field(s), while being submerged in a potential fluid. Therefore, to aid the design of the motion control system, the \mathcal{LP} equations from Theorem 3.2

Chapter 3 are used to describe the FRM dynamics in this chapter as,

$$\underbrace{\begin{bmatrix} \Lambda_{b}(q) & 0_{6,n} \\ 0_{n,6} & \Lambda_{q}(q) \end{bmatrix}}_{\Lambda(q)} \begin{bmatrix} \dot{\mu} \\ \ddot{q} \end{bmatrix} + \underbrace{\begin{bmatrix} \frac{1}{2}P(q,\dot{q}) & 0_{6,n} \\ 0_{n,6} & \tilde{\Gamma}'_{q}(q,\dot{q}) \end{bmatrix}}_{\mathcal{D}_{\dot{q}}(q,\dot{q})} \underbrace{\begin{bmatrix} \mu \\ \dot{q} \end{bmatrix}}_{\xi} = \underbrace{\begin{bmatrix} \operatorname{ad}_{\mu}^{\top} \Lambda_{b} & -\frac{1}{2}S(q,\mu) - \operatorname{ad}_{\Lambda_{b}\mu}^{\sim} \mathcal{A}_{l} \\ \frac{1}{2}S(q,\mu)^{\top} - \mathcal{A}_{l}^{\top} \operatorname{ad}_{\Lambda_{b}\mu}^{\sim} & -\tilde{\mathcal{B}}(q,\mu) \end{bmatrix}}_{\mathcal{D}_{\mu}(q,\mu)} \begin{bmatrix} \mu \\ \dot{q} \end{bmatrix} \qquad (5.3)$$

$$+ \begin{bmatrix} \mathbb{I} & 0 \\ -\mathcal{A}_{l}^{\top} & \mathbb{I} \end{bmatrix} \begin{pmatrix} \mathcal{F}_{b} \\ \tau \end{bmatrix} + \begin{bmatrix} F_{d} \\ \tau_{d} \end{bmatrix} - \begin{bmatrix} d_{b}\mathcal{U}(g_{1},q) \\ d_{q}\mathcal{U}(g_{1},q) \end{bmatrix} \end{pmatrix}$$

where Λ is the block-diagonal inertia consisting of the locked inertia, Λ_b , and reduced shape inertia [29], Λ_q , which include the additional inertia effects of the surrounding potential fluid flow. The CC matrices $\mathcal{D}_{\dot{q}}$, \mathcal{D}_{μ} depend only on \dot{q} and μ , respectively¹. Also, $\tilde{\Gamma}'_q$ is the reduced CC matrix [29] and $\tilde{\mathcal{B}}(\mu)\dot{q}$ is the mixed (μ,\dot{q}) CC-coupling in the bottom row of (5.3) arising from curvature. In (5.3), $P(\dot{q}) = \frac{d}{dt}\Lambda_b$ and $S(\mu)^{\top}\mu = \frac{\partial}{\partial q}\langle\mu,\mu\rangle_{\Lambda_b}$, are two fundamental matrices that arise in the \mathcal{LP} equations. The effective symmetry breaking potential is denoted by \mathcal{U} , and d_b, d_q denote the differentials of the argument relative to g_b and q coordinates, respectively. The FRM-base pose kinematics is rewritten as,

$$\dot{g}_b = g_b V_b^{\wedge} = g_b (\mu - \mathcal{A}_l(q)\dot{q})^{\wedge}, \ g_b(R_b, p_b)$$

$$(5.4)$$

5.3 Passivity-Based Control (PBC) Framework

PBC broadly consists of two stages: potential shaping and damping injection [3]. In the former, the mechanism's potential energy is modified in a way that its minimum defines the new equilibrium for the mechanism's configuration. In damping injection, the mechanism is damped along the geodesic resulting from the potential shaping stage to stabilize around the new equilibrium. In the following, I will review aspects of PBC for the FRM, or more generally for any \mathcal{LP} system.

5.3.1 Potential Shaping

The motion stabilization task for the FRM can be broken down into two aspects: relative equilibria stabilization to regulate the internal motion, and group stabilization to regulate the external motion. The former is achieved through shape potentials and the latter through symmetry-breaking potentials.

¹The (1, 1) block matrix in \mathcal{D}_{μ} here is written using the Natural \mathcal{EP} body-level factorization, see Sec. 2.6.1.1 in Chap. 2.6.

5.3.1.1 Shape Potentials

The stabilization of the relative equilibria, i.e., the shape (joints), e.g. controlling the end-effector of the FRM relative to the FRM-base, is achieved by shaping the shape potential energy. The control task(s) is formulated as a potential $\Phi_q(q): \mathbb{R}^n \to \mathbb{R}_+$. Formally, $\Phi_q(q)$ is a potential on the shape-space of the \mathcal{LP} system, i.e., $\Phi_q(q): \mathrm{SE}(3) \times \mathbb{R}^n/\mathrm{SE}(3) \cong \mathbb{R}^n \to \mathbb{R}_+$. Note that $\Phi_q(q)$ is the effective potential, i.e., the sum of k task potentials on the shape variables, $\Phi_q(q) = \sum_i^k \Phi_{q,i}(q)$. Each of the task potentials can be formulated on some desired configuration space, e.g. only p-variables of the shape (\mathbb{R}^p), SE(3), SO(3) etc. Let the i^{th} operational space be \mathcal{Q}_i , with a forward kinematics map, $f_i: \mathbb{R}^n \to \mathcal{Q}_i$. The differential kinematics is given by the push-forward as, $d_q f_i(q)(\dot{q}) = J_i(q)\dot{q}$, where $J_i = \frac{\delta f_i(q)}{\delta q}$ is the Jacobian. Hence, the time-derivative of $\Phi_q(q)$ is given by its directional derivative (or the Lie derivative) along the shape trajectory q, i.e.,

$$\dot{\Phi}_q(q) = \langle \frac{\delta \Phi_q}{\delta q}, \dot{q} \rangle = \sum_{i=1}^k \langle \frac{\delta f_i}{\delta q}^\top \frac{\delta \Phi_{q,i}}{\delta f_i}, \dot{q} \rangle = \sum_{i=1}^k \langle J_i^\top d_{f_i} \Phi_{q,i}, \dot{q} \rangle$$
 (5.5)

where d_{f_i} refers to the differential w.r.t. the i^{th} operational space.

Assumption 5.1. The task potential $\Phi_q(q)$, is at least positive semi-definite in the FRM-shape with upper and lower bounds $0 \leq \underline{\Phi}_q < \overline{\Phi}_q < \overline{\Phi}_q, \underline{\Phi}_q, \overline{\Phi}_q \geq 0$, and is quadratic.

5.3.1.2 Symmetry-Breaking Potentials

For the \mathcal{LP} system, potential shaping consists of restoring the symmetry of the \mathcal{LP} equations by removing the effect of the symmetry-breaking potential $\mathcal{U}(g_b,q)$ (e.g. gravity, buoyancy) in (5.3), and imposing the behaviour of another symmetry-breaking task potential, $\Phi(g_b,q)$, that explicitly depends on the group variable (FRM-base). As before, $\Phi = \sum_{i=1}^{l} \Phi_i(g_b,q)$ is the effective symmetry-breaking potential. In this case, each task consists of a symmetry-breaking forward kinematics map(s), $h_i(g_b,q): SE(3) \times \mathbb{R}^n \to \hat{\mathcal{Q}}_i$. Since h_i depends on g_b , the corresponding task potential, $\Phi_i(h_i(g_b,q)): \mathcal{Q} \to \mathbb{R}$, is symmetry-breaking. The time-derivative of $\Phi(g_b,q)$ is given by its directional derivative (or the Lie derivative) along the

system trajectory (g_b, q) , i.e.,

$$\frac{d}{dt}\Phi(g_b,q) = \langle d_b\Phi, V_b \rangle + \langle d_q\Phi, \dot{q} \rangle = \langle d_b\Phi, \mu \rangle + \langle d_q\Phi - \mathcal{A}_l^{\top}d_b\Phi, \dot{q} \rangle
= \sum_{i=1}^l \left(\langle \frac{\delta\Phi_i}{\delta h_i} \left(g_b^{-1} \frac{\delta h_i}{\delta g_b} \right), \mu \rangle + \langle \frac{\delta\Phi_i}{\delta h_i} \frac{\delta h_i}{\delta q} - \mathcal{A}_l^{\top} \frac{\delta\Phi_i}{\delta h_i} \left(g_b^{-1} \frac{\delta h_i}{\delta g_b} \right), \dot{q} \rangle \right)
= \sum_{i=1}^l \left(\langle T_i(q)^{\top} d_{h_i}\Phi_i, \mu \rangle + \langle (J_i^{\top} - \mathcal{A}_l^{\top} J_b) d_{h_i}\Phi_i, \dot{q} \rangle \right)
= \sum_{i=1}^l \left(\langle T_i(q)^{\top} d_{h_i}\Phi_i, \mu \rangle + \langle \tilde{J}_i^{\top} d_{h_i}\Phi_i, \dot{q} \rangle \right)$$
(5.6)

where $T_i = \left(g_b^{-1} \frac{\delta h_i}{\delta g_b}\right)$ and \tilde{J}_i are known as the FRM-base and generalized Jacobians, respectively, and $d_{h_i}\Phi_i$ is the differential of Φ_i relative to the h_i variable.

Assumption 5.2. The task potential $\Phi(g_b, q)$, is at least positive semi-definite in the FRM configuration (g_b, q) with upper and lower bounds $0 \leq \underline{\Phi} < \Phi < \overline{\Phi}$, $\underline{\Phi} \geq 0$, and is quadratic.

Assumptions 5.1 and 5.2 are standard in passivity-based and Lyapunov-based control design [3, 10], and are required for ascertaining passivity/stability through functional analysis.

Remark 24. Note that the proportional actions in (5.5) and (5.6) are obtained as the effective sum of the pullback operations (transposed Jacobian) on the potential differentials in their respective task configuration spaces. This is a consequence of the well-known result of superposition of stiffness actions. Hence, this type of control approach is the pullback-type controller, wherein the potential from a task space is pulled back to the configuration space for motion stabilization.

To this end, the actuation (\mathcal{F}_b, τ) in (5.3) is decomposed as,

$$\begin{bmatrix} \mathcal{F}_b \\ \tau \end{bmatrix} = \begin{bmatrix} \hat{\mathcal{F}}_b(\mathcal{U}(.,q)) \\ \hat{\tau}(\mathcal{U}(.,q)) \end{bmatrix} + \begin{bmatrix} \tilde{\mathcal{F}}_b(\Phi(.,q)) \\ \tilde{\tau}(\Phi(.,q)) \end{bmatrix} + \begin{bmatrix} \overline{\mathcal{F}}_b(\mu,\dot{q}) \\ \overline{\tau}(\mu,\dot{q}) \end{bmatrix}$$
(5.7)

where $(\hat{\bullet})$, $(\tilde{\bullet})$ and $(\bar{\bullet})$ denote the symmetry-restoring, potential shaping task control, and damping injection actions, and (.) is the argument for the measurement (or estimate) for the FRM-base configuration.

5.3.2 Structure-Preserving Damping Injection

An intuitive choice for damping injection is $(\overline{\mathcal{F}}_b, \overline{\tau}) = -(D_b(q)\mu, D_q(q)\dot{q})$, where $D_b, D_q \succ 0$. However, using the FRM Hamiltonian, $\mathcal{H} = \mathcal{H}_{\mu} + \mathcal{H}_{\dot{q}}$ (Theorem 3.4), and computing its time-derivative assuming $\mathcal{U}, \Phi = 0$ and $(F_d, \tau_d) = (0, 0)$,

$$\dot{\mathcal{H}} = -\begin{bmatrix} \mu^{\top} & \dot{q}^{\top} \end{bmatrix} \begin{bmatrix} D_b & 0 \\ \mathcal{A}_l^{\top} D_b & D_q \end{bmatrix} \begin{bmatrix} \mu \\ \dot{q} \end{bmatrix}$$
 (5.8)

which is an asymmetric damping on the FRM velocities. Hence, in the following, the damping injection is performed as,

$$(\overline{\mathcal{F}}_b, \overline{\tau}) = (-D_b(q)\mu + D_b(q)\mathcal{A}_l\dot{q}, D_q(q)\dot{q})$$
(5.9)

which results in the dissipation of the Hamiltonian as,

$$\dot{\mathcal{H}} = -\langle \mu, \mu \rangle_{D_b} - \langle \dot{q}, \dot{q} \rangle_{\tilde{D}_q}, \ \tilde{D}_q = D_q - \mathcal{A}_l^{\top} D_b \mathcal{A}_l$$
 (5.10)

Remark 25. Note that the particular choice of $\overline{\mathcal{F}}_b$ in (5.9) creates a negative feed-back interconnection through the off-diagonal terms in the effective damping matrix, which generates no net power flow between momentum and shape subsystems. In that respect, this choice is structure-preserving, and is exploited in the PBC approach here. It is worth pointing out that the damping can be chosen directly in the symmetry-breaking task-space by disregarding the structure. However, this approach does not exploit the structural properties of the \mathcal{LP} system for the FRM. That being said, $D_b(q)$ can be set in the desired symmetry-breaking task-space basis, e.g. the end-effector, using the push-forward maps as $D_b(q) = T_i(q)^{\top} \overline{D}_b T_i(q)$, where $\overline{D}_b \succ 0$ is the required damping.

5.3.3 PBC Design: \mathcal{LP} Systems

FRM is a \mathcal{LP} system with a symmetry group (SE(3)), which results in a momentum continuity equation. Consequently, this leads to a block-diagonalized inertia, and a feedback interconnection of momentum and shape subsystems, as I showed in Fig. 3.7a. Motion stabilization for such systems can be achieved in two ways. In the first approach, namely direct PBC, the passivity of the whole system is exploited in motion control and the subsystem decomposition is ignored. This means that all tasks in motion control assume equal priority. In the second approach, subsystem PBC, one subsystem is prioritized for convergence by strengthening its passivity property to OSP through control action. These two approaches were motivated by motion stabilization of the generalized AC motor [3, pp. 9.3]. In fact, the momentum and shape subsystems of the FRM are analogous to the electrical and mechanical subsystems of an electromechanical machine, see [3, Fig. 9.2]. In the following, I bring forward the two PBC approaches through two novel Lemmas for subsystem OSP analysis.

5.3.3.1 Direct PBC

Lemma 5.1. Given a \mathcal{LP} system with $\mathcal{U} = 0$, like the floating FRM, let the damping injection be (5.9). The negative feedback interconnection of the momentum and shape subsystems is rendered OSP because the shape subsystem is OSP, and the momentum subsystem is passive in a way that it would be OSP in the

absence of the interconnection. In particular, the OSP map is,

$$\begin{bmatrix} \tilde{\mathcal{F}}_b + F_d \\ \tilde{\tau} + \tau_d - \mathcal{A}_l^{\top} (\tilde{\mathcal{F}}_b + F_d) \end{bmatrix} \mapsto \begin{bmatrix} \mu \\ \dot{q} \end{bmatrix}$$
 (5.11)

with storage function $\mathcal{H} = \mathcal{H}_{\mu} + \mathcal{H}_{\dot{a}}$.

Proof. Taking the time-derivative of the momentum subsystem (Σ_2) storage function, \mathcal{H}_{μ} , using (5.3),

$$\dot{\mathcal{H}}_{\mu} = -\langle \mu, \mu \rangle_{D_b} - \langle \dot{q}, \frac{D\hat{l}_{\mu}}{Dq} - \mathcal{A}_l^{\top} D_b \mu \rangle + \langle \mu, \tilde{\mathcal{F}}_b + F_d \rangle$$
 (5.12)

which creates the passivity map $(\tilde{\mathcal{F}}_b + F_d, \dot{q}) \mapsto (\mu, \frac{D\hat{l}_{\mu}}{Dq} - \mathcal{A}_l^{\top} D_b \mu)$. Note that Σ_2 is not OSP. Taking the time-derivative of the shape subsystem (Σ_1) storage function, $\mathcal{H}_{\dot{q}}$,

$$\dot{\mathcal{H}}_{\dot{q}} = -\langle \dot{q}, \dot{q} \rangle_{\tilde{D}_q} + \langle \dot{q}, \tilde{\tau} + \tau_d - \mathcal{A}_l^{\top} (\tilde{\mathcal{F}}_b + F_d) + (\frac{D\hat{l}_{\mu}}{Dq} - \mathcal{A}_l^{\top} D_b \mu) \rangle$$
 (5.13)

which creates the OSP map $\tilde{\tau} + \tau_d - \mathcal{A}_l^{\top}(\tilde{\mathcal{F}}_b + F_d) + (\frac{D\hat{l}_{\mu}}{Dq} - \mathcal{A}_l^{\top}D_b\mu) \mapsto \dot{q}$. Thus computing $\dot{\mathcal{H}}$ using (5.12) and (5.13), the result follows.

Remark 26. Note that Lemma 5.1 is a relaxed version of the standard feedback interconnection result in literature, which requires both subsystems in a feedback interconnection to be OSP to preserve this property [189, Appendix A.3]. Lemma 5.1 is a useful result that applies specifically to \mathcal{LP} systems, which are characterized by a block-diagonal inertia and a Lagrangian symmetry variable, e.g. g_b for the FRM.

5.3.3.2 Subsystem PBC: Prioritized Shape

Alternatively, for performance reasons, the motion control of shape can be prioritized for convergence. In this case, the OSP of the shape subsystem is strengthened, which results in a cascade system. This approach is outlined below.

Lemma 5.2. Given a \mathcal{LP} system with $\mathcal{U} = 0$, like the floating FRM, choosing $\tau = \tilde{\tau} - (\frac{D\hat{l}_{\mu}}{Dq} - \mathcal{A}_{l}^{\top}D_{b}\mu) - D_{q}(\dot{q})$ to compensate for μ -disturbances, and $\mathcal{F}_{b} = \tilde{\mathcal{F}}_{b} - D_{b}(q)\mu + D_{b}(q)\mathcal{A}_{l}\dot{q}$ transforms the negative feedback into a cascade interconnection with the shape subsystem driving the momentum subsystem. The cascade interconnection is rendered OSP as the shape subsystem is OSP, and the momentum subsystem is passive in a way that it would be OSP in the absence of the interconnection. An additional secant condition must be satisfied as follows,

$$D_b - \frac{1}{4} \mathcal{X}^{\top} \tilde{D}_q^{-1} \mathcal{X} \succ 0 \tag{5.14}$$

where $\mathcal{X} = \left(\frac{1}{2}S(\mu) + \operatorname{ad}_{\Lambda_b\mu}^{\sim} \mathcal{A}_l - D_b(q)\mathcal{A}_l\right)$. In particular, the OSP map is,

$$\begin{bmatrix} \tilde{\mathcal{F}}_b + F_d \\ \tilde{\tau} + \tau_d - \mathcal{A}_l^{\top} (\mathcal{F}_b + F_d) \end{bmatrix} \mapsto \begin{bmatrix} \mu \\ \dot{q} \end{bmatrix}$$
 (5.15)

with storage function $\mathcal{H} = \mathcal{H}_{\mu} + \mathcal{H}_{\dot{q}}$.

Proof. From Lemma 5.1, the momentum subsystem Σ_2 has the passivity map $(\tilde{\mathcal{F}}_b + F_d, \dot{q}) \mapsto (\mu, \frac{D\hat{l}_{\mu}}{Dq} - \mathcal{A}_l^{\top} D_b)$. Taking the time-derivative of $\mathcal{H}_{\dot{q}}$,

$$\dot{\mathcal{H}}_{\dot{q}} = -\langle \dot{q}, \dot{q} \rangle_{\tilde{D}_{a}} + \langle \dot{q}, \tilde{\tau} + \tau_{d} - \mathcal{A}_{l}^{\top} (\tilde{\mathcal{F}}_{b} + F_{d}) \rangle \tag{5.16}$$

where $\tilde{D}_q = D_q - \mathcal{A}_l^{\top} D_b \mathcal{A}_l$, which creates the OSP map $\tilde{\tau} + \tau_d - \mathcal{A}_l^{\top} (\tilde{\mathcal{F}}_b + F_d) \mapsto \dot{q}$. Thus computing $\dot{\mathcal{H}}$ using (5.12) and (5.16),

$$\dot{\mathcal{H}} = -\begin{bmatrix} \mu^{\top} & \dot{q}^{\top} \end{bmatrix} \underbrace{\begin{bmatrix} D_b & \frac{1}{2}\mathcal{X} \\ \frac{1}{2}\mathcal{X}^{\top} & \tilde{D}_q \end{bmatrix}}_{\mathcal{Y}(\mu)} \begin{bmatrix} \mu \\ \dot{q} \end{bmatrix} + \langle \tilde{\mathcal{F}}_b + F_d, \mu \rangle + \langle \dot{q}, \tilde{\tau} + \tau_d - \mathcal{A}_l^{\top} (\tilde{\mathcal{F}}_b + F_d) \rangle \quad (5.17)$$

and OSP follows from the Schur's complement for positive-definiteness of $\mathcal{Y}(\mu)$ to get the secant condition in (5.14).

Corollary 4. The condition of positive-definiteness of $\mathcal{Y}(\mu)$ to ensure OSP of the cascade interconnection in Theorem 5.2 can be reformulated using commutativity in Prop. 3.34 and the mapping between $\operatorname{ad}^{\sim} \mapsto \operatorname{ad}^{\top}$ operators as,

$$\begin{bmatrix} \mu^{\top} & \dot{q}^{\top} \end{bmatrix} \mathcal{Y}(\mu) \begin{bmatrix} \mu \\ \dot{q} \end{bmatrix} = \begin{bmatrix} \mu^{\top} & \dot{q}^{\top} \end{bmatrix} \begin{bmatrix} D_b + \frac{1}{2} P(\dot{q}) + \operatorname{ad}_{\mathcal{A}_l \dot{q}}^{\top} \Lambda_b & -\frac{1}{2} D_b \mathcal{A}_l \\ -\frac{1}{2} \mathcal{A}_l^{\top} D_b & \tilde{D}_q \end{bmatrix} \begin{bmatrix} \mu \\ \dot{q} \end{bmatrix}$$
(5.18)

resulting in a modified secant condition from Schur's complement,

$$D_b + \frac{1}{2}P(\dot{q}) + \operatorname{ad}_{\mathcal{A}_l\dot{q}}^{\top}\Lambda_b - \frac{1}{4}D_b\mathcal{A}_l\tilde{D}_q^{-1}\mathcal{A}_l^{\top}D_b \succ 0$$
 (5.19)

which depends only on the shape state-space, (q, \dot{q}) , instead of μ .

Remark 27. In prior works on hierarchical control [196], OSP of a lower priority task is ensured only in the set of convergence of a higher priority task. Lemma 5.2 is a stronger condition, as it affirms the OSP of the whole subsystem (not just each subsystem), while prioritizing the convergence of the shape subsystem.

Lemmas 5.1 and 5.2 will serve as a foundation to address the OFC problem. Analogously two variants of IM-PBC, which will additionally estimate (g_b, μ) , using an internal model of the Ver (\mathcal{LP}) dynamics will be postulated.

5.4 Proposed Method: IM-PBC

To achieve full-state feedback PBC for the FRM, a measurement of μ is required in Lemmas 5.1 and 5.2. I recall that the shape measurements (q) are available at a fast rate, through proprioceptive local sensors, e.g. joint encoders, and hence using a dirty derivative or a first order observer is sufficient for velocities (\dot{q}) . However, the group variable measurements, (g_b, V_b) , are obtained either through an exteroceptive sensor or a localizer algorithm. Since such a method is outlier-proper due to occlusions, IMU drifts, and feature-loss, the controller stability is often afflicted. Furthermore, the estimate of μ or V_b cannot be reliably obtained through a dirty derivative (like the shape) due to the slow-sampling and outlier discontinuities in the signal.

The proposed control design is motivated by the internal model principle from classical control theory and cybernetics, i.e., the control approach must utilize the feedback of the regulated variable, and, additionally, the plant model in the feedback path [197, 198]. In other words, a good regulator must be a model of the system. In essence, the passivity-based OFC approach in [3] is a realization of this philosophy, as the controller was an \mathcal{EL} system itself. In neuroscience, the internal model controller is a well-accepted model of the cerebellum as a sensorimotor controller. In particular, the motion model is used to generate an efferent copy (prediction) that is actively used in the feedback loop to achieve fast-reaching motions despite slow visual sensing [199]. In this vein, I denote the proposed method as Internal Model-PBC (IM-PBC) for \mathcal{LP} systems, i.e., mechanisms with symmetry, e.g. FRM. The key idea is to exploit the knowledge of the applied effort to predict the motion, and utilize it in the feedback loop. In this thesis, I shall focus on the control-theoretic aspects of the methods and their validation. The design is motivated by a future outlook of enabling the localizer system to benefit from the predicted motion.

5.4.1 Differential-Geometric Perspective

In this subsection, key geometric concepts of the FRM from Chapter 3 are revisited to develop an analogous concept for the estimation problem to address the OFC problem. Let $\hat{r} = (\hat{g}_b, q) \in SE(3) \times \mathbb{R}^n$ denote the estimated configuration, where \hat{g}_b is the FRM-base pose estimate of a virtual frame $\{\hat{B}\}$, recall Fig. 3.1 for typical FRMs. The corresponding velocity of this configuration is $\hat{V} = (\hat{V}_b, \dot{q})$. The configuration state estimation error, $\eta \in SE(3)$ between $\hat{g}_b(t)$ and g_b , is defined² as $\eta(g_b, \hat{g}_b) = \hat{g}_b^{-1}g_b$.

To elucidate the concept, I recall the illustration of the FRM configuration space in Fig. 3.2. This abstraction is modified in Fig. 5.6 to address the OFC problem. The proposed observer's configuration trajectory, $\hat{r}(t)$, is shown as yellow dot

 $^{^{2}\}eta$ is a left-invariant error [12, eq. 6], i.e $\eta(gg_{b}, g\hat{g}_{1}) = \eta, g \in SE(3)$.

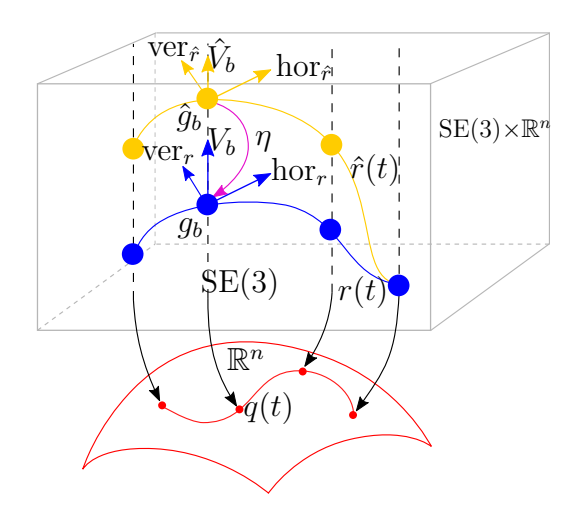


Figure 5.6: A differential-geometric illustration of the estimation problem for the \mathcal{LP} system. The trajectories of the physical system (r, blue trajectory) and its observer $(\hat{r}, \text{ yellow trajectory})$ evolve in $SE(3) \times \mathbb{R}^n$, grey-box.

trajectory in Fig. 5.6. Note that the quantities, Λ_b , M_{bq} , and hence, \mathcal{A}_l , are trivialized at the frame $\{B\}$ in Fig. 3.1. Therefore, given the pose error, η (magenta), the transport operator, Ad_{η} , transforms \mathcal{A}_l to the observer frame, $\{\hat{B}\}$. Thus, the mechanical connection at \hat{r} is obtained using (3.6) as, $\hat{\mathcal{A}} = \mathrm{Ad}_{\hat{b}} \left[\mathbb{I}_{6,6} \quad \mathrm{Ad}_{\eta} \mathcal{A}_l(q) \right] \hat{V}$. Correspondingly, the horizontal part is obtained as, $\mathrm{hor}_{\hat{r}} = (-\mathrm{Ad}_{\eta} \mathcal{A}_l \dot{q}, \dot{q})$ and the vertical part as, $\mathrm{ver}_{\hat{r}} = \hat{V} - \mathrm{hor}_{\hat{r}} = (\hat{V}_b + \mathrm{Ad}_{\eta} \mathcal{A}_l \dot{q}, 0_n) = (\hat{\mu}, 0_n)$. $\mathrm{hor}_{\hat{r}}$, $\mathrm{ver}_{\hat{r}}$, \hat{V}_b have been marked as yellow arrows. Since (q, \dot{q}) , are considered known, the reduced shape trajectory (red) is identical for both, the FRM and its observer. The key idea is to use the estimation error, η , in the SE(3) direction (fiber), however, instead of estimating also in the fiber, the estimation is performed along $\mathrm{ver}_{\hat{r}}$ while stabilizing the \mathcal{LP} dynamics in (5.3).

The group (SE(3)) velocities $(\hat{V}, \hat{\mu})$ in the estimation frame, $\{\hat{B}\}$, are transported to the FRM-base frame, $\{B\}$ using the $\mathrm{Ad}_{\eta}^{-1}\hat{V}$ operator. The main idea is to ensure that in $\mathrm{ver}_{\hat{r}}$, the state $\hat{\mu}(t) \to \mu(t)$ as $\hat{g}_b \to g_b$, which subsequently results in $\hat{V}_b(t) \to V_b(t)$.

5.4.2 Direct Internal Model-PBC (IM-PBC)

In the following, the direct IM-PBC approach is proposed, which exploits the passivity of the whole \mathcal{LP} dynamics for motion stabilization.

5.4.2.1 Motion with Symmetry-breaking Potentials

The proposed IM-PBC consists of an observer to estimate $(\hat{g}_b, \hat{\mu})$ and, additionally, a motion control law to stabilize the \mathcal{LP} dynamics of the whole FRM using the estimates.

As a first approach, the measured (not estimated) g_b is used in closed-loop feedback, as in [188, 189]. Thus, the control law is chosen as,

$$\begin{bmatrix} \tilde{\mathcal{F}}_b \\ \tilde{\tau} \end{bmatrix} = \underbrace{\begin{bmatrix} -d_b \Phi(g_b, q) \\ -d_q \Phi(g_b, q) - d_q \Phi_q(q) \end{bmatrix}}_{\text{Task regulation}}, \begin{bmatrix} \overline{\mathcal{F}}_b \\ \overline{\tau} \end{bmatrix} = \underbrace{\begin{bmatrix} -D_b(q)\hat{\mu}_o + D_b(q)\mathcal{A}_l\dot{q} \\ -D_q(q)\dot{q} \end{bmatrix}}_{\text{Damping}}$$

$$\begin{bmatrix} \hat{\mathcal{F}}_b \\ \hat{\tau} \end{bmatrix} = \underbrace{\begin{bmatrix} d_b \mathcal{U}(g_b, q) \\ d_q \mathcal{U}(g_b, q) - \mathcal{A}_l^{\top} d_b \mathcal{U}(g_b, q) \end{bmatrix}}_{\text{Symmetry-restoring}}$$
(5.20)

where $D_q(q), D_b(q) \succ 0$ are the damping gains.

5.4.2.2 Group Observer: SE(3)

Corresponding to the configuration error, η , the group error potential is denoted as $\Psi(\eta) : SE(3) \to \mathbb{R}_+$, which provides the error injection for the observer feedback loop through its differential (gradient). The group observer is chosen with the same geometric structure as (5.4) with an error injection term as follows,

$$\dot{\hat{g}}_b = \hat{g}_b \left(\underbrace{\check{\mu} - \operatorname{Ad}_{\eta} \left(\mathcal{A}_l \dot{q} - \operatorname{grad} \Psi(\eta) \right)}_{\hat{V}_b} \right)^{\wedge}$$
(5.21)

where $\check{\mu} \in \mathbb{R}^6 \cong \mathfrak{se}(3)$ is an internal model locked velocity, and grad is the Riemannian gradient operator computed at g_b , which is related to the differential through the locked kinetic energy metric as, $\langle d\Psi, y \rangle = \langle \operatorname{grad} \Psi, y \rangle_{\Lambda_b}$, given $y \in \mathbb{R}^6 \cong \mathfrak{se}(3)$.

In (5.21), note that $\hat{\mu} = \check{\mu} + \operatorname{Ad}_{\eta} \operatorname{grad} \Psi(\eta)$ is the output locked velocity estimate in the estimation basis $\{B\}$, and Ad_{η} operator is used to correctly map the body quantities from the basis of $\{B\}$ to the estimation basis of $\{\hat{B}\}$ (Fig. 3.1). This concept was introduced in the differential geometric approach earlier, and will also be examined further in Sec. 5.4.2.4.

5.4.2.3 Error kinematics

The observer error kinematics are derived by taking the time derivative of the pose error, $\eta = \hat{g}_b^{-1} g_b$, as,

$$\dot{\eta} = -\hat{g}_b^{-1} \dot{\hat{g}}_b \hat{g}_b^{-1} g_b + \hat{g}_b^{-1} \dot{g}_b
\Rightarrow \dot{\eta} = \eta (\mu - \operatorname{Ad}_{(\eta^{-1})} \check{\mu} - \operatorname{grad} \Psi(\eta))^{\wedge}
\Rightarrow (\eta^{-1} \dot{\eta})^{\vee} = \underbrace{\mu - \left(\operatorname{Ad}_{(\eta^{-1})} \check{\mu} + \operatorname{grad} \Psi(\eta)\right)}_{\mu_e}$$
(5.22)

where μ_e is the observer velocity error.

5.4.2.4 $Ver(\mathcal{LP})$ Observer: Momentum

Before proceeding to the observer equations for the $\text{Ver}(\mathcal{LP})$ equation (or the momentum equation), a vector comparison between the locked velocity (μ) and the observer velocity $(\hat{\mu})$ is obtained. The $\text{Ad}_{\eta^{-1}}$ term acts as the transport operator, which helps in defining the correct velocity error as $\mu_e = \mu - \hat{\mu}_o$, where $\hat{\mu}_o = \text{Ad}_{\eta^{-1}}\hat{\mu}$, as is evident in (5.22).

Following the discussion above, we compute the velocity error dynamics by taking the time-derivative of μ_e and using (5.22), as follows,

$$\frac{d}{dt}\mu_e = \frac{d}{dt}(\mu - \mathrm{Ad}_{\eta}^{-1}\hat{\mu})$$

$$= \dot{\mu} - \left(\mathrm{Ad}_{\eta}^{-1}\dot{\dot{\mu}} + \frac{d}{dt}\operatorname{grad}\Psi(\eta) - \mathrm{ad}_{\mu_e}\hat{\mu}_o\right)$$
(5.23)

Note that $\frac{d}{dt} \operatorname{grad} \Psi(\eta)$ along trajectories $(\eta, \mu_e, q, \dot{q})$ resolves as,

$$\frac{d}{dt}\operatorname{grad}\Psi(\eta) = \Lambda_b^{-1}\operatorname{Hess}(\Psi)\mu_e - \Lambda_b^{-1}P(\dot{q})\operatorname{grad}\Psi$$
 (5.24)

using the chain rule differentiation. Furthermore, substituting for $\hat{\mu}_o = \mu - \mu_e$ and using the properties, $\mathrm{ad}_x x = 0$ and $\mathrm{ad}_x y = -\mathrm{ad}_y x$ in (5.23),

$$\frac{d}{dt}\mu_e = \dot{\mu} - \left(\operatorname{Ad}_{\eta}^{-1}\dot{\ddot{\mu}} + \Lambda_b^{-1}\operatorname{Hess}(\Psi)\mu_e - \Lambda_b^{-1}P(\dot{q})\operatorname{grad}\Psi + \operatorname{ad}_{\mu}\mu_e\right)$$
(5.25)

Therefore, the observer goal is to determine the internal model $\mathrm{Ad}_{(\eta^{-1})}\dot{\check{\mu}}$. To this end, the observer for the momentum equation (first row of (5.3)) is proposed as the dynamics of $\check{\mu}$ with the geometric structure of the $\mathrm{Ver}(\mathcal{LP})$ equation, as follows,

$$\Lambda_b \operatorname{Ad}_{\eta}^{-1} \dot{\tilde{\mu}} + P(\dot{q}) \operatorname{Ad}_{\eta}^{-1} \tilde{\mu} - \operatorname{ad}_{\Lambda_b \hat{\mu}_o}^{\sim} (\hat{\mu}_o - \mathcal{A}_l \dot{q}) = \tilde{\mathcal{F}}_b + l.d\Psi(\eta) + \mathcal{F}_o
\Rightarrow \operatorname{Ver}(\hat{\mathcal{LP}})_{\operatorname{direct}} = \tilde{\mathcal{F}}_b + l.d\Psi(\eta) + \mathcal{F}_o$$
(5.26)

where l > 0 is an observer parameter, $\mathcal{F}_o \in \mathbb{R}^6 \cong \mathfrak{se}(3)^*$ is a virtual observer force (wrench) that shall be used to passivate the error dynamics with *optional* measurements (or estimates), as we shall see later.

Velocity error dynamics

Substituting (5.26) into (5.25), and using actual locked dynamics ($\dot{\mu}$) from (5.3),

$$\frac{d}{dt}\mu_e = \Lambda_b^{-1} \left(-\frac{1}{2} P(\dot{q}) \mu_e - \left(\frac{1}{2} P(\dot{q}) + \operatorname{ad}_{\mathcal{A}_l \dot{q}}^{\top} \Lambda_b \right) \mu_e - D_b(q) \hat{\mu}_o + D_b(q) \mathcal{A}_l \dot{q} \right)
- \operatorname{Hess}(\Psi) \mu_e + \left(\operatorname{ad}_{\Lambda_b \mu}^{\sim} \mu - \operatorname{ad}_{\Lambda_b \hat{\mu}_o}^{\sim} \hat{\mu}_o - \Lambda_b \operatorname{ad}_{\mu} \mu_e \right) + l.d\Psi(\eta) + F_d - \mathcal{F}_o \right)$$
(5.27)

To simplify the bracketed ad^{\top} terms, I provide the following skew-symmetry property, which is crucial for stability analysis later.

Lemma 5.3. For body velocities, V_1 , V_2 , $V_e \in \mathbb{R}^6 \cong \mathfrak{se}(3)$, such that a velocity error, $V_e = V_1 - V_2$, given inertia Λ , the following holds for the natural and bilinear Body-level factorization (BLF)s (Sec. 2.6.1.1),

$$\operatorname{ad}_{V_1}^{\top} \Lambda V_1 - \operatorname{ad}_{V_2}^{\top} \Lambda V_2 = \operatorname{ad}_{\Lambda V_1}^{\sim} V_1 - \operatorname{ad}_{\Lambda V_2}^{\sim} V_2 = \mathcal{C}(V_1, V_e) V_e$$
 (5.28)

where $C(V_1, V_e) = (\operatorname{ad}_{V_1}^{\top} \Lambda + \operatorname{ad}_{\Lambda V_1}^{\sim} - \Lambda \operatorname{ad}_{\Lambda V_e}^{\sim})$. Furthermore, given $x \in \mathbb{R}^6 \cong \mathfrak{se}(3)$, C satisfies a skew-symmetry property as follows,

$$\langle x, (\mathcal{C}(V_1, V_e)V_e - \Lambda \operatorname{ad}_{V_1})x \rangle = \langle x, \tilde{\mathcal{C}}(V_1, V_e)x \rangle = 0 \Rightarrow \tilde{\mathcal{C}}^{\top} = -\tilde{\mathcal{C}}$$
 (5.29)

Proof. For the first part in (5.28),

L.H.S =
$$\operatorname{ad}_{V_{1}}^{\top} \Lambda(V_{e} + V_{2}) - \operatorname{ad}_{(V_{1} - V_{e})}^{\top} \Lambda V_{2}$$

= $\operatorname{ad}_{V_{1}}^{\top} \Lambda V_{e} + \operatorname{ad}_{V_{1}}^{\top} \Lambda V_{2} - \operatorname{ad}_{V_{1}}^{\top} \Lambda V_{2} + \operatorname{ad}_{V_{e}}^{\top} \Lambda V_{2}$
= $\operatorname{ad}_{V_{1}}^{\top} \Lambda V_{e} + \operatorname{ad}_{V_{e}}^{\top} \Lambda(V_{1} - V_{e})$
= $(\operatorname{ad}_{V_{1}}^{\top} \Lambda + \operatorname{ad}_{\Lambda V_{1}}^{\top} - \operatorname{ad}_{\Lambda V_{e}}^{\sim}) V_{e} = \mathcal{C}(V_{1}, V_{e}) V_{e}$ (5.30)

For the second part in (5.29),

L.H.S =
$$\langle x, (\operatorname{ad}_{V_{1}}^{\top} \Lambda + \operatorname{ad}_{\Lambda V_{1}}^{\sim} - \operatorname{ad}_{\Lambda V_{e}}^{\sim} - \Lambda \operatorname{ad}_{V_{1}}) x \rangle$$

= $\langle x, (\operatorname{ad}_{V_{1}}^{\top} \Lambda + \operatorname{ad}_{\Lambda V_{1}}^{\sim} - \Lambda \operatorname{ad}_{V_{1}}) x \rangle - \langle x, \operatorname{ad}_{\Lambda V_{e}}^{\sim} x \rangle$ (5.31)

Note that the first and second inner product terms in (5.31) contain the Riemannian connection and bilinear factorization BLF of the rigid body CC matrix, respectively, see Subsection 2.6.1.1. Moreover, both these factorizations are skew-symmetric. Hence, $\langle x, \tilde{\mathcal{C}}(V_1, V_e)x \rangle = 0$.

Corollary 5. The matrix operator C in Lemma 5.3 satisfies the following property,

$$\langle x, \mathcal{C}(\mu, y)z \rangle = \langle x, \operatorname{ad}_{\Lambda y}^{\sim} z \rangle = \langle x, \operatorname{ad}_{z}^{\top} \Lambda y \rangle$$
 (5.32)

Proof. Using the properties $ad_x y = -ad_y x$, and the bilinear factorization BLF, the result follows.

In (5.27), using $\tilde{\mathcal{C}}$ from Lemma 5.3, and denoting $\tilde{P}(\dot{q}) = \left(\frac{1}{2}P(\dot{q}) + \operatorname{ad}_{\mathcal{A}_l\dot{q}}^{\top}\Lambda_b\right)$,

$$\frac{d\mu_e}{dt} = \Lambda_b^{-1} \left(\tilde{\mathcal{C}}(\mu, \mu_e) \mu_e - \frac{1}{2} P(\dot{q}) \mu_e - l.d\Psi(\eta) + F_d - \mathcal{F}_o \right)
- \left(\text{Hess}(\Psi) + \tilde{P}(\dot{q}) \mu_e - D_b(q) \right) \mu_e - D_b(q) \mu + D_b(q) \mathcal{A}_l \dot{q} \right)$$
(5.33)

Note that the velocity error dynamics in (5.33) is a function of the controlled quantities μ, \dot{q} . Thus a separation principle between observer and controller design is not feasible since *both*, μ and \dot{q} must be additionally stabilized.

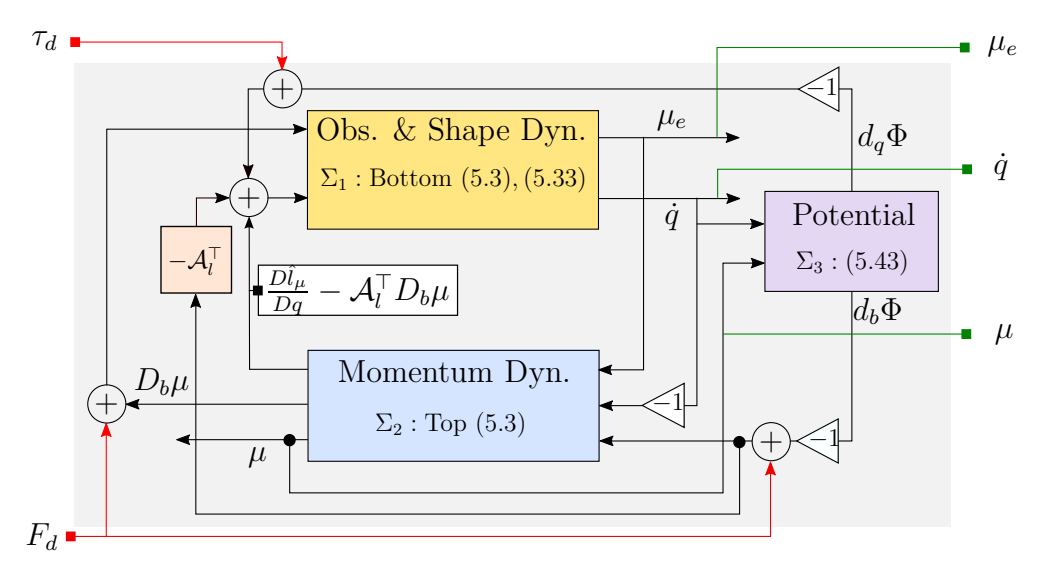


Figure 5.7: Direct IM-PBC as passive interconnection of observer-shape, momentum and the symmetry-breaking potential subsystems, with external inputs (red) on left, and outputs of the IM-PBC (green) on right.

5.4.3 Stability/Passivity Analysis of Direct IM-PBC

The stability analysis of the proposed IM-PBC is based on passive interconnection of the momentum and shape subsystems for the FRM in Theorem 3.4 of Chap. 3, and its extension to symmetry-breaking potentials in Corollary 3. In particular, the error dynamics for the observer and shape are considered as one subsystem, which is interconnected with the momentum subsystem in a negative feedback. Furthermore, the symmetry-breaking potential is also in a negative feedback interconnection with both these subsystems. The interconnection block diagram is shown in Fig. 5.7, which will be systematically explained through storage function analysis next.

5.4.3.1 OSP of Observer & Shape dynamics

As mentioned above, the error dynamics of the observer and shape are considered to be one subsystem, Σ_1 in Fig. 5.7, with states $z = (\eta, \mu_e, q, \dot{q})$. In the following, I prove OSP for this subsystem.

Lemma 5.4. Given the FRM with equations of motion as in (5.3), its shape dynamics (bottom row) and the observer error dynamics in (5.33) satisfy OSP,

$$\Sigma_{1}: \begin{bmatrix} F_{d} - \mathcal{F}_{o} - D_{b}(q)\mu \\ \tau_{d} - \mathcal{A}_{l}^{\top} F_{d} + \frac{D\hat{l}_{\mu}}{Dq} - \mathcal{A}_{l}^{\top} D_{b}(q)\mu - \left(d_{q}\Phi - \mathcal{A}_{l}^{\top} d_{b}\Phi\right) \end{bmatrix} \mapsto \begin{bmatrix} \mu_{e} \\ \dot{q} \end{bmatrix}$$
 (5.34)

provided that the observer parameters satisfy $(\Lambda_b^{-1} \mathrm{Hess}(\Psi) + \tilde{P}(\dot{q}) - D_b(q)) \succ 0$

with storage function as,

$$W = \underbrace{l\Psi(\eta)}_{W1} + \underbrace{\frac{l}{2}\langle\mu_e,\mu_e\rangle_{\Lambda_b}}_{W2} + \underbrace{\frac{1}{2}\langle\dot{q},\dot{q}\rangle_{\Lambda_q}}_{W3} + \Phi_q(q)$$
(5.35)

such that l > 0. Furthermore, W is bounded as, $\underline{\alpha}(z) \leq W(x) \leq \overline{\alpha}(z)$, due to the corresponding bounds for the kinetic energy metric and the potentials, $\Psi(\eta)$, $\Phi_a(q)$.

Proof. Differentiating W along trajectories $(\eta, \mu_e, q, \dot{q})$ and using the error dynamics in bottom row of (5.3) and (5.33),

$$\dot{W} = \langle \mu_{e}, \frac{1}{2} (-P(\dot{q}) + P(\dot{q})) \mu_{e} \rangle + \langle \dot{q}, \frac{D\hat{l}_{\mu}}{Dq} - \mathcal{A}_{l}^{\top} D_{b}(q) \mu \rangle
+ \langle \mu_{e}, \tilde{\mathcal{C}}(\mu, \mu_{e}) \mu_{e} \rangle + \langle \dot{q}, (\frac{1}{2} \frac{d}{dt} \Lambda_{q} - \Gamma_{q}(\dot{q}, \mu)) \dot{q} \rangle + \langle \mu_{e}, F_{d} - \mathcal{F}_{o} \rangle
- \langle \mu_{e}, (\text{Hess}(\Psi) + \tilde{P}(\dot{q}) - D_{b}(q)) \mu_{e} \rangle - \langle \dot{q}, \dot{q} \rangle_{\tilde{D}_{q}(q)} - \langle \mu_{e}, -D_{b}(q) \mu \rangle
+ \langle \dot{q}, (\tau_{d} - \mathcal{A}_{l}^{\top} F_{d}) - (d_{q} \Phi(g_{b}, q) - \mathcal{A}_{l}^{\top} d_{b} \Phi(g_{b}, q)) \rangle$$
(5.36)

Note that the first term in the top row of (5.36) cancels out. In the second row of (5.36), the first term is 0 due to the skew-symmetry of \tilde{C} in Lemma 5.3. Furthermore, the second term is also 0 owing to the skew-symmetry in Prop. 3.2. Therefore, (5.36) is rewritten as,

$$\dot{W} = -\langle \mu_e, (\text{Hess}(\Psi) + \tilde{P}(\dot{q}) - D_b(q))\mu_e \rangle - \langle \dot{q}, \dot{q} \rangle_{\tilde{D}_q(q)}$$

$$+ \langle \dot{q}, (\tau_d - \mathcal{A}_l^{\top} F_d) + (\frac{D\hat{l}_{\mu}}{Dq} - \mathcal{A}_l^{\top} D_b(q)\mu) - (d_q \Phi - \mathcal{A}_l^{\top} d_b \Phi) \rangle$$

$$+ \langle \mu_e, F_d - \mathcal{F}_o - D_b(q)\mu \rangle$$

$$(5.37)$$

If the observer gain parameters satisfy $H = (\text{Hess}(\Psi) + \tilde{P}(\dot{q}) - D_b(q)) > 0$,

$$\dot{W} \leq -\underline{\sigma}(H)||\mu_e||^2 -\underline{\sigma}(\tilde{D}_q)||\dot{q}||^2 + \langle F_d - F_o - D_b(q)\mu, \mu_e \rangle + \left\langle (\tau_d - \mathcal{A}_l^{\top} F_d) + (\frac{D\hat{l}_{\mu}}{Da} - \mathcal{A}_l^{\top} D_b(q)\mu) - \left(d_q \Phi - \mathcal{A}_l^{\top} d_b \Phi\right), \dot{q} \right\rangle$$
(5.38)

which proves the result.

In Fig. 5.7, the input-output map of Lemma 5.4 can be verified for the Σ_1 subsystem (yellow block).

5.4.3.2 Passivity of the Momentum Dynamics

The second subsystem, Σ_2 , in Fig. 5.7 is the momentum subsystem parameterized by μ . For this, I provide the following result.

Lemma 5.5. Given the FRM with equations of motion as in (5.3), its momentum dynamics (top row) is passive,

$$\Sigma_2 : \begin{bmatrix} F_d - d_b \Phi(g_b, q) \\ -\dot{q} \\ \mu_e \end{bmatrix} \mapsto \begin{bmatrix} \mu \\ \frac{D\hat{l}_{\mu}}{Dq} - \mathcal{A}_l^{\top} D_b(q) \mu \\ D_b(q) \mu \end{bmatrix}$$
 (5.39)

with storage function as

$$\mathcal{W} = \frac{1}{2} \langle \mu, \mu \rangle_{\Lambda_b}, \ \frac{1}{2} \underline{\sigma}(\Lambda_b) ||\mu||^2 \le \mathcal{W}(\mu) \le \frac{1}{2} \overline{\sigma}(\Lambda_b) ||\mu||^2$$
 (5.40)

Proof. Taking the time-derivative, and exploiting the fact that $\frac{d}{dt}\Lambda_b = P(\dot{q})$,

$$\dot{\mathcal{W}} = -\langle \mu, \mu \rangle_{D_b} + \langle \mu, F_d - d_b \Phi + D_b \mu_e - (\frac{1}{2} S + \operatorname{ad}_{\Lambda_b \mu}^{\sim} \mathcal{A}_l - D_b \mathcal{A}_l) \dot{q}) \rangle$$

$$\leq -\underline{\sigma}(D_b) ||\mu||^2 + \langle F_d - d_b \Phi, \mu \rangle - \langle \dot{q}, \frac{D \hat{l}_{\mu}}{D q} + \mathcal{A}_l^{\top} D_b \mu \rangle + \langle \mu_e, D_b \mu \rangle$$
(5.41)

which proves the result.

In Fig. 5.7, the input-output map of Lemma 5.4 can be verified for the Σ_2 subsystem (blue block). Note that in the inequality of (5.41), the latter two terms denote the negative feedback interconnection with the OSP system Σ_1 .

5.4.3.3 Passivity of the Symmetry-breaking Potential

The passivity of the potential subsystem, Σ_3 in Fig. 5.7, follows from the Corollary 3 of Chap. 3.

Lemma 5.6. The task-oriented symmetry-breaking potential $\Phi(g_b, q)$, which satisfies bounds, $\underline{\Phi} \leq \underline{\Phi} \leq \overline{\Phi}$, is passive,

$$\Sigma_3 : \begin{bmatrix} \mu \\ \dot{q} \end{bmatrix} \mapsto \begin{bmatrix} d_b \Phi(g_b, q) \\ d_q \Phi(g_b, q) - \mathcal{A}_l^\top d_b \Phi(g_b, q) \end{bmatrix}$$
 (5.42)

Proof. Taking the time-derivative of Φ ,

$$\frac{d}{dt}\Phi(g_b, q) = \langle \mu, d_b \Phi(g_b, q) \rangle + \langle \dot{q}, d_q \Phi(g_b, q) - \mathcal{A}_l^{\top} d_b \Phi(g_b, q) \rangle$$
 (5.43)

yields the result.

In Fig. 5.7, the input-output map of Lemma 5.6 can be verified for the Σ_3 subsystem (purple block). Note that Σ_3 is in a negative feedback interconnection with both Σ_1 and Σ_2 .

5.4.3.4 L2-&-Asymptotic Stability of the IM-PBC

In the following, the proposed IM-PBC is proved to be OSP, i.e., L2-stable, with the disturbance forces as inputs. In the absence of the disturbances, the IM-PBC is asymptotically stable about an equilibrium defined by the potentials Φ , Φ_q . This is formalized in the theorem below.

Theorem 5.1. Given the FRM with equations of motion as in (5.3), the proposed IM-PBC consisting of

- 1. SE(3) group observer defined as (5.21) with an error function $\eta = \hat{g}_b^{-1} g_b$ such that $tr(\eta(0)) \neq -1$,
- 2. $a \operatorname{Ver}(\mathcal{LP}) observer as (5.26),$
- 3. a motion control law as (5.20),

is OSP with the map,

$$\begin{bmatrix} \mathcal{F}_o \\ F_d \\ \tau_d \end{bmatrix} \mapsto \begin{bmatrix} -\mu_e \\ \mu + \mu_e - \mathcal{A}_l \dot{q} \\ \dot{q} \end{bmatrix}$$
 (5.44)

with the storage function $\mathcal{H} = W(\eta, \mu_e, \dot{q}) + \mathcal{W}(\mu) + \Phi(g_b, q)$. Furthermore, if the effective task potential, $\Phi(g_b, q) + \Phi_q(q)$, yields a unique equilibrium in $SE(3) \times \mathbb{R}^n$, and $(F_d, \tau_d, \mathcal{F}_o) = 0$, the closed-loop dynamics is asymptotically stable, i.e., $\eta \to \mathbb{I}_{4,4}$, $f(g_b, q) \to \bar{f}$, $q \to \bar{q}$ and $(\mu_e, \mu, \dot{q}) = 0$.

Proof. I recall that Σ_1 is OSP from Lemma 5.4. Also, Σ_2 is a passive system in a feedback interconnection with Σ_1 , which would be OSP without the interconnection, see (5.41). Thus, using the relaxed OSP concept in Lemma 5.1 for interconnection of the shape-momentum subsystems in \mathcal{LP} dynamics, the resulting feedback interconnection of $\Sigma_1 - \Sigma_2$ is OSP with (5.44). To this end, the storage function is $\tilde{\mathcal{H}} = W(\eta, \mu_e, \dot{q}) + W(\mu)$. This further emphasizes how the observer error dynamics serve as a part of the shape, as shown in Fig. 5.7. Furthermore, the symmetry-breaking potential Φ is a passive system (with no input), which is in a negative feedback interconnection with an effective OSP of $\Sigma_1 - \Sigma_2$, which preserves the OSP property by the invariance of passivity in Def. 2.14. Thus, the proposed IM-PBC is L2-stable. For the asymptotic stability analysis, Lemmas 5.4-5.6 are considered with no input, i.e., $(F_o, F_d, \tau_d) = 0$. In particular,

$$\dot{\mathcal{H}} \le -\underline{\sigma}(H)||\mu_e||^2 - \underline{\sigma}(\tilde{D}_q)||\dot{q}||^2 - \underline{\sigma}(D_b)||\mu||^2 \tag{5.45}$$

which implies uniform stability of the IM-PBC states $(\eta, \mu_e, g_b, q, \mu, \dot{q})$ about the origin $(\mathbb{I}_{4,4}, 0, \bar{g}_b, \bar{q}, 0, 0)$. Thus, in the set $\Omega = \{\eta, \mu_e, g_b, q, \mu, \dot{q} | \dot{\mathcal{H}} = 0 \}$, the closed-loop dynamics in (5.33), and the top and bottom rows of (5.3) are determined

by,

$$\begin{bmatrix} l.\mathbb{I} & 0 & 0 \\ 0 & \mathbb{I} & -\mathcal{A}_l^{\top} \\ 0 & 0 & \mathbb{I} \end{bmatrix} \begin{bmatrix} d\Psi \\ d_q \Phi_q(q) + d_q \Phi(g_b, q) \\ d_b \Phi(g_b, q) \end{bmatrix} = 0$$
 (5.46)

In (5.46), $d\Psi$ is independent of the task potentials, Φ_q , Φ . If the effective task potential, $\Phi(g_b, q) + \Phi_q(q)$, yields a unique equilibrium in the FRM configuration space, SE(3)× \mathbb{R}^n , then the IM-PBC is ZSO by Lemma 2.12. Thus, from Def. 2.13, the closed-loop dynamics is asymptotically stable.

5.4.4 Subsystem IM-PBC

In the subsystem IM-PBC, the shape subsystem is given precedence for convergence by exploiting the PBC design outlined in Lemma 5.2. Naturally, the change in control approach also results in a consequent modification to the observer feedback law.

5.4.4.1 Motion Control Law

To this end, the motion control law in (5.47) is modified as,

$$\begin{bmatrix} \tilde{\mathcal{F}}_{b} \\ \tilde{\tau} \end{bmatrix} = \underbrace{\begin{bmatrix} -d_{b}\Phi(g_{b}, q) \\ -d_{q}\Phi_{q}(q) \end{bmatrix}}_{\text{Task regulation}}, \begin{bmatrix} \overline{\mathcal{F}}_{b} \\ \overline{\tau} \end{bmatrix} = \underbrace{\begin{bmatrix} -D_{b}(q)\hat{\mu}_{o} + D_{b}(q)\mathcal{A}_{l}\dot{q} \\ -D_{q}(q)\dot{q} \end{bmatrix}}_{\text{Damping}}$$

$$\begin{bmatrix} \hat{\mathcal{F}}_{b} \\ \hat{\tau} \end{bmatrix} = \underbrace{\begin{bmatrix} d_{b}\mathcal{U}(g_{b}, q) \\ d_{q}\mathcal{U}(g_{b}, q) - \mathcal{A}_{l}^{\top}d_{b}\mathcal{U}(g_{b}, q) \end{bmatrix}}_{\text{Symmetry-restoring}} + \underbrace{\begin{bmatrix} 0 \\ D\hat{l}_{\mu} \\ Dq}(\hat{\mu}_{o}) + \mathcal{A}_{l}^{\top}(\overline{\mathcal{F}}_{b} + \tilde{\mathcal{F}}_{b}) \end{bmatrix}}_{\text{Decoupling}}$$

$$(5.47)$$
Symmetry-restoring action

where $\frac{D\hat{l}_{\mu}}{Dq}(\hat{\mu}_{o}) = \frac{1}{2}S(\hat{\mu}_{o})^{\top}\hat{\mu}_{o} - \mathcal{A}_{l}^{\top}\operatorname{ad}_{\hat{\mu}_{o}}^{\top}\Lambda_{b}\hat{\mu}_{o}$, is a part of the decoupling action that isolates the shape dynamics from the momentum subsystem, however, using the estimated locked velocity, $\hat{\mu}_{o}$.

Remark 28. The group observer for the subsystem IM-PBC remains identical in structure to (5.21) of the direct IM-PBC. Consequently, the error kinematics in (5.22) also is the same.

5.4.4.2 $Ver(\mathcal{LP})$ Observer: Momentum

The observer system for the momentum equation, i.e., the $Ver(\mathcal{LP})$ equation, however, is simplified as,

$$\Lambda_b \operatorname{Ad}_{\eta}^{-1} \dot{\tilde{\mu}} + P(\dot{q}) \operatorname{Ad}_{\eta}^{-1} \operatorname{grad} \Psi - \operatorname{ad}_{\Lambda_b \hat{\mu}_o}^{\sim} \hat{\mu}_o - \overline{\mathcal{F}}_b = + \tilde{\mathcal{F}}_b + l.d\Psi(\eta) + \mathcal{F}_o
\operatorname{Ver}(\hat{\mathcal{LP}})_{\text{subsystem}} = \tilde{\mathcal{F}}_b + l.d\Psi(\eta) + \mathcal{F}_o$$
(5.48)

where \mathcal{F}_o is the virtual wrench that is used to passivate the dynamics, as in (5.26).

Note that in contrast to (5.26), (5.48) is structurally different. This is a direct consequence of the new control law in (5.47). This shall become evident through the stability analysis later.

Velocity Error Dynamics

Using (5.48), the observer velocity error dynamics are computed, as in (5.33), as,

$$\frac{d\mu_e}{dt} = \Lambda_b^{-1} \Big(\tilde{\mathcal{C}}(\mu, \mu_e) \mu_e - P(\dot{q}) \mu - \operatorname{ad}_{\Lambda_b \mu}^{\sim} \mathcal{A}_l \dot{q} - l.d\Psi(\eta) \\
+ F_d - \mathcal{F}_o - \operatorname{Hess}(\Psi) \mu_e \Big)$$
(5.49)

Shape (joints) velocity dynamics

The shape velocity dynamics are written by substituting (5.47) in second row of (5.3), with $\Gamma_q(\dot{q}, \mu) = \tilde{\Gamma}'_q(\dot{q}) + \tilde{\mathcal{B}}(\mu)$ to ease notation, as,

$$\ddot{q} = \Lambda_q^{-1} \left(-\Gamma_q(\dot{q}, \mu) \dot{q} + \frac{1}{2} (S(\mu)^\top \mu - S(\hat{\mu}_o)^\top \hat{\mu}_o) - \mathcal{A}_l^\top \left(\operatorname{ad}_{\Lambda_b \mu}^\sim \mu - \operatorname{ad}_{\Lambda_b \hat{\mu}_o}^\sim \hat{\mu}_o \right) - d_q \Phi_q(q) - D_q(q) \dot{q} \right)$$
(5.50)

The quadratic terms in (5.53) are simplified by, firstly, substituting $\mu_e = \mu - \hat{\mu}_o$ and, then applying the commutative Prop. 3.34 for S^{\top} to get

$$S(\mu)^{\mathsf{T}}\mu - S(\hat{\mu}_o)^{\mathsf{T}}\hat{\mu}_o = \left(2S(\mu)^{\mathsf{T}} - S(\mu_e)^{\mathsf{T}}\right)\mu_e \tag{5.51}$$

Secondly, using Lemma 5.3 for the \mathcal{C} operator, we get,

$$\mathcal{A}_{l}^{\top}(\operatorname{ad}_{\Lambda_{b}\mu}^{\sim}\mu - \operatorname{ad}_{\Lambda_{b}\hat{\mu}_{o}}^{\sim}\hat{\mu}_{o})$$

$$= \mathcal{A}_{l}^{\top}(\operatorname{ad}_{\mu}^{\top}\Lambda_{b}\mu - \operatorname{ad}_{\hat{\mu}_{o}}^{\top}\Lambda_{b}\hat{\mu}_{o}) = \mathcal{A}_{l}^{\top}\mathcal{C}(\mu, \mu_{e})\mu_{e}$$
(5.52)

Finally, using (5.51) and (5.52), (5.53) is rewritten as,

$$\ddot{q} = \Lambda_q^{-1} \left(-\Gamma_q(\dot{q}, \mu)\dot{q} + \frac{1}{2} \left(2S(\mu)^\top - S(\mu_e)^\top \right) \mu_e - \mathcal{A}_l^\top \mathcal{C}(\mu, \mu_e) \mu_e - d_q \Phi_q(q) - D_q(q) \dot{q} \right)$$

$$(5.53)$$

Momentum Dynamics

The momentum dynamics in closed-loop is rewritten as,

$$\dot{\mu} = \Lambda_b^{-1} \left(-\frac{1}{2} P(\dot{q}) \mu + \operatorname{ad}_{\mu}^{\top} \Lambda_b \mu - \left(\frac{1}{2} S(\mu) - \operatorname{ad}_{\Lambda_b \mu}^{\sim} \mathcal{A}_l \right) \dot{q} - d_b \Phi(g_b, q) - D_b(q) \mu + D_b(q) \left(\mu_e + \mathcal{A}_l \dot{q} \right) \right)$$
(5.54)

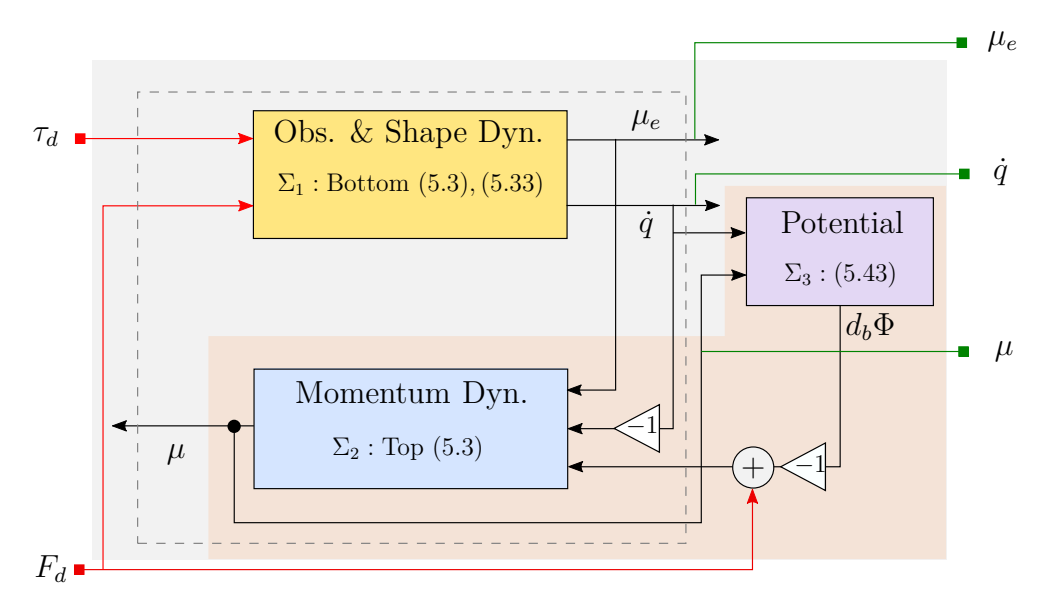


Figure 5.8: Subsystem IM-PBC as passive interconnection of observer-shape, momentum and the symmetry-breaking potential subsystems, with external inputs (red) on left, and outputs of the IM-PBC (green) on right.

5.4.5 Stability/Passivity Analysis of Subsystem IM-PBC

In this subsection, the stability and passivity properties of the subsystem IM-PBC, see Fig. 5.8, is proved. In particular, the observer and shape subsystem, Σ_1 , does not have any interconnection inputs from the other subsystems, and is proved to be OSP in a prioritized manner. In the set that Σ_1 is mechanically stable, the subsystem $\Sigma_2 - \Sigma_3$ consisting of the momentum and symmetry-breaking potential is OSP. In the absence of disturbance inputs, both systems are asymptotically stable in a hierarchical fashion.

5.4.5.1 OSP & Asymptotic Stability of Observer & Shape Dynamics

Lemma 5.7. Consider the FRM with \mathcal{LP} dynamics as in (5.3). Given the shape motion control law chosen as $\tau = \overline{\tau} + \tilde{\tau} + \hat{\tau}$ in (5.47), and the observer feedback laws as (5.21) and (5.48), the observer and the shape dynamics are OSP,

$$\Sigma_1 : \begin{bmatrix} F_d - \mathcal{F}_o \\ \tau_d - \mathcal{A}_l^\top F_d \end{bmatrix} \mapsto \begin{bmatrix} \mu_e \\ \dot{q} \end{bmatrix}$$
 (5.55)

with storage function as

$$W = \underbrace{l\Psi(\eta)}_{W1} + \underbrace{\frac{l}{2}\langle\mu_e,\mu_e\rangle_{\Lambda_b}}_{W2} + \underbrace{\frac{1}{2}\langle\dot{q},\dot{q}\rangle_{\Lambda_q}}_{W3} + \Phi_q(q)$$
(5.56)

such that l > 0. Furthermore, if the inputs $(F_d, \tau_d, \mathcal{F}_o) = 0$, then the shape and observer dynamics are asymptotically stable.

Proof. Differentiating W along trajectories $(\eta, \mu_e, q, \dot{q})$, and using the error dynamics from (5.49) and (5.53),

$$\dot{W} = -\langle \mu_{e}, P(\dot{q})\mu \rangle + \frac{1}{2}\langle \mu_{e}, P(\dot{q})\mu_{e} \rangle + \frac{1}{2}\langle \dot{q}, 2S(\mu)^{\top}\mu_{e} \rangle - \langle \dot{q}, S(\mu_{e})^{\top}\mu_{e} \rangle$$

$$+ \langle \mu_{e}, \tilde{\mathcal{C}}(\mu, \mu_{e})\mu_{e} \rangle + \langle \dot{q}, (\frac{1}{2}\frac{d}{dt}\Lambda_{q} - \Gamma_{q}(\dot{q}, \mu)\dot{q}) \rangle + \langle \mu_{e}, F_{d} - \mathcal{F}_{o} \rangle$$

$$- \langle \mu_{e}, \text{Hess}(\Psi) \rangle - \langle \dot{q}, \dot{q} \rangle_{D_{q}(q)} + \langle \dot{q}, \tau_{d} - \mathcal{A}_{l}^{\top} F_{d} \rangle$$

$$- \langle \dot{q}, \mathcal{A}_{l}^{\top} \mathcal{C}(\mu, \mu_{e})\mu_{e} \rangle - \langle \mu_{e}, \text{ad}_{\Lambda_{b}\mu}^{\sim} \mathcal{A}_{l} \dot{q} \rangle$$

$$(5.57)$$

The first row in (5.57) cancels out. This is a direct consequence of the commutativity properties that I revealed in Prop. 3.34 for the FRM, and is shown below.

$$-\langle \mu_e, P(\dot{q})\mu \rangle + \frac{1}{2}\langle \mu_e, P(\dot{q})\mu_e \rangle + \frac{1}{2}\langle \dot{q}, 2S(\mu)^{\top}\mu_e \rangle - \langle \dot{q}, S(\mu_e)^{\top}\mu_e \rangle =$$

$$-\langle \dot{q}, S(\mu)^{\top}\mu_e \langle +\frac{1}{2}\langle \dot{q}, S(\mu_e)^{\top}\mu_e \rangle + \langle \dot{q}, S(\mu)^{\top}\mu_e \rangle - \langle \dot{q}, S(\mu_e)^{\top}\mu_e \rangle = 0$$

$$(5.58)$$

where the second of Prop. 3.34 is applied to the first two inner products.

Next, note that the first item in the second row of (5.57) cancels out due to the skew-symmetry of \tilde{C} , see Lemma 5.3. The second item in the second row also cancels out due to the skew-symmetry property of the shape dynamics in Prop. 3.2. Using the Corollary 5 on the last row of (5.57),

$$- \langle \mathcal{A}_{l}\dot{q}, \mathcal{C}(\mu, \mu_{e})\mu_{e} \rangle - \langle \mu_{e}, \operatorname{ad}_{\Lambda_{b}\mu}^{\sim} \mathcal{A}_{l}\dot{q} \rangle$$

$$= -\langle \mathcal{A}_{l}\dot{q}, \operatorname{ad}_{\mu_{e}}^{\top} \Lambda_{b}\mu_{e} \rangle - \langle \mu_{e}, \operatorname{ad}_{\Lambda_{b}\mu}^{\sim} \mathcal{A}_{l}\dot{q} \rangle = \langle \mu_{e}, \underbrace{\left(\Lambda_{b}\operatorname{ad}_{\mathcal{A}_{l}\dot{q}} - \operatorname{ad}_{\mathcal{A}_{l}\dot{q}}\Lambda_{b}\right)}_{\text{skew-symmetric}} \mu_{e} \rangle$$
(5.59)

=0

Thus, (5.57) yields,

$$\dot{W} = -\langle \mu_e, \operatorname{Hess}(\Psi) \mu_e \rangle - \langle \dot{q}, \dot{q} \rangle_{D_q(q)} + \langle \mu_e, F_d - \mathcal{F}_o \rangle + \langle \dot{q}, \tau_d - \mathcal{A}_l^{\top} F_d \rangle
\leq -\underline{\sigma}(\operatorname{Hess}(\Psi)) ||\mu_e||^2 - \underline{\sigma}(D_q) ||\dot{q}||^2 + \langle F_d - \mathcal{F}_o, \mu_e \rangle + \langle \tau_d - \mathcal{A}_l^{\top} F_d, \dot{q} \rangle$$
(5.60)

which proves the result.

To prove asymptotic stability, consider the shape and observer dynamics with $(F_d, \tau_d, \mathcal{F}_o) = 0$, which results in,

$$\dot{W} \le -\underline{\sigma}(\operatorname{Hess}(\Psi))||\mu_e||^2 - \underline{\sigma}(D_q)||\dot{q}||^2$$
(5.61)

which implies $W(t) \leq W(0)$, for $t \to \infty$, i.e., W(0) defines a positively invariant set, $\{(\eta, \mu_e, q, \dot{q}) | W(t) \leq W(0)\}$. Let $E = \{(\eta, \mu_e, q, \dot{q}) | \dot{W} = 0 \Rightarrow (\mu_e, \dot{q}) = 0\}$, and the largest invariant set in E is $(ld\Psi(\eta), d_q\Phi_q(q)) = (0, 0)$, which is convergent if $\Phi_q(q)$ is positive-definite in the shape configuration q.

5.4.5.2 Convergence of Momentum and Symmetry-breaking Potential

The asymptotic stability (convergence) of the momentum (Σ_2) and the symmetry-breaking potential (Σ_3) is achieved in the positively invariant set, E, from Lemma 5.7 for Σ_1 subsystem. In particular, the following Lemma states the result.

Theorem 5.2. Consider the FRM with \mathcal{LP} dynamics as in (5.3). Given the external actuation $\mathcal{F}_b = \overline{\mathcal{F}}_b + \hat{\mathcal{F}}_b + \hat{\mathcal{F}}_b$ in (5.47), the dynamics of the momentum and the symmetry-breaking potential, $\Phi(g_b, q)$, in the positively invariant set defined as $E = \{(\eta, \mu_e, q, \dot{q}) | (\mu_e, \dot{q}) = 0\}$ are OSP,

$$\Sigma_2: \mathcal{F}_d \to \mu$$
 (5.62)

with the storage function as,

$$W = \frac{1}{2} \langle \mu, \mu \rangle_{\Lambda_b(q)} + \Phi(g_b, q)$$
 (5.63)

If the disturbance, $F_d = 0$, then $\Sigma_2 - \Sigma_3$ subsystem is asymptotically stable in E.

Proof. Differentiating W along trajectories in the set E, using (5.54) and (5.43),

$$\dot{\mathcal{W}} = -\langle \mu, \mu \rangle_{D_b(q)} \le \underline{\sigma}(D_b(q))||\mu||^2 \tag{5.64}$$

due to the first of skew-symmetry Prop. 3.2, which proves the uniform stability of μ and g_b about 0 and the desired setpoint for the FRM-base in $\Phi(g_b, q)$, respectively. This means, $\mathcal{W}(t) \leq \mathcal{W}(0)$, for $t \to \infty$, i.e., $\mathcal{W}(0)$ defines a positively invariant set, $\{(\mu, g_b)|\mathcal{W}(t) \leq \mathcal{W}(0)\}$. Let $\mathcal{E} = \{(\mu, g_b)|\dot{\mathcal{W}} = 0 \Rightarrow \mu = 0\}$, and the largest invariant set in \mathcal{E} is defined by, $d_b\Phi(g_b, q) = 0$, which is asymptotically stable if Φ is positive-definite.

5.4.5.3 Transient OSP of Subsystem IM-PBC

According to Lemma 5.2, the subsystem comprising of $\Sigma_2 - \Sigma_3$ is OSP in the set \mathcal{E} . Note that, the $\Sigma_1 - \Sigma_2$ subsystem is a cascade interconnection (dashed box in Fig. 5.8), i.e., the observer and shape dynamics drive the momentum subsystem. In the subsystem IM-PBC, the shape convergence is given precedence, and the symmetry-breaking potential is an external subsystem. Thus, as in Lemma 5.2, a stronger condition for OSP of the $\Sigma_1 - \Sigma_2$ cascade is given next.

Lemma 5.8. Consider the FRM with \mathcal{LP} dynamics as in (5.3). Given the shape motion control law as $\tau = \overline{\tau} + \hat{\tau} + \hat{\tau}$ and the external actuation $\mathcal{F}_b = \overline{\mathcal{F}}_b + \tilde{\mathcal{F}}_b + \hat{\mathcal{F}}_b$ in (5.47), and the observer feedback laws as (5.21) and (5.48), the cascade interconnection $\Sigma_1 - \Sigma_2$ in Fig. 5.8 (dashed box) is OSP,

$$(\mathcal{F}_o, F_d, \tau_d) \mapsto (-\mu_e, \mu + \mu_e - \mathcal{A}_l \dot{q}, \dot{q}) \tag{5.65}$$

with storage function $\mathcal{H} = W + \frac{1}{2} \langle \mu, \mu \rangle_{\Lambda_b(q)}$, if it satisfies the secant condition given as,

$$\mathcal{R}(q, \dot{q}) = \begin{bmatrix} \operatorname{Hess}(\Psi) & -\frac{1}{2}D_b & 0\\ -\frac{1}{2}D_b & D_b + \frac{1}{2}P(\dot{q}) + \operatorname{ad}_{\mathcal{A}_l\dot{q}}\Lambda_b & -\frac{1}{2}D_b\mathcal{A}_l\\ 0 & -\frac{1}{2}\mathcal{A}_l^{\top}D_b & D_q \end{bmatrix} \succ 0$$
(5.66)

Proof. Differentiating \mathcal{H} along the system trajectory,

$$\dot{\mathcal{H}} = -\langle \mu_e, \text{Hess}(\Psi)\mu_e \rangle - \langle \dot{q}, \dot{q} \rangle_{D_q} - \langle \mu, \mu \rangle_{D_b} + \langle \mu, D_b(q)(\mu_e + \mathcal{A}_l \dot{q}) \rangle - \langle \dot{q}, \frac{D\hat{l}_{\mu}}{Dq} \rangle$$
 (5.67)

which can be rewritten as,

$$\dot{\mathcal{H}} = -\begin{bmatrix} \mu_e^{\top} & \mu^{\top} & \dot{q}^{\top} \end{bmatrix} \mathcal{R}(q, \dot{q}) \begin{bmatrix} \mu_e \\ \mu \\ \dot{q} \end{bmatrix} + \begin{bmatrix} \mathcal{F}_o^{\top} & F_d^{\top} & \tau_d^{\top} \end{bmatrix} \begin{bmatrix} -\mu_e \\ \mu + \mu_e - \mathcal{A}_l \dot{q} \\ \dot{q} \end{bmatrix}$$
(5.68)

and the result follows from the condition in (5.66).

Remark 29. Lemma 5.8 is the extended variant of Lemma 5.2 for output feed-back motion control, with an additional output related to the observer error μ_e . Importantly, the condition in (5.66) is purely determined by the state-space of the FRM's shape. To satisfy the secant condition in (5.66), it is worth noting that the matrices $P(\dot{q})$ and \mathcal{A}_l , $\operatorname{ad}_{\mathcal{A}_l\dot{q}}^{\top}\Lambda_b$ are upper bounded as,

$$||P(q,\dot{q})|| \le \kappa_1 ||\dot{q}||, ||\operatorname{ad}_{\mathcal{A}_l(q)\dot{q}}^{\top} \Lambda_b(q)|| \le \kappa_2 ||\dot{q}||.$$
 (5.69)

Thus, the secant condition of Lemma 5.8 is satisfied by choosing $\operatorname{Hess}(\Psi)$ D_b, D_q , i.e., the gain parameters for the observer and motion control law, respectively, in a way that dominates the \dot{q} -dependent upper bounds. This aspect of dominating the velocity-dependent terms was observed also in output-feedback control of fixed-base robotic mechanisms, see [141].

5.5 Sensory/Model Extension of IM-PBC

In this section, I extend the proposed IM-PBC to include additional sensing and model information, which serves as a template for motion control of the FRM. The following extensions are not strictly required, but provide a stronger passivity property for the closed-loop system. Rather than performing a passivity analysis of these extensions case by case, only the fully-extended case is analysed, and the nuances are remarked.

5.5.1 Velocity: Sensing and Models

In many scenarios, the FRM-base velocity, V_b , might be available from the localizer or the navigation filter if an IMU is integrated into it. In this case, a measurement of μ is available using the relationship $\mu = V_b + \mathcal{A}_l \dot{q}$ in (5.4). However, the estimation of IMU biases and the exteroceptive nature of the pose measurement of g_b in the localizer makes the velocity estimate outlier-prone, and also possibly slow-sampled (as in the case of orbital robots). The ROAM-2 ISS experiment for the Astrobee free-flyer highlighted this aspect, as shown in Fig. 5.3. Hence, it is advantageous to use the effort-flow framework of the IM-PBC from Fig. 5.2b and extend it to use the available μ measurements in the IM-PBC-observer. In this way, the proposed IM-PBC can predict $\hat{\mu}$ based on the effort applied, and serve as a fault detection algorithm in case of measurement outliers. To that end, the error injection, \mathcal{F}_o , in (5.26) is determined using the negative differential of a Rayleigh dissipation function on the velocity error, μ_e , as,

$$\mathcal{F}_{o1} = -d_{\mu_e} W_e = -D_{\mu} \mu_e, \ W_e = \langle \mu_e, \mu_e \rangle_{D_{\mu}}$$
 (5.70)

Note that \mathcal{F}_o serves to increase the OSP index of Lemmas 5.4 and 5.7, and hence Σ_1 has a stronger dissipation.

In some situations, the FRM might be additionally constrained with a holonomic or a homogeneous non-holonomic constraint, e.g. a humanoid in a non-slipping single or double support phase has zero feet velocities. In this case, the proposed IM-PBC-observer is extended to consider such pseudo measurements. For the holonomic case, let the constraint act at a material point $\{X\}$ of the FRM, such that the constraint is either SE(3), or its subgroup. Suppose that the dimension of the constraint space is d, and its position is denoted as g_x , which is given by a forward kinematics map, $g_x = f(g_b, q) = \text{const.}$, and translates to a velocity-level constraint as,

$$V_x = (g_x^{-1}\dot{g}_x) = \underbrace{\left[\mathcal{T}_1(q) \quad \mathcal{T}_2(q)\right]}_{\mathcal{T}(q)} \begin{bmatrix} \mu \\ \dot{q} \end{bmatrix} = 0$$
 (5.71)

where $\mathcal{T} \in \mathbb{R}^{d \times (n+6)}$ is the Jacobian (push-forward), i.e., $df(\xi) = T(q)\xi$. Note that form in (5.71) is also applicable to homogeneous non-holonomic constraints. The corresponding estimated constraint velocity at $\{X\}$ is $\hat{V}_x = T(q)\hat{\xi}$, yielding the constraint velocity error as, $V_e = V_x - \hat{V}_x = T_1(q)\mu_e$. The error injection term at $\{X\}$ is based on the negative differential of a Rayleigh dissipation function, $W_x = \frac{1}{2}\langle V_e, V_e \rangle_{D_x} > 0$, as $-d_{V_e}W_x = -D_x(\mathcal{T}\xi - \mathcal{T}\hat{\xi}) = -\mathcal{T}\hat{\xi}$, which is pulled back to $\{B\}$ as

$$\mathcal{F}_{o2} = -\mathcal{T}_1^{\mathsf{T}} D_x \mathcal{T} \hat{\xi} = -\mathcal{T}_1^{\mathsf{T}} D_x \mathcal{T} (\xi - \hat{\xi}) = -\mathcal{T}_1^{\mathsf{T}} D_x \mathcal{T}_1 \mu_e \tag{5.72}$$

Remark 30. In case d < 6, the error injection due to the constraint alone in (5.48) does not strictly increase OSP index of Σ_1 through Lemma 5.4, as the

correction is restricted to the constraint directions only. However, it serves to use the pseudo-measurements for improving the internal model locked velocity, $\check{\mu}$.

In view of the aforementioned treatment, the $Ver(\mathcal{LP})$ observer equations in direct IM-PBC, (5.26), and subsystem IM-PBC, (5.48), are extended with velocity measurements and constraint models as,

$$\operatorname{Ver}(\hat{\mathcal{LP}})_{\bullet} = \tilde{\mathcal{F}}_b + l.d\Psi(\eta) - D_{\mu}\mu_e - \mathcal{T}_1(q)^{\top}D_x\mathcal{T}(q)\begin{bmatrix} \hat{\mu}_o \\ \dot{q} \end{bmatrix}$$
 (5.73)

5.5.2 Force: Sensing, Models and Estimation

In many cases, the disturbance wrench, F_d , (or a component of it) might be available through an explicit measurement from a FTS, e.g. the foot contact of a humanoid, or a wrench model of the disturbance, e.g. the Voxelmap-Pointshell (VPS) algorithm [200] for contact wrenches. In this case, simply using $\mathcal{F}_{o3} = F_d$ simplifies the OSP map in Theorem 5.1 for direct IM-PBC as $(F_d, \tau_d) \mapsto (\mu, \dot{q})$ and the OSP map in Lemma 5.7 as $(\tau_d \mapsto \dot{q})$, i.e., the contribution of μ_e to the output is completely eliminated.

However, instead of directly introducing F_d into the feedback loop, it can be estimated using the proposed IM-PBC-observers. In particular, the IM-PBC is further extended to estimate the unmodeled wrench for purposes of contact detection. To this end, the following assumption is required for convergence (if F_d is not directly measured).

Assumption 5.3. The disturbance wrench F_d is a constant (quasi-static) disturbance, i.e., $\dot{F}_d = 0$.

Let the estimate of F_d be denoted as $\hat{F}_d \in \mathbb{R}^6 \cong \mathfrak{se}(3)^*$, which is trivialized at $\{\hat{B}\}$. As pointed out in Sec. 5.4.1, the Ad_{η} operator provides a transport for the force as $\mathrm{Ad}_{\eta}^{\top}\hat{F}_d$ trivialized at $\{B\}$. Thus, the force estimation error is defined as, $F_e = F_d - \mathrm{Ad}_{\eta}^{\top}\hat{F}_d$. The observer for the force estimation is proposed as,

$$\frac{d}{dt}(\operatorname{Ad}_{\eta}^{\top}\hat{\mathcal{F}}_{d}) = -K_{\mu}\mu_{e} - K_{f}F_{e}, \ \mathcal{F}_{o3} = \operatorname{Ad}_{\eta}^{\top}\hat{\mathcal{F}}_{d}, \ K_{\mu}, K_{f} \in \mathbb{R}^{6\times6} \succ 0$$
 (5.74)

Hence, combining the contributions to \mathcal{F}_o using all the above additional measurements and model information, $\mathcal{F}_o = \sum_{i=1}^3 \mathcal{F}_{oi}$,

Theorem 5.3. Given the FRM with equations of motion as in (5.3), the proposed IM-PBC extended with additional measurement and model information through \mathcal{F}_o as,

$$\mathcal{F}_o = -D_\mu \mu_e - \mathcal{T}_1^\top D_x \mathcal{T} \hat{\xi} + \operatorname{Ad}_{\eta}^\top \hat{\mathcal{F}}_d$$
 (5.75)

has the following consequences.

The direct IM-PBC in Theorem 5.1 is OSP,

$$\begin{bmatrix} F_d \\ \tau_d \end{bmatrix} \mapsto \begin{bmatrix} \mu - \mathcal{A}_l \dot{q} \\ \dot{q} \end{bmatrix} \tag{5.76}$$

with the storage function $\mathcal{H}' = W'(\eta, \mu_e, \dot{q}) + \mathcal{W}(\mu) + \Phi(g_b, q)$, where the subsystem function for Σ_1 is augmented as $W' = W(\eta, \mu_e, \dot{q}) + \langle F_e, F_e \rangle_{K_n^{-1}}$.

For the subsystem IM-PBC, the shape and observer subsystem (Σ_1) in Lemma 5.7 is OSP,

$$\tau_d - \mathcal{A}_l^{\top} F_d \mapsto \dot{q} \tag{5.77}$$

where the subsystem storage function for Σ_1 is augmented as W', as for direct IM-PBC.

Proof. Firstly, for direct IM-PBC, using the time-derivative of W from (5.38) in Lemma 5.4, and applying (5.75), $\frac{d}{dt}W'$ yields,

$$\dot{W}' \leq -\underline{\sigma}(lH + \mathbb{D})||\mu_e||^2 -\underline{\sigma}(\tilde{D}_q)||\dot{q}||^2 -\underline{\sigma}(K_f)||F_e||^2 + \langle -D_b(q)\mu, l\mu_e \rangle + \left\langle (\tau_d - \mathcal{A}_l^{\top} F_d) + (\frac{D\hat{l}_{\mu}}{Dq} - \mathcal{A}_l^{\top} D_b(q)\mu) - (d_q \Phi - \mathcal{A}_l^{\top} d_b \Phi), \dot{q} \right\rangle$$
(5.78)

where $\mathbb{D} = D_{\mu} + \mathcal{T}_1^{\top} D_x \mathcal{T}_1$. Using (5.78), with Lemmas 5.5 and 5.6, the result follows straightforwardly from $\dot{\mathcal{H}}'$.

Similarly, for subsystem IM-PBC, computing the time-derivative of W',

$$\dot{W}' = \leq -\underline{\sigma}(\operatorname{Hess}(\Psi) + \mathbb{D})||\mu_e||^2 - \underline{\sigma}(D_a)||\dot{q}||^2 + \langle \tau_d - \mathcal{A}_l^{\top} F_d, \dot{q} \rangle \tag{5.79}$$

which proves the result.

Remark 31. Note that, (5.78) yields the OSP map, $(-D_b\mu, \tau_d - \mathcal{A}_l^{\top} F_d) \mapsto (l\mu_e, \dot{q})$, which is satisfied even if $K_f, D_{\mu} \geq 0$ (not strictly positive-definite). Hence, the extensions with velocity measurements, FTS or a force model, are not strictly required. However, if available, the observer performance can be improved by exploiting them in the proposed framework.

5.5.3 Integral Action for $Ver(\mathcal{LP})$ in Direct IM-PBC

In Theorem 5.3, I provided a variation of the IM-PBC methods that are capable of estimation of disturbance wrenches, F_d . In practice, F_d might be required for motion control of the FRM. In Fig. 5.5, I highlighted the problem of limit cycles generated in the FRM during coordinated control of the shape and its base. This issue arises specifically in direct IM-PBC, when symmetry-breaking potentials are used, e.g. end-effector pose and base control simultaneously. In such cases, the differential of the potential projects to the shape as $d_q\Phi$ and the group as $d_b\Phi$, as is observed in (5.43). It is often assumed that these commanded forces are

realized uniformly. However, due to heterogeneity in actuation, this is seldom the case. In particular, the limit cycles are generated due to a combination of static friction (τ_d) , and the slow actuator dynamics of the FRM-base, which create a regenerative feedback loop. The net effect is that a resultant F_d enters the control loop, where F_d is the disturbance wrench representing the magnitude of failure of the actuators to achieve the commanded forces. In this case, $\mathrm{Ad}_{\eta}^{\mathsf{T}} \hat{F}_d$, can be exploited to provide an integral action in the momentum equation $(\mathrm{Ver}(\mathcal{LP}))$.

Lemma 5.9. Consider the FRM with \mathcal{LP} dynamics in (5.3), for which the direct IM-PBC control approach in Theorem 5.3 is utilized. Instead of adding the estimated disturbance wrench $\operatorname{Ad}_{\eta}^{\mathsf{T}} \hat{F}_d$ to the observer loop through \mathcal{F}_o , consider it added to the external actuation loop as,

$$\mathcal{F}_b = \overline{\mathcal{F}}_b + \tilde{\mathcal{F}}_b + \hat{\mathcal{F}}_b - \operatorname{Ad}_n^{\mathsf{T}} F_d$$
 (5.80)

In this case, the closed-loop \mathcal{LP} dynamics is OSP,

$$\begin{bmatrix} F_e \\ \tau_d - \mathcal{A}_l^\top F_d \end{bmatrix} \mapsto \begin{bmatrix} \mu \\ \dot{q} \end{bmatrix} \tag{5.81}$$

with the storage function, \mathcal{H}' , from Theorem 5.3.

Proof. The time-derivative of the augmented storage function W' for the observer and shape subsystem, Σ_1 , remains the same as in Theorem 5.3. For the $\text{Ver}(\mathcal{LP})$ equation (Σ_2) , computing the time-derivative of W using (5.80), the passivity map in Lemma 5.5 changes to,

$$\Sigma_2 : \begin{bmatrix} F_e - d_b \Phi(g_b, q) \\ -\dot{q} \\ \mu_e \end{bmatrix} \mapsto \begin{bmatrix} \mu \\ \frac{D\hat{l}_{\mu}}{Dq} - \mathcal{A}_l^{\top} D_b(q) \mu \\ D_b(q) \mu \end{bmatrix}$$
(5.82)

Finally, the time-derivative of \mathcal{H}' yields the result.

Remark 32. By adding an integral action to the motion control of the momentum subsystem, i.e., $Ver(\mathcal{LP})$ dynamics, we forego its ability to provide a compliant response to a interaction-borne disturbance wrench in F_d . However, note that the shape (joints) does not actively perform disturbance rejection through the integral action in Lemma 5.9. Thus, for interaction-oriented tasks, the shape exhibits a compliant behaviour if the interaction occurs along the structure that includes the shape.

5.6 Validation of the Proposed Methods

In this section, I provide the validation of the subsystem IM-PBC and direct IM-PBC through simulation and experimental results, respectively.

5.6.1 Simulation Results: Subsystem IM-PBC

An orbital robot was considered as the FRM with spacecraft (FRM-base) mass, $m_b = 350 [\mathrm{Kg}]$, and principal inertia moments, $I_b = \mathrm{blkdiag}(128, 147, 147) [\mathrm{Kg.m^2}]$. A KUKA LWR4+ manipulator with with n = 7 joints and parameters reported in [27] was considered as the articulated mechanism of the FRM. Note that in orbit, $\mathcal{U}(g_b, q) = 0$, i.e., there is no symmetry-breaking potential field on the unforced FRM and $(\hat{\mathcal{F}}_b, \hat{\tau}) = (0, 0)$ in (5.20). In this validation, the main goal is to demonstrate the convergence properties and estimation performance of Σ_1 subsystem, which is prioritized in subsystem IM-PBC. To this end, the symmetry-breaking task potential was not considered, i.e., $\Phi(g_b, q) = 0$ and $(\tilde{\mathcal{F}}_b, \tilde{\tau}) = (0, 0)$, the the total damping in $(\overline{\mathcal{F}}_b, \overline{\tau})$ was restricted to the shape, i.e., $\overline{\mathcal{F}}_b = 0$. This allows evaluating the convergence properties of Σ_1 . A shape-space stiffness potential was chosen as $\Phi_q = \frac{1}{2} \langle \Delta q, \Delta q \rangle_{K_q}$, where q_d , $q_{di} = q_i(0) + 3^{\circ}$ was the desired set-point. The control law parameters were chosen as,

$$K_q = \text{blkdiag}(6, 6, 4.8, 4.8, 1.2, 1.2, 1.2)[\text{Nm/rad.}]$$

 $D_q = \text{blkdiag}(0.4, 0.4, 0.3, 0.2, 0.1, 0.1, 0.1)[\text{Nm/(rad./s)}]$
(5.83)

Note that, the parameters K_p , D_q were chosen to have an underdamped motion with a large settling time (> 20[s]) to emphasize the convergence properties even during rapid shape motions.

5.6.1.1 Convergence of Σ_1

For analysing the convergence property of method, 10 simulations were performed with uniformly distributed initial conditions as follows,

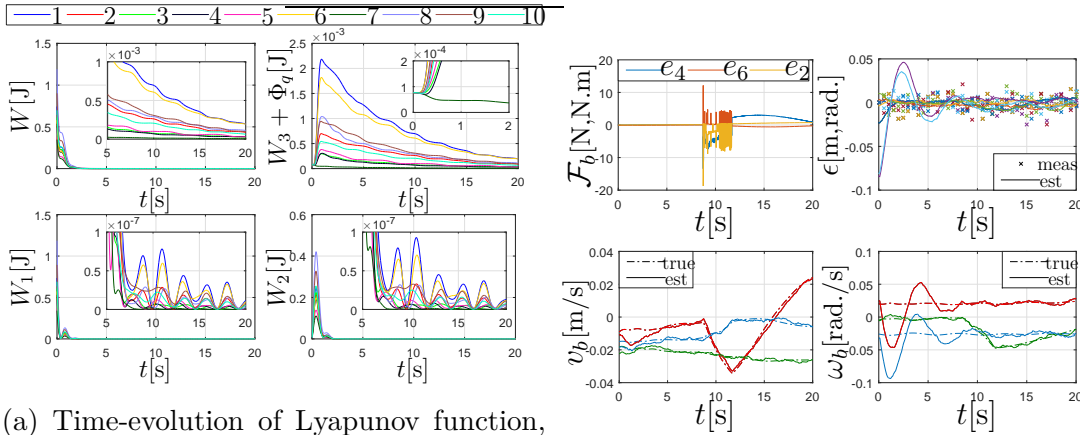
$$v_{bi}(0) \in [-0.1, 0.1][\text{m/s}], \ \omega_{bi}(0) \in [-0.1, 0.1][\text{rad./s}]$$

 $p_{bi}(0) \in [-0.3, 0.3][\text{m}], \ R_b(\theta_b) : \theta_{bi}(0) \in [-30, 30]^{\circ}$

$$(5.84)$$

The observer states were initialized as $\hat{g}_b = \mathbb{I}_{4,4}$ and $\hat{\mu} = 0_6$. The observer potential was paratermized as $\Psi(\eta) = \frac{1}{2} \langle \epsilon, \epsilon \rangle_{k\mathbb{I}_{6,6}}$, where $\epsilon = \log(\eta)^{\vee}$ is the parameterized observer pose error in exponential coordinates, log: SE(3) $\to \mathfrak{se}(3)$ is the group log map (see [9]). Its parameters were set as k = 2.7, l = 450. In Fig. 5.9a, the convergence is shown through the Lyapunov function, W (top-left), and its constituents for 10 simulations. In particular, W is seen to be non-increasing (plot inset). This validates the uniform stability proved in Lemma 5.7. Note that after t > 5, the biggest contributing factor to W is the shape-space energy, i.e. $W_3 + \Phi_q$ (top-right). In the inset, I show that $\frac{d}{dt}(W_3 + \Phi_q) > 0$ during t > 0. This is due to the interconnection term, $\langle \dot{q}, \frac{D\hat{l}_{\mu}}{Dq} \rangle > 0$, during the observer convergence phase. After the observer converges, t > 1, $\frac{d}{dt}(W_3 + \Phi_q) \leq 0$. In fact, this is expected, since $\{W_3 + \Phi_q | W_1 + W_2 = 0\}$ is the Lyapunov candidate for the full state feedback case. In the bottom row, the pose error energy, W_1 , and velocity error

kinetic energy, W_2 , are shown to converge. Note that, in the plot insets although W_1, W_2 are non-decreasing but overall $W \leq 0$, which proves asymptotic stability of Σ_1 .



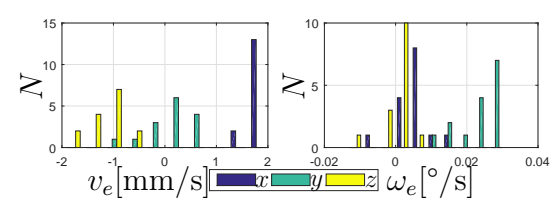
- W (top-left), shape-space energy W_3 + Φ_q (top-right), spacecraft-pose error potential, W_1 (bottom-left) and locked kinetic energy-like velocity error function, velocity, v_b , and bottom-right: angular velocity W_2 (bottom-right) for 20[s] in 10 different locity, ω_b , with xyz (e_i) coloured in RGB. simulations (coloured, see legend).
 - (b) Top-left: Actuation forces, \mathcal{F}_b in e_2, e_4, e_6 bases. Top-right: Pose error, ϵ , in all bases, e_i , $i \in [1,6]$. Bottom-left: Linear

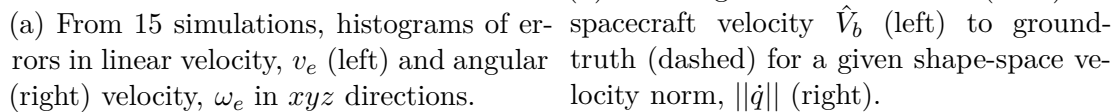
Figure 5.9: Convergence evidence of Subsystem IM-PBC.

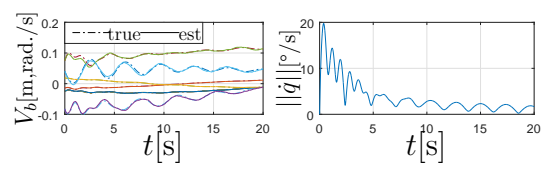
Sensor characteristics and Disturbances 5.6.1.2

In this part, the effectiveness of the subsystem IM-PBC-observer is established, while considering sensor characteristics of the exteroceptive sensor and spacecraft disturbances. The sensor is simulated with sampling time of 0.1[s] and a Gaussian noise model as $\tilde{g}_b = g_b \exp(\gamma^{\wedge})$, where $\gamma \in \mathbb{R}^6 \cong \mathfrak{se}(3)$ has a mean 0_6 and variance $5e^{-5}\mathbb{I}_{6.6}$. In the following, e_i , i=1,2,3 (4,5,6) are the rotational (translational, respectively) basis of the frame $\{B\}$ in xyz convention. A disturbance force, F_d , in e_2, e_4, e_6 basis of $\{B\}$ was applied, see top-left of Fig. 5.9b. I performed 15 simulations with initial conditions given in (5.84) and the observer initialization with 30% error in its states $(\hat{g}_b(\hat{p}_b, \hat{R}_b(\hat{\theta}_b)), \hat{\mu}_b)$. In Fig. 5.9b, I highlight the convergence results for one simulation. The pose errors (top-right) converge at t=7, after which it is shown that the estimates (solid) have a smaller variation, in contrast to the measurements (\times) . At the same time, in the bottom row, the estimates (solid) of linear (left) and angular (right) velocities converge to the ground-truth (dashed). At t > 7, the effect of \mathcal{F}_b on V_b is tracked by the estimate despite slow-sampled measurements.

The observer's error statistics for the last 5[s] were evaluated for N=15simulations. The standard deviation for the estimation errors in position, r_b , and







(b) Convergence of estimates (solid) of locity norm, $||\dot{q}||$ (right).

Figure 5.10: Velocity convergence in Subsystem IM-PBC.

orientation, ψ_b , varied between [1, 3.5][mm] and [0.1, 0.18][°], respectively, which was lower than that of the measurements, [6.2, 7.5] [mm] and [0.36, 0.41][°]. In Fig. 5.10a, for the velocity errors, $V_e = [\omega_e^\top v_e^\top]^\top = V_b - \hat{V}_b$, the histograms for linear $(v_e, \text{ left})$ and angular $(\omega_e, \text{ right})$ parts are reported, which are in the range of $\pm 1.8 \text{[mm/s]}$ and $\pm 0.02 \text{[°/s]}$, respectively.

To emphasize that the proposed observer equations do not require a rigidized system for convergence, I considered a lighter spacecraft (20% of m_b , I_b) for validation. Fig. 5.10b shows that \hat{V}_b (left) in solid colours converges to the ground-truth (dashed) despite high variation of $||\dot{q}||$ (right), and its effect on V_b is tracked well by V_b in all components.

5.6.2Experimental Results: Direct IM-PBC

While the previous subsection focused on the observer performance, here I focus on the full motion stabilization of the FRM at DLR OOS-SIM, while using an exteroceptive measurement of group state-space (g_b, V_b) . The DLR OOS-SIM, see Fig. 5.11, is a hardware-in-the-loop facility to simulate FRM dynamics, especially for orbital robots. The FRM consists of a KUKA-LWR4+ (orange manipulator) with n=7 joints as the articulated mechanism, and the FRM-base (spacecraft mock-up with gold insulation) is computed using a rigid multibody dynamics model, and effected using an industrial KUKA-KR120 robot [201].

For the experiment, an orbital robot was considered with mass 800[Kg], and principal inertia moments blkdiag(800, 600, 500)[Kg.m²]. While g_b was obtained directly from an image-processing algorithm (see [73] for details), V_b was obtained using the direct kinematics of the KUKA-KR120 robot. Since the OOS-SIM provides a 0-g environment, $\mathcal{U}=0$, or $(\hat{\mathcal{F}}_b,\hat{\tau})=(0,0)$. The control task was posed as regulation of the end-effector about a setpoint (star) in Fig. 5.11, which was (0,0,0.1)[m] and (5,0,0)[deg] from its initial configuration, and also the regulation of its spacecraft pose, which was (0.02, 0.02, 0.02) m and (5, 0, 0) [deg] from its initial configuration. The sensory information was considered as (g_b, V_b, q, \dot{q}) , in which (g_b, V_b) was available only at 10[Hz], while the spacecraft actuation \mathcal{F}_b was limited to 10[Hz]. The values for sensing and actuation of the FRM-base are

representative of the typical Guidance, Navigation & Control (GNC) bus speeds in space robotics [179].

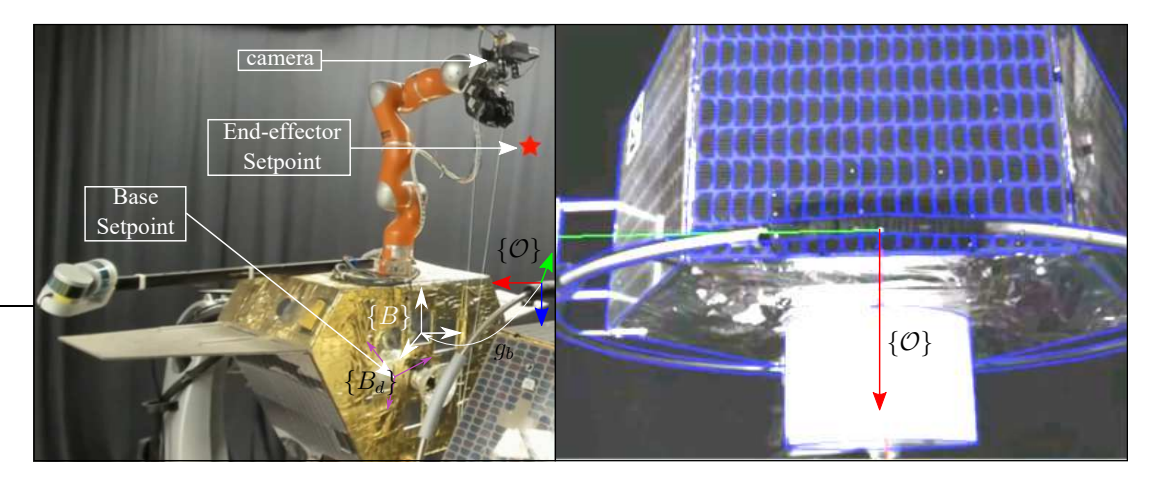


Figure 5.11: Experimental setup for validation of direct PBC. Left: Orbital robot on DLR OOS-SIM; Right: Image processing to obtain g_b , i.e., pose of $\{B\}$ relative to $\{\mathcal{O}\}$.

5.6.2.1 Motion Control without Integral Action

In the first experimental validation, the direct IM-PBC was implemented without any integral action (Sec. 5.5.3) for disturbance rejection. Due to this, the following results exhibit the limit cycle behaviour, I introduced in Fig. 5.5. However, the results still serve to provide insights into performance characteristics. The experimental results are shown through the Figures 5.12-5.15. In Fig. 5.12, the FRM-base pose $g_b(p_b, \theta_b)$ are shown for the image-processing measurements (blue) and the internal state of the direct IM-PBC, \hat{g}_b . The desired setpoint for the FRM-base, which was (-0.02, -0.02, 0.02)[m] and (-3, 2, -4)[deg] from its initial configuration, is also shown (yellow dashed). Firstly, note that the observer imparts a filtering effect, in contrast to the noisy camera signals, while tracking the oscillatory dynamics (due to the limit cycle) of the FRM-base. Thus, the observer does not introduce a perceptible phase lag like a first order filter. Also observe that the limit cycles are occurring about the equilibrium (setpoint), i.e., the velocities have a 0-crossing, which is symptomatic of deadzone non-linearity. This is verified by juxtaposing the 0-crossings of μ in Fig. 5.12. It is worth highlighting that despite fast oscillatory dynamics and 10[Hz] vision-based feedback, the observer estimate tracks the measurement well. The combined heterogeneous actuation of the shape, τ , and the FRM-base is shown in Fig. 5.14, which illustrates the source of the limit cycle. Finally, although the $\mathrm{Ad}_n^{\top} \hat{F}_d$ was not used in feedback, I provide the estimated disturbances in Fig. 5.15. This hints towards the disturbances that are likely to appear from the heterogeneous actuation, since

the FRM did not undergo any interactions.

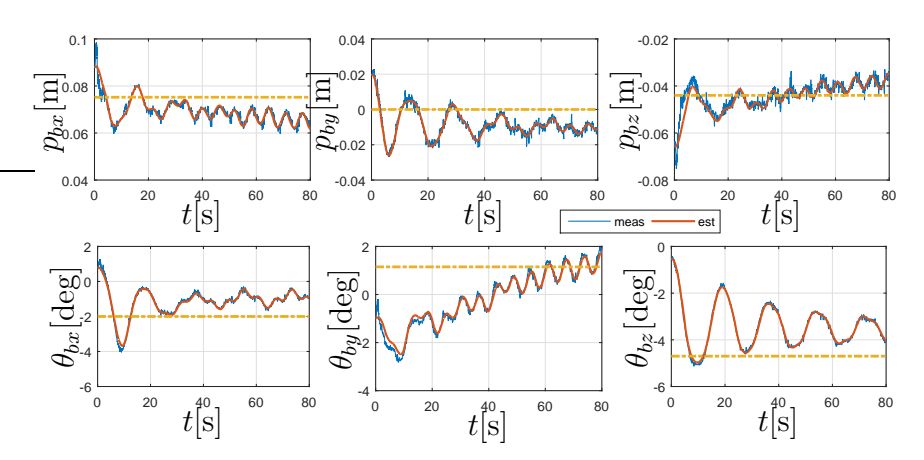


Figure 5.12: Group variable, FRM-base pose $g_b(p_b, \theta_b)$. Top row: Position; Bottom row: Orientation (Euler parameterization XYZ). Vision-based measurement in blue, observer state \hat{g}_b in red, and setpoint for control task in dashed yellow.

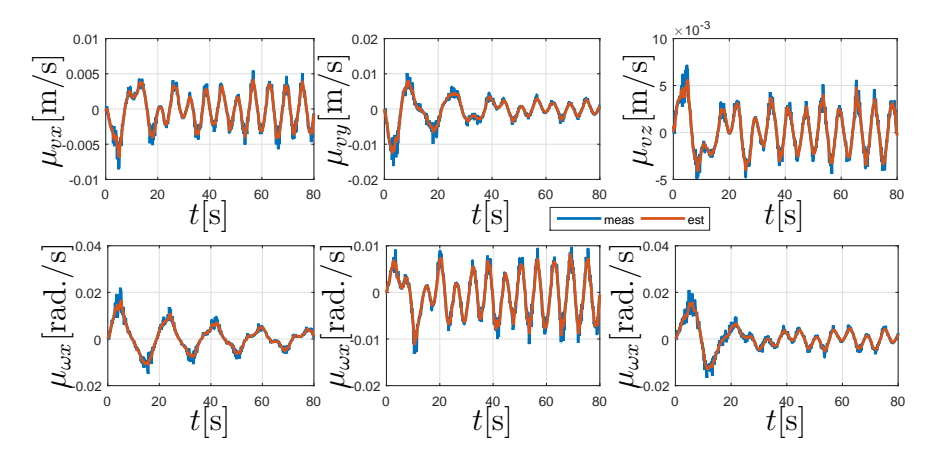


Figure 5.13: Locked velocity, μ . Top row: Linear component (μ_v) ; Bottom row: Angular component (μ_ω) . Measurement in blue, and observer output $\hat{\mu}_o$ in red.

5.6.2.2 Motion Control with Integral Action

To attenuate the limit cycle, the integral action in the FRM-base action (see (5.80) in Sec. 5.5.3) is exploited. The experimental results are shown through Figures 5.16-5.21. It is observed in the plots that the limit cycle is attenuated. In Fig. 5.16, the vision-based measurement (blue) and the observer internal estimate, \hat{g}_b , are shown. In particular, in p_{bz} and θ_{bx} subplots, outliers are noted at t = 8, 23[s], respectively, in the measured data. However, the observer remains physically consistent, which results in a continuous estimate of μ in Fig. 5.17. Note that a naive differentiation with such outliers would result in discontinuous feedback.

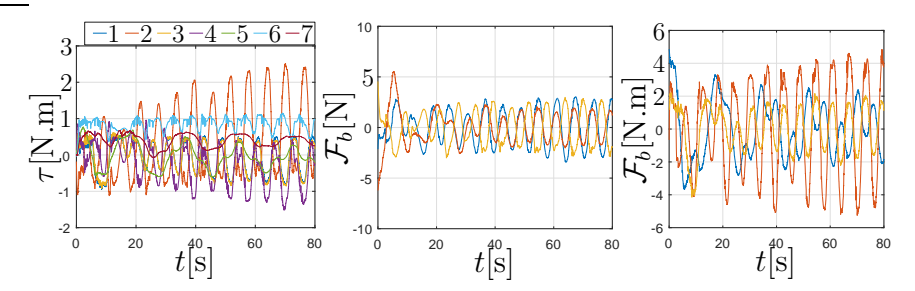


Figure 5.14: Total actuation for the direct IM-PBC. Left: Shape actuation (τ) ; Center: FRM-base forces (\mathcal{F}_b) ; Right: FRM-base torque (\mathcal{F}_b) .

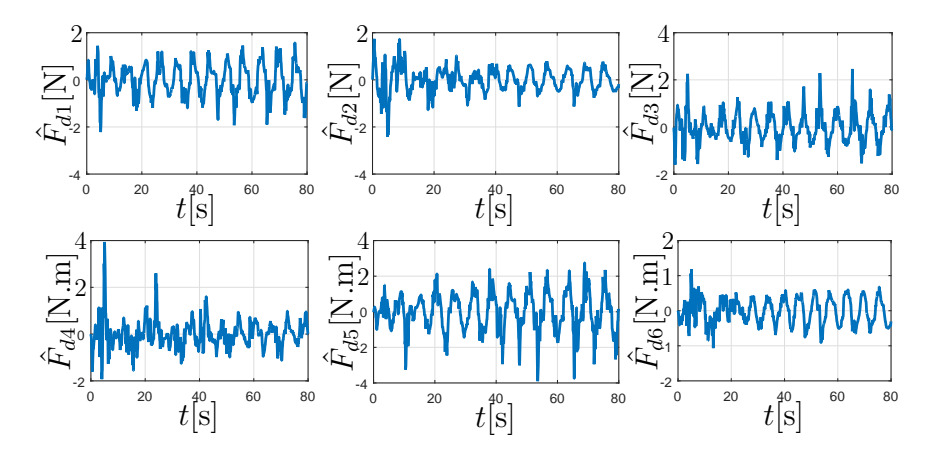


Figure 5.15: Estimated disturbance, \hat{F}_d . Top row: Forces; Bottom row: Torques

Fig. 5.17 shows the net momentum of the FRM being damped.

Two symmetry-breaking tasks were considered for the poses of the FRM-base and the end-effector of the manipulator. In Figures 5.18-5.19, the desired setpoints (dashed blue) and the actual state (red) are shown. In particular, Fig. 5.18 shows the position of the control tasks for FRM-base (top) and end-effector (bottom), and Fig. 5.19 shows the corresponding orientation values. The plots indicate successful execution of the motion control tasks. A slightly underdamped behaviour is exhibited owing to the 10[Hz] actuation of the FRM-base, which has been highlighted in the insets of Fig. 5.20 for \mathcal{F}_b . Fig. 5.20 shows the combined effort applied to achieve the tasks. Note that in contrast to (5.14), limit cycles are attenuated. The final offsets in τ are attributed to gravity compensation errors in the facility and static friction in the manipulator. The estimated disturbance, \hat{F}_d , which is exploited in the control law is shown in Fig. 5.21. It can be seen that the disturbances are at their highest magnitudes at the initial phase of motion, and get attenuated over time due to the control action.

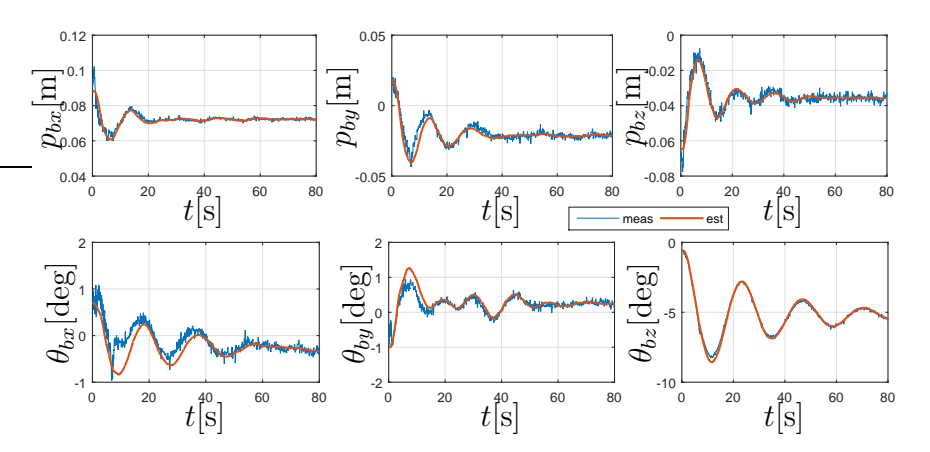


Figure 5.16: Group variable, FRM-base pose $g_b(p_b, \theta_b)$. Top row: Position; Bottom row: Orientation (Euler parameterization XYZ). Vision-based measurement in blue, observer state \hat{g}_b in red, and setpoint for control task in dashed yellow.

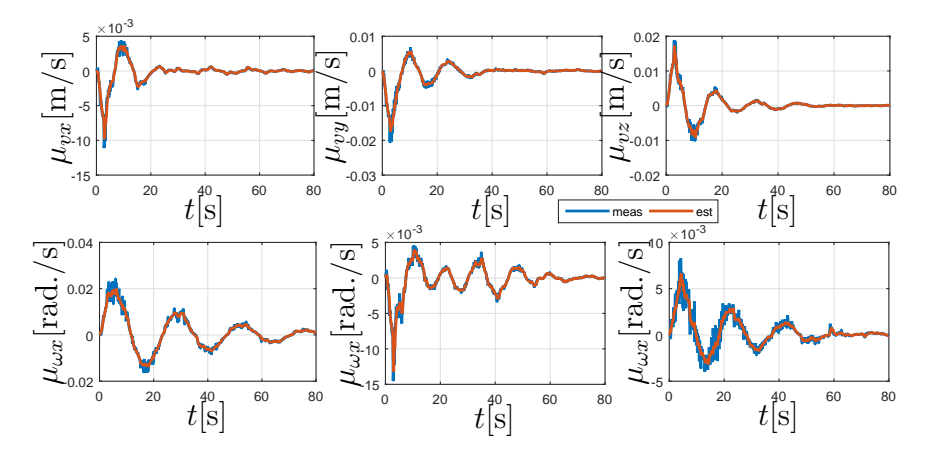


Figure 5.17: Locked velocity, μ . Top row: Linear component (μ_v) ; Bottom row: Angular component (μ_ω) . Measurement in blue, and observer output $\hat{\mu}_o$ in red.

5.6.2.3 Motion Control during Interactions

The key driving factor behind the direct IM-PBC design was to enable a compliant behaviour during interactions. Hence, in the next validation, the controller response (with integral action) is evaluated during interactions. External forces were applied to the FRM by pulling the string attached to the gripper in Fig. 5.11. The key experimental results are shown in Figures 5.22-5.25. The controller was engaged at t = 8[s], and two interaction events were performed at t = 36.5[s] and t = 51.5[s]. In Fig. 5.22, the vision-based measurement and observer estimate of g_b are shown together. During the interaction events, it can be seen that the measured data exhibits outliers up to 5[cm], but the observer estimate is unaffected by it. In particular, during the interactions, the FRM gets displaced from its equilibrium compliantly. The integral action should intuitively weaken the

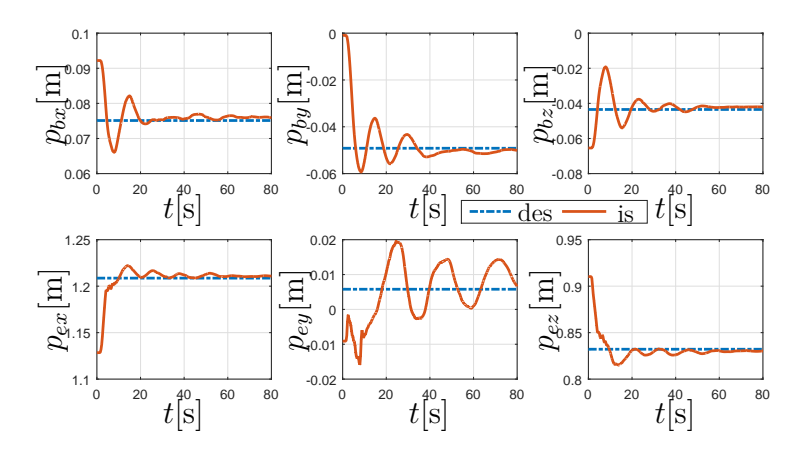


Figure 5.18: Regulation of symmetry-breaking tasks. Top row: FRM-base position; Bottom row: End-effector position.

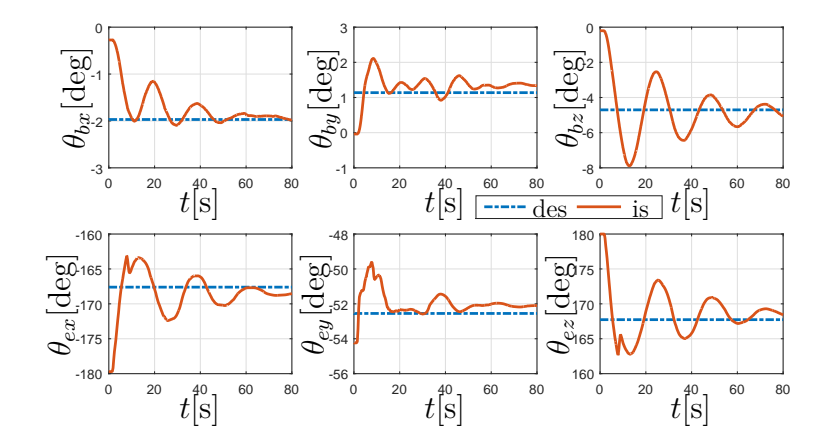


Figure 5.19: Regulation of symmetry-breaking tasks. Top row: FRM-base orientation; Bottom row: End-effector orientation.

compliant behaviour in the Ver(\mathcal{LP}) dynamics. However, in the direct IM-PBC design, the symmetry-breaking potential projects to the FRM-base actuation, see Fig. 5.7. Consequently, the task-related wrench generates a compliant FRM-base displacement corresponding to the end-effector displacement, when interactions occur. This is also exhibited in the time-evolution of μ in Fig. 5.23, which stabilizes to 0 after removal of the external interactions. The coordinated effort applied by the shape (τ) and the FRM-base (\mathcal{F}_b) are shown in Fig. 5.24. It is seen that during interactions, both subsystems generate control actions to ensure a force balance compliantly. The estimated disturbances are shown Fig. 5.24, and in particular, \hat{F}_{d1} , \hat{F}_{d3} , \hat{F}_{d5} show the directions along which the interactions were directed. It can been that the direct IM-PBC observer was able to estimate the disturbance wrench accurately. This proves that the proposed direct IM-PBC is not only compliant but also a contact-aware control approach.

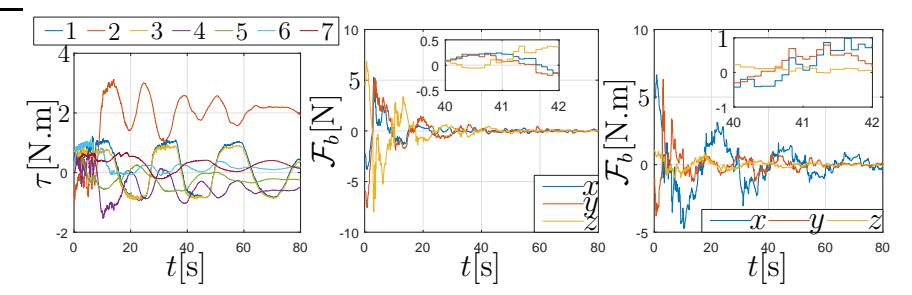


Figure 5.20: Total actuation for the direct IM-PBC. Left: Shape actuation (τ) ; Center: FRM-base forces (\mathcal{F}_b) ; Right: FRM-base torque (\mathcal{F}_b) .

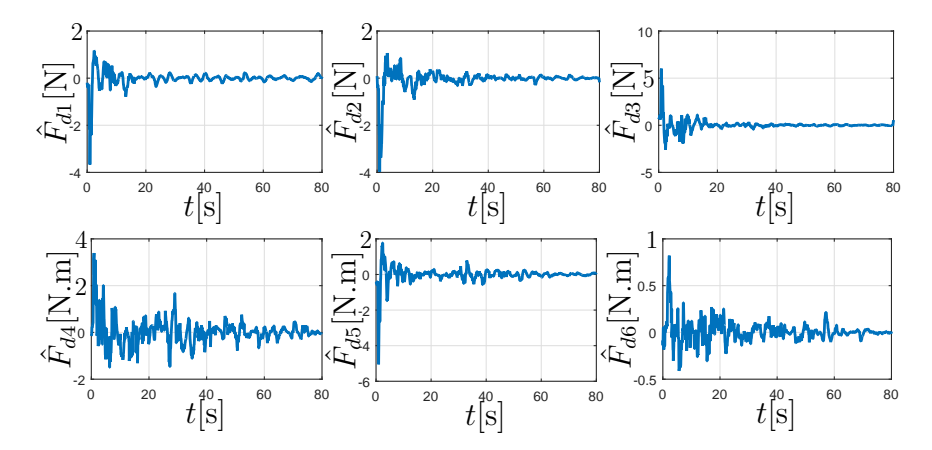


Figure 5.21: Estimated disturbance, \hat{F}_d . Top row: Forces; Bottom row: Torques

5.7 Conclusion

In this chapter, a novel IM-PBC framework was proposed to achieve full motion stabilization of an \mathcal{LP} system, namely the FRM. Within the framework, two methods, namely direct IM-PBC and subsystem IM-PBC were provided. While the former exploited the passivity of the \mathcal{LP} dynamics in the presence of a symmetry-breaking potential, the latter prioritized the shape subsystem's convergence. Both approaches used a minimal set of measurements from the shape state-space and the exteroceptive group variable for motion stabilization, even in the presence of symmetry-breaking potentials. The key novelty was the use of the \mathcal{LP} dynamics to exploit, firstly, the block-diagonal inertia to obviate shape acceleration measurements and, secondly, the properties in the CC matrix to aid the stability analysis. Both approaches were proved to be asymptotically stable and OSP in the absence and presence of disturbances, respectively. The effectiveness and convergence properties of subsystem IM-PBC were validated through simulation results, while direct IM-PBC was validated experimentally at the DLR OOS-SIM. The proposed control framework was shown to be extensible with additional measurements if available, and therefore, is applicable to a

5.7 Conclusion 155

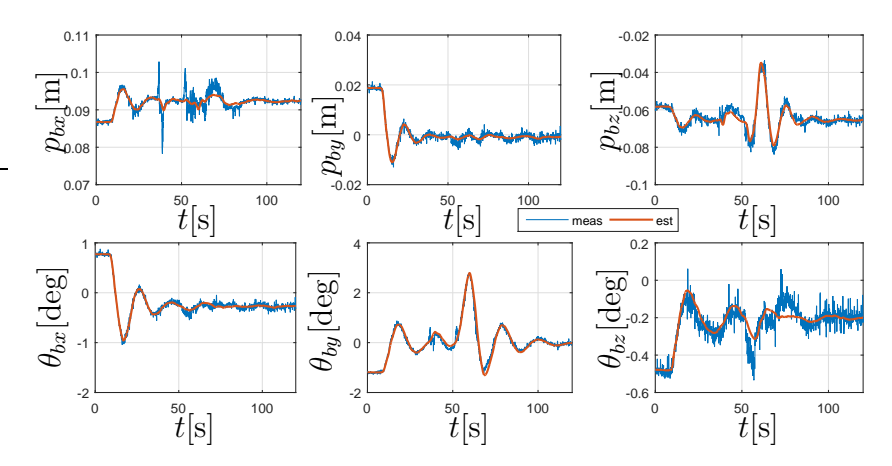


Figure 5.22: Group variable, FRM-base pose $g_b(p_b, \theta_b)$. Top row: Position; Bottom row: Orientation (Euler parameterization XYZ). Vision-based measurement in blue, observer state \hat{g}_b in red, and setpoint for control task in dashed yellow.

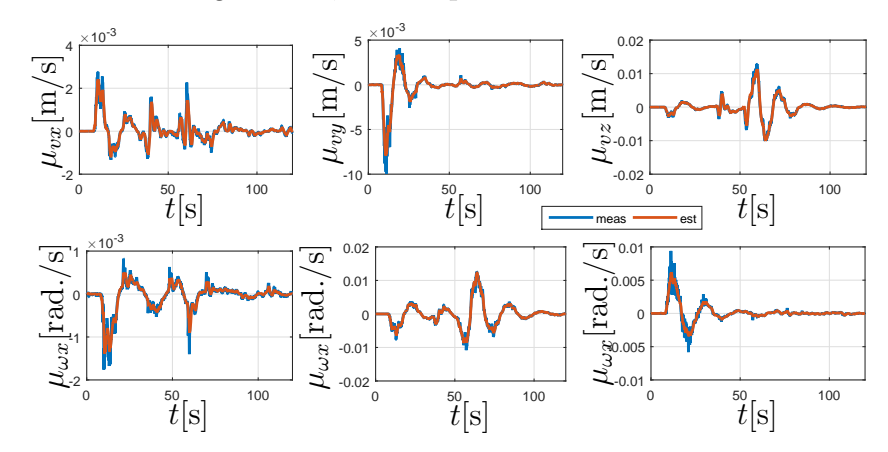


Figure 5.23: Locked velocity, μ . Top row: Linear component (μ_v) ; Bottom row: Angular component (μ_ω) . Measurement in blue, and observer output $\hat{\mu}_o$ in red.

wide variety of FRMs. The approach was proved to be contact-aware, and importantly, address the problems of heterogeneity in sensing and actuation within the FRM construction. Although kinematic/dynamic uncertainty in Λ_b , S, P and spacecraft-actuator model errors (\mathcal{F}_b) is a limiting factor for the framework's performance, the performance benefits of a model-based fast-feedback due to the observer was shown to be effective for motion control. The publications resulting from the contributions of this chapter are:

- 1. H. **Mishra**, M. De Stefano, A. M. Giordano, and C. Ott, "A nonlinear observer for free-floating target motion using only pose measurements", in 2019 American Control Conference (ACC), 2019, pp. 1114–1121
- 2. H. Mishra, M. De Stefano, A. M. Giordano, and C. Ott, "Output feed-

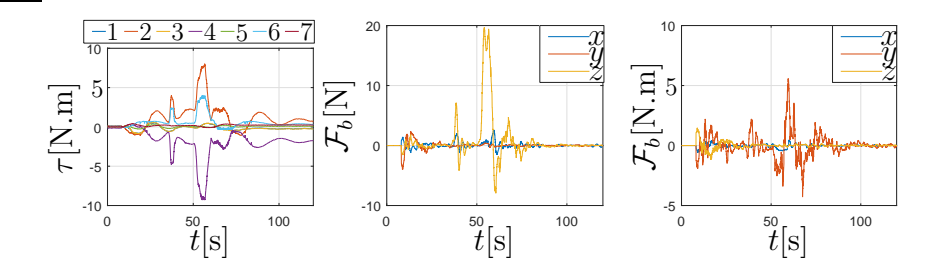


Figure 5.24: Total actuation for the direct IM-PBC. Left: Shape actuation (τ) ; Center: FRM-base forces (\mathcal{F}_b) ; Right: FRM-base torque (\mathcal{F}_b) .

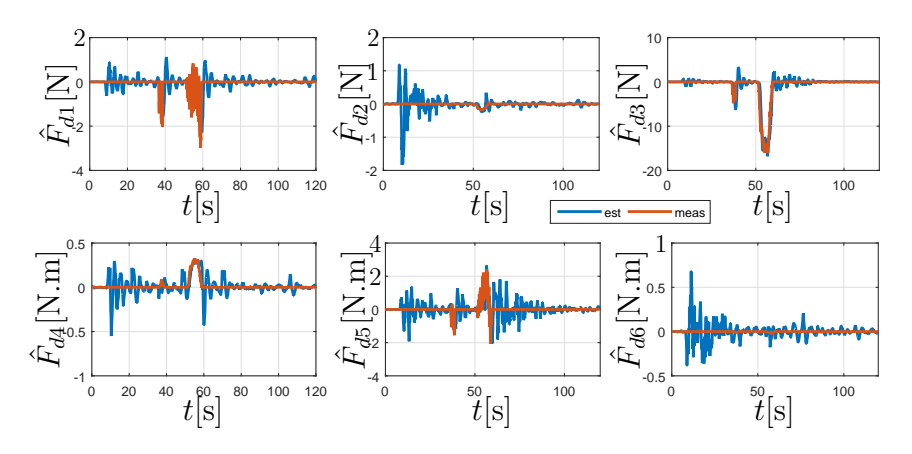


Figure 5.25: Estimated disturbance, \hat{F}_d . Top row: Forces; Bottom row: Torques.

back stabilization of an orbital robot", in 2020 59th IEEE Conference on Decision and Control (CDC), 2020, pp. 1503–1501

- 3. H. **Mishra**, G. Garofalo, A. M. Giordano, M. De Stefano, C. Ott, and A. Kugi, "Reduced Euler-Lagrange equations of floating-base robots: Computation, properties, and applications", *IEEE Transactions on Robotics*, pp. 1–19, 2022
- 4. M. Rothammer, A. Coelho, H. **Mishra**, C. Ott, A. Franchi, and A. Albu-Schaeffer, "A rigid body observer (BObs) considering pfaffian constraints with a pose regulation framework", *IEEE Control Systems Letters*, vol. 7, pp. 163–168, 2023
- 5. H. Mishra, M. De Stefano, and C. Ott, "Is there a closed-loop lagrangian for hierarchical motion control?", *IEEE Control Systems Letters (first review)*, 2025

The shape-prioritized control approach presented here is the key principle behind hierarchical motion control. The shape here assumes the role of the primary task, whereas the symmetry-breaking potential assumes the role of the secondary

5.7 Conclusion 157

task. However, the hierarchy was possible because the FRM is a special \mathcal{LP} system with a Lie group as its fiber. Therefore, for general \mathcal{EL} systems, it is evident that this structure needs to be replicated using inertia shaping. This approach will be employed in the next chapter. A key motivating factor behind the proposed IM-PBC approach is to close the loop with the perception system, see Fig. 5.2b. This will enable the latter's point-set registration algorithm to exploit the predicted output of the IM-PBC as a priori information to improve perception performance and reduce computational time. By closing the loop between mechanical effort and optical flow, the goal is to impart a muscle memory for fast-reaching agile movements in the FRM. This active perception-oriented control approach will be pursued as a sequel to this work.

22

Task-induced Variational Symmetry in Motion Control

(6 Noether symmetry reflects invariance under a transformation, and therefore there must exist a quantity that remains invariant or conserved [203].

Gian F. Giudice, A Zeptospace Odyssey: A Journey into the Physics of the LHC, 2009

6.1 Introduction

A large class of contemporary engineering systems, e.g., mechanical systems, are modeled as \mathcal{EL} systems, which are based on variational principles emerging from the definition of energy functions [3]. The interrelated methods of PBC [3] and CL [5, pp. 467–514] are popular approaches for motion stabilization of \mathcal{EL} systems. While the latter includes shaping of kinetic energy and the scalar potential in the Lagrangian, the former usually leaves the kinetic energy (metric tensor) unchanged. In this context, the full-motion stabilization, either in the configuration space or as a local diffeomorphism to an alternative operational space, is well-understood. The latter has been useful for multiple task-specific motion control, e.g., in robotic systems, using the superposition of impedances [204], see RMP Flow framework by [205]. However, quite often, it is required to establish the notion of hierarchy (or priority), see right of Fig. 6.1, when the \mathcal{EL} system is redundant, i.e., it has more Degrees-of-Freedom (DoF) than the task-specific motion [206], [207], [52], [208], [209], [210], [211, §2.3.2].

6.1.1 Related Work

The two levels of hierarchy in [207] was extend to N arbitrary levels in [52], while the tracking case for N levels was addressed in [209]. In the above works, a matrix transformation of the tangent space was used to rewrite the original \mathcal{EL} dynamics as the dynamics of a subspace called the primary task and decoupled nullspace velocities. The off-diagonal CC terms were compensated to prove Lyapunov stability with semi-definite functions. However, such a transformation lacks a physical intuition because the underlying physical principle is concealed [56]¹. In fact, due to matrix transformations, the exact nature of the dynamics and the closed-loop inertia metric tensor was not clearly known, which forced the usage of semi-definite functions. Moreover, it is not clear if the control solution is variational, i.e., does there exist a CL for the control problem?. Without a Lagrangian framework, it is difficult to query geometric properties like: Does the closed-loop system possess a symmetry (momentum conservation)? Is a geodesic in configuration space also a geodesic in prioritized subspace? Do there exist natural energy functions in subspaces?

Motion on a subspace, like task-specific motion, are often encountered in geometric control, in which NPS is used to perform dynamics reduction. In [5, Ch. 9], energy-based motion stabilization was shown for nonholonomic systems with symmetry. In [212], systems with Killing vectors, i.e., directions of symmetry in the inertia tensor, were exploited for reduction to achieve simultaneous stabilization of relative equilibria (shape) and a non-stationary motion along symmetry. However, in such systems, the symmetry is evident already in the Lagrangian. Generally, \mathcal{EL} systems might not possess natural symmetries along desirable directions (primary subspace). However, motion control might require the imposition of symmetry by virtue of hierarchy (or priority). To this end, in [213], the concept of task-induced Lie group symmetry was introduced for a needle-steering system, however, at a purely kinematic level. Thus, the concept of task-induced symmetry for \mathcal{EL} systems is an open research topic.

6.1.2 Motivating Case

This work is inspired by the PFB [5] topology of the FRM, i.e., its configuration consists of Lie group (SE(3), see Fig. 6.1), which acts isometrically w.r.t. the inertia metric tensor [56]. In other words, the Lie algebra of this symmetry group acts as *Killing vectors* for the inertia, i.e., the inertia does not change along the group variable. In general, for any \mathcal{EL} system, the kinematics of the high priority task defines an algebraic symmetry, i.e., task-specific orthogonal decomposition of the tangent space. However, the algebraic symmetry is not necessarily a variational (dynamics) symmetry of the \mathcal{EL} system. Hence, the

¹This was shown for the FRM in Chapter 3, but is generally a problem with matrix transformations.

6.1 Introduction 161

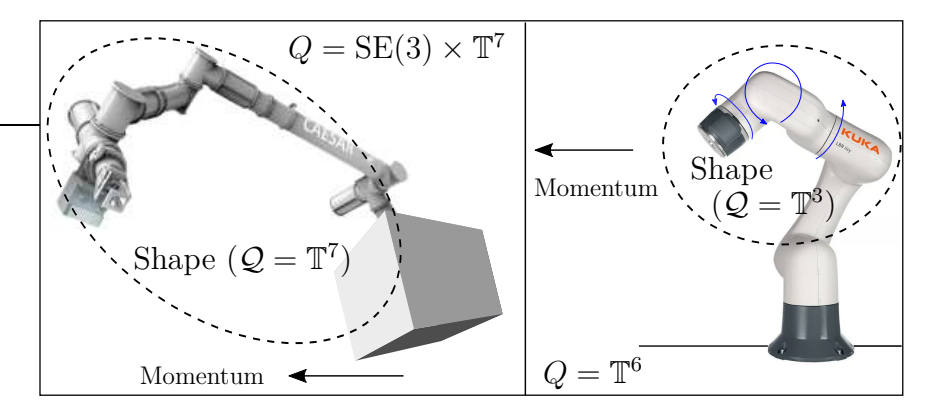


Figure 6.1: Lie group symmetry results in reduction of dynamics into shape and group subspaces. Left: A FRM with the set of joints as the shape-space, while the SE(3) group defines the conserved momentum direction. Right: Hierarchy in motion control of a fixed-base robot, the shape-space comprises of the last three joints, while the nullspace momentum determines motion along the fiber.

key idea in this work is the generation of synthetic symmetry w.r.t. the primary operational space task, so that the induced metric tensor is invariant to the motion along the nullspace directions. This symmetry decomposes the dynamics into those corresponding to the internal shape (for the task), and a conserved momentum, as in the case of the FRM. In particular, control actions generate a topological PFB. This physical intuition in the proposed method of imposing hierarchy was missing in former approaches [206], [207], [52], [208], [209].

6.1.3 Key Contributions

The key novelty in this work are the following.

- 1. In Lemma 6.5, I develop the Symmetry Generating Controller (SGC), which performs a CC compensation to transform the general \mathcal{EL} system into an \mathcal{LP} system with symmetry along the nullspace to the *primary operational space*. In this \mathcal{LP} system, the primary space acts as the internal shape, while the vertical subspace (nullspace) serves as Killing vectors.
- 2. In Lemma 6.9, an additional CC compensation is performed in the shape dynamics of the resulting \mathcal{LP} system so that its closed-loop behaviour is characterized by a time-invariant electromagnetic geodesic. The magnetic-like effect is due to the conserved momenta (vector potential) along the nullspace (Killing vectors). To the best of my knowledge, this Lagrangian framework for hierarchical control of an \mathcal{EL} system has never been proposed before. As a result of this formulation, the shape subsystem is proved to be

stable using its natural energy (Hamiltonian) as the Lyapunov candidate, in contrast to [207] which required semi-definite functions.

- 3. For a secondary task using the fiber (nullspace), the controller design uses two approaches for stabilization. Firstly, in Theorem 6.1, the fiber energy is used in stabilization. Secondly, in Theorem 6.2, the *squared momentum Casimir invariant* is used in the Lyapunov function, which is also conserved due to the symmetry in the \mathcal{LP} system.
- 4. The proposed approach is validated through simulations and experiments that emphasize the correctness of the proposed theory.
- 5. I bring forward the concepts of symmetry, submersion and Killing vector fields from geometric mechanics, to provide a physically intuitive solution to the problem of hierarchical motion control of \mathcal{EL} systems with redundancy.

The paper is structured as follows. In Sec. 6.2, the preliminary concepts of Killing vector fields and symmetry generation is provided. To impose a task-hierarchy, the task-induced fiber bundle is introduced in Sec. 6.3. In Sec. 6.4, the horizontal subspace is introduced to write the \mathcal{EL} equations on the fiber bundle in Sec. 6.5. In Sec. 6.6, the SGC is derived with relevant stability/passivity analysis. The SGC is validated through simulations in Sec. 6.7 that highlight conserved quantities. Finally, the concluding remarks are outlined in Sec. 6.8.

6.2 Preliminaries

In this chapter, the \mathcal{EL} system in (2.15) from Chapter 2 is considered, and the equations are reported here for completeness.

$$\frac{d}{dt}\frac{\delta L}{\delta \dot{q}} - \frac{\delta L}{\delta q} = \tilde{\tau} \text{ (Lagrangian)}, \quad \nabla_{\dot{q}} \dot{q} = (\tilde{\tau} - \frac{\partial V}{\partial q})^{\sharp} \text{ (Riemannian)}$$
 (6.1a)

$$M(q)\ddot{q} + C(q,\dot{q})\dot{q} = \tilde{\tau} - \frac{\partial V}{\partial q}, \text{ (Robotics)}$$
 (6.1b)

Assumption 6.1. Given the \mathcal{EL} system in (2.15), the effect of V is removed for potential shaping [13], i.e., $\tilde{\tau} \mapsto \tilde{\tau} = \frac{\partial V}{\partial q} + \tau$.

Assumption 6.1 is standard in motion control, see [207], and τ is used to design the relevant proportional actions in this paper.

Property 6.1. Given the \mathcal{EL} system descriptions in (2.15), the motion dynamics satisfy the passivity property for $\tau = 0$, correspondingly written as,

$$\frac{d}{dt}\left(\langle \frac{\delta L}{\delta \dot{q}}, \dot{q} \rangle - L\right) = 0 \ [3, \ eq. \ 2.10], \ \langle \nabla_{\dot{q}} \dot{q}, \dot{q} \rangle_M = 0[10, \ eq. \ 2] \tag{6.2a}$$

$$\langle \dot{q}, (\dot{M} - 2C(q, \dot{q}))\dot{q} \rangle = 0 \ [8, Lemma 4.2]$$
 (6.2b)

6.2 Preliminaries 163

A corollary of this property is that it remains invariant under the action of an invertible linear map, $\xi = T(q)\dot{q}$, i.e., the dynamics in terms of ξ also satisfies passivity [8, Lemma 4.11].

In the following Lemma, I derive the Killing equation from Sec. 2.3.1 in a robotics notation as the contribution to make it accessible. This will be useful in designing the control action to generate symmetry of the kinetic energy.

Lemma 6.1. Consider the system in (2.15), the Killing equation in (2.24) can be rewritten as,

$$\mathcal{L}_{\xi}\mathcal{K} = \frac{1}{2} \left\langle \dot{q}, \left(M_v(q, \xi) + P(q, \xi) \right) \dot{q} \right\rangle = 0 \tag{6.3}$$

where $M_v \in \mathbb{R}^{n \times n}$ is the symmetric Inertia Velocity matrix (Def. 2.15), which is written as $M_v(q, \dot{q})\dot{q} = \dot{M}\dot{q}$, and $P = \left(\frac{\partial \xi(q)}{\partial q}\right)^{\top} M(q)$.

Proof. The metric for the \mathcal{EL} system in (2.15) is $\mathcal{K}(q,\dot{q}) = \frac{1}{2}\langle \dot{q},\dot{q}\rangle_M$. Computing $\mathcal{L}_{\mathcal{E}}\mathcal{K}$ using (2.20),

$$\mathcal{L}_{\xi}\mathcal{K} = \frac{1}{2} \langle \xi, \frac{\partial \langle \dot{q}, \dot{q} \rangle_{M}}{\partial q} \rangle + \langle \dot{\xi}, M \dot{q} \rangle = \frac{1}{2} \langle \xi, M_{d}(q, \dot{q})^{\top} \dot{q} \rangle + \langle \frac{\partial \xi(q)}{\partial q} \dot{q}, M \dot{q} \rangle$$

$$= \frac{1}{2} \langle \dot{q}, M_{v}(q, \xi) \dot{q} \rangle + \langle \dot{q}, P(q, \xi) \dot{q} \rangle = 0$$
(6.4)

where in the second line, $M_d \in \mathbb{R}^{n \times n}$ is $\frac{\partial \langle x, y \rangle_{M(q)}}{\partial q} = M_d^{\top}(q, x)y$ for $x, y \in T_qQ$, and called the Inertia Derivative matrix, see Def. 2.15. In the second line, the property $M_d(q, x)y = M_v(q, y)x$ [127, Prop. 6] is used for simplification of the first term for the result.

6.2.1 Symmetry Generation: Concept

In the following, a general concept for creating synthetic symmetry is derived. This is the core idea behind this chapter. A preliminary approach towards this was shown in [97] through quasi-linearization. However, the derivation therein was based on Einstein-notation which is abstract for the motion control and robotics communities. Furthermore, the applications were restricted to systems with trivial Lagrangians with few DoF. In the following, I derive a matrix-based formulation that generalizes to an arbitrary robotic mechanism, and can be computed using standard dynamics libraries [22].

Lemma 6.2. Consider the system in (2.15) without any scalar potential (V = 0), but with actuation τ on the R.H.S. A synthetic symmetry is required along the flow of the vector field $\xi(q) = T(q)\dot{q}$, where $T \in \mathbb{R}^{n \times n}$ is a linear map. Let τ be chosen as,

$$\tau = -T^{\top} \left(\frac{1}{2} T^{-\top} M_d(q, T^{-1} \xi)^{\top} T^{-1} + \dot{T}^{-\top} M T^{-1} \right) \xi \tag{6.5}$$

where M_d is the ID matrix of M. Then, the momenta along ξ is conserved about the neighbourhood of the initial configuration, $q_0 \in Q$, and ξ is the Killing vector.

Proof. The dynamics in (2.15) can be written locally around the initial configuration q_0 using the Newtonian transformation in Lemma 2.15 from Chapter 2.6 as,

$$\Lambda(q)\dot{\xi} + \Gamma(q,\xi)\xi = F = T^{-\top}\tau \tag{6.6}$$

where $\Lambda(q)$ is the transformed inertia metric, and its CC matrix assumes the form $\Gamma(q,\xi) = T^{-\top} \left(C(q,\dot{q}) T^{-1} + M \dot{T}^{-1} \right)$. Factorizing Γ further using the ID and IV matrices, we get,

$$\Gamma(q,\xi) = T^{-\top} \Big(M_v(q,\dot{q}) - \frac{1}{2} M_d^{\top}(q,\dot{q}) \Big) T^{-1} + T^{-\top} M \dot{T}^{-1}$$
 (6.7)

Applying τ in (6.6),

$$\Lambda(q)\dot{\xi} + T^{-\top} \Big(M_v(q, \dot{q}) - \frac{1}{2} M_d^{\top}(q, \dot{q}) \Big) T^{-1} \xi + T^{-\top} M \dot{T}^{-1} \xi
= - \Big(\frac{1}{2} T^{-\top} M_d(q, T^{-1} \xi)^{\top} T^{-1} + \dot{T}^{-\top} M T^{-1} \Big) \xi$$
(6.8)

By cancelling the CC terms, we obtain,

$$\Rightarrow \frac{d}{dt}p = 0, \ p = \Lambda(q)\xi \tag{6.9}$$

which proves the result.

Note that in Lemma 6.2, the control law τ is chosen in a way that ensures the fulfilment of the matrix-based Killing equation in Lemma 6.1.

Remark 33. From Lemma 6.2, it is concluded that the control action τ ensures two integrals of motion. Firstly, the squared momentum Casimir invariant, p^2 is conserved. Consequently, the energy-like function is obtained $\hat{\mathcal{K}} = \frac{1}{2} \langle p, p \rangle_{\Lambda(q_0)^{-1}}$, which is rewritten as, $\frac{1}{2} \langle \mu, \mu \rangle_{\Lambda(q_0)}$, where $\mu = \Lambda(q_0)^{-1} \Lambda(q) \xi$ is a quasivelocity [120]. Thus, there exist n Killing vectors and according to Lemma 2.7, the effective metric tensor $\Lambda(q_0)$ is independent of the configuration, q.

Consider a simple scenario where, $T = \mathbb{I}_n$, i.e., it is our goal to generate Killing vectors of M along the $\frac{\partial}{\partial q}$ directions. In this case, and the control action simplifies to $\tau = -\frac{1}{2}M_d^{\top}(q,\dot{q})\dot{q}$. Since the vector $\xi = \frac{\partial}{\partial q}$ is not configuration-dependent, the last term in (6.4) of Lemma 6.1 is 0, giving,

$$\mathcal{L}_{\xi}\hat{\mathcal{K}} = \frac{1}{2}\mathcal{L}_{\xi}\langle\mu,\mu\rangle_{M(q_0)} = 0, \tag{6.10}$$

Note that the approach in Lemma 6.2 uses feedback linearization, but differs from standard approaches in literature [8, §5.2]. Specifically, the approach in

this chapter is intended to generate a Killing symmetry of the metric tensor. In the non-trivial case, when the vector field is dependent on the configuration, $\xi \equiv \xi(q)$, the control law in Lemma 6.2 can be used to generate symmetries of the metric along the vector field.

Note that creating a synthetic symmetry in Lemma 6.2 comes at the cost of giving up the property of energy conservation with the metric M(q). Momentum conservation results from symmetry in space, whereas energy conservation implies symmetry in time [95]. Hence, in Lemma 6.2, a design choice is made to give up the latter to obtain the former. However, as shown in Remark 33, the momentum conservation property can be used to rewrite an alternative energy-like description that holds in the neighbourhood of q_0 . Note that imposing a momentum conservation property does not imply that the underlying manifold is of a flat curvature. As we shall see, I will use Lemma 6.2 to generate a symmetry of the metric tensor along the fiber (nullspace) of the primary task. This will ensure that the primary task geodesic equation can be written on a level set of the conserved momenta in the fiber.

Using Lemma 2.7 after symmetry generation from Lemma 6.2, the effective inertia is rendered independent of the flow due to the Killing vectors. This is crucial for generating a variational symmetry of the Lagrangian and the \mathcal{EL} system is transformed into an \mathcal{LP} system. In the next section, the task-induced fiber bundle topology of the \mathcal{EL} system is revisited from Chapter 2.

6.3 Task-induced Fiber Bundle

In motion control for redundant \mathcal{EL} systems, instead of the natural configuration manifold Q, the motion in a primary operational space, $R_1 \subset \mathbb{R}^{n_1}$, is relevant. As defined in Def. 2.3 of Chapter 2.1, the forward kinematics map, $\pi_1 : Q \to R_1$ gives the operational space configuration as $r_1 \in R_1 = \pi_1(q)$, and is a surjective submersion if its differential $d\pi_1(q) = J_1$ has $\operatorname{rank}(J_1) = n_1$. Likewise, there might also be a secondary operational space submersion, $\pi_2 : Q \to R_2$, where $d\pi_2(q) = J_2$ has $\operatorname{rank}(J_2) = n_2$, which is required to optimize motion characteristics around the primary task. Let $r_i \in R_i$ be the configuration in the R_i operational space. For motion control, a task is posed as a scalar potential on R_i as, $\Phi_i : R_i \to \mathbb{R}$ such that $\Phi_i(r_i, \overline{r_i})$ has an equilibrium at $\overline{r_i} \in R_i$.

Assumption 6.2. The operational spaces, R_i , satisfy $\dim(R_i) = n_i$ and $\sum n_i = n$, and the total task posed on the operational spaces satisfies a unique point in Q.

Assumption 6.2 implies that $\Phi_1 + \Phi_2$ is positive-definite in Q. This is important for full-motion stabilization. Using both operational spaces, the overall operational space configuration is

$$r = (r_1, r_2) = \pi(q) = (\pi_1(q), \pi_2(q))$$
(6.11)

where π is a *locally* invertible transformation by Assumption 6.2, i.e., $\pi: Q \to R$, $R = R_1 \times R_2$ is the total operational space, i.e., the Cartesian product of the primary and secondary operational spaces. The differential of the task maps π_i , $d\pi_i: T_qQ \to T_{r_1}R_1$, give the total operational space Jacobian map as,

$$\dot{r} = J(q)\dot{q} = \begin{bmatrix} J_1(q) \\ J_2(q) \end{bmatrix} \dot{q}, \ J_i = d\pi_i = \frac{\partial \pi_i}{\partial q}^{\top}$$
(6.12)

The following property enables the pullback of forces from R_i to Q, and is the foundation for control based on transposed Jacobian [8].

Property 6.2. For the forward kinematics submersion $\pi_i: Q \mapsto R_i$, corresponding to the scalar field, $\Phi_i(r_i, \overline{r}_i)$, there exists $\Phi_i^q(q): Q \mapsto \mathbb{R}$ such that $\frac{\partial \Phi_i^q}{\partial q} = J_i^{\top} \frac{\partial \Phi_i}{\partial r_i}$ and $\Phi_i^q = \Phi_i$. This is because the pullback of exact covectors is also exact by Poincaré Lemma [89, Th. 11.49].

The formulation in (6.11) and (6.12) was used in the superposition of pullback of the diffeomorphism maps (impedances) [204], see RMP Flow framework by [205]. However, this approach generally violates the notion of hierarchy (or priority) because the pullback of the secondary task conflicts with the pullback of the primary task to the configuration space Q, i.e.,

$$\langle (J_1^{\top} \frac{\partial \Phi_1}{\partial r_1})^{\sharp}, (J_2^{\top} \frac{\partial \Phi_2}{\partial r_2})^{\sharp} \rangle_M \neq 0$$
 (6.13)

Hierarchy can be achieved instead by modeling the system as a fiber bundle. The reader is encouraged to review the preliminaries in Sec. 2.4 for the next section. The surjective submersion, π_1 , of the primary task from Def. 2.3 results in a fibered manifold, denoted as a triplet (Q, π_1, R_1) . The task-induced fiber bundle can be denoted by the short exact sequence as,

where $\Psi_1: \pi_1^{-1}(r_1) \to Q$ is the inclusion map of the embedded submanifold at each r_1 . In the particular case of task-induced symmetry, the function Ψ_1 can be determined locally using,

$$\pi_1(q) = r_1, \ \pi_2(q) = r_2, \ s(q) = 0$$
 (6.15)

where s determines the fiber origin, i.e., the zero of the fiber at a given $\pi_1(q) = r_1$. The fiber bundle formalism charts the configuration of the \mathcal{EL} system as (r_1, s) , which denote the shape and the fiber origin w.r.t. the given r_1 , respectively. In

order to exploit this coordinate structure, trivialization morphisms and transition functions need to be identified to establish the charts [214, Th. 1.1.4]. We are, however, interested in the tangent space of the exact sequence in (6.14).

For each $q \in Q$, the primary submersion π_1 describes the vertical subspace, \mathbb{V}_1 , on the tangent bundle TQ, as, $\mathbb{V}_{1q} = \text{Kern}(J_1(q))$, where \mathbb{V}_{1q} is a vector space of dimension k_1 . The fibered manifold provides canonical exact sequences for the tangent and the cotangent spaces as follows [104, eq. 1.4.3],

$$\mathbb{V}_{1}q \xrightarrow{Z_{1}} T_{q}Q \xrightarrow{J_{1}} T_{r_{1}}R_{1}$$

$$\downarrow^{J_{2}Z_{1}} \downarrow^{J_{2}} \downarrow^{J}$$

$$\downarrow^{J_{1}} T_{r_{2}}R_{2} \qquad T_{r}R$$

$$(6.16)$$

$$T_{r_1}^{\top} R_1 \xrightarrow{J_1^{\top}} T_q^{\top} Q \xrightarrow{Z_1^{\top}} \mathbb{V}_1 q^{\top}$$

$$\downarrow^{J^{\top}} J_2^{\top} \uparrow^{Z_1^{\top} J_2^{\top}} \downarrow^{Z_1^{\top} J_2^{\top}}$$

$$T_r^{\top} R \qquad T_{r_2}^{\top} R_2 \qquad (6.17)$$

Let the vertical velocity be $(q, \tilde{\mu}) \in \mathbb{V}_{1q}$, where $\tilde{\mu} \in \mathbb{R}^{k_1}$. The velocity $\tilde{\mu}$ is canonically projected to a vertical component $\dot{q}_{v1} \in \mathrm{Ver}(T_qQ)$ on the tangent space, as $\dot{q}_{v1} = Z_1(q)\tilde{\mu}$, where $Z_1 \in \mathbb{R}^{n \times k_1}$ denotes the set of vertical (nullspace) basis. Motion along Z_1 ensures the invariance of $\pi_1(q) = r_1$. Note that by Property 2.2, Z_1 plays the role of the Ad action in \mathbb{V}_{1q} , and thus $\tilde{\mu}$ assumes a right-invariant form, i.e., like a spatial velocity twist in rigid body motion. The numerical procedure to find Z_1 basis is reported in the Lemma below, and the contribution here is the geometric perspective of algebraic symmetry.

Lemma 6.3. Consider the system in (2.15) with forward kinematics of the primary task, $\pi_1(q) = r_1$. Let $\Phi_1(r_1, \overline{r}_1) : R_1 \to \mathbb{R}$ be a potential on the primary operational space. The condition of Algebraic Symmetry determines the basis vectors Z_1^j using the condition that the Lie derivative of Φ_1 along Z_1^j is 0, i.e., $\mathcal{L}_{Z_1^j}\Phi_1(r_1,\overline{r}_1) = 0$, where \mathcal{L} denotes the Lie derivative of Φ_1 along Z_1^j . This condition can be obtained using the Singular Value Decomposition (SVD) of the differential kinematics, J_1 as,

$$J_1 = U \Sigma V^{\top} = U \begin{bmatrix} \Sigma_1 & 0 \\ 0 & 0 \end{bmatrix} \underbrace{\begin{bmatrix} V_1^{\top} \\ Z_1^{\top} \end{bmatrix}}_{\mathcal{D}}$$
 (6.18)

where $U \in \mathcal{O}(n_1), \mathcal{R} \in \mathcal{O}(n)$ are matrices of the orthogonal group.

Proof. The power flow due to the proportional action in the operational space R_1 is given by the time-derivative of the corresponding potential,

$$\mathcal{L}_{\dot{r}_1}\Phi_1(r_1,\overline{r}_1) = \frac{d}{dt}\Phi_1(r_1,\overline{r}_1) = \langle \frac{\partial \Phi_1}{\partial r_1}, \dot{r}_1 \rangle \tag{6.19}$$

The differential in R_1 is then pulled back (Property 6.2) to the configuration space Q as,

 $\mathcal{L}_{\dot{q}}\Phi_{i}(r_{i}, \overline{r}_{i}) = \langle \frac{\partial \Phi_{i}}{\partial r_{i}}, \dot{r}_{i} \rangle = \langle J_{i}^{\top} \frac{\partial \Phi_{i}}{\partial r_{i}}, \dot{q} \rangle$ (6.20)

Using the Lie derivative in (6.20) for R_1 and Q, and restricting the R.H.S of (6.20) to V_{1q} in the fiber,

$$\langle J_1^{\top} \frac{\partial \Phi_1}{\partial r_1}, \dot{q}_{v1} \rangle = \langle \frac{\partial \Phi_1}{\partial r_1}, \underline{J_1 Z_1} \tilde{\mu} \rangle = 0$$
 (6.21)

Note that applying the decomposition in (6.18), I get the R.H.S in (6.21), which proves the result.

The following concepts from Chapter 2 are revisited to set up the theory. In Lemma 6.3, the nullspace basis Z_1 defines a CPT as in Def. 2.1, which is a symmetry of Φ_1 . Assumption 2.2 is invoked so that the fibers are isomorphic, and the \mathcal{EL} system does not suffer from algorithmic singularity [106]. Using Def. 2.4, the induced metric on the submanifold π_1^{-1} is written as $\mathcal{M}_2(q) = Z_1^{\top} M Z_1$.

6.4 The Horizontal subspace

Note that by virtue of pullback, given a covector (force) $F_1 \in T_{r_1}^{\top} R_1$ in the primary operational space, it can be pulled back canonically to $T_q^{\top} Q$ as $J_1^{\top} F_1$. Unfortunately, there is no more canonical geometric machinery available to pullback forces from the fiber $\pi_1^{-1}(r_1)$ to $T_q^{\top} Q$. The Ehresmann connection from Def. 2.5 is chosen to aid this step as the map $\mathcal{A}_q: T_qQ \mapsto \mathbb{V}_{1q}$, which satisfies $\mathcal{A}(\operatorname{Ver}(\tilde{\mu})) = \tilde{\mu}$, where $\tilde{\mu} \in \mathbb{V}_1$.

Thus, Def. 2.5 determines a specific vertical velocity $\tilde{\mu}$ given \dot{q} . In Robotics, the Ehresmann connection is referred to as the nullspace projector [206, 207], and appears in literature in the form, $\mathcal{A} = (Z_1^\top W Z_1)^{-1} Z_1^\top W$, where $W \in \mathbb{R}^{n \times n}$ is a weighing matrix. In particular, the connection defines the endomorphism map, $T_q Q \to T_q Q$, through the projector matrix $\mathcal{Z} = Z_1 \mathcal{A}$, which splits any tangent velocity vector $\dot{q}^* \in T_q Q$ as,

$$\dot{q}^* = \dot{q}_v^* + \dot{q}_h^* = (\mathcal{Z})\dot{q}^* + \text{Kern}(\mathcal{Z})\dot{q}^*$$
(6.22)

which decomposes the tangent space into two distributions as $T_qQ = \mathbb{V}_{1q} + \mathbb{H}_{1q}$.

Property 6.3. The endomorphism $\mathcal{Z}: T_qQ \mapsto T_qQ$ given by $\mathcal{Z}(q) = Z_1\mathcal{A}$, is an Ehresmann connection form on Q, see [14, Def. 2.2], which is compatible with the forward kinematics submersion, π_1 . It satisfies the projection properties:

$$\mathcal{Z}^2 = \mathcal{Z}, \ \mathcal{Z}v = v, \forall v \in \mathbb{V}_{1q}$$
 (6.23)

Using \mathcal{Z} , the horizontal subspace at q is defined as $\mathbb{H}_{1q} = \operatorname{Kern}(\mathcal{Z}(q))$, with a horizontal velocity defined as, $\dot{q}_h = \dot{q} - \mathcal{Z}(q)\dot{q}$.

In the next part, the connection is explicitly shown with its geometric interpretation. To this end, let $x \in T_q^{\top}Q$ be a force covector in Q. Computing the power flow due to x in the submanifold $\pi_1^{-1}(r_1)$,

$$\langle x, \dot{q} \rangle \Big|_{\pi_1^{-1}(r_1)} = \langle x, \dot{q}_{v1} \rangle = \underbrace{\langle Z_1^\top x, \tilde{\mu} \rangle}_{\text{force-velocity pair in fiber}}$$
 (6.24)

The connection \mathcal{A} can be computed as:

Def. 6.1. Statically Consistent: If $W = \mathbb{I}_{n,n}$: In this case, the R.H.S. of (6.24) is written as,

$$\langle Z_1 Z_1^\top x, Z_1 \tilde{\mu} \rangle, \ \because Z_1^\top Z_1 = \mathbb{I}_{k_1 \times k_1} \tag{6.25}$$

to determine the force-velocity pairing in Q.

Def. 6.2. Dynamically Consistent: If W = M(q): In this case, the R.H.S. of (6.24) is written using the canonical metric, \mathcal{M}_2 , on the fiber, see Def. 2.4, as,

$$\langle (Z_1^\top x)^\sharp, \tilde{\mu} \rangle_{\mathcal{M}_2} = \langle Z_1 (Z_1^\top x)^\sharp, Z_1 \tilde{\mu} \rangle_M$$

$$= \langle M Z_1 \mathcal{M}_2^{-1} Z_1^\top x, Z_1 \tilde{\mu} \rangle = \langle \left(Z_1 (Z_1^\top x))^\sharp \right)^\flat, Z_1 \tilde{\mu} \rangle$$
(6.26)

Thus, we see that both projection formulae satisfy the force-velocity pairing in (6.24), and hence, are equally valid iff $\dot{r}_1=0$. In geometric mechanics, the former is called a trivial Ehresmann connection and the latter is called the *mechanical* connection, see [5]. In the latter case, $\tilde{\mu}$ obtained from the connection is known as the locked velocity, i.e., the velocity corresponding to the momentum in the fiber space. Given the system velocity, \dot{q} , the conjugate momentum is written as $\frac{\delta L}{\delta \dot{q}}=M(q)\dot{q}$, and the cotangent vertical space is $\mathbb{V}_{1q}^{\top}\subset T_q^{\top}Q$, $p=Z_1^{\top}\frac{\delta L}{\delta \dot{q}}$, $p\in\mathbb{V}_{1q}^{\top}$. Using the canonical metric on the vertical subspace (see Def. 2.4), the velocity corresponding to p, i.e., the locked velocity, is obtained as,

$$\tilde{\mu} = \mathcal{M}_2^{-1} Z_1^{\top} \frac{\delta L}{\delta \dot{q}} = \mathcal{M}_2^{-1} p = \mathcal{A}(q) \dot{q}, \tag{6.27}$$

which defines the vertical velocity as $\dot{q}_v = Z_1 A \dot{q} = \mathcal{Z}(q) \dot{q}$. The bundle velocity is obtained as a locally invertible linear transformation of the velocity on T_qQ , i.e.,

$$\begin{bmatrix} \dot{r}_1 \\ \tilde{\mu} \end{bmatrix} = T(q)\dot{q}, \ T = \begin{bmatrix} J_1(q) \\ \mathcal{A}(q) \end{bmatrix}$$
 (6.28)

which is called the extended Jacobian in robotics. However, note that T does not emerge as the differential of a kinematic map.

Lemma 6.4. Given the mechanical connection, \mathcal{A} , the contribution of the horizontal velocity, i.e., motion purely in the shape, \dot{q}_h , towards fiber displacement is, $\tilde{\mathcal{A}}_l \dot{r}_1$, and $\tilde{\mu} = Z_1^{\top} \dot{q} + \tilde{\mathcal{A}}_l \dot{r}_1$, where $\tilde{\mathcal{A}}_l = -Z_1^{\top} T^{-1} \begin{bmatrix} \mathbb{I} \\ 0 \end{bmatrix}$ is the right-trivialized (spatial) local form of the mechanical connection [14].

Proof. The velocity of the \mathcal{EL} system is, $\dot{q} = T^{-1} \begin{bmatrix} \dot{r}_1^\top & \tilde{\mu}^\top \end{bmatrix}^\top$, using which,

$$\dot{q} = T^{-1} \begin{bmatrix} \dot{r}_1 \\ \tilde{\mu} \end{bmatrix} = \dot{q}_h + \dot{q}_v = T^{-1} \begin{bmatrix} \dot{r}_1 \\ 0 \end{bmatrix} + T^{-1} \begin{bmatrix} 0 \\ \tilde{\mu} \end{bmatrix}$$

$$(6.29)$$

The trivial connection gives the pure fiber velocity, i.e., $\tilde{\mu}|_{\dot{r}_1=0}$, as shown in (2.30) of Chapter 2, as $\tilde{\mu}|_{\dot{r}_1=0}=Z_1^{\top}\dot{q}$. Thus, the contribution of the horizontal velocity towards fiber displacement is simply,

$$(\mathcal{A} - Z_1^{\mathsf{T}})\dot{q}_h = (\mathcal{A} - Z_1^{\mathsf{T}})T^{-1}\begin{bmatrix} \dot{r}_1 \\ 0 \end{bmatrix} = \mathcal{A}\dot{q}_h - Z_1^{\mathsf{T}}T^{-1}\begin{bmatrix} \dot{r}_1 \\ 0 \end{bmatrix}$$

$$= -Z_1^{\mathsf{T}}T^{-1}\begin{bmatrix} \dot{r}_1 \\ 0 \end{bmatrix}, :: \mathcal{A}\dot{q}_h = 0$$

$$(6.30)$$

which yields the form of $\tilde{\mathcal{A}}_l$. Consequently, $\tilde{\mu}$ is written as the sum of the pure fiber velocity and the horizontal contribution as $\tilde{\mu} = Z_1^{\top} \dot{q} + \tilde{\mathcal{A}}_l \dot{r}_1$.

6.4.1 Restriction of the Secondary Task

Instead of using the pullback of Φ_2 directly, hierarchy is imposed by first restricting it to the submanifold, $\pi_1^{-1}(r_1)$. Consider the secondary task potential, $\Phi_2(r_2, \overline{r}_2)$. Using Property 6.2, it is concluded that $\forall \Phi_2(r_2, \overline{r}_2)$, $\exists \Phi_2^q(q)$. Recall that the fiber π_1^{-1} is an embedded submanifold of Q. Hence, smooth functions on Q have a restriction to the domain in the submanifold, $\pi_1^{-1}(r_1)$, i.e., the fiber [89, Th. 5.27]. The domain restriction applied to the scalar field Φ_2^q results in another restricted scalar field $\Phi_2: \pi_1^{-1} \to \mathbb{R}$, whose domain is a point in the submanifold at r_1 . This is the restriction of the potential $\Phi_2 = \Phi_2(r_2, \overline{r}_2) \Big|_{\pi_1^{-1}(r_1)}$ at each r_1 .

For the next treatment, the Lie derivative of $\tilde{\Phi}_2$ along \mathbb{V}_1 is computed by restricting the Lie derivative of Φ_2 to π_1^{-1} . Computing this,

$$\mathcal{L}_{\dot{q}}\Phi_{2}\Big|_{\pi_{1}^{-1}(r_{1})} = \left\langle J_{2}^{\top} \frac{\partial \Phi_{2}}{\partial r_{2}}, \dot{q} \right\rangle \Big|_{\pi_{1}^{-1}(r_{1})}$$

$$\Rightarrow \mathcal{L}_{\dot{q}_{v1}}\tilde{\Phi}_{2} = \left\langle J_{2}^{\top} \frac{\partial \Phi_{2}}{\partial r_{2}}, \dot{q}_{v1} \right\rangle = \underbrace{\left\langle Z_{1}^{\top} J_{2}^{\top} \frac{\partial \Phi_{2}}{\partial r_{2}}, \tilde{\mu} \right\rangle}_{\text{force-velocity pair in fiber}} \tag{6.31}$$

which is projected to Q using the connection \mathcal{A} . The mechanical connection satisfies an additional orthogonality (symmetry) condition between the proportional actions of the primary and secondary tasks, i.e.,

$$\langle (J_1^{\top} \frac{\partial \Phi_1}{\partial r_1})^{\sharp}, (\mathcal{A}^{\top} Z_1^{\top} J_2^{\top} \frac{\partial \Phi_2}{\partial r_2})^{\sharp} \rangle_M = 0$$
 (6.32)

which is useful to impose a task-induced symmetry, in contrast to direct pullback (6.13). Note that the definition of \mathcal{A} is a choice, and does not affect power flows in dynamics, but it simplifies the \mathcal{EL} equations of motion.

6.5 \mathcal{EL} equations of Motion on the Fiber Bundle

Recall from Sec. 2.4.7 that for a general \mathcal{EL} system without symmetry, the quotient map $\pi_1: Q \to Q/G_{r_1}$ holds locally for each r_1 , where G_{r_1} is the Lie group locally defined at r_1 . In this case, the tangent space that is isomorphic to the groupoid yields a Lie algebroid. Hence, the dynamics of $(\dot{r}_1, \tilde{\mu})$ correspond to the dynamics of the shape velocity and the Lie algebroid of G_{r_1} . The equations of motion are given below for an arbitrary connection. In robotics notation, the dynamics are obtained using the Newtonian transformation in Lemma 2.15 from Chapter 2.6 corresponding to (6.28) as,

$$\mathcal{M}(q) \begin{bmatrix} \ddot{r}_1 \\ \dot{\tilde{\mu}} \end{bmatrix} + \Gamma(q, \dot{r}_1, \tilde{\mu}) \begin{bmatrix} \dot{r}_1 \\ \tilde{\mu} \end{bmatrix} = \begin{bmatrix} F_1 \\ f \end{bmatrix}$$
 (6.33)

where $\tau = T^{\top}(F_1, f)$ denote the forces in the shape and fiber, $\mathcal{M} = T^{-\top}MT^{-1}$ is the metric tensor (fully-coupled for arbitrary \mathcal{A}) in the fiber bundle, and $\Gamma = T^{-\top}(CT^{-1} - M\dot{T}^{-1})$ is the matrix of CC terms. For further treatment, the forces are decomposed as,

$$F_1 = \hat{F}_1 + \overline{F}_1 + F_{1d}, \ f = \hat{f} + \overline{f} + f_d$$
 (6.34)

where $(\hat{\bullet})$ are used for feedback action, whereas $(\overline{\bullet})$ are used to provide feedforward action, while $(\bullet)_d$ are disturbance forces in the fiber bundle cotangent space. In the control design aspect, first \hat{f} will be used to generate a symmetry of the metric tensor, then \overline{F}_1 will be used to render the shape subsystem (primary space) time-invariant, and (\hat{F}_1, \hat{f}) for the hierarchy-based control.

Remark 34. Note that the inertia tensor \mathcal{M} is block-diagonalized

$$\mathcal{M}(q) = \begin{bmatrix} \mathcal{M}_1(q) & 0\\ 0 & \mathcal{M}_2(q) \end{bmatrix} \tag{6.35}$$

if \mathcal{A} is chosen to be the mechanical connection, as was shown in [207, 215]. In the following, \mathcal{A} is chosen as the mechanical connection to simplify the derivation, i.e., $\tilde{\mu}$ is the locked velocity. But the trivial connection can be alternatively used.

Remark 35. The dynamics in (6.33) satisfy the passivity property by the corollary in Property 6.1, i.e., the kinetic energy $\frac{1}{2}\langle(\dot{r}_1,\tilde{\mu}),(\dot{r}_1,\tilde{\mu})\rangle_{\mathcal{M}}$ in the bundle coordinates is conserved.

For the motion control of a redundant \mathcal{EL} system, it cannot be a priori assumed that the forward kinematics surjective submersion $\pi_1: Q \mapsto R_1$ has a fixed point, i.e., constrained. In fact, it is required to regulate the motion along the operational space R_1 , such that $r_1(t) = \pi_1(q(t))$ is steered to a desired setpoint, and in a way that the resulting motion in R_1 is geodesic in nature. To achieve

this, the key objective is to generate an inertia metric tensor $\hat{\mathcal{M}}$ from \mathcal{M} , which satisfies $\mathcal{L}_{Z_1^i}\hat{\mathcal{M}}=0$, $\forall i$. This means that the vectors Z_1^i act as infinitesimal (Killing) symmetries of $\hat{\mathcal{M}}$ according to Lemma 6.1, and in the horizontal lift basis, $\hat{\mathcal{M}} \equiv \hat{\mathcal{M}}(r_1)$. It will be shown next that $\hat{\mathcal{M}}(r_1)$ is the metric for the space $\hat{Q} = G_0 \times R_1$, where G_0 is the Lie group arising from the closed Lie algebra V_{1q} .

6.6 Symmetry Generating Controller Design

In this section, the motion control design is derived to generate the required motion on $\hat{Q} = G_0 \times R_1$ using the \mathcal{EL} system residing on Q. To that end, we first define the subspaces relevant to motion control.

Def. 6.3. Primary Subspace: Given a \mathcal{EL} system with configuration space \hat{Q} , the primary subspace is the operational space, R_1 , which is isomorphic to to the quotient (shape) space, $R_1 \cong Q/G_0$, where G_0 is the structural Lie group acting along the fibers (nullspace). A task-oriented motion on the primary subspace is determined by a time-invariant "electromagnetic" geodesic on R_1 [216], in which the task-oriented potential, Φ_1 , defines the equilibrium, and the magnetic potential is determined by the momenta in the fiber (nullspace).

The electromagnetic geodesic differs from the commonly known geodesic with scalar potentials [217] in that the former features gyroscopic torques, similar to the magnetic torques in the Lorentz force law, see Lemma A.5 in the Appendix. On the left of Fig. 6.2, the geodesic motions under the influence of a purely scalar potential field on \mathbb{S}^2 sphere are shown. In [217, 218], such geodesic motions were used to create periodic motions. However, geodesic motions can be generalized for a general gauge potential (with an additional vector potential), and can also be periodic, see [216]. The vector potential causes purely gyroscopic torques that provide a turning effect around the guiding center. Such an electromagnetic geodesic is shown on the right of Fig. 6.2. Note that both systems possess identical Hamiltonians, which is conserved if the potentials are time-invariant.

Def. 6.4. Secondary Subspace: In the context of task-induced symmetry, given a \mathcal{EL} system with configuration space \hat{Q} , the secondary subspace is another operational space, R_2 , which drives the momentum subsystem (maybe periodic) along the fibers (nullspace).

6.6.1 Shaping the Inertia Metric Tensor

Firstly, through control action, a G_0 -invariant metric, $\hat{M}(r_1)$, has to be generated from M(q) that corresponds to the PFB $\hat{Q} = G_0 \times R_1$. This is achieved through the application of Lemma 6.2 to the \mathcal{EL} equations in 6.33. This means that the control action is chosen so that the metric, $\hat{M}(r)$ has the group Lie algebra Z_1

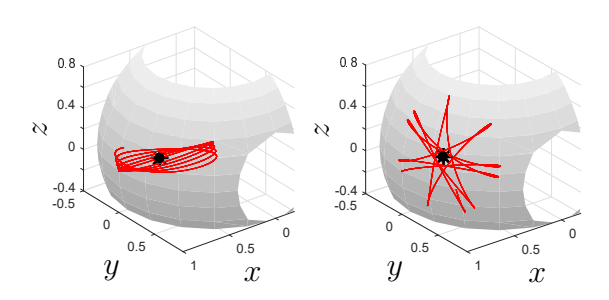


Figure 6.2: Geodesics on \mathbb{S}^2 sphere. Left: Geodesic motion due to a central scalar potential field. Right: Electromagnetic geodesic motion due to a gauge potential, consisting of a central scalar potential and a vector potential.

as its Killing vectors. While Lemma 6.2 provides a framework to generate a full symmetry, in task-induced hierarchy, it might be required to generate a partial symmetry, i.e., only along nullspace. To this end, the following Lemma illustrates the way forward.

Lemma 6.5. Given the \mathcal{EL} system in (6.33) with actuation forcing τ with the Ehresmann connection as the mechanical connection. Let \overline{f} be the component of τ along the fiber space for feedforward action. If

$$\overline{f} = \frac{1}{2} Z_1(q)^{\top} M_d(q, \dot{q})^{\top} \dot{q} + \dot{Z}_1(q, \dot{q})^{\top} M(q) \dot{q}, \tag{6.36}$$

then the \mathcal{EL} system on Q transforms into a PFB, $\hat{Q} = G_0 \times R_1$.

Proof. As shown in Sec. 6.4, the momenta along fiber is $p = Z_1^{\top} \frac{\partial l(q,\dot{q})}{\partial q}$. Thus, the condition to conserve momenta along the fiber is,

$$\frac{d}{dt}\langle Z_1(q), \frac{\delta l(q, \dot{q})}{\delta \dot{q}} \rangle = 0 \Rightarrow \langle \dot{Z}, \frac{\delta l}{\delta \dot{q}} \rangle + \langle Z_1, \frac{d}{dt} \frac{\delta l}{\delta \dot{q}} \rangle = 0$$

$$\Rightarrow \langle \dot{Z}_1, \frac{\delta l}{\delta \dot{q}} \rangle + \langle Z_1, \frac{\delta l}{\delta q} \rangle = 0 \Rightarrow \langle Z_1, \frac{1}{2} M_d(q, \dot{q})^\top \dot{q} \rangle + \langle \dot{Z}_1, M(q) \dot{q} \rangle = 0$$
(6.37)

which is the matrix-based Killing equation in Lemma 6.1. Thus, choosing (6.36), the system behaves as if there exist Killing symmetries about the Lie algebra, $\xi \cong Z_1$, and the momentum is forced to be conserved along these directions. To see this, computing the inner product using (6.37) with $\hat{f} = f_d = 0$,

$$\langle \tilde{\mu}, f \rangle = \langle \tilde{\mu}, \frac{1}{2} Z_1^{\top} M_d(q, \dot{q})^{\top} \dot{q} + \dot{Z}_1^{\top} M(q) \dot{q} \rangle = 0$$
 (6.38)

which is actually the Rund-Trautman expression in Def. 2.2.

Since momenta is conserved along the fiber, the topology of the resulting \mathcal{EL} system is characterized as a Lie group action of a group $G_0(q(0))$ on the shape R_1 ,

i.e., $\hat{Q} = G_0 \times R_1$. Note that in Lemma 6.5, $G_0(q(0))$ is the group that gets fixed at q(0). As remarked in Sec. 6.5, since Q does not in general have symmetry, at each $r_1(t)$, there is a group action $G_t(r_1(t))$ which is a function of $r_1(t)$. So, in Lemma 6.5, the control law ensures that the group at $G_0(r_1(0))$ is fixed resulting in a PFB topology. This proves the result.

Consider the \mathcal{EL} dynamics in (6.33) with $\dot{r}_1 = 0$. In this case, the fiber dynamics with f as in Lemma 6.5 results in the conservation of the squared-momentum Casimir-invariant p^2 . Let $\hat{\mathcal{M}}_2$ be the new locked metric tensor after application of Lemma 6.5. This can be used to derive an energy-like quantity as,

$$\frac{1}{2} \langle p, p \rangle_{\hat{\mathcal{M}}_{2}(r_{1}(0))^{-1}} = \frac{1}{2} \langle \mathcal{M}_{2}(q)\tilde{\mu}, \mathcal{M}_{2}(q)\tilde{\mu} \rangle_{\hat{\mathcal{M}}_{2}(r_{1}(0))^{-1}}
= \frac{1}{2} \langle \mathcal{S}\tilde{\mu}, \mathcal{S}\tilde{\mu} \rangle_{\hat{\mathcal{M}}_{2}(r_{1}(0))} = \frac{1}{2} \langle \mu, \mu \rangle_{\hat{\mathcal{M}}_{2}(r_{1}(0))}$$
(6.39)

where $S = \hat{\mathcal{M}}_2(r_1(0))^{-1}\mathcal{M}_2(q)$ and $\mu = S(q)\tilde{\mu}$ is the basis change from spatial to body frame for G_0 . In the case, $\dot{r}_1 \neq 0$, the kinetic energy in the fiber is $\frac{1}{2}\langle \mu, \mu \rangle_{\hat{\mathcal{M}}_2(r_1)}$, i.e., varies with r_1 only. Note that Lemma 6.5 is not restricted only to the fiber, rather it generates symmetry along the fiber for the entire \mathcal{EL} system. In fact, (6.38) leads to,

$$\langle \left(\frac{\partial Z_1 \tilde{\mu}}{\partial q}\right) \dot{q}, M(q) \dot{q} \rangle + \langle \frac{1}{2} M_d(q, \dot{q})^\top Z_1 \tilde{\mu}, \dot{q} \rangle = \langle \dot{q}, \dot{q} \rangle_{\Psi} = 0$$
 (6.40)

where $\Psi = \left(\frac{\partial Z_1\tilde{\mu}}{\partial q}\right)^{\top}M(q) + M_v(q, Z_1\tilde{\mu})$, which is exactly the R.H.S. of (6.4) in Lemma 6.1. The second term is the symmetric part of $\nabla_{\dot{q}}\dot{q}$ along $Z_1\tilde{\mu}$, leaving only the skew-symmetric part, and the first term removes the variation due to basis change of Z_1 . This means that Lemma 6.5 generates a metric tensor \hat{M} in Q, which does not vary along $Z_1\tilde{\mu}$. Consequently, we also get $\hat{\mathcal{M}}_1 = \hat{\mathcal{M}}_1(r_1)$. Thus, the total kinetic energy assumes the form,

$$\hat{\mathcal{K}} = \hat{\mathcal{K}}_1(r_1, \dot{r}_1) + \hat{\mathcal{K}}_2(r_1, \mu) = \frac{1}{2} \langle \dot{r}_1, \dot{r}_1 \rangle_{\hat{\mathcal{M}}_1(r_1)} + \frac{1}{2} \langle \mu, \mu \rangle_{\hat{\mathcal{M}}_2(r_1)}$$
(6.41)

which is G_0 -invariant. Note in (6.38), the pair (Z_1, \dot{Z}_1) are the first prolongation of Z_1 (as in (2.20)), and (6.38) proves that Z_1 defines a CPT symmetry of the closed-loop kinetic energy, $\hat{\mathcal{K}}$.

Property 6.4. Let $x, y \in \mathbb{V}_{1q}$ be the spatial and body forces for the fiber group G_0 . In the spatial and body basis, the power flows are related as, $\langle \tilde{\mu}, x \rangle = \langle \mu, \mathcal{S}^{-\top} x \rangle$.

Property 6.5. The left-trivialized (body) form of the local mechanical connection that contributes to the fiber motion is $A_l = -\mathcal{S}Z_1^{\top}T^{-1}\begin{bmatrix} \mathbb{I} \\ 0 \end{bmatrix}$.

Proof. Using Lemma 6.4, $\tilde{\mathcal{A}}_l = -Z_1^{\top} T^{-1} \begin{bmatrix} \mathbb{I} \\ 0 \end{bmatrix}$, and $\tilde{\mathcal{A}}_l \dot{r}_1$ gives the right-trivialized (spatial) form of the local mechanical connection. Thus, using the basis change \mathcal{S} , the result follows straight-forwardly, and $\mathcal{A}_l \dot{r}_1$ gives the left-trivialized (body) contribution of the horizontal velocity towards fiber motion.

I point out that in the final control law, we use the spatial pairing $\langle \tilde{\mu}, x \rangle$. But, the body formulation is used to show that the resulting system is an \mathcal{LP} system.

Thus, we can write a G_0 -invariant Lagrangian for the \mathcal{LP} system under the effect of primary task potential, i.e.,

$$l(r_1, \dot{r}_1, \mu) = \hat{\mathcal{K}}_1(r_1, \dot{r}_1) - \Phi_1(r_1, \overline{r}_1) + \hat{\mathcal{K}}_2(r_1, \mu), \quad \mathcal{L}_{Z_1^i} l(r_1, \dot{r}_1, \mu) = 0$$
 (6.42)

and this is a consequence of Lemma 2.7, i.e., in the fiber bundle coordinates, the metric (and thus, the Lagrangian) is independent of the group variable, G_0 . This is the meaning of variational symmetry, or NPS.

Lemma 6.6. Consider the \mathcal{EL} system described in (2.15) with actuation τ , with forcing chosen as in Lemma 6.5. This generates a kinetic energy function for the PFB as $\hat{\mathcal{K}} = \frac{1}{2} \langle \dot{r}_1, \dot{r}_1 \rangle_{\hat{\mathcal{M}}_1(r_1)} + \frac{1}{2} \langle \mu, \mu \rangle_{\hat{\mathcal{M}}_2(r_1)}$. Using the mechanical connection as the Ehresmann connection with the local form \mathcal{A}_l (Property 6.5), the state of the \mathcal{EL} system is written as (r, x, \dot{r}_1, μ) , where $x \in G_0$. This system is known as the Lagrange-Poincaré system (\mathcal{LP}) , and its motion is dictated by the \mathcal{LP} equations, which are also called as the Reduced Euler-Lagrange equations or Wong's equations [219], and is G_0 -invariant as,

$$\operatorname{Hor}(\mathcal{LP}) = \frac{d}{dt} \frac{\delta \hat{\mathcal{K}}_{1}}{\delta \dot{r}_{1}} - \frac{\delta \hat{\mathcal{K}}_{1}}{\delta r_{1}} = \frac{\delta \hat{\mathcal{K}}_{2}}{\delta r_{1}} + \mathcal{A}_{l}^{\top} \operatorname{ad}_{\mu}^{\top} \frac{\delta \hat{\mathcal{K}}_{2}}{\delta \mu} - \left(D \mathcal{A}_{l}(r_{1}, \dot{r}_{1})\right)^{\top} \frac{\delta \hat{\mathcal{K}}_{2}}{\delta \mu} + F_{1}$$

$$\operatorname{Ver}(\mathcal{LP}) = \frac{d}{dt} \frac{\delta \hat{\mathcal{K}}_{2}}{\delta \mu} = \operatorname{ad}_{(\mu - \mathcal{A}_{l} \dot{r}_{1})}^{\top} \frac{\delta \hat{\mathcal{K}}_{2}}{\delta \mu} + \vartheta$$

$$(6.43)$$

where $D\mathcal{A}_l$ refers to the curvature, or the covariant exterior derivative of the mechanical connection \mathcal{A}_l , see [19], which measures the non-integrability of the horizontal subspace \mathbb{H}_{1q} , and $\vartheta = \mathcal{S}^{-\top}(\hat{f} + f_{1d})$.

Proof. Given a G_0 -invariant Lagrangian, the motion is described by the \mathcal{LP} equations, as shown by [5, 123, 149].

The geometric concept in the control approach is shown in Fig. 6.3. We started with an \mathcal{EL} system having a configuration space Q (dotted) that was not endowed with any natural symmetry. This is an obstruction to generating geodesic motion in a primary operational space R_1 (red). Thus, through control action, a symmetry is created along the fiber (Lie group G_0) so that there is a right transitive group action $x(0) \cdot g = x(1)$, resulting in a configuration space

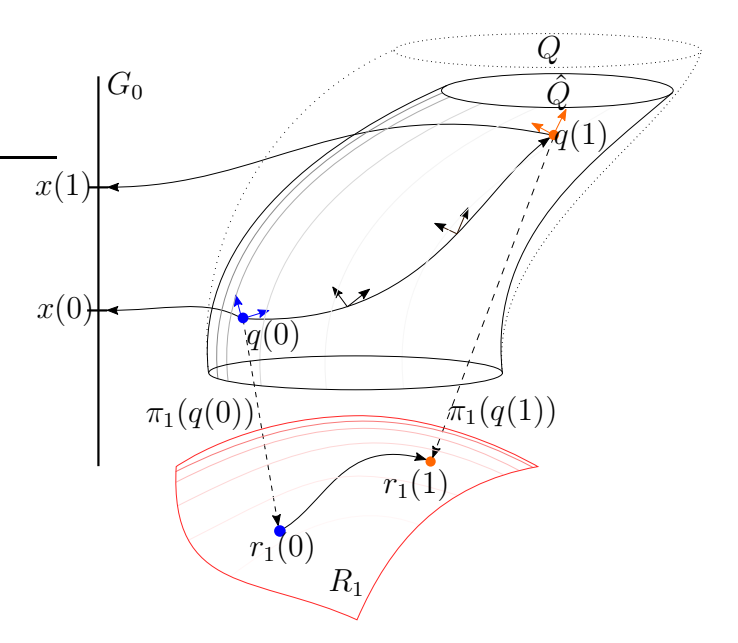


Figure 6.3: Motion control concept: A redundant \mathcal{EL} system with configuration space Q (dotted) is given, which might not have any natural symmetry, and it is required to create geodesic motions in an operational space R_1 (red). Through control action, a symmetry is created along the fiber (Lie group G_0) so that there is a transitive group action $g \cdot x(0) = x(1)$, resulting in a configuration space resembling a PFB, $\hat{Q} = G_0 \times R_1$. Consequently, as a geodesic motion is generated in R_1 , a momentum conservation principle along the fibers is ensured.

that is a PFB, $\hat{Q} = G_0 \times R_1$. This Lie group, G_0 , is frozen at $r_1(0)$ to simplify the Groupoid action of a general fiber bundle to group action of PFB. Consequently, we shall see next that a geodesic motion is generated in R_1 , as a momentum conservation principle or a continuity equation along the fibers is ensured. In the following, the first principles of the subsystem prioritized controller approach from Chapter 5 will be employed to achieve task-induced symmetry.

6.6.2 Passive Interconnection of Subsystems

In this subsection, it is proved that the \mathcal{LP} dynamics from Lemma 6.6 are a feedback interconnection of passive subsystems composed of the motion on the primary subspace and its nullspace (fiber), as shown in Fig. 6.4. I recall that this is identical to the concept in Theorem 3.4 for the FRM. In the shape dynamics (top row of (6.43)), the CC terms with (μ, μ) coupling are the covariant derivative of the locked kinetic energy, $\hat{\mathcal{K}}_2$, relative to the shape, see [149, §4.2], i.e.,

$$\frac{D\hat{\mathcal{K}}_2}{Dr_1} = \frac{\delta\hat{\mathcal{K}}_2}{\delta r_1} - \mathcal{A}_l^{\mathsf{T}} \mathrm{ad}_{\mu}^{\mathsf{T}} \frac{\partial\hat{\mathcal{K}}_2}{\delta \mu}$$
 (6.44)

177

which provides the time-varying torques from the momentum dynamics for the motion in the primary subspace $R_1 = \hat{Q}/G_0$.

Lemma 6.7. Consider the system in Lemma 6.6. The shape subsystem, $Hor(\mathcal{LP})$, is passive with the map,

$$\frac{D\hat{\mathcal{K}}_2}{Dr_1} + F_1 \mapsto \dot{r}_1 \tag{6.45}$$

with the shape subsystem Hamiltonian as the storage function, which is written as $\mathcal{H}_1 = \frac{1}{2} \langle \dot{r}_1, \dot{r}_1 \rangle_{\hat{\mathcal{M}}_1(r_1)}$.

Proof. The motion on $R_1 = \hat{Q}/G_0$ for the internal shape Σ_1 is described by the magnetic Lagrangian,

$$l_1 = \hat{\mathcal{K}}_1(r_1, \dot{r}_1) - \langle \dot{r}_1, \mathcal{A}_l^{\mathsf{T}} \hat{\mathcal{M}}_2(r_1) \mu \rangle \tag{6.46}$$

which models the primary subspace motion. Its time-derivative is computed as,

$$\dot{l}_1 = \langle \frac{\delta l_1}{\delta r_1}, \dot{r}_1 \rangle + \langle \frac{\delta l_1}{\delta \dot{r}_1}, \ddot{r} \rangle = \langle \frac{\delta l_1}{\delta r_1}, \dot{r}_1 \rangle + \frac{d}{dt} \langle \frac{\delta l_1}{\delta \dot{r}_1}, \dot{r}_1 \rangle - \langle \frac{d}{dt} \frac{\delta l_1}{\delta \dot{r}_1}, \dot{r}_1 \rangle$$
 (6.47)

Using (6.46), the Hamiltonian is obtained as $\mathcal{H}_1 = \langle \frac{\delta l_1}{\delta r_1}, \dot{r}_1 \rangle - l_1$. Hence, using (6.47) to compute the time-derivative of \mathcal{H}_1 ,

$$\dot{\mathcal{H}}_1 = \frac{d}{dt} \langle \frac{\delta l_1}{\delta \dot{r}_1}, \dot{r}_1 \rangle - \dot{l}_1 = \langle \dot{r}_1, \frac{D\hat{\mathcal{K}}_2}{Dr_1} + F_1 \rangle \tag{6.48}$$

which proves passivity of Σ_1 with Hamiltonian \mathcal{H}_1 as the storage function.

Next, we analyze the passivity of the nullspace subsystem, $Ver(\mathcal{LP})$, denoted as Σ_2 in Fig. 6.4.

Lemma 6.8. Given the system in Lemma 6.6, the momentum subsystem, denoted as $Ver(\mathcal{LP})$, is passive with the map,

$$\begin{bmatrix} \vartheta \\ -\dot{r}_1 \end{bmatrix} \mapsto \begin{bmatrix} \mu \\ \frac{D\hat{\mathcal{K}}_2}{Dr_1} \end{bmatrix} \tag{6.49}$$

with the subsystem Hamiltonian as the storage function, $\mathcal{H}_2 = \hat{\mathcal{K}}_2(r_1, \mu)$.

Proof. For Σ_2 , computing the time-derivative of \mathcal{H}_2 ,

$$\dot{\mathcal{H}}_2 = \langle \mu, \vartheta \rangle + \langle \frac{D\hat{\mathcal{K}}_2}{Dr_1}, -\dot{r}_1 \rangle \tag{6.50}$$

which proves the result.

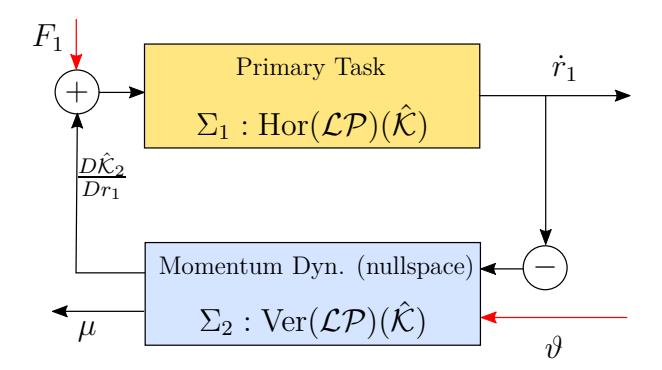


Figure 6.4: Passive interconnection of $Hor(\mathcal{LP})$ and $Ver(\mathcal{LP})$ subsystems.

Thus, the \mathcal{LP} dynamics form an interconnection between the two passive subsystems: shape (Σ_1) and momentum (Σ_2) . It can be trivially proved that the total system is a passive interconnection with $\sum_{i=1}^2 \mathcal{H}_i$ as the storage function. This has been summarized in Fig. 6.4. Note that Lemmas 6.7 and 6.8 also hold in the presence of a primary task potential, Φ_1 , in Σ_1 . In this case, F_1 will correspondingly change, and the shape Hamiltonian is $\mathcal{H}_1 = \frac{1}{2} \langle \dot{r}_1, \dot{r}_1 \rangle_{\hat{\mathcal{M}}_2} + \Phi_1$. This trivial result is left to the reader. In the next part, both subsystems are treated independently for motion stabilization.

6.6.3 Stabilizing the Shape Space

As mentioned earlier, $r_1 \in R_1 \cong \hat{Q}/G_0$, denotes the configuration of the shape space or the reduced space. For motion control, this space is considered as the primary subspace. Its dynamic system is denoted as Σ_1 , whose variation is given by the first of (6.43) in Lemma 6.6. The key objective for motion stabilization is to ensure that Σ_1 is OSP.

Lemma 6.9. Given the system in Lemma 6.6, the shape subsystem, Σ_1 , is rendered OSP, $F_{1d} \mapsto \dot{r}_1$, with the storage function as \mathcal{H}_1 from Lemma 6.7, if the control action is $\hat{F}_1 = -\frac{\partial \Phi_1}{\partial r_1} - D_{r1}\dot{r}_1$, $\overline{F}_1 = -\frac{D\hat{\mathcal{K}}_2}{Dr_1}$. Furthermore, if the disturbance torques, $F_{1d} = 0$, Σ_1 is asymptotically stable about the equilibrium of Φ_1 .

Proof. Taking the time-derivative of \mathcal{H}_1 using F_1 ,

$$\dot{\mathcal{H}}_1 = -\langle \dot{r}_1, \dot{r}_1 \rangle_{D_{r1}} + \langle F_{1d}, \dot{r}_1 \rangle \tag{6.51}$$

which proves the first part of the result. In the case that $F_{1d} = 0$, Σ_1 is proved ZSO (recall Def. 2.12) by using the set $\mathfrak{A} = \{(r, \dot{r}_1) \in T_r R_1 | \dot{\mathcal{H}}_1 = 0\}$. In this set, $\frac{\delta\Phi_1}{\delta r_1} = 0$, and thus, by LaSalle's invariance principle, asymptotic stability follows for the second part [220].

Remark 36. In Lemma 6.9 \overline{F}_1 cancels $\frac{D\hat{K}_2}{Dr_1}$, which is actually the time-varying input for Σ_1 from the nullspace subsystem, Σ_2 . This force is actually related to \mathcal{M}_2 being r_1 -dependent. Thus, by cancelling this force, the resultant PFB is further made geodesic-invariant, i.e., $\hat{\mathcal{M}}_2$ is constant, recall Fig. 2.9 from Chapter 2. Note that in F_1 , we did not explicitly cancel the curvature term $\left(D\mathcal{A}_l(r,\dot{r}_1)\right)^{\top}\frac{\delta l}{\delta \mu}$, because it provides purely gyroscopic torques from the vector potential, $\mathcal{A}_l^{\top}\frac{\delta \hat{K}_2}{\delta \mu}$. Thus, if $D_{r1} = 0$ and $F_{1d} = 0$, we obtain the the electromagnetic geodesic equation in $R_1 = \hat{Q}/G_0$, which is written in a coordinate invariant form as,

$$\nabla_{\dot{r}_1}^{R_1} \dot{r}_1 = -D\mathbb{A}(r, \dot{r}_1, \mu) \tag{6.52}$$

where $\mathbb{A} = (\Phi_1, A)$ is the gauge potential, $A = \mathcal{A}_l^{\top} \frac{\delta \hat{\mathcal{K}}_2}{\delta \mu}$ with $\frac{\delta \hat{\mathcal{K}}_2}{\delta \mu}$ held constant. It is worth pointing out that (6.52) is the Lorentz force law on R_1 . This is the physical interpretation of Lemma 6.9.

6.6.4 Stabilizing the Momentum

Lemma 6.10. Given the system in Lemma 6.6, the nullspace momentum subsystem, Σ_2 , is rendered OSP, in the set \mathfrak{A} , if $\hat{f} = -D_{\tilde{\mu}}\tilde{\mu}$, and is asymptotically stable.

Proof. Computing the time-derivative of \mathcal{H}_2 using \hat{f} , and using Prop. 6.4,

$$\dot{\mathcal{H}}_2 = -\langle \tilde{\mu}, \tilde{\mu} \rangle_{D_{\tilde{\mu}}} + \langle f_d, \tilde{\mu} \rangle \tag{6.53}$$

which proves the first part, and also asymptotic stability follows if $f_d = 0$.

6.6.5 Symmetry-breaking Potential: I

The Lagrangian for the \mathcal{LP} system evolving on $\hat{Q} = G_0 \times R_1$ depends only on the configuration of the primary subspace, $r_1 \in R_1$. However, for motion control purposes, there might arise a need to pose another task on a secondary subspace, R_2 , e.g., maintaining an optimal configuration in the joint space, while performing the primary task on \mathbb{S}^2 in Fig. 2.3-B. Note that using a potential on any other configuration variable other than r_1 breaks the symmetry of the Lagrangian, l, in (6.42), and thus, such a potential for the secondary task is called as a *symmetry-breaking potential* [221]. Let the secondary configuration be $r_2 \in R_2$, with a task potential $\Phi_2(r_2, \overline{r}_2)$, as described in Sec. 6.3. Then, its time-derivative provides a passivity map,

$$\dot{\Phi}_2 = \langle \frac{\partial \Phi_2(r_2, \overline{r}_2)}{\partial r_2}, \dot{r}_2 \rangle = \langle J_2^{\top} \frac{\partial \Phi_2(r_2, \overline{r}_2)}{\partial r_2}, \dot{q} \rangle$$
 (6.54)

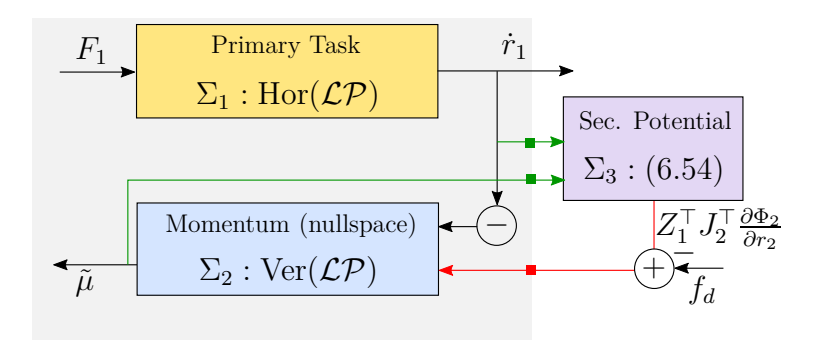


Figure 6.5: Interconnection of primary task and nullspace subsystems with symmetry-breaking potential.

Note that the set \mathfrak{A} , i.e., $\dot{r}_1 = 0$ is the submanifold $\pi_1^{-1}(\overline{r}_1)$ at the primary equilibrium. Evaluating (6.54) in this set yields

$$\tilde{\mu} \mapsto Z_1^{\top} J_2^{\top} \frac{\partial \Phi_2(r_2, \overline{r}_2)}{\partial r_2}.$$
 (6.55)

Theorem 6.1. Given the system in Lemma 6.6 in the set \mathfrak{A} , i.e., $\dot{r}_1 = 0$, the feedback interconnection $\Sigma_2 - \Sigma_3$ is OSP if $\hat{f} = -Z_1^{\top} J_2^{\top} \frac{\partial \Phi_2}{\partial r_2} - D_{\tilde{\mu}} \tilde{\mu}$. The system converges to the equilibrium (\bar{r}_2) of Φ_2 , if $f_d = 0$, and Assumption 6.2 holds.

Proof. Computing the time-derivative of \mathcal{H}_2 using \hat{f} ,

$$\dot{\mathcal{H}}_2 = -\langle \tilde{\mu}, \tilde{\mu} \rangle_{D_{\tilde{\mu}}} + \langle \tilde{\mu}, f_d - Z_1^{\top} J_2^{\top} \frac{\partial \Phi_2}{\partial r_2} \rangle$$
 (6.56)

which yields the OSP map $f_d - Z_1^{\top} J_2^{\top} \frac{\partial \Phi_2}{\partial r_2} \mapsto \tilde{\mu}$. We also recall the passivity of the symmetry-breaking potential in (6.55). Using the fact that a feedback interconnection of passive subsystems $(\Sigma_2 - \Sigma_3)$ is OSP if one (Σ_2) is OSP (Def. 2.14), the first part follows. In the set that $f_d = 0$, the system converges to the set $\mathfrak{B} = \{\dot{q} \in T_q Q | \dot{r}_1, \tilde{\mu} = 0\}$. In this set, $Z_1^{\top} J_2^{\top} \frac{\partial \Phi_2}{\partial r_2} = 0$, which is only satisfied under Assumption 6.2, i.e., if the configuration desired in \overline{r}_2 is compatible with \overline{r}_1 and there is a unique $\overline{q} \in Q = \pi^{-1}(\overline{r})$, where $\overline{r} = (\overline{r}_1, \overline{r}_2)$.

Using Lemma 6.9 transforms the feedback interconnection of the shape and momentum subsystems to a cascade interconnection between them, as shown in Fig. 6.5. This enables converging to the set \mathfrak{A} without the need for discharging power from Σ_3 into Σ_1 , and is the physical intuition behind task-induced symmetry (hierarchy).

Remark 37. The control laws in Lemma 6.9 and Theorem 6.1 provides an elegant Lagrangian alternative to the seminal works on task-induced hierarchy in robotics

[51, 52]. In these works, a skew-symmetric CC term was cancelled to create a so-called dynamic decoupling without analysing its effect on the metric tensor. The geometry of the control problem and the passive interconnection in Fig. 6.4 were also missing. In this Chapter, we have provided a rigorous mathematical proof that this dynamic decoupling can be achieved by generating Killing symmetry of the metric tensor, and the primary task motion is geodesic.

6.6.6 Symmetry-breaking Potential: II

Although the locked energy \mathcal{H}_2 is a valid storage function to analyse stability/passivity properties, it is not the only way. The key idea behind Lyapunov or energy-based passivity analysis is the existence of a level-set at t=0 for which dissipative behaviour drives the system towards a desired equilibrium. Due to the SGC action that generates symmetry in the fiber (Lie group), there is a conservation law on the momentum, p which gives the squared momentum Casimir invariant, $||p||^2$, as a level-set for such an analysis. The main advantage of this approach is that it removes the interconnection between the shape and momentum subsystems, as shown next. Let the system with the new storage function be denoted $\tilde{\Sigma}_2$. Naturally, this changes the control law as follows.

Theorem 6.2. Consider the system in Lemma 6.6 described using the $\Sigma_1 - \tilde{\Sigma}_2$ description. They are independently OSP (without an interconnection), and in the set \mathfrak{A} , i.e., $\dot{r}_1 = 0$, $\tilde{\Sigma}_2 - \Sigma_3$ are OSP, if, $\hat{f} = -\mathcal{M}_2^{-1} Z_1^{\top} J_2^{\top} \frac{\partial \Phi_2}{\partial r_2} - D_p p$. The system converges to the equilibrium of $\Phi_2(r_2, \overline{r}_2)$, if $f_d = 0$, and if it is compatible with the primary task, Φ_1 .

Proof. Choosing the storage function as $\tilde{\mathcal{H}}_2 = \frac{1}{2}||p||^2$, and taking its derivative using the new \hat{f} ,

$$\dot{\tilde{\mathcal{H}}}_2 = -||p||_{D_p}^2 + \langle p, \left(f_d - \left(\mathcal{M}_2^{-1} Z_1^\top J_2^\top \frac{\partial \Phi_2}{\partial r_2} \right) \right) \rangle$$
 (6.57)

which proves the OSP for the momentum subsystem, $f_d - \left(\mathcal{M}_2^{-1} Z_1^{\top} J_2^{\top} \frac{\partial \Phi_2}{\partial r_2}\right) \mapsto p$. Thus, $\Sigma_1 - \tilde{\Sigma}_2$ are not interconnected. Furthermore, as in Lemma 6.1, considering (6.55) and the interconnection of passive subsystems, OSP of the $\tilde{\Sigma}_2 - \Sigma_3$ is proved. In the set that $f_d = 0$, the system converges to the set $\mathfrak{B} = \{\dot{q} \in T_q Q | \dot{r}_1, \tilde{\mu} = 0\}$. In this set, $\mathcal{M}_2^{-1} Z_1^{\top} J_2^{\top} \frac{\partial \Phi_2}{\partial r_2} = 0$, which is only satisfied under Assumption 6.2, i.e., if the configuration desired in Φ_2 is compatible with Φ_1 , as in Lemma 6.1. \square

The interconnection of subsystems is shown in Fig. 6.6, in which clearly Φ_2 only discharges through the momentum subsystem. Hence, it does not affect the shape (primary task) and this is task-induced symmetry. In this chapter, the second method of motion control using symmetry-breaking potential is used for the validation. The experimental validation of the former approach is shown later in the Chapter 8 for an application.

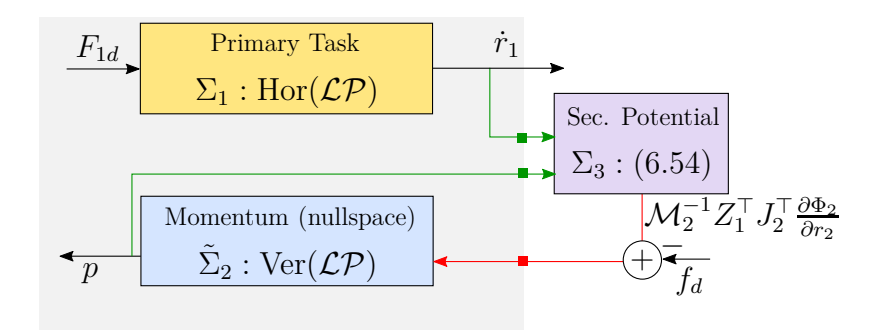


Figure 6.6: Interconnection of primary task and nullspace (momentum-squared) subsystems with symmetry-breaking potential.

6.6.7 Relation to Floating-base Mechanics

The control approach presented here was inspired by the PFB topology and \mathcal{LP} dynamics of the FRM from Chapter 3, and hence, it is prudent to draw parallels between both. The configuration space of a floating-base robot is a principal G-bundle by nature, $\hat{Q} = G_0 \times R_1$, where R_1 refers to the space of joint motions and, $G_0 = SE(3)$ is the Lie group representation of the position and orientation of the mechanism in an inertial frame. The configuration of the FRM is q=(s,x)with $s \in R_1$ and $x \in G_0$. In this case, $\pi(q) : \hat{Q} \mapsto R_1$, is the mapping to the shape space, i.e., $R_1 = \hat{Q}/G_0$. The group acts on \hat{Q} , as $q \cdot g = (s, x \cdot g)$, and the action is transitive and isometric, i.e., the inertia metric tensor, M, on \hat{Q} does not depend upon the Lie group configuration x, i.e., $M \equiv M(s)$. Obviously, this means that the Lie algebra of \mathfrak{g} , corresponding to G_0 , is a symmetry for the metric tensor, i.e., they are Killing vector fields. Thus, it is a matter of fact that the momentum map of floating-base mechanisms have a conserved momenta. The conservation of momentum is modeled in geometric mechanics as a velocity-level Pfaffian-like constraint, called the mechanical connection [14]. The body representation of the connection is the locked velocity, μ , of the FRM. Using the connection, the FRM motion is given by the \mathcal{LP} equations.

While the FRM has natural symmetries arising due to Lie group action, in this chapter, we developed synthetic task-induced symmetries. Thus, there are conserved momenta in both cases. Additionally, the *primary task* serves as the internal shape, while the nullspace motions constitute a Lie group (fiber). Consequently, just like the FRM, we obtain electromagnetic-like geodesic motions on the shape, $R_1 = \hat{Q}/G_0$, while the motion along the nullspace is purely Killing.

6.7 Validation

In this section, simulation results are used to demonstrate evidence to validate the proposed theory. In particular, the key focus is to validate the conservation 6.7 Validation 183

properties and the passive interconnection of the shape and nullspace subsystems. To this end, the metric tensors $\hat{\mathcal{M}}_1(r_1)$, $\hat{\mathcal{M}}_2(r_1)$ that correspond to the \mathcal{LP} dynamics rendered by SGC are required to be computed for the kinetic energies, $\hat{\mathcal{K}}_1 = \frac{1}{2} \langle \dot{r}_1, \dot{r}_1 \rangle_{\hat{\mathcal{M}}_1}$ and $\hat{\mathcal{K}}_2 = \frac{1}{2} \langle \tilde{\mu}, \tilde{\mu} \rangle_{\hat{\mathcal{M}}_2}$ such that they are only r_1 -dependent. This is computed using the standard computation methods in robotics outlined in Chapter 2.6, with a special implementation shown in Fig.6.7. Note that this is only required here for validation purposes, and these quantities are not needed for motion control.

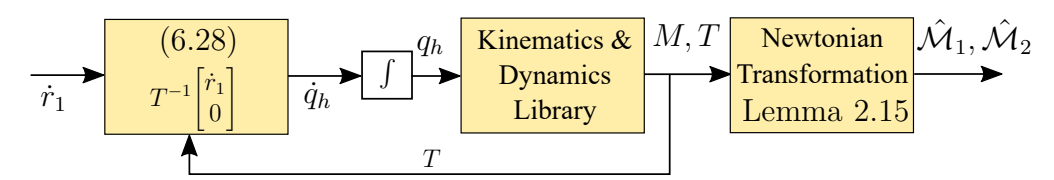


Figure 6.7: Computation of inertias $\hat{\mathcal{M}}_1(r_1)$, $\hat{\mathcal{M}}_2(r_1)$ of the effective \mathcal{LP} system using standard robotics libraries.

In the following, to implement \overline{f} in 6.5, the multibody dynamics software [22] was used, which provides recursive computation of M, C matrices and its derivatives for the \mathcal{EL} equations of mechanisms. It requires the computation of forces related to the ID matrix M_d , which is obtained as,

$$C(q, \dot{q}) = \dot{M}(q, \dot{q}) - \frac{\delta L(q, \dot{q})}{\delta q} \Rightarrow M_d(q, \dot{q})^{\top} \dot{q} = C(q, \dot{q}) \dot{q} - M_v(q, \dot{q}) \dot{q}$$
(6.58)

and \dot{Z}_1 is computed numerically using a numerical differentiation.

To enforce Lemma 6.9, the partial derivative of the locked kinetic energy $(\hat{\mathcal{K}}_2)$ with respect to r_1 is required. This is computed as follows. Note that, $\langle \tilde{\mu}, \tilde{\mu} \rangle_{\mathcal{M}_2} = \langle Z_1 \tilde{\mu}, Z_1 \tilde{\mu} \rangle_M$. Thus,

$$\overline{F}_{1} = \frac{\delta\langle \tilde{\mu}, \tilde{\mu} \rangle_{\mathcal{M}_{2}}}{\delta r_{1}} = \begin{bmatrix} 1_{2,2} & 0_{2,5} \end{bmatrix} T^{-\top} \frac{\delta\langle Z_{1}\tilde{\mu}, Z_{1}\tilde{\mu} \rangle_{M}}{\delta q}
= \begin{bmatrix} 1 & 0 \end{bmatrix} T^{-\top} M_{d}(q, Z_{1}\tilde{\mu})^{\top} Z_{1}\tilde{\mu}$$
(6.59)

where M_d^{\top} is computed in the same way as (6.58), but with the vertical component $Z_1\tilde{\mu}$. Using these tools, the validation is performed in two stages below.

6.7.1 Symmetry Generation and Shape Regulation

An articulated robotic mechanism consisting of n=7 revolute joints was considered with $Q=\mathbb{T}^7$, see Fig. 6.8. This mechanism was manufactured during the ESA-funded MIRROR project for In-Orbit Assembly tasks [47, 66]. The operational space was considered to be the comprise of the first two joints, i.e., $R_1=\mathbb{T}^2$

with configuration $r=(q_1,q_2)\in\mathbb{T}^2$. Thus, the forward kinematics of the surjective submersion is a constant map, $r_1=\pi_1(q)=J_1q$, with $J_1=\begin{bmatrix} 1 & 0 & 0_5 \\ 0 & 1 & 0_5 \end{bmatrix}$, and its differential is $\dot{r}_1=d\pi_1\dot{q}=J_1\dot{q}$. The differential map is used to define the vertical space as, $\mathbb{V}_{1q}=Z_1=\mathrm{Kern}(J_1)$, such that $Z_1=\begin{bmatrix} 0_5 & 0_5 & \mathbb{I}_{5,5} \end{bmatrix}^\top$. A linear primary potential, $\Phi_1=\frac{1}{2}\langle r_1,r_1\rangle_k$, with equilibrium $\overline{r}_1=0$, where $k=\mathrm{diag}(20,20)$ is the spring stiffness is used to generate harmonic motions on $R_1=\mathbb{T}^2$.

The proposed control approach was implemented so that the mechanism is forced to behave as if it operates in the configuration space, $\hat{Q} = \mathbb{T}^2 \times \mathbb{R}^5$, that is a PFB, instead of Q. Applying Lemma 6.5, $\overline{f} = Z_1^{\top}(C - M_v)\dot{q}$. This creates the synthetic symmetry in the considered \mathcal{EL} system. The motion characteristics on the total space, Q, are shown in Fig. 6.8. As remarked in Sec. 6.2.1, the energy in Q is not a conserved quantity. In the right of Fig. 6.8, the motion (\dot{q}) can be seen to be dynamic. Recall that the objective is to enforce a priority on the motion in $R_1 = \mathbb{T}^2$.

The variation in the proposed kinetic $(\hat{\mathcal{K}}_1)$ and potential (Φ_1) energies are shown in the left of Fig. 6.10. Note that the reduced Hamiltonian, $\mathcal{H}_1 = \hat{\mathcal{K}}_1 + \Phi_1$, remains conserved. This allows motion control design in an independent manner on $R_1 = \mathbb{T}^2$. This is aided by the fact that the fiber (nullspace) consisting of motions on $(q_3...q_7)$ conserves momentum. This is shown in the center and right. In the center, the squared momentum Casimir invariant, p^2 , is shown. Since it is conserved, it provides a level-set for further stabilization of a secondary task along the fiber. On the right, it can also be seen that the momenta along the basis (3...7) corresponding to the $(q_3...q_7)$ joints is conserved.

Using the same robotic system, another simulation was performed for a non-trivial primary task, which was posed on the Cartesian position of the end-effector, $r_1 = \pi_1(q) \in \mathbb{R}^3$. In this case, $d\pi_1 = J_1$ is configuration dependent, and consequently, the nullspace basis Z_1 , i.e., $\dot{Z}_1 \neq 0$. To implement Lemma 6.5, computations in the previous simulation were used. On the left of Fig. 6.11, it can be seen that the shape Hamiltonian, \mathcal{H}_1 is conserved resulting in a geodesic motion in Cartesian position. Due to the enforced symmetry, the remaining 4 momenta are conserved as seen on the right. This validates symmetry generation of the proposed SGC and shape stabilization in Lemmas 6.5 and 6.9.

6.7.2 Motion Control with Symmetry-breaking Potential

In this subsection, the shape control law in Lemma 6.9 is employed for the Cartesian position, $r_1 \in \mathbb{R}^3$ of the end-effector on a KUKA LBR iisy R1300 (n = 6) robot, such that $\dot{r}_1 = J_1(q)\dot{q}$. The shape potential was, $\Phi_1 = \frac{1}{2}\langle \delta r_1, \delta r_1 \rangle_{k_1}$, where $\delta r_1 = r_1 - \overline{r}_1$, $\overline{r}_1 \in \mathbb{R}^3$ is the desired setpoint and $k_1 = 5[\text{N/m}]$ is the spring potential. The Rayleigh damping is chosen with gain, $D_{r1} = 2[\text{N/(m/s)}]$. The secondary subspace comprises the last three joint positions in the configura-

6.7 Validation 185

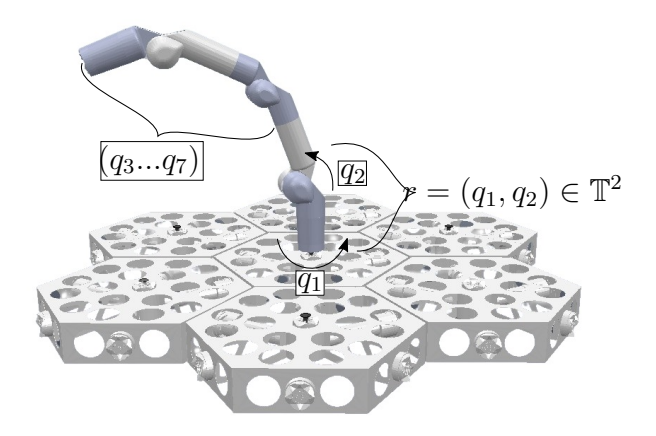


Figure 6.8: Simulation using the ESA-funded MIRROR robot with n=7 joints meant for In-Orbit Assembly. In the simulation, the operational space was considered to be $R_1 = \mathbb{T}^2$ with configuration $r_1 = (q_1, q_2) \in \mathbb{T}^2$, i.e., $n_1 = 2$. The motion in the remaining joints forms the fiber.

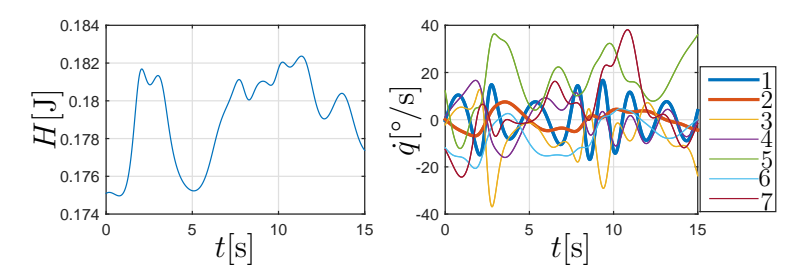


Figure 6.9: Motion characteristics on the total space, Q. Left: Total energy is not conserved during motions; Right: System Velocity with bases 1 (blue) and 2 (red) under the influence of a potential on $R_1 = Q/G_0$.

tion space, i.e., $R_2 = \mathbb{T}^3$. In this subspace, the stiffness potential is chosen as, $\Phi_2 = \frac{1}{2} \langle \delta r_2, \delta r_2 \rangle_{k_2}$, where $\delta r_2 = r_2 - \overline{r}_2$, $\overline{r}_2 \in R_2$ is the setpoint with joint stiffness $k_2 = 1$ [N.m/rad]. Note that no damping is applied to the momentum subspace, i.e., $D_p = 0$ in Theorem 6.2, to demonstrate that even during harmonic motions, the momentum-subsystem provides an energy-like level-set.

For the symmetry generation in Lemma 6.5 and shape regulation in Lemma 6.9, computations similar to the previous simulation were used. On the left of Fig. 6.12, the shape Hamiltonian \mathcal{H}_1 is shown to monotonically decay over time due to the damping, according to Lemma 6.9. In the center, motion characteristics in the nullspace (fiber) subsystem are shown. In particular, it can be seen that the energy-like function, $E_p = \tilde{\mathcal{H}}_2 + \Phi_2$ reaches a level-set for t > 15[s], i.e., in the set, $\mathcal{H}_1 = 0$. The corresponding momentum variation under the potential is shown on the right. This proves empirically the Lemma 6.9 and Theorem 6.2,

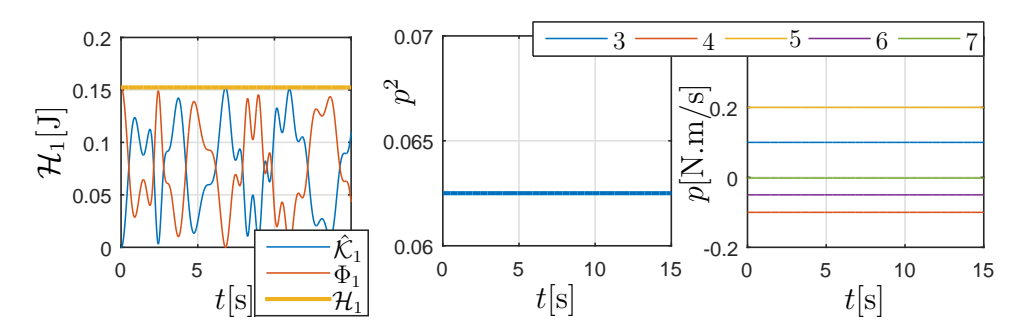


Figure 6.10: Left: Conservation of shape Hamiltonian (\mathcal{H}_1). Center: Squared-momentum Casimir invariant, p^2 along symmetry directions. Right: Momentum, p, is conserved along symmetry during motions.

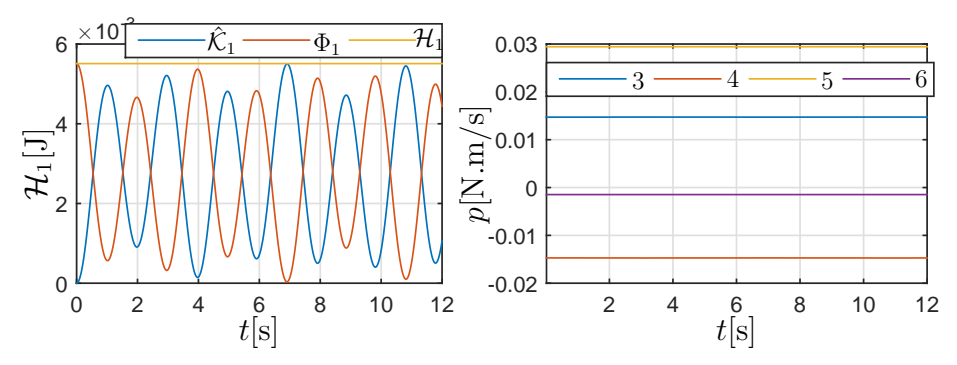


Figure 6.11: Left: Shape Hamiltonian, \mathcal{H}_1 , is conserved because motion on R_1 is geodesic. Right: Momentum, p, along nullspace (fiber) which constitutes the symmetry directions is conserved during motions.

and provides the necessary conditions for motion control with hierarchy. To further demonstrate robustness of the proposed approach, the secondary setpoint, \overline{r}_2 , was given two step increments, as shown in Fig. 6.13, in which the arrows mark the instant of the step. It is seen on the left that E_p simply reaches a new level-set, with an increase in limit-cycle amplitude. On the right, the limit-cycle are shown through the variation in the momenta of the nullspace. Of course, as proved in Lemma 6.9, the shape subsystem remained invariant to the step increases in Φ_2 , and consequently E_p .

With these results, the key results of this chapter were validated in terms of conserved energies and momenta. In particular, the novel control law that implements task-induced variational symmetry comprising of Lemmas 6.5, 6.9 and Theorem 6.2 have been validated through simulation results. In Chapter 8, the experimental validation of Theorem 6.2 will be demonstrated for a practical application.

6.8 Conclusion 187

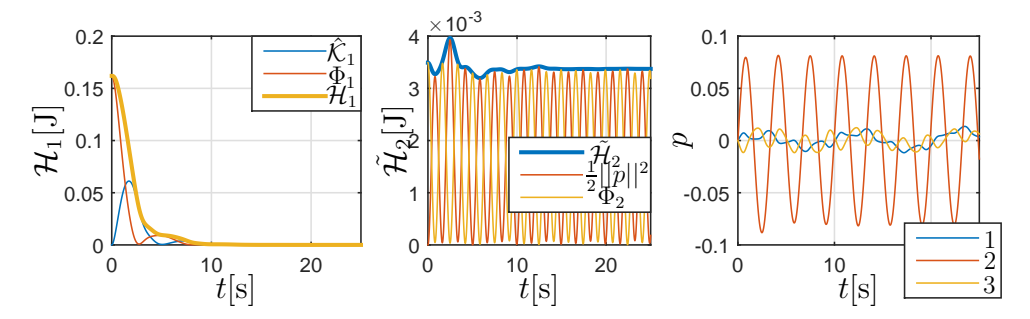


Figure 6.12: Left: Asymptotic convergence on shape space (operational space), $R_1 = Q/G_0$ with damping. Center: The Energy function based on Casimir invariant, $\tilde{\mathcal{H}}_2$, provides a level-set when $\mathcal{H}_1 = 0$, even with harmonic motion. Right: Momentum, p, is not conserved during motions.

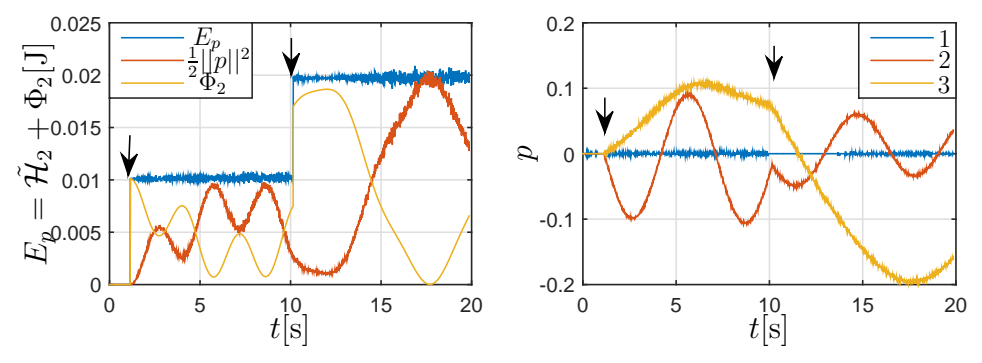


Figure 6.13: Motion characteristics on the fiber space, i.e., along directions of generated symmetry. Left: The Energy function based on Casimir invariant, $E_p = \tilde{\mathcal{H}}_2 + \Phi_2$, provides level-sets (for step changes in Φ_2 , arrows) when $\mathcal{H}_1 = 0$, even with harmonic motion. Right: Time-evolution of Momentum, p.

6.8 Conclusion

The narrative in this chapter is from space to earth. Indeed, the PFB topology, \mathcal{LP} dynamics, and the passive feedback interconnection of shape and momentum subsystems of an orbital FRM served as building blocks to achieve task-induced variational symmetry (hierarchy) in motion control of general \mathcal{EL} systems that might not possess symmetry. The proposed approach starts with Lemma 6.5, which generates a Lagrangian symmetry in a way that the closed-loop inertia metric tensor only depends on the primary task configuration. This step transforms the \mathcal{EL} system into an \mathcal{LP} system, in which the shape (primary task) dynamics is a time-varying electromagnetic geodesic equation. Lemma 6.9 cancels CC terms to ensure geodesic invariance by resulting a time-varying electromagnetic geodesic equation, which provides a subspace Hamiltonian to ascertain stability. To completely realized task-induced symmetry, two approaches were exploited that used the natural locked energy and the momentum squared Casimir invariant in the

energy descriptions. We recall that both of these are conserved quantities in \mathcal{LP} systems. In the set that the primary task has converged, stabilization of the secondary task was proved using Theorems 6.2 and 6.2. While the former used the natural energy function, the latter employed the squared momentum in the stability analysis. The energy-momentum concepts proposed in this chapter were investigated thoroughly and results prove their correctness. Recently, new methods have been developed to learn Lyapunov functions for multi-task execution. However, the key challenge is in specifying the metric tensor. As future work, the metric behaviour in the proposed control approach here will be used to fill this gap, and create a physics-informed learning method to achieve hierarchical motion control. Convergence of hierarchical motion control was proved here by stabilizing the shape and momentum subsystem energies sequentially. This begs the question if it can be achieved with a single energy function, as was done using Direct PBC approach in Chapter 5. This subject will be addressed in the next chapter.

99

Task-induced Algebraic Symmetry in Motion Control

(As far as I see, all a priori statements in physics find their origin in symmetry [222].

Hermann Weyl, Symmetry, 1952

7.1 Introduction

In motion control, the \mathcal{EL} system often has more DoF than the dimension of its primary operational space. The resulting redundancy not only needs to be stabilized but enables improving the system configuration by virtue of another task on a secondary operational space. This should be realized such that the primary task assumes precedence over the secondary, see Fig. 7.1, unlike in superposition of impedances. This means that the control action due to the secondary task should be an algebraic symmetry of the primary. In particular, it is required to establish a hierarchy (or priority), [215, 223, 224], [52, 206–209]. In Chapter 6, this task-induced symmetry was achieved at a variational level, i.e., control action transformed the \mathcal{EL} system into an \mathcal{LP} system, in which the inertia metric tensor was rendered independent of the fiber (nullspace) position. This enabled a hierarchical stabilization mechanism in which the primary task (shape) converged first resulting in an invariant set in which the secondary task also converged. This resulted from employing two energy-like functions hierarchically. However, this approach does not give any stability guarantee for the fiber during the transient state of the primary. Therefore, it is natural to ask if the task-induced algebraic

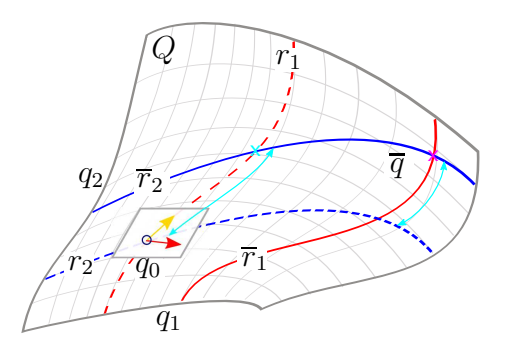


Figure 7.1: Motion control scenario for a particle on $Q \subset \mathbb{R}^3$, $q = (r_1, r_2) \in Q$. The primary (secondary) operational spaces are the lines in red (blue), $r_i = \pi_i(q) \in R_i$. The initial configuration is $q_0 \in Q$, which is the intersection of the current operational space configurations (dashed lines). The desired equilibrium is $\overline{q} \in Q$, which is an intersection of $(\overline{r}_1, \overline{r}_2)$. It is required to impose an algebraic symmetry such that the proportional action for the secondary task is projected along the dual basis of the orthogonal subspace to the primary action, i.e., prioritizes R_1 .

symmetry can be enforced through a single energy-like function, as in Theorem 5.1. This is the main contribution of this chapter.

7.1.1 Related Work

The concept of hierarchy was proposed almost 20 years ago in the form of kinematic and dynamic decoupling of maps of the tangent space [215, 223]. Motion control was realized by the superposition of the proportional action due to the primary task, and an endomorphism (nullspace projection) of the proportional action due to the secondary task. In these schemes, kinematic decoupling was achieved using a configuration-dependent map, whereas dynamic decoupling used a metric-dependent map [215, 224]. In the early days, hierarchy was imposed using feedback linearization [215, 223].

In the realm of hierarchical PBC, two levels of hierarchy was seminally resolved in [207] (see also [52]). In these above works, the dynamic decoupling of the tangent space was used to rewrite the original \mathcal{EL} dynamics as the dynamics of a subspace called the primary task and decoupled nullspace velocities. The CC torques corresponding to the block off-diagonal parts of the CC matrix were compensated to prove Lyapunov stability with semi-definite functions. However, in the aforementioned prior works, stability and passivity properties were ascertained through hierarchical level-sets, and system-wide transient behaviour was inconclusive. Task hierarchy is also useful when there is a limit-cycle requirement in one of the operational spaces. In [225], the method in [207] was extended to stabilize a limit cycle in the nullspace after the primary task was converged.

7.1 Introduction 191

However, the analysis fails if the limit cycle requirement is placed on the primary space, e.g., hip motion during walking. Thus, a conserved Hamiltonian (natural energy) for the entire \mathcal{EL} system under task hierarchy is required. The main obstruction earlier was that the nullspace projection of the secondary task potential results in non-Hamiltonian dynamics with non-zero curl of the control forces. This is a rare topic in classical mechanics, see [226, 227], and prevents energy-based stability analysis.

In the theory of \mathcal{EL} systems, a hierarchy is a special form of *symmetry*, i.e., invariance of a quantity, e.g., a potential scalar, w.r.t. motions along a vector field [95]. In the context of PBC without inertia-shaping [3], the symmetry of the shaped potential is of importance because it implies an orthogonality condition for the proportional actions. In this chapter, I show that the task hierarchy indeed is: a task-induced symmetry of the algebraic system of the proportional actions.

7.1.2 Key Contributions

The contributions of this work are the following.

- 1. For the first time, task-induced algebraic symmetry (hierarchy) and the associated motion control problem have been addressed and solved using a single Hamiltonian, which characterizes the whole \mathcal{EL} system. Thus, the contribution of this chapter is fundamental and toward the explanation of motion phenomena under task-induced algebraic symmetry.
- 2. In Lemma 7.4, it is shown that the projection of the proportional action of the secondary task to the fiber (nullspace) results in a *restriction* of the secondary task potential. However, the fiber equilibrium of this restricted potential is state-dependent, and varies with the primary task configuration. This generates inertial forces and imparts a non-conservative nature to the dynamics.
- 3. In Theorem 7.1, I derive a novel control law that tracks the wandering equilibrium in the fiber and conserves a new Hamiltonian. Although the proposed Hamiltonian is different from that of the \mathcal{EL} system, it preserves the natural metric tensor for the non-conservative \mathcal{EL} system. This Hamiltonian serves as a candidate function in the context of Lyapunov and PBC approaches using which I prove full motion stabilization with damping injection and limit cycle behaviour.
- 4. Simulation results for a simple \mathcal{EL} system are used to illustrate the key ideas (e.g., conserved Hamiltonian, variation of equilibrium, limit cycle), so that the audience can grasp the motion phenomena with ease.

The chapter is organized as follows. In Sec. 7.2, the preliminaries of \mathcal{EL} mechanics in the context of operational spaces is described. In Sec. 7.3, I use the tools from geometric mechanics on fibered manifolds to formulate the problem of task-induced algebraic symmetry between two operational spaces. In Sec. 7.4, I show that the task-induced algebraic symmetry is inherently a non-Hamiltonian problem resulting in a system with curl forces. I derive a novel proportional action that conserves a new Hamiltonian, but preserves the metric tensor. Finally in, Sec. 7.5, concluding remarks and the future scope of work are described.

7.2 Preliminaries

In this section, the relevant theory of \mathcal{EL} mechanics under proportional actions arising from scalar potential fields in context of operational spaces is described.

7.2.1 The considered \mathcal{EL} system

The \mathcal{EL} system in (2.15) from Chapter 2 is considered in this chapter, as in Chapter 6. It is assumed that Assumption 6.1 is fulfilled and Property 6.1 is satisfied.

Example 5. Let us consider a particle with configuration $q = (q_1, q_2) \in Q \equiv \mathbb{R}^2$, see Fig. 7.2. Let its mass be $M = \begin{bmatrix} 10 & 4 \\ 4 & 5 \end{bmatrix}$ [Kg], which gives the kinetic energy, $K = \frac{1}{2} \langle \dot{q}, \dot{q} \rangle_M$. Its Euler-Lagrange equations are,

$$\nabla_{\dot{q}}\dot{q} = \tau^{\sharp} \Rightarrow \frac{d}{dt}(M\dot{q}) = \tau \tag{7.1}$$

where $\tau \in \mathbb{R}^2$ is the control action.

Although Example 5 has a configuration-independent affine metric, it serves as a strong candidate (inertia coupling) to show that task hierarchy is a non-Hamiltonian problem. However, the theory is developed with generality to \mathcal{EL} systems and their motion control.

For this, it might be required to regulate the motion on operational spaces, R_i , such that $\dim(R_i) = n_i \leq n$. Consider the primary (secondary) task i = 1 (i = 2) on the corresponding operational spaces. There is a map $\pi_i : Q \to R_i$ to each operational space, R_i , and the corresponding operational space configuration $r_i \in R_i$ is the forward kinematics map as the following,

$$r = (r_1, r_2) = \pi(q) = (\pi_1(q), \pi_2(q))$$
(7.2)

where π is a *locally* invertible transformation, i.e., $\pi: Q \to R$, $R = R_1 \times R_2$ is the total operational space, i.e., the Cartesian product of the primary and secondary operational spaces.

7.2 Preliminaries 193

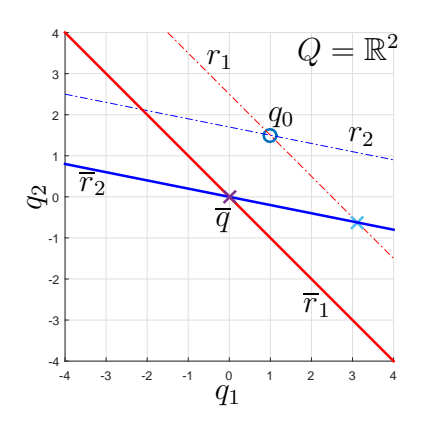


Figure 7.2: Motion control scenario for a particle in affine space $Q = \mathbb{R}^2$, $q = (q_1, q_2) \in Q$. The primary (secondary) operational spaces are the lines in red (blue), $r_i = \pi_i = \begin{bmatrix} k_i & 1 \end{bmatrix} q$. The initial configuration is $q_0 \in Q$, and the desired equilibrium is $\overline{q} \in Q$, which is an intersection of $(\overline{r}_1, \overline{r}_2)$.

Assumption 7.1. The operational spaces, R_i , satisfy $\dim(R_i) = n_i$ and $\sum n_i = n$ and the total task posed on the operational spaces should satisfy a unique point in Q.

Assumption 7.1 is standard as in Chapter 6.

Def. 7.1. For a \mathcal{EL} system, let Q be the configuration space and $R_i \subset \mathbb{R}^{n_i}$, i = 1, 2, be the operational spaces, which are differentiable manifolds. Then, the differentiable map $\pi_i : Q \mapsto R_i$ is a surjective submersion at $q \in Q$ if its differential, $J_i : T_qQ \mapsto T_{\pi_i(q)}R_i$ is a surjective linear map.

In Example 5, each map $\pi_i : \mathbb{R}^2 \to \mathbb{R}$ is considered as a line of slope k_i such that,

$$r = \begin{bmatrix} r_1 \\ r_2 \end{bmatrix} = \pi(q) = \begin{bmatrix} \pi_1(q) \\ \pi_2(q) \end{bmatrix} = \begin{bmatrix} k_1 & 1 \\ k_2 & 1 \end{bmatrix} \begin{bmatrix} q_1 \\ q_2 \end{bmatrix}$$
 (7.3)

with $k_1 = 1$ and $k_2 = 0.2$. Obviously, $q \equiv (r_1, r_2)$, i.e., the current configuration is uniquely given by the configurations on the two operational spaces. Note that in Fig. 7.2, the initial condition $q_0 = (1, 1.5) \in Q$ is the intersection of the primary (red) and secondary (blue) dashed lines denoting the current configuration in the respective spaces.

The differential of the task maps π_i , $d\pi_i: T_qQ \mapsto T_{r_1}R_1$, give the total operational space Jacobian map as,

$$\dot{r} = J(q)\dot{q} = \begin{bmatrix} J_1(q) \\ J_2(q) \end{bmatrix} \dot{q}, \ J_i = d\pi_i = \frac{\partial \pi_i}{\partial q}^{\top}$$
 (7.4)

which for Example 5 is,

$$\dot{r} = J\dot{q} = \begin{bmatrix} k_1 & 1\\ k_2 & 1 \end{bmatrix} \dot{q} \tag{7.5}$$

To understand the nature of task conflict, I refer to [215, I for two key definitions.

Def. 7.2. Kinematic decoupling: Consider the \mathcal{EL} system in (2.15) with two tangent space maps $\mathcal{T}_1 \in \mathbb{R}^{n_1 \times n}$ and $\mathcal{T}_2 \in \mathbb{R}^{n_2 \times n}$, which may not be Jacobians of a kinematics submersion, satisfying $n = n_1 + n_2$. Let $\mathcal{T}^{\top} = \begin{bmatrix} \mathcal{T}_1^{\top} & \mathcal{T}_2^{\top} \end{bmatrix}$. Then, the velocities resulting from these maps, $\mathcal{T}_1\dot{q}$ and $\mathcal{T}_2\dot{q}$, are kinematically decoupled if,

$$\mathcal{T}_1 \mathcal{T}^{-1} \begin{bmatrix} 0 \\ \mathcal{T}_2 \end{bmatrix} \dot{q} = 0 = \mathcal{T}_2 \mathcal{T}^{-1} \begin{bmatrix} \mathcal{T}_1 \\ 0 \end{bmatrix} \dot{q}$$
 (7.6)

Def. 7.2 is, however, a tautology (always true) if \mathcal{T} is invertible. This can be proved as follows. Let $\mathcal{T}^{-1} = \begin{bmatrix} A & B \end{bmatrix}$. Using $\mathcal{T}\mathcal{T}^{-1} = \mathbb{I}_{n,n}$, I get, \mathcal{T}_1B and \mathcal{T}_2A are 0. Using these properties, (7.6) always follows. Thus, the following definition is a better representation of task conflict for this chapter.

Def. 7.3. Geometric decoupling: Given Def. 7.2, the velocities $\mathcal{T}_1\dot{q}$ and $\mathcal{T}_2\dot{q}$, are geometrically decoupled if,

$$\left\langle \mathcal{T}^{-1} \begin{bmatrix} 0 \\ \mathcal{T}_2 \end{bmatrix} \dot{q}, \mathcal{T}^{-1} \begin{bmatrix} \mathcal{T}_1 \\ 0 \end{bmatrix} \dot{q} \right\rangle_W = 0 \tag{7.7}$$

where $W \succ 0$ is a weighing matrix that determines the geometry for decoupling. Obviously by Def. 7.3, the operational space velocities in (7.4), \dot{r}_1 and \dot{r}_2 , are not necessarily geometrically decoupled for a given W.

Lemma 7.1. Given a \mathcal{EL} system with a point transformation, i.e., a locally invertible transformation $r = \pi(q)$, it is described by a local Lagrangian as, $\hat{L}(r, \dot{r})$. The \mathcal{EL} equations remain invariant and are described as [91, pp. 30],

$$\frac{d}{dt}\frac{\delta\hat{L}}{\delta\dot{r}} - \frac{\delta\hat{L}}{\delta r} = F \Rightarrow \hat{\nabla}_{\dot{r}}\dot{r} = F^{\sharp} \Rightarrow \Lambda(q)\ddot{r} + \mathcal{C}(r,\dot{r})\dot{r} = F \tag{7.8}$$

where $F = J^{-\top}\tau \in T_r^{\top}R$, $\Lambda = J^{-\top}MJ^{-1}$ is the total operational space inertia metric tensor on $R_1 \times R_2$, and $C = J^{-\top}(CJ^{-1} - M\dot{J}^{-1})$ is the corresponding CC matrix, and $\hat{\nabla}$ is the covariant derivative on R.

Let us consider the equilibria $\overline{r} = (\overline{r}_1, \overline{r}_2) \in R$ which gives a unique point $\overline{q} = \pi^{-1}(\overline{r}) = \pi^{-1}(\overline{r}_1, \overline{r}_2)$, purple \times in Fig. 7.2. The unique equilibrium \overline{q} is also the intersection point of the two surfaces denoting the desired operational space configurations in R_1, R_2 .

7.2 Preliminaries 195

7.2.2 Proportional Action

Typically in motion control in PBC approaches [13, 189], the proportional action arises from the differential of a potential function on the operational space, R_i , denoted as, $\Phi_i : R_i \to \mathbb{R}$. Motion stabilization about an equilibrium is then achieved through damping injection. In this work, the motion of \mathcal{EL} system (e.g., particle in Fig. 7.2) is analysed from a mechanics perspective to emphasize the conserved Hamiltonian associated with task-induced algebraic symmetry in \mathcal{EL} systems. This is required to bring forward the key contribution, i.e., Lyapunov-based motion stabilization, while considering a class of non-conservative systems with curl forces. To that end, the proposed theory of motion is developed while presupposing the effect of scalar potentials corresponding to the proportional terms. Damping injection for motion stabilization is treated later. The power flow due to the proportional action in the operational space R_i is given by the time-derivative of the corresponding potential,

$$\mathcal{L}_{\dot{r}_i}\Phi_i(r_i, \overline{r}_i) = \frac{d}{dt}\Phi_i(r_i, \overline{r}_i) = \langle \frac{\partial \Phi_i}{\partial r_i}, \dot{r}_i \rangle \tag{7.9}$$

The differential in R_i is then pulled back to the configuration space Q as,

$$\mathcal{L}_{\dot{q}}\Phi_{i}(r_{i}, \overline{r}_{i}) = \langle \frac{\partial \Phi_{i}}{\partial r_{i}}, \dot{r}_{i} \rangle = \langle J_{i}^{\top} \frac{\partial \Phi_{i}}{\partial r_{i}}, \dot{q} \rangle$$
 (7.10)

In the case of superposition of proportional actions [204, 205], the total force acting is,

$$\tau = \sum_{i=1} F_i = -\sum_{i=1}^2 J_i^{\top} \frac{\partial \Phi_i(r_i, \overline{r}_i)}{\partial r_i}$$
 (7.11)

Lemma 7.2. Given the \mathcal{EL} system in (2.15), the proportional action in (7.11) conserves the Hamiltonian, $H = K(q, \dot{q}) + \sum \Phi_i(r_i, \overline{r_i})$.

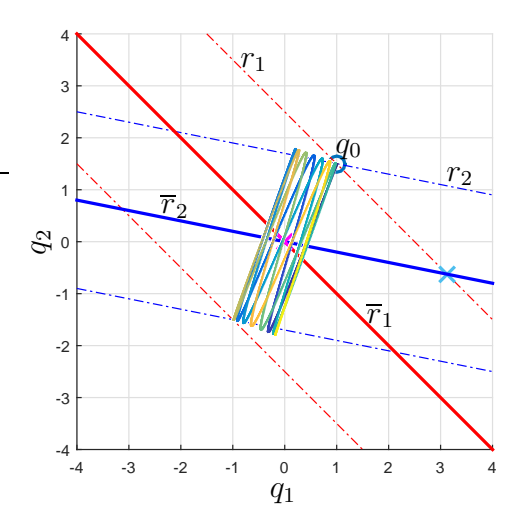
Proof. Taking the time-derivative of H, using (7.10) and Prop. 6.1, $\dot{H} = 0$.

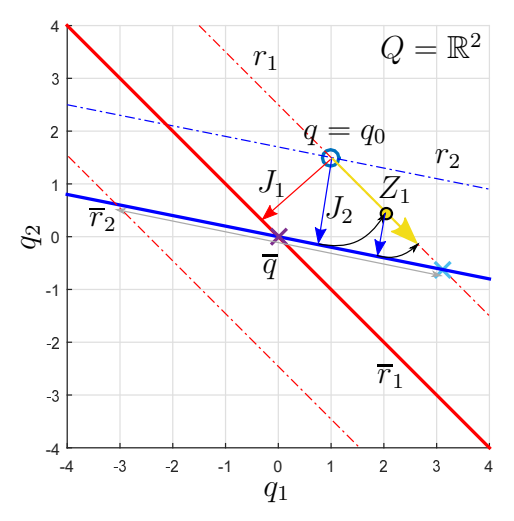
For the configuration space in Example 5, $Q = \mathbb{R}^2$, the orbit (due to the undamped motion) of the particle due to superposition proportional action in Lemma 7.2 is confined in a bounded rectangular region, as shown in Fig. 7.3a, and the shape of the rectangular region is determined by the magnitudes of $\text{Hess}(\Phi_i)$. In this example, linear spring-like scalar potentials, $\Phi_i = \frac{1}{2} \langle \delta r_i, \delta r_i \rangle_{P_i}$, are used where $\delta r_i = r_i - \overline{r}_i$ and $P_1 = 4$, $P_2 = 20$, which gives $\text{Hess}(\Phi_i) = P_i$.

The following property is introduced here to apply Property 2.1, and will be used later to write the operational space potentials, Φ_i as functions in Q.

While Lemma 7.2 provides a conserved Hamiltonian, H, that serves as a Lyapunov candidate, both potentials, Φ_i , charge and discharge in a way that can conflict with each other. This means that

$$\langle J_1^{\top} \frac{\partial \Phi_1(r_1, \overline{r}_1)}{\partial r_1}, J_2^{\top} \frac{\partial \Phi_2(r_2, \overline{r}_2)}{\partial r_2} \rangle_{M(q)^{-1}} \neq 0,$$
 (7.12)





sition of proportional actions in Lemma (red and blue arrows) J_i are not orthog-7.2, $P_1 = 4$ and $P_2 = 20$. Trajectory is onal. The basis orthogonal to J_1 is Z_1 colour-graded from blue $(t=0[\mathbf{s}])$ to yel- (yellow). The equilibrium of the secondary rectangular region.

(a) Orbit of the 2D particle with superpo- (b) Example 5: The Jacobian directions low (t = 30[s]). Motion is bounded in a task, \overline{r}_2 , projected along Z_1 is at its intersection with current r_1 , the blue \times .

which results because the operational space configurations, R_1 and R_2 , do not satisfy a surface orthogonality condition relative to each other. In the example of Fig. 7.2, this means that r_1 and r_2 are not orthogonal. Consequently, J_1 and J_2 are also not orthogonal, as is explicitly shown in Fig. 7.3b. In the following section, \mathcal{EL} mechanics on fibered manifolds is introduced to impose task-induced algebraic symmetry.

7.3 \mathcal{EL} Mechanics on Fibered Manifolds

In this section, the key concepts from geometric mechanics on fibered manifolds are revisited from Chapter 6. Using this formalism, I prove that the projection of the proportional action of the secondary task to the fiber (nullspace) actually corresponds to a restricted potential in the manifold of self-motions. Using the \mathcal{EL} equations of motion in the fibered bundle formalism, energy conservation is proved while considering a fiber potential with a stationary equilibrium.

In robotics, often the secondary potential is pulled back along the nullspace projector (yellow arrow in Fig. 7.3b) of the primary task differential (Jacobian) [52, 207, 224]. Let the nullspace basis of the map J_1 be $Z_1 \in \mathbb{R}^{n \times (n-n_1)}$. In this work, I assume that each nullspace basis satisfies the orthogonality and unity norm criteria, i.e.,

$$\langle Z_1^j, Z_1^i \rangle_A = 0, \ i \neq j, \ \langle Z_1^j, Z_1^j \rangle_A = 1$$
 (7.13)

where $A \in \mathbb{R}^{n \times n}$ is a weighing matrix for the inner product. While the local operational space transformation $\pi: Q \to R$ in (6.11) is useful, there is an alternative way to describe the system.

7.3.1 Task-induced Fiber Bundle

The task-induced fiber bundle is identical to the one presented in Chapter 6. In the following, the key points are summarized. The surjective submersion, π_1 , of the primary task from Def. 2.3 results in a fibered manifold, denoted as a triplet (Q, π_1, R_1) . Each fiber $\pi_1^{-1}(r_1)$ for $r_1 \in R_1$ is an embedded submanifold of Q with dimension $k_1 = n - n_1$ [100], which is also known as the manifold of self-motions [101]. The task-induced fiber bundle is denoted by the short exact sequence as,

where $\Psi_1: \pi_1^{-1}(r_1) \to Q$ is the inclusion map of the embedded submanifold at each r_1 . The function Ψ_1 can be determined locally using the secondary task submersion,

$$\pi_1(q) = r_1, \ \pi_2(q) = r_2, \ s(q) = 0$$
 (7.15)

where s determines the fiber origin, i.e., the zero of the fiber at a given $\pi_1(q) = r_1$. For every $q \in Q$, the primary submersion π_1 , the canonical vertical subspace is, \mathbb{V}_1 , on the tangent bundle TQ, written as, $\mathbb{V}_{1q} = \mathrm{Kern}(J_1(q))$, where \mathbb{V}_{1q} is a k_1 -dimensional vector space. The fibered manifold provides canonical exact sequences for the tangent and the cotangent spaces as follows [104, eq. 1.4.3],

$$\mathbb{V}_{1}q \xrightarrow{Z_{1}} T_{q}Q \xrightarrow{J_{1}} T_{r_{1}}R_{1}$$

$$\downarrow^{J_{2}Z_{1}} \downarrow_{J_{2}} \downarrow^{J}$$

$$\downarrow^{J_{1}Z_{1}} T_{r_{2}}R_{2} \qquad T_{r}R$$

$$(7.16)$$

$$T_{r_1}^{\top} R_1 \xrightarrow{J_1^{\top}} T_q^{\top} Q \xrightarrow{Z_1^{\top}} \mathbb{V}_1 q^{\top}$$

$$\downarrow^{J^{\top}} J_2^{\top} \uparrow^{Z_1^{\top} J_2^{\top}} \qquad (7.17)$$

$$T_r^{\top} R \qquad T_{r_2}^{\top} R_2$$

Let the vertical velocity be $(q, \tilde{\mu}) \in \mathbb{V}_{1q}$, where $\tilde{\mu} \in \mathbb{R}^{k_1}$. The velocity $\tilde{\mu}$ is canonically projected to a vertical component $\dot{q}_{v1} \in \operatorname{Ver}(T_qQ)$ on the tangent space, as $\dot{q}_{v1} = Z_1(q)\tilde{\mu}$, where $Z_1 \in \mathbb{R}^{n \times k_1}$ denotes the set of vertical (nullspace) basis. Motion along Z_1 ensures the invariance of $\pi_1(q) = r_1$. The numerical procedure to find Z_1 basis is reported in the Lemma 6.3 of Chapter 6.

Before proceeding, let us revisit some key ideas from Chapter 2. Assumption 2.2 is invoked so that the fibers are isomorphic, and the \mathcal{EL} system does not suffer from algorithmic singularity [106]. In Example 5, the nullspace basis is $Z_1 = \frac{1}{\sqrt{1+k_1^2}} \begin{bmatrix} 1 & -k_1 \end{bmatrix}^{\mathsf{T}}$. Another consequence of the sequences in (7.16) and (7.17) is the canonically defined metric on the submanifold π_1^{-1} , see Def. 2.4, $\mathcal{M}_2 = Z_1^{\mathsf{T}} M Z_1$.

7.3.2 Restriction of the Secondary Task

Consider the secondary task potential, $\Phi_2(r_2, \overline{r}_2)$. Using Property 6.2, it is concluded that $\forall \Phi_2(r_2, \overline{r}_2)$, $\exists \Phi_2^q(q)$. Recall that the fiber π_1^{-1} is an embedded submanifold of Q. Hence, smooth functions on Q have a restriction to the domain in the submanifold, $\pi_1^{-1}(r_1)$, i.e., the fiber [89, Th. 5.27]. The domain restriction applied to the scalar field Φ_2^q results in another restricted scalar field $\Phi_2: \pi_1^{-1} \to \mathbb{R}$, whose domain is a point in the submanifold at r_1 . This is the restriction of the potential $\Phi_2 = \Phi_2(r_2, \overline{r}_2) \Big|_{\pi_1^{-1}(r_1)}$ at each r_1 .

This potential, $\tilde{\Phi}_2$, is restricted to the fiber (nullspace), and it is characterized by its origin, its equilibrium and the local Hessian form in the fiber space. The fiber origin was already identified using the inclusion map Ψ_1 in (7.14) as the point s which satisfies $\Psi_1(r_1,s)=q$. Using the same map the equilibrium can be identified as follows. The key idea is that, there exists an equilibrium $\hat{q} \in Q$, which must satisfy the current primary configuration (r_1) and the desired secondary configuration \overline{r}_2 , i.e., $\forall r_1 \in R_1, \ \exists (r_1, \overline{s}) \in \pi_1^{-1}(r_1)$, such that $\hat{q} = \Psi_1(r_1, \overline{s})$ and $\pi_2(\hat{q}) = r_2$, where \overline{s} determines the fiber equilibrium. Note that the restricted potential, Φ_2 , depends on the relative distance between s and \overline{s} . Consequently, $\frac{\partial \Phi_2(s,\overline{s})}{\partial s} = -\frac{\partial \Phi_2(s,\overline{s})}{\partial \overline{s}}$.

For the next treatment, the Lie derivative of $\tilde{\Phi}_2$ along \mathbb{V}_1 is computed by restricting the Lie derivative of Φ_2 to π_1^{-1} . Computing this,

$$\mathcal{L}_{\dot{q}}\Phi_{2}\Big|_{\pi_{1}^{-1}(r_{1})} = \left\langle J_{2}^{\top} \frac{\partial \Phi_{2}}{\partial r_{2}}, \dot{q} \right\rangle \Big|_{\pi_{1}^{-1}(r_{1})}$$

$$\Rightarrow \mathcal{L}_{\dot{q}_{v_{1}}}\tilde{\Phi}_{2} = \left\langle J_{2}^{\top} \frac{\partial \Phi_{2}}{\partial r_{2}}, \dot{q}_{v_{1}} \right\rangle = \underbrace{\left\langle Z_{1}^{\top} J_{2}^{\top} \frac{\partial \Phi_{2}}{\partial r_{2}}, \tilde{\mu} \right\rangle}_{\text{force-velocity pair in fiber}} \tag{7.18}$$

From (7.18), the fiber force $f_e = -Z_1^{\top} J_2^{\top} \frac{\partial \Phi_2(r_2, \overline{r}_2)}{\partial r_2}$ is the differential of the restricted potential in the submanifold at r_1 , i.e., $f_e = -\frac{\partial \tilde{\Phi}_2(s, \overline{s})}{\partial s}$. Locally, its Hessian in the fiber is obtained as, $\operatorname{Hess}(\tilde{\Phi}_2) = Z_1^{\top} J_2^{\top} \operatorname{Hess}(\Phi_2) J_2 Z_1$ by taking the second derivative. The restricted potential in the fiber is therefore determined locally as,

$$\tilde{\Phi}_2 = \frac{1}{2} \langle s_e, s_e \rangle_{\text{Hess}(\tilde{\Phi}_2)}, \ s_e = s - \overline{s}, \tag{7.19}$$

Remark 38. Note that in (7.19), the local fiber potential $\tilde{\Phi}_2(s_e)$ generates a conservative force field $-\frac{\partial \tilde{\Phi}_2}{\partial s}$. But, the fiber potential, which is local, is not like the global potential forms, $\Phi_i(r_i, \overline{r}_i)$. The key difference is that the latter can be pulled back trivially as corresponding potential forms in the configuration space Q, see Prop. 6.2. However, the $\tilde{\Phi}_2$ corresponds to an analogous potential in Q iff $\dot{r}_1 = 0$.

Note that the final R.H.S of (7.18) agrees with the cotangent space exact sequence in (7.17). After the domain restriction, I obtain a force in the fiber space, however, to apply control forces, the force must be brought back to T_qQ . Unfortunately, there is no more canonical geometric machinery available. As in Chapter 6, a connection (see Def. 2.5), $\mathcal{A}_q:T_qQ\mapsto \mathbb{V}_{1q}$, is chosen to aid this step, which satisfies $\mathcal{A}\big(\mathrm{Ver}(\tilde{\mu})\big)=\tilde{\mu}$, where $\tilde{\mu}\in\mathbb{V}_1$.

Thus, Def. 2.5 determines a specific vertical velocity $\tilde{\mu}$ given \dot{q} . In Robotics, the Ehresmann connection is referred to as the nullspace projector [206, 207], and appears in literature in the form, $\mathcal{A} = (Z_1^\top W Z_1)^{-1} Z_1^\top W$, where $W \in \mathbb{R}^{n \times n}$ is a weighing matrix. In particular, the connection defines the endomorphism map, $T_q Q \to T_q Q$, through the projector matrix (endomorphism in Property 6.3) $\mathcal{Z} = Z_1 \mathcal{A}$, which splits any tangent velocity vector $\dot{q}^* \in T_q Q$ as,

$$\dot{q}^* = \dot{q}_v^* + \dot{q}_h^* = (\mathcal{Z})\dot{q}^* + \text{Kern}(\mathcal{Z})\dot{q}^*$$
(7.20)

which decomposes the tangent space into two distributions as $T_qQ = \mathbb{V}_{1q} + \mathbb{H}_{1q}$. The connection can be defined as statically consistent using $W = \mathbb{I}_{n,n}$ and $\mathcal{A} = Z_1^{\top}$ or dynamically consistent using W = M(q) and $\mathcal{A} = \mathcal{M}_2^{-1} Z_1^{\top} M$.

Both projection formulae satisfy the force-velocity pairing in (7.18), and hence, are equally valid iff $\dot{r}_1 = 0$. In geometric mechanics, the former is called a trivial Ehresmann connection and the latter is called the *mechanical* connection, see Def. 2.7. In the latter case, $\tilde{\mu}$ obtained from the connection is known as the locked velocity, i.e., the velocity corresponding to the momentum in the fiber space. The bundle velocity is obtained as a locally invertible linear transformation of the velocity on T_qQ , i.e.,

$$\begin{bmatrix} \dot{r}_1 \\ \tilde{\mu} \end{bmatrix} = T(q)\dot{q}, \ T = \begin{bmatrix} J_1(q) \\ \mathcal{A}(q) \end{bmatrix}$$
 (7.21)

which is called (with an abuse of wording), the extended Jacobian in robotics. However, T does not emerge as the differential of a kinematic map. Note that from Def. 7.3, the shape velocity \dot{r}_1 and the vertical velocity $\tilde{\mu}$ are geometrically decoupled for any arbitrary connection, \mathcal{A} , as

$$\left\langle T^{-1} \begin{bmatrix} 0 \\ \tilde{\mu} \end{bmatrix}, T^{-1} \begin{bmatrix} \dot{r}_1 \\ 0 \end{bmatrix} \right\rangle_W = 0 \tag{7.22}$$

However, the mechanical connection satisfies an additional orthogonality (symmetry) condition between the proportional actions of the primary and secondary tasks, i.e.,

$$\langle (J_1^{\top} \frac{\partial \Phi_1}{\partial r_1})^{\sharp}, (\mathcal{A}^{\top} Z_1^{\top} J_2^{\top} \frac{\partial \Phi_2}{\partial r_2})^{\sharp} \rangle_M = 0$$
 (7.23)

which is not satisfied by the trivial one. Thus, (7.21) and (7.23) give the conditions of algebraic symmetry that needs to be satisfied by the motion control. Note that definition of \mathcal{A} is a choice, and does not affect power flows in dynamics, but it simplifies the \mathcal{EL} equations of motion. With the aforementioned machinery, it is prudent to investigate a simple example to recollect the concepts in task-induced algebraic symmetry (hierarchy).

Example 6. Consider an \mathcal{EL} system with configuration $q = (q_1, q_2) \in Q = \mathbb{R}^2$, see Fig. 7.4, with kinematic submersions for primary task $r_1 = \pi_1(q) = \sqrt{\sum_i q_i^2}$, and secondary task $r_2 = \pi_2(q) = 1 - \cos(q_2)$. Note that Def. 7.3 is not satisfied, see top of Fig. 7.4. Considering the tasks independently, the potentials are, $\Phi_i(r_i) = \frac{1}{2}k_ir_i^2$, $k_1 = 1$, $k_2 = 2.5$. For task-induced symmetry, (7.19) yields a restricted potential $\tilde{\Phi}_2(s_e)$, and (7.23) holds on Q. The potential $\tilde{\Phi}_2$ is compared with $\Phi_2(r_2, \overline{r}_2)$ at the bottom of Fig. 7.4, which shows the effect on $\tilde{\Phi}_2$ due to the projection. In this plot, $\tilde{\Phi}_2$ is computed using (7.19) over the domain Q.

Note that $\tilde{\Phi}_2$ gets truncated in Q in regions where J_1 (blue) and J_2 (red) are aligned, which indicates conflicting primary and secondary objectives. Consequently, $J_2\mathcal{Z}$ is singular in these regions, and the restricted potential $\tilde{\Phi}_2$ is 0, along the diagonal. This shows that the domain of $\tilde{\Phi}_2$ is actually a disjoint union of 4 sets. The analysis in this work considers motion in the interior of one set such that the ensuing motion does not encounter the submanifold boundary. This is ensured by the Assumptions 2.1, 2.2 and 2.3.

7.3.3 \mathcal{EL} equations of Motion on the Fiber Bundle

As in Sec. 6.5 from Chapter 6, note that for a general \mathcal{EL} system without symmetry considered here, the quotient map $\pi_1: Q \to Q/G_{r_1}$ holds locally for each r_1 , where G_{r_1} is the Lie group locally defined at r_1 . The dynamics of $(\dot{r}_1, \tilde{\mu})$ globally correspond to the dynamics of the shape velocity and the Lie algebroid of G_{r_1} . The equations of motion are given as in (6.33) from Chapter 6.

$$\mathcal{M}(q) \begin{bmatrix} \ddot{r}_1 \\ \dot{\tilde{\mu}} \end{bmatrix} + \Gamma(q, \dot{r}_1, \tilde{\mu}) \begin{bmatrix} \dot{r}_1 \\ \tilde{\mu} \end{bmatrix} = \begin{bmatrix} F_1 \\ f \end{bmatrix}$$
 (7.24)

where $\tau = T^{\top}(F_1, f)$ denote the forces in the shape and fiber, $\mathcal{M} = T^{-\top}MT^{-1}$ is the metric tensor (fully-coupled for arbitrary \mathcal{A}) in the fiber bundle, and $\Gamma = T^{-\top}(CT^{-1} - M\dot{T}^{-1})$ is the matrix of CC terms.

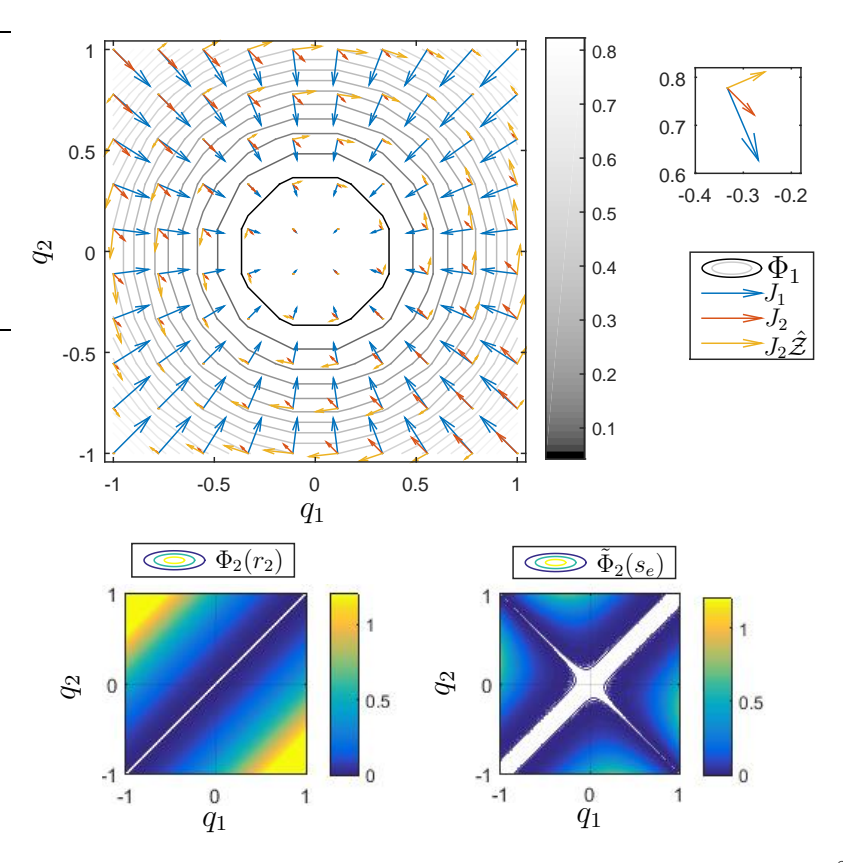


Figure 7.4: Example \mathcal{EL} system: Configuration: $q = (q_1, q_2) \in Q = \mathbb{R}^2$, with submersions maps $r_1 = \pi_1(q) = \sqrt{\sum_i q_i^2}$, $r_2 = \pi_2(q) = q_2 - q_1$. Top: The scalar potential field, Φ_1 , with vector fields J_1 , J_2 and $J_2\hat{\mathcal{Z}}$. Bottom: Comparison of independent $\Phi_2(r_2)$ and restricted $\tilde{\Phi}_2$.

Remark 39. Note that the inertia tensor \mathcal{M} is block-diagonalized

$$\mathcal{M}(q) = \begin{bmatrix} \mathcal{M}_1(q) & 0\\ 0 & \mathcal{M}_2(q) \end{bmatrix}$$
 (7.25)

if \mathcal{A} is chosen to be the mechanical connection, as was shown in [207, 215]. In the following, \mathcal{A} is chosen as the mechanical connection to simplify the derivation. But the trivial connection can be alternatively used.

Remark 40. The dynamics in (7.24) satisfy the passivity property by the corollary in Prop. 6.1, i.e., there exists a conserved Hamiltonian.

Lemma 7.3. Given a \mathcal{EL} system in 2.15, the submersion of the primary task kinematics, $\pi_1: Q \to R_1$, results in a fiber bundle description, i.e., local coordinates $(r_1, s) \in \pi_1^{-1}$. Let the kinetic energy of the \mathcal{EL} system in (2.15) be rewritten as $K = \frac{1}{2} \langle (\dot{r}_1, \tilde{\mu}), (\dot{r}_1, \tilde{\mu}) \rangle_{\mathcal{M}}$. Consider the motion under static scalar potentials,

 $\Phi_1(r_1, \overline{r}_1)$ and $\tilde{\Phi}_2(s, \overline{s})$ as $F_1 = -\frac{\partial \Phi_1}{\partial r_1}$ and $f = -\frac{\partial \tilde{\Phi}_2}{\partial s}$, such that $\overline{r}_1, \overline{s}$ are time-invariant. In terms of this description, the equations of motion are given by the \mathcal{EL} equations in (7.24), which conserve the Hamiltonian, $\hat{H} = K(\dot{r}_1, \tilde{\mu}) + \Phi(r_1, s)$, where $\Phi = \Phi_1 + \tilde{\Phi}_2$.

Proof. Taking the time-derivative of \hat{H} along the trajectory using (7.24),

$$\dot{\hat{H}} = \langle (\dot{r}_1, \tilde{\mu}), \left(\frac{\dot{\mathcal{M}}}{2}(\dot{r}_1, \tilde{\mu}) - \Gamma(\dot{r}_1, \tilde{\mu})\right) \rangle
+ \langle (\dot{r}_1, \tilde{\mu}), (F_1, f) \rangle + \langle \frac{\partial \Phi_1}{\partial r_1}, \dot{r}_1 \rangle + \langle \frac{\partial \tilde{\Phi}_2}{\partial s}, \tilde{\mu} \rangle = 0$$
(7.26)

where Remark 40 is used to assert passivity as $\langle (\dot{r}_1, \tilde{\mu}), (\dot{r}_1, \tilde{\mu}) \rangle_{\dot{\mathcal{M}} = 2\Gamma} = 0$.

Lemma 7.3 provides the analytical machinery to design the proportional action which ensures that the state (r_1, r_2) is driven towards $(\overline{r}_1, \overline{r}_2)$ in a manner that imposes task-induced algebraic symmetry. To that end, I consider the proportional action of the form,

$$\tau = \tau_1 + \tau_2 + \tau_u$$

$$\tau_1 = -J_1^{\top} \frac{\partial \Phi_1(r_1, \overline{r}_1)}{\partial r_1})$$

$$\tau_2 = -\mathcal{A}^{\top} Z_1^{\top} J_2^{\top} \frac{\partial \Phi_2(r_2, \overline{r}_2)}{\partial r_2}$$

$$(7.27)$$

where $\Phi_i = \frac{1}{2} \langle (r_i - \overline{r}_i), (r_i - \overline{r}_i) \rangle_{P_i}$ is the spring-like potential with $P_i \succ 0$, and τ_u is a control action to be determined later. In robotics, $\tau_u = 0$ is often used, or has some compensation terms for CC forces [207]. However, I will show next that this naive imposition of task hierarchy destroys the Hamiltonian nature of the \mathcal{EL} system.

Remark 41. Given that a secondary task potential, $\Phi_2(r_2, \overline{r}_2)$, has a restriction to the fiber, $\tilde{\Phi}_2(s, \overline{s})\Big|_{\pi_1^{-1}(r_1)}$, as shown in Sec. 7.3.2, it is enticing to use $\tilde{\Phi}_2$ and apply Lemma 7.3 to prove the Hamiltonian nature of the system. However, the fiber equilibrium \overline{s} in task-hierarchy is not time-invariant, and imparts curl forces to the dynamics as I will show next. This makes the problem non-Hamiltonian, and (7.27) applied to (7.24) does not conserve \hat{H} .

7.4 Conserved Hamiltonian and Motion Control

In this section, firstly, I use Example 5 to demonstrate the non-conservative nature of task-induced algebraic symmetry under conventional proportional actions

(with $\tau_u = 0$ in (7.27)). Secondly, I prove that this is due to a wandering equilibrium of the restricted potential in the fiber space. Thirdly, I derive a novel proportional action that conserves a new Hamiltonian which characterizes the \mathcal{EL} system with task hierarchy while preserving the metric tensor.

7.4.1 Comparison of Force Fields

For the 2D case in Fig. 7.2, comparing the force field portraits for the proportional term in Lemma 7.2 and the one in (7.27) (with $\tau_u = 0$) reveals the nature of the forces. In particular, the force fields are shown in Fig. 7.5 for scalar potentials, with Hessians $P_1 = 4$ and $P_2 = 20$. The potential parameters were chosen to highlight the difference in the resulting force fields. On the left, the force field portrait with superposition of proportional actions from Lemma 7.2 is shown, while the portrait with the projection of the secondary proportional action from (7.27) is shown. Note that in both cases, the forces turn towards the equilibrium strongly in the conical region between the lines $(\bar{\tau}_1, \bar{\tau}_2)$. However, the latter turns strongly in a way that resembles motion with vorticity [228]. Vorticity is quantified by the curl of the force field, i.e., $\nabla \times \tau$. For the case of Lemma 7.2, obviously $\nabla \times \tau = 0$ because the proportional actions are obtained as differentials of primary and secondary potentials. Mathematically, it is computed as the following,

$$\nabla \times \tau = \begin{bmatrix} \frac{\partial}{\partial q_1} & \frac{\partial}{\partial q_2} \end{bmatrix} \begin{bmatrix} 0 & 1 \\ -1 & 0 \end{bmatrix} \begin{bmatrix} \tau_1 \\ \tau_2 \end{bmatrix}$$

$$= \sum_{i=1}^{2} \left(v_1^{\top} J_i^{\top} \operatorname{Hess}(\Phi_i) J_i v_2 - v_2^{\top} J_i^{\top} \operatorname{Hess}(\Phi_i) J_i v_1 \right) = 0$$

$$(7.28)$$

where $v_1^{\top} = \begin{bmatrix} 1 & 0 \end{bmatrix}$ and $v_2^{\top} = \begin{bmatrix} 0 & 1 \end{bmatrix}$ are the unit vectors. Note that in (7.28), the null curl condition results due to the symmetric nature of the Hessian forms $J_i^{\top} \operatorname{Hess}(\Phi_i) J_2$. It is worth noting that these Hessians correspond to the potentials (0-forms) in the configuration space Q, which result from the pullbacks from the operational spaces R_1, R_2 , see Prop. 6.2.

However, the case with (7.27) has $\nabla \times \tau \neq 0$, thus, generating a system with curl forces. As in (7.28), the curl is computed using $\hat{Z}_1 = Z_1 \mathcal{A}$, as,

$$\nabla \times \tau = v_1^{\top} C v_2 - v_2^{\top} C v_1, \ C = \hat{Z}_1^{\top} J_2^{\top} \text{Hess}(\Phi_2) J_2 = v_1^{\top} (C - C^{\top}) v_2$$
 (7.29)

As expected, due to the non-symmetric nature of C in (7.29), which arises due to the projection, the curl is not null. Thus, the system becomes non-conservative. This poses a challenge in characterizing the motion of the particle using level-sets of a scalar Hamiltonian. Consequently, Lyapunov-based stabilization also becomes difficult because the system is non-Hamiltonian, i.e., the motion equations do not arise from a Lagrangian or Hamiltonian, which precludes the natural energy as a candidate. In mechanics terminology, (7.27) with (7.1) defines a purely

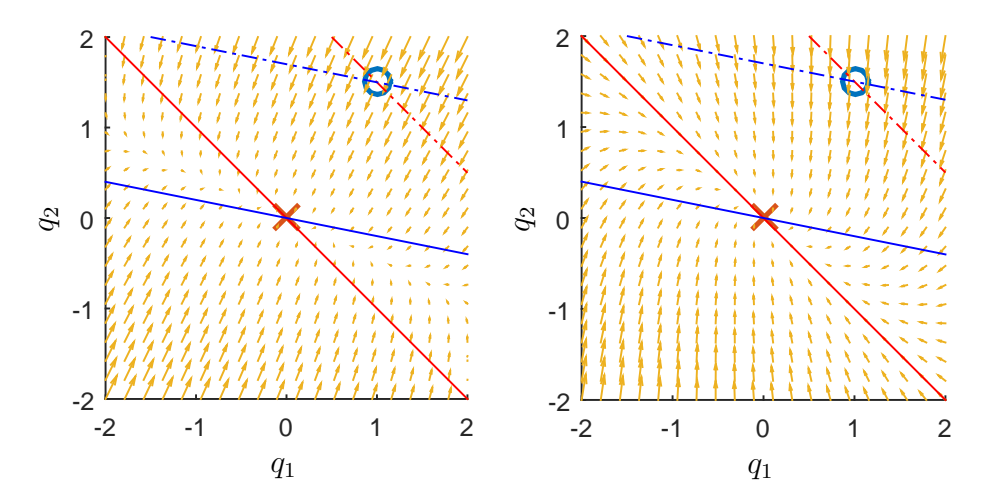


Figure 7.5: Force fields with scalar potential parameters: $P_1 = 4$, $P_2 = 20$. Left: Superposition of primary/secondary proportional actions, Right: Using Projection of secondary proportional action.

Newtonian system with curl forces, see related works in [226, 227]. In the next part, I will prove that these curl forces arise because the equilibrium, \bar{s} of the fiber-restricted potential, $\tilde{\Phi}_2(s,\bar{s})$, varies as $r_1(t)$ changes due to the primary potential Φ_1 . This makes the control problem non-conservative.

7.4.2 Wandering Equilibrium in the Fiber

In (7.18), I derived the Lie derivative of the fiber-restricted potential, Φ_2 in the submanifold $\pi_1^{-1}(r_1)$ for a fixed r_1 . To attribute for the complete motion, the total derivative of this potential must be computed, and is stated below. The proof requires the following Assumption.

Assumption 7.2. The current primary configuration $r_1 \in R_1$, and the desired secondary configuration, $\overline{r}_2 \in R_2$, satisfy a unique point in Q, i.e.,

$$\pi(\hat{q}) = (r_1, \overline{r}_2) \Rightarrow \hat{q} = \pi^{-1}(r_1, \overline{r}_2) \tag{7.30}$$

Assumption (7.2) only requires that π be a proper map, i.e., the total operational space Jacobian, J, is full rank.

Lemma 7.4. Given the fiber bundle of the primary task, $\pi_1: Q \to R_1$, the total derivative of the fiber-restricted secondary potential, $\tilde{\Phi}_2$, under Assumption 7.2 is,

$$\mathcal{L}_{\dot{q}}\tilde{\Phi}_{2} = \langle Z_{1}^{\top} \frac{\partial \tilde{\Phi}_{2}(s, \overline{s})}{\partial q}, \tilde{\omega} \rangle, \ \tilde{\omega} = \tilde{\mu} - \overline{\omega}(\dot{r}_{1})$$
 (7.31)

where $\overline{\omega}(\dot{r}_1) = \mathcal{A}J^{-1}\begin{bmatrix} \dot{r}_1 \\ 0 \end{bmatrix}$ is the velocity of the potential's equilibrium \overline{s} in the fiber, $\pi_1^{-1}(r_1)$, trivialized at the frame located in s = 0, while r_1 varies in R_1 .

Proof. Computing the total derivative of $\tilde{\Phi}_2$ along \dot{q} , and using (7.20) to decompose $\dot{q} = \dot{q}_v + \dot{q}_h$,

$$\mathcal{L}_{\dot{q}}\tilde{\Phi}_{2} = \langle \frac{\partial \tilde{\Phi}_{2}(s, \overline{s}(r_{1}))}{\partial q}, \dot{q}_{v} \rangle + \langle \frac{\partial \tilde{\Phi}_{2}(s, \overline{s}(r_{1}))}{\partial q}, \dot{q}_{h} \rangle
= \langle \underbrace{\frac{\partial \tilde{\Phi}_{2}(s, \overline{s}(r_{1}))}{\partial q}, Z_{1}\tilde{\mu} \rangle}_{\text{Ver}} - \underbrace{\langle \frac{\partial \tilde{\Phi}_{2}(s, \overline{s}(r_{1}))}{\partial r_{1}}, \dot{r}_{1} \rangle}_{\text{Hor} \neq 0} \tag{7.32}$$

where the negative sign in the second line follows from

$$\frac{\partial \tilde{\Phi}_2(s,\overline{s})}{\partial s} = -\frac{\partial \tilde{\Phi}_2(s,\overline{s})}{\partial \overline{s}}.$$
 (7.33)

The identity in (7.33) is because the magnitude of $\tilde{\Phi}_2(s, \overline{s})$ depends on the relative distance between the origin s and the equilibrium \overline{s} . In (7.32), the Ver-part of the R.H.S. is equivalent to $\langle \frac{\partial \tilde{\Phi}_2}{\partial s}, \dot{s} \rangle$, as described in Sec. 7.3.2. Note that the Hor-part of the power flow (7.32) is generally not 0, and it is simplified next. From (6.14), \hat{q} is obtained using the inclusion map, Ψ_1 , from the fiber as,

$$\Psi_1(r_1, \overline{s}) = \pi_1^{-1}(r_1, \overline{r}_2) = \hat{q} \Rightarrow \frac{\partial \Psi_1}{\partial r_1} \dot{r}_1 + Z_1 \overline{\omega} = J^{-1} \begin{bmatrix} \dot{r}_1 \\ 0 \end{bmatrix} = \dot{\hat{q}}_h + \dot{\hat{q}}_v$$
 (7.34)

where the differential form is considered in the second line of (7.34). Using $\mathcal{A}\hat{q}_h = 0$, I get the form of $\overline{\omega}$ in the Lemma. The Hor-part in the R.H.S. of (7.32) is therefore,

$$\langle \frac{\partial \tilde{\Phi}_2}{\partial r_1}, \dot{r}_1 \rangle = \langle J^{\top} \begin{bmatrix} \frac{\partial \tilde{\Phi}_2}{\partial r_1} \\ 0 \end{bmatrix}, J^{-1} \begin{bmatrix} \dot{r}_1 \\ 0 \end{bmatrix} \rangle = \langle Z_1 \frac{\partial \tilde{\Phi}_2}{\partial q}, \mathcal{A} J^{-1} \begin{bmatrix} \dot{r}_1 \\ 0 \end{bmatrix} \rangle = \langle Z_1 \frac{\partial \tilde{\Phi}_2}{\partial q}, \overline{\omega} \rangle \quad (7.35)$$

Thus, using (7.35) in (7.32) proves the result.

Note that in Lemma 7.4, the wandering velocity of the fiber equilibrium is exactly the horizontal contribution of the shape (primary task) towards motion in the fiber, as shown in Lemma 6.4 in Chapter 6. This is the physical intuition behind Lemma 7.4, and it brings forth a very surprising observation.

Remark 42. Although the vertical (nullspace) velocities along Z_1 basis are orthogonal to the proportional action of the primary task, $J_1^{\top} \frac{\partial \Phi_1}{\partial r_1}$, recall Lemma 6.3, the horizontal velocities (emerging purely from \dot{r}_1) are not necessarily orthogonal to the proportional action of the secondary task, even when restricted to the manifold of self-motions. In other words, even if the motion occurs purely in R_1 , the

magnitude of the fiber restricted potential $\tilde{\Phi}_2$ varies along the path in R_1 . This observation proves instrumental in finding the Hamiltonian for the task-hierarchy problem.

It is instructive to visualize this effect using Example 5, see Fig. 7.3b. The equilibrium of the submanifold (nullspace) is not located at the projection of the force field $F_2 = -J_2^{\top} \frac{\partial \Phi_2}{\partial r_2}$. To see this, consider the point $q = q_0$. At this point, the pullback of the secondary proportional action, F_2 is projected along the nullspace basis using, $f = Z_1^{\top} F_2$. However, after projection, the equilibrium is not located at the yellow dot. In fact, at this point, there is another non-zero proportional term. The actual equilibrium, i.e., f = 0 is located at the blue \times , which is the intersection of $(r_1, \overline{r_2})$, i.e., intersection of the line given by r_1 and the line of the secondary equilibrium $\overline{r_2}$. Given the point in primary space, r_1 , the configuration point is $\hat{q} = \pi^{-1}(r_1, \overline{r_2})$, which varies with r_1 .

This variation of equilibrium is highlighted in Fig. 7.6. In particular, the \mathcal{EL} system trajectory is plotted in magenta, and 10 points are numbered on it to identify the equilibrium \overline{s} as red circles on the \overline{r}_2 line. Note that in transition from 1 to 2, the equilibrium has shifted left along $\pi_2^{-1}(\overline{r}_2)$, i.e., along the nullspace (fiber) of the secondary equilibrium. At the points 7 and 10, the primary equilibrium is reached, $r_1 = \overline{r}_1$. Hence, the proportional action of the secondary task is pointed along the nullspace (fiber) of the primary equilibrium, $\pi_1^{-1}(\overline{r}_1)$. The pairs 1-9, 2-8 and 4-6, respectively, are non-identical points in Q, but have the same value of r_1 , and the corresponding fiber equilibria. Thus, for the 1-9 pair, the proportional action at 9 is stronger than in 1, as the former is further away. The equilibria varies between the limits shown by the black arrowed line.

Generally, it is not trivial to find the fiber variables s, \overline{s} in \mathcal{EL} systems. However, Example 5 enables the study of the behaviour of the origin and the equilibrium in the fiber. The origin in the fiber is determined by the map, $\Psi_1(r_1, s) = q$, where $(r_1, s) \in \pi_1^{-1}(r_1) \equiv \mathbb{R}^1$. This origin is obtained as,

$$s = \Psi_1^{-1}(q) = Z_1^{\top} J^{-1} r = Z_1^{\top} q \tag{7.36}$$

The state-dependent equilibrium in the fiber is $\overline{s} = \Psi_1^{-1} \circ \pi^{-1}(r_1, \overline{r}_2)$. I use the map,

$$\Psi_1(q,\overline{s}) = \hat{q} \Rightarrow \overline{s} = \Psi_1^{-1} \circ \pi^{-1}(\hat{r}) = Z_1^{\top} \hat{q}$$

$$(7.37)$$

where $\hat{r} = (r_1, \overline{r}_2)$. In Fig. 7.7, the motion of s and \overline{s} are shown for the trajectory in Fig. 7.6. Recall that, the proportional actions are given by (7.27) with $\tau_u = 0$. It can be seen that the fiber origin, s has a poor tracking performance relative to the wandering fiber equilibrium, \overline{s} . Due to the varying nature of the equilibrium in the fiber, the conventional \mathcal{EL} equations are not suitable. Instead, it is required to use a anisotropic form of the kinetic energy which is common in tracking control [229]. This idea will be followed to design a novel proportional action that preserves the Hamiltonian structure of the \mathcal{EL} system.

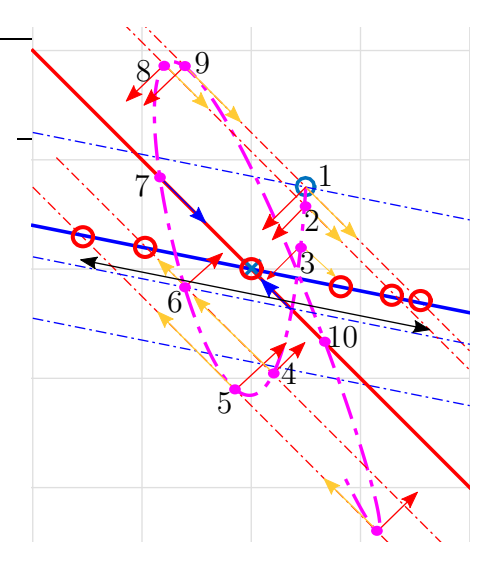


Figure 7.6: Time-evolution of the fiber equilibrium, \bar{s} , (red circles) due to conventional projected position-dependent forcing in (7.27) with $\tau_u = 0$. The equilibria vary along $\pi_2^{-1}(\bar{r}_2)$.

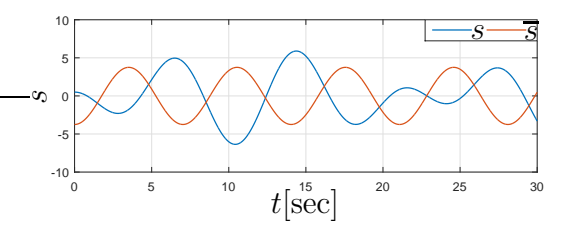


Figure 7.7: Time-evolution of the fiber origin, s, and the fiber equilibrium, \overline{s} , due to conventional projected position-dependent forcing in (7.27) with $\tau_u = 0$. Fiber coordinate is unable to track the state-dependent equilibrium.

7.4.3 The Conserved Hamiltonian

In the context of PBC [3] and Lagrangian matching [13], for a given \mathcal{EL} system with natural Hamiltonian $H(q,\dot{q}) = K(q,\dot{q}) + \mathcal{V}(q)$, a desired closed-loop Hamiltonian is chosen as $\mathcal{H} = \mathcal{K}(q,\dot{q}) + \Phi(q)$, and the proportional actions are derived such that \mathcal{H} is a conserved quantity of motion. In PBC, $\mathcal{K} = K$ is often chosen to preserve the metric structure of the \mathcal{EL} system, while potential shaping is performed so that V is replaced by Φ in closed-loop. Recall that by virtue of Assumption 6.1, the effect of V is already removed, and it remains to impose the potential Φ that exhibits the task-induced algebraic symmetry. In hierarchical PBC approaches for motion control with redundancy, however, a closed-loop Hamiltonian \mathcal{H} for the entire \mathcal{EL} system has never been reported. To that end, in the following Theorem as the main result, I report a Hamiltonian, \mathcal{H} , which is a conserved quantity of motion, while imposing a task-induced algebraic symmetry.

Theorem 7.1. Consider the \mathcal{EL} system in (6.33) with the natural Hamiltonian, \hat{H} , in Lemma. 7.3 as the integral of motion. For the task-induced algebraic symmetry, let surjective submersions imposed by the forward kinematics to the operational spaces, $\pi_1: Q \to R_1$, as in Def. 2.3, where i = 1 (i = 2) denotes the primary (secondary, respectively) task satisfy Assumption 7.1. The proportional action chosen as (7.27), where

$$\begin{bmatrix}
F_1 \\
f
\end{bmatrix} = \underbrace{-\begin{bmatrix}
\frac{\partial \Phi_1}{\partial r_1} \\
Z_1^{\top} J_2^{\top} \frac{\partial \Phi_2}{\partial r_2}
\end{bmatrix}}_{proportional\ action} + \underbrace{\begin{bmatrix}
0 \\
\mathcal{M}_2 f_u^{\sharp}
\end{bmatrix}}_{feedforward} + \underline{\Gamma(\dot{r}_1, \tilde{\mu})} \begin{bmatrix} \dot{r}_1 \\
\overline{\omega} \end{bmatrix} \\
tracking$$

$$f_u^{\sharp} = \underbrace{\mathcal{N}(q, \dot{q})} \begin{bmatrix} \dot{r}_1 \\ 0 \end{bmatrix}}_{CC\ terms} + \underbrace{\mathcal{A}J^{-1} \mathcal{M}_1^{-1}}_{proportional\ action\ (primary)} \\
\mathcal{N} = (\dot{\mathcal{A}}J^{-1} + \mathcal{A}\dot{J}^{-1} - \mathcal{M}^{-1}\Gamma(\dot{r}_1))$$
(7.38)

conserves a new Hamiltonian given as,

$$\mathcal{H} = \underbrace{\frac{1}{2} \left\langle (\dot{r}_1, \tilde{\omega}), (\dot{r}_1, \tilde{\omega}) \right\rangle_{\mathcal{M}}}_{\kappa} + \underbrace{\Phi_1(r_1, \overline{r}_1) + \tilde{\Phi}_2(s, \overline{s})}_{\Phi}$$
(7.39)

which preserves the inertia tensor \mathcal{M} along trajectories.

Proof. Subtracting the time-derivative of the wandering fiber velocity from the L.H.S. and R.H.S. of (6.33),

$$\mathcal{M}(q) \begin{bmatrix} \ddot{r}_1 \\ \dot{\tilde{\omega}} \end{bmatrix} + \Gamma(q, \dot{r}_1, \tilde{\mu}) \begin{bmatrix} \dot{r}_1 \\ \tilde{\mu} \end{bmatrix} = \begin{bmatrix} F_1 \\ f \end{bmatrix} - \mathcal{M}(q) \begin{bmatrix} 0 \\ \dot{\overline{\omega}} \end{bmatrix}$$
 (7.40)

As remarked in Remark 39, \mathcal{A} is chosen as the mechanical connection. Thus, the dynamics of the wandering equilibrium in the fiber (R.H.S. of (7.40)) is written as,

$$\mathcal{M}_{2}\dot{\overline{\omega}} = \mathcal{M}_{2}\frac{d}{dt}\left(\mathcal{A}J^{-1}\begin{bmatrix}\dot{r}_{1}\\0\end{bmatrix}\right) = \mathcal{M}_{2}\left(\left(\dot{\mathcal{A}}J^{-1} + \mathcal{A}\dot{J}^{-1}\right)\begin{bmatrix}\dot{r}_{1}\\0\end{bmatrix} + \mathcal{A}J^{-1}\begin{bmatrix}\ddot{r}_{1}\\0\end{bmatrix}\right) \quad (7.41)$$

In (7.41), \ddot{r}_1 can be either measured or computed using the top row in (6.33). In this work, I follow this model-based approach to compute \ddot{r}_1 as,

$$\begin{bmatrix} \ddot{r}_1 \\ 0 \end{bmatrix} = -\mathcal{M}^{-1} \Gamma(\dot{r}_1) \begin{bmatrix} \dot{r}_1 \\ 0 \end{bmatrix} + \begin{bmatrix} \mathcal{M}_1^{-1} F_1 \\ 0 \end{bmatrix}$$
 (7.42)

Applying (7.42) in (7.41),

$$\mathcal{M}_{2}\dot{\overline{\omega}} = \mathcal{M}_{2} \left(\dot{\mathcal{A}} J^{-1} + \mathcal{A} \dot{J}^{-1} - \mathcal{A} J^{-1} \mathcal{M}^{-1} \Gamma(\dot{r}_{1}) \right) \begin{bmatrix} \dot{r}_{1} \\ 0 \end{bmatrix} + \mathcal{M}_{2} \mathcal{A} J^{-1} \begin{bmatrix} \mathcal{M}_{1}^{-1} F_{1} \\ 0 \end{bmatrix}$$

$$(7.43)$$

Computing the time-derivative of \mathcal{H} ,

$$\dot{\mathcal{H}} = \langle (\dot{r}_1, \tilde{\omega}), (F_1, f) \rangle - \langle (\dot{r}_1, \tilde{\omega}), \mathcal{M}(0, \dot{\bar{\omega}}) \rangle
+ \langle \frac{\partial \Phi_1(r_1, \overline{r}_1)}{\partial r_1}, \dot{r}_1 \rangle + \langle \frac{\partial \tilde{\Phi}_2(s, \overline{s})}{\partial q}, Z_1 \tilde{\omega} \rangle + \langle (\dot{r}_1, \tilde{\omega}), \frac{\dot{\mathcal{M}}}{2} \begin{bmatrix} \dot{r}_1 \\ \tilde{\omega} \end{bmatrix} - \Gamma \begin{bmatrix} \dot{r}_1 \\ \tilde{\mu} \end{bmatrix} \rangle$$
(7.44)

where the time-derivatives are computed using (7.9) for $\Phi_1(r_1, \overline{r}_1)$ and Lemma 7.4 for $\tilde{\Phi}_2(s, \overline{s})$. Note that the final term in (7.44) does not cancel out by the passivity property in Prop. 6.1 (see Remark 40) because the fiber velocities are not identical. Thus, a CC compensation is required, as in tracking control. This term shows up as the final term on the R.H.S. of the first of (7.38). Thus, if the shape-fiber actuation is chosen as the first of (7.38), it ensures the conservation of \mathcal{H} , i.e., $\dot{\mathcal{H}} = 0$, which proves the result. Note that in the first of (7.38), the second term is the feedforward term to track the wandering equilibrium acceleration, $\dot{\omega}$, which appears as an inertial acceleration, whereas the final term compensates for the CC terms, like in tracking for motion control, see [229]. It is worth pointing out that although \mathcal{H} resembles a tracking control problem, the problem of task-induced hierarchy is not explicitly time-varying, i.e., the level-set of \mathcal{H} is time-invariant.

Remark 43. In (7.38), apart from velocity-dependent CC terms, there is also a position-dependent term related to the primary task that is projected to the fiber (nullspace). For relatively slow motions, the velocity-dependent terms might be ignored at the cost of accuracy. However, the proportional term is only small iff $r_1 \to \overline{r}_1$, and therefore, cannot be ignored even in practice.

Remark 44. Theorem 7.1 is important because it provides a conserved quantity for stabilization using damping injection, as in PBC approaches. Physically, the compensation in τ_u ensures tracking of the wandering potential, $\tilde{\Phi}_2$, in the fiber space by removing the inertial effects of the moving frame. This creates a conserved Hamiltonian as, $\dot{\mathcal{H}} = 0$, and renders the system integrable, although it continues to have the presence of curl force. This is a rare example of a system with curl forces possessing an integral of motion, that can be exploited for energy-based stabilization.

Remark 45. Another consequence of Theorem 7.1 is that the stability property is applicable to the entire system, as opposed to the hierarchical property in [51, 52, 206]. To the best of my knowledge, motion stabilization for the entire system, while providing a hierarchy of convergence has not been provided earlier.

Remark 46. In Theorem 7.1, task-induced algebraic symmetry is mathematically imposed as the inner product,

$$\langle J_1^{\top} \frac{\partial \Phi_2(r_1, \overline{r}_1)}{\partial r_1}, \mathcal{A}^{\top} Z_1^{\top} \frac{\partial \Phi_2(r_2, r_2)}{\partial r_2} \rangle_{M^{-1}} = 0$$
 (7.45)

which was the main goal of this chapter.

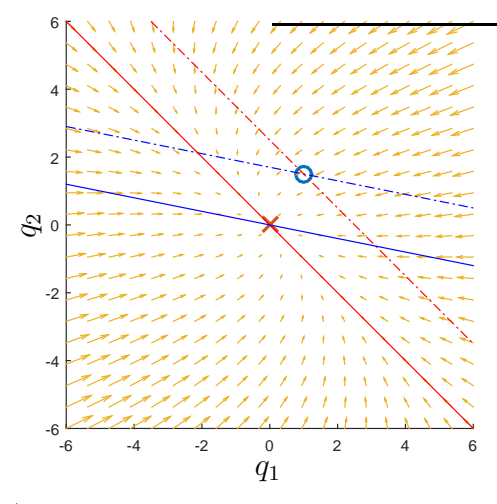
It is instructive to validate Theorem 7.1 for the case considered in Example 5. In this particular case, the underlying coordinate system is non-orthogonal, and hence, the mechanical connection $\mathcal{A} \neq Z_1^{\top}$. Before writing the Hamiltonian, it is worth noting that the inertia in the directions of the primary subspace and the fiber (nullspace), is $\mathcal{M} = T^{-\top}MT = \operatorname{diag}(m_1, m_2)$. The velocity of the wandering equilibrium (Lemma 7.4) in the fiber is, $\overline{\omega} = Z_1^{\top}J^{-1}\begin{bmatrix} \dot{r}_1 \\ 0 \end{bmatrix}$. For the application of Theorem 7.1, only the proportional term in (7.38) is required as,

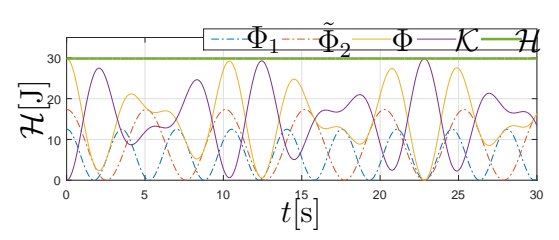
$$\tau_u = \mathcal{A}^{\top} m_2 \mathcal{A} J^{-1} \begin{bmatrix} m_1^{-1} \frac{\partial \Phi_1(r_1, \overline{r}_1)}{\partial r_1} \\ 0 \end{bmatrix}$$
 (7.46)

which is required to preserve the Hamiltonian \mathcal{H} .

Firstly, the force fields of the total proportional action in Theorem 7.1 is shown in Fig. 7.8a. The force fields preserve the nature of motion in the right of Fig. 7.5, which considered a naive projection of the secondary proportional action, $\tau_u = 0$ in (7.27). As before, the fields turn strongly in a way that resembles motion with *vorticity*, but arise from a conserved Hamiltonian \mathcal{H} . The Hamiltonian was computed using (7.19), (7.36) and (7.37) for $\tilde{\Phi}_2$, and is plotted in Fig. 7.8b. Clearly, \mathcal{H} (green) is a constant of motion, while the anisotropic form of the kinetic energy (yellow) proposed in this chapter, \mathcal{K} , and the total potential energy $\Phi = \Phi_1 + \tilde{\Phi}_2$ (purple) exchange energy with each other. Note that $\tilde{\Phi}_2$ (red) is comparable in magnitude to Φ_1 (blue). The observations in the aforementioned figures prove the correctness of the proposed theory in this chapter.

To evaluate the tracking performance in the fiber, the proportional gain in the secondary task was chosen as, $P_2 = 0$, and the result is plotted in Fig. 7.9a. Evidently, the fiber origin s tracks the wandering fiber equilibrium \overline{s} with a constant offset. This shows that even without the secondary proportional gain, the terms in Theorem 7.1 ensure that the fiber origin follows the fiber equilibrium in an equidistant manner, as is seen with only the feedforward terms of tracking control. The motion in fiber while considering $P_2 \neq 0$ is shown in Fig. 7.9b. In contrast to Fig. 7.7, it is seen that the tracking performance is considerably improved due to the terms in Theorem 7.1. Finally, the trajectory in \mathbb{R}^2 for $t \in [0, 30]$ is shown in Fig. 7.10a in a colour-graded manner, i.e., from blue (t = 0)to yellow (t=30). The trajectory is starkly different from that in superposition, Fig. 7.3a. In particular, the motion is bounded in a rhombus with sides defined by the considered operational space $r_i \in [r_i(0), 2\overline{r}_i - r_i(0)]$. The trajectory in Fig. 7.10a also indicates the anisotropic form of the inertia metric, as the standard Lissajous figure in Fig. 7.3a is now skewed into a rhombus. It is worth noting here that, setting the primary task gain as $P_1 = 0$, results in a motion along the fiber (nullspace) of the primary task $\pi_1^{-1}(r_1(0))$ toward \overline{r}_2 , while using $P_2=0$, results in a motion along the fiber (nullspace) of the secondary task $\pi_2^{-1}(r_2(0))$ toward \overline{r}_1 . This is an intuitive behaviour of task-induced algebraic symmetry,





(b) Time-evolution of the non-conservative system due to projection of the secondary potential to the fiber (nullspace) with the inertial compensation in Theorem 7.1.

(a) Force field with the proportional action in Theorem 7.1 resulting in a non-conservative system with a conserved Hamiltonian.

Figure 7.8: Motion Characteristics with proposed control action in Theorem 7.1.

and was verified in simulation. As a corollary of Theorem 7.1, the asymptotic stabilization of the \mathcal{EL} system about the equilibrium is proved next while adding damping terms.

Corollary 6. Consider the \mathcal{EL} system in Theorem 7.1 with τ in (7.27) as the control law having τ_u as a feedforward with additional damping for setpoint regulation, such that,

$$\tau = \tau_1 + \tau_2 + \tau_u, \begin{cases} \tau_1 = J_1^{\top} F_1, \ F_1 = -\left(\frac{\partial \Phi_1(r_1, \overline{r}_1)}{\partial r_1}\right) + D_1 \dot{r}_1\right) \\ \tau_2 = \mathcal{A}^{\top} f, \ f = -\left(Z_1^{\top} J_2^{\top} \frac{\partial \Phi_2(r_2, \overline{r}_2)}{\partial r_2} + D_2 \tilde{\omega}\right) \end{cases}$$
(7.47)

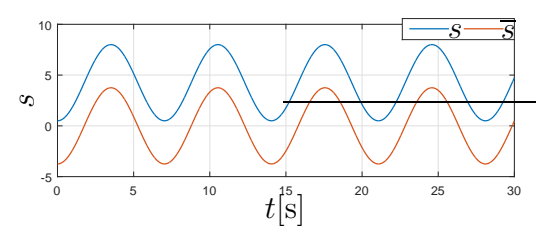
where $D_1, D_2 \succ 0$. The closed-loop dynamics of the \mathcal{EL} system ensures asymptotic stability, i.e., $(r_1, r_2) \rightarrow (\overline{r}_1, \overline{r}_2)$.

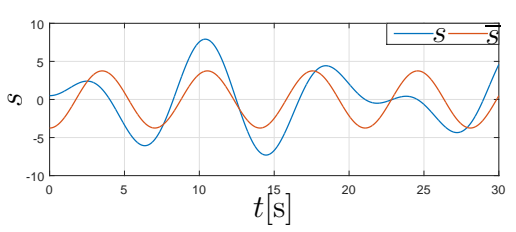
Proof. The Hamiltonian, \mathcal{H} , in Theorem 7.1 serves as the Lyapunov candidate. Taking its time-derivative,

$$\dot{\mathcal{H}} = -\langle \dot{r}_1, \dot{r}_1 \rangle_{D_1} - \langle \tilde{\omega}, \tilde{\omega} \rangle_{D_2} \tag{7.48}$$

which proves uniform stability. Importantly, the problem is time-invariant, as proved in Theorem 7.1. Hence, LaSalle's invariance principle [220] is employed, i.e., in the set $\{\mathcal{H}(r_1,\dot{r}_1,s,\tilde{\omega})\big|\dot{\mathcal{H}}=0\}$, we get,

$$\begin{bmatrix} J_1^{\top} & \mathcal{A}^{\top} \end{bmatrix} \begin{bmatrix} \frac{\partial \Phi_1}{\partial r_1} \\ Z_1^{\top} J_2^{\top} \frac{\partial \Phi_2}{\partial r_2} \end{bmatrix} = \begin{bmatrix} J_1^{\top} & \mathcal{A}^{\top} \end{bmatrix} \begin{bmatrix} \frac{\partial \Phi_1}{\partial r_1} \\ \frac{\partial \Phi_2}{\partial s} \end{bmatrix} = 0 \Rightarrow (r_1, s) \to (\overline{r}_1, \overline{s}). \tag{7.49}$$





the equilibrium \overline{s} with constant offset.

(a) Variation of the fiber origin, s, and equi- (b) Time-evolution of the fiber origin, s, librium, \overline{s} , due to change in r_1 with $P_2 = 0$ and the fiber equilibrium, \overline{s} , during moin Lemma 7.1. Fiber coordinate s tracks tion described in Theorem 7.1. Fiber coordinate s tracks the equilibrium \overline{s} .

Figure 7.9: Time evolution of fiber origin and equilibrium with proposed control action.

Furthermore, in the set $\{\mathcal{H} | \dot{\mathcal{H}} = 0, \dot{r}_1 = 0\}, \ \overline{\omega} = 0$, i.e., the fiber equilibrium stabilizes to a stationary point. In this condition, since $(\overline{r}_1, \overline{s})$ must satisfy $\pi^{-1}(\overline{r}_1, \overline{r}_2), (r_1, s) \to (\overline{r}_1, \overline{s})$ also implies, $(r_1, r_2) \to (\overline{r}_1, \overline{r}_2)$, which proves the result.

As mentioned earlier, Corollary 6 is significant because the control law in (7.47) achieves task-induced symmetry, while employing a single energy-like quantity \mathcal{H} . This is in contrast to prior works [51, 52] which exploited a hierarchy of energy functions to achieve the same functionality.

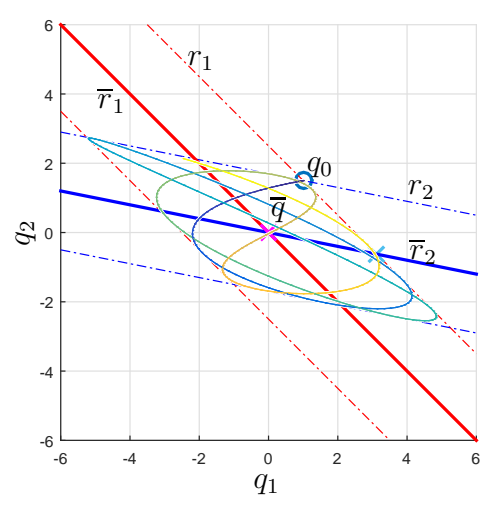
The results from the application of Corollary 6 to Example 5 are shown in Figures 7.10b and 7.11a. In Fig. 7.11a, it is seen that the Lyapunov function \mathcal{H} (green) decreases to origin in a non-increasing manner which validates Corollary 6. Commensurately, the fiber motion is emphasized in the Fig. 7.11b, in which it is observed that the wandering equilibrium in the fiber, \overline{s} (red) reaches a limit value, and the actual fiber motion (blue) tracks it. The actual trajectory is shown in Fig. 7.10b, in which the \mathcal{EL} system is shown to asymptotically converge to $\overline{q} \equiv (\overline{r}_1, \overline{r}_2)$.

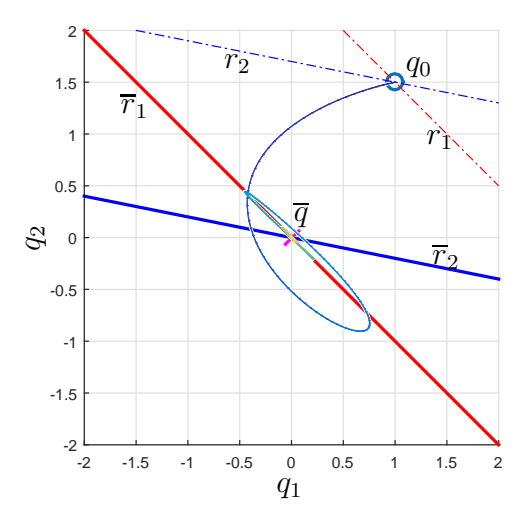
In the next part, limit cycle phenomena are proved separately for the primary operational space and the fiber. For this analysis, recall that \mathcal{A} chosen as the mechanical connection results in a block-diagonal inertia \mathcal{M} . This eases the following stability analysis.

Corollary 7. Consider the \mathcal{EL} system in Theorem 7.1 with τ in (7.27) as the control law having τ_u as feedforward with additional damping only for regulation in the primary space, R_1 , and initial condition as $\mathcal{K}(0) = 0$, such that,

$$\tau = \tau_1 + \tau_2 + \tau_u, \begin{cases} \tau_1 = J_1^{\top} F_1, & F_1 = -\frac{\partial \Phi_1(r_1, \overline{r}_1)}{\partial r_1} - D_1 \dot{r}_1 \\ \tau_2 = \mathcal{A}^{\top} f, & f = -Z_1^{\top} J_2^{\top} \frac{\partial \Phi_2(r_2, \overline{r}_2)}{\partial r_2} \end{cases}$$
(7.50)

where $D_1 \succ 0$. The closed-loop dynamics of the \mathcal{EL} system ensures orbital stability in the fiber $\pi_1^{-1}(\overline{r}_1)$, i.e., $\mathcal{H} \to \mathcal{H}|_{\dot{r}_1=0}$, and \mathcal{EL} system converges to a limit





- (a) Orbit of the 2D particle per Theorem 7.1 with conserved \mathcal{H} about the desired equilibrium $\overline{q} \equiv (\overline{r}_1, \overline{r}_2)$ with initial condition $q_0 \equiv (r_1, r_2)$. Trajectory is colour-graded from blue (t = 0[s]) to yellow (t = 30[s]). Motion is bounded in a rhombus.
- (b) Damped trajectory of the 2D particle as dictated by Corollary 6 with Lyapunov function \mathcal{H} towards the desired equilibrium $\overline{q} \equiv (\overline{r}_1, \overline{r}_2)$ with initial condition $q_0 \equiv (r_1, r_2)$. Trajectory is colour-graded from blue (t = 0[s]) to yellow (t = 30[s]).

Figure 7.10: 2D particle orbit: undamped and damped.

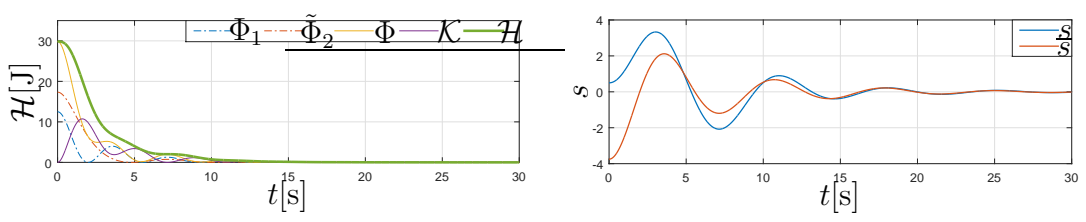
cycle in the fiber.

Proof. The Hamiltonian, \mathcal{H} , in Theorem 7.1 serves as the Lyapunov candidate. Taking its time-derivative, we get $\dot{\mathcal{H}} = -\langle \dot{r}_1, \dot{r}_1 \rangle_{D_1}$, which proves stability. The problem is rendered time-invariant, see Theorem 7.1. Hence, the \mathcal{EL} system converges to the set $\{\mathcal{H} \middle| \dot{r}_1 = 0\}$, in which $\dot{\mathcal{H}} = 0$. In this set, the wandering equilibrium in Lemma 7.4 becomes stationary, i.e., $\overline{\omega} = 0$. Thus, due to block-diagonal inertia, \mathcal{M} , the top row of \mathcal{EL} dynamics in (6.33) vanishes, resulting in $J^{\top} \frac{\partial \Phi_1}{\partial r_1} = 0$, i.e., $r_1 \to \overline{r}_1$. Only the bottom row of the \mathcal{EL} dynamics in (6.33) remains, which is simply the geodesic equation in the fiber $\pi_1^{-1}(\overline{r}_1)$ under the scalar potential $\tilde{\Phi}_2$, i.e., $\hat{\nabla}_{\tilde{\mu}}^{G_{\overline{r}_1}} \tilde{\mu} = -\left(\frac{\partial \tilde{\Phi}_2}{\partial s}\right)^{\sharp}$, where $\nabla^{G_{\overline{r}_1}}$ is the covariant derivative on the specific fiber $\pi_1^{-1}(\overline{r}_1)$. Furthermore, if $\mathcal{K}(0) = 0$, then in the limit set,

$$\mathcal{H}\Big|_{\dot{r}_1=0} = \frac{1}{2} \langle \tilde{\mu}, \tilde{\mu} \rangle_{\mathcal{M}_2} + \tilde{\Phi}_2(s, \overline{s}(\overline{r}_1))$$

which proves the result.

Corollary 8. Consider the \mathcal{EL} system in Theorem 7.1 with τ in (7.27) as the control law having τ_u as a feedforward with additional damping only for fiber



(a) Time-evolution of the \mathcal{EL} system under (b) Variation of the fiber, s, and the fiber Corollary 6 in which $\hat{\mathcal{H}}$ is driven to 0. equilibrium, \overline{s} , under Corollary 6.

Figure 7.11: Fully damped control motion characteristics.

regulation and initial condition as K(0) = 0, such that,

$$\tau = \tau_1 + \tau_2 + \tau_u, \begin{cases} \tau_1 = J_1^{\top} F_1, \ F_1 = -\frac{\partial \Phi_1(r_1, \overline{r}_1)}{\partial r_1} \\ \tau_2 = \mathcal{A}^{\top} f, \ f = -\left(Z_1^{\top} J_2^{\top} \frac{\partial \Phi_2(r_2, \overline{r}_2)}{\partial r_2} + D_2 \tilde{\omega}\right) \end{cases}$$
(7.51)

where $D_2 \succ 0$. The closed-loop dynamics of the \mathcal{EL} system ensures orbital stability of the primary task, i.e., $\mathcal{H} \to \mathcal{H}|_{\tilde{\omega}=0}$, and \mathcal{EL} system converges to a limit cycle in the primary operational space along $\pi_2^{-1}(\overline{r}_2)$.

Proof. The Hamiltonian, \mathcal{H} , in Theorem 7.1 serves as the Lyapunov candidate. Taking its time-derivative, we get $\dot{\mathcal{H}} = -\langle \tilde{\omega}, \tilde{\omega} \rangle_{D_2}$, which proves stability. The problem is rendered time-invariant, see Theorem 7.1. Hence, the \mathcal{EL} system converges to the set $\{\mathcal{H} \middle| \dot{\tilde{\omega}} = 0\}$, in which $\dot{\mathcal{H}} = 0$. In this set, the L.H.S. of the bottom row of (7.40) vanishes, resulting in $\mathcal{A}^{\top} \frac{\partial \tilde{\Phi}_2}{\partial s} = 0$, i.e., $s \to \overline{s} \ \forall r_1 \in R_1$. Thus, only the top row of the \mathcal{EL} dynamics in (7.40) remains, which is simply the geodesic equation in the primary operational R_1 under the scalar potential Φ_1 , i.e., $\hat{\nabla}_{\dot{r}_1}^{R_1} \dot{r}_1 = -\left(\frac{\partial \Phi_1}{\partial r_1}\right)^{\sharp}$, where ∇^{R_1} is the covariant derivative on R_1 . Furthermore, if $\mathcal{K}(0) = 0$, then in the limit set,

$$\mathcal{H}\Big|_{\tilde{\omega}=0} = \frac{1}{2} \langle \dot{r}_1, \dot{r}_1 \rangle_{\mathcal{M}_1} + \Phi_1(r_1, \overline{r}_1), \tag{7.52}$$

which proves the result. Also note that, since $\tilde{\Phi}_2 \to 0$ as $t \to \infty$, $r_2 \to \overline{r}_2$.

In [225], limit cycle stabilization was achieved in the fiber, while regulating on the primary operational space, R_1 . In contrast, Corollary 8 implies that limit cycle stabilization can be achieved on R_1 while regulating motion on the fiber. This is significant because, the generated limit cycle is a geodesic of motion on R_1 . To achieve this, the proposed Hamiltonian, \mathcal{H} , which is a single quantity for the entire \mathcal{EL} system, is exploited in contrast to the hierarchy of two Hamiltonian functions (one each for primary and fiber spaces) in [225].

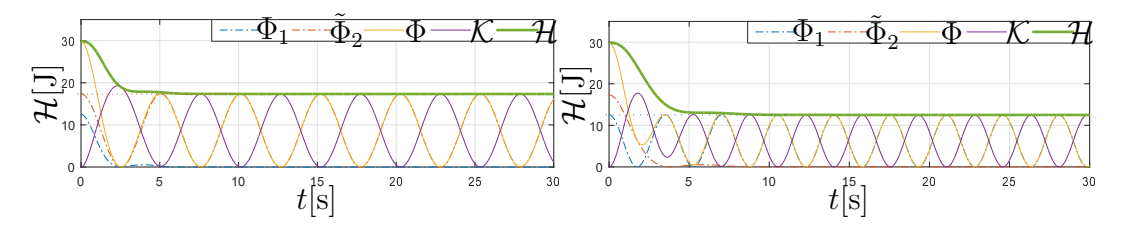


Figure 7.12: Time-evolution of the \mathcal{EL} system under Corollaries 7 (left) and 8 (right), in which the Hamiltonian \mathcal{H} reaches a steady state value by damping out motion in one subspace.

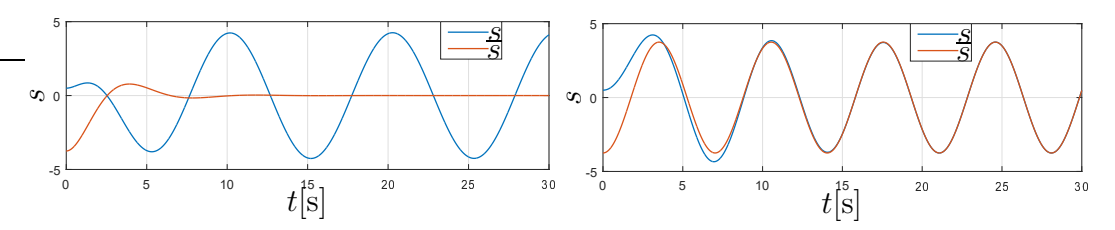


Figure 7.13: Variation of the fiber origin, s, and the fiber equilibrium, \overline{s} , under Corollaries 7 (left) and 8 (right). Left: Fiber equilibrium \overline{s} assumes a steady state, while the fiber coordinate tracks it. Right: Fiber coordinate s tracks the equilibrium \overline{s} , which varies due to the limit cycle in R_1 .

Remark 47. Note that in Corollaries 7 and 8, the Hamiltonian \mathcal{H} does not necessarily converge $(t \to \infty)$ to the initial energies, $\tilde{\Phi}_2(s(r_1(0)), \overline{s})$ and $\Phi_1(r_1(0), \overline{r}_1)$, respectively. It will however, converge to a value that satisfies $\mathcal{H}(t) \leq \mathcal{H}(0)$.

The results for the Corollaries 7 and 8 applied to Example 5 are shown in Figures 7.12-7.14. In particular, the results of Corollary 7 and Corollary 8 are shown on the left and right side, respectively. In Fig. 7.12, it is seen that the Hamiltonian \mathcal{H} converges to steady-state values, as postulated in the Corollaries. In the case of Example 5, $\mathcal{H} \to \tilde{\Phi}_2(s(r_1(0)), \overline{s})$ and $\mathcal{H} \to \Phi_1(r_1(0), \overline{r}_1)$ on the left and right, respectively. However, note that, in general, as in Remark 47, this might not be the case. In Corollary 7, the \mathcal{EL} system converges to $\dot{r}_1 \to 0$, or $\overline{\omega} = 0$, i.e., the equilibrium in fiber becomes stationary. This is seen clearly in the left of Fig. 7.13, while the \mathcal{EL} system assumes a limit cycle in the fiber. In contrast, on the right, the limit cycle is on R_1 , and \overline{s} does not assume a steady state. However, the proposed feedforward in Theorem 7.1 ensures tracking. In Fig. 7.14, the orbit of the \mathcal{EL} system is shown. On the left, as proved in Corollary 7, the \mathcal{EL} system converges to a limit cycle on $\pi_1^{-1}(\overline{r}_1)$. In contrast, on the right, as proved in Corollary 8, the convergence is to a limit cycle on $\pi_2^{-1}(\overline{r}_2)$.

With these results from the application of aforementioned Theorems and the corollaries, the proposed mechanism of imposing task-induced algebraic symmetry

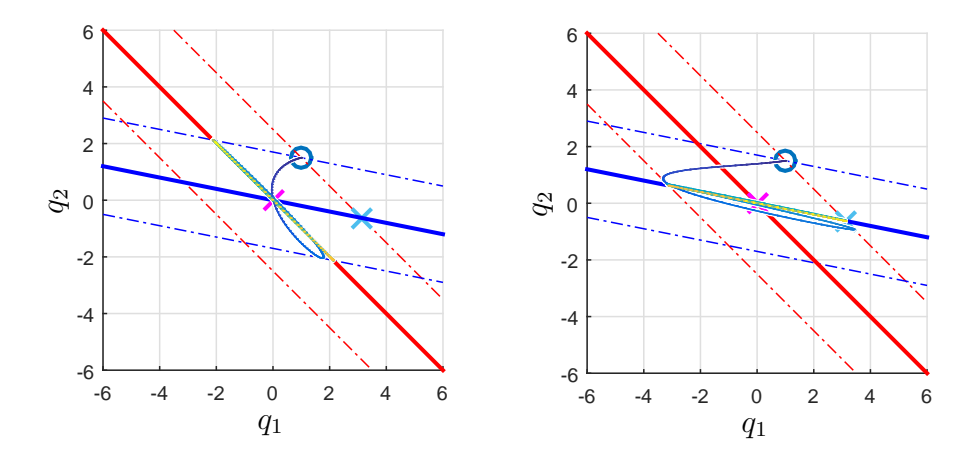


Figure 7.14: Orbit of the 2D particle as dictated by Corollaries 7 (left) and 8 (right). Left: Motion is regulated to the primary desired equilibrium \bar{r}_1 with a limit cycle along its fiber. Right: Motion is regulated on the fiber with a limit cycle along the primary operational space. Trajectory is colour-graded from blue (t = 0[s]) to yellow (t = 30[s]).

is validated. In particular, I recall that the stabilization results here are evaluated using a single Lyapunov candidate, in contrast to the work presented in Chapter 6. Therefore, the stability claims are applicable for the whole \mathcal{EL} system at all times. This type of hierarchical control was not done before.

7.5 Conclusion

In this chapter, the problem of task-induced algebraic symmetry (hierarchy) in motion control has been solved from a Hamiltonian perspective for the entire \mathcal{EL} system for the first time. In motion control with redundancy, the \mathcal{EL} equations on the task-induced fiber bundle is sufficient to ascertain stabilization with a single task. However, introducing a secondary task makes the problem non-Hamiltonian due to the wandering equilibrium of the fiber (nullspace) potential that varies with the motion in the primary operational space. This phenomena was proved analytically and demonstrated through simulation results. To pose the control problem in the Hamiltonian framework, a novel proportional action was proposed to ensure that a new Hamiltonian which describes the \mathcal{EL} system with task hierarchy is conserved. Although the new proposed Hamiltonian is different from the original Hamiltonian of the \mathcal{EL} system, it preserves the metric tensor. The conserved Hamiltonian was demonstrated through simulation results. The main value of this work is that it introduces the notion of motion stabilization using non-conservative force fields. As future work, the proposed

7.5 Conclusion 217

theory will be applied for PBC of robotic systems to experimentally validate the system-wide stability and passivity properties. From that perspective, it appears that task-induced algebraic symmetry could be imposed without any force sensing requirement, in contrast to traditional methods in [52, 207, 209]. However, this remains to be proved analytically.

Applications

In this chapter, the applications which have directly benefited from the contents of the theoretical contribution of this thesis are summarized. This gives the reader an overview of the impact of this thesis in practice. Obviously, in some applications, the contributions of the thesis have been modified for engineering considerations. The mathematical aspect of these modifications can be found in the corresponding publication related to this thesis (Tables 1.1 and 1.3), and are referenced explicitly in each section below. The key findings are summarized with instructive figures and plots to aid the understanding of the key concept. As is evident from the earlier chapters, the contributions include the topics of sensor-based control, Validation & Verification for orbital robotics, motion control and shared control (teleoperation). The contributions are: one intravehicular ISS mission, a dedicated V&V strategy for orbital robotics, four projects (EU,ESA) in orbital robotics, and two KUKA-supported innovation awards.

8.1 NASA/DLR/MIT ROAM/Tumbledock: ISS Experiments

This work focuses on the results of an experimental campaign for autonomous rendezvous using two Astrobee robots on the International Space Station (ISS), conducted under the ROAM/TumbleDock test campaign, a collaboration between NASA, DLR and MIT [230]. In these experiments, one robot serves as the autonomously controlled Chaser, and another as the unknown Target. The Target mimics the anticipated tumble of the ENVISAT satellite, which is of interest for active debris removal [42].

220 8 Applications

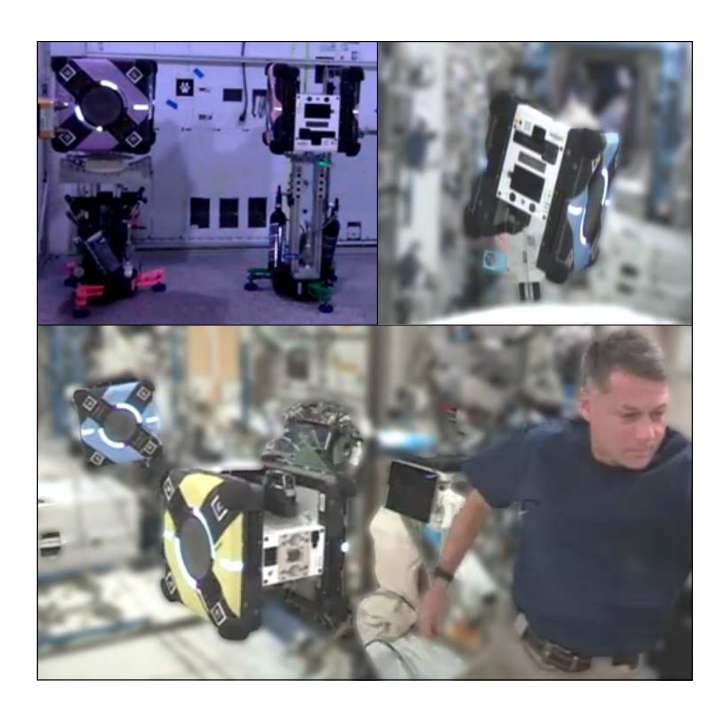


Figure 8.1: Validation of the Observer during on-ground testing at NASA Ames (top left), ISS Crew minimal (top right) and the final Tumbledock/ROAM2 experiments in the Japanese Experiment Module on the ISS (bottom).

NASA's Astrobee robots are free-flying robots which operate aboard the Japanese Experiment Module in the ISS. The Astrobees enable microgravity autonomy research through a sensor-suite and three reconfigurable general-purpose processors. The Astrobees utilize impellers to provide full actuation by propulsion, with multiple sensors for navigation including cameras and an IMU. On-orbit testing during the first campaign faced a significant challenge with Astrobee's default localization module, which was prone to infeasible jumps and general high root mean square error [230].

To this end, based on my work in Chapter 5 on internal model control, I proposed a two-layer state estimation approach to the localization to overcome these discontinuities. The proposed approach is shown in Fig. 8.2, where the extension is highlighted in yellow. In particular, the i^{th} Astrobee robot's configuration in the ISS is $g_i \in \text{SE}(3)$ with the body velocity V_i . First, the state $(\tilde{g}_i, \tilde{V}_i)$ is roughly estimated by the default localization pipeline using a kinematic sensor fusion of exteroceptive (cameras) and proprioceptive (IMU) measurements. However, the transitioning of optical features (s) from the field of view might result in estimation discontinuities, which negatively affect control performance. This was already observed in ROAM 1 test campaign earlier. Furthermore, air circulation in the ISS can cause a disturbance (F_i) that perturbs the desired Astrobee motion. The proposed observer was added to estimate not only the motion state

 (\hat{g}_i, \hat{V}_i) in a smooth and precise manner, but also the disturbance wrenches (\hat{F}_i) . In particular, Theorem 5.3 was employed while linearizing the observer error dynamics about $g_i^{-1}\hat{g}_i = \mathbb{I}_{4,4}, \hat{V}_i - V_i = 0$ to formulate an EKF for \mathcal{LP} dynamics. This was done in order to enable outlier rejection based on a stochastically-significant threshold and measurement noise modeling for the localization pipeline, as was shown in [231]. Additionally, in the neighbourhood of the linearization point, the observer and the controller dynamics become decoupled, which simplified testing.

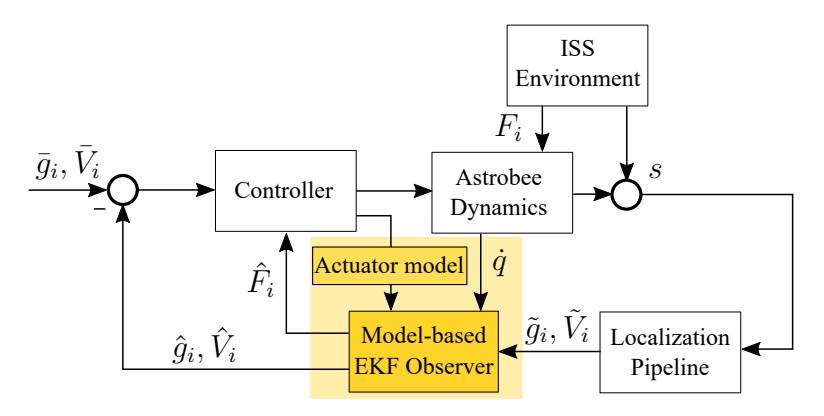


Figure 8.2: Controller block diagram for the i^{th} Astrobee, i = C for the Chaser and i = T for the Target. Extensions to the default Localization Pipeline are indicated in yellow.

.

The proposed observer was validated sequentially in three phases, as shown in Fig. 8.1: On-ground validation using air-bearing test-bed at NASA Ames, followed by Crew Minimal on the ISS, and the final ROAM test campaign. The observer was successful in 19 out of 20 experiments in the final ROAM 2 test campaign on the ISS, with one failure being attributable to a prolonged image processing error. Here, I show the key experimental results for the Target Astrobee in Figs. 8.3-8.4; the observer was also used on subset of runs for Chaser localization improvement. The position and velocity estimates provided by the localization pipeline (blue) and the observer (red) from Fig. 8.2 are shown in Fig. 8.3. It can be seen that the localization estimates tend to suffer sporadic discontinuities (dashed ellipses). The model-based observer is not affected by these discontinuities as they are not in agreement with the Astrobee's dynamic model. Note that both position and velocity estimates are required for the motion stabilization of the Astrobee, and the removal of discontinuities was a major benefit. To validate the estimation of disturbance forces, F_i , the Astrobee actuators were turned off so that the commanded forces of the controller serve as a disturbance. In Fig. 8.4, the actual (red) and the estimated (blue) disturbance forces are shown, which demonstrates the estimation convergence. The success of this ISS test campaign has sparked the interest of NASA to have the filter as a part of the permanent Astrobee software stack.

222 8 Applications

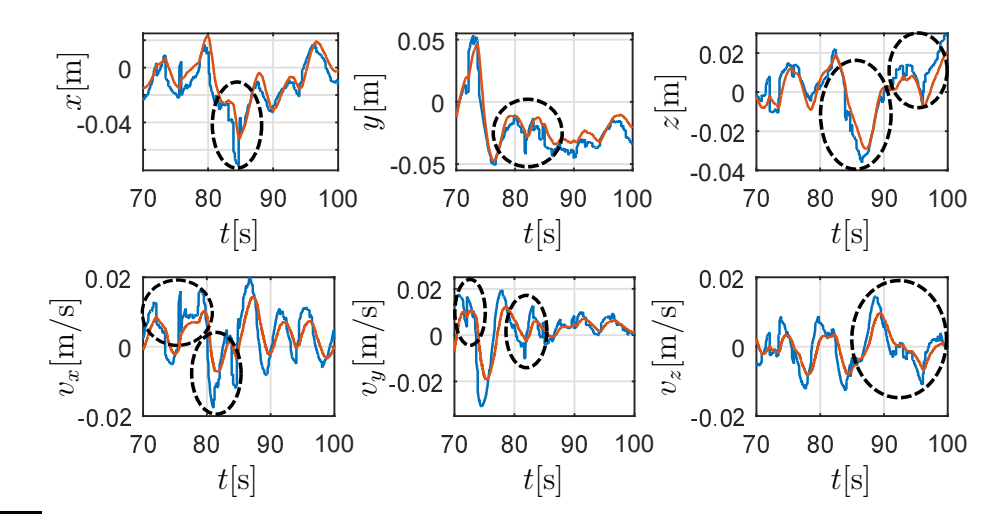


Figure 8.3: Position (top row) and velocity (bottom row) state estimation results. The localization pipeline is shown in blue, and the Model-based EKF in red. Dashed circles indicate localization discontinuities

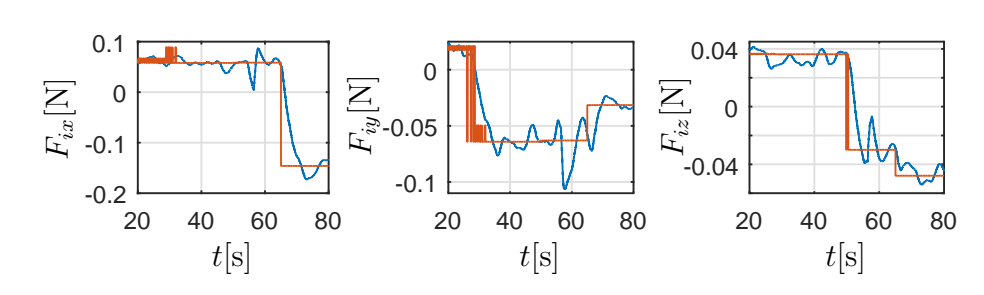


Figure 8.4: Disturbance force, F_i : actual (red) and estimated (blue).

8.2 V&V Strategy for Orbital Robotics

With the rapid development of robotics technologies and powerful computing, orbital robotic missions have emerged as a key driver to address problems, e.g., on-orbit servicing. Such missions require multiple subsystems, e.g., planning, perception, motion control software, autonomy, and shared control modalities to work reliably, especially during proximity operations. This necessitates a more structured validation plan, to be started already during the preliminary stages of the mission. In traditional space missions, approaches for V&V of GNC algorithms have been instrumental in derisking mission preparatory activities. However, the extension to robotic missions requires a commensurate extension of the V&V tools to possess robotics-oriented dynamic models, sensor/actuator models, onboard computers, and math libraries. In this section, I outline my contribution towards the approach adopted at DLR for V&V of orbital robotics technologies.

8.2.1 Co-simulation: MIL/SIL/PIL

Once the mission requirements are roughly available, the initial phase A/B1 progresses through a sequence of rapid prototyping using model-based design tools [232, 233]. However, contemporary tools have been aimed at GNC applications, and the topics relevant to robotics prototyping, e.g. multibody dynamics, momentum conservation, capture dynamics, have been missing. At DLR, during the research activity for this thesis, I have developed a co-simulation framework that enables model/software/processor-in-the-loop, also known as MIL/SIL/PIL, see Fig. 8.5. In particular, the framework is composed of CoppeliaSim [234] as the physics provider and MATLAB/Simulink as the control prototyping environment. The inter-process communication between the orbital robot and control software was developed using Links and Nodes, while high-bandwidth data communication, e.g. for synthetic camera images, was developed using SensorNet, both of which are developed at DLR [235]. The main novelty over the the state-of-the-art [236] is that, my approach allows the CoppeliaSim simulation to run with a lower time-step of 10[ms], while the communication for robot joints runs at a faster and synchronized time-step of 1[ms] with the control software for high-fidelity torque control. This ensures that the non-dynamics modules, e.g., graphics rendering, are computed slower than the dynamics engine, which is not possible with the supported API of CoppeliaSim. To achieve this, I developed an unsupported API around the supported API, which communicates directly with the underlying dynamics engine that runs with a finer time-step. This co-simulation framework was exploited in multiple projects, e.g., ESA MIRROR [66], EU EROSS+/IOD [41] each of which will be described later. The official deliverables of these projects have directly featured results from the co-simulation developed during this thesis. In this co-simulation, the motion of FRM is simulated using Open Dynamics Engine because it preserves the symmetry of FRM's \mathcal{LP} dynamics, i.e., momentum conservation [237].

8.2.2 HIL on OOS-SIM

In the Phase D of such projects, the control software was validated on the DLR OOS-SIM facility: a robotic facility to simulate capture dynamics for orbital robotics. The \mathcal{LP} dynamics from Chapter 3 was implemented on a real-time computer to simulate the motion of an orbital FRM. As shown in Chapter 4, this implementation preserved the symmetry, i.e., momentum conservation, of the FRM. In fact, for the mission phases of approach, grasping and post-grasping, the total momentum of the orbital robot (\mathcal{J}_s) and the client satellite (\mathcal{J}_c) was also conserved, as is shown in Fig. 8.6. In the shown scenario, the satellite was spinning around its docking axis at 1[°/s], while the orbital FRM grasped it using a free-floating controller [29]. After the grasp event (arrow), momentum was transferred from the satellite to the FRM. During this simulation, the bottom plot shows that

224 8 Applications

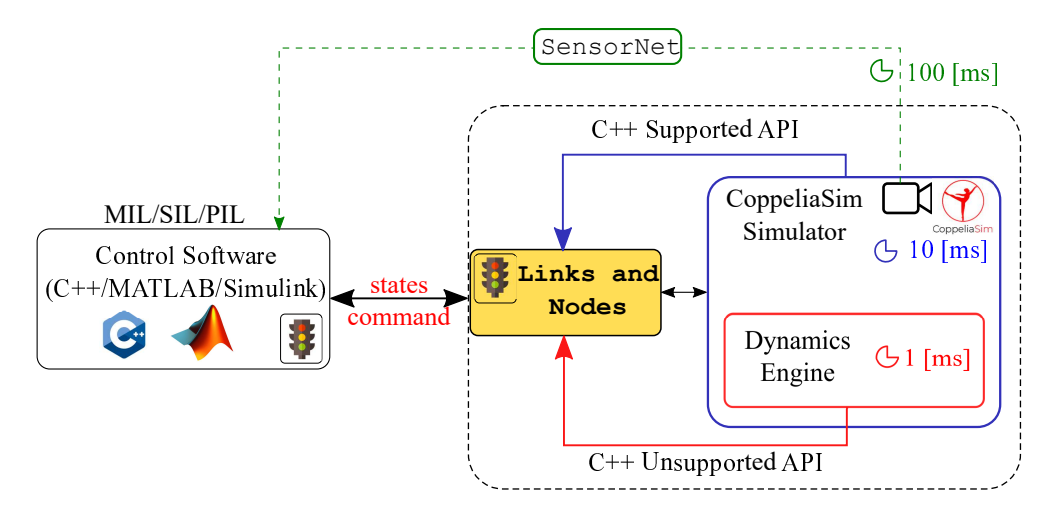


Figure 8.5: Co-simulation environment for control prototyping in orbital robotics missions developed during this thesis.

the total momentum $\mathcal{J}_c + \mathcal{J}_s$ is conserved. This proves the high-fidelity and the real-time computation capability of the \mathcal{LP} dynamics from Chapter 3.

Thus, through the aforementioned contributions, I extended the incremental V&V strategy for orbital robotics at DLR, which is summarized in the Fig. 8.7. This approach was successfully employed during the EROSS+/IOD mission development, which was funded by the European Union [41].

8.3 EU EROSS+: On-orbit Servicing

The objective of European Robotic Orbital Support Services (EROSS+) is to demonstrate the European solutions for the Servicers and the Serviced LEO/GEO satellites, enabling a large range of efficient and safe orbital support services. The demonstration mission concept includes the complete orbital rendezvous phase of a Servicer spacecraft (FRM) with a collaborative Client satellite prepared for On-Orbit Servicing that shall be followed by the capture and then servicing operations. The whole idea is to validate the capability of carrying out on-orbit operations of this type for future missions [41, 172].

8.3.1 Co-simulation: Initial Analysis

Within this project, DLR was responsible for the robotic arm subsystem, which consisted of the CAESAR robotic manipulator [170]. For rapid control prototyping, the co-simulation framework in Sec. 8.2.1 was constructed to reflect the anticipated concept of operations [41], see 8.8. This framework was used to evaluate the controller, and an example of manoeuvre performed with the co-simulation

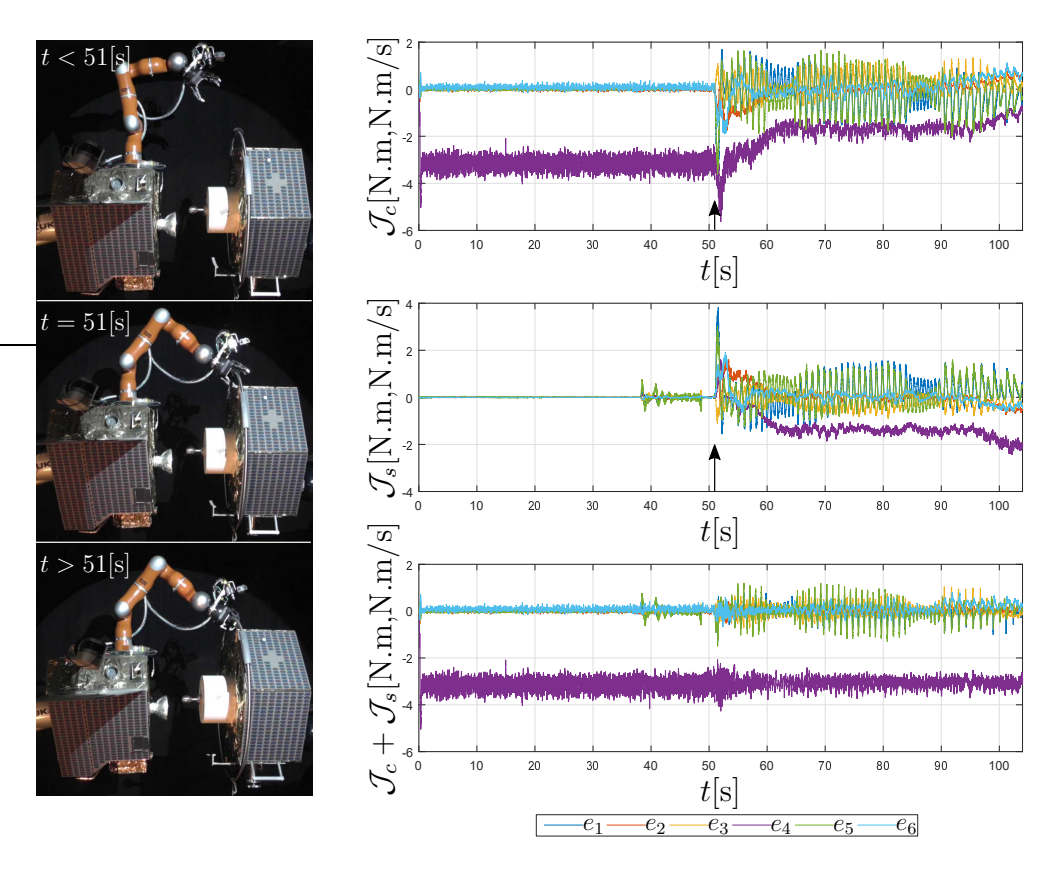


Figure 8.6: Conservation of total momentum $(\mathcal{J}_c + \mathcal{J}_s)$ of the orbital robot and the client satellite on the DLR OOS-SIM facility during approach, grasp and post-grasping phases of an experiment.

for the EROSS+ project is shown in Fig. 8.8 from the initial configuration to the capture configuration. To deal with this exteroceptive sensing, the IM-PBC approach in Theorem 5.1 was employed, as is. The client satellite was considered with a residual velocity of $1[^{\circ}/s]$ when the CAESAR arm begins its approach. During the approach, the spacecraft was required to regulate its pose using a combined control approach. The tracking control errors were less than 5[mm] and $0.02[^{\circ}]$ for the platform, and less than 5[mm] and $0.5[^{\circ}]$ for the end-effector, as shown in Figures 8.9a and 8.9b. In compliance with the mission requirements, the sampling rates of sensors/actuators for the platform, as well as the visual input were considered at 10[Hz].

226 8 Applications

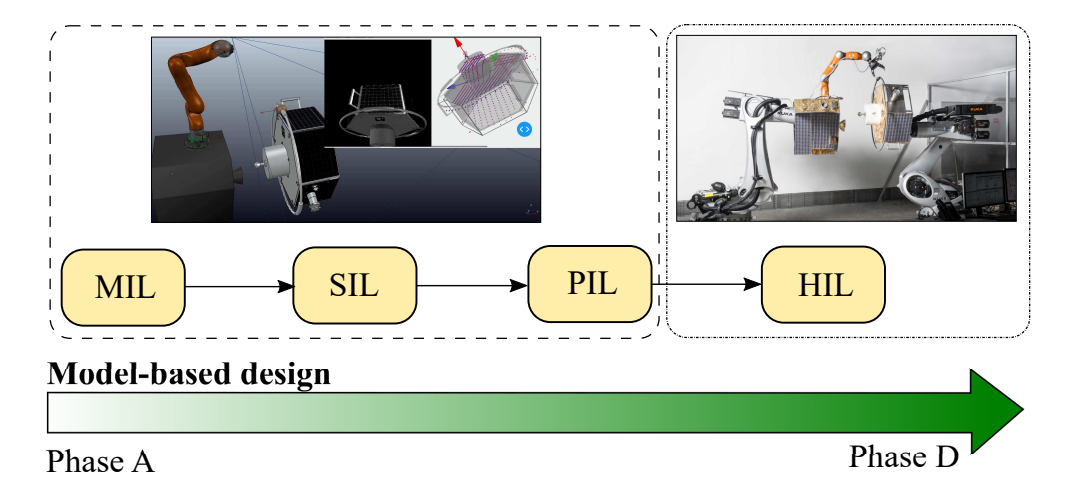


Figure 8.7: An incremental V&V strategy using the co-simulator framework (dynamics, synthetic images, LIDAR point clouds) and HIL during thesis research.

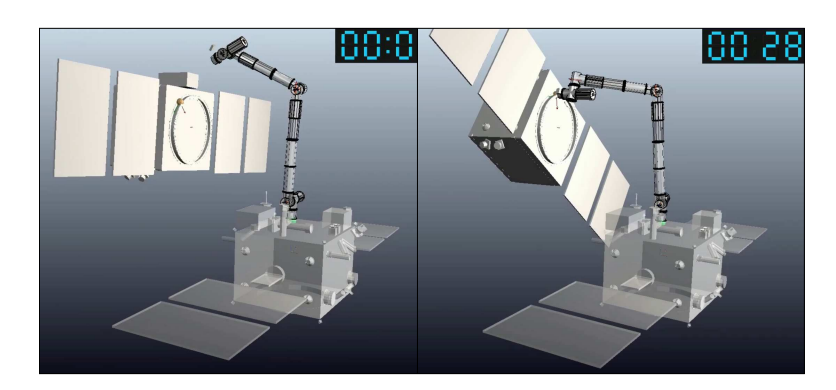
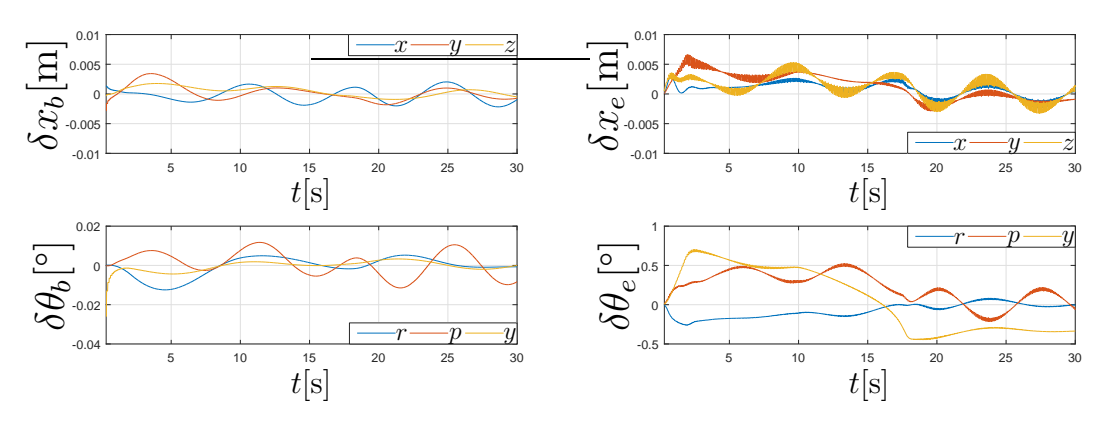


Figure 8.8: EROSS+: Co-simulation environment for control prototyping. Orbital FRM approaches client satellite spinning at $1[^{\circ}/s]$. Left: Initial approach configuration. Right: Final capture configuration.

8.3.2 HIL: Control Prototyping

The robotic HIL facility: DLR OOS-SIM from Sec. 8.2.2 was configured with the anticipated masses of the spacecraft 345[Kg] and satellite 400[Kg] to validate the control approach. Following the co-simulation from the previous section, the IM-PBC approach from Theorem 5.1 was also used for HIL validation. The validation results of the proposed method on the OOS-SIM are detailed therein in Sec. 5.6.2, and are not explicitly repeated here. The reader is encouraged to review the results. This also proves the effectiveness of the incremental V&V approach, which begins with the MIL at an early stage (shown here), and followed by HIL process. Through these processes, technical mission requirements, e.g., maximum acceptable displacement of the FRM-base, were obtained. Although



- (a) Spacecraft pose error (left) of the (b) EROSS+' CAESAR arm end-effector EROSS+ Servicer during the regulation tracking pose error (right) of the Servicer task.
- during the regulation task.

Figure 8.9: EROSS+ results from Co-simulation environment.

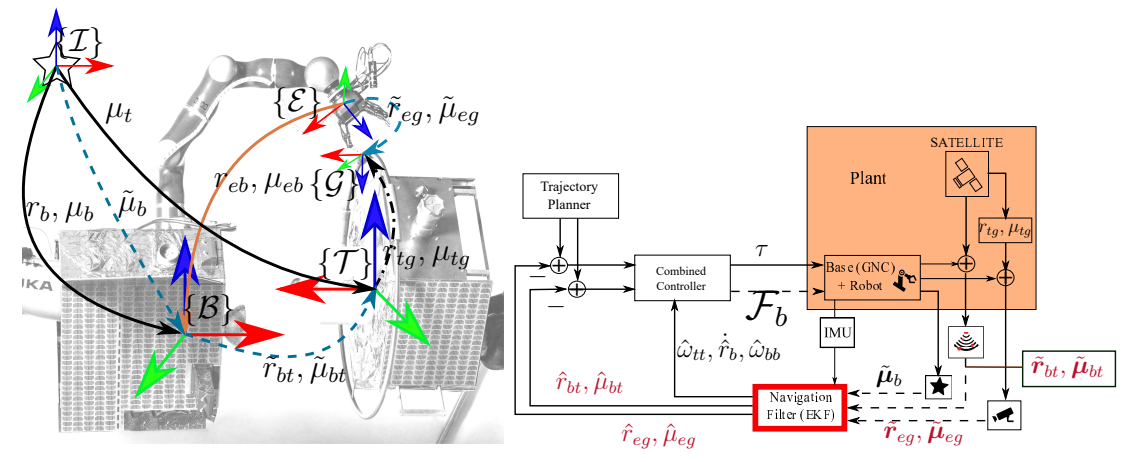
the robotic manipulator on the OOS-SIM was the LWR4+, the dynamic coupling between it and the spacecraft was analysed while keeping the identical inertia ratios.

ESA COMRADE: Active Debris Removal 8.4

This work deals with the early phase analysis of the robotic capture of the EN-VISAT satellite. The satellite was decommissioned in 2012 and has acquired a complex tumbling motion in orbit which creates a hazard for neighbouring space assets. Hence, it is being considered for debris removal using an orbital FRM that will require *combined control*, i.e., use the combined effort of spacecraft and the robotic manipulator, to approach it in a safe manner. The dynamic nature of the mission posed challenges in motion control design and the HIL validation [42]. In the following, I list down my contributions related to these topics.

Robot Navigation EKF 8.4.1

A Robot Navigation EKF was designed for the capture phase to simultaneously estimate the inertial states of the two agents: FRM platform, which will undergo combined actuation of the robotic arm and the spacecraft, and ENVISAT, which is tumbling with nearly 2.5[°/s]. The scenario is shown in Fig. 8.10a, and the corresponding sensor-suite is given in Table 8.1. On the ISS, the current method uses an estimator for the FRM-base (ISS) followed by another one for the Target (incoming cargo vessel) [238]. However, note that the ISS does not produce dynamic motions and the Target is also controlled, which simplifies the



(a) ESA COMRADE: Orbital FRM (b) Block diagram of the controller for the or-(left) approaches a free-floating target bital FRM to approach the ENVISAT using the satellite (ENVISAT, right). proposed filter.

Figure 8.10: The grasping frame, $\{\mathcal{G}\}$, is observed in an end-effector-mounted camera frame, $\{\mathcal{E}\}$, and the CoM frame, $\{\mathcal{T}\}$ is observed using a base-mounted LiDAR, $\{\mathcal{B}\}$, to estimate the inertial motion states of both, the FRM-base and the target, w.r.t. $\{\mathcal{I}\}$.

estimation problem. Therefore, estimation errors are likely to propagate with a difficult-to-model correlation, when motions are dynamic, as in ESA COMRADE. The proposed combined EKF is advantageous over the cascaded scheme since it performs a combined state estimation.

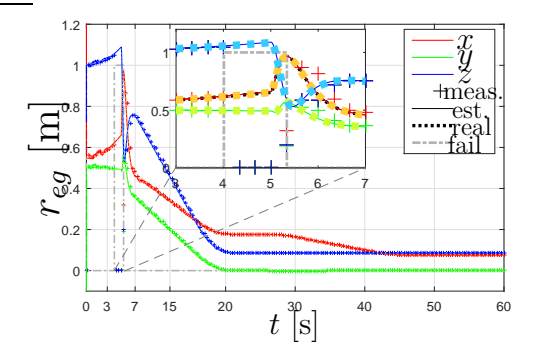
Sensor	LiDAR	Camera	Star	\mathbf{IMU}
			Tracker	
Meas.	$\{ ilde{m{r}}_{bt}, ilde{m{\mu}}_{bt}\}$	$\{ ilde{m{r}}_{eg}, ilde{m{\mu}}_{eg}\}$	$ ilde{oldsymbol{\mu}}_b$	$\{ ilde{m{\omega}}_{bb}, ilde{m{a}}_{bb}\}$
Rate [Hz]	10	10	10	1000

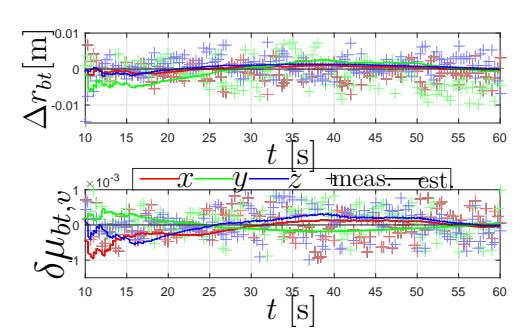
Table 8.1: Available Measurements on Orbital Robot

Combined state estimation poses a design challenge that the correlation mentioned above needs to be explicitly modeled. Traditionally, a multiplicative quaternion filter is used that only models the quaternion error vector while assuming that the scalar part is unity when errors are small [238]. In the proposed filter, two inertial orientation states (Target and FRM) were to be estimated from relative measurements which are composed of both. This lack of observability is resolved by using the inertial star tracker measurement, however, the main issue lies in the linearization of the measurement error model. This is because both inertial quaternion states are coupled, and this needs to be accounted for in the measurement matrix of the filter. In [75, App. B], I derived this correlation

model, which enabled the design within the multiplicative filtering framework. The EKF also employed the symmetry of ENVISAT's \mathcal{EP} dynamics, i.e., momentum conservation of its unforced motion, to improve estimation accuracy. For the Phase B1 of the project, the controller structure in [64, 134] was used to track the tumbling ENVISAT, which is based on the combined controller presented in [44], for the reach phase and the proposed filter was implemented in the GNC Development Environment [233, 239]. It is an integrated development environment that provides tools which are able to support the analysis, synthesis, evaluation activities and data management, especially for a GNC design process, and was the tool chosen for COMRADE. The results are summarized below.

Firstly, due to the limited range of operation of the camera, in the initial part of the *capture* phase, there is a high possibility of the camera going out of range. This is clearly emphasized in $t \in [4, 5.2]$ [s] (dashed grey) of Figure 8.11a, in which the component-wise camera position measurement, for measured (plus), estimated (solid) and real (dotted) are provided. It is observed that despite the camera being out of range, the EKF provides robust reconstruction of the relative transforms that it measures. This ensures the normal operation of the controller. Furthermore, it is also seen that the estimate (solid) tracks the real (dotted) line better than the measured (plus) quantity. Secondly, noise levels are high in unfiltered LiDAR pose measurements. This negatively affects the performance of the base body GNC system which, in turn, affects end-effector accuracy. Figure 8.11b shows the residuals (obtained by subtracting from ground truth) of measurements (marked as +) and reconstructed measurements from estimates (solid). It is evident that the proposed EKF successfully filters out the noise of the LIDAR signal.





(a) Camera position for measured (plus), (b) Estimation error in LiDAR position reconstructed from estimates (solid) and (top) and quaternion (bottom), for meaground-truth (dotted) with camera failure sured (+) and reconstructed from esti-(dashed grey) during $t \in [4, 5.2]$ s.

mates (solid) relative to ground truth.

Figure 8.11: ESA COMRADE: Estimation results for camera and LiDAR.

Using the proposed filter, the end-effector performance in terms of position

and orientation control errors were 1 [mm] and 0.05[°] respectively. It is worth pointing out that the combined controller architecture (relying on unfiltered measurements) in [44] had a nominal end-effector control error of 1 [cm] and 0.5° in orientation due to LiDAR noise. This confirms the noise reduction of the proposed filter and the controller performance improvement. The details of the filter were published in [75].

8.4.2 V&V using HIL

A typical approach to replicate a desired motion between an orbital FRM and the client satellite on a robotic facility is to use an absolute formulation, i.e. the motion of the simulated body with respect to an inertial frame is commanded exactly on a HIL facility with respect to its inertial frame [49, 50, 73, 240]. The absolute representation of the dynamics can have limited applicability when replicating the tumbling velocity of a large satellite (e.g. ENVISAT) due to workspace constraints. Although a kinematic scaling might be useful to address this problem, however, it will lead to a non-physical simulation because model-based and measured forces will be different. Therefore, a relative formulation of the dynamics is an attractive solution.

In contrast to prior work on relative dynamics implementations in [161, 165], the proposed method ensured dynamic consistency. Specifically, the fictitious forces of the space analogue scenario, e.g. CC forces, are experienced on the HIL facility by commanding additional feed-forward terms. To achieve this, the method of Lagrangian matching from Chapter 4 was applied. The key novelty was its application while considering motions of the orbital FRM (i.e., a multibody Hamel's equations) and ENVISAT (i.e., rigid-body \mathcal{EP} equations) relative to the nominal unforced motion of ENVISAT for a client satellite. This choice of the nominal trajectory was motivated to employ the symmetry in the \mathcal{EP} dynamics of ENVISAT, i.e., momentum conservation. This means that the time-evolution of motion on the HIL facility can be seen as relative dynamics on the momentum level-set of ENVISAT. This novel application of the method enabled HIL simulation while reproducing only the relative motions on the OOS-SIM, and was crucial to achieving the V&V results of the COMRADE scenario.

The manipulator on the FRM was equipped with a gripper, which was used to grasp the launch-adapter-ring profile attached to the client mock-up. The phases of the experiments are shown in Fig. 8.12. The OBSW controller for the HIL validation was designed as a nonlinear compliant controller (see [179, §6.2.1]), which provides the actuation to perform synchronisation, approach and capture of ENVISAT. Fig. 8.13 summarises the experimental results. On the top row, the relative error of the manipulator and FRM-base is shown. ENVISAT was initialised with an angular velocity of $2.5[^{\circ}/s]$ about its major axis of inertia and between $t \in [0, 9][s]$ the synchronisation phase occurs, i.e. the spacecraft regulates its pose with respect to ENVISAT. At t = 9.1[s], the manipulator arm

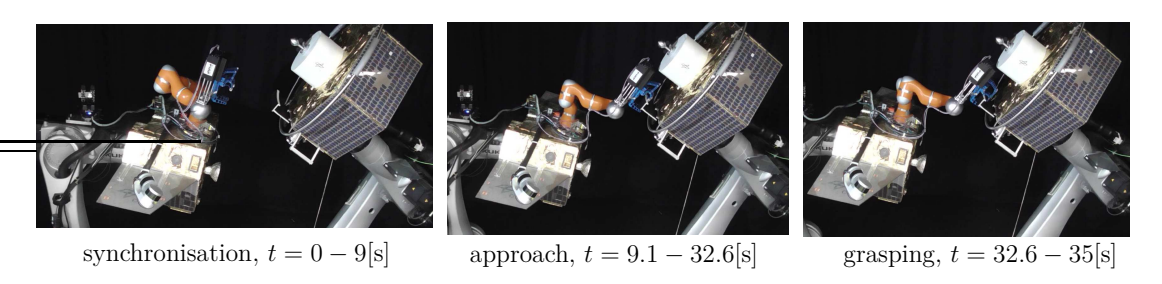


Figure 8.12: ESA COMRADE scenario of robotic capture of ENVISAT (right) using a FRM on the OOS-SIM facility.

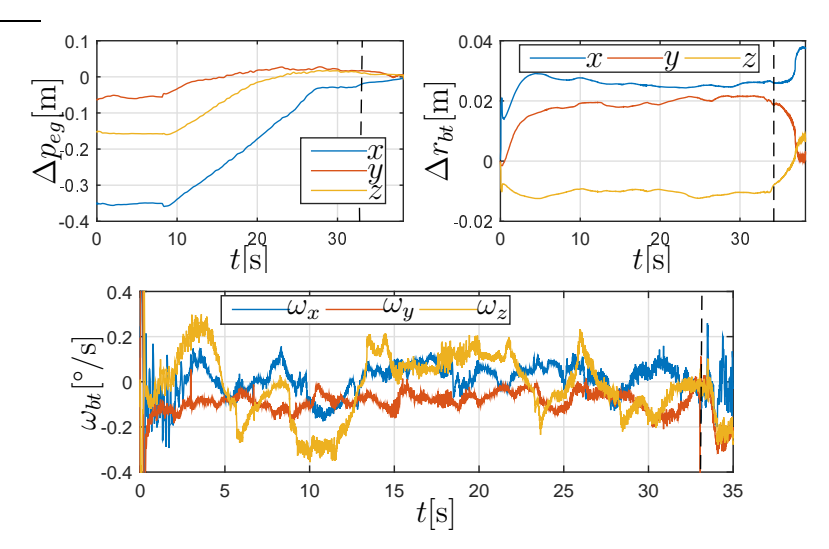


Figure 8.13: Top: Controller position errors: End-effector: Δ and FRM-base error Δr_{bt} . Bottom: FRM angular velocity (ω_{bt}) with respect to the ENVISAT CoM.

starts the approach and the capture of the ENVISAT occurs at t=32.6[s] (see the dashed-line) in Fig. 8.13. The bottom of Fig. 8.13 shows the relative velocity of the servicer with respect to the client. It can be seen that before the grasping, the angular error is approximately $0.2[^{\circ}/s]$ component-wise (see between $t \in [15, 32.6][s]$). This validation of the controller for the ENVISAT capture was enabled by the proposed relative dynamics formulation. Commonly, a rigidisation phase (see [179, §6.2.2]) follows after the grasping and the manipulator arm damps the remaining relative velocity, however, it was not considered within this validation.

8.5 ESA MIRROR: On-Orbit Assembly

Autonomous on-orbit assembly is a key technology for building larger space assets. This technology is crucial for structures which are too large to be self-deployed as

a monolithic component. For example, the new generation of space telescopes for deep-space observations require a larger diameter, however, the sizes are currently limited by launch vehicle sizes [241]. Hence, a suitable solution is to deliver the structural components into the orbit in single or multiple launches to perform the so-called in-orbit assembly.

In the ESA-funded project, MIRROR, a novel modular MAR system has been proposed, see [47]. The MAR is composed of three modules: a torso and two symmetrical 7-DoF anthropomorphic robotic arms that are functionally independent and can be connected through the Standard Interfaces (SIs) to the torso. The modular design of the MAR reduces the complexity of the robotic system by separating it into a smaller atomic components and recombining the manipulators in different morphologies. Examples of the MAR morphology are: 1-arm, 1-arm+torso and 2-arms, which are shown in Fig. 8.14 A, B and C, respectively. The main operations foreseen for the MAR are pick-and-place of the tiles (Fig. 8.14-D) with the torso or the arm(s), and transportation of the tiles by walking on the telescope structure through the SIs. These operations will enable the onorbit assembly of larger telescope structures. In the project, a unified PBC was designed in order to accommodate all the MAR operations for each morphology shown in Fig. 8.14. This approach featured a primary task on the end-effector pose without a secondary task, and stabilized the entire MAR system using a single energy function. This is a simplified version of Theorem 7.1, in which there is no potential in the fiber (nullspace), only damping. The proposed unified control law was compliant against the constraint forces arising during SI closure. A key advantage of the proposed controller is that it can operate in both decentralized and centralized manner, and enables the usage of OBSW in each MAR atomic component.

For control prototyping, the co-simulation framework from Sec. 8.2.1 was used, see Fig. 8.15 and the control software was developed in MATLAB/Simulink. The holonomic constraints of the SIs were implemented using the suctionPad functionality in CoppeliaSim, which creates an overlap constraint, i.e., the two pertinent objects in close proximity will overlap their respective position/orientation to create dynamics loop closure constraints. Specifically, the suctionPad objects were added on each of the tiles of the breadboard shown in Fig. 8.14-D in a way that reflected the kinematics (not geometry) of the SIs. Thus, in the event that the end-effector of the MAR was in close proximity (below a specified threshold) of the suctionPad object, the former will be constrained to the tile structure.

In this section, the co-simulation results of the walking operation using the dual arm system with torso are shown for walking motion using 5 tiles. The sequence snapshots of the walking procedure are shown in Fig. 8.15, where the system moves from its initial position at t=0[s] to the first tile with the Arm-1. At t=39[s], the SI is engaged and later Arm-2 moves towards the second tile (t=50[s]) to perform a second latch with the SI at t=60[s]. In Fig. 8.16, the error in position (left) and orientation (right) of the corresponding arm in use

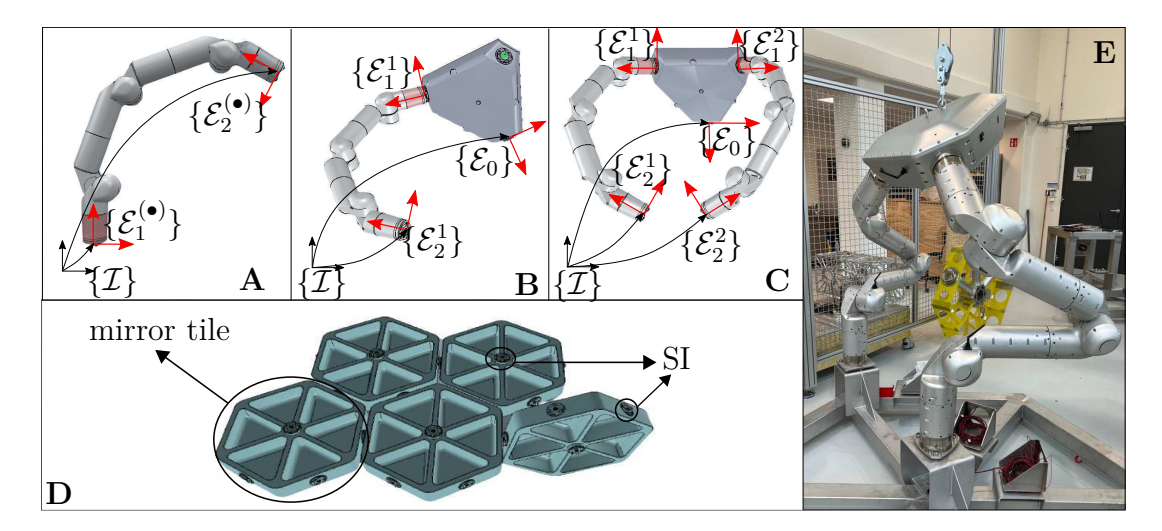


Figure 8.14: Morphologies of the MAR system in MIRROR project. **A**: Morphology 1-arm, **B**: Morphology 1-arm+torso, **C**: Morphology 2-arms, **D**: Breadboard of mirror tiles equipped with standard interfaces (SI), **E**: The manufactured MAR prototype in MIRROR.

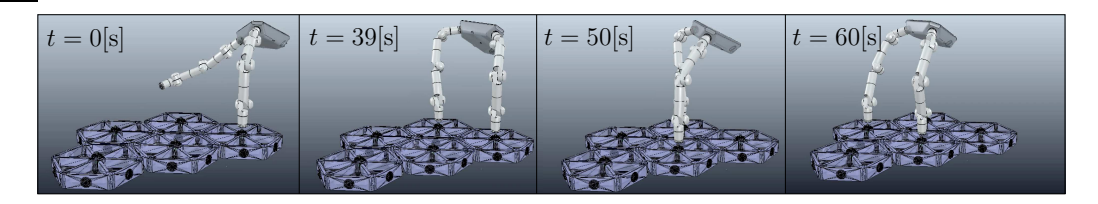


Figure 8.15: 2-arms MAR-morphology: Snapshots of walking operation.

during this walking operation is shown. The results show the effectiveness of the developed unified controller in performing multi-contact walking. The unified PBC, proof of stability and simulation results of different MAR-morphologies within the project were published in [66].

8.6 EU ORU-BOAS: On-Orbit Assembly

To support in-orbit assembly, the EU has commissioned the ORU-BOAS project [168], which considers the deployment of orbital modules to perform life-extension operations. These modules are autonomous small satellites, equipped with onboard Reaction Control System (RCS) and reaction wheels (RWs), i.e., they are fixed-inertia multibody systems. For assembly, two modules are mechanically connected through a SIROM SI, as shown in [168]. Within ORU-BOAS project, the goals were to design a centralized motion control system that can achieve docking for assembly and its HIL V&V, see Fig. 8.17. For this scenario, a HIL framework that replicates the relative motion of the agents in a dynamically con-

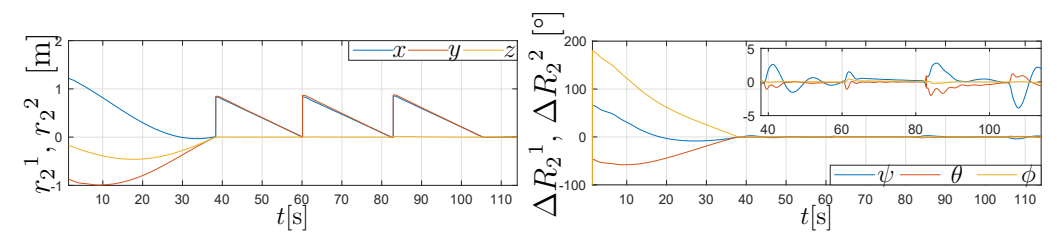


Figure 8.16: 2-arms MAR-morphology: Control errors in position (left) and orientation (right).

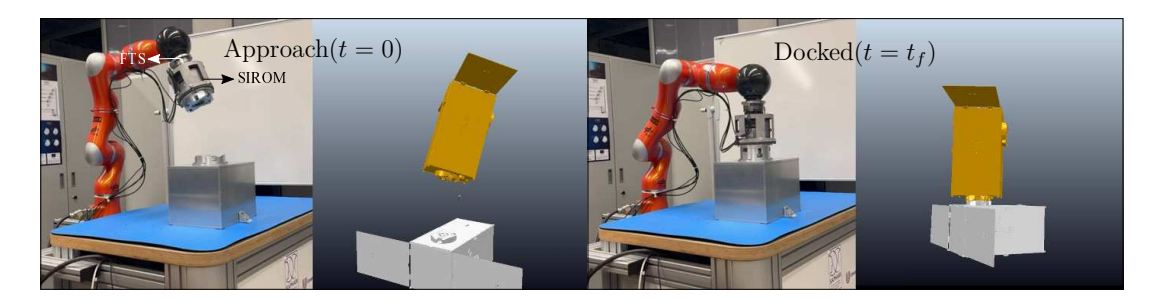


Figure 8.17: ORU-BOAS Scenario: Two satellite modules approach and dock with each using the SIROM SI. The HIL facility for V&V was developed using a single robotic system, while ensuring that the total momentum of both satellites is integrated in software for dynamic consistency.

sistent way is a promising solution, as was shown in Sec. 8.4.2. However, therein the formulation was considered relative to a nominal trajectory, which required the computation of two dynamic models and also acceleration measurements, which are computational and sensory overheads.

To address these problems, a momentum-shape dynamics formulation for a fleet of multibody modules was proposed in ORU-BOAS. The contribution was the sequential application of reduction theory (\mathcal{LP} -dynamics from Chapter 3) for each module followed by passive decomposition theory [242, 243] for the fleet of modules. The latter step describes the formation using a global \mathcal{LP} -dynamics formulation that splits the formation's motion into the total momentum and the relative configurations (shape). Two complementary control laws: Free-flying and Hierarchical, are proposed to enable on-orbit assembly by regulating the total and relative motions of the modules. The free-flying control law is an extension of Theorem 5.1. In this, the observer was not considered to retain focus on pure motion control, and the shape potential $\Phi_q = 0$ because the reaction wheels are not controlled in position but velocity. The hierarchical control law prioritizes the momentum subsystem and converges in shape as a secondary task, and hence, its convergence sequence is exactly the opposite of Theorem 5.2. However, note that even this sequence is an outcome of the passive feedback interconnection of \mathcal{LP} systems in Theorem 3.4. The free-flying control law prioritizes convergence, while

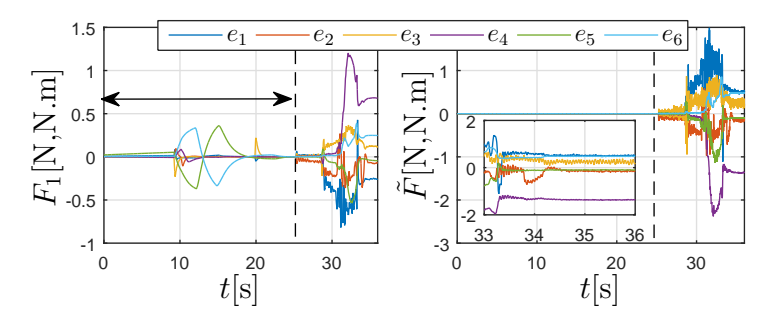


Figure 8.18: Control (left, Sat-1) and Interaction (right) wrenches on the HIL during approach and docking maneuver.

the hierarchical controller optimizes fuel efficiency. The Cartesian tasks in such missions are time-constrained and necessitate a fast response from the actuators. To achieve this, both control approaches are based on inertia-shaping of RWs' actuator dynamics and passivity-based control of the Cartesian dynamics. Third, a novel HIL framework is realized and experimentally validated on the DLR OOS-SIM and LWR4+, wherein the relative motion is reconstructed on the hardware while simulating momentum in software. The key benefit of this approach is that acceleration measurements are avoided in contrast to [54]. Furthermore, a single robotic system is used to generate relative motions, see Fig. 8.17. The proposed free-flying controller is experimentally validated using this HIL approach.

The results from an experiment in the V&V campaign is shown in Figures 8.18-8.20. The two satellites with initial conditions, as shown in Fig. 8.17, were required to achieve docking using the SIROM SI. In the left of Fig. 8.18, the actuation of the Sat-1, F_1 resulting from the free-flying controller [57, Th. 1] is shown on the left, and in the centralized scheme Sat-2 has an equal and opposite actuation. In particular, the initial phase (double arrow) is the actuation required for the approach phase, whereas the docking happens in t > 25[s]. Note that the actuation forces during docking are due to the control action to compensate for the initial misalignment when the satellites are constrained by the SIROM SI. The interaction wrench, \tilde{F} , measured using the FTS in the HIL is shown on the right. In particular, in the inset, it can be seen that the wrenches stabilize in t > 33[s] which validates the docking procedure. The torques (τ_1) , saturated at 0.1[N.m]) and velocities (θ_1) of the reaction wheels, which were considered in the dynamic model of the HIL during the experiment are shown in Fig. 8.19. For the controller, the tracking (left) and the setpoint (right) position errors are shown in Fig. 8.20. Note that after docking there are some residual position errors, which are responsible for the forces in Fig. 8.18.

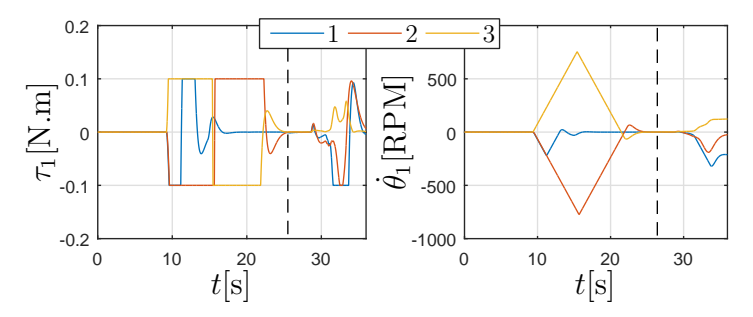


Figure 8.19: Reaction wheel motion. Left: Actuator torques; Right: Velocities.

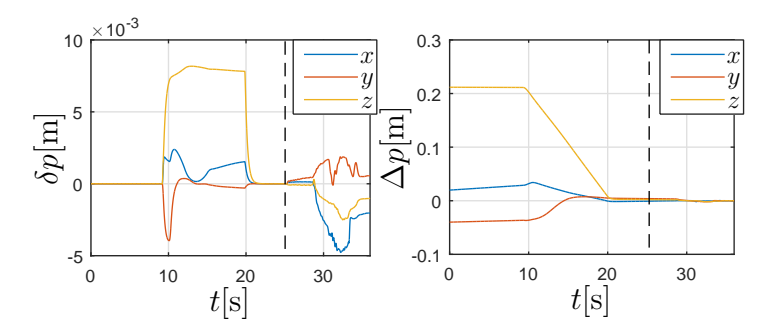


Figure 8.20: Tracking (left) and final setpoint (right) position errors of the centralized free-flying controller on the HIL during approach and docking maneuver.

8.7 KUKA Innovation Awards

This section deals with industrial engagement of topics in this thesis through KUKA Innovation Award [244]. In this annual competition, KUKA AG provides a robot to demonstrate research solutions that address a specific class of industry-relevant challenge. Although the focus is on technological implementation, it enables prototyping research results through a demonstrator. The specific events listed below are those in which I was a part of the team. Naturally, for engineering purposes, the corresponding thesis contributions are used in a modified form for engineering purposes, which I explicitly outline in the descriptions below.

8.7.1 Automatica (2023): Open Platform challenge

For a FRM, although automatic control [35, 134, 245] is the crowning glory, its technology-readiness for unplanned tasks, e.g. tactile inspection, opening-closing fluid values, might not be satisfactory [246]. In this case, teleoperated control [246, 247], emerges as a pragmatic approach because it employs the advantage of human intuition for corrective actions, see Fig. 8.22. Such a method was exploited in [247] to grasp a satellite. This approach, however, does not consider

prolonged interactions encountered in a inspection/maintenance task, which requires the fully-actuated (*free-flying*) control of the FRM to avoid drifts. In the KUKA Innovation Award 2023, the objective for our team (SPIRIT) was to demonstrate robotic maintenance of industrial infrastructure using the DLR Suspended Aerial Manipulator (SAM) system [248]. To this end, the motion control required the teleoperated control of the to open/close a fluid value, see Fig. 8.21.

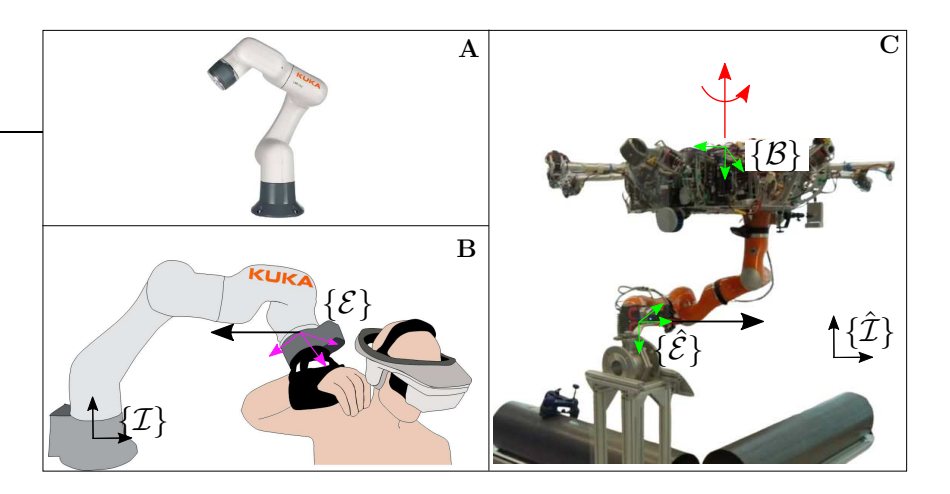


Figure 8.21: KUKA Innovation Award 2023 scenario: **A**: KUKA LBR iisy 3 R760 used as haptic device, **B**: Teleoperation system for human guidance, **C**: Remote SAM system closing a fluid value in an industrial maintenance activity.

This demonstration of shared control required the following features:

- 1. Bilateral Teleoperation Controller (BTC) [249–251]: An archetypal teleoperation approach which stabilizes a coordination task error, i.e., the error between the desired motion generated by the human operator using a haptic device and the motion of the remote robot. In this method, the measurements of positions (P) and interaction forces (F) from the two agents are transmitted over communication channels.
- 2. Partitioned Shared Controller (PSC) [252]: Fully-actuated control of FRM introduces redundancy for *in situ* execution of a secondary task, e.g., regulation of the FRM-base configuration within safety limits during interaction-oriented tasks while considering the BTC task as primary.

To this end, I proposed a novel passivity-based *free-flying* PSC, which performs a primary interaction-oriented coordination task, e.g. tactile sensing, and an *in situ* secondary task for operational safety, e.g. collision avoidance. The preliminary validation of this approach was performed for the orbital FRM, which might also require the aforementioned features, e.g., to perform extravehicular

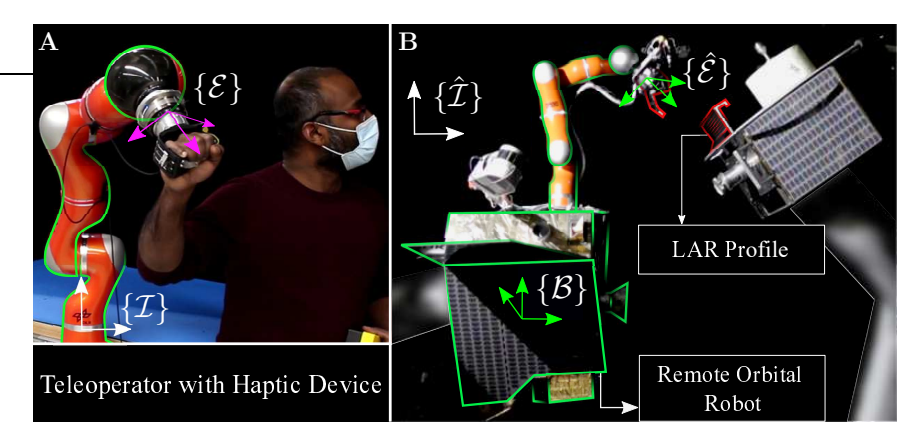


Figure 8.22: Teleoperation scenario. A: Teleoperator with haptic device; B: Remote orbital FRM and its environment.

tactile inspection, see Fig. 8.22. The \mathcal{LP} dynamics of the orbital FRM from Chapter 3 are exploited in the control design, which avoids the ideal velocity tracking assumption in [246], to obviate acceleration measurements of the haptic device and human-related sensitivity in the spacecraft actuation. In particular, the control law assumes the form in Theorem 5.1. However, the analysis was performed without the observer to retain focus on the PSC concept. This means that the control law assumes the form as in (5.20), in which the symmetry-breaking potential Φ_b consists of both the BTC coordination task and the secondary FRM-base regulation task, while $\Phi_q = 0$. Additionally, the BTC coordination task requires tracking the human guidance input, so (5.20) was augmented with tracking feedforward terms. This control law is published in [55, Th. 1].

For the validation, the control sequence is summarized in Fig. 8.23, which consists of: free approach, maintain static contact, and perform sliding contact. The end-effectors of the haptic device and the remote orbital robot in Fig. 8.22 were equipped with FTS to measure the teleoperator and environment interaction wrenches, respectively. The results of the experiment are summarized through the plots in Figures 8.24-8.25, wherein 1-3 and 4-6 are the translational and rotational bases, respectively. In the plots, the time intervals for static ($t \in [48, 95][s]$) and sliding ($t \in [120, 145][s]$) contacts are highlighted using solid and dashed vertical lines, respectively. The tracking performance of the BTC coordination task, i.e., the position errors, r_e , and the orientation errors, $\Delta R = \text{sk}(\check{\eta}_e)^{\vee} \cdot \frac{180}{\pi}$, between the end-effector poses of the orbital robot and the haptic device are shown in Fig. 8.24.A-8.24.B, respectively. The component-wise mean errors for the whole experiment were (-4.6, -9.1, -3.1)[mm] and $(-2.2, 2.5, 0.24)[^{\circ}]$, respectively. The measurements of the dynamically consistent teleoperator wrench¹, \hat{F}_h , and the negated end-effector interaction wrench, $-\mathcal{F}_e$, are shown in Fig. 8.25.A-8.25.B,

¹The wrench is scaled correctly to account for differences in inertia tensor between the haptic and remote robotic systems.

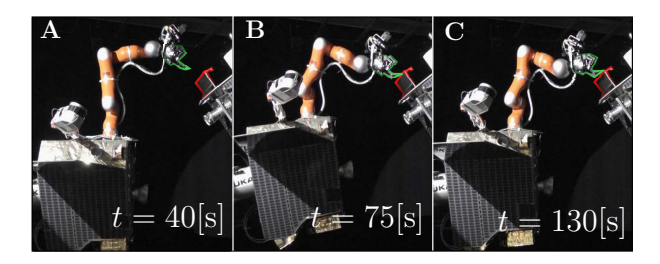


Figure 8.23: Control sequence in the experiment. **A**: Approach; **B**: Static contact; **C**: Sliding contact.

respectively. During interactions, \hat{F}_h is opposite in sign and approximately equal to \mathcal{F}_e , which indicates a high degree of transparency for the teleoperator. In Fig. 8.25.C, the spacecraft actuation in the orbital robot's end-effector frame, $\{\hat{\mathcal{E}}\}$, i.e., $\hat{\mathcal{F}}_b$, is shown. Juxtaposing this with Fig. 8.25.B shows that the spacecraft actuation provides the exact stabilizing wrench during interactions, and highlights the free-flying functionality of the proposed method. At the end (t > 150[s]), the biases in $(r_e, \Delta R)$ and \hat{F}_h in Figures 8.24, and 8.25.A, respectively, are due to common HIL modeling errors, e.g. gravity compensation and static friction, which appear as a quasi-static disturbance for the proposed method. However, the stability of the system equilibrium holds, as proved in [55, Lemma 2].

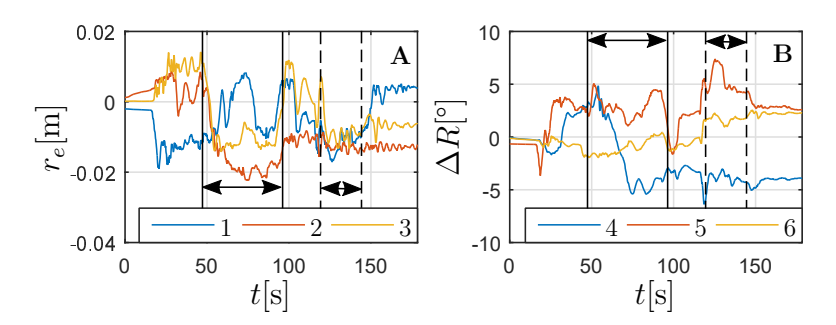


Figure 8.24: BTC coordination task error, **A**: position error, r_e ; **B**: orientation error, ΔR .

It is worth pointing out some differences of the proposed method w.r.t. the orbital FRM and the SAM system. In the orbital case, the spacecraft has 6-DoF actuation through thrusters, whereas in SAM system, the thrust is generated using propellers. Notably, SAM's propellers are designed for pendulum motion stabilization, not gravity compensation. Therefore, the controllability of the propellers is limited to the yaw and horizontal plane, red arrow in Fig. 8.21. Therefore, while the FRM-base task is posed on SE(3) for the orbital robot, it is limited to SE(2) for SAM. With these modalities in view, the motion control system featuring BTC and PSC features were implemented on SAM for the KUKA innovation Award 2024, as shown in [Jongseok]. Therefore, the findings in [55]

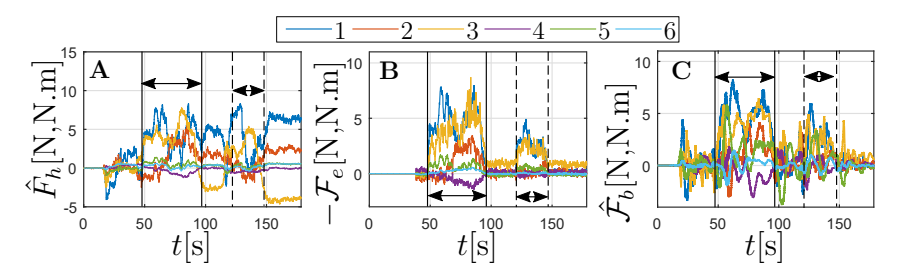


Figure 8.25: **A**: Dynamically consistent teleoperator wrench, \hat{F}_h ; **B**: Negated endeffector interaction wrench, $-\mathcal{F}_e$, **C**: Spacecraft actuation in the orbital robot's
end effector frame $(\{\hat{\mathcal{E}}\})$, $\hat{\mathcal{F}}_b$.

for orbital robotics proved to be the basis for the industrial maintenance application, which was implemented by co-contributors for the event with additional features like extended reality and deep-learning based perception. In fact, our work in KUKA Innovation Award 2024 has secured funding from DLR to perform market research towards a business case in which the work proposed in [55] is a key technology for shared control functionality.

8.7.2 Hannovermesse (2024): Robots for the people

In KUKA Innovation Award 2024, the objective for our team (YANTRA) was to demonstrate robotic assistance for handloom sustainable textiles. For the project development, the robotic manipulator provided by KUKA was LBR iisy R1300 (6-DoF), see left of Fig. 8.26. In this robot, the tool center point (TCP) that is required to be controlled has a non-collocated set of three joints that contribute towards the orientation task, see right of Fig. 8.26. This was due to the long links towards the end of the serial kinematic chain to increase the robot's reachability [253]. However, this had the negative effect that a small change in the desired orientation translates to a large reconfiguration of the arm. Consequently, the uncertainties like friction and gravity errors on the large inertia elements negatively affected the overall orientation accuracy of the end-effector. During development, it was observed that the conventional Cartesian impedance control law [254, eq. 3] provided unsatisfactory orientation control.

Additionally, in the considered tasks, the main goal of the end-effector was to achieve a desired pointing with respect to the surface. Due to the axial symmetry of the end-effector, the rotation about the pointing axis is of secondary importance. To address the orientation control problem, I proposed the approach in Theorem 6.1 to create a task-induced variational symmetry, i.e., it prioritizes the pointing requirement as a primary task (along with the translational part), while utilizing the nullspace (fiber) of the robot to achieve the secondary requirement of rotation about the pointing axis. The details of the primary and secondary potentials are outlined below.

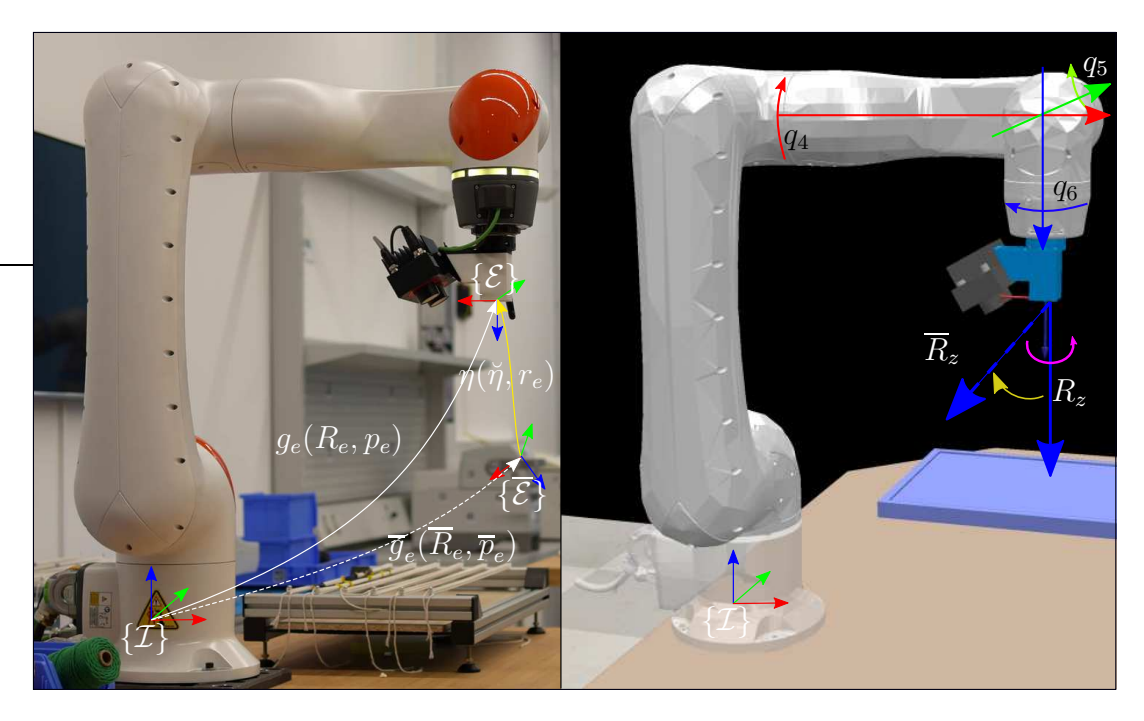


Figure 8.26: Cartesian control of robotic manipulator. Left: In traditional Cartesian control, the pose of $\{\mathcal{E}\}$ w.r.t. $\{\mathcal{I}\}$, i.e., $g_e \equiv (R_e, p_e)$ is regulated about a desired setpoint $\overline{g}_e \equiv (\overline{R}_e, \overline{p}_e)$. Right: A primary pointing requirement such that the Direction Cosine Vector (DCV) R_z aligns with \overline{R}_z (yellow), while the angle around the pointing axis (magenta) is secondary.

The end-effector body Jacobian is written as translational and rotational parts as, $J^{\top} = \begin{bmatrix} J_v^{\top} & J_{\omega}^{\top} \end{bmatrix}$ [8, §3.4]. The rotational part can be further written componentwise as, $J_{\omega}^{\top} = \begin{bmatrix} J_{\omega x}^{\top} & J_{\omega y}^{\top} & J_{\omega z}^{\top} \end{bmatrix}$. The rotation matrix for the end-effector is written as,

$$R_e = \begin{bmatrix} R_x & R_y & R_z \end{bmatrix} \tag{8.1}$$

where $R_{(\bullet)} \in \mathbb{R}^3$ is the DCV along the direction indicated by the superscript. For example, R_z is the vector $e_z = \begin{bmatrix} 0 & 0 & 1 \end{bmatrix}$ in $\{\mathcal{E}\}$ expressed in $\{\mathcal{I}\}$. Note that the DCV satisfies the condition of the sphere, i.e., $R_z^{\top}R_z = 1$, $R_z \in \mathbb{S}^2$. Thus, controlling the variable R_z results in control on the \mathbb{S}^2 sphere. The time-derivative of the DCV is written as,

$$\dot{R}_z = \omega_{e_{\times}} R_z = -(R_z)_{\times} \omega_e = \underbrace{-(R_z)_{\times} J_{\omega}(q)}_{J_1} \dot{q}$$
(8.2)

The pointing error is indicated using a scalar potential function as,

$$\Phi_{1p}: \mathbb{S}^2 \to \mathbb{R}_+, \ \Phi_{1p}(R_z, \overline{R}_z) = \mathcal{K}_1(1 - \langle R_z, \overline{R}_z \rangle), \ \mathcal{K}_1 > 0$$
(8.3)

Its time-derivative is written as,

$$\frac{d}{dt}\Phi_{1p} = \mathcal{K}_1 \langle \overline{R}_z, (R_z)_{\times} \omega_e \rangle = \langle (\mathcal{K}_1 \overline{R}_z)_{\times} R_z, \omega_e \rangle = \langle (\mathcal{K}_1 \overline{R}_z)_{\times} R_z, J_{\omega} \dot{q} \rangle \tag{8.4}$$

Note that $J_1 \in \mathbb{R}^{3 \times n}$, however, is not full-rank because of the sphere constraint $R_z^{\mathsf{T}} R_z = 1$. Thus, using SVD, its nullspace basis can be obtained as, shown in Lemma 6.3. In this work, the proportional control torques for the axial angle error are projected to the fiber (nullspace). To that end, let the current angle about the R_z axis be $\theta \in \mathbb{S}^1$ and its desired setpoint be $\overline{\theta} \in \mathbb{S}^1$. Therefore, the axial error is determined as, $\tilde{\theta} = \theta - \overline{\theta}$. Thus, the total primary task potential and the secondary potential are written as,

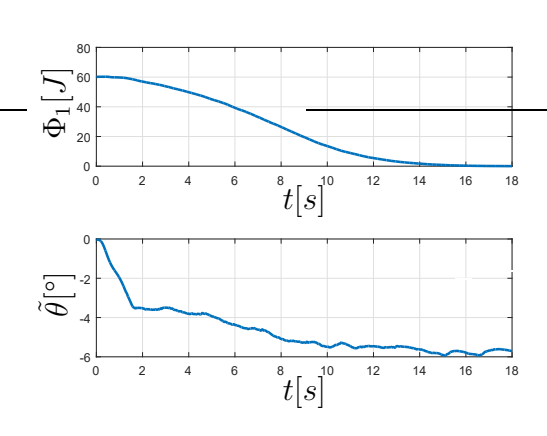
$$\Phi_1 = \frac{1}{2} ||r_e||_K^2 + \Phi_{1p}, \ \Phi_2 = \frac{1}{2} \langle \tilde{\theta}, \tilde{\theta} \rangle_k$$
(8.5)

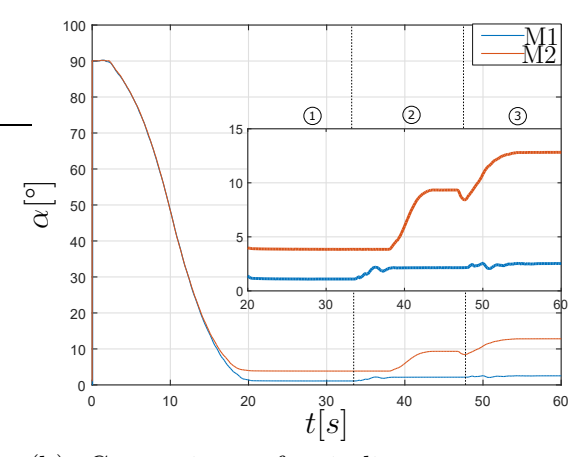
where $r_e \in \mathbb{R}^3$ is the position error, $K \succ 0$ and k > 0. The control law with variational symmetry was obtained using Theorem 6.1, and applied to the robot. The results are shown in Fig. 8.27. In particular, on the top left, it is seen that the robot converges in the primary operational space, while the secondary configuration error (bottom) suffers from a steady-state error due to inaccurate gravity errors, friction etc. On the right, the SE(3) impedance control is compared with the proposed control in terms of the misalignment error (α) by commanding three successive trajectories. While the former suffers errors upto 12[°], the proposed approach reduces the alignment error, thus, enabling task execution using the provided robot.

8.8 Conclusion

This chapter presented practical applications of the work developed during the thesis research. These applications were a part of international projects with a consortium of space agencies, eminent aerospace companies and robot manufacturers. The methods have been validated either on real robotic hardware or tools that have been recommended by space agencies. These applications have been officially a part of work packages in funded projects, and hence, the impact of the thesis contributions have a financial value attached to it.

The practical applications from this thesis, however, are a part of an incremental progress narrative. Indeed, in the on-going ESA-funded RISE/ADRIOS-II mission, the co-simulation tool from Sec. 8.2.1 is being used in collaboration with the spacecraft manufacturer, D-Orbit, and the robotics manufacturer, Kinetik. The digital twin of the mission is used for integration of developments by both manufacturers so that the MIL/SIL/PIL phases can be achieved for evaluation by the ESA. In this mission, the pointing-prioritized motion control law from





- (a) Top: The scalar potential on the point- (b) Comparison of misalignment errors ing error, Φ_1 , converges. Bottom: The ax- between ial error, $\hat{\theta}$, treated as a secondary goal, (M1, blue) and the conventional SE(3) and its proportional action is projected to impedance control (M2, red). The robot the primary's nullspace.
 - proposed control was commanded 3 motions sequentially.

Figure 8.27: Controller performance for KUKA Innovation Award 2024.

Sec. 8.7.2 has been proposed to grasp a the launch adapter ring using a circularly symmetric multi-contact mechanism. The combined state estimation for the FRM-base and the client statellite proposed in Sec. 8.4.1 that employs the robotic manipulator's kinematics has become a mission-standard now, see the ESA-funded follow-up of COMRADE in [255]. This approach is also being used currently within the EU-funded EROSS-IOD mission. The output-feedback combined control approach from this research [64], as in Sec. 8.4, is being used in early phase mission analysis within the CNES-funded DIANE mission for grasping a spinning satellite. Even in academia, the published works from Table 1.1 that have been referenced in this chapter have featured in high-impact survey papers on space robotics [256–260].

CHAPTER 9

Conclusion

In the current age, robotic mechanisms have emerged as a practical reality to address conveniences and contingencies of human endeavour across all media: land, sea, air and space. Over the years, these robotic mechanisms have evolved into articulated systems, which are characterized by variable inertia with a non-Euclidean geometry in their configuration spaces. For such a mechanism, it is intuitive to model the dynamics as an Euler-Lagrange (\mathcal{EL}) system and analyze its motion control stability in terms of geometric quantities like energy. This general approach is the geometric principle behind Passivity-Based Control (PBC). For the special class of \mathcal{EL} systems with symmetry, known as Lagrange-Poincaré (\mathcal{LP}) systems, Noether's invariance (symmetry) was instrumental in developing the view of a higher dimensional motion as variations of a lower dimensional shape in level-sets of momenta (possibly conserved). Our knowledge of the dynamics of contemporary robotic mechanisms is already on the precipice that requires a deeper understanding of symmetry for solving practical motion control problems. In particular, Lagrangian symmetry occurs naturally in a Floating-base Robotic Mechanism (FRM), and is a behavioural requirement in hierarchical motion control. However, a common theory based on symmetry that unifies the dynamics and control synthesis for this class of problems in robotics was missing. Thus, this development was imminent, and is the primary contribution of this thesis.

The research towards this thesis has made one of the first strides towards employing symmetry in dynamics and motion control of robotic mechanisms. I have exploited the symmetry of FRM to develop a deeper understanding of its dynamics, which aided the design of a motion control framework for \mathcal{LP} systems. For systems that do not have a natural symmetry, but require a behavioural symmetry, as in hierarchical motion control, I developed an approach that synthesizes an artificial symmetry to create a \mathcal{LP} system. This enables the direct

246 9 Conclusion

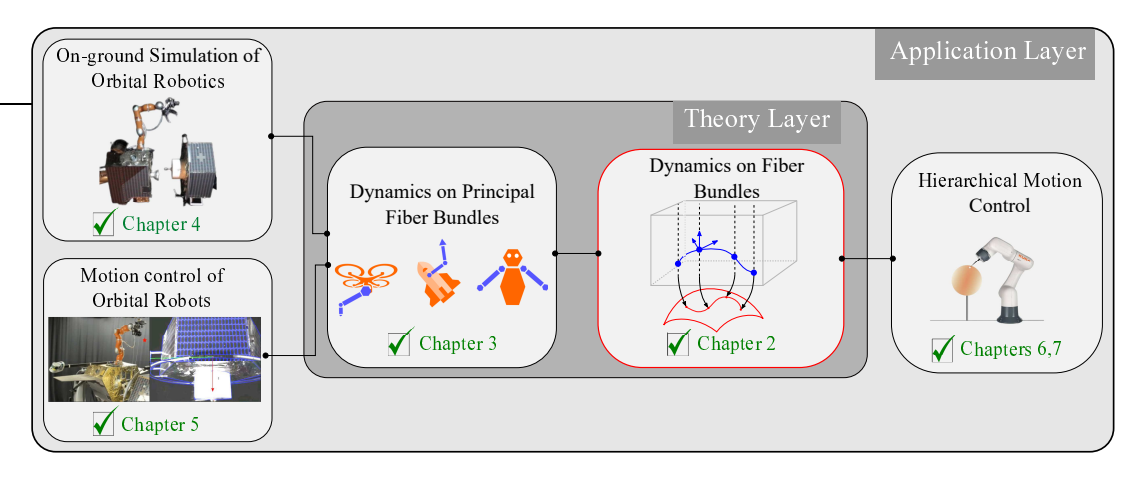


Figure 9.1: Employing symmetry in dynamics and motion control of robotic mechanisms: From theory to application.

application of the aforementioned control framework. In this way, the proposed theory in this thesis exploits symmetry when available, or gives an approach to synthesize it when required.

This thesis fills the identified research gaps, while amalgamating the topics of symmetry from geometric mechanics with dynamics and motion control from robotics. Using the symmetry of FRMs, I derived a novel computation of its \mathcal{LP} dynamics. This novel computation was employed to design a momentum-consistent HIL simulation framework for orbital robotic missions. Following this, the \mathcal{LP} dynamics derived in this thesis were also used to design observer-based PBC control approaches for such systems with inherent symmetry. By revealing the passive feedback interconnection between the shape and momentum subsystems of \mathcal{LP} systems, I derived a formal framework for hierarchical motion control. On the other hand, for \mathcal{EL} systems that lack symmetry, the proposed control theory was employed to impose a hierarchy in task execution after synthesizing an artificial symmetry. The multidisciplinary topics in the thesis were structured in an incremental flow of theoretical treatment, which were validated by simulations and hardware experiments. A brief outline of the contributions are summarized in Fig. 9.1, and is also written below.

Chapter 2 proposed a comprehensive theory of constrained \mathcal{EL} systems and linked it to the concept of symmetry. I showed that the presence of a constraint results in a fiber bundle topology of the total configuration space. In this bundle formalism, the shape space refers to the motion orthogonal to the constraint. This approach helped generalize the modeling of motion for two key subtopics in robotics: dynamics of FRM and the dynamics of hierarchical motion control. While the former is characterized by the special structure of a *Principal Fiber Bundle* (PFB) topology, the latter results in a general fiber bundle topology.

Corresponding to the PFB of a FRM, a novel computation of its \mathcal{LP} dynam-

ics was derived in Chapter 3. This computation split the CC matrix into two parts according to the velocity dependencies. In particular, the first one varied with the shape, while the latter varied with momentum. This decomposition was pivotal in revealing the passive feedback interconnection between the shape and momentum subsystems. This interconnection provided the stepping stone for designing PBC approaches for motion control. Furthermore, using the \mathcal{LP} dynamics, a generalized Poinsot theorem was proved, which provided a geometric visualization of the FRM's motion.

In Chapter 4, the proposed \mathcal{LP} dynamics for the FRM was employed to develop an on-ground HIL framework for performing V&V of orbital missions. In particular, the proposed dynamics were a significant improvement in eliminating sensory overheads, like acceleration measurements, and ensuring momentum consistency. The proposed HIL framework was advantageous in that it unified the use of different On-ground Robotic facilities that are developed during the course of an orbital mission through a substructuring approach.

Chapter 5 used the passive interconnection from Chapter 3 to propose sensor-based PBC approaches for the FRM. In practice, the floating-base and the articulated mechanism of the FRM are equipped with sensors and actuators that have different underlying physical principles. To this end, the proposed sensor-based PBC was proved to be effective against practical problems (e.g., sensor noise, actuation lag) arising from the hybrid nature of FRM.

Chapters 6 and 7 generalize the aforementioned PBC approach for \mathcal{LP} systems to general \mathcal{EL} systems. This is relevant for practical robotic applications that require a task-induced hierarchy in motion control, but might not possess a symmetry in the desirable directions of the configuration space, e.g., using a fixed-base robot. In Chapter 6, a control approach was proposed to ensure hierarchical convergence of energy functions, while the approach in Chapter 7 ensured hierarchical convergence of the tasks with a single energy function. In contrast to prior works, the key advantage in the above two approaches is that the hierarchical behaviour of the \mathcal{EL} system is prescribed by virtue of its metric tensor and task potentials.

As detailed in Chapter 8, the work in this thesis contributed towards several projects/missions funded by ESA (MIRROR and COMRADE), EU (ORU-BOAS and EROSS-IOD), NASA (TUMBLEDOCK) and KUKA (Innovation awards 2023/24). The contributions of this thesis are a part of ongoing development in robotics, and it is prudent to have an overview of future work. The on-ground HIL framework is used in EU EROSS-SC and ESA GEA-RISE missions. The sensor-based motion control approaches are being integrated into the overall on-board architecture for these missions. The output-feedback combined control approach from this thesis will be used in early phase mission analysis within the CNES-funded DIANE mission for grasping a spinning satellite. The fiber bundle framework and the hierarchical motion control approaches of this thesis will be used to create a geometry-informed control policy generator, e.g., NVIDIA

248 9 Conclusion

RMPflow. The benefit of having a priori knowledge of the desirable metric behaviour will be exploited for integrating with physics-informed learning methods to achieve hierarchical motion control.

Thus, the key achievements of the thesis have enabled subtopics, each of which will exploit symmetry to improve the utility of robots in practical applications. This thesis is multidisciplinary in that it makes contributions to the diverse fields of dynamics, simulation, observer-based motion control and hierarchical control, which are unified within the context of symmetry. In conclusion, it has provided a framework to address a class of motion control problems in robotics using the same formalism that is used today to explain motion phenomena in the universe.

An intellect which at a certain moment would know all forces that set nature in motion, and all positions of all items of which nature is composed, if this intellect were also vast enough to submit these data to analysis, it would embrace in a single formula the movements of the greatest bodies of the universe and those of the tiniest atom; for such an intellect nothing would be uncertain and the future just like the past would be present before its eyes [261].

P.S. Laplace, Essai philosophique sur les probabilités, 1825

APPENDIX A

Appendix

Lemma A.1. Equivalence of inner products: Given $\rho \in \mathbb{R}^n$ and $\sigma \in \mathbb{R}^n$ as body trivializations of a vector and its covector respectively, and likewise $\rho' \in \mathbb{R}^n$ and $\sigma' \in \mathbb{R}^n$ as corresponding trivializations in inertial space, then,

$$\langle \rho, \sigma \rangle = \langle \rho', \sigma' \rangle = c_0, \ c_0 \ge 0$$

A.1 SE(3) Group and Properties

A.1.1 Introduction

In this section, relevant details about motion on the SE(3) group are provided. The reader is referred to the Appendix A.1.2 for the matrix descriptions of introduced quantities. The pose of a rigid-body is a matrix representation of SE(3), which is written as $g \equiv g(R, p)$, where $R \in SO(3)$ is the rotation matrix and $p \in \mathbb{R}^3$ is the position. The identity of the SE(3) group is $\mathbb{I}_{4,4}$, where $\mathbb{I}_{k,k}$ is an identity matrix of dimension $k \times k$. The tangent space at $\mathbb{I}_{4,4}$ is the $\mathfrak{se}(3)$ algebra, which is referenced in body and spatial frames. Analogously, the cotangent space at $\mathbb{I}_{4,4}$ is denoted as $\mathfrak{se}(3)^*$. The $\mathfrak{se}(3)$ algebra and its dual $\mathfrak{se}(3)^*$ are isomorphic to the space of velocity twists and wrenches on \mathbb{R}^6 using $(\bullet)^{\wedge}: \mathbb{R}^6 \to \mathfrak{se}(3), \mathfrak{se}(3)^*$ and $(\bullet)^{\vee}: \mathfrak{se}(3), \mathfrak{se}(3)^* \to \mathbb{R}^6$, e.g. given a twist, $\mathcal{V} \in \mathbb{R}^6$, $\mathcal{V}^{\wedge} \in \mathfrak{se}(3)$. The adjoint action, Ad: $\mathfrak{se}(3) \to \mathfrak{se}(3)$, of a pose g transforms elements of $\mathfrak{se}(3)$ algebra between spatial and body frames as $\mathcal{V}^s = \mathrm{Ad}_q \mathcal{V}$, see [10]. The adjoint map of the $\mathfrak{se}(3)$ algebra onto itself is $ad:\mathfrak{se}(3)\to\mathfrak{se}(3)$. This is denoted by $ad_{\mathcal{V}}$ and its coadjoint map is $\operatorname{ad}_{\mathcal{V}}^{\top}:\mathfrak{se}(3)^*\to\mathfrak{se}(3)^*$. The SE(3) group and its algebra are endowed with a diffeomorphism map, $\exp:\mathfrak{se}(3)\to SE(3)$ and its inverse map, $\log : SE(3) \to \mathfrak{se}(3) \text{ (see [62])}.$

250 A Appendix

A.1.2 Matrix Representation

Given a rigid-body pose $g \equiv (R, p) \in SE(3)$ with body velocity $\mathcal{V} = \begin{bmatrix} \omega^\top & v^\top \end{bmatrix}^\top$, the following quantities are detailed,

$$g = \begin{bmatrix} R & p \\ 0_{1,3} & 1 \end{bmatrix}, \ \mathcal{V}^{\wedge} = \begin{bmatrix} \omega_{\times} & v \\ 0_{1,3} & 0 \end{bmatrix},$$

$$Ad_{g} = \begin{bmatrix} R & 0_{3,3} \\ p_{\times}R & R \end{bmatrix}, \ ad_{\mathcal{V}} = \begin{bmatrix} \omega_{\times} & 0_{3,3} \\ v_{\times} & \omega_{\times} \end{bmatrix},$$
(A.1)

where $(\bullet)_{\times}$ is a skew-symmetric matrix for the vector, and ω (v) is the angular (linear, respectively) velocity. For k^{th} -link (see Sec. 2.6.1) with mass, $m_k > 0$, the moment of inertia, $I_k \in \mathbb{R}^{3\times 3} \succ 0$, and momentum $h_k = \begin{bmatrix} h_\omega^T & h_v^T \end{bmatrix}^T = M_k V_k$,

$$M_k = \begin{bmatrix} I_k & 0_{3,3} \\ 0_{3,3} & m_k \mathbb{I}_{3,3} \end{bmatrix}, \text{ ad}_{M_k V_k}^{\sim} = \begin{bmatrix} h_{\omega \times} & h_{v \times} \\ h_{v \times} & 0_{3,3} \end{bmatrix}.$$
 (A.2)

Property A.1. Corresponding to a SE(3) action of $g \in SE(3)$, the following properties hold,

•
$$\operatorname{Ad}_g \operatorname{ad}_{\mathcal{V}} \operatorname{Ad}_g^{-1} = \operatorname{ad}_{\operatorname{Ad}_g \mathcal{V}}$$
 (A.3a)

•
$$\operatorname{Ad}_g^{\top} a d_{MV}^{\sim} \operatorname{Ad}_g = a d_{\operatorname{Ad}_g^{\top} MV}^{\sim}$$
 (A.3b)

Property A.2. [262, Lemma 1]: Given $x \in \mathbb{R}^6$ and a pose $g \in SE(3)$, which varies as $\dot{g} = gV^{\wedge}$ with body velocity $V \in \mathbb{R}^6 \cong \mathfrak{se}(3)$, the following holds,

$$\frac{d\mathrm{Ad}_g}{dt}x = \mathrm{Ad}_g\mathrm{ad}_V x. \tag{A.4}$$

Property A.3. [262, Lemma 2]: Given a frame with a pose $g \in SE(3)$, which is time-varying as $\dot{g} = gV^{\wedge}$, where $V \in \mathbb{R}^6 \cong \mathfrak{se}(3)$ is the frame body velocity, the time-derivative of a covector $y \in \mathbb{R}^6 \cong \mathfrak{se}(3)^*$ in this frame is given by,

$$\frac{d}{dt}y = \mathring{y} - \operatorname{ad}_{V}^{\mathsf{T}}y,\tag{A.5}$$

where \mathring{y} is the componentwise time-derivative (see [23, §2.10]), and $\operatorname{ad}_{V}^{\top}y$ accounts for the basis change of the time-varying frame, and encapsulates the SE(3) structural coefficients.

A.1.3 Proof in Property 2.3

The first part follows because M_k is a constant and $\mathrm{ad}_{M_k V_k}^{\sim}$ is skew-symmetric. For the corollary, a time-varying frame $\{C\}$ with a pose $g_c \in \mathrm{SE}(3)$ is considered, which is a right translation of g_k , i.e., $g_c = g_k g_{kc}$, where $g_{kc} \in \mathrm{SE}(3)$ evolves as

 $\dot{g}_{kc} = g_{kc}V_{kc}^{\wedge}$. In the basis of $\{C\}$, $\bar{V}_k = \mathrm{Ad}_{kc}^{-1}V_k$, and taking its time-derivative using (2.52) and Prop. A.1 from Appendix A.1 leads to,

$$\bar{M}_k \dot{\bar{V}}_k + (-\mathrm{ad}_{\bar{M}_k \bar{V}_k}^{\sim} + \bar{M}_k \mathrm{ad}_{V_{kc}}) \bar{V}_k = \bar{F}_k, \tag{A.6}$$

where $\bar{M}_k = \mathrm{Ad}_{kc}^{\top} M_k \mathrm{Ad}_{kc}$ and $\bar{F}_k = \mathrm{Ad}_{kc}^{\top} F_k$. In (A.8), for $x \in \mathbb{R}^6$,

$$x^{\top} \left(\frac{d}{dt} \bar{M}_k - 2(-\operatorname{ad}_{\bar{M}_k \bar{V}_k}^{\sim} + \bar{M}_k \operatorname{ad}_{V_{kc}}) \right) x = 0$$
(A.7)

is satisfied, which proves the invariance of the skew-symmetry to a change (time-varying) of basis, i.e., a frame transformation.

A.2 Multibody Dynamics

A.2.1 Passivity/Skew-symmetry

Given a mechanical system with velocity $V \in \mathbb{R}^m$ and inertia M, the unforced motion equations result from the kinetic energy, $\kappa = \frac{1}{2} \langle V, V \rangle_M$, as,

$$M\dot{V} + C(V)V = 0, (A.8)$$

where CV is the CC force.

Passivity in (A.8), i.e., $V^{\top}(\dot{M}-2C)V=0$, is pivotal in Lyapunov stability analysis of controller designs [25, 27], in which, the time-derivative of kinetic energy, $\dot{\kappa}$ is computed. Using (A.8), $\dot{\kappa}=V^{\top}(\frac{\dot{M}}{2}-C)V$, and passivity implies $\dot{\kappa}=0$, i.e., 0 power flow due to the CC force.

In specific control problems like tracking [134] and observer design [62], a kinetic-like energy function appears as $\hat{\kappa} = \frac{1}{2} \langle w, w \rangle_M$, where $w \in \mathbb{R}^m$ is, for example, a velocity error. In such cases, the time-derivative of $\hat{\kappa}$ contains $w^{\top} \left(\frac{\dot{M}}{2} - C \right) w$, which is not 0 despite passivity. Hence, a stronger skew-symmetry property is desired for the C matrix to conclude 0 power flow due to the CC wrench.

A.2.2 Proof of Lemma 2.14

The velocity of the k^{th} link is $V_k = T_k(q)V$ and its time-derivative is written as $\dot{V}_k = T_k(q)\dot{V} + \dot{T}_k(V)V$. Substituting this in (2.52) for all links, pre-multiplying T_k^{\top} on both sides and considering that the constraint reaction wrenches disappear after projection results in (3.1) with M, C as in (3.2). Note that an iterative loop is required in Lemma 2.14, and T_k and \dot{T}_k are obtained beforehand in this loop through a recursive computation, as shown in [22, §VI].

252 A Appendix

A.2.3 Proof of Lemma 3.2

Substituting $\dot{V} = L\dot{\xi} + \dot{L}\xi$ in (3.1), and multiplying L^{\top} on the L.H.S results in (3.4) with Λ, Γ as numerical transformations of M, C (in underbraces of (3.4)).

Property A.4. Given the FRM (see Fig. 3.1) defined in Def. 3.1, for $V \in \mathbb{R}^6 \cong \mathfrak{se}(3)$,

$$\sum_{k} A d_{1k}^{-\top} \operatorname{ad}_{A d_{1k}^{-1} \mathcal{V}}^{\top} M_k A d_{1k}^{-1} = \operatorname{ad}_{\mathcal{V}}^{\top} M_b.$$
 (A.9)

Proof. Using (A.3a) in Prop. A.1 from Appendix A.1 for simplification of L.H.S, followed by substitution of the iterative expansion of M_b from (3.3), the result follows.

The following identities related to \tilde{J}_k will be used for the proof of Theorem 3.2.

Lemma A.2. The following identities hold true.

$$\sum_{k} A d_{1k}^{-\top} M_k \, \tilde{J}_k = 0_{6,n} \tag{A.10a}$$

$$\sum_{k} A d_{1k}^{-\top} M_{k} \, \dot{\tilde{J}}_{k} = \sum_{k} A d_{1k}^{-\top} a d_{J_{k}\dot{q}}^{\top} M_{k} \, \tilde{J}_{k}$$
 (A.10b)

$$\sum_{k} A d_{1k}^{-\top} a d_{M_k \tilde{J}_k \dot{q}} A d_{1k}^{-1} = 0_{6,n}$$
(A.10c)

$$\sum_{k} A d_{1k}^{-\top} \operatorname{ad}_{A d_{1k}^{-1} \mu}^{\top} M_{k} \tilde{J}_{k} = 0_{6,n}$$
(A.10d)

$$\sum_{k} A d_{1k}^{-\top} (\operatorname{ad}_{J_{k}\dot{q}}^{\top} - \operatorname{ad}_{\tilde{J}_{k}\dot{q}}^{\top}) M_{k} \tilde{J}_{k} = 0_{6,n}$$
(A.10e)

Proof. To prove (A.10a), in the iteration of (3.3), the expression of \tilde{J}_k is used instead of J_k , while all the other identities are a direct consequence of (A.10a), (A.3a) and (A.3b) from the Prop. A.1 in Appendix A.1.

A.3 Stokes' Theorem for the FRM

A.3.1 Stokes' Theorem

Let us assume $\mathcal{J} = 0_6 \Rightarrow \mu = 0_6$ for simplicity of exposition, which reduces (5.4) to

$$\dot{g}_1 = g_1(-\mathcal{A}_l \dot{q})^{\wedge},\tag{A.11}$$

and that the initial condition is $g_1(0) = \mathbb{I}_{4,4}$. Under an abelian group assumption¹ for g_1 , the solution for (A.11) is [124],

$$g_1(t_f) = \exp\left(\int_{t_0}^{t_f} -\mathcal{A}_l \dot{q} dt\right) = \exp\left(\int_{\partial \mathcal{U}} -\mathcal{A}_l dq\right),$$
 (A.12)

where for $X \in \mathbb{R}^6$, $\exp(X) \equiv \exp(X^{\wedge})$ is the SE(3) exponential [10]. Note that the time-integral is replaced by a path-integral over a path $\partial \mathcal{U}$. For a closed path, i.e., gait, Stokes' theorem [124] is applied to convert the path integral in (A.12) to an area integral over the area \mathcal{U} ,

$$g_1(t_f) = \exp\left(-\int \int_{\mathcal{U}} D\mathcal{A}_l dA\right),$$
 (A.13)

where, $(D\mathcal{A}_l)(x)y = (d\mathcal{A}_l)(x)y - \operatorname{ad}_{\mathcal{A}_l x}\mathcal{A}_l y$ is a map $D\mathcal{A}_l : \mathbb{R}^n \times \mathbb{R}^n \to \mathfrak{se}(3)$ and is the local curvature, i.e., the covariant derivative of the local connection form $\mathcal{A}_l x$ along shape trajectories given by y, and dA is a differential area that is parameterized by the basis vectors $x, y \in \mathbb{R}^n$. The integral of $(d\mathcal{A}_l)(x)y$ in (A.13) is the nonconservative contribution and captures the change in mechanical connection due to change in shape. Likewise, the integral of the Lie bracket term $-\operatorname{ad}_{\mathcal{A}_l x} \mathcal{A}_l y$ is the the primary non-commutative contribution and captures the change in mechanical connection due to non-commutativity of SE(3) [20].

A.3.2 FRM-base Displacement over a Gait

Plotting the curvature, DA_l , component-wise over the gait's domain produces the CCF surfaces, see Fig. A.1. By computing the CCF surface volume under the gait area, we obtain the corrected Body Velocity Integral (cBVI), i.e., ζ in (2.48). Using this, an approximate $\delta \hat{g}_1 = \exp(\zeta)$ per gait cycle is obtained [20]. We elaborate the main idea for a 2-joint FRM (see Fig. 2.11), and hence the gait is defined by the shape basis vectors $(q_1, q_2) \in \mathbb{R}^2$. In Fig. A.1, the CCF for the k^{th} component², $(DA_l)_k$ is plotted on the left as a surface with an overlay of a circular gait (red). On the right of Fig. A.1, the volumetric mesh of the CCF surface under the gait area (red) is shown. The positive sense (arrows) is given by the direction of gait is execution. By computing the volume of the CCF surfaces for each component (k), we obtain the corresponding component, ζ_k . Finally, $\exp(\zeta) = \delta \hat{g}_1$ is the approximation of the net displacement of the FRM-base, δg_1 , over the gait.

¹The assumption is used to explain the main idea. However, SE(3) is not an abelian group, and despite the failure of the assumption, the presented theory was shown to be an approximation of the exact solution [20, 124].

 $^{{}^{2}}$ In $\mathfrak{se}(3) \cong \mathbb{R}^{6}$, k = 1, ..., 6, where the first three indices refer to the rotational and the last three to the translational bases, respectively.

254 A Appendix

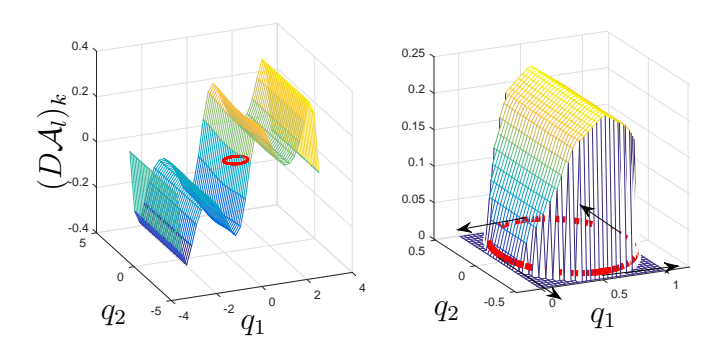


Figure A.1: CCF surface for the k^{th} basis corresponding to a gait (red circle) using 2-joints, and its zoomed in mesh volume (right) under that gait area, which provides an approximate estimate of FRM-base displacement per gait.

A.4 Derivations in Lemma 3.3

A.4.1 Proof of (3.7)

The momentum equation [16, eq. 6] is,

$$\langle \frac{dp}{dt}, \eta \rangle = \langle p, [(-\mathcal{A}_l \dot{q} + M_b^{-1} p)^{\wedge}, \eta^{\wedge}]^{\vee} \rangle, \ \eta \in \mathbb{R}^6.$$
 (A.14)

Moving η to the left on L.H.S and R.H.S after using SE(3) Lie-bracket isomorphism, $[x^{\wedge}, y^{\wedge}]^{\vee} = \operatorname{ad}_{x} y$, $x, y \in \mathbb{R}^{6}$, substituting $p = M_{b}\mu$ and, eliminating η yields the result.

A.4.2 Proof of (3.8)

To obtain closed form expression for \tilde{N} in (3.8), we recall [5, eq. 3.11.19]³, which provides a scalar product form in terms of body momentum, $p = M_b \mu$, as,

$$\langle \tilde{N}, \delta q \rangle = - \left\langle p, (d\mathcal{A}_l)(q, \dot{q}, \delta q) - [(\mathcal{A}_l \dot{q})^{\wedge}, (\mathcal{A}_l \delta q)^{\wedge}]^{\vee} + \frac{1}{2} \frac{\partial (M_b^{-1} p)}{\partial q} \delta q + [(M_b^{-1} p)^{\wedge}, (\mathcal{A}_l \delta q)^{\wedge}]^{\vee} \right\rangle.$$
(A.15)

In (A.15), as in Appendix A.4.1, the isomorphism, $[x^{\wedge}, y^{\wedge}]^{\vee} = \mathrm{ad}_x y$ is used. Also, in vector notation, $(d\mathcal{A}_l)(q, \dot{q}, \delta q) = (d\mathcal{A}_l)(q, \dot{q})\delta q$. Furthermore, we get $\frac{\partial (M_b^{-1}p)}{\partial q} = -M_b^{-1} \frac{\partial M_b (M_b^{-1}p)}{\partial q}$. Moving all δq terms towards the left in both L.H.S and R.H.S of (A.15), and substituting p, we get,

 $^{^3}$ In [5, eq. 3.11.19], the μ -dependent terms are on the L.H.S.

$$\langle \delta q, \tilde{N} \rangle = \left\langle \delta q, \left(- (d\mathcal{A}_l)(q, \dot{q})^\top - \mathcal{A}_l^\top \operatorname{ad}_{\mathcal{A}_l \dot{q}}^\top \right) M_b \mu + \frac{1}{2} \frac{\partial \mu^\top M_b(q) \mu}{\partial q} - \mathcal{A}_l^\top \operatorname{ad}_{\mu}^\top M_b \mu \right\rangle.$$
(A.16)

Removing δq variations, we get \tilde{N} in (3.8).

A.5 Computation of LID Matrix: Lemma 3.7

The following Lemma, which is an application of [22, Prop. 4], is key to the proof in Lemma A.4.

Lemma A.3. Given a column-wise detail of link Jacobian as, $J_k = \begin{bmatrix} J_k^1 & \dots & J_k^n \end{bmatrix}$ for the k^{th} link, using [22, Prop. 4] for the j^{th} joint and a velocity $X \in \mathbb{R}^6 \cong \mathfrak{se}(3)$, we have,

$$\frac{\partial A d_{1k}^{-1} X}{q_j} = -\operatorname{ad}_{J_k^j} A d_{1k}^{-1} X$$

$$\Rightarrow \frac{\partial A d_{1k}^{-1} X}{\partial q} = \begin{bmatrix} -\operatorname{ad}_{J_k^1} A d_{1k}^{-1} X & \dots \end{bmatrix}.$$
(A.17)

Lemma A.4. The partial derivative of the scalar form $\langle x, y \rangle_{M_b}$, $x, y \in \mathbb{R}^6$ with respect to q is computed as,

$$\frac{\partial}{\partial q} \langle x, y \rangle_{M_b} = \sum_{k} \left(\Pi_k(x)^\top + \tilde{\Pi}_k(x) \right) y = S(x)^\top y, \tag{A.18}$$

$$\sum_{k} \Pi_{k}(x)^{\top} = \sum_{k} J_{k}^{\top} \operatorname{ad}_{Ad_{1k}^{-1} x}^{\top} M_{k} A d_{1k}^{-1}, \tag{A.19}$$

$$\sum_{k} \tilde{\Pi}_{k}(x) = \sum_{k} J_{k}^{\top} \operatorname{ad}_{M_{k} A d_{1k}^{-1} x}^{\sim} A d_{1k}^{-1}.$$
(A.20)

Proof. Considering that $Ad_{1k} \equiv Ad_{1k}(q)$, note that,

$$\frac{\partial}{\partial q} \langle x, y \rangle_{M_b} = \sum_{k} \frac{\partial}{\partial q} \left(\left(\underbrace{\operatorname{Ad}_{1k}^{-1} x}_{r(q)} \right)^{\top} M_k \left(\underbrace{\operatorname{Ad}_{1k}^{-1} y}_{s(q)} \right) \right)
= \sum_{k} \left(\left(\frac{\partial r(q)}{\partial q} \right)^{\top} M_k s(q) + \left(\frac{\partial s(q)}{\partial q} \right)^{\top} M_k r(q) \right)
= \sum_{k} \Pi_k(x)^{\top} y + \Pi_k(y)^{\top} x,$$
(A.21)

where $\Pi_k(z) = \operatorname{Ad}_{1k}^{-\top} M_k \frac{\partial \operatorname{Ad}_{1k}^{-1} z}{\partial q}$. Now, we invoke Lemma A.3, and apply the property, $\operatorname{ad}_{J_k^j} \operatorname{Ad}_{1k}^{-1} x = -\operatorname{ad}_{\operatorname{Ad}_{1k}^{-1} x} J_k^j$ in it. Isolating, J_k^j to obtain J_k , we first obtain $\frac{\partial \operatorname{Ad}_{1k}^{-1} x}{\partial q} = \operatorname{ad}_{\operatorname{Ad}_{1k}^{-1} x} J_k$. Substituting this in Π_k yields (A.19).

256 A Appendix

The result in second of (A.21) can be conveniently rewritten as a linear operator form as (A.18) such that $\Pi_k(y)^{\top}x = \tilde{\Pi}_k(x)y$. This velocity exchange property appears similar to the one in (2.56) and is actually a consequence of it. By simply exploiting the property in (2.56) in $\Pi_k(y)^{\top}x$, we obtain (A.20).

A.6 Proofs about Key Properties in Sec. 3.6

A.6.1 Proof of Prop. 3.2

The first follows straightforwardly. The second follows by using the corresponding matrix expansions in (3.26a) and (3.26d). For the third, fourth and fifth, $\mathrm{ad}_{M_b\mu}^{\sim}$, $\tilde{\mathcal{B}}$ in (3.26e) and \mathcal{D}_{μ} in (5.3), respectively, are skew-symmetric. The final claim is evident in the velocity dependencies of $\mathcal{D}_{\dot{q}}$, \mathcal{D}_{μ} .

A.6.2 Proof of Prop. 3.4

Using the first of (3.39) in (3.26a), we conclude that Λ_q is invariant. The second of (3.39) implies that the reduced joint torques, $\tau - \mathcal{A}_l^{\top} \mathcal{F}_1$, in (5.3) are also invariant. In (3.26d), $\tilde{\Gamma}'_q$ is invariant because its computation depends on body Jacobians, \tilde{J}_k , which are invariant to spatial frame transformations. Finally, substituting $\mu = \mathrm{Ad}_{1c}\mu_c$ in (5.3) and using (3.40), we conclude that the CC torques are invariant. Thus, the invariance of the shape dynamics in (5.3) to frame transformations follows. The second follows straightforwardly from Prop. 3.3. In particular, $x^{\top}(\frac{d}{dt}\bar{M}_b - 2\bar{P})x = 0$ for $x \in \mathbb{R}^6$ is the multibody equivalent of the corollary in Prop. 2.3.

A.6.3 Proof of Theorem 3.3

The iterative form of the curvature is obtained by matching (3.8) and the bottom row of (5.3). Following Remark 19, by elimination, the only remaining terms are $-\tilde{\mathcal{B}}(\mu)\dot{q}$ in (5.3) and $-((D\mathcal{A}_l)(q,\dot{q}))^{\top}M_b\mu$ in (3.8), which are equal⁴. Considering a generalized velocity x instead of \dot{q} , (3.26e) is reformulated as $-\tilde{\mathcal{B}}(\mu)x = \mathcal{B}(q,x)\mu$ to obtain the new matrix operator in (3.43). This reformulation of $-\tilde{\mathcal{B}}(\mu)x$ is performed by applying the properties $\mathrm{ad}_X Y = -\mathrm{ad}_Y X$, (2.56), and the proposed Prop. 3.1. Hence, by equating, $-\tilde{\mathcal{B}}(\mu)x = \mathcal{B}(x)\mu = -((D\mathcal{A}_l)(q,x))^{\top}M_b\mu$, we get the result in Theorem 3.3. In particular, we further isolate the exterior derivative

⁴This observation has also been remarked in [145, §4]

operator as,

$$(d\mathcal{A}_l)(x)y = -M_b^{-1} \left(-S(\mathcal{A}_l x) + P(x)\mathcal{A}_l + \sum_k \left(J_k^{\top} (M_k \nabla_{J_k X} + 2M_k \operatorname{ad}_{J_k x}) \operatorname{Ad}_{1k}^{-1} \right)^{\top} \right).$$
(A.22)

A.6.4 Proof of Corollary 2

Substituting x = y, the final term in \mathcal{B}^T cancels out because $\operatorname{ad}_X X = 0$. Applying Prop. 3.1, the two middle terms cancel each other. In the first term, using (3.27), all the terms cancel out and yield the result.

A.6.5 Proof of Prop. 3.5

The transformed curvature, $D\mathcal{A}_{l}^{c}$, is obtained using (3.42), but with the dynamics matrices M_{b} , \mathcal{B} referred in the basis of g_{c} , i.e., $\hat{M}_{b} = \mathrm{Ad}_{1c}^{\mathsf{T}} M_{b} \mathrm{Ad}_{1c}$ and $\mathcal{B}_{c}(q,x) = \mathcal{B}(q,x) \mathrm{Ad}_{1c}$, as $D\mathcal{A}_{l}^{c} = \hat{M}_{b}^{-1} \mathcal{B}_{c}(x)^{\mathsf{T}}$. Substituting the constituent matrices yields the result.

A.6.6 Proofs used in Theorem 3.2

A.6.6.1 Proof of Lemma 3.9

The partitions of the CC matrix, Γ , in (3.28) are expanded by using partitions of \tilde{T} from (3.21) of Remark 17. The main idea of this proof is to start from these expressions and separate the terms according to their velocity dependencies for each of the four blocks of Γ in (3.28). In fact, the key feature of the CC matrix structure in (5.3) is the isolation of different terms according to the dependency on shape (\dot{q}) and locked (μ) velocities. This step will also reveal the LIV matrix structure defined above in (3.22).

Expanding the CC matrix, Γ , using (3.21) yields

$$\Gamma_b = \sum_k \mathrm{Ad}_{1k}^{-\top} (-\mathrm{ad}_{V_k}^{\top} M_k - M_k \, \mathrm{ad}_{J_k \dot{q}}) \mathrm{Ad}_{1k}^{-1}$$
 (A.23a)

$$\Gamma_{bq} = \sum_{k} \operatorname{Ad}_{1k}^{-\top} \left(-\operatorname{ad}_{V_{k}}^{\top} M_{k} \tilde{J}_{k} + M_{k} \dot{\tilde{J}}_{k} \right)$$

$$= \sum_{k} \operatorname{Ad}_{1k}^{-\top} \left(-\operatorname{ad}_{V_{k}}^{\top} M_{k} + \operatorname{ad}_{J_{k}\dot{q}}^{\top} M_{k} \right) \tilde{J}_{k}$$
(A.23b)

$$\Gamma_{qb} = \sum_{k} \tilde{J}_k^{\top} (-\operatorname{ad}_{V_k}^{\top} M_k - M_k \operatorname{ad}_{J_k \dot{q}}) \operatorname{Ad}_{1k}^{-1}$$
(A.23c)

$$\Gamma_q = \sum_k \tilde{J}_k^{\top} (-\operatorname{ad}_{V_k}^{\top} M_k \tilde{J}_k + M_k \dot{\tilde{J}}_k), \tag{A.23d}$$

⁵In the new basis, $\mu_c = \mathrm{Ad}_{1c}^{-1}\mu$, which is substituted in \mathcal{B} to get \mathcal{B}_c .

258 A Appendix

where (A.10b) is used to get (A.23b). For the proof, Γ is factorized to obtain (\dot{q}, \dot{q}) , (\dot{q}, μ) and (μ, μ) coupling forces. The key idea is to use (3.21) to write $V_k = \mathrm{Ad}_{1k}^{-1} \mu + \tilde{J}_k \dot{q}$ and split $\mathrm{ad}_{V_k}^{\top} M_k$ in (A.23) as the sum of contributions depending on \dot{q} and μ , as,

$$\operatorname{ad}_{V_k}^{\top} M_k = (\operatorname{ad}_{\operatorname{Ad}_{1k}^{-1}\mu}^{\top} + \operatorname{ad}_{\tilde{J}_k \dot{q}}^{\top}) M_k. \tag{A.24}$$

• Γ_b in (3.29): We simplify (A.23a) by splitting $\operatorname{ad}_{V_k}^{\top}$ as,

$$\Gamma_b = \sum_{k} A d_{1k}^{-\top} \left(-\left(a d_{Ad_{1k}^{-1}(\mu - \mathcal{A}_l \dot{q})}^{\top} + a d_{J_k \dot{q}}^{\top} \right) M_k - M_k \, a d_{J_k \dot{q}} \right) A d_{1k}^{-1}$$
(A.25)

The summation in (A.25) is eliminated after using the expansion for $P(\dot{q})$ from (3.22), and applying Prop. A.4 (Appendix A.2). This yields (3.29) in Lemma 3.9.

• Γ_{bq} in (3.30): After expanding \tilde{J}_k in (A.23b), we obtain,

$$\Gamma_{bq} = \sum_{k} \operatorname{Ad}_{1k}^{-\top} \left(\operatorname{ad}_{(-\operatorname{Ad}_{1k}^{-1}\mu - \tilde{J}_{k}\dot{q} + J_{k}\dot{q})}^{\top} M_{k} \right) \tilde{J}_{k}$$

$$= -\sum_{k} \operatorname{Ad}_{1k}^{-\top} \left(\operatorname{ad}_{\operatorname{Ad}_{1k}^{-1}\mu}^{\top} + \operatorname{ad}_{(\tilde{J}_{k}\dot{q} - J_{k}\dot{q})}^{\top} \right) M_{k} \tilde{J}_{k}$$
(A.26)

Using Prop. A.4 (Appendix A.2) and applying (A.10d) and (A.10e) straightforwardly yields (3.30).

• Γ_{qb} in (3.31): Using (A.24) and the form of \tilde{J}_k from (3.21) to expand the terms in (A.23c), we get,

$$\Gamma_{qb} = \sum_{k} \tilde{J}_{k}^{\top} \left(-\operatorname{ad}_{(\operatorname{Ad}_{1k}^{-1}\mu + \tilde{J}_{k}\dot{q})}^{\top} M_{k} - M_{k} \operatorname{ad}_{J_{k}\dot{q}} \right) \operatorname{Ad}_{1k}^{-1}$$

$$= \sum_{k} \left(\left(-J_{k}^{\top} \operatorname{ad}_{\operatorname{Ad}_{1k}^{-1}\mu}^{\top} + \mathcal{A}_{l}^{\top} \operatorname{Ad}_{1k}^{-\top} \operatorname{ad}_{\operatorname{Ad}_{1k}^{-1}\mu}^{\top} \right) - \tilde{J}_{k}^{\top} \operatorname{ad}_{\tilde{J}_{k}\dot{q}} \right) M_{k} - \tilde{J}_{k}^{\top} M_{k} \operatorname{ad}_{J_{k}\dot{q}} \operatorname{Ad}_{1k}^{-1}.$$
(A.27)

Upon expanding, followed by invoking Prop. A.4 (Appendix A.1.2) for the second term, the matrix $\mathcal{A}_l^{\mathsf{T}} \mathrm{ad}_{\mu}^{\mathsf{T}} M_b$ is obtained. Therefore, (A.27) is rewritten as in (3.31).

• Γ_q in (3.32): The Γ_q matrix in (A.23d) is expanded as in (3.32) by simply using (A.24).

A.6.6.2 Proof of Lemma 3.10

In the proof, the following identities are used for the block matrix expansions (underbraced parts) of Γ_{qb} and Γ_q , which were obtained in Lemma 3.9.

$$B_{1}(\dot{q})\mu = \sum_{k} \tilde{J}_{k}^{\top} \left(\operatorname{ad}_{M_{k} \operatorname{Ad}_{1k}^{-1} \mu}^{\sim} \tilde{J}_{k} - M_{k} \operatorname{ad}_{\operatorname{Ad}_{1k}^{-1} \mu}^{\sim} J_{k} \right) \dot{q}$$

$$= B_{3}(q, \mu) \dot{q}$$
(A.28)

$$\Gamma'_{q}(\dot{q})\dot{q} = \sum_{k} \tilde{J}_{k}^{\top} (-\operatorname{ad}_{M_{k}\tilde{J}_{k}\dot{q}}^{\sim} \tilde{J}_{k} + M_{k} \dot{\tilde{J}}_{k})\dot{q}$$

$$= \tilde{\Gamma}'_{q}(q, \dot{q})\dot{q}$$
(A.29)

$$\tilde{S}(\mu)^{\top} \mu = \frac{1}{2} \sum_{k} (\Pi_{k}^{\top} + \tilde{\Pi}_{k}) \mu = \frac{1}{2} S(\mu)^{\top} \mu$$
 (A.30)

These three identities follow straight forwardly by using (2.56) and $\operatorname{ad}_X Y = -\operatorname{ad}_Y X$ for rearrangement. Applying these identities to the L.H.S of Lemma 3.10, we obtain all the terms, but $\tilde{\mathcal{B}} = -(B_2 + B_3)$. Expanding $\tilde{\mathcal{B}}$, using \tilde{J}_k , and (A.10d) to cancel terms results in (3.26e).

Lemma A.5. Consider an \mathcal{EL} system with $q \in Q$, which is moving due to a time-invariant gauge potential comprising of a scalar potential, V(q), a magnetic potential A(q). The motion equations describe the electromagnetic geodesic for this system as,

$$M(q)\ddot{q} + C(q, \dot{q})\dot{q} = -dV - \mathcal{B}(q)\dot{q} \tag{A.31}$$

where $\mathcal{B} = \frac{\partial A}{\partial q} - \frac{\partial A}{\partial q}^{\top}$ is skew-symmetric, i.e., $x^{\top} \mathcal{B} x = 0$ for $x \in \mathbb{R}^n$.

Proof. In this case, the magnetic Lagrangian [94, §3] is used and written as,

$$L = T - V + \langle \dot{q}, A(q) \rangle \tag{A.32}$$

We obtain the two parts of the L.H.S in (A.31) as.

$$\frac{d}{dt}\frac{\partial L}{\partial \dot{q}} = M(q)\ddot{q} + \dot{M}(q,\dot{q})\dot{q} + \dot{A}(q,\dot{q}) \tag{A.33}$$

$$\frac{\partial L}{\partial q} = \frac{1}{2} \frac{\partial}{\partial q} \langle \dot{q}, \dot{q} \rangle_{M(q)} - \frac{\partial V}{\partial q} + \frac{\partial}{\partial q} \langle \dot{q}, A(q) \rangle \tag{A.34}$$

In (A.33) and (A.34), respectively, through algebraic manipulation, we get,

$$\dot{A}(q,\dot{q}) = \dot{q}^{\top} \frac{\partial A(q)}{\partial q} = \mathcal{A}(q)\dot{q}, \ \frac{\partial \langle \dot{q}, A \rangle}{\partial q} = \mathcal{A}(q)^{\top} \dot{q}$$
 (A.35)

Using (A.35) in (A.33) and (A.34), and writing (A.31), we obtain $\mathcal{B} = \mathcal{A} - \mathcal{A}^{\top}$, and hence, (A.31).

Note that Lemma A.5 generalizes the Lorentz force law, see [263, eq. 16], for a curved configuration space, Q, (Christoffel symbols in C) and replaces the magnetic force using a skew-symmetric tensor \mathcal{B} . A corollary is that the Hamiltonian is written as $\mathcal{H} = \frac{1}{2} \langle \dot{q}, \dot{q} \rangle_Q + V(q)$, and is conserved.

Bibliography

- [1] H. Weyl, Levels of infinity: selected writings on mathematics and philosophy. Courier Corporation, 2013.
- [2] J. Wheeler, A Journey Into Gravity and Spacetime, ser. Library series. Scientific American Library, 1990.
- [3] R. Ortega, A. Loría, P. J. Nicklasson, and H. Sira-Ramírez, "Euler-lagrange systems", in *Passivity-based Control of Euler-Lagrange Systems: Mechanical, Electrical and Electromechanical Applications*. London: Springer London, 1998, pp. 15–37.
- [4] J. E. Marsden and T. S. Ratiu, Introduction to Mechanics and Symmetry: A Basic Exposition of Classical Mechanical Systems. Springer Publishing Company, Incorporated, 2010.
- [5] A. Bloch and B Brogliato, "Nonholonomic mechanics and control", Appl. Mech. Rev., vol. 57, no. 1, B3–B3, 2004.
- [6] F. Bullo and A. D. Lewis, "Lie groups, systems on groups, and symmetries", in *Geometric Control of Mechanical Systems: Modeling, Analysis, and Design for Simple Mechanical Control Systems.* New York, NY: Springer New York, 2005, 247–310.
- [7] T. Kurfess, Robotics and Automation Handbook. Taylor & Francis, 2005.
- [8] R. M. Murray, Z. Li, and S. S. Sastry, A mathematical introduction to robotic manipulation. CRC press, 2017.
- [9] F. Bullo and R. Murray, "Proportional derivative (pd) control on the euclidean group", 1995.
- [10] —, "Tracking for fully actuated mechanical systems: a geometric framework", *Automatica*, vol. 35, no. 1, pp. 17–34, 1999.

262 BIBLIOGRAPHY

[11] S. Bonnabel, P. Martin, and P. Rouchon, "Symmetry-preserving observers", *IEEE Transactions on Automatic Control*, vol. 53, no. 11, pp. 2514–2526, 2008.

- [12] C. Lageman, J. Trumpf, and R. Mahony, "Gradient-like observers for invariant dynamics on a lie group", *IEEE Transactions on Automatic Control*, vol. 55, no. 2, pp. 367–377, 2010.
- [13] A. M. Bloch, N. E. Leonard, and J. E. Marsden, "Controlled lagrangians and the stabilization of mechanical systems. i. the first matching theorem", *IEEE Transactions on automatic control*, vol. 45, no. 12, pp. 2253–2270, 2000.
- [14] A. M. Bloch, P. S. Krishnaprasad, J. E. Marsden, and R. M. Murray, "Nonholonomic mechanical systems with symmetry", Archive for Rational Mechanics and Analysis, vol. 136, no. 1, pp. 21–99, 1996.
- [15] J. P. Ostrowski, "Computing reduced equations for robotic systems with constraints and symmetries", *IEEE Transactions on Robotics and Automation*, vol. 15, no. 1, pp. 111–123, 1999.
- [16] R. M. Murray, "Nonlinear control of mechanical systems: A lagrangian perspective", *Annual Reviews in Control*, vol. 21, pp. 31–42, 1997.
- [17] S. D. Kelly and R. M. Murray, "Geometric phases and robotic locomotion", Journal of Robotic Systems, vol. 12, no. 6, pp. 417–431, 1995.
- [18] K. A. McIsaac and J. P. Ostrowski, "A geometric approach to gait generation for eel-like locomotion", in *Proceedings. 2000 IEEE/RSJ International Conference on Intelligent Robots and Systems (IROS 2000) (Cat. No.00CH37113)*, vol. 3, 2000, 2230–2235 vol.3.
- [19] R. L. Hatton and H. Choset, "Geometric motion planning: The local connection, stokes' theorem, and the importance of coordinate choice", *The International Journal of Robotics Research*, vol. 30, no. 8, pp. 988–1014, 2011.
- [20] R. Hatton and H. Choset, "Nonconservativity and noncommutativity in locomotion", The European Physical Journal Special Topics, vol. 224, no. 17, pp. 3141–3174, 2015.
- [21] D. Rollinson, R. L. Hatton, and H. Choset, "Coordinates matter: Virtual chassis and minimum perturbation coordinate representations", in *Adaptive Mobile Robotics*, pp. 183–190.
- [22] G. Garofalo, C. Ott, and A. Albu-Schäffer, "On the closed form computation of the dynamic matrices and their differentiations", in 2013 IEEE/RSJ International Conference on Intelligent Robots and Systems, 2013, pp. 2364–2359.

[23] R. Featherstone, *Rigid Body Dynamics Algorithms*. Berlin, Heidelberg: Springer-Verlag, 2007.

- [24] M. Zefran and F. Bullo, "Lagrangian dynamics", Robotics and Automation Handbook, pp. 5–1, 2005.
- [25] G. Garofalo, B. Henze, J. Englsberger, and C. Ott, "On the inertially decoupled structure of the floating base robot dynamics", *IFAC-Papers-OnLine*, vol. 48, no. 1, pp. 322 –327, 2015, 8th Vienna International Conferenceon Mathematical Modelling.
- [26] P. J. From, I. Schjølberg, J. T. Gravdahl, K. Y. Pettersen, and T. I. Fossen, "On the boundedness and skew-symmetric properties of the inertia and coriolis matrices for vehicle-manipulator systems", *IFAC Proceedings Volumes*, vol. 43, no. 16, pp. 193 –198, 2010, 7th IFAC Symposium on Intelligent Autonomous Vehicles.
- [27] M. De Stefano, R. Balachandran, A. M. Giordano, C. Ott, and C. Secchi, "An energy-based approach for the multi-rate control of a manipulator on an actuated base", in 2018 IEEE International Conference on Robotics and Automation (ICRA), 2018, pp. 1072–1077.
- [28] S. R. Ploen, "A skew-symmetric form of the recursive newton-euler algorithm for the control of multibody systems", in 1999 American Control Conference (ACC), vol. 6, 1999, 3770–3773 vol.6.
- [29] K. Yoshida and D. N. Nenchev, "A general formulation of under-actuated manipulator systems", in *Robotics Research*, Y. Shirai and S. Hirose, Eds., London: Springer London, 1998, pp. 33–44.
- [30] O. Egeland and K. Y. Pettersen, "Free-floating robotic systems", in *Control Problems in Robotics and Automation*, B. Siciliano and K. P. Valavanis, Eds., Berlin, Heidelberg: Springer Berlin Heidelberg, 1998, 119–134.
- [31] A. Saccon, S. Traversaro, F. Nori, and H. Nijmeijer, "On centroidal dynamics and integrability of average angular velocity", *IEEE Robotics and Automation Letters*, vol. 2, no. 2, pp. 943–950, 2017.
- [32] K. Nanos and E. Papadopoulos, "On the use of free-floating space robots in the presence of angular momentum", *Intelligent Service Robotics*, vol. 4, no. 1, pp. 3–15, 2011.
- [33] H. Nakanishi and K. Yoshida, "Impedance Control for Free-flying Space Robots -Basic Equations and Applications-", in *Intelligent Robots and Systems*, *IEEE/RSJ International Conference on*, 2006.
- [34] A. M. Giordano, G. Garofalo, and A. Albu-Schaffer, "Momentum dumping for space robots", in 2017 IEEE 56th Annual Conference on Decision and Control (CDC), 2017, pp. 5243–5248.

[35] —, "Momentum dumping for space robots", in 2017 IEEE 56th Annual Conference on Decision and Control (CDC), 2017, pp. 5243–5248.

- [36] A. M. Giordano, C. Ott, and A. Albu-Schäffer, "Coordinated control of spacecraft's attitude and end-effector for space robots", *IEEE Robotics and Automation Letters*, vol. 4, no. 2, pp. 2108–2115, 2019.
- [37] A. M. Giordano, "Whole-body control of orbital robots", Ph.D. dissertation, Technische Universität München, 2020.
- [38] S. A. A. Moosavian and E. Papadopoulos, "Free-flying robots in space: An overview of dynamics modeling, planning and control", *Robotica*, vol. 25, no. 5, pp. 537–547, 2007.
- [39] D. E. Orin, A. Goswami, and S.-H. Lee, "Centroidal dynamics of a humanoid robot", *Autonomous robots*, vol. 35, pp. 161–176, 2013.
- [40] P. M. Wensing and D. E. Orin, "Improved computation of the humanoid centroidal dynamics and application for whole-body control", *International Journal of Humanoid Robotics*, vol. 13, no. 01, p. 1550 039, 2016.
- [41] M. A. Roa, A. Beyer, I. Rodriguez, M. Stelzer, M. de Stefano, J.-P. Lutze, H. Mishra, F. Elhardt, G. Grunwald, et al., "Eross: In-orbit demonstration of european robotic orbital support services", in 2024 IEEE Aerospace Conference, 2024, pp. 1–9.
- [42] P. Colmenarejo, N. Santos, P. Serra, J. Telaar, H. Strauch, M. De Stefano, A. M. Giordano, H. **Mishra**, R. Lampariello, C. Ott, et al., "Results of the comrade project: Combined control for robotic spacecraft and manipulator in servicing missions: Active debris removal and re-fuelling", in 11th International ESA Conference on Guidance, Navigation & Control Systems, 2020, pp. 10–23.
- [43] S. Jaekel, R. Lampariello, W. Rackl, et al., "Design and operational elements of the robotic subsystem for the e.Deorbit debris removal mission", Frontiers in Robotics and AI, vol. 5, p. 100, 2018.
- [44] P. Colmenarejo, D. Henry, G. Visentin, et al., "Methods and outcomes of the COMRADE project Design of robust coupled control for robotic spacecraft in servicing missions", in *International Astronautical Congress (IAC)*, 2018.
- [45] H. Benninghoff, F. Rems, E. A. Risse, et al., "RICADOS rendezvous, inspection, capturing and detumbling by orbital servicing", in *International Conference on Astrodynamics Tools and Techniques*, 2018.
- [46] A. Flores-Abad, O. Ma, K. Pham, and S. Ulrich, "A review of space robotics technologies for on-orbit servicing", *Progress in Aerospace Sciences*, vol. 68, pp. 1–26, 2014.

[47] M. Deremetz, M. Debroise, M. De Stefano, H. **Mishra**, B. Brunner, G. Grunwald, M. A. Roa Garzon, M. Reiner, M. Závodník, M. Komarek, et al., "Design and integration of a multi-arm installation robot demonstrator for orbital large assembly", in 73rd International Astronautical Congress, IAC 2022, 2022.

- [48] W Smith, J Nuth, J Leary, D Wegel, J Church, M Grebenstein, and S. Voelk, "Low risk technique for sample acquisition from remote and hazardous sites on a comet", in *International Workshop Instrumentation for Planetary Missions (IPM) 2018*, 2018.
- [49] F. Aghili and J. Piedboeuf, "Hardware-in-loop simulation of robots interacting with environment via algebraic differential equation", in *IEEE/RSJ International Conference on Intelligent Robots and Systems (IROS)*, vol. 3, 2000, 1590–1596 vol.3.
- [50] J. A. et al., "The oos-sim: An on-ground simulation facility for on-orbit servicing robotic operations", in 2015 IEEE International Conference on Robotics and Automation (ICRA), 2015.
- [51] C. Ott, Cartesian impedance control of redundant and flexible-joint robots. Springer, 2008.
- [52] C. Ott, A. Dietrich, and A. Albu-Schäffer, "Prioritized multi-task compliance control of redundant manipulators", *Automatica*, vol. 53, pp. 416–423, 2015.
- [53] M. Mukadam, C.-A. Cheng, D. Fox, B. Boots, and N. Ratliff, "Riemannian motion policy fusion through learnable lyapunov function reshaping", in *Conference on robot learning*, PMLR, 2020, pp. 204–219.
- [54] M. De Stefano, H. Mishra, A. M. Giordano, R. Lampariello, and C. Ott, "A relative dynamics formulation for hardware- in-the-loop simulation of on-orbit robotic missions", *IEEE Robotics and Automation Letters*, vol. 6, no. 2, pp. 3569–3576, 2021.
- [55] H. **Mishra**, R. Balachandran, M. De Stefano, and C. Ott, "A compliant partitioned shared control strategy for an orbital robot", *IEEE Robotics and Automation Letters*, vol. 6, no. 4, pp. 7317–7324, 2021.
- [56] H. **Mishra**, G. Garofalo, A. M. Giordano, M. De Stefano, C. Ott, and A. Kugi, "Reduced Euler-Lagrange equations of floating-base robots: Computation, properties, and applications", *IEEE Transactions on Robotics*, pp. 1–19, 2022.
- [57] H. **Mishra**, T. Vicariotto, and M. De Stefano, "Dynamics, simulation & control of orbital modules for on-orbit assembly", *IEEE Robotics and Automation Letters*, vol. 10, no. 1, pp. 200–207, 2025.

[58] H. Mishra, M. De Stefano, and C. Ott, "Is there a closed-loop lagrangian for hierarchical motion control?", *IEEE Control Systems Letters (first review)*, 2025.

- [61] H. Mishra, M. De Stefano, A. M. Giordano, and C. Ott, "Tracking control with robotic systems for a moving target: A vector lyapunov function approach", *IFAC-PapersOnLine*, vol. 51, no. 22, pp. 471–478, 2018, 12th IFAC Symposium on Robot Control SYROCO 2018.
- [62] H. **Mishra**, M. De Stefano, A. M. Giordano, and C. Ott, "A nonlinear observer for free-floating target motion using only pose measurements", in 2019 American Control Conference (ACC), 2019, pp. 1114–1121.
- [63] —, "Output feedback stabilization of an orbital robot", in 2020 59th IEEE Conference on Decision and Control (CDC), 2020, pp. 1503–1501.
- [64] H. Mishra, M. De Stefano, A. M. Giordano, R. Lampariello, and C. Ott, "A geometric controller for fully-actuated robotic capture of a tumbling target", in 2020 American Control Conference (ACC), 2020, pp. 2150– 2157.
- [65] H. Mishra, A. M. Giordano, M. De Stefano, R. Lampariello, and C. Ott, "Inertia-decoupled equations for hardware-in-the-loop simulation of an orbital robot with external forces", in 2020 IEEE/RSJ International Conference on Intelligent Robots and Systems (IROS), 2020, pp. 1879–1886.
- [66] H. Mishra, M. De Stefano, and C. Ott, "Dynamics and control of a reconfigurable multi-arm robot for in-orbit assembly", IFAC-PapersOnLine, vol. 55, no. 20, pp. 235–240, 2022, 10th Vienna International Conference on Mathematical Modelling MATHMOD 2022.
- [67] M. De Stefano, C. Ott, R. Vijayan, H. **Mishra**, and F. Elhardt, "Method for controlling a robot device", pat. US20240391102, 2024.
- [68] R. Balachandran and H. Mishra, "Verfahren zum Kooperativen Kontrollieren eines Autonomen Systems durch einen Menschlichen Operator und/oder ein Automatisches Kontrollsystem und Computerprogrammprodukt", pending (DE) DE102020114574.8A, 2021.
- [73] R. Lampariello, H. **Mishra**, N. Oumer, et al., "Tracking control for the grasping of a tumbling satellite with a free-floating robot", *IEEE Robotics and Automation Letters*, vol. 3, no. 4, pp. 3638–3645, 2018.
- [74] M. De Stefano, H. Mishra, R. Balachandran, R. Lampariello, C. Ott, and C. Secchi, "Multi-rate tracking control for a space robot on a controlled satellite: A passivity-based strategy", *IEEE Robotics and Automation Let*ters, vol. 4, no. 2, pp. 1319–1326, 2019.

[75] A. Poó Gallardo, H. **Mishra**, A. Massimo Giordano, and R. Lampariello, "Robust estimation of motion states for free-floating tumbling target capture", in 2019 IEEE Aerospace Conference, 2019, pp. 1–11.

- [76] R. Balachandran, H. **Mishra**, M. Cappelli, B. Weber, C. Secchi, C. Ott, and A. Albu-Schaeffer, "Adaptive authority allocation in shared control of robots using bayesian filters", in *2020 IEEE International Conference on Robotics and Automation (ICRA)*, 2020, pp. 11298–11304.
- [77] A. Coelho, Y. Sarkisov, X. Wu, H. **Mishra**, H. Singh, A. Dietrich, A. Franchi, K. Kondak, and C. Ott, "Whole-body teleoperation and shared control of redundant robots with applications to aerial manipulation", *Journal of Intelligent & Robotic Systems*, vol. 102, pp. 1–22, 2021.
- [78] R. Balachandran, H. **Mishra**, M. Panzirsch, and C. Ott, "A finite-gain stable multi-agent robot control framework with adaptive authority allocation", in 2021 IEEE International Conference on Robotics and Automation (ICRA), 2021, pp. 1579–1585.
- [79] A. M. Giordano, D. Calzolari, M. De Stefano, H. **Mishra**, C. Ott, and A. Albu-Schäffer, "Compliant floating-base control of space robots", *IEEE Robotics and Automation Letters*, vol. 6, no. 4, pp. 7485–7492, 2021.
- [80] R. Lampariello, H. **Mishra**, N. W. Oumer, and J. Peters, "Robust motion prediction of a free-tumbling satellite with on-ground experimental validation", *Journal of Guidance, Control, and Dynamics*, vol. 44, no. 10, pp. 1777–1793, 2021.
- [81] I. Rodríguez, J.-P. Lutze, H. **Mishra**, P. Lehner, and M. A. Roa, "Hybrid planning to minimize platform disturbances during in-orbit assembly tasks", in *2022 IEEE Aerospace Conference (AERO)*, 2022, pp. 1–11.
- [82] J. Jeong, H. **Mishra**, C. Ott, and M. J. Kim, "A memory-based so(3) parameterization: Theory and application to 6d impedance control with radially unbounded potential function", in 2022 International Conference on Robotics and Automation (ICRA), 2022, pp. 8338–8344.
- [83] M. Rothammer, A. Coelho, H. **Mishra**, C. Ott, A. Franchi, and A. Albu-Schaeffer, "A rigid body observer (bobs) considering pfaffian constraints with a pose regulation framework", *IEEE Control Systems Letters*, vol. 7, pp. 163–168, 2023.
- [84] A. Coelho, A. Albu-Schaeffer, A. Sachtler, H. **Mishra**, D. Bicego, C. Ott, and A. Franchi, "Eigenmpc: An eigenmanifold-inspired model-predictive control framework for exciting efficient oscillations in mechanical systems", in 2022 IEEE 61st Conference on Decision and Control (CDC), 2022, pp. 2437–2442.

[85] J.-P. Lutze, R. Schuller, H. **Mishra**, I. Rodríguez, and M. A. Roa, "Optimization of multi-arm robot locomotion to reduce satellite disturbances during in-orbit assembly", in *IEEE Aerospace Conference*, 2023, pp. 1–11.

- [86] R. Balachandran, M. De Stefano, H. **Mishra**, C. Ott, and A. Albu-Schaeffer, "Passive arbitration in adaptive shared control of robots with variable force and stiffness scaling", *Mechatronics*, vol. 90, p. 102 930, 2023.
- [87] M. De Stefano, M. A. Roa, R. Balachandran, A. M.Giordano, H. Mishra, N. Oumer, B. Brunner, M. Lingenauber, M. Stelzer, and R. Lampariello, "Design and validation of orbital robotic missions", in *Space Robotics: The State of the Art and Future Trends*, X. T. Yan and G. Visentin, Eds. Cham: Springer Nature Switzerland, 2024, pp. 281–304.
- [88] B. Basu, The Sacred Books of the Hindus, Vol. 6: Vaisesika Sutra (1915, Classic Reprint). 1kg Limited, 2018.
- [89] J. Lee, *Introduction to Smooth Manifolds*, ser. Graduate Texts in Mathematics. Springer New York, 2013.
- [90] R. M. Murray, J. W. Burdick, S. D. Kelly, and J. Radford, "Trajectory generation for mechanical systems with application to robotic locomotion", in *Proceedings of the Third Workshop on the Algorithmic Foundations of Robotics on Robotics: The Algorithmic Perspective: The Algorithmic Perspective*, ser. WAFR '98, Houston, Texas, USA: A. K. Peters, Ltd., 1998, pp. 81–90.
- [91] H. Goldstein, C. Poole, and J. Safko, *Classical Mechanics*. Addison Wesley, 2002.
- [92] D. D. Holm, Geometric Mechanics-Part II: Rotating, Translating and Rolling. World Scientific, 2011.
- [93] O. Esen and S. Sütlü, "Lagrangian dynamics on matched pairs", *Journal of Geometry and Physics*, vol. 111, pp. 142–157, 2017.
- [94] J. E. Marsden and J. Scheurle, "The reduced euler-lagrange equations", in *Dynamics and Control of Mechanical Systems: The Falling Cat and Re-lated Problems*, ser. Crm Proceedings & Lecture Notes, American Mathematical Society, 1993.
- [95] R. Leone, "On the wonderfulness of noether's theorems, 100 years later, and routh reduction", arXiv preprint arXiv:1804.01714, 2018.
- [96] A. K. Halder, A. Paliathanasis, and P. G. Leach, "Noether's theorem and symmetry", *Symmetry*, vol. 10, no. 12, 2018.
- [97] D. E. Chang and R. G. McLenaghan, "Geometric criteria for the quasilinearization of the equations of motion of mechanical systems", *IEEE Transactions on Automatic Control*, vol. 58, no. 4, pp. 1046–1050, 2013.

[98] M. O. Katanaev, "Killing vector fields and a homogeneous isotropic universe", *Physics-Uspekhi*, vol. 59, no. 7, p. 689, 2016.

- [99] D. Krupka and J. Janyška, *Lectures on Differential Invariants*, ser. Folia Facultatis Scientiarum Naturalium Universitatis Purkynianae Brunensis: Mathematica. Purkynianae University, 1990.
- [100] M. J. Gotay, J. E. Marsden, and V. Moncrief, Mathematical Aspects of Classical Field Theory: Proceedings of the AMS-IMS-SIAM Joint Summer Research Conference Held July 20-26, 1991, with Support from the National Science Foundation. American Mathematical Soc., 1992, vol. 132.
- [101] J. W. Burdick, "On the inverse kinematics of redundant manipulators: Characterization of the self-motion manifolds", in *Advanced Robotics*, K. J. Waldron, Ed., Berlin, Heidelberg: Springer Berlin Heidelberg, 1989, pp. 25–34.
- [102] A. Albu-Schäffer and A. Sachtler, "Redundancy resolution at position level", *IEEE Transactions on Robotics*, pp. 1–22, 2023.
- [103] N. Steenrod, *The Topology of Fibre Bundles*, ser. Princeton Landmarks in Mathematics and Physics. Princeton University Press, 1999.
- [104] G. Giachetta, L. Mangiarotti, and G. A. Sardanashvily, New Lagrangian and Hamiltonian methods in field theory. World Scientific, 1997.
- [105] T. Shamir and Y. Yomdin, "Repeatability of redundant manipulators: Mathematical solution of the problem", *IEEE Transactions on Automatic Control*, vol. 33, no. 11, pp. 1004–1009, 1988.
- [106] C. Altafini, "Redundant robotic chains on riemannian submersions", *IEEE Transactions on Robotics and Automation*, vol. 20, no. 2, pp. 335–340, 2004.
- [107] P. J. Olver, Applications of Lie groups to differential equations. Springer Science & Business Media, 1993, vol. 107.
- [108] T. Bendokat, R. Zimmermann, and P.-A. Absil, "A grassmann manifold handbook: Basic geometry and computational aspects", *Advances in Computational Mathematics*, vol. 50, no. 1, p. 6, 2024.
- [109] J. E. Humphreys, Introduction to Lie algebras and representation theory. Springer Science & Business Media, 2012, vol. 9.
- [110] W. A. Rodrigues and E. C. de Oliveira, *The many faces of Maxwell, Dirac and Einstein equations*. Springer, 2007, vol. 722.
- [111] A. Cohen, An Introduction to the Lie Theory of One-parameter Groups: With Applications to the Solution of Differential Equations, ser. Cornell University Library historical math monographs. D.C. Health & Company, 1911.

[112] I. Kolář, J. Slovák, and P. W. Michor, *Bundles and Connections*. Berlin, Heidelberg: Springer Berlin Heidelberg, 1993, pp. 76–115.

- [113] "A generalized exponential formula for forward and differential kinematics of open-chain multi-body systems", *Mechanism and Machine Theory*, vol. 73, pp. 61–75, 2014.
- [114] S. B. Andersson, "Geometric phases in dissipative systems with symmetry", *IFAC Proceedings Volumes*, vol. 37, no. 13, pp. 231–236, 2004, 6th IFAC Symposium on Nonlinear Control Systems 2004 (NOLCOS 2004), Stuttgart, Germany, 1-3 September, 2004.
- [115] C. Altafini, "Explicit Wei–Norman formulae for matrix lie groups via Putzer's method", Systems & Control Letters, vol. 54, no. 11, pp. 1121–1130, 2005.
- [116] M. Crampin, D. Saunders, et al., "Cartan geometries and their symmetries", Atlantis Stud. Var. Geom, vol. 4, 2016.
- [117] A. Weinstein, "Groupoids: Unifying internal and external symmetry", *Notices of the AMS*, vol. 43, no. 7, pp. 744–752, 1996.
- [118] I. Moerdijk and J. Mrčun, "On the integrability of lie subalgebroids", Advances in Mathematics, vol. 204, no. 1, pp. 101–115, 2006.
- [119] S. Li, A. Stern, X. Tang, et al., "Lagrangian mechanics and reduction on fibered manifolds", SIGMA. Symmetry, Integrability and Geometry: Methods and Applications, vol. 13, p. 019, 2017.
- [120] J. E. M. Anthony M. Bloch and D. V. Zenkov, "Quasivelocities and symmetries in non-holonomic systems", *Dynamical Systems*, vol. 24, no. 2, pp. 187–222, 2009.
- [121] F Bullo, "On controllability and symmetries in simple mechanical systems", Technical project, California Institute of Technology, 1996.
- [122] J. W. Burdick, "On the inverse kinematics of redundant manipulators: Characterization of the self-motion manifolds", in *Advanced Robotics: Proceedings of the 4th International Conference on Advanced Robotics Columbus, Ohio, June 13–15, 1989*, Springer, 1989, pp. 25–34.
- [123] M. J. Enos, Dynamics and Control of Mechanical Systems: The Falling Cat and Related Problems. USA: American Mathematical Society, 1993, pp. 139–164.
- [124] J. B. Melli, C. W. Rowley, and D. S. Rufat, "Motion planning for an articulated body in a perfect planar fluid", *SIAM Journal on Applied Dynamical Systems*, vol. 5, no. 4, pp. 650–669, 2006.

[125] R. Mason and J. Burdick, "Propulsion and control of deformable bodies in an ideal fluid", in *Proceedings 1999 IEEE International Conference on Robotics and Automation (Cat. No.99CH36288C)*, vol. 1, 1999, 773–780 vol.1.

- [126] H. K. Khalil, *Nonlinear systems (3rd edition)*. Upper Saddle River, NJ: Prentice-Hall, 2002.
- [127] J. I. Mulero, "A new factorization of the coriolis/centripetal matrix", *Robotica*, vol. 27, no. 5, 689–700, 2009.
- [128] J. Y. S. Luh, M. W. Walker, and R. P. C. Paul, "On-Line Computational Scheme for Mechanical Manipulators", *Journal of Dynamic Systems, Measurement, and Control*, vol. 102, no. 2, pp. 69–76, 1980.
- [129] J. M. Hollerbach, "A recursive lagrangian formulation of maniputator dynamics and a comparative study of dynamics formulation complexity", *IEEE Transactions on Systems, Man, and Cybernetics*, vol. 10, no. 11, pp. 730–736, 1980.
- [130] D. Parsons and J. F. Canny, "Geometric problems in molecular biology and robotics.", in *ISMB*, 1994, pp. 322–330.
- [131] Lee, "Robot arm kinematics, dynamics, and control", *Computer*, vol. 15, no. 12, pp. 62–80, 1982.
- [132] J. Uicker J. J., "Dynamic Force Analysis of Spatial Linkages", *Journal of Applied Mechanics*, vol. 34, no. 2, pp. 418–424, 1967.
- [133] W. M. Silver, "On the equivalence of lagrangian and newton-euler dynamics for manipulators", *The International Journal of Robotics Research*, vol. 1, no. 2, pp. 60–70, 1982.
- [134] M. De Stefano, H. Mishra, R. Balachandran, R. Lampariello, C. Ott, and C. Secchi, "Multi-rate tracking control for a space robot on a controlled satellite: A passivity-based strategy", *IEEE Robotics and Automation Letters*, vol. 4, no. 2, pp. 1319–1326, 2019.
- [135] S. Echeandia and P. M. Wensing, "Numerical Methods to Compute the Coriolis Matrix and Christoffel Symbols for Rigid-Body Systems", *Journal of Computational and Nonlinear Dynamics*, vol. 16, no. 9, 2021.
- [136] G. Niemeyer and J.-J. E. Slotine, "Performance in adaptive manipulator control", *The International Journal of Robotics Research*, vol. 10, no. 2, 149–161, 1991.
- [137] F. Park, J. Bobrow, and S. Ploen, "A lie group formulation of robot dynamics", *The International Journal of Robotics Research*, vol. 14, no. 6, pp. 609–618, 1995.
- [138] G. J. Gbur, "Falling felines and fundamental physics", in *Falling Felines* and Fundamental Physics. Yale University Press, 2019, pp. 243–263.

[139] L. Poinsot, Théorie nouvelle de la rotation des corps, 143. Bachelier, 1851.

- [140] A. M. Giordano, G. Garofalo, M. D. Stefano, C. Ott, and A. Albu-Schäffer, "Dynamics and control of a free-floating space robot in presence of nonzero linear and angular momenta", in *IEEE 55th Conference on Decision and Control (CDC)*, 2016, pp. 7527–7534.
- [141] S. Nicosia and P. Tomei, "Robot control by using only joint position measurements", *IEEE Transactions on Automatic Control*, vol. 35, no. 9, pp. 1058–1061, 1990.
- [142] S. Ramasamy and R. L. Hatton, "The geometry of optimal gaits for drag-dominated kinematic systems", *IEEE Transactions on Robotics*, vol. 35, no. 4, pp. 1014–1033, 2019.
- [143] E. Shammas, K. Schmidt, and H. Choset, "Natural gait generation techniques for multi-bodied isolated mechanical systems", in *Proceedings of the 2005 IEEE International Conference on Robotics and Automation*, 2005, pp. 3664–3669.
- [144] A. De Luca and L. Ferrajoli, "A modified newton-euler method for dynamic computations in robot fault detection and control", in 2009 IEEE International Conference on Robotics and Automation, 2009, pp. 3359–3364.
- [145] J. Ostrowski, "Reduced equations for nonholonomic mechanical systems with dissipative forces", Reports on Mathematical Physics, vol. 42, no. 1, pp. 185 –209, 1998, Proceedings of the Pacific Institute of Mathematical Sciences Workshop on Nonholonomic Constraints in Dynamics.
- [146] D. Rollinson, A. Buchan, and H. Choset, "Virtual chassis for snake robots: Definition and applications", Advanced Robotics, vol. 26, no. 17, pp. 2043–2064, 2012.
- [147] J. E. Marsden and T. S. Ratiu, Introduction to Mechanics and Symmetry: A Basic Exposition of Classical Mechanical Systems. Springer Publishing Company, Incorporated, 2010.
- [148] O. Itani and E. Shammas, "Motion planning for a redundant planar snake robot", in 2020 IEEE/ASME International Conference on Advanced Intelligent Mechatronics (AIM), 2020, pp. 1483–1488.
- [149] H. Cendra, J. E. Marsden, and T. S. Ratiu, "Lagrangian reduction by stages", *Memoirs of the American Mathematical Society*, vol. 152, no. 722, pp. 1–108, 2001.
- [150] G. Nava, F. Romano, F. Nori, and D. Pucci, "Stability analysis and design of momentum-based controllers for humanoid robots", in 2016 IEEE/RSJ International Conference on Intelligent Robots and Systems (IROS), 2016, pp. 680–687.

[151] S. Fahmi, C. Mastalli, M. Focchi, and C. Semini, "Passive whole-body control for quadruped robots: Experimental validation over challenging terrain", *IEEE Robotics Autom. Lett.*, vol. 4, no. 3, pp. 2553–2560, 2019.

- [152] B. Henze, "Whole-body control for multi-contact balancing", in Whole-Body Control for Multi-Contact Balancing of Humanoid Robots: Design and Experiments. Cham: Springer International Publishing, 2022, pp. 65–128.
- [153] E. Kanso, J. E. Marsden, C. W. Rowley, and J. B. Melli-Huber, "Locomotion of articulated bodies in a perfect fluid", *Journal of Nonlinear Science*, vol. 15, pp. 255–289, 2005.
- [154] G. Antonelli, "Modelling of underwater robots", in *Underwater Robots*. Cham: Springer International Publishing, 2018, pp. 33–110.
- [155] J. de Gea Fernández, C. Ott, and B. Wehbe, "Machine learning and dynamic whole body control for underwater manipulation", in *AI Technology for Underwater Robots*, F. Kirchner, S. Straube, D. Kühn, and N. Hoyer, Eds. Cham: Springer International Publishing, 2020, pp. 107–115.
- [156] "Seakeeping theory", in *Handbook of Marine Craft Hydrodynamics and Motion Control*. John Wiley & Sons, Ltd, 2011, ch. 5, pp. 81–107.
- [157] N. Sinha, The Sacred Books of the Hindus, Vol. 11: Samkhya Philosophy (1915, Classic Reprint). Fb&c Limited, 2016.
- [158] D. de Klerk, D. J. Rixen, and S. N. Voormeeren, "General framework for dynamic substructuring: History, review and classification of techniques", *AIAA Journal*, vol. 46, no. 5, pp. 1169–1181, 2008.
- [159] T. ESA, Technology readiness levels handbook for space applications, issue 1, rev. 6, 2008.
- [160] J. Straub, "In search of technology readiness level (trl) 10", Aerospace Science and Technology, vol. 46, pp. 312–320, 2015.
- [161] H. Shimoji, M. Inoue, K. Tsuchiya, et al., "Simulation system for a space robot using 6 axis servos", IFAC Proceedings Volumes: IFAC Symposium on Automatic Control in Aerospace, vol. 22, no. 7, pp. 115–120, 1989.
- [162] S. K. Agrawal, G. Hirzinger, K. Landzettel, and R. Schwertassek, "A new laboratory simulator for study of motion of free-floating robots relative to space targets", *IEEE Transactions on Robotics and Automation*, vol. 12, no. 4, pp. 627–633, 1996.
- [163] J. Piedboeuf, F. Aghili, M. Doyon, and E. Martin, "Dynamic emulation of space robot in one-g environment using hardware-in-the-loop simulation", in *Romansy 14: Theory and Practice of Robots and Manipulators (CISM-IFTOMM Symposium)*, 2002, pp. 213–229.

[164] S. Dubowsky, W. Durfee, T. Corrigan, A. Kuklinski, and U. Muller, "A laboratory test bed for space robotics: The VES II", in *IEEE/RSJ International Conference on Intelligent Robots and Systems (IROS)*, vol. 3, 1994, 1562–1569 vol.3.

- [165] R. Takahashi, H. Ise, A. Konno, M. Uchiyama, and D. Sato, "Hybrid simulation of a dual-arm space robot colliding with a floating object", *IEEE International Conference on Robotics and Automation (ICRA)*, pp. 1201–1206, 2008.
- [166] C. Carignan, N. Scott, and S. Roderick, "Hardware-in-the-loop simulation of satellite capture on a ground-based robotic testbed", *International Symposium on Artificial Intelligence, Robotics and Automation in Space* (i-SAIRAS), 2014.
- [167] D. E. Chang and J. E. Marsden, "Reduction of controlled lagrangian and hamiltonian systems with symmetry", SIAM Journal of Control and Optimization, vol. 43, no. 1, 277–300, 2004.
- [168] A. Ruiz, M. Diaz-Carrasco, J. Viñals, I. Prieto, A. Rozas, and S. García, "Oru-boas: Developing reusable building blocks for satellite modularisation", in 74th International Astronautical Congress, 2023.
- [169] C. Space, "E.deorbit implementation plan", European Space Research and Technology Centre, ESA unclassified Releasable to the Public 1.0, 2015.
- [170] A. Beyer, G. Grunwald, M. Heumos, M. Schedl, R. Bayer, W. Bertleff, B. Brunner, R. Burger, J. Butterfaß, R. Gruber, et al., "Caesar: Space robotics technology for assembly, maintenance, and repair", in Proceedings of the International Astronautical Congress, IAC, 2018.
- [171] T. Boge, T. Wimmer, O. Ma, and T. Tzschichholz, "Epos-using robotics for rvd simulation of on-orbit servicing missions", in AIAA Modeling and Simulation Technologies Conference, 2010, p. 7788.
- [172] V. Dubancheta, J. A. B. Romerob, I. S. Paraskevasc, P. L. Negroa, A. Cuffoloa, F. Mayea, A. R. Reinab, P. R. Manriqueb, M. Alonsob, and S. Torralbo, "Eross project—ground validation of an autonomous gnc architecture towards future european servicing missions", 2021.
- [173] M. De Stefano, R. Vijayan, A. Stemmer, and C. Ott, "A gravity compensation strategy for on-ground validation of orbital manipulators", in *IEEE International Conference on Robotics and Automation*, 2023.
- [174] R. Chhabra and M. R. Emami, "A generalized exponential formula for forward and differential kinematics of open-chain multi-body systems", *Mechanism and Machine Theory*, vol. 73, pp. 61–75, 2014.
- [175] D. E. Chang, "Controlled lagrangian and hamiltonian systems", Ph.D. dissertation, California Institute of Technology, 2002.

[176] N. Hogan, "Impedance Control: An Approach to Manipulation: Part II— Implementation", Journal of Dynamic Systems, Measurement, and Control, vol. 107, no. 1, pp. 8–16, 1985.

- [177] M. Maier, M. Chalon, M. Pfanne, R. Bayer, et al., "TINA: Small torque controlled robotic arm for exploration and small satellites", in *International Astronautical Congress (IAC)*, 2019.
- [178] G. Jha, *The Nyaya-Sutras Of Gautama (4 Vols.)* Motilal Banarsidass Publishers Pvt. Limited, 1999.
- [179] P. Colmenarejo, D. Henry, G. Visentin, and F. Ankersen et al., "Methods and outcomes of the COMRADE project Design of robust coupled control for robotic spacecraft in servicing missions", in *International Astronautical Congress*, Germany, 2018.
- [180] J. Telaar, I. Ahrns, S. Estable, W. Rackl, and M. De Stefano et al., "GNC architecture for the e.Deorbit mission", in 7th European Conference for Aeronautics and Space Sciences (EUCASS), 2017.
- [181] G. Heredia, R. Cano, A. Jimenez-Cano, and A. Ollero, "Modeling and design of multirotors with multi-joint arms", in *Aerial Robotic Manipulation: Research, Development and Applications*, A. Ollero and B. Siciliano, Eds. Cham: Springer International Publishing, 2019, pp. 15–33.
- [182] J. Lee, R. R. Balachandran, K. Kondak, A. Coelho, M. D. Stefano, M. Humt, J. Feng, T. Asfour, and R. Triebel, "Virtual reality via object pose estimation and active learning: Realizing telepresence robots with aerial manipulation capabilities", *Field Robotics*, vol. 3, pp. 323–367, 2023.
- [183] E. Kelasidi, P. Liljeback, K. Y. Pettersen, and J. T. Gravdahl, "Innovation in underwater robots: Biologically inspired swimming snake robots", *IEEE Robotics & Automation Magazine*, vol. 23, no. 1, pp. 44–62, 2016.
- [184] K. Nanos and E. G. Papadopoulos, "On the dynamics and control of free-floating space manipulator systems in the presence of angular momentum", Frontiers in Robotics and AI, vol. 4, p. 26, 2017.
- [185] M. Bloesch, M. Hutter, M. A. Hoepflinger, and S. Leutenegger et al., "State estimation for legged robots-consistent fusion of leg kinematics and IMU", *Robotics*, vol. 17, pp. 17–24, 2013.
- [186] S. Kuindersma, R. Deits, M. Fallon, et al., "Optimization-based locomotion planning, estimation, and control design for the atlas humanoid robot", Autonomous robots, vol. 40, no. 3, pp. 429–455, 2016.
- [187] D. Rollinson, A. Buchan, and H. Choset, "State estimation for snake robots", in *IEEE/RSJ International Conference on Intelligent Robots and Systems*, 2011, pp. 1075–1080.

[188] D. Maithripala, J. Berg, and W. Dayawansa, "Almost-global tracking of simple mechanical systems on a general class of lie groups", *IEEE Transactions on Automatic Control*, vol. 51, no. 2, pp. 216–225, 2006.

- [189] R. Ortega, A. Loria, R. Kelly, and L. Praly, "On passivity-based output feedback global stabilization of euler-lagrange systems", *International Journal of Robust and Nonlinear Control*, vol. 5, no. 4, pp. 313–323, 1995.
- [190] N. Aghannan and P. Rouchon, "An intrinsic observer for a class of lagrangian systems", *IEEE Transactions on Automatic Control*, vol. 48, no. 6, pp. 936–945, 2003.
- [191] P. Corke and M. Good, "Dynamic effects in visual closed-loop systems", *IEEE Transactions on Robotics and Automation*, vol. 12, no. 5, pp. 671–683, 1996.
- [192] K. Dupree, N. R. Gans, W. MacKunis, and W. E. Dixon, "Euclidean calculation of feature points of a rotating satellite: A daisy-chaining approach", *Journal of guidance, control, and dynamics*, vol. 31, no. 4, pp. 954–961, 2008.
- [193] G. Fink and C. Semini, "Proprioceptive sensor fusion for quadruped robot state estimation", in 2020 IEEE/RSJ International Conference on Intelligent Robots and Systems (IROS), 2020, pp. 10914–10920.
- [194] N. Mansard, A. Remazeilles, and F. Chaumette, "Continuity of Varying-Feature-Set Control Laws", *IEEE Transactions on Automatic Control*, vol. 54, no. 11, pp. 2493–2505, 2009.
- [195] R. Bajcsy, Y. Aloimonos, and J. K. Tsotsos, "Revisiting active perception", *Autonomous Robots*, vol. 42, no. 2, pp. 177–196, 2018.
- [196] A. Dietrich, C. Ott, and A. Albu-Schäffer, "Multi-objective compliance control of redundant manipulators: Hierarchy, control, and stability", in 2013 IEEE/RSJ International Conference on Intelligent Robots and Systems, 2013, pp. 3043–3050.
- [197] B. Francis and W. Wonham, "The internal model principle of control theory", *Automatica*, vol. 12, no. 5, pp. 457–465, 1976.
- [198] R. C. CONANT and W. R. ASHBY, "Every good regulator of a system must be a model of that system", *International Journal of Systems Science*, vol. 1, no. 2, pp. 89–97, 1970.
- [199] M. Desmurget and S. Grafton, "Forward modeling allows feedback control for fast reaching movements", *Trends in cognitive sciences*, vol. 4, no. 11, pp. 423–431, 2000.
- [200] M. Sagardia, "Virtual manipulations with force feedback in complex interaction scenarios", Ph.D. dissertation, Technische Universität München, 2019.

[201] G. Hirzinger, K. Landzettel, and et al, "Dlr's robotics technologies for on-orbit servicing", *Advanced Robotics*, vol. 18, no. 2, pp. 139–174, 2004.

- [202] M. Rothammer, A. Coelho, H. **Mishra**, C. Ott, A. Franchi, and A. Albu-Schaeffer, "A rigid body observer (BObs) considering pfaffian constraints with a pose regulation framework", *IEEE Control Systems Letters*, vol. 7, pp. 163–168, 2023.
- [203] G. F. Giudice, A Zeptospace Odyssey: A Journey into the Physics of the LHC. Oxford University Press, USA, 2010.
- [204] N. Hogan, "Impedance control: An approach to manipulation", in *American Control Conference (ACC)*, 1984, pp. 304–313.
- [205] C.-A. Cheng et al., "RMPflow: A geometric framework for generation of multitask motion policies", *IEEE Transactions on Automation Science and Engineering*, vol. 18, no. 3, pp. 968–987, 2021.
- [206] A. Dietrich, A. Albu-Schäffer, and G. Hirzinger, "On continuous null space projections for torque-based, hierarchical, multi-objective manipulation", in *IEEE International Conference on Robotics and Automation (ICRA)*, 2012, pp. 2978–2985.
- [207] C. Ott, A. Kugi, and Y. Nakamura, "Resolving the problem of non-integrability of nullspace velocities for compliance control of redundant manipulators by using semi-definite lyapunov functions", in *IEEE International Conference on Robotics and Automation (ICRA)*, 2008, pp. 1999–2004.
- [208] A. Dietrich, X. Wu, K. Bussmann, C. Ott, A. Albu-Schäffer, and S. Stramigioli, "Passive hierarchical impedance control via energy tanks", *IEEE Robotics and Automation Letters*, vol. 2, no. 2, pp. 522–529, 2016.
- [209] A. Dietrich and C. Ott, "Hierarchical impedance-based tracking control of kinematically redundant robots", *IEEE Transactions on Robotics*, vol. 36, no. 1, pp. 204–221, 2020.
- [210] J. Lachner, F. Allmendinger, S. Stramigioli, and N. Hogan, "Shaping impedances to comply with constrained task dynamics", *IEEE Transactions on Robotics*, vol. 38, no. 5, pp. 2750–2767, 2022.
- [211] S. Stramigioli and H. Bruyninckx, "Geometry and Screw Theory for Robotics", Tutorial from IEEE International Conference on Robotics and Automation (ICRA), Seoul, 2001.
- [212] F. Bullo and A. D. Lewis, "Reduction, linearization, and stability of relative equilibria for mechanical systems on riemannian manifolds", *Acta Applicandae Mathematicae*, vol. 99, no. 1, pp. 53–95, 2007.

[213] V. Kallem, D. E. Chang, and N. J. Cowan, "Task-induced symmetry and reduction in kinematic systems with application to needle steering", in 2007 IEEE/RSJ International Conference on Intelligent Robots and Systems, 2007, pp. 3302–3308.

- [214] G Sardanashvily, "Fibre bundles, jet manifolds and lagrangian theory. lectures for theoreticians", arXiv preprint arXiv:0908.1886, 2009.
- [215] J. Park, W. Chung, and Y. Youm, "On dynamical decoupling of kinematically redundant manipulators", in *IEEE/RSJ International Conference on Intelligent Robots and Systems (IROS)*, vol. 3, 1999, 1495–1500 vol.3.
- [216] M. Schneider, "Closed magnetic geodesics on closed hyperbolic Riemann surfaces", *Proceedings of the London Mathematical Society*, vol. 105, no. 2, pp. 424–446, 2012.
- [217] A. Albu-Schäffer and C. Della Santina, "A review on nonlinear modes in conservative mechanical systems", *Annual Reviews in Control*, vol. 50, pp. 49–71, 2020.
- [218] C. D. Santina, D. Lakatos, A. Bicchi, and A. Albu-Schaeffer, "Exciting nonlinear modes of conservative mechanical systems by operating a master variable decoupling", in 2021 60th IEEE Conference on Decision and Control (CDC), 2021, pp. 2448–2455.
- [219] S. Storchak, "Wong's equations in yang-mills theory", Central European Journal of Physics, vol. 12, no. 4, pp. 233–244, 2014.
- [220] J P. La Salle, "An invariance principle in the theory of stability.", 1967.
- [221] F. Gay-Balmaz and C. Tronci, "Reduction theory for symmetry breaking with applications to nematic systems", *Physica D: Nonlinear Phenomena*, vol. 239, no. 20-22, pp. 1929–1947, 2010.
- [222] H. Weyl, *Symmetry*, ser. Princeton Science Library. Princeton University Press, 1952.
- [223] J. Park, W.-K. Chung, and Y. Youm, "Specification and control of motion for kinematically redundant manipulators", in *IEEE/RSJ International Conference on Intelligent Robots and Systems (IROS)*, vol. 3, 1995, 89–94 vol.3.
- [224] A. Albu-Schaffer, C. Ott, U. Frese, and G. Hirzinger, "Cartesian impedance control of redundant robots: Recent results with the dlr-light-weight-arms", in *IEEE International Conference on Robotics and Automation (ICRA)*, vol. 3, 2003, 3704–3709 vol.3.
- [225] G. Garofalo, C. Ott, and A. Albu-Schäffer, "Orbital stabilization of mechanical systems through semidefinite lyapunov functions", in 2013 American Control Conference, 2013, pp. 5715–5721.

[226] M. V. Berry and P. Shukla, "Hamiltonian curl forces", *Proceedings of the Royal Society A: Mathematical, Physical and Engineering Sciences*, vol. 471, no. 2176, p. 20150002, 2015.

- [227] M. V. Berry and P. Shukla, "Curl force dynamics: Symmetries, chaos and constants of motion", New Journal of Physics, vol. 18, no. 6, p. 063 018, 2016.
- [228] S. Stramigioli, "The principal bundle structure of continuum mechanics", Journal of Geometry and Physics, vol. 200, p. 105 172, 2024.
- [229] B. Paden and R. Panja, "Global asymptotically stable pd+ controller for robot manipulator", vol. 47, pp. 1697–1712, 1988.
- [230] K. Albee, C. Specht, H. **Mishra**, C. Oestreich, B. Brunner, R. Lampariello, and R. Linares, "Autonomous rendezvous with an uncertain, uncooperative tumbling target: The tumbledock flight experiments", in 16th Symposium on Advanced Space Technologies in Robotics and Automation (ASTRA 2022), 2022.
- [231] H. **Mishra**, "Designing robust pose estimator for non-cooperative space targets for visual servoing during approach maneuvers", M.S. thesis, Technical University of Munich, 2016.
- [232] V. Muralidharan, M. R. Makhdoomi, A. Žinys, B. Razgus, M. Klimavičius, M. Olivares-Mendez, and C. Martinez, "On-ground validation of orbital gnc: Visual navigation assessment in robotic testbed facility", *Astrodynamics*, pp. 1–25, 2024.
- [233] P. Colmenarejo, F. Gandía, A. G. Casas, A. Tomassini, et al., "GNCDE: An integrated GNC Development Environment", Guidance, Navigation and Control Systems, vol. 606, p. 29, 2006.
- [234] E. Rohmer, S. P. N. Singh, and M. Freese, "Coppeliasim (formerly v-rep): A versatile and scalable robot simulation framework", in *Proc. of The International Conference on Intelligent Robots and Systems (IROS)*, 2013.
- [235] M. J. Schuster, C. Brand, S. G. Brunner, P. Lehner, et al., "The LRU rover for autonomous planetary exploration and its success in the Space-BotCamp challenge", in 2016 International Conference on Autonomous Robot Systems and Competitions (ICARSC), 2016, pp. 7–14.
- [236] R. Spica, G. Claudio, F. Spindler, and P. Robuffo Giordano, Interfacing Matlab/Simulink with V-REP for an Easy Development of Sensor-Based Control Algorithms for Robotic Platforms, 2014 IEEE International Conference on Robotics and Automation (ICRA) Workshop on MAT-LAB/Simulink for Robotics Education and Research, Hong Kong, China, 2014.

[237] T. Erez, Y. Tassa, and E. Todorov, "Simulation tools for model-based robotics: Comparison of bullet, havok, mujoco, ode and physx", in 2015 IEEE international conference on robotics and automation (ICRA), IEEE, 2015, pp. 4397–4404.

- [238] J. Galante, J. Van Eepoel, C. D'Souza, and B. Patrick, "Fast Kalman filtering for relative spacecraft position and attitude estimation for the RAVEN ISS hosted payload", 39th AAS Guidance and Control Conference, 2016.
- [239] F. Gandía, A. Paoletti, A. Tomassini, et al., "GNCDE: Exploiting the capabilities of development environments for GNC design", 4th International Conference On Spacecraft Formation Flying Mission & Technologies (SFFMT), 2011.
- [240] F. Aghili and M. Namvar, "Scaling inertia properties of a manipulator payload for 0-g emulation of spacecraft.", *I. J. Robotic Res.*, vol. 28, no. 7, pp. 883–894, 2009.
- [241] M. A. Roa et al., "Robotic technologies for in-space assembly operations", in Symposium on Advanced Space Technologies in Robotics and Automation (ASTRA), 2017.
- [242] D. Lee and P. Y. Li, "Passive Decomposition Approach to Formation and Maneuver Control of Multiple Rigid Bodies", *Journal of Dynamic Systems Measurement and Control-transactions of The Asme*, vol. 129, pp. 662–677, 2007.
- [243] D. Lee and P. Y. Li, "Passive Decomposition of Mechanical Systems with Coordination Requirement", *IEEE Transactions on Automatic Control*, vol. 58, no. 1, pp. 230–235, 2012.
- [244] W. Kim, M. Lorenzini, P. Balatti, P. D. Nguyen, U. Pattacini, V. Tikhanoff, L. Peternel, C. Fantacci, L. Natale, G. Metta, and A. Ajoudani, "Adaptable workstations for human-robot collaboration: A reconfigurable framework for improving worker ergonomics and productivity", *IEEE Robotics & Automation Magazine*, vol. 26, no. 3, pp. 14–26, 2019.
- [245] E. Papadopoulos and S. Dubowsky, "Coordinated manipulator/spacecraft motion control for space robotic systems", in *IEEE International Conference on Robotics and Automation (ICRA)*, 1991, 1696–1701 vol.2.
- [246] J. R. Spofford and D. L. Akin, "Redundancy control of a free-flying teler-obot", *Journal of Guidance, Control, and Dynamics*, vol. 13, no. 3, pp. 515–523, 1990.
- [247] J. Artigas *et al.*, "Teleoperation for on-orbit servicing missions through the ASTRA geostationary satellite", in *IEEE Aerospace Conference (AE-ROCONF)*, 2016, pp. 1–12.

[248] Y. S. Sarkisov, M. J. Kim, D. Bicego, D. Tsetserukou, C. Ott, A. Franchi, and K. Kondak, "Development of sam: Cable-suspended aerial manipulator", in 2019 International Conference on Robotics and Automation (ICRA), IEEE, 2019, pp. 5323–5329.

- [249] Y. Yokokohji and T. Yoshikawa, "Bilateral control of master-slave manipulators for ideal kinesthetic coupling-formulation and experiment", *IEEE Transactions on Robotics and Automation*, vol. 10, no. 5, pp. 605–620, 1994.
- [250] P. F. Hokayem and M. W. Spong, "Bilateral teleoperation: An historical survey", *Automatica*, vol. 42, no. 12, pp. 2035–2057, 2006.
- [251] D. Lawrence, "Stability and transparency in bilateral teleoperation", *IEEE Transactions on Robotics and Automation*, vol. 9, no. 5, pp. 624–637, 1993.
- [252] T. Inagaki et al., "Adaptive automation: Sharing and trading of control", Handbook of cognitive task design, vol. 8, pp. 147–169, 2003.
- [253] C. Taesi, F. Aggogeri, and N. Pellegrini, "Cobot applications—recent advances and challenges", *Robotics*, vol. 12, no. 3, p. 79, 2023.
- [254] A. Albu-Schaffer and G. Hirzinger, "Cartesian impedance control techniques for torque controlled light-weight robots", in *Proceedings IEEE International Conference on Robotics and Automation (Cat. No.02CH37292)*, vol. 1, 2002, 657–663 vol.1.
- [255] F. Basana, Z. Pavanello, F. Branz, A. Francesconi, G. Borelli, D. Invernizzi, M. Massari, M. Lovera, A. Nocerino, R. Opromolla, et al., "Satellite and robotic arm combined control for spacecraft close-proximity operations", CEAS Space Journal, pp. 1–27, 2024.
- [256] S. A. Chien, G. Visentin, and C. Basich, "Exploring beyond earth using space robotics", *Science Robotics*, vol. 9, no. 91, eadi6424, 2024.
- [257] M. C. Rai, M. H. Nair, D. Schaefer, R. Detry, M. Poozhiyil, J. Rybicka, S. Dulanty, J. Gotz, M. A. Roa, R. Lampariello, et al., "Robotic upcycling and recycling: Unraveling the era of sustainable in-space manufacturing", CEAS Space Journal, pp. 1–15, 2024.
- [258] B. Ma, Z. Jiang, Y. Liu, and Z. Xie, "Advances in space robots for on-orbit servicing: A comprehensive review", *Advanced Intelligent Systems*, vol. 5, no. 8, p. 2 200 397, 2023.
- [259] E. Papadopoulos, F. Aghili, O. Ma, and R. Lampariello, "Robotic manipulation and capture in space: A survey", *Frontiers in Robotics and AI*, vol. 8, p. 686723, 2021.
- [260] W. Zhang, F. Li, J. Li, and Q. Cheng, "Review of on-orbit robotic arm active debris capture removal methods", *Aerospace*, vol. 10, no. 1, p. 13, 2022.

[261] P. S. marquis de Laplace, Essai philosophique sur les probabilités. Bachelier, 1825.

- [262] J. Kim, "Lie group formulation of articulated rigid body dynamics", Technical report, Carnegie Mellon University, Tech. Rep., 2012.
- [263] M. D. Semon and J. R. Taylor, "Thoughts on the magnetic vector potential", *American Journal of Physics*, vol. 64, no. 11, pp. 1361–1369, 1996.